Co-pyrolysis of Coal and Biomass Blends

A Thesis

Submitted in Partial Fulfilment of the Requirements

for the Degree of

DOCTOR OF PHILOSOPHY

Munmi Bhattacharyya

(156151012)

School of Energy Science and Engineering

Indian Institute of Technology Guwahati

Guwahati – 781039, Assam

January 2024

This Thesis is dedicated to my parents who have constantly guided and inspired me throughout my life

DECLARATION

I do hereby declare that the content embodied in this thesis entitled ***"Co-pyrolysis of coal and biomass blends"*** is the result of investigations carried out by myself, else stated, under the guidance of Prof. Pinakeswar Mahanta and Prof. Kaustubha Mohanty.

In keeping with the general practice of reporting scientific observations, due acknowledgments have been made wherever the work described is based on the findings of other investigators.

Any part of this work has not been submitted for the award of degree, diploma, fellowship, associate-fellowship or its equivalent to any university or institution.

Date: May 2023

Munmi Bhattacharyya
(Roll No: 156151012)
School of Energy Science and Engineering
Indian Institute of Technology Guwahati
Assam, India

CERTIFICATE

It is certified that the work contained in the thesis titled ***"Co-pyrolysis of coal and biomass blends"*** submitted by Miss Munmi Bhattacharyya to Indian Institute of Technology Guwahati for the award of degree of Doctor of Philosophy has been carried out under my supervision in the School of Energy Science and Engineering, Indian Institute of Technology Guwahati. This work has not been submitted elsewhere for the award of any other degree or diploma.

Date:

Prof. Pinakeswar Mahanta
Professor, Department of Mechanical Engineering
Indian Institute of Technology Guwahati
Guwahati-781039, Assam, India

CERTIFICATE

It is certified that the work contained in the thesis titled ***"Co-pyrolysis of coal and biomass blends"*** submitted by Miss Munmi Bhattacharyya to Indian Institute of Technology Guwahati for the award of degree of Doctor of Philosophy has been carried out under my supervision in the School of Energy Science and Engineering, Indian Institute of Technology Guwahati. This work has not been submitted elsewhere for the award of any other degree or diploma.

Date:

Prof. Kaustubha Mohanty
Professor & Head, Department of Chemical Engineering
& Adjunct Professor, School of Energy Science and Engineering
Indian Institute of Technology Guwahati
Guwahati-781039, Assam, India

Acknowledgement

It gives me immense delight to express my heartfelt gratitude to them, whose unconditional guidance and support has culminated in making this thesis possible. At the outset, I would like to thank the Almighty for showering his blessings on me for sustaining myself during my academic and research tenure at Indian Institute of Technology Guwahati.

I would like to express my sincere gratitude to my supervisors, Prof. Pinakeswar Mahanta and Prof. Kaustubha Mohanty, for their professional supervision, encouragement, and continuous support. Their cordial suggestions, constructive feedback, recommendations, and insightful remarks at every stage of my research work has helped me in completion of the thesis. Without their keen interest and the myriad of knowledge they provided me in the project work, I would not have been able to put my best foot forward in this domain of expertise. I would also to thank my doctoral committee members: Prof. G. Pugazhenthi, Prof. Vinayak Kulkarni and Dr. Pankaj Kalita, for their constant guidance and support. Their willingness to share their colossal knowledge in pyrolysis kinetics and reaction engineering has made me understand the project vividly and its manifestations in great depths.

I would also like to thank the Head of the School of Energy Science and Engineering, Prof. V. V. Goud for his constant motivation in carrying out the work. I would also like to thank other faculty members of the School for their valuable help, particularly Prof. V. S. Moholkar for providing the reactor facility for carrying out the pyrolysis experiments. I would also bestow my sincere gratitude to the faculty members of School of Energy Science and Engineering: Dr. Farrukh Khalid, Dr. Ranjith Thangavel, Dr. E S N Raju P for their constant motivation and encouragement. I am also highly grateful to one of my seniors, Dr. Krushna Prasad Shadangi for his timely technical guidance and suggestions in carrying out the project work, to whom I am indebted for all the positive discussions on the project.

I owe my sincere thanks to the School of Energy Science and Engineering, Department of Chemical Engineering, Department of Mechanical Engineering, Centre for Environment, Central Workshop, Central Instruments Facility of IIT Guwahati and Guwahati Biotech Park for providing the required analytical facilities for my research. I am grateful to the staff members: Dr. Lepakshi Barbora, Mr. Dhiren Huzuri, Mr. Debarshi Baruah and Mr. Harsaraj Biswanath, for their constant cooperation and encouragement in completion of the project work. I would like to gratefully acknowledge Ministry of Human Resource Development (MHRD) for providing fellowship.

I would like to thank all my fellow lab-mates Dr. Velentina, Dr. Bikash, Dr. Sounak, Dr. Sachankar, Dr. Dhananjay, Dr. Hirakh, Dr. Deep, Santosh, Anindita and Deepesh for all the enriching and valuable discussions we had to work together in completion of the experiments. I would also like to deeply thank my lab-mates of Energy Efficiency Lab: Dr. Philip, Dr. Barasa, Rishiraj, Nayan, Phenicia, Umesh, Pranab, Pushpita, Jyotishman, Aradhana and Ramanuj who has provided unleashed motivation, encouragement, and a positive companionship. I would also like to deeply thank my friends at the Institute premises Dr. Needhi, Dr. Nilakshi, Dr. Bandana, Dr. Viswanth, Dr. Joy, Jaishree, Juhi, Aparupa, Neepu, Sureandar and Tanuj for their constant support and motivation during my tenure.

Last, but not the least I owe my sincere gratitude to my parents, Dr. Hirendra Kumar Bhattacharyya, Dr. Dipti Devi and my late grandmother, Niru Bhattacharyya for being a constant support system and being the guiding light during my tenure. I would also like to thank my late brother, Uttkarsh Bhattacharyya for his innumerable blessings who has always been a source of inspiration throughout my life and instilled in me the motto to never stop chasing my dreams.

Munmi Bhattacharyya

May 2023

CONTENTS

List of Figures

List of Tables

Nomenclature

TGA	Thermogravimetric analyzer
DTG	Derivative Thermogravimetric analysis
FTIR	Fourier Transform Infrared Spectroscopy
EDX	Energy Dispersive X-ray Spectroscopy
XRD	X-ray Diffraction technique
FESEM	Field Emission Scanning Electron Microscopy
FETEM	Field Emission Transmission Electron Microscopy
HRTEM	High-Resolution Transmission Electron Microscopy
SAED	Selected Area Electron Diffraction Technique
FFT	First Fourier Transform
AFM	Atomic Force Microscopy
BET-N_2	Brunnaeur-Emmett-Teller Nitrogen Adsorption analysis
XPS	X-ray photoelectron spectroscopy
ESR	Electron Spin Resonance Spectroscopy
T_{in} or T_1	Initial devolatilization temperature (K)
T_{peak}	Maximum degradation temperature (K)
T_{offset} or T_2	Temperature at which active pyrolytic zone ends (K)
R_d	Rate of decomposition
R_i	Instantaneous reactivity
ρ	Intrinsic reaction rate
D_i	Devolatilization index (10^{-8} mg min^{-1} K^{-3})
CPI	Comprehensive pyrolysis index (10^{-6} % min^{-1} K^{-2})
AAEM	Alkali and alkaline earth metal
PAH	Polyaromatic hydrocarbon
VPR	Vapour residence time
M	Moisture content (%)
VM	Volatile matter content (%)
A	Ash content (%)
FC	Fixed carbon content (%)

HHV	High heating value (MJ/ kg)
LHV	Low heating value (MJ/kg)
KAS	Kissinger-Akahira-Sunose method
E	Activation energy (kJ mol^{-1})
A	Pre-exponential factor (s^{-1})
k	Rate constant (s^{-1})
ΔH	Enthalpy (kJ mol^{-1})
ΔG	Gibbs free energy (kJ mol^{-1})
ΔS	Entropy (kJ mol^{-1}. K^{-1})
GC/MS	Gas chromatography mass spectrometry

Greek Symbols

f(α)	Differential form of reaction model
β	Heating rate, K min^{-1}
g(α)	Integral form of reaction model
α	Conversion
β	Heating rate (K min^{-1})
R	Gas constant (8.314×10^{3} kJ mol^{-1}. K^{-1})
n	Reaction order
h	Plank's constant, 6.626×10^{-34} J s^{-1}
k_B	Boltzmann's constant, 1.381×10^{-23} J K^{-1}

Subscripts

onset	Initial devolatilization temperature (K)
offset	Final devolatilization temperature (K)
max	Maximum peak temperature (K)

Abstract

Coal and sawdust are viable feedstock substitutes for fuel production. It generates liquid oil, char residue, and fuel gas as the crucial elements of pyrolytic products during the co-pyrolysis process. The blending of biomass with coal helped to decrease the thermal stability of coal. However, the lower thermal stability, lesser viscosity, high oxygen content, high water content and lower calorific value of liquid fuel renders it economically precarious. In addition, fuel gas and char residue also hold as a salient yardstick to this technology since its applications are multifarious. To incessantly mark this challenge, the present study aims to develop a sustainable process that implements functional composite nano-catalysts synthesized by incipient wetness impregnation technique. In the present study, the blended feeds at 10 %, 30 %, 50 %, 70 %, 90 %, 100 % and 200 % were visualized for their degradation potential, and their poitive and negative chemical synergistic effects were estimated from 303-1173 K temperature at various heating rates 10-40 K min^{-1} under nitrogen as purge gas (20 mL min^{-1}) in a thermogravimetric analyzer. The blends with the highest reactivity were studied for their devolatilization kinetics via the Kissinger-Akahira-Sunose method and thermodynamics along with their prediction of theoretical reaction mechanistic pathways. The synthesized catalysts, 10% and 20% NiO and Ni (II) aluminate composite nano-catalysts showed a significant observation in their purity of elements, purity of phases, crystallinity, higher thermal stability, lesser particle sizes, and porosity. The highest degradability and conversion % in the active pyrolytic zone of catalytic pyrolysis of sawdust and catalytic co-pyrolysis of blends ensued the selected (catalyst/sawdust) and (catalyst/blend) ratio for further pyrolytic experiments. The pyrolytic experiments were conducted in a fixed-bed reactor with nitrogen as the purge gas (18 L h^{-1}) at 30 K min^{-1} heating rate from 773–873 K temperature at 1 bar pressure. Due to a larger number of surface-active sites and enhanced oxygen-carrying capacity, the conversion % increased substantially in sawdust pyrolysis with a 20 % Ni loading catalyst. This is mainly accountable to the increased pyrolytic syngas yield with increased H_2 content due to reverse water-gas shift reaction. Aromatic content increased for bio-oil with 20 % Ni loading catalyst due to the catalytic cracking at higher temperatures. The catalyst decreases the oxygen and nitrogen content in bio-oil, thus increasing its fuel quality. Biochar revealed amorphous graphitic multilayer nanosheets with a hexagonal crystal system and a porous carbon structure. However, for thermal pyrolysis of coal, coal char yield % decreased with an increase in temperature from 773–873 K with negligible liquid oil generated as a product. In thermal co-

pyrolysis of coal and 100 % sawdust blend, with an increase in temperature from 773–873 K, liquid oil yield increased while biochar yield decreased significantly. However, char residue similarly revealed amorphous graphitic multilayer nanosheets with a hexagonal crystal system. At a coal-sawdust blending of 50 %, 100 % and 200 %, the conversion, wt. % increased from 27.97 % and 37.35 % to a significant rise of 92.8 % respectively. This was due to the synergistic interactions of alkali and alkaline earth metals (AAEM) in the feeds which have an autocatalytic effect on the long-chain aromatic hydrocarbons of coal. With the integration of catalyst to the blends, higher conversion, wt. % was observed significantly with a higher gas yield with a higher metal loading %. Aromatics content increased in the liquid oil for co-pyrolysis of blend with 20 % Ni loaded catalyst, enhancing its fuel quality. This proves that 10 % and 20 % NiO and Ni (II) aluminate composite nano-catalysts are effective functional materials for the catalytic upgradation of pyrolytic products.

Keywords: Coal, Sawdust, Composite catalysts, Co-pyrolysis, Liquid oil, Hydrogen, Char residue

CHAPTER I

INTRODUCTION

1.1 Motivation

Energy serves as a significant yardstick in the economic growth and development of a nation. The energy supply-demand chain for all countries is facing immediate attention in various sectors such as agriculture, transport, industry, commercial, and domestic. Instead of mitigation of global anthropogenic greenhouse gas emissions, ozone layer depletion, and market oil shocks in the early 1970s, there is a pressing need to pacify the ardent environmental pollution for future resource utilization *(Morgan and Kandiyoti, 2014)*. Coal is composed of an organic macromolecular skeletal matrix structure embedded with mineral matter along with low-weight molecular compounds. The burning of coal produces heat energy with a bond dissociation energy of 1000 kJ mol^{-1} to produce unfaltering free radicals and hydrogen molecules *(Reddy and Vinu, 2018; Jayanti et al., 2012).* It sustains a high calorific value index. Hence, it is being used as a substantial source to produce heat and power *(Mallick et al., 2018).* Its demand is about ~29% of the underlying requisite for global energy and substantiates ~39% of global electricity concerns *(Mallick et al., 2018).* The global coal capacity sustained between 2000 and 2018 has nearly doubled from 1,066 GW to 2,024 GW. In India, the coal production capacity is expected to reach up to 238 GW by *2027 (Evans and Pierce, 2020).* Indian coal is higher in ash content, and sulfur content, and low in thermal efficiency. Hence, the possibility of formation of less energy is also evident *(Sharma et al., 2014).* However, the production and utilization of such fossil-based resources and waste disposal of its products pollute the environment *(Morgan and Kandiyoti, 2014)*. To add on, fossil fuel resources are on the verge of depletion in the 21st century, since their inception during the industrialization age for energy generation, electricity requirements, and steel and cement production *(Morgan and Kandiyoti, 2014)*. Thus, there is an urgent need to provide constant fuel supplies and energy security to the upscaling world economic growth for reinforcing key supply chain management goals and better living standards. At the utmost need of the hour, this necessitated the utilization of renewable substitutes to sustain the fuels and electricity demand and in turn, pacify the global pollution index for a circular economy.

Lignocellulosic biomass is CO_2 neutral, and consists of high volatile matter, moisture, and H content. The occurrence of cellulose, hemicellulose, and lignin results in pyrolytic vapor, once it gets pyrolyzed with bond dissociation energy of 380-420 kJ mol^{-1} *(Reddy and Vinu, 2018)*. The pyrolysis of cellulose and hemicellulose leads to the formation of abundant free radicals, hydrogen forming light aliphatic radicals along with some furan compounds. However, lignin generates oxygenated compounds in the form of tar such as guaiacol, syringol, methyl guaiacol, vinyl guaiacol, vanillin, and vanillic acid *(Reddy and Vinu, 2018).*

The yield of such products varies with the process parameters along with the presence of high alkaline and alkali earth metal contents such as K, Mg, and Ca. The high alkaline and alkali earth metal content in the biomass has the potential to catalyze pyrolysis reactions. According to the International Energy Agency (IEA) 2022 report, clean energy transition in emerging economies foster sustainable innovation for net zero emissions and rapid decarbonization. The momentum for low-emission hydrogen and biofuel generation from renewable substitutes such as biomass through certain thermochemical routes has gained considerable addendum.

The blending of coal with biomass in a process termed co-pyrolysis appears quite appealing scientifically owing to its environmental pollution control through mitigation of NO_x, SO_x, and particulate matter, and the flexibility of its operation facilitating the production of volatile gas and liquid oil. Blending of biomass to coal during high-temperature pyrolysis decreases the significant emissions of the CO_2, volatile organic compounds and polyaromatic hydrocarbon (PAH). The high hydrogen content of biomass is believed to stabilize the higher molecular weight free radicals of coal thus enhancing the quality and yield of liquid oil products. Co-pyrolysis of biomass and coal produces better energy in terms of gaseous and liquid fuel *(Reddy and Vinu, 2018, Idris et al., 2010, Cordero et al., 2004, Moghtaderi et al., 2004, Vuthaluru, 2004, Blesa, et al., 2003, Collot et al., 1999).* It was also reported that the quality of co-pyrolytic oil is better as compared to the pyrolytic oil obtained from coal and biomass alone *(Yang et al., 2019).* Correspondingly the yield of pyrolytic oil and the quality of char is also better.

In a need to protract global carbon emissions, the motivation and focus gearing up the drivers behind coal/biomass energy research is the sustainable formulation of energy products, primarily biofuel through catalytic upgradation techniques by metal precursors (salts). The design of catalytic materials and their implementation into biomass or coal/biomass mixture would suffice tar generation during the pyrolytic process and increase light chain aromatic and aliphatic compounds. Catalytic materials imbibing high surface area, and effective dispersion of the metal active sites onto the support, increases the reaction rate of the substrate to selective products. In advanced research, nano-catalysts with a higher volume-to-surface area ratio would impart adequate binding sites for the reactant molecules, thus increasing its activity and selectivity towards selective products. However, this approach requires tremendous strides from the research community since a rational design is cumbersome. Although, the catalytic pyrolysis of biomass research is progressing rapidly, the fundamental research into the underlying phenomena of catalytic co-pyrolysis research of

coal/biomass blends, which is a recent development, is relatively lagging and hence has remained obscure. Henceforth, there is an impending call for a thorough investigation of thermal and catalytic co-pyrolysis of coal and biomass blends.

1.2 Coal and biomass as energy substitutes for fuel production

According to sustainable development goals 7.2 and recent IEA 2019 reports, the share of global electricity generation was 23.2% and renewables share in final energy consumption was 17.7%. The global demand for biofuels is set to accelerate at a continuum pace by 41 billion liters, or 28%, over 2021-2026 with a 2026 NZE demand of 342 billion liters. However, accessing the biofuels generation index by region, the Asian continent would surpass from 10.8 billion liters/year, 11.5% to 34 billion liters/year, 40.2% in 2026. This might be due to the prolific weather conditions in the region, vehement land resource potential for agricultural cultivation, generation of agricultural and forestry waste residues from fertile lands, a varsity in biodiversity prospect in non-edible food crops, and non-edible oil seeds production. In the global energy paradigm, India is a driving force towards the global energy economy. According to India Energy Outlook Report 2022, total energy demand in India steadily increased for coal from 33–44%, natural gas from 5-6%, renewables from 1–3%, and decreased for traditional biomass from 26–13% from 2010–2020 respectively. The majority of the CO_2 emissions occurred from coal-fired power stations (1104 Mt CO_2) and the energy sector and agriculture (98 Mt CO_2) in 2019. According to this report, global electricity demand increased from 717–1273 TWh from 2010–2021 for India with a steady increase in renewables share. In this scenario, the blending of biomass substitutes with coal-based non-renewable resources in a thermal process termed co-pyrolysis negates greenhouse gas emissions and produces CO_2-neutral fuel. The hydrogen donor capacity of biomass decreases the thermal stability of coal and increases its fuel grade quality during pyrolysis.

1.3 Catalytic valorization of biomass pyrolysis and co-pyrolysis of blends by nano-composite catalysts

Biomass pyrolysis renders the generation of liquid bio-oil, bio-char, and evolved volatile gas as pyrolyzed products. Despite higher char generation in slow pyrolysis reactions, fast pyrolysis generates myriad volumes of bio-oil due to moderate temperature, higher heating rate and shorter vapor residence time (VRT) *(Liu et al., 2017).* However, bio-oil produced from biomass pyrolysis has inadvertently high oxygen content (~35-45%), high water content (~15-30%), an inconsiderable calorific value index (HHV, MJ kg^{-1}) as compared to fossil

fuels, lesser thermal stability, substantial viscosity and acidity, rendering it immiscible with traditional liquid fuels *(Zhang et al., 2022).* These factors of biofuel could be delineated by transition metal catalysts.

Transition metal catalysts such as metal precursors (salts) *(Kumar et al. 2021),* transition metal oxides *(Santamaria et al. 2021),* natural clay catalysts *(Fernandez et al. 2021),* red mud *(Santosa et al. 2020),* hydrotalcites *(Prabhakara et al. 2022)* employed for the valorization of biomass to biofuels have gained considerable attention in the recent decades. Heterogeneous metal-based catalysts are momentous catalytic substances that have metallic active sites with variable surface binding energy properties. Transition metal catalysts, especially nickel-based catalysts surpass the properties of traditional heterogeneous catalysts in activity, stability and selectivity terms toward targeted reactions at the molecular level. However, nano-catalysts offer better properties than conventional heterogeneous catalysts in pyrolysis research. Due to their smaller sizes, nanoparticles have higher surface area and increased exposed active sites. Other guiding attributes to its prominence over traditional micro-catalysts include uniform active site distribution on the catalyst surface, lesser surface roughness, greater number of active phases, higher surface binding energies, higher thermal stability and uniform pore size distribution. Li et al. conducted several studies on supported and unsupported nickel nanoparticle catalysts for biomass pyrolysis. Thermogravimetric analysis done on catalytic pyrolysis of biomass showed lower onset temperatures for hemicellulose and lignin pyrolysis, which indicated that the nanoparticle catalyst helped to lower the activation energies of the thermal degradation process *(Li et al., 2009).* Supported nanoparticle catalysts, Ni/Al_2O_3 and $Ni\text{-}La\text{-}Fe/Al_2O_3$ developed by Li et al. led to excellent tar conversion (>99 %) at a temperature of 1073 K, significantly improving the yields of product gas. They also studied catalyst deactivation for 10 h and showed that the catalyst was highly stable. Richardson et al. studied the catalytic pyrolysis of biomass especially beechwood for cleaning of gasification producer gas. This is implicated by in-situ generated Ni metal nanoparticles synthesized by microwave-assisted polyol method measuring 2-4 nm in diameter. They are impregnated on wood chips by nickel nitrate using vacuum as the medium. The pyrolysis tests conducted in a horizontal tube furnace reactor to a temperature of 700^{o}C rendered an effective covalent combination of π orbitals from the aromatic conversion of benzene and naphthalene with the unoccupied d orbitals from the metal. It was observed that during catalytic pyrolysis when Ni content increased from 0.19-0.66mol/dnf wood, hydrogen gas production increased from 68-83%, solid yield increased from 16.7-16.9g/100g dnf wood and water yield decreased from 16.3-15.9g/100g dnf wood. It was also seen that tar conversion increased for furans,

decreased for phenolic compounds, increased for non-oxygenated aromatic compounds, decreased for the presence of polycyclic aromatic hydrocarbons, and increased significantly for oxygenated compounds from 0.19-0.66mol/dnf wood as nickel content increased in the nanoparticles. This effectuated aromatic tar conversion during the overall gasification process *(Richardson et al., 2013)*. Zirconia-based nano-catalysts, both zirconia-based nanoparticles and nanocomposites are another group of functional nanomaterials for heavy oil upgrading. This is implicated due to their high oxygen storage capacity and high acidity factor which transfers hydrogen groups to recipient atoms, such as the direct decarboxylation of benzoic acid to benzaldehyde *(Masudi and Muraza, 2018).* For viscosity reduction of heavy oil, tungstate zirconia also played a vital role as reported by Wang et al. *(Wang et al., 2012).* Ahmadi et al. studied prepared CoMo catalysts supported on various nano-structured materials (activated carbon, MCM-41, HZSM-5, γ-alumina, SBA-15) and an industrial catalyst Ru/C for hydrodeoxygenation of fast pyrolysis oil from hardwood sawdust in an autoclave reactor. It was observed that among all the supported catalysts, CoMo/MCM-41 produced the highest oil fraction yield, while CoMo/γ-alumina and CoMo/HZSM-5 produced the highest heavy oil (~20 wt.%) and coke (~10 wt.%) yields respectively. The Van Krevelen plot of the feed and HDO oil suggested that lighter oil has higher atomic H/C and O/C attributes than the heavy oils due to its aliphatic nature and due to the presence of more oxygenate compounds. Regeneration of CoMo/γ-alumina catalysts was performed which led to similar oil yields as the fresh catalyst *(Ahmadi et al., 2016)*. However, there was a study on recyclable monolithic nano-porous graphitic supported nano-catalysts (Fe, Au, Pd, Rh, Pt, and Ni) via pyrolysis using a tube furnace at a temperature from 400-1400°C under flowing hydrogen gas (150 mL min^{-1}). The Fe (0) nano-porous carbon was trans-metalated to noble-metal doped nano-porous carbon using ferrocene as a monomer repeat unit along with polyamide aerogels. The porous metal-doped carbons oxidized benzyl alcohol to benzaldehyde with metal-doped Au or Pt, the reduction of nitrobenzene by hydrazine to aniline catalyzed with carbon-supported Fe and two Heck coupling reactions of iodobenzene with styrene or butyl acrylate, catalyzed with carbon-supported Pd *(Saeed et al., 2016).*

Effective size and shape of the catalyst and a high surface-to-volume ratio defines the atomic utilization efficiency of the catalyst by unifying the physicochemical environment of its active sites. This could be achievable with a homogeneous distribution of active centers on its supports. This substantially necessitates the profundity of its structure-activity-relationship implications through the precise engineering and design of its molecular active site structure

and functionalities. One such technique is the wetness impregnation technique, where a metal (active) precursor is dissolved in an aqueous or an organic solution and subsequently heated and calcined for the generation of its metallic active sites onto the support. This substantially green process generates a limited amount of waste with a broad pore-size distribution of the catalysts.

1.4 Scope of the present work

From the preceding studies, it is observed that many authors have investigated biomass pyrolysis, its kinetics and product evaluation. However, few such kinds of literature are available on the co-pyrolysis of coal/biomass blends, its thermal pyrolysis kinetics and product profile distribution. Catalytic valorization of biomass to high-grade quality bio-oil could be effectuated by the implementation of catalysts, thus increasing its activity and selectivity towards selective products. This part of the work is still a challenge for research in the case of co-pyrolysis of coal/biomass blends. Although the catalytic pyrolysis of biomass research is progressing rapidly, the fundamental research into the underlying phenomena of catalytic co-pyrolysis research of coal/biomass blends, which is a recent development, is relatively lagging and hence has remained obscure.

The scopes of the work are as follows,

- Kinetic analysis (model-free integral) and thermodynamic analysis of coal and biomass and its blends using non-isothermal techniques (Kissinger-Akahira-Sunose model). The feeds are also investigated for their physicochemical characterization towards the production of renewable fuel and value-added chemicals.
- Preparation and detailed physicochemical characterization of 10% and 20% NiO and Ni (II) aluminate-based nano-composite catalysts for their applications in catalytic pyrolysis and catalytic co-pyrolysis of blends research.
- Effect of temperature and biomass blending ratio on co-pyrolysis of coal/biomass blends with product evaluation.
- Catalytic valorization of biomass for higher value yield of bio-oil and pyrolytic syngas generation with an evaluation of char residue formation using 10% and 20% NiO and Ni (II) aluminate-based nano-composite catalysts.
- Catalytic upgradation of coal/biomass blends for enhanced pyrolytic product generation using 10% and 20% NiO and Ni (II) aluminate-based nano-composite catalysts.

1.5 Outline of the Thesis

The thesis comprises of nine chapters. Chapter 1 discusses the relevance and significance of coal/biomass co-pyrolysis and the development of robust catalysts specifically nano-catalysts towards catalytic valorization of biomass, co-valorization of coal/biomass blends and catalytic upgradation of pyrolyzed products. In the final context, the motivation behind the work carried out and the outline of the thesis are also focused extensively. Chapter 2 reports the review of literature on various aspects of pyrolysis of coal and biomass as viable feedstocks for the generation of feasible pyrolytic end-products and co-pyrolysis of coal/biomass blends alongside a review of thecatalytic valorization of the mentioned processes. Chapter 3 describes the materials and methods section which emphasizes on the preparation and characterization techniques of the feedstocks and the synthesized catalysts. Chapter 4 describes the characterization of raw feedstock materials, coal and sawdust and prepared catalysts, 10% and 20% NiO and Ni (II) aluminate composite nano-catalysts for biomass pyrolysis and co-pyrolysis respectively. In Chapter 5, an experimental approach of the positive and negative upshots of blending sawdust with high ash content coal on the thermal stability of coal during the co-pyrolysis process is visualized. Optimization of biomass blending to coal in a thermogravimetric experiment and its studies on devolatilization characteristics affecting conversion % in the active pyrolytic zone is done comprehensively. Further, the thermal pyrolysis kinetics of coal and biomass as individual feedstocks and their blended feeds are evaluated by the KAS method. In Chapter 6, the study reveals the estimation of the mechanistic pathway and the thermo-kinetic parameters of thermal and catalytic pyrolysis of sawdust and catalytic co-pyrolysis coal/sawdust blends via 10% and 20% Ni-based nano-composite catalysts. Kinetics and thermodynamic estimation of the pyrolysis kinetics process was evaluated by the KAS method and a comparative assessment was done for both thermal and catalytic pyrolysis kinetics of sawdust and coal/sawdust blends. Chapter 7 describes the thermal and catalytic pyrolysis of sawdust in the presence of functional Ni-based nanocomposite catalysts, further substantiated with detailed product analysis and characterization for liquid bio-oil, product bio-char, and char residues. Fuel gas analysis along with the prominence in hydrogen gas generation is also elucidated in this Chapter. Chapter 8 describes the thermal and catalytic co-pyrolysis of coal/sawdust blends in the presence of functional Ni-based nanocomposite catalysts as elucidated, further substantiated with detailed product analysis and characterization for liquid oil, product gas and char residues. Fuel gas analysis along with the prominence in hydrogen

gas generation is also elucidated in this Chapter. Chapter 9 summarizes the research findings and elucidates the recommendations and scope for future work.

References

- Morgan, T.J. and Kandiyoti, R., 2014. Pyrolysis of coals and biomass: analysis of thermal breakdown and its products. *Chemical Reviews*, *114*(3), pp.1547-1607.
- Reddy, B.R. and Vinu, R., 2018. Microwave-assisted co-pyrolysis of high ash Indian coal and rice husk: product characterization and evidence of interactions. *Fuel Processing Technology*, *178*, pp.41-52.
- Jayanti, S., Saravanan, V. and Sivaji, S., 2012. Assessment of retrofitting possibility of an Indian pulverized coal boiler for operation with Indian coals in oxy-coal combustion mode with CO2 sequestration. *Proceedings of the Institution of Mechanical Engineers, Part A: Journal of Power and Energy*, *226*(8), pp.1003-1013.
- Mallick, D., Mahanta, P. and Moholkar, V.S., 2018. Synergistic effects in gasification of coal/biomass blends: analysis and review. *Coal and biomass gasification*, pp.473-497.
- Evans, S. and Pearce, R., 2020. Mapped: The world's coal power plants. *Carbon Brief*.
- Sharma, A., Saikia, A., Khare, P., Dutta, D.K. and Baruah, B.P., 2014. The chemical composition of tertiary Indian coal ash and its combustion behaviour–a statistical approach: Part 2. *Journal of earth system science*, *123*(6), pp.1439-1449.
- Blesa, M.J., Miranda, J.L., Moliner, R., Izquierdo, M.T. and Palacios, J.M., 2003. Low-temperature co-pyrolysis of a low-rank coal and biomass to prepare smokeless fuel briquettes. *Journal of Analytical and Applied Pyrolysis*, *70*(2), pp.665-677.
- Cordero, T., Rodrıguez-Mirasol, J., Pastrana, J. and Rodrıguez, J.J., 2004. Improved solid fuels from co-pyrolysis of a high-sulphur content coal and different lignocellulosic wastes. *Fuel*, *83*(11-12), pp.1585-1590.
- Collot, A.G., Zhuo, Y., Dugwell, D.R. and Kandiyoti, R., 1999. Co-pyrolysis and co-gasification of coal and biomass in bench-scale fixed-bed and fluidised bed reactors. *Fuel*, *78*(6), pp.667-679.
- Idris, S.S., Abd Rahman, N., Ismail, K., Alias, A.B., Abd Rashid, Z. and Aris, M.J., 2010. Investigation on thermochemical behaviour of low rank Malaysian coal, oil palm biomass and their blends during pyrolysis via thermogravimetric analysis (TGA). *Bioresource technology*, *101*(12), pp.4584-4592.
- Moghtaderi, B., Meesri, C. and Wall, T.F., 2004. Pyrolytic characteristics of blended coal and woody biomass. *Fuel*, *83*(6), pp.745-750.

- Vuthaluru, H.B., 2004.: Investigations into the pyrolytic behaviour of coal/biomass blends using thermogravimetric analysis.
- Yang, Z., Wu, Y., Zhang, Z., Li, H., Li, X., Egorov, R.I., Strizhak, P.A. and Gao, X., 2019. Recent advances in co-thermochemical conversions of biomass with fossil fuels focusing on the synergistic effects. *Renewable and Sustainable Energy Reviews*, *103*, pp.384-398.
- Liu, W.J., Li, W.W., Jiang, H. and Yu, H.Q., 2017. Fates of chemical elements in biomass during its pyrolysis. *Chemical Reviews*, *117*(9), pp.6367-6398.
- Zhang, P., Chen, Z., Zhang, Q., Zhang, S., Ning, X. and Zhou, J., 2022. Co-pyrolysis characteristics and kinetics of low metamorphic coal and pine sawdust. *RSC advances*, *12*(34), pp.21725-21735.
- Kumar, R. and Strezov, V., 2021. Thermochemical production of bio-oil: A review of downstream processing technologies for bio-oil upgrading, production of hydrogen and high value-added products. *Renewable and Sustainable Energy Reviews*, *135*, p.110152.
- Santamaria, L., Lopez, G., Fernandez, E., Cortazar, M., Arregi, A., Olazar, M. and Bilbao, J., 2021. Progress on catalyst development for the steam reforming of biomass and waste plastics pyrolysis volatiles: a review. *Energy & Fuels*, *35*(21), pp.17051-17084.
- Fernandez, E., Santamaria, L., Artetxe, M., Amutio, M., Arregi, A., Lopez, G., Bilbao, J. and Olazar, M., 2021. In line upgrading of biomass fast pyrolysis products using low-cost catalysts. *Fuel*, *296*, p.120682.
- Santosa, D.M., Zhu, C., Agblevor, F.A., Maddi, B., Roberts, B.Q., Kutnyakov, I.V., Lee, S.J. and Wang, H., 2020. In situ catalytic fast pyrolysis using red mud catalyst: Impact of catalytic fast pyrolysis temperature and biomass feedstocks. *ACS Sustainable Chemistry & Engineering*, *8*(13), pp.5156-5164.
- Prabhakara, H.M., Bramer, E.A. and Brem, G., 2022. Hydrotalcite as a deoxygenation catalyst in fast pyrolysis of biomass for the production of high-quality bio-oil. *Journal of Analytical and Applied Pyrolysis*, *161*, p.105431.
- Li, J., Xiao, B., Yan, R. and Liu, J., 2009. Development of a nano-Ni-La-Fe/Al_2O_3 catalyst to be used for syn-gas production and tar removal after biomass gasification. *BioResources*, *4*(4), pp.1520-1535.

- Richardson, Y., Motuzas, J., Julbe, A., Volle, G. and Blin, J., 2013. Catalytic investigation of in situ generated Ni metal nanoparticles for tar conversion during biomass pyrolysis. *The Journal of Physical Chemistry C*, *117*(45), pp.23812-23831.
- Masudi, A. and Muraza, O., 2018. Zirconia-based nanocatalysts in heavy oil upgrading: a mini review. *Energy & fuels*, *32*(3), pp.2840-2854.
- Wang, H., Wu, Y., He, L. and Liu, Z., 2012. Supporting tungsten oxide on zirconia by hydrothermal and impregnation methods and its use as a catalyst to reduce the viscosity of heavy crude oil. *Energy & fuels*, *26*(11), pp.6518-6527.
- Ahmadi, S., Yuan, Z., Rohani, S. and Xu, C.C., 2016. Effects of nano-structured CoMo catalysts on hydrodeoxygenation of fast pyrolysis oil in supercritical ethanol. *Catalysis Today*, *269*, pp.182-194.
- Saeed, A.M., Wisner, C.A., Donthula, S., Majedi Far, H., Sotiriou-Leventis, C. and Leventis, N., 2016. Reuseable monolithic nanoporous graphite-supported nanocatalysts (Fe, Au, Pt, Pd, Ni, and Rh) from pyrolysis and galvanic transmetalation of ferrocene-based polyamide aerogels. *Chemistry of Materials*, *28*(13), pp.4867-4877.

CHAPTER II

Review of Literature

2.1 Introduction

This chapter reports the literature review on various aspects of pyrolysis of coal and biomass as viable feedstocks for the generation of pyrolytic products. Trends of research on the co-pyrolysis technology, and selected literature highlighting experimental research work on co-pyrolysis processes are also reported along with the comparison of research findings. The chapter also reviews the chemistry behind the synergistic interactions among the coal-biomass blends, the kinetic modeling strategies applicable to the co-pyrolysis process, and the variation of the kinetic parameters with operational conditions of the feedstocks and process parameters. An in-depth kaleidoscopic review of reaction kinetics and thermodynamics evaluated from co-pyrolysis process kinetics integrated with designing a co-pyrolysis system is therefore crucial and indispensable. Section 2.5 and 2.6 presents a comprehensive and concise description of catalytic valorization of such carbonaceous wastes, biomass, and coal in the presence of metallic catalysts and nano-catalysts. Summary of the literature review, an attempt to improvise its research gaps to formulate the objectives of the present research are presented at the end of the chapter in sections 2.7 and 2.8.

2.2 General overview of pyrolysis of coal and biomass

A succinct explanation of the pyrolysis of coal and biomass as feedstocks, its historical perspective, and its gradual transition towards renewables is given in the present context. Coal production and utilization have been rising at an alarming rate, with its trend exceeding seven billion tonnes in 2010. Pulverized coal combustion generates abundant power and steam by inducing excess air/fuel ratio into the system. Whereas coal gasification imbues incomplete or partial combustion in the presence of a gasifying agent to convert a non-ash fraction of coal to gas with a significant calorific value. In underground coal gasification where the underground coal seam acts as a reactor generates massive amounts of product gases with the release of carbon dioxide (CO_2), carbon monoxide (CO), minimal amounts of methane (CH_4), and hydrogen sulfide (H_2S). Henceforth, massive waste disposal sites of coal derivatives lead to environmental pollution which necessitates a pressing concern. This engenders a critical concern about clean coal technologies through which carbon dioxide (CO_2) is sequestered from the atmosphere. Integrated gasification combined cycle (IGCC) plays a prime role in the carbon footprint scenario by integrating gasification-based produced synthesis gas (a mixture of carbonmonoxide and hydrogen) into the turbine for the generation of electricity and by reclaiming lost heat into the exhaust thereby maximizing energy efficiency. However, keeping a critical eye on GHG emissions, pulverized coal power plants produce SO_x (84.75 lb $MMBtu^{-1}$), NO_x (70.00 lb $MMBtu^{-1}$), particulate matter (13.00 lb

MMBtu^{-1}), whereas IGCC power plants produce SO_x (12.53 lb MMBtu^{-1}), NO_x (57.33 lb MMBtu^{-1}), particulate matter (7.10 lb MMBtu^{-1}) *(Haslback J et al., 2013)*. Even though coal liquefaction, an established technology dates back to the aftermath of 1970s oil shocks where coal utilization routes were designed, coal pyrolysis emerges as a bottleneck on the unequivocal exacerbation of the anthropogenic CO_2 emissions into the atmosphere and produces clean fuel to increase the added value of coal-based products.

However, the demand for renewables in the present energy context has put forth an incumbent implementation of biomass. Biomass acts as a profuse carbon-neutral resource, and gears up maximal waste recovery through minimal greenhouse gas emissions for directing waste management practices toward a circular economy *(Diamantis et al., 2021).* Lignocellulosic biomass complements the major agricultural residues *(Fu et al., 2019),* forestry residues *(Yuan et al., 2019),* crop residues *(He et al., 2018),* biogas generated from anaerobic digestion of lipid-rich sludge *(Diamantis et al., 2021),* indigenous crop stalks *(Gupta et al., 2020),* invasive plant weeds *(Sahoo et al., 2021),* aquatic plants *(Huang et al., 2020, Muradov et al., 2010),* municipal solid waste *(Lee et al., 2020),* landfill *wastes (Jagodzińska et al., 2021)* and non-edible seeds *(Shadangi and Mohanty, 2014)* to be used as a viable renewable resource for the production of value-added products through various thermochemical conversion technologies such as pyrolysis *(Kan et al., 2016),* gasification *(George et al., 2019),* combustion *(Ajimotokan et al., 2019, Antwi-Boasiako and Acheampong, 2016),* hydrothermal liquefaction *(Jasiūnas et al., 2017),* hydrothermal gasification *(Selvi Gökkaya et al., 2020)* and hydrothermal carbonization *(Monedero et al., 2019).* In this context, pyrolysis emerges as a reliable technology for the thermal degradation of biomass cost-effectively *(Kan et al., 2016, Bridgewater, 2003).*

2.3 General overview of co-pyrolysis of coal and biomass blends

A brief exposition on co-pyrolysis of coal and biomass blends explores the sustainable development of energy resources to pacify the ongoing oil crisis. From the grassroots level to market research analysis, the need for process economics to estimate the cost of biomass processing and coal utilization is a matter of vital concern that must be rendered pivotal by designing new technologies. Despite the many advantages of biomass energy, its use at commercial scale is still minimal because of the many challenges associated with supply chain management and conversion technologies. To sum up, biomass availability is a source of major issue as is the availability of fertile lands for its cultivation. Despite these facts, coal has its disadvantages which are high ash content, high sulphur content, and requires higher

energy for its thermal degradation. To avoid such lacunae, the concept of co-pyrolysis of coal and biomass has irrevocably geared to produce CO_2-neutral fuel. Despite producing CO_2-neutral fuel, the high hydrogen content of biomass is believed to stabilize the higher molecular weight free radicals of coal thus enhancing the quality and yield of liquid product. Literature reveals that the co-pyrolysis of biomass and coal produces better energy in terms of gaseous and liquid fuel *(Shafizadeh, 1981; Jenkins, 1989*). When the proportion of coal in coal-biomass blends is higher, the calorific value increases due to a higher concentration of carbon in the sample along with a lower degree of oxidation than the biomass sample. For every 1% increase in carbon concentration, it would elevate the calorific value by approximately 0.39 MJ kg^{-1} *(Shafizadeh, 1981*) and for every 1 % decrease in ash content in woods, there is a rough decrease of calorific value of 0.2 MJ kg^{-1} because ash released is not a significant contributory factor to the heat released during combustion *(Jenkins, 1989).* This appears quite appealing scientifically owing to its environmental pollution control through mitigation of NO_x, SO_x, and particulate matter, and the flexibility of its operation facilitating the production of volatile gas and liquid oil.

Many researchers have reviewed the pyrolysis of coal and biomass as feedstocks. Literature on pyrolysis and co-pyrolysis processes, chemistry related to coal and biomass co-pyrolysis including thermodynamics and reaction kinetics, process parametric effects on the reaction (mainly particle size, temperature, heating rate, gas flow rate, biomass feeding ratios) and its catalytic co-processing are reported. The literature exude a review on the product yields when biomass is co-pyrolyzed with coal; few of which shed light on its blending characteristics, devolatilization properties and others on its kinetics *(Biagini et al., 2002, Idris et al., 2010, Aboyade et al., 2013, Wang et al., 2014, Wang et al., 2015, Messina et al., 2015, Yan et al., 2016, Dalluge et al., 2017, Guo et al., 2017, Li et al., 2019, Wu et al., 2019, Zhu et al., 2021, Zhang et al., 2022, Zhao et al., 2022).*

The knowledge of the properties and behavior of coal and biomass with temperature is quintessential for designing an efficient pyrolysis unit. Thermal analysis has been widely used in pyrolysis research (*Shadangi and Mohanty, 2014*). The thermogravimetric analysis measures the degradation pattern of the sample as a function of increasing temperature or time under the kinetic regime. It can accurately model and predict the composition, cure kinetics, reaction kinetics, thermodynamics, thermal stability and aging process of the feedstock. Alongside this, catalytic processing of products using bulk and supported metal catalysts has also been reviewed. It would therefore be an aim of this review to look at

potential advances in this light, assessing the status quo and fate of co-pyrolyzed products and capturing the modes of improvements that are needed or could be useful in formulating the whole mechanism.

2.3.1 Types of coal and biomass pyrolyzed

Pyrolysis is one of the methods to get solid, liquid, and gaseous fuels from coal and biomass. However, such an energetic process majorly depends on the intrinsic and extrinsic factors of the feedstock. For coal, the intrinsic factors are accounting for the structure, composition, rank and particle size. The external factors relying on the pyrolysis process are temperature, pressure, medium of gas purging, and heating rate. Coal has an intricate carbon molecular structure with strong covalent linkages and high sulfur and ash content. As compared to coal, lignocellulosic biomass renders upstanding pyrolytic characteristics depending on its hemicellulose, cellulose, and lignin content. The occurrence of cellulose, hemicellulose and lignin results in pyrolytic vapor, once it gets pyrolyzed with bond dissociation energy of 380-420 kJ mol^{-1}. The composition of carbonaceous material of biomass and coal are also evaluated in terms of proximate (volatile matter, fixed carbon and ash) and ultimate analysis (carbon content, hydrogen content, sulfur content, nitrogen and oxygen content). Coal has higher carbon content while biomass has higher volatile matter and oxygen content, although coal and biomass have similar nitrogen content. One more interesting characteristic of coal and biomass is the ash compositional analysis to evaluate silica, alumina and other alkali and alkaline earth metals in the mixture in the form of K_2O and CaO respectively. The polymers of hemicellulose, cellulose and lignin which encase the total fiber content in the biomass macromolecular structure and other wood materials apart from extractives, constitute the major and most valuable components of biomass. Table 2.1-2.4 illustrates the ultimate analysis, proximate analysis, and properties of selected biomass fuels, and coal for pyrolysis reactions.

Table 2.1 Chemical proximate analysis and properties of selected biomass feeds

Feed	Moisture, %	Ash content, %	Volatile matter, %	Fixed carbon, %	Reference
Licorice residue	-	2.02	75.1	22.8	*Zhou et al., 2023*
Green Microalgae *Botryococcus braunii*	5.01 ± 0.42	27.44 ± 1.11	-	-	*Dirgarini et al., 2021*
Cedar	3.04	4.08	84.59	-	*Zhu et al., 2020*
Beechwood	-	0.95	77.81	21.24	*Ismail et al., 2020*
Cellulose	1.91	0.06	91.28	6.75	*Zhao et al., 2020*

(Continued)

Walnut seed	8.16	0.70	81.66	9.48	*Yang et al., 2019*
Freshwater macroalgae, Oedogonium sp.	7.0	8.0	77.3	14.7	*Zhu et al.,2015*
Sawdust	3.13	1.64	79.67	15.56	*Wang et al., 2012*
Rice straw	3.63	11.83	64.82	19.72	*Wang et al., 2012*
Safflower seed	5.7	2.2	80.8	11.3	*Onay et al., 2007*

Table 2.2 Chemical proximate analysis and properties of selected coal feeds

Feed	**Moisture, %**	**Ash content, %**	**Volatile matter, %**	**Fixed carbon, %**	**Reference**
Naomaohu coal	2.10	1.82	41.27	54.81	*Chen et al., 2021*
Zhundong brown coal	-	4.34	30.86	64.79	*Ismail et al., 2020*
Lignite	4.12	11.98	34.14	49.76	*Zhao et al., 2020*
Shenfu coal	9.37	6.43	33.18	51.02	*Yang et al., 2019*
Loy Yang coal	6.0	4.80	46.50	48.80	*Zhu et al.,2015*
Pingshuo coal	2.16	31.26	29.21	19.72	*Wang et al., 2012*
Lignite	11.2	39.6	32.7	16.5	*Onay et al., 2007*

Table 2.3 Chemical ultimate analysis and properties of selected biomass feeds

Feed	**C, %**	**H, %**	**O, %**	**N, %**	**S, %**	**HHV, MJ kg^{-1}**	**Reference**
Licorice residue	42.5	6.41	49.5	1.3	0.24	-	*Zhou et al., 2023*
Cedar	50.86	6.04	41.94	0.12	1.04	-	*Zhu et al., 2020*
Beechwood	49.66	6.29	43.95	0.1	-	-	*Ismail et al., 2020*
Cellulose	44.48	6.38	49.02	0.12	-	15.4	*Zhao et al., 2020*
Walnut seed	48.47	6.23	45.12	0.18	-	-	*Yang et al., 2019*
Jatropha curcas seed cake	45.5	6.7	45.3	-	-	17.05	*Naik et al., 2016*
Freshwater macroalgae, *Oedogonium sp.*	46.00	6.00	35.40	3.93	0.20	19.1	*Zhu et al.,2015*

(Continued)

Sawdust	46.92	5.63	41.78	0.86	0.04	17.79	*Wang et al., 2012*
Rice straw	45.26	4.15	34.71	0.30	0.12	14.94	*Wang et al., 2012*
Safflower seed	61.1	9.2	26.9	2.8	-	26.8	*Onay et al., 2007*

Table 2.4 Chemical ultimate analysis and properties of selected coal feeds

Feed	**C, %**	**H, %**	**O, %**	**N, %**	**S, %**	**HHV, MJ kg^{-1}**	**Reference**
Naomaohu coal	73.10	5.61	19.49	0.95	0.85	-	*Zhu et al., 2020*
Zhundong brown coal	75.39	3.48	15.19	1.19	0.42	-	*Ismail et al., 2020*
Lignite	60.13	4.16	34.20	1.16	0.35	22.4	*Zhao et al., 2020*
Shenfu coal	66.64	5.86	26.45	0.77	0.28	-	*Yang et al., 2019*
Indian bituminous coal	77.7	5.0	2.5	1.0	-	31.03	*Naik et al., 2016*
Loy Yang coal	65.40	4.50	24.40	0.47	0.44	25.7	*Zhu et al., 2015*
Pingshuo coal	52.05	3.07	8.31	0.79	0.12	14.94	*Wang et al., 2012*
Lignite	36.8	3.4	56.9	1.1	1.8	6.6	*Onay et al., 2007*

2.3.2 Review on the proportion of biomass on coal and biomass blends

It is of utmost necessity to shed light on the prominence of the pyrolytic products as obtained from the pyrolysis of coal and biomass blends. The proportion of biomass in the co-pyrolysis process influences the product distribution profile. Numerous researchers have studied the effect of biomass ratio on coal for the blending characteristics and also tried to study its feedstock interactions and synergistic interactions. Wang et al. studied four different fuels, Zhundong brown coal, Datong bituminous coal, wheat husk biomass, and corn stalk biomass at three different mixing ratios, coal:biomass = 80:20, 50:50 and 20:80 in a quartz reactor. They stated that coal−biomass blends indicate the absence of a synergistic effect between the coal and biomass pyrolysis. A chemical percolation devolatilization (CPD) model with a particle energy equation was employed which agreed well with the experimental data for different particle diameters, fuel types, and blend mixing conditions *(Wang et al. 2015)*. Zhao et al. worked on co-pyrolysis of Hulunbeier coal and walnut shells in a drop-tube furnace at a 50:50 ratio, where M1 operated from 298-673 K and M2 operated from 673-873 K at a heating rate of 5^{o}C min^{-1}. They reported that M1 achieved a higher tar

yield and lower water content than M2. The M1-generated tar exhibited a lower free-radical concentration, higher H/C ratio, higher levels of uncondensed aromatic hydrogen, and shorter side-chains than that produced by M2 *(Zhao et al., 2022)* Zhang et al. reported on the co-pyrolysis characteristics of low metamorphic coal and pine sawdust in a fixed-bed pyrolysis reactor and showed that addition of 30 % biomass addition to coal improved tar and gas yields. Synergistic interaction was more pronounced where polycyclic aromatic hydrocarbons (PAH) in the co-pyrolysis tar were converted into phenolic substances which improve the tar quality. However, alcohols and acids in the tar interact further to generate high amounts of esters *(Zhang et al., 2022).* Wu et al. reported the co-pyrolysis of low-rank coal from Shannxi Province, China, and cellulose from Sigma-Aldrich at 25 %, 50 % and 75 % of cellulose addition to coal in a NETZSCH SAT-449 thermogravimetric analyzer with process conditions as nitrogen gas flow (50 mL min^{-1}), temperature of 1273 K and heating rate of 10, 20 and 40 K min^{-1}. They reported the synergistic interaction between the maceral components with positive synergy from volatile products observed with the addition of vitrinite at 25%. Inertinite inhibited the formation of volatiles during co-pyrolysis with negative synergy. However, negligible synergy was observed for acid-washed low-rank coal with cellulose at the hating rate of 10 or 20 ℃ min^{-1} *(Wu et al., 2021).* Wu et al. reported the co-pyrolysis of low-grade coal and wheat straw in a drop-tube furnace at 25 %, 50 % and 75 % of wheat straw with coal from temperatures 873-1273 K with nitrogen as purge gas (100 mL min^{-1} flow rate). They observed both positive and negative synergic effects from the gaseous product distribution profile due to presence of cellulose (cause of generation of CO and CO_2), hemicellulose (cause of generation of CH_4) and lignin (cause of generation of C_2H_4 and C_2H_6) *(Wu et al., 2021).* Messina et al. reported the co-pyrolysis of commercial peanut (*Arachis hypogaea*) shells and cassava (*Manihot esculenta*) starch with particle diameter between 250 μm and 500 μm for the reactor assays in a fixed-bed reactor, while samples with a particle diameter between 44 μm and 74 μm were selected for thermogravimetric studies. Microcrystalline cellulose was used to investigate the synergistic effects between the two biomasses. They proved that synergistic effects were predominant. A mixture composed of 75 wt.% of starch and 25 wt.% of peanut shells led to maximize the yield of the bio-oil (58.2 wt.%), while its water content was reduced to 3.4%. The addition of starch to the peanut shells led to a bio-char with less ash content *(Messina et al., 2015).* Wang et al. reported the fast pyrolysis of coal/biomass blends in a fluidized bed reactor. Yilan sub-bituminous coal and corncob at mass ratios (0–100 %) were used to yield higher pyrolysis oil at coal blending ratios of less than 60 %. GC/MS results indicate that co-pyrolysis oil has higher alcohol,

aldehydes, ketones, and carboxylic acids *(Wang et al., 2014)*. Table 2.5 illustrates the proportion of biomass on coal and biomass blended mixtures for various co-pyrolysis processes.

Table 2.5 Summary of literature on proportion of biomass on co-pyrolysis of coal-biomass blends

Equipment used	Type of coal	Type of biomass	Coal/Biomass percentage	Process conditions	Reference
Fixed-bed quartz tube pyrolysis reactor unit	Low metamorphic coal	Pine sawdust	0 %, 10 %, 20 %, 30 %, 40 %, 50 % and 100 % pine sawdust addition to coal	Nitrogen gas with a holding time of 30 min, temperature of 948 K, and a heating rate of 10 K min^{-1}	*Zhang et al., 2022*
Drop-tube fixed-bed reactor (I.D., 34 mm; length, 300 mm)	Hulunbeier coal (20-40 mesh size)	Walnut shells (20-40 mesh size)	50:50	Nitrogen gas flow (200 mL min^{-1}) with M1 and M2 processes where M1 operated from 298-673 K and M2 operated from 673-873 K at a heating rate of 5°C min^{-1}	*Zhao et al., 2022*
NETZSCH SAT-449 Thermogravimetric analyzer	Low-rank coal from Shannxi Province, China	Cellulose	25 %, 50 % and 75 % of cellulose addition to coal	Nitrogen gas flow (50 mL min^{-1}), temperature of 1273 K and heating rate of 10, 20 and 40 K min^{-1}	*Wu et al., 2021*
Drop-tube furnace (I.D., 35 mm, height, 800 mm)	Low-quality coal	Wheat straw	25 %, 50 % and 75 % of wheat straw addition to coal	Temperature of 873-1273 K, Purge gas was nitrogen (100 mL min^{-1})	*Wu et al., 2019*
Single particle reactor system	Zhundong brown coal, Datong bituminous coal	Wheat husk biomass, corn stalk biomass	Coal:biomass = 80:20, 50:50, 20:80	Nitrogen flow (5 L min^{-1}), pressure of 1 atm	*Wang et al., 2015*

(Continued)

Stainless steel fixed bed reactor	-	Peanut (*Arachis hypogaea*) shells and cassava (*Manihot esculenta*) starch processed by wet granulation	75 wt.% shells – 25 wt.% starch (PS75); 50 wt.% shells – 50 wt.% starch (PS50); 25 wt.% shells – 75 wt.% starch (PS25)	Temperature 773 K at a heating rate of 5°C/min, nitrogen flow rate 300 mL min^{-1}	*Messina et al., 2015*
Fluidized-bed reactor unit	Yilan sub-bituminous coal	Corncob	0 – 100 %	Higher pyrolysis oil yields at coal blending ratios of less than 60 %	*Wang et al., 2014*

2.3.3 Chemistry behind co-pyrolysis of coal and biomass mixtures

Co-pyrolysis is an integral section of the chemical industry and has several positive upshots concerning emissions, energy requirements, and pyrolytic product quality. It negates the emissions of SO_x, and NO_x during pyrolysis and has resulted in higher calorific value fuel including various oxygenated compounds. However, coal and biomass are accumulators of solar energy. This instils a difference in their H/C and O/C atomic ratios signifying the Van Krevelen diagram. As compared to coal, biomass has a higher H/C ratio (1.26–1.58) and O/C ratio (0.4–0.8) which renders biomass having high hydrogen donating capacity to coal during co-pyrolysis reactions. The high oxygen content in biomass accelerates its reactivity and devolatilization characteristics, thereby contributing to the conversion of coal. The hydrocarbon released from coal during co-pyrolysis with biomass enhances the quality of pyrolytic vapor and as a result, the oil quality improves. However, blending biomass with coal during high-temperature pyrolysis decreases the emissions of the carbon dioxide, volatile organic compounds, and polyaromatic hydrocarbon (PAH). It is noticed that the PAH is accounted to be high in the pyrolytic oil when the amount of biomass is less in feed (coal-biomass blends). However, it gets reduced once the concentration of biomass increases in the blends by yielding a higher amount of aliphatic and oxygenated compounds. This is attributed to the presence of organic components in the biomass that influence the formation of alkene and reduce the aromaticity of the pyrolytic oil due to free-radical stabilization and cross-linking reactions.

Many researchers reviewed the chemistry behind the co-pyrolysis of coal and biomass, its synergistic interactions of alkali and alkaline earth metals (AAEM) presence in biomass, the fluid behavior of coal, and the probable fate of its extractable/pyrolyzed products. Zhu et al. analyzed the composition of liquid bio-oil from the fast co-pyrolysis of cedar sawdust with low rank coal. Their results showed that there were more generations of single-ring and two-ring aromatic compounds and less formation of three-ring and four-ring aromatic compounds. They ascribed this to the hydrogen supply by the pyrolysis of cedar sawdust, thereby restraining the secondary polymerization of volatiles in fast co-pyrolysis. Besides the role of hydrogen donors, alkali and alkaline-earth metals in biomass also influence the co-pyrolysis process *(Zhu et al., 2021).* Li et al. studied the co-pyrolysis of Xilinhot lignite and rice husk, and they revealed that the secondary cracking of volatiles from both feedstocks was promoted by alkali and alkaline-earth metals in biomass which enhances the synergistic interactions *(Li et al., 2019).* Yan et al. reported the co-pyrolysis of bamboo from Huzhou, Zhejiang Province of South China and Mengxi coal from China's Inner Mongolia of particle size ~106 μm at three different mass ratios, i.e., 10, 30 and 50 wt.%. Thermogravimetric analysis was employed from 303-1073 K temperature at heating rates, 5, 20 and 50 K min^{-1} under nitrogen as purge gas and the devolatilization aspects of coal and bamboo were observed inherently. Bamboo devolatilized at a lesser temperature (453 K) than coal (573 K) and theoretical and experimental TG-DTG curves suggested no synergistic interactions among the two feedstocks. However, mineral co-processing in the blends via Na, K and Ca in the order NaCl>KCl>$Ca(NO_3)_2$ led to significant synergistic effects thus increasing its reactivity *(Yan et al., 2016).* Later, Dalluge et al. compared the influence of seven AAEM salts on char and volatile yields issued from the fast pyrolysis of lignin *(Dalluge et al., 2017).*

The thermal stability of biomass is lower than that of coal which induces degradation of coal at higher temperatures by the free radicals generated from biomass devolatilization, particularly lignin. Overall seeing from an in-depth perspective, co-pyrolysis of coal with biomass induces several free radical mechanisms including initiation, secondary radical formation, and termination by radical disproportionation or recombination. In this scenario, secondary radical formation involving depolymerization, hydrogen transfer reactions, monomer formation, intermolecular hydrogen transfer and isomerization facilitate the scission of polymer chains and their derivatives.

2.3.4 Review on kinetic models for thermal degradation kinetics

Theoretical exploration of model kinetics embarks upon basic mathematical fundamentals and principles. An incumbent rigor imbibing chemical kinetics in the area of pyrolysis is the evolution of reliable algorithms for process design, biofuel, and gas exploration, crystallization transitions of char, and lifetime assessment of the process cycle. This instills the involvement of conceptual and algorithmic advances toward the fabrication of model parameters for reliable data. Conceptualization of models generates an intense procedure of gathering rate or conversion data over a wide range of temperatures and time factors to adequately decouple activation energies and pre-exponential dependencies in the Arrhenius equation. Theoretical reaction mechanistic pathways of such thermal processes via solid-state kinetic models are also crucial in this study as evaluated by thermo-analytical methods.

2.3.4.1 Significance of solid-state kinetic models

The impetus gearing solid-state chemistry research is seen in the area of solid-state physics, solid-state chemistry, material sciences, catalysis, and chemistry of polymers. Theoretical solid-state kinetic models exude new dimensions to the synthesis, structure, properties, and applications of solid-state materials, specifically to thermal degradation processes such as coal and biomass co-pyrolysis. Solid-state kinetic models encompass a range of non-isothermal reaction models based on nucleation and nuclei growth in the lattice of the reactants, geometrical shape of the crystals, diffusion-based, and reaction order-based models *(Khawam and Flanagan, 2006).* Nucleation is the formation of a new product phase at reactive points or nucleation sites of the reactants which might happen at single-step or multi-stepped mechanisms in solid-state reactions as denoted by the nucleation models. These reactions include crystallization *(Yang et al., 2005),* crystallographic transition *(Burnham et al., 2004)* and decomposition *(Graetz et al., 2005, Wang et al., 2005).* However, in thermal degradation of coal and biomass co-pyrolysis processes, decomposition reaction is predominant with a deceleration trend of sigmoidal α-time curve. The shape of the curve is indicative of the dedicated reaction mechanism and the solid-state kinetic model of the thermal process but is independent of the heating rate of the reaction.

2.3.4.2 Significance of model-fitting integral kinetic methods

At the onset of delving into the correlations of solid-state processes to reaction kinetics, kinetic terms such as reaction rate, $\frac{d\propto}{dt}$, Arrhenius preexponential factor, A, gas constant, R and activation energy, E, requires a pre-emptive focus and an inquisitive consideration.

Considering the pressure dependency term, h(P) = 0, the reaction rate, *dα/dt*, of a solid-state process can be given in Eq. (2.1) as,

$$\frac{d\propto}{dt} = Aexp^{\frac{-E}{RT}} f\ (\propto) \tag{2.1}$$

If the sample temperature is related to the reference temperature, and even the sample temperature is different than the reference temperature then presenting a new term $g(\alpha)$, we can write Eq. (2.2) as,

$$g(\alpha) = \int_0^{\propto} \frac{d(\propto)}{f(\propto)} = A \int \exp\left(-\frac{E}{RT}\right) dT \tag{2.2}$$

where g(α) is the integral form of the reaction model.

Based on assumptions prioritized on the mathematical functions which are used to describe the reaction mechanism of any solid-state processes, model fitting kinetic methods are rigorously fitted for the estimation of kinetic parameters such as activation energies, $E_{\alpha,}$ and pre-exponential factor terms, A by the goodness of data fitting or maximizing linear regression coefficient values. Such methods are limited to single-step processes since they are invariably determined by pre-existing solid-state kinetic models *(Sbirrazzuoli, 2013)*. The extent of conversion, α = 0.20 - 0.80, is considered for accurate computations in Arrhenius dependency parameters. The differential methods of Borchardt–Daniels or Achar–Brindley–Sharp *(Borchardt and Daniels, 1957), (Sharp et al., 1966)* are obtained by taking the logarithm of Eq. (2.1) and given as Eq. (2.3),

$$\ln\left[\frac{1}{\gamma(1-\alpha(T))}.\frac{d\alpha(T)}{dT}\right] \tag{2.3}$$

where the slope is $-\frac{E}{R}$ and intercept is ln $(\frac{A}{\beta})$.

Coats-Redfern method is used to calculate the kinetic triplets: activation energy, pre-exponential factor, and order of the reaction in a single stage of the reaction *(Coats and Redfern, 1964)* as given by Eq. (2.4),

$$ln\frac{\beta}{T^2} = ln\frac{AR}{E.g(\alpha)} - \frac{E}{RT} \tag{2.4}$$

where the slope is $-\frac{E}{R}$ and intercept is $ln\frac{AR}{E.g(\propto)}$

However, the precision of this method for the determination of apparent activation energy values without neglecting the low-temperature integral in the thermal decomposition process is yet to be studied.

Van-Krevelen using the same methodology as Coats and Redfern, obtained, for n # 1 as given in Eq. (2.5) *(Van Krevelen, 1951),*

$$ln\left(\frac{(1-\alpha)^{1-n}-1}{1-n}\right) = Ln\left(\frac{A}{\beta}\left(\frac{0.368}{T_n}\right)^{\frac{E}{RT}}\left(\frac{1}{\frac{E}{RT_n}+1}\right)\right) + \left(\frac{E}{RT_n}+1\right) Ln\, T \quad (2.5)$$

where T_n is the temperature at the maximum rate (K).

The Horowitz and Metzger method is a simplification of that of Coats and Redfern. Based on Eq. (2.2), a deviation of characteristic temperature is defined as $\theta = T - T_s$, where T is the temperature at any time (K), and T_s = the TGA differential curve peak temperature. For n # 1 the following expression is obtained as given in Eq. (2.6) *(Horowitz and Metzger, 1963),*

$$\ln\left((1-\alpha)^{1-n}\right) = \frac{-E\theta}{RT_{s^2}} + \ln(1-n) \quad (2.6)$$

Sharp and Wentworth estimated activation energies from $\left(\frac{dc}{dt}\right)$, rate of change of fraction of weight with the change in temperature, where a linear plot of log $\frac{\frac{dc}{dt}}{1-c}$ versus 1/T gives a slope of E_α and intercept of A as given in Eq. (2.7) *(Sharp and Wentworth, 1969),*

$$\log\left[\frac{dc/dT}{(1-c)}\right] = \frac{\log(A}{\beta}) - \left[\frac{E}{2.303R}\right].\ 1/T \quad (2.7)$$

Kennedy-Clark equation estimates activation energies at constant heating rate conditions as given in Eq. (2.8) *(Kennedy and Clark, 1997),*

$$\ln\left[\frac{\beta.g(\alpha)}{(T-T_0)}\right] = \ln A - \frac{E}{RT} \quad (2.8)$$

Kissinger's method involves using the maximum reaction rate as a function of the heating rate to derive activation energy and pre-exponential factor terms. It is rigorously applicable and iso-conversional for first-order reactions. It is an excellent approximation for nth-order, nucleation-growth, and distributed reactivity reactions. At the peak reaction rate, the derivative of the reaction rate (second derivative of conversion) is equal to zero *(Kissinger, 1957)*. For a first-order reaction, *df(x)/dx* =−1, the equation Eq. (2.9) is,

$$ln\frac{\beta}{Tm^2} = ln\frac{AR}{E} - \frac{E}{RTm} \quad (2.9)$$

where the slope is -E/R and intercept is $ln\frac{AR}{E}$.

2.3.4.3 Significance of model-free kinetic methods

Kinetic modeling methods free from rigorous fitting to phenomenological theoretical models without any assumptions of reaction mechanism are termed iso-converional or model-free kinetic methods. They render more reliable kinetic data from thermo-analytical procedures since vital knowledge is vested upon dependence of apparent activation energies with the extent of conversion, E_α-dependency *(Sbirrazzuoli, 2013).* To shed light on the

prominence of the historical evolution of model-free kinetic methods, an in-depth knowledge about the significance and advantage of each model and to relinquish the added flaws in them is preemptive.

Model-free kinetic methods are initiated from a differential form of rate equations as deduced by Freeman and Carroll as given in Eq. (2.10) *(Freeman and Carroll, 1958),*

$$Y=-\frac{E}{R}X+n;\ Y=\frac{\Delta \ln\left(\frac{d\alpha}{dt}\right)}{\Delta \ln(1-\alpha)};\ X=\frac{\Delta\left(\frac{1}{t}\right)}{\ln(1-\alpha)} \quad (2.10)$$

Friedman deduced an equation where the rate equation was devoid of pressure dependency term as given by Eq. (2.11) *(Friedman, 1964),*

$$ln(d\alpha/dt) = ln\,(A) + ln\,f\,(\alpha) - (E/RT) \quad (2.11)$$

Friedman suggested that if the conversion steps are minimalistic, those effective first-order frequency factors can be used for each instantaneous reaction rate and incremental fraction reacted *(Friedman, 1964).* In this study, a value of E_α was computed for each value of α lying between 0.01 and 0.99 with a step of 0.01. The advantages of differential methods such as Friedman's method are that they make no approximations and can be applied to any temperature program. This does not hold for usual integral methods. Ozawa and Flynn and Wall independently observed that the approximation of the temperature integral proposed by Doyle leads to the equation as given in Eq. (2.12),

$$ln\,(\beta) = ln\,((A.\,E)/(f(\alpha)R)) - 5.331 - 1.052\,(E/RT) \quad (2.12)$$

This is known as the OFW equation *(Ozawa, 1965; Flynn and Wall, 1966).* Plotting ln (βi) versus $1/T_i$ at conversion α gives a slope of E/R at that α *(Flynn and Wall, 1996; Ozawa, 1965).*

A more accurate simplification of the temperature integral leads to the KAS (Kissinger-Akahira-Sunose) equation *(Ozawa, 1992)* as given in Eq. (2.13),

$$ln\frac{\beta}{T^2} = ln\frac{AR}{E\,g(\propto)} - \frac{E}{RT} \quad (2.13)$$

where the slope is $-\frac{E}{R}$ and intercept is $ln\frac{AR}{E\,g(\propto)}$.

The algorithm used in this study allows the computation of kinetic parameters using an integral non-isothermal method, according to a generalized form of Eq. (2.14) *(Sbirrazzouli, 2013),*

$$ln\frac{\beta.g(\alpha)}{T^m} = B - C\,(\frac{E}{RT}) \quad (2.14)$$

More accurate approximations were proposed by Tang et al. *(Tang et al., 2003)* and Madhusudanan et al. *(Madhusudanan et al., 1986).* The equation deduced by Tang et al. can be estimated using m = 1.894661, B = ln (AR/E) + 3.63504095 -1.894661 ln E and C =

1.00145033. Madhusudanan et al. (1986) equation corresponds to m = 1.921503, B = ln (AR/E) + 3.772050 – 1.921503 ln E and ln C = 1.000956 after identification with Eq. (2.9) *(Sbirrazzouli, 2013).* Therefore, the Tang kinetics method is expressed as given in Eq. (2.15),

$$B = \ln (AR/E) + 3.63504095 - 1.894661 \ln E \quad (2.15)$$

Madhusudanan kinetics method is expressed as given in Eq. (2.16),

$$B = \ln (AR/E) + 3.772050 - 1.921503 \ln E \quad (2.16)$$

Slightly more accurate activation energies can be obtained by replacing the square of the temperature with a power of 1.92 and adding a coefficient of 1.0008 in front of the right-hand term as given in the Starink method *(Starink, 2003)* as given below,

$$ln\left[\frac{\beta.g(\alpha)}{T^m}\right] = B - C\left(\frac{E}{RT}\right);\ m = 1.92 \quad (2.17)$$

In this case, the slope is -1.0008 (E/R) and the intercept is $\ln\left(\frac{AR}{E}\right)$ + 3.7545411– 1.92 ln E.

The distributed activation energy method *(Miura and Maki, 1998)* presented a simple method with which to estimate both *f(E)* and $k_0(E)$ from three sets of experimental data with higher experimental accuracy obtained at different heating rates without assuming functional forms for *f(E)* and $k_0(E)$ as given in Eq. (2.18),

$$\ln\frac{\beta}{T^2} = \ln\left(\frac{k_0 R}{E}\right) + 0.6075 - \frac{E}{RT} \quad (2.18)$$

where 0.6075 – E/RT is the slope and $\ln\left(\frac{k_0 R}{E}\right)$ is the intercept of the equation.

Table 2.6 summarizes the literature on linear model-free and model-fitting kinetic methods chronologically with their significance.

Table 2.6 Summary of literature on linear model-free and model-fitting kinetic methods

Method	Equation	Slope	Intercept	Reference
Van-Krevelen method	$Ln\left(\frac{(1-\alpha)^{1-n}-1}{1-n}\right) = Ln\left(\frac{A}{\beta}\left(\frac{0.368}{T_n}\right)^{\frac{E}{RT}}\left(\frac{1}{\frac{E}{RT_n}+1}\right)\right) + \left(\frac{E}{RT_n}+1\right) Ln\, T$	$\left(\frac{E}{RT_n}+1\right)$	$Ln\left(\frac{A}{\beta}\left(\frac{0.368}{T_n}\right)^{\frac{E}{RT}}\left(\frac{1}{\frac{E}{RT_n}+1}\right)\right)$	*Van Krevelen, 1951*
Kissinger method	$ln\frac{\beta}{Tm^2} = ln\frac{AR}{E} - \frac{E}{RTm}$	$-\frac{E}{R}$	$ln\frac{AR}{E}$	*Kissinger, 1957*
Freeman Carroll method	Y=- $\frac{E}{R}X + n$; Y= $\frac{\Delta \ln\left(\frac{d\alpha}{dt}\right)}{\Delta \ln(1-\alpha)}$; X= $\frac{\Delta\left(\frac{1}{T}\right)}{\ln(1-\alpha)}$	$-\frac{E}{R}$	n	*Freeman and Carroll, 1958*
Horowitz method	ln [-ln (1-α)] = ln [$\frac{ART}{\beta E}$(1- $\frac{2RT}{E}$)] - $\frac{E}{RT}$, n = 1	$-\frac{E}{R}$	ln [$\frac{ART}{\beta E}$(1-$\frac{2RT}{E}$)]	*Horowitz and Metzger, 1963*
Coats Redfern method	$\ln\frac{\beta}{T^2} = \ln\frac{AR}{E.g(\alpha)} - \frac{E}{RT}$	$-\frac{E}{R}$	$ln\frac{AR}{E.g(\propto)}$	*Coats and Redfern, 1964*
od	ln(dα/dt) = ln (A) + ln f (α) - (E/RT)	$-\frac{E}{R}$	Ln (A) + ln f (α)	*Friedman, 1964*
Ozawa-Flynn-Wall method	ln (β) = ln ((A. E)/(f(α)R)) – 5.331 – 1.052 (E/RT)	– 1.052 (E/RT)	ln ((A. E)/(f(α)R))	*Flynn and Wall., 1996; Ozawa, 1965*
Achar-Brindley Sharp method	$\ln\left[\frac{1}{\gamma(1-\alpha(T))}.\frac{d\alpha(T)}{dT}\right]$	$-\frac{E}{R}$	ln $(\frac{A}{\beta})$	*Sharp et al., 1966*
Sharp-Wentworth method	log $[\frac{dc/dT}{(1-c)}] = \frac{\log(A}{\beta}) - [\frac{E}{2.303R}]$. 1/T	$-\frac{E}{2.303R}$	$\frac{\log(A}{\beta})$	*Sharp and Wentworth, 1969*
Madhusudanan method	ln $[\frac{\beta.g(\alpha)}{T^m}]$ = B -C $(\frac{E}{RT})$; m= 1.921503	-1.000956 (E/R)	ln (AR/E) + 3.772050 – 1.921503 ln E	*Madhusudanan et al., 1986*
Kissinger-Akahira-Sunose method	$\ln\frac{\beta}{T^2} = \ln\frac{AR}{E\,g(\propto)} - \frac{E}{RT}$	$-\frac{E}{R}$	$ln\frac{AR}{E\,g(\propto)}$	*Ozawa, 1992*
Kennedy-Clark method	ln $[\frac{\beta.g(\alpha)}{(T-T_0)}]$ = ln A - $\frac{E}{RT}$	$-\frac{E}{R}$	ln A	*Kennedy and Clark, 1997*
Distributed Activation Energy Method	$\ln\frac{\beta}{T^2} = \ln(\frac{k_0R}{E}) + 0.6075 - \frac{E}{RT}$	0.6075 $-\frac{E}{R}$	$\ln(\frac{k_0R}{E})$	*Miura and Maki, 1998*
Li Tang method	ln $[\frac{\beta.g(\alpha)}{T^m}]$ = B - C $(\frac{E}{RT})$; m= 1.894661	-1.00145033 (E/R)	ln $(\frac{AR}{E})$ + 3.63504095 – 1.894661 lnE	*Tang et al., 2003*
Starink method	ln $[\frac{\beta.g(\alpha)}{T^m}]$ = B -C $(\frac{E}{RT})$; m= 1.92	-1.0008 (E/R)	ln $(\frac{AR}{E})$ + 3.75 45411– 1.92 lnE	*Starink, 2003*

2.3.4.4 Significance of non-linear model-fitting kinetic methods

The activation energy, *E*, as a function of the reacted fraction can be determined from iso-conventional methods without any previous assumption on the kinetic model fitted by the reaction. The combined kinetic analysis allows determining the kinetic triplet (*E*, *A*, and *f(α)*) from the simultaneous analysis of a set of different curves measured under any different temperature programs. In this method, the kinetic model is determined in the following general form of Eq. (2.19),

$$f(\alpha) = c(1-\alpha)^n \alpha^m \tag{2.19}$$

This equation can accurately fit every ideal kinetic model *(Khawam and Flanagan, 2006)*. Besides, this equation Eq. (2.19) can also describe deviations of the ideal kinetic models due to inhomogeneities in the shape and size of the solid particles as given in Eq. (2.20),

$$\ln\left(\frac{d\alpha}{dt}\right) - \ln(1-\alpha)^n \alpha^m = \ln(cA) - \frac{E}{RT} \tag{2.20}$$

Values of *n* and *m* that maximize the correlation coefficient, *r* are evaluated, and the values of activation energies and pre-exponential factor are estimated eventually from the slope and intercept of the linear plot respectively. For evaluation of the reaction mechanism, the kinetic model is discriminated by the shape of the *f(α)* function resulting from the optimization procedure *(Perejon et al., 2011).*

Vyazovkin's method confers rate equations by integrating the time or temperature integral in a way that the activation energy is assumed to be constant only over small steps. Vyazovkin's advanced iso-convensational integral method considers the variation of E_α in the computation of the temperature integral. This method overcomes the drawbacks of classical integral methods, applies to any temperature program, and uses a numerical integration of the temperature integral *(Vyazovkin, 2001).* The resulting advanced method allows one to handle a set of *n* experiments carried out under different arbitrary temperature programs, $T_i\ (t)$ as given in Eq. (2.21),

$$J[E_\alpha, \mathrm{T}(t_\alpha)] = \int_{t_{\alpha-\Delta\alpha}}^{t_\alpha} exp^{\frac{-E_\alpha}{RT(t)}} dt \tag{2.21}$$

where *E* is the activation energy (J mol^{-1}), *T* is temperature, *t* is the time at conversion factor, *α* and *R* is the gas constant.

Scott's algorithm assumes a range of mass component fractions characterized by *M(t),* reacting at each assumed first-order parallel reaction. By assuming the range of mass component fractions in the char, the heterogeneity of the reacting compound is considered

(Scott et al., 2006). It is also assumed that a reaction is dominating at a unique conversion when a constant heating rate is applied.

$$\frac{M(t)}{M_0} = w + \sum_i f_{i,0} \exp[-A_i \int_0^{\tau} \exp(-\frac{Ei}{RT(t)})\, dt] = w + \sum f_{i,0} \exp[\int_{x0}^{x} \frac{\delta x}{f(x)}] \quad (2.22)$$

where *M(t)* is the sample mass of the initial value, M_0 containing a fraction w of inert material, $f_{i,0}$ is the initial mass fraction of M_0 which decomposes with E_i and A_i *(Scott et al., 2006).*

Eq. (2.23) stands as a linear matrix problem on the knowledge of reactions occurring with each value of *E* and *A*. The mass of solid fuel remaining at a time is the sum of the masses of each of the components remaining. The equation may then be written in a matrix format such that for any set of times *(t_1, t_2, t_3)* the remaining mass *M(t)* of fuel is given by Eq. (2.23) as,

$$\begin{Bmatrix} \psi_1(t_0) & \psi_2(t_0) & \psi_n(t_0) \\ \psi_1(t_1) & \psi_2(t_1) \ldots & \psi_n(t_1) \\ \psi_1(t_2) & \psi_2(t_2) & \psi_n(t_2) \end{Bmatrix} \begin{matrix} 1 \\ 1 \\ 1 \end{matrix} \text{ x } \begin{Bmatrix} f_{1,0} \\ f_{2,0} \\ f_{3,0} \end{Bmatrix} = \frac{1}{M_0} \begin{Bmatrix} M(t_0) \\ M(t_1) \\ M(t_2) \end{Bmatrix} \quad (2.23)$$

such that M = ψf. When $\frac{dT}{dt} = \beta$,

$$\psi_i(t) = \psi_i(T) = \exp[\frac{-A_i}{\beta} \int_{T_0}^{T} \exp(^{-E_i/RT(t)}) dT] = \quad exp^{\int_x^x \frac{\delta x}{f(x)}} \quad (2.24)$$

Regarding the deconvolution methods, the DTG profile of solid-state material can be separated using symmetric or asymmetric functions. The symmetric functions such as Gaussian, Logistic, Lorentz functions have been investigated by Chen et al. *(Chen et al., 2015)* and Naya et al. *(Naya et al., 2006),* and the asymmetric Weibull, bi-Gaussian, Fraser–Suzuki functions was used by Cai et al. *(Cai et al., 2009)* and Cheng et al. *(Cheng et al., 2014).* Pérez-Maqueda et al. *(Perezon et al., 2011)* considered that the asymmetric functions are more suitable for deconvolution procedures in TGA, especially for the Fraser–Suzuki function.

The activation energy, *E*, as a function of the reacted fraction can be determined from iso-conventional methods without any previous assumption on the kinetic model fitted by the reaction. Different fitting functions have been used for the deconvolution process, namely

Gaussian deconvolution method *(Perejon et al., 2011)* as given in Eq. (2.25),

$$y = a_0 \exp[-\frac{1}{2}(\frac{x-a1}{a2})^2 \quad (2.25)$$

where a_0, a_1, a_2 are amplitude, center, and width of the curve.

Lorentzian deconvolution method *(Perejon et al., 2011)* as given in Eq. (2.26),

$$y = \frac{a_0}{1+(\frac{x-a2}{a2})2} \quad (2.26)$$

where, a_0, a_1, a_2 are amplitude, center, and width of the curve.

Weibull deconvolution method *(Perejon et al., 2011)* as given in Eq. (2.27),

$$y = a_0(a3 - 1/a3)^{(1-a3)/a3}(\frac{x-a1}{a2} + (\frac{a3-1}{a3})^{1/a3})^{a3}\exp[-(\frac{x-a1}{a2} + (\frac{a3-1}{a3})^{1/a3})^{a3}+\frac{a3-1}{a3}] \quad (2.27)$$

where a_0, a_1, a_2, a_3 are amplitude, center, width, and shape of the curve.

Fraser-Suzuki deconvolution method *(Perejon et al., 2011*) as given in Eq. (2.28),

$$y = a_0 exp[-ln2[\frac{ln\,(1+2a_3\frac{x-a_1}{a_2})}{a_3}]^2] \quad (2.28)$$

where, a_0, a_1, a_2, a_3 are amplitude, position, half-width, and asymmetry of the curve.

The Fraser-Suzuki deconvolution method treats the *dα/dT* signal of i-th pseudo component as a Fraser-Suzuki function (FSF) of temperature as given in Eq. (2.29*) (Hu et al., 2016),*

$$\frac{\delta\alpha}{\delta T} = \sum_{i=1}^{3} c_i H_{p,i} \text{ - } \exp(-\frac{ln}{A_{s,i}^2} \ln [1 + A_{s,i}\frac{(T-T_{p,i})}{w_{h,f,i}}]^2 \quad (2.29)$$

where the FSF parameters are H_p, $A_{s,i}$, T_p, w_h denotes height (K), asymmetry (dimensionless), peak temperature (K), and half-width (K) of the peak (K) of *dα/dT* vs. *T* profile for i-th pseudo component, respectively.

1- DAEM was evaluated for Sulcis coal and Russian coal based on global kinetics phenomena from single step kinetics pathway where on the transition towards the gas phase, the particle becomes more porous. This is inherent due to the decomposition of the functional groups to light gas and aliphatic chains producing lighter fragments (tar) *(de Caprariis et al., 2012).* At a constant heating rate, β the pyrolysis reaction starting from a lower temperature, T_0 at a linear heating time, *t* gives Eq. (2.30) as,

$$\frac{v}{v*} = \int_0^{\propto} exp(\frac{-k_0}{\propto}\int_0^T exp(-\frac{E}{RT})\,dT)\,f(E)dE \quad (2.30)$$

where, *v, v** are parameters that indicate volatile released at a time, *t* and total volatile yield loss, α is a constant heating rate, *E* is the activation energy (J mol^{-1}), *T* is temperature, *f(E)* is the distribution function of activation energy, *R* is gas constant, k_0 is pre-exponential factor (sec^{-1}).

2- DAEM (Double Gaussian model) was assumed for pyrolysis with two step kinetics behaviours, the tar and light hydrocarbon gas formation during the primary pyrolysis and the char condensation, cross-linking reactions and a further gas production during the secondary pyrolysis. Two sets of parallel reactions occur, sharing the same pre-exponential factor but not the same distributed activation energy *(de Caprariis et al., 2012).* The 2-DAEM equation can be written as in Eq. (2.31),

$$1-\frac{v}{v*} = \int_0^{\propto} exp(\frac{-k_0}{\propto}\int_0^T exp(-\frac{E}{RT})\,dT)\,(\mathrm{w}f_1(E) + (1-w)f_{2\,(E)})\,\mathrm{dE} \quad (2.31)$$

where, w is a parameter that weighs reaction classes varying from 0 to 1, *v, v** are parameters that indicate the volatiles released at the time, *t* and total volatile yield loss, α is a constant heating rate, *E* is the activation energy (J mol^{-1}), *T* is temperature, *f(E)* is the distribution function of activation energy, *R* is gas constant, k_0 is a pre-exponential factor (sec^{-1}).

3-DAEM is developed by assuming that the pyrolysis process occurs in three stages with different kinetic behaviors and kinetic distribution (three sets of parallel reactions with the same pre-exponential factor with different distributed activation energy) *(Wang et al., 2016)* as given in Eq. (2.32),

$$1-\frac{v}{v*} = \int_0^{\propto} exp(\frac{-k_0}{\propto}\int_0^T exp(-\frac{E}{RT})\,dT)\,(\mathrm{w}f_1(E) + (w)_2 f_{2\,(E)}) + (1-w_1-w_2)\,f_3(E)]\,dE) \quad (2.32)$$

where, w is a parameter that weighs reaction classes varying from 0 to 1, *v, v** are parameters that indicate the volatiles released at the time, *t* and total volatile yield loss, α is a constant heating rate, *E* is the activation energy (J mol^{-1}), *T* is temperature, *f(E)* is the distribution function of activation energy, *R* is gas constant, k_0 is a pre-exponential factor (sec^{-1}).

Non-isothermal nth- DAEM pyrolysis of forest waste using the Gaussian distribution and the asymptotic solution was proposed by Vand *(Vand, 1943)* and adopted in coal devolatilization by Pitt *(Pitt, 1962)* postulates that the decomposition mechanism takes a large

number of independent, parallel, and the first order chemical reactions with different activation energies exhibiting variation in the bond strength of constituent species of biomass. The non-isothermal nth order DAEM is given in Eq. (2.33) as,

$$1-\mathrm{X} = \int_0^{\propto}[1-(1-n)\int_{T_0}^T \frac{A}{\beta} exp(-\frac{E}{RT})\,dT)]^{1-n}\,f(E)dE \quad (2.33)$$

where *E* is the activation energy, β is the heating rate, *A* is the frequency factor, *R* is the ideal gas constant, *n* is the reaction order, *T* is absolute temperature, T_o is the initial reaction temperature, *X* is the conversion rate and *f(E)* is the initial distribution function of activation energies *(Dhaundiyal and Singh, 2016)*.

Considering a parabolic increase of temperature with time, the Ø function can be written as given in Eq. (2.34) *(Soria et al., 2016),*

$$T = b.t^2 = \text{Ø}\,(\mathrm{E,\,T}) = \exp\,(\frac{k_0}{2\,(b^{1.5})}\int_0^T (\frac{e^{\frac{-E}{RT}}}{T^{1.5}}dT)) \quad (2.34)$$

The Ø function can be approximated as given in Eq. (2.35),

$$\text{Ø}\,(\mathrm{E,\,T}) = \exp\,(\frac{k_0\,RT^{1.5}}{2\,(bE)^{0.5}}e^{-\frac{E}{RT}}) \quad (2.35)$$

The Arrhenius equation for a parabolic temperature profile is obtained as in Eq. (2.36),

$$ln\frac{(b)^{0.5}}{(T)^{1.5}} = ln\left(\frac{k_0 R}{2E_\alpha}\right) - \ln\left[-\ln\left(\emptyset_{par}\right)\right] - \frac{E_\alpha}{RT} \quad (2.36)$$

where E is the activation energy, k_0 is the frequency factor, R is the ideal gas constant, and T is the absolute temperature.

The $\emptyset$ function for an exponential temperature increase is expressed as in Eq. (2.37),

$$T = c_0.exp^{ct} = \emptyset\ (E, T) = \exp\left(\frac{k_0}{c}\int_0^T \left(\frac{e^{\frac{-E}{RT}}}{T}dT\right)\right) \quad (2.37)$$

The $\emptyset$ function can be approximated as given in Eq. (2.38),

$$\emptyset\ (E, T) = \exp\left(\frac{k_0\ RT}{cE}e^{-\frac{E}{RT}}\right) \quad (2.38)$$

The Arrhenius equation for an exponential temperature profile is obtained as in Eq. (2.39),

$$ln\frac{c}{T} = ln\left(\frac{k_0 R}{E_\alpha}\right) - \ln\left[-\ln\left(\emptyset_{exp}\right)\right] - \frac{E_\alpha}{RT} \quad (2.39)$$

Where E is the activation energy, k_0 is the frequency factor, R is the ideal gas constant, and T is the absolute temperature.

The Gaussian form of DAEM is explicated to obtain kinetic values over an activation energy distribution function. However, it is not appropriate to indicate the initial and final stages of the thermal decomposition process. In this regard, the logistic form of DAEM with slightly thicker tails in the logistic curve function is used to analyze the thermal decomposition process *(Dong et al., 2018).* To better describe the thermal decomposition of solid fuels, which involves two subprocesses, the double logistic distribution is used to represent the activation energy distribution as given in Eq. (2.40 - 2.42),

$$f\ (E) = w\ f_1\ (E) + (1- w)\ f_2\ (E) \quad (2.40)$$

$$f_1(E) = \frac{\pi}{\sqrt{3\pi}\sigma_1}\frac{exp\left[-\pi\left(E-\mu_1\right)/(\sqrt{3}\sigma_1)\right]}{\{1+\exp[-\pi\frac{E-\mu_1}{\sqrt{3\sigma_1}}]\}^2} \quad (2.41)$$

$$f_2(E) = \frac{\pi}{\sqrt{3\pi}\sigma_1}\frac{exp\left[-\pi\left(E-\mu_2\right)/(\sqrt{3}\sigma_2)\right]}{\{1+\exp[-\pi\frac{E-\mu_2}{\sqrt{3\sigma_2}}]\}^2} \quad (2.42)$$

where, w is a constant, 0<w<1, μ is the mean value (J mol^{-1}), σ is the standard deviation of E, and 1, 2 represent the value of first and second subprocesses.

Since the assignment of the Gaussian distribution to *f(E)* does not always reflect real situations, a discrete distribution for the global devolatilization was proposed by Giuntoli et al. *(Guintoli et al., 2009).* Eq. (2.43) can be rewritten as given in Eq. (2.43) *(He et al., 2020),*

$$1-\frac{v}{v*} = \sum_{i=0}^{n}\phi\ (E_i, T)\ D\ (E_i) \quad (2.43)$$

where *v, v** are parameters that indicate the volatiles released at time, *t,* and total volatile yield loss, α is a constant heating rate, *E* is the activation energy (J mol^{-1}), *T* is temperature, and *D* (E_i) is the discrete distribution function.

For the dissociation profiles of solid fuels obtained during char conversion, typical solid reaction models applicable for gas-solid reactions are used as grain model, random pore model (RPM), and shrinking core model (SPM). De Micco gives an overall expression to char conversion *(De Micco et al., 2012)* as given in Eq. (2.44),

$$r = \frac{dx}{dt} = k(T)G\left(C_g\right)f\left(x\right) \tag{2.44}$$

where *r* is the instantaneous char reactivity, $G(C_g)$ is a parameter related to the concentration of the gaseous reactant, *f(x)* is the reaction model, and *k(T)* is a function of temperature.

The grain model or homogeneous or volume reaction model is based on the assumption that the reaction takes place homogeneously throughout the char particle *(Seo et al., 2010*) as given in Eq. (2.45),

$$f(x) = 1 - x \tag{2.45}$$

The random pore model (RPM) is based on pore size distribution with randomly interconnected/overlapping sets of cylindrical pores *(Rafsanjani and Jamshidi, 2008).* It describes the competitive mechanism of surface area increase and decrease related to pore growth and intersection, as the reaction proceeds *(Bhatia and Vartak, 1996).* Eq. (2.46) expresses the RPM model,

$$f(x) = \frac{S_0}{1-\varepsilon_0}(1-x)\sqrt{1-\emptyset\ln(1-x)} \tag{2.46}$$

where, $\emptyset = \frac{4\pi L0\ (1-\varepsilon 0)}{S_0^2}$

where, S_0 is initial area per unit volume, ε_0 is the initial porosity of the material and L_0 initial pore segment of length per unit volume.

The shrinking core model (SCM) is based on the assumption that the reaction occurs on the char's external surface and gradually moves inside *(Seo et al., 2010).* The space between an assembly of non-uniform grains constitutes the porous network *(Lu, 1994)* where shrinking core behavior applies to those grains. However, as the reaction proceeds, the micro pores begin to coalesce into larger macro-pores and meso-pores, hence reducing the surface area and reaction rate. The expression is given in Eq. (2.47) as,

$$f(x) = \frac{S_0\ (1-x^h)}{(1-\varepsilon_0} \tag{2.47}$$

where, S_0 is initial surface per unit volume, Ɛ is initial porosity, and h is the shape factor dependent on grain geometry. Table 2.7 gives the summary of the literature on the evolution of such non-linear model fitting methods.

Table 2.7 Summary of literature on the evolution of non-linear model-fitting kinetic methods

Method	Equation	Parameters	Reference
Vyazovkin's Method	$J[E_\alpha, T(t_\alpha)] = \int_{t_{\alpha-\Delta\alpha}}^{t_\alpha} exp^{\frac{-E_\alpha}{RT(t)}} dt$	E is the activation energy (J/mol), T is temperature, t is the time at conversion factor, α, and R is the gas constant	*Vyazovkin, 2001*
Scott's algorithm	$\frac{M(t)}{M_0} = w + \sum_i f_{i,0} \exp[-A_i \int_0^\tau \exp(-\frac{Ei}{RT(t)})\, dt] = w + \sum f_{i,0} \exp[\int_{x0}^{x} \frac{\delta x}{f(x)}]$	$M(t)$ is the sample mass of the initial value, M_0 containing a fraction w of inert material, $f_{i,0}$ is the initial mass fraction of M_0 which decomposes with E_i and A_i	*Scott et al., 2006*
Gaussian deconvolution method	$y = a_0 \exp[-\frac{1}{2}(\frac{x-a1}{a2})^2$	a_0, a_1, a_2 are the amplitude, center, and width of the curve	*Perejon et al., 2011*
Lorentzian deconvolution method	$y=\frac{a_0}{1+(\frac{x-a2}{a2})2}$	a_0, a_1, a_2 are the amplitude, center, and width of the curve	*Perejon et al., 2011*
Weibull deconvolution method	$y = a_0(a3 - 1/a3)^{(1-a3)/a3}(\frac{x-a1}{a2} + (\frac{a3-1}{a3})^{1/a3})^{a3} \exp[-(\frac{x-a1}{a2} + (\frac{a3-1}{a3})^{1/a3})^{a3} + \frac{a3-1}{a3}]$	a_0, a_1, a_2, a_3 are amplitude, center, width, and shape of the curve	*Perejon et al., 2011*
Fraser-Suzuki deconvolution method	$y = a_0 exp[-ln2[\frac{ln(1+2a_3\frac{x-a_1}{a_2})}{a_3}]^2]$	a_0, a_1, a_2, a_3 are amplitude, position, half-width, and asymmetry of the curve	*Perejon et al., 2011*
Fraser-Suzuki deconvolution method	$\frac{\delta\alpha}{\delta T} = \sum_{i=1}^{3} c_i H_{p,i} \exp(-\frac{ln}{A_{s,i}^2} \ln[1 + A_{s,i}\frac{(T-T_{p,i})}{w_{h,f,i}}]^2$	H_p, $A_{s,i}$, T_p, w_h denotes height (K), asymmetry (dimensionless), peak temperature(K), and half-width (K) of the peak (K) of $d\alpha/dT$ vs. T profile for i-th pseudo component	*Hu et al., 2016*

(Conitnued)

1- Distributed Activation energy Model (1-DAEM)	1- $\frac{v}{v*} = \int_0^{\propto} exp(\frac{-k_0}{\propto} \int_0^T exp(-\frac{E}{RT})\, dT)\, f(E) dE$	v, v* are parameters that indicate the volatiles released at the time, *t* and total volatile yield loss, *α* is a constant heating rate, *E* is the activation energy (J mol^{-1}), *T* is temperature, *f€* is the distribution function of activation energy, *R* is gas constant, k_0 is a pre-exponential factor (s^{-1})	*de Caprariis et al., 2012*
2- Distributed Activation energy Model (2-DAEM)	1- $\frac{v}{v*} = \int_0^{\propto} exp(\frac{-k_0}{\propto} \int_0^T exp(-\frac{E}{RT})\, dT)\, (\mathrm{w} f_1(E) + (1-w) f_{2\,(E)})\, \mathrm{dE}$	*w* is a parameter that weighs reaction classes varying from 0 to 1, *v, v** are parameters that indicate the volatiles released at the time, *t* and total volatile yield loss, *α* is a constant heating rate, *E* is the activation energy (J mol^{-1}), *T* is temperature, *f€* is the distribution function of activation energy, *R* is gas constant, k_0 is a pre-exponential factor (s^{-1})	*de Caprariis et al., 2012*
3- Distributed Activation energy Model (3-DAEM)	1- $\frac{v}{v*} = \int_0^{\propto} exp(\frac{-k_0}{\propto} \int_0^T exp(-\frac{E}{RT})\, dT)\, (\mathrm{w} f_1(E) + (w)_2 f_{2\,(E)}) + (1- w_1\text{-}w_2)\, f_3(E)]\, dE$	w is a parameter that weighs reaction classes varying from 0 to 1, are parameters that indicate the volatiles released at the time, *t* and total volatile yield loss, *α* is a constant heating rate, *E* is the activation energy (J mol^{-1}), *T* is temperature, *f€* is the distribution function of activation energy, *R* is gas constant, k_0 is a pre-exponential factor (s^{-1})	*Wang et al., 2016*

(Continued)

n-order Distributed Activation energy Model (n^{th} DAEM)	$1\text{- X} = \int_0^{\infty}[1-(1-n)\int_{T_0}^{T}\frac{A}{\beta}exp(-\frac{E}{RT})\,dT)]^{1-n}\,f(E)dE$	where E is the activation energy, β is the heating rate, A is the frequency factor, R is the ideal gas constant, n is the reaction order, T is absolute temperature, To is the initial reaction temperature, X is the conversion rate and $f(E)$ is the initial distribution function of activation energies	*Dhaundiyal and Singh, 2016*
Exponential form of DAEM	$ln\frac{c}{T} = ln(\frac{k_0R}{E_\alpha}) - \ln[-\ln(\emptyset_{exp})] - \frac{E_\alpha}{RT}$	where E is the activation energy, k_0 is the frequency factor, R is the ideal gas constant, T is the absolute temperature	*Soria-Verdugo et al., 2016*
Parabolic form of DAEM	$ln\frac{(b)^{0.5}}{(T)^{1.5}} = ln(\frac{k_0R}{2E_\alpha}) - \ln[-\ln(\emptyset_{par})] - \frac{E_\alpha}{RT}$	where E is the activation energy, k_0 is the frequency factor, R is the ideal gas constant, T is the absolute temperature	*Soria-Verdugo et al., 2016*
Double Logistic Distributed Activation Energy Model	$f(E) = w\,f_1(E) + (1-w)\,f_2(E)$, where $f_1(E) = \frac{\pi}{\sqrt{3\pi}\sigma_1}\frac{exp\,[-\pi\,(E-\mu_1)/(\sqrt{3}\sigma_1)]}{\{1+\exp[-\pi\frac{E-\mu_1}{\sqrt{3\sigma_1}}]\}^2}$ $f_2(E) = \frac{\pi}{\sqrt{3\pi}\sigma_1}\frac{exp\,[-\pi\,(E-\mu_2)/(\sqrt{3}\sigma_2)]}{\{1+\exp[-\pi\frac{E-\mu_2}{\sqrt{3\sigma_2}}]\}^2}$	w is a constant, 0<w<1, μ is the mean value (J mol^{-1}), σ is the standard deviation of E and 1, 2 represent the value of the first and second subprocesses	*Dong et al., 2018*
Discrete Distributed Activation Energy Model	$1-\frac{v}{v*} = \sum_{i=0}^{n}\phi\,(E_i,T)\,D(E_i)$	v, v^* are parameters that indicate the volatiles released at time, t and total volatile yield loss, α is a constant heating rate, E is the activation energy (J mol^{-1}), T is temperature, $D(E_i)$ is the discrete distribution function.	*He et al., 2020*

(Continued)

Char gasification models

Random pore model,	$f(x) = \frac{S_0}{1-\varepsilon_0}(1\text{- x})\sqrt{1-\emptyset \ln(1-x)}$ Where, $\emptyset = \frac{4\pi L0\ (1-\varepsilon 0)}{S_0^2}$	S_0 is the initial area per unit volume ε_0 is the initial porosity of the material L_0 is initial pore segment length per unit volume	*Bhatia and Perlmutter, 1981*
Grain model	$\frac{d\propto}{dt} = k_{VRM}\ (1\text{- }\alpha)$ $\alpha = 1 - \exp\ (-\ (A_0 \exp\ (\frac{-E}{RT})\ t)\ (1 + \frac{A1}{4} \exp\ (-$ E/RT) t) where, $A_0 = \frac{k_0\ C^n\ S_0}{1-\epsilon 0}$, $A_1 = \frac{4\pi L_0 k_0\ C^n}{S_0}$	α is conversion, A_0, A_1 are surface pore parameters, k_{VRM} is the pre-exponential factor, E is activation energy (kJ mol^{-1}), R is gas constant, T is the temperature (K)	*Seo et al., 2010*
Shrinking core model	$f(x) = \frac{S_0\ (1-x^h)}{(1-\varepsilon_0}$	S_0 is initial surface per unit volume, $\mathcal{E}$ is initial porosity, h is shape factor dependent on grain geometry	*Homma et al., 2005*

2.4 Review on reaction kinetics and thermodynamics

Thermogravimetric analysis is a suitable technique to observe pyrolysis kinetics and thermodynamics. Various iso-conversional and non-iso- conversional integral methods could be bought to light in the review of kinetic modeling studies. In place of differential methods where there is a variation in the temperature term, accuracy can be limited due to variations in the reaction temperature of the experimental data and baseline determination inefficacy *(Sbirrazzouli, 2013)*. The integral methods consider a fixed temperature integral approximation and render stable calculations for kinetic exponents making it more reliable and accurate to use *(Sbirrazzouli, 2013)*. The kinetics and thermodynamics of coal-biomass co-pyrolysis using model-free integral methods are reported by various authors *(Guo et al., 2017, Aboyade et al., 2013, Idris et al., 2010, Vuthaluru et al., 2004, Biagini et al., 2002)*. Guo et al. studied Zhundong lignite and pine sawdust co-pyrolysis in a micro-fluidized reactor at a temperature of 1173 K and achieved varied activation energies for the individual producer gas components *(Guo et al., 2017)*. Aboyade et al. studied the co-pyrolysis of sugarcane bagasse and corn stalks blended with coal in a thermogravimetric analyzer. It was stated that the reaction favored synergistic interactions till the devolatilization of biomass occurred during the co-pyrolysis experiment. The iso-conversional model-free kinetic

analysis in the study revealed that apparent activation energy values were varied between 165–180 kJ mol^{-1} for sugarcane bagasse, 162–190 kJ mol^{-1} for corn cob, 160–175 kJ mol^{-1} for corn stover, and 225–260 kJ mol^{-1} for coal in between 10-80 % conversion range. This study also revealed that blending of biomass to coal produced about 7–11 % higher volatile yields (on a dry and ash-free basis) than the coal shows a purely additive behavior of biomass *(Aboyade et al., 2013).* Idris et al. studied Malaysian low-rank coal and empty fruit brunches co-pyrolysis from 303–1173 K temperature and achieved variable activation energies at different stages of conversion by the Kissinger equation *(Idris et al., 2010).* Table 2.8 shows a summary of the literature on reaction kinetic parameters for co-pyrolysis of coal/biomass mixtures.

Table 2.8 Summary of literature on reaction kinetic parameters for co-pyrolysis of coal/biomass mixtures

Feed	Blend, %	Reactor	Process conditions	Thermal event	Kinetic model equation	E_a, kJ mol^{-1}	*n*	Reference
Zhundong Lignite and Pine Sawdust (particle size: 150 – 250 µm)	Biomass mass ratios of 100, 75, 50, 25, and 0% (weight %, dry basis)	Micro-fluidized bed reactor equipped with a mass spectrometer	Temperature : 1173 K, Purge gas: Argon (~99.9 % purity) (300 mL min^{-1})	G3 (Three-dimensional diffusion (Jander)	$\ln [k(T)] = \frac{-E}{RT} + \ln(A)$; where E_a is the apparent activation energy (kJ mol^{-1}), A: pre-exponential factor (s^{-1}), T: temperature (K), and R: gas constant (8.314 J $mol^{-1} K^{-1}$)	E_{H2}: 63.9, 57.0, 46.6, 58.5, 39.5, E_{CO}: 32.5, 27.0, 20.7, 23.0, 27.1, E_{CO2}: 18.3, 21.8, 19.9, 17.1, 23.4, E_{CH4}: 30.7, 23.9, 31.4, 26.5, 19.8	-	*Guo et al., 2017*
				Order-based model (n = 3/2)		E_{H2}: 64.2, 57.6, 48.7, 59.1, 40.0, E_{CO}: 33.1, 27.2, 21.3, 26.0, 27.2, E_{CO2}: 19.8, 21.9, 20.4, 20.6, 25.2, E_{CH4}: 31.0, 24.4, 35.3, 26.8, 18.7	-	
A blend of low-grade South African hard coals and sugarcane bagasse (particle size: < 212 µm)	Coal: biomass: 100:0, 90:10, 80:20, 60:40, 0:100	Mettler Toledo TGA/DCS 1 analyzer	Temperature : 303 – 1173 K, Heating rate of single fuel samples: 5, 10, 20, 30,	Conversion range: 0.1 – 0	$t_\alpha = \frac{\frac{1}{\beta} exp \int_{T_0}^{T_\alpha} exp^{-\frac{E}{RT}}}{exp^{\frac{E}{RT}}}$	245.6, 240, 183, 173, 165 180	-	*Aboyade et al., 2013*

(Continued)

Blend of low-grade South African hard coals and biomass corn cob (particle size: < 212 µm)			40, 50 and 150 °C min^{-1}, Blended samples: 5, 10 and 50 °C min^{-1}, Purge gas: 150 mL min^{-1}			245.6, 170 – 246, 179 – 283, 180 -240, 162 – 190	-	
The blend of low-grade South African hard coals and corn stover (particle size: < 212 µm)						245.6, 160 - 175	-	
Malaysian low-rank coal and biomass, empty fruit brunches (particle size: < 212 µm)	Biomass: coal: 0:100, 20:80, 40:60, 50:50, 60:40, 80:20, 100:0	Mettler Toledo TGA/SD RA51e thermobalance	Temperature: 303 - 1173 K, Heating rates: 10, 20, 40 and 60 K min^{-1}	I	Kissinger equation: $ln\frac{\beta}{Tm^2} = ln\frac{AR}{E} - \frac{E}{RTm}$; β is the heating rate, A is the pre-exponential factor, R is the gas constant, T_m is the peak temperature (K), E_a is the activation energy (kJ mol^{-1})	-	-	*Idris et al., 2010*
				II		0, 181.55, 189.92, 194.11, 207.12, 226.85, 209.68	-	
				III		272.88, 266.61, 263.60, 262.95, 243.24, 239.13	-	
				IV		-	-	
Malaysian low-rank coal and biomass palm kernel shell (particle size: < 212 µm)				I		0, 138.97, 137.84, 142.72, 144.66, 149.59, 150.13	-	
				II		0, 174.35, 176.43, 176.43, 187.64, 186.35, 192.12	-	
				III		272.88, 254.93, 264.34, 261.69, 233.97, 223.72, 0	-	
				IV		0, 234.74,	-	

						251.29, 245.79, 255.61, 260.58, 277.11		
Malaysian low-rank coal and biomass, palm mesocarp fibre (particle size: < 212 µm)				I		0, 157.71, 161.48, 162.55, 163.83, 165.64, 166.24	-	
				II		0, 198.19, 202.59, 206.97, 202.62, 205.55, 216.10	-	
				III		272.88, 258.71, 271.37, 266.04, 263.66, 262.84, 0	-	
				IV		-	-	
Collie coal from Western Australia (particle size: ~ 1 mm, biomass wood waste (particle size: ~1 mm)	Coal/ wood waste = 50:50, 0:100	NETZSCH Simultaneous Thermal Analyzer STA 409 C (TGA-MS)	Temperature: 303 – 1523 K, Heating rate: 20 K min^{-1}, Purge gas: Argon (50 mL min^{-1})	I	$\frac{d\propto}{dt} = \frac{A}{\emptyset} exp_{RT}^{-E}(1-\propto)^n$; where α: conversion of reactant, t (min): time, A (min^{-1}): pre-exponential factor (frequency factor), $\emptyset$: heating rate (K min^{-1}), E_a (J mol^{-1}): activation energy, R (J mol^{-1} K^{-1}): universal gas constant (8.314), T (K): temperature, n is the reaction order.	46.9, 64.9	0.22, 0.4	*Vuthaluru, 2004*
	Coal/ wood waste = 90:10, 80:20, 70:30, 50:50			II		115.3, 90.9, 99.1, 135.4, 118	1.6, 0.46, 0.4, 0.62, 0.42	
	Coal/ wood waste = 100:0, 50:50, 30:70, 20:80, 10:90			III		183.6, 59.9, 54.4, 76.9	1.07, 0.38, 0.38, 0.36	
Collie coal from Western	Coal/ wheat straw =			I		68.7, 80.2	0.85, 0.8	

Australia (particle size: ~ 1 mm, biomass wheat straw (particle size: ~1 mm)	50:50, 0:100							
	Coal/ wheat straw = 90:10, 80:20, 70:30, 50:50, 0:100			II		124.3, 78.7, 119.6, 123.9, 114.8	0.41, 0.21, 0.42, 0.44, 0.52	
	Coal/ wheat straw = 100:0, 50:50, 30:70, 20:80, 10:90			III		183.6, 76.9, 49.9, 68	0.48, 0.24, 0.39	
Two coal samples, Coal US and coal, JW, two biomasses, pine sawdust and biogras	Coal US, Coal JW, Pine sawdust, Biogran: (100% wt.%)	Mettler TA 3000 system	Temperature : 373 – 1173 K, Heating rate: 20 K min^{-1}, Purge gas: Nitrogen (300 mL min^{-1})	Isothermal conversion: 50%	Single first-order reaction ($\frac{-dW}{dt} = k\,(W - W\infty)$; where W is the mass of the sample, $W\infty$ = W_{ash} + W_{char} is the final solid residue of the sample, k is the Arrhenius rate constant	38.6, 24.6, 29.1, 21.2	-	*Biagini et al., 2002*
				Isothermal conversion: 90%		32.8, 22.5, 24.4, 18.1	-	

2.5 Review of emerging heterogeneous catalysts for catalytic pyrolysis of biomass

In Section 2.5, an extensive review is comprehensively indulged upon emerging heterogeneous catalysts for catalytic pyrolysis of biomass feedstocks. The catalytic upgradation of biomass is precariously substantiated by the application of bulk and supported catalysts into the biomass mixture, thus increasing the liquid oil and gas yield.

Pyrolysis is an energy-intensive process with peculiar thermodynamic characteristics. The major products of biomass pyrolysis, when purged into a non-oxidative thermal

degradation environment, are liquid bio-oil, gas products and solid biochar *(Kan et al., 2016)*. These products have myriad implementations in the industry due to their highly prominent properties *(Kumar and Strezov, 2021)*. CH_4, C_nH_m and H_2 are the predominant energy fuels, and CO and H_2 in the ratio of 1:1 can be sufficed as a major component of syngas or power-gas *(Kumar and Strezov, 2021, Bridgewater, 2003)*. However, bio-oil was devoid of the prime fuel properties of ideal content of oxygen and water and acidity inherent in a fuel. Lower calorific value, lesser thermal stability and poor immiscibility with petroleum oils were other dismal fuel characteristics of bio-oil *(Kumar and Strezov, 2021, Chai et al., 2020)* as compared to fossil fuels, lesser thermal stability and substantial viscosity and acidity rendering it immiscible with traditional liquid fuels as pointed out by Zheng et al. *(Zheng et al., 2022)*. Zheng et al. also showed that this is precariously substantiated since lighter aromatic hydrocarbons such as benzene, toluene, and xylene (BTX), the basic organic compounds present in fossil fuels have minimal usage as a carbon neutral precursor in fine chemicals generation as compared to bio-based fuel products *(Zheng et al., 2022)*.

A plethora of studies have suggested the myriad applications of catalysts in biomass pyrolysis. The introduction of a catalyst to the biomass system decreases the temperature of its degradation and removes oxygen through various reactions such as dehydration, decarbonylation, and decarboxylation *(Hernando et al., 2018)*. Metal oxides act as supporters, promoters, and active components (enhanced acid, base, specific surface area, and pore size distribution properties) due to lattice imperfections such as planar defects and electron holes *(Wang et al. 2017)* in such reactions. In the reforming and pyrolysis reactions of biomass, various supports are usually used such as Al_2O_3, SiO_2, TiO_2, CeO_2, MgO, Cr_2O_3, and ZrO_2. Al_2O_3 supports which have high surface areas and high mechanical crushing strength have many Lewis acid sites. It has a high-water retention capacity (30 wt.%) and oxidizes metallic precursors to their oxide form in the presence of an excess amount of water causing catalyst deactivation. However, Al_2O_3 supported Ni-based catalyst is reviewed to have higher activity than nickel supported on MgO, TiO_2, CeO_2, ZrO_2, and SiO_2 *(Furusawa et al., 2013, Santamaria et al., 2018)*. In addition to serving as an exemplary observation, Al_2O_3 and SiO_2-Al_2O_3 (acidic metal oxides) and MgO and CaO (basic metal oxide), transition metal oxides (NiO, CuO, MoO_3, CoO) have been strikingly studied. This could catalytically crack organic molecules into lighter aromatic molecules *(Wang et al. 2017)*. Ly et al. worked on bamboo biomass, which was subjected to a pyrolytic temperature from 400-550 ^oC in a bubbling fluidized bed reactor using nitrogen (100 g/h) as the purge gas and also subjected to catalytic pyrolysis of biomass, HZSM-5, and red mud. The thermal pyrolytic oil was obtained

as 53.44 % at 475ºC and decreased to 45.77 % as the temperature increased to 550ºC. Contrary to the char, the gas yield increased from 18.62-28.59 wt. %; and reached the highest value at 550°C. Upon catalytic pyrolysis of bamboo biomass, red mud catalyst gave the highest oil yield of 50.34 % because it promotes de-methoxylation and improves the production of saturated phenol. However, HZSM-5 promoted the formation of aromatic compounds and methoxy phenolic groups with 49.14 % liquid yield due to cracking of the pyrolysis vapor into lower molecular compounds and non-condensable gas, followed by the deoxygenation through dehydration, decarboxylation, and decarbonylation *(Ly et al., 2020).* Ni-based catalysts are reactive in the following order in the pyrolysis process: Ni-Cu/CeO_2> Ni-Cu/Al_2O_3>Ni/Al_2O_3>Ni/ZrO_2>Ni-Cu/ZrO_2>Ni/SiO_2>Ni/Cr_2O_3. However, Ni-based alumina-supported catalysts are highly favorable for reforming volatiles from biomass pyrolysis *(Ren et al., 2022).* Liu et al. studied the isothermal pyrolysis of rice husk catalyzed by Ni and Fe affecting the kinetics (mainly activation energies) of the evolved gas components *(Liu et al., 2017).* With the inclusion of Fe and Ni contents into the biomass pyrolysis mix, CO_2 and H_2 gases were promoted while CH_4 was inhibited. The apparent activation energies for H_2 and CO_2 reduced from 91.15-67.72 kJ mol^{-1} and 35.15-30.44 kJ mol^{-1} for Fe catalyzed rice husk and 91.15 - 55.13 kJ mol^{-1} and 35.15-33.99 kJ mol^{-1} for Ni catalyzed rice husk, while CO increased from 34.50 - 37.15 kJ mol^{-1} and CH_4 increased from 40.65–51.71 kJ mol^{-1} in the presence of Fe catalyzed rice husk. However, in the presence of Ni-catalyzed rice husk CH_4 increased from 40.65–46.65 kJ mol^{-1}, while CO decreased from 34.50–30.26 kJ mol^{-1}. Nickel catalysts are extensively used in the methanation of the carbon-dioxide process where candidate supports such as alumina with a substantive surface area and thermal stability characteristics were potentially applied. A one-step strategy incorporating the EISA method was developed by Xu et al. for mesoporous support with effective metal-support interaction *(Xu et al., 2017).* The method of partial hydrolysis devoid of any organic, alkaline surfactants was incorporated by Lin et al. into mesoporous γ-Al_2O_3 support to destabilize the sintering of active metallic Ni sites on the support. The incorporation of a higher number of NiO species into the Ni/MA catalyst accentuated the degree of active metallic nickel sites *(Lin et al., 2019).* Li et al. studied supported nano-catalysts, Ni/Al_2O_3 and Ni-La-Fe/Al_2O_3 for sawdust pyrolysis reaction and achieved >99 % tar conversion *(Li et al., 2008, 2009).* Another reported study of thermal pyrolysis and catalytic upgradation of pine wood sawdust over H-ZSM 5 (Si/Al=38) was studied over a temperature range of 773–973 K for thermal pyrolysis and catalytic upgradation experiment at ~873 K. It was observed that the liquid yields increased to a maximum 55.28 % at 873 K and further decreased as the

temperature increased. The highest gas (28.81 %) and char (22.86 %) yield was achieved at 973 K and 773 K respectively. Liquid yield was reduced from 50–55 % for thermal pyrolysis to 35−45 % after catalytic upgrading by H-ZSM 5. The the highest liquid yield was achieved at the highest catalyst bed temperature, with a maximum yield of 45.43 % at 370°C and a C/B ratio of 1:1 (H-ZSM5; Si/Al= 38)) since catalytic upgrading removes oxygen in the form of water, carbon dioxide, and carbon monoxide. Catalytic upgrading with H-ZSM5 decreased the yield of ketones, aldehydes, phenols, and alcohols with conventional heating and furfurals with inductive heating as compared to thermal pyrolysis of pinewood sawdust biomass. The use of a catalyst produces a higher yield of nonoxygenated hydrocarbons, such as aromatic hydrocarbons (C_5–C_{10}). These hydrocarbons have a higher-octane number (comparative to those of petroleum fuel) and are of interest for fuel replacement and additives *(Muley et al., 2015).* Zheng et al. reviewed the integration of catalyst materials, H-ZSM-5-30, ZSM-5, Ni/ZSM-5, Ni/ZSM-5, Ni-Ce/HZSM-5 into the biomass pyrolytic systems, pine wood sawdust, pine, pine, Jatropha residues and sugarcane bagasse in its synergistic action with the feedstock, higher reactivity by stabilizing free radical fragments occurring on account of homolytic and heterolytic free radical substitution reactions and increasing the yield of highly selective products of benzene, toluene and xylene yields (23.1 %, 30.1 %, 13.9 %), (20.8 %, 37.1 %, 38.0 %), (7.4 %, 10.6 %, 10.0 %) and aromatic yields of 20.9 % and 13.8 % respectively. Zheng et al. stated that when biomass is thermally cracked, the free radical intermediates undergo numerous competitive reactions which makes it susceptible to coupling reactions, rearrangement and polymerization reactions *(Zheng et al., 2022).* Zheng et al. observed that due to the higher oxygen content and lesser hydrogen content in biomass (less H/C ratio and higher O/C ratio), minimal levels of hydrogen molecules are donated into the thermal pyrolysis system producing less bio-oil yield and more of detrimental coke. The hydrogen donor precursors are supplemented by such catalytic materials, which also serve as a bottleneck in the enhancement and the catalytic upgradation of bio-oil for producing specific targeted products *(Zheng et al., 2022).*

The physicochemical characteristics of Ni/Al_2O_3 catalysts are reviewed by several researchers who reported on biomass pyrolysis, reforming of volatiles, and reforming of methane. Nandini et al. reported Ni/Al_2O_3 catalyst with different Ni loading values (2, 5, 7, 10, 15 and 20 wt. %) by impregnation technique for stable CO_2 reforming of CH_4. XRD patterns revealed weak nickel diffraction peaks due to the formation of $NiAl_2O_4$ spinel from NiO and Al_2O_3 support. Nickel crystallites having diameters of less than 3 nm cannot be

observed by XRD. This is because, as the catalytic reaction proceeds, some of the $NiAl_2O_4$ would be reduced to Ni under the reaction atmosphere. However, with increasing Ni loading, surface area and pore volume decreased considerably from 227.8-119.4 m^2 g^{-1} and 0.367–0.268 m^3 g^{-1} respectively. They exhibited type IV isotherm with hysteresis loop of type IV with a mesoporous structure *(Nandini, 2005).*

Despite having a deluge of studies on catalytic pyrolysis reaction of biomass and reforming of volatiles/gases from biomass pyrolysis, catalytic pyrolytic kinetic and thermodynamic studies are still lacking in a wider perspective. However, few papers on Ni-based promoted and bimetallic alloy-based supported catalysts shed light in this review instead on kinetics, thermodynamics, and mechanistic studies of biomass catalytic pyrolysis. Yang et al. studied catalytic biomass pyrolysis using Ni-based functional materials *(Yang et al., 2019).* This study elucidates the application of Ni-CaO-Ca_2SiO_4 and Ni-Ca_2SiO_4 to three biomass materials such as cellulose, sawdust, and straw by non-isothermal modeling free methods that, Ozawa-Flynn-Wall Method (OFW), Kissinger-Akahira-Sunose Method (KAS), Starink Method and Distributed Activation Energy Method (DAEM). Ni enhances the cracking of C-H, C-C and C-O bonds *(Ji et al., 2017),* CaO is the CO_2 sorbent to enhances water-gas shift reaction towards more hydrogen generation potential *(Yan and Zhang, 2019, Cruz-Hernández et al., 2017)* and Ca_2SiO_4 works as a chemical stabilizer to stabilize catalyst sintering and CO_2 capture. For the case of sawdust, lower activation energy (E_a) was noticed for Ni-CaO-Ca_2SiO_4 than the catalyst Ni-Ca_2SiO_4 due to the cracking efficiency of CaO and its behavior as sorbent. Gupta and Mondal worked on catalytic pyrolysis of waste pine needles with nickel-doped gamma-alumina catalysts *(Gupta and Mondal, 2021).* As compared to the Al_2O_3 catalyst, the Ni/Al_2O_3 catalyst acts as a promising candidate catalyst because of its oxygen reduction potential, higher hydrocarbon, and phenolic compounds generation in bio-oil. The bio-oil yield gets further reduced and product gas yield is enhanced due to the demolition of oxygenated hydrocarbons to lighter volatiles such as CO_2, CO, H_2 and CH_4. The average value of activation energy for pine needle's thermal pyrolysis is 125.602 kJ mol^{-1} by the OFW method and 121.359 kJ mol^{-1} by the KAS method. However, pine needle catalytic pyrolysis via Al_2O_3 catalyst estimated an E_a of 111.076 kJ mol^{-1} and 106.625 kJ mol^{-1} by OFW and KAS method thus reducing E_a by 11.56 %. Whereas, pine needle catalytic pyrolysis via Ni/Al_2O_3 catalyst estimated 105.346 kJ mol^{-1} and 100.594 kJ mol^{-1} by OFW and KAS method, thus enhancing the rate of the reaction and reducing E_a by 16.12 %. Yang et al. utilized a novel NiO/Al_2O_3 catalyst in tobacco rob and observed a

curtailment of E_a from 78.39–62.28 kJ mol^{-1} *(Yang et al., 2011).* Table 2.9 summarizes on review of catalysts for catalytic pyrolysis of biomass.

Table 2.9 Summary of review of catalysts for catalytic pyrolysis of biomass

Catalyst	Biomass	Reactor	Process conditions	Significance	Reference
Metal precursors (salts) Mono-metallic (Cu10%/zeolite and Ni10%/zeolite) and bi-metallic catalysts (Cu 5%-Ni5%/zeolite) catalysts was prepared by incipient wetness impregnation technique	Pine wood biomass	Infrared image gold furnace (SINKU-RIKO)	Heating rate – 100 K min-1, Helium gas flow rate – 50 mL min-1, Inventory of biomass – 100 mg, three catalyst-to-biomass ratios: CuZ: NiZ-1, CuZ: NiZ-2 and CuZ: NiZ-3	CuNi/zeolite showed better deoxygenation activity of bio-oil. Cu/zeolite-Ni/zeolite preferred the production of aromatic hydrocarbons. All the catalysts equally favored decarboxylation and decarbonylation reactions.	*Kumar et al., 2019*
Transition metal oxides (Ni catalysts on different supports such as Al_2O_3, SiO_2, MgO, TiO_2, ZrO_2) (0.4 – 0.8 mm)	Pine wood (pinus insignis) (1 - 2 mm)	Two reactors with a conical spouted bed reactor (CSBR) in which the biomass pyrolysis is carried out, and a fluidized bed reactor (FBR) for the in-line reforming of pyrolysis volatiles. Diameter: 38.1 mm, Length: 440 mm. The reactor was placed in a radiant oven (550 W)	Pyrolysis temperature - 773 K, Reforming temperature - 873 – 973 K, continuous biomass feed rate- 0.75 g min^{-1}, water feed rate- 3 mL min^{-1}, molar steam/carbon ratio - 7.7, space-time – 20 gcatmin^{-1} g $volatiles^{-1}$	Ni/Al_2O_3, Ni/ZrO_2, and Ni/MgO are the most active and stable. Ni/TiO_2 has less performance regarding Ni/TiO_2 catalyst due to phase transformation affects.	*Santamaria et al., 2019*

(Continued)

Red mud was produced from a bauxite residue and was formulated with a colloidal alumina binder and a colloidal silica (250 – 600 µm)	Pinyon juniper (~2 mm), pine (420 µm), forest thinning waste (< 1 mm)	Fluidized – bed reactor	Temp – 673 - 723 K, 28L min^{-1} of nitrogen gas flow rate, used for fluidization, nitrogen gas was gradually replaced with the non-condensable gases from the catalytic pyrolysis until the fluidizing gas was made up of 11 L min^{-1} of nitrogen and 62 L min^{-1} of recycled non-condensable gases.	Catalytic fast pyrolysis with red mud gives improved bio-oil and improved hydrocarbon range along with hydrotreating of gas.	*Santosa et al., 2020*

2.6 Review of advances in catalysts for catalytic co-valorization of coal and biomass blends

A substantial review is endowed upon transpiring catalysts for catalytic co-pyrolysis of coal and biomass blended feedstocks. The catalytic upgradation of product yields is precariously substantiated by the autocatalytic effect of alkali and alkaline earth metals (AAEM's) of char gasification during co-pyrolysis of coal and biomass blends as explained below.

Literature suggests a manifold number of papers published on coal pyrolysis, low tar yields, and its generation of heavy polycyclic aromatic hydrocarbon compounds during the process *(Williams et al., 2000, Sun et al., 2019).* This is a crucial setback to the energy and chemical industry since the majority of the thermal power plants are dependent on coal. The underlying solution is vested upon high hydrogen donor feedstocks such as biomass, plastics and heavy oil which can improve the yield of coal tar, improve the selectivity of the desired aromatic compounds, and reduce coke formation *(Dorado et al., 2014, Yao et al., 2015, Wang et al., 2015, Zhao et al., 2022, Zhang et al., 2022, Wu et al., 2019, Wu et al., 2021, Messina et al., 2015, Wang et al., 2014).* A paper on the utilization of low-rank Shandong coal by Yang et al. reports the catalytic co-pyrolysis with coal tar catalyzed by hematite,

chalcopyrite, nickel laterite, and molybdenite. This promotes the production of light tar, especially mono-aromatics, aliphatic, and phenol, and increases the gas yield *(Yang et al., 2022).* In another work, the importance of the catalytic effect of mineral matter, alkali, and alkaline earth metals (AAEM) (mainly Na, Mg and Ca) on product yield distribution and profile has its pre-eminence apart from other elements such as carbon, hydrogen, nitrogen, sulfur and oxygen *(Yan et al., 2016).* The catalytic effect of AAEM is contained in the blended char which increases globally with a decrease in the coal rank, thus increasing the reactivity of the process *(Quan et al., 2016, Zhao et al., 2020).* In a study, industrial solid waste coal fly ash and agricultural solid waste corn stalk are studied on their catalytic co-pyrolysis aspects *(Hong et al., 2022).* Bio-oil yield was improved as the content of oxy-compounds decreased from 43.32-32.44 % upon integration of coal fly ash due to ketonization taking place. The selectivity of aliphatic hydrocarbons was also increased by 7.89 % due to coal fly ash acting as a catalyst. In a study by Bie et al., the in-situ release of AAEM's during the co-pyrolysis of coal and biomass was monitored by laser-induced breakdown spectroscopy and showed that the temporal release of alkali metals during the biomass pyrolysis and co-pyrolysis initiated with an increase and eventually decrease over time, independent of pyrolysis temperature, mass ratio of biomass to coal, and minerals in coal. Besides, pyrolysis temperature had a decisive effect on the maximum release concentration and ratio of alkali metals, while co-pyrolysis limited the volatilization of alkali metals via the interaction between coal and biomass *(Bie et al., 2023).* Song et al. found that by inductively coupled plasma optical emission spectroscopy (ICP-OES) and inductively coupled plasma mass spectrometry (ICP-MS) during co-pyrolysis of coal and biomass blends, 65.0 wt. % K migrated into the coal char, 15.9 wt. % K was released into the gas phase, and 19.1 wt. % K remained in the biomass char *(Song et al., 2019).* The interactions may be caused by volatile-char interaction, volatile-volatile interaction, and catalysis of mineral matter *(Tian et al., 2022).* Chansa et al. determined the alkali release during co-combustion of biomass and coal using laser-induced breakdown spectroscopy and found that the potassium release rate increased with increasing biomass content *(Chansa et al., 2021).* However, Dayton et al. investigated the effect of coal minerals on the release of alkali metals during co-combustion of coal and biomass and believed that minerals in coal inhibited the release of potassium from biomass *(Dayton et al., 1999).*

2.7 Summary and Limitations of Existing Literature

As observed in the review of literature, co-pyrolysis of coal/biomass blends has proved reliable, and cost-effective processes in producing CO_2-neutral fuel. Oodles of research

papers are available on various aspects of biomass pyrolysis, co-pyrolysis of coal/biomass blends, synergistic effects of alkali and alkaline earth metals in co-pyrolysis and catalytic pyrolysis of biomass. Numerous research works have been conducted on the pyrolysis of lignocellulosic biomass using a fixed-bed reactor unit or a drop-tube furnace. Co-pyrolysis of coal/biomass blends has several positive upshots concerning emissions, energy requirements, and pyrolytic product quality. The review of literature on the effect of biomass blending ratio on the co-pyrolysis and chemistry of co-pyrolysis processes is presented in sections 2.3.2 and 2.3.3 respectively. Reaction kinetics, thermodynamics and reaction mechanism are three crucial attributes of optimization of the co-pyrolysis process as mentioned in section 2.4. Based on the review, it was found that the majority of the published research on pyrolysis was primarily on deducing kinetic triplets – activation energies, pre-exponential, and order of the reaction and also on thermodynamic parameters, enthalpy, Gibbs free energy and entropy change during the process. However, more research is required to see extensive and flourishing progress in this area. Very little information on the quality of biofuel and gas production on operating temperatures has been found in the open literature. Studies on the blending of biomass with coal and its effect on devolatilization were found in literature. Hence, more studies are required to understand the presence and effect of synergistic interactions between the two feedstocks. However, there is scanty research available in the realm of catalytic co-pyrolysis research of coal/biomass blends. The catalytic pyrolysis of biomass approach may offer viable and attractive options over the traditional approaches of thermal pyrolysis since it enhances the quality of bio-oil and removes tar from liquid products generating clean pyrolytic syn-gas. However, challenges remain in considering catalyst selection and screening and put forth a methodical challenge in its synthesis and characterization since a homogeneous distribution of active elements, a high surface binding energy and a high surface-to-volume ratio are highly effectuated and crucial. Continued research efforts are necessary for the development of catalyst materials that deal with the abundantly available reactive biomass fuels. A plethora of studies have suggested the myriad application of catalysts in biomass pyrolysis as reported (*Kumar et al., 2019; Santamaria et al., 2019; Fernandez et al., 2021, Santosa et al., 2020).* However, the catalytic upgradation of product yields is precariously substantiated by the autocatalytic effect of alkali and alkaline earth metals (AAEM's) of char gasification during co-pyrolysis of coal and biomass blends. The details of the review are presented in the sections 2.5 through 2.6.

A kaleidoscopic review of the literature evinces the multifaceted relevance and significance of such elegant transition metal catalysts in the chemical reaction engineering

paradigm. The demand to gear the wheels to curb the global pollution index for a circular economy, leveraging the environmental sustainability index by mitigation air pollution, aggravating biofuel production and fostering sustainable innovation in the chemical industry, transition metal catalysts play a vital role. In this context, nanomaterials appear as momentous catalytic substances which have standout metallic active sites with effective surface binding energy properties. The morphological irregularities such as kinks, terraces, holes, vacancies and surface defects in the heterogeneous nano-catalyst structure exacerbate its surface reactivity and selectivity in an incongruous seat of thermal and chemical reactions. Effective size and shape of the catalyst and a high surface-to-volume ratio define the atomic utilization efficiency of the catalyst by unifying the physicochemical environment of its active sites. This substantially necessitates the profundity of its structure-activity-relationship implications in multifarious applications through the precise engineering and design of its molecular active site structure and functionalities.

Because of the above, in the present work, an attempt has been made to investigate the effect of various operating parameters (effect of temperature, type of coal and biomass, biomass blending proportion on coal/biomass mixtures, effect of catalyst type, catalyst loading, metal loading in catalyst) on product distribution (liquid product, evolved volatile gas and char) in a horizontal furnace of ID: 76.5 mm, length: 600 mm and volume: 2700 mL. It was attached to a condenser unit with cooled recirculating water to condense the non-condensable gases into liquid oil. The coal used in this study was low-grade coal available in the North-Eastern region of India and sawdust (teak wood) was locally collected from Guwahati, Assam. The optimization of pyrolysis and co-pyrolysis of coal/sawdust blends was done in a mathematical complaisant way for evaluation of kinetic triplets – activation energies, pre-exponential factor and order of the reaction. The pyrolysis kinetics of sawdust and co-pyrolysis kinetics of coal/sawdust blends with and without catalyst, Ni (II) and NiO aluminate nanocomposite catalyst were done. Subsequently, the pyrolytic behaviour of coal and sawdust as feedstocks, their product profile distribution, assessment of pyrolytic oil compounds in liquid oil, their thermal characteristics and char reactivity, and their feasibility as a co-product during the pyrolysis process were thoroughly assessed. It is expected that the information gathered in the present study would be quintessential for understanding different aspects of pyrolysis, co-pyrolysis of various other bed materials such as municipal sewage sludge, plastic or polyethylene terephthalate (PET) and integration of different catalyst materials such as zeolites, dolomites, mineral clay catalysts, hydrotalcite and red mud. This might be integrated as catalyst bed materials or as direct supports for transition metals such as

Ni, Pd, Pt, Ru, Rd or Cu. Further, this novel approach may be adopted for the design of an efficient pyrolysis process with built-in smart functional materials as catalysts which surpass the disadvantages of traditional heterogeneous catalysts.

2.8 Objectives of the present work

The key objectives which are addressed in the present investigation are,

1. Physico-chemical characterization of selected biomass and coal towards the production of renewable fuel and value-added chemicals. Kinetic analysis (model-free integral) and thermodynamic analysis of coal and biomass and its blends using non-isothermal techniques (Kissinger-Akahira-Sunose model).
2. Preparation and detailed physicochemical characterization of 10 % and 20 % NiO and Ni (II) aluminate-based nano-composite catalysts for their applications in catalytic pyrolysis of biomass and catalytic co-pyrolysis of coal-biomass blends.
3. Studies on both thermal and catalytic pyrolysis kinetics of sawdust and catalytic co-pyrolysis kinetics of coal/sawdust blends using 10 % and 20 % NiO and Ni (II) aluminate-based composite nano-catalysts.
4. Studies on the effect of temperature and biomass blending ratio on co-pyrolysis of coal/biomass blends with product evaluation.
5. Studies on catalytic effect on the yield, quality and composition of biomass and coal/biomass blends pyrolytic oil, along with the evaluation and characteristic properties of char and gas.

References

- Haslback, J., Kuehn, N., Lewis, E., Pinkerton, L.L., Simpson, J., Turner, M.J., Varghese, E. and Woods, M., 2013. *Cost and Performance Baseline for Fossil Energy Plants, Volume 1: Bituminous Coal and Natural Gas to Electricity, Revision 2a* (No. DOE/NETL-2010/1397). National Energy Technology Laboratory (NETL), Pittsburgh, PA, Morgantown, WV, and Albany, OR (United States).
- Diamantis, V., Eftaxias, A., Stamatelatou, K., Noutsopoulos, C., Vlachokostas, C. and Aivasidis, A., 2021. Bioenergy in the era of circular economy: Anaerobic digestion technological solutions to produce biogas from lipid-rich wastes. *Renewable Energy*, *168*, pp.438-447.
- Fu, P., Yi, W., Li, Z. and Li, Y., 2019. Comparative study on fast pyrolysis of agricultural straw residues based on heat carrier circulation heating. *Bioresource technology*, *271*, pp.136-142.
- Yuan, R., Yu, S. and Shen, Y., 2019. Pyrolysis and combustion kinetics of lignocellulosic biomass pellets with calcium-rich wastes from agro-forestry residues. *Waste Management*, *87*, pp.86-96.
- He, X., Liu, Z., Niu, W., Yang, L., Zhou, T., Qin, D., Niu, Z. and Yuan, Q., 2018. Effects of pyrolysis temperature on the physicochemical properties of gas and biochar obtained from pyrolysis of crop residues. *Energy*, *143*, pp.746-756.
- Gupta, A., Thengane, S.K. and Mahajani, S., 2020. Kinetics of pyrolysis and gasification of cotton stalk in the central parts of India. *Fuel*, *263*, p.116752.
- Sahoo, A., Kumar, S., Kumar, J. and Bhaskar, T., 2021. A detailed assessment of
- pyrolysis kinetics of invasive lignocellulosic biomasses (Prosopis juliflora and Lantana camara) by thermogravimetric analysis. *Bioresource Technology*, *319*, p.124060.
- Huang, H., Liu, J., Liu, H., Evrendilek, F., Buyukada, M., 2020. Pyrolysis of water hyacinth biomass parts: Bioenergy, gas emissions, and by-products using TG-FTIR and Py-GC/MS analyses. *Energy Conversion and Management, 207*, p.112552.
- Muradov, N., Fidalgo, B., Gujar, A.C., Ali, T., 2010. Pyrolysis of fast-growing aquatic biomass–Lemna minor (duckweed): Characterization of pyrolysis products. *Bioresource technology, 101(21),* pp. 8424-8428.
- Lee, D.J., Lu, J.S., Chang, J.S., 2020. Pyrolysis synergy of municipal solid waste (MSW): A review. *Bioresource technology, 1 (318)*, p. 123912.

- Jagodzińska, K., Zaini, I.N., Svanberg, R., Yang, W., Jönsson, P.G., 2021. Pyrolysis of excavated waste from landfill mining: Characterisation of the process products. Journal of Cleaner Production, 10 (279), p. 123541.
- Shadangi, K.P. and Mohanty, K., 2014. Kinetic study and thermal analysis of the pyrolysis of non-edible oilseed powders by thermogravimetric and differential scanning calorimetric analysis. *Renewable Energy*, *63*, pp.337-344.
- Kan, T., Strezov, V. and Evans, T.J., 2016. Lignocellulosic biomass pyrolysis: A review of product properties and effects of pyrolysis parameters. *Renewable and sustainable energy reviews*, *57*, pp.1126-1140.
- George, J., Arun, P. and Muraleedharan, C., 2019. Experimental investigation on co-gasification of coffee husk and sawdust in a bubbling fluidised bed gasifier. *Journal of the Energy Institute*, *92*(6), pp.1977-1986.
- Ajimotokan, H.A., Ehindero, A.O., Ajao, K.S., Adeleke, A.A., Ikubanni, P.P. and Shuaib-Babata, Y.L., 2019. Combustion characteristics of fuel briquettes made from charcoal particles and sawdust agglomerates. *Scientific African*, *6*, p.e00202.
- Antwi-Boasiako, C. and Acheampong, B.B., 2016. Strength properties and calorific values of sawdust-briquettes as wood-residue energy generation source from tropical hardwoods of different densities. *Biomass and Bioenergy*, *85*, pp.144-152.
- Jasiūnas, L., Pedersen, T.H., Toor, S.S. and Rosendahl, L.A., 2017. Biocrude production via supercritical hydrothermal co-liquefaction of spent mushroom compost and aspen wood sawdust. *Renewable Energy*, *111*, pp.392-398.
- Gökkaya, D.S., Sert, M., Sağlam, M., Yüksel, M. and Ballice, L., 2020. Hydrothermal gasification of the isolated hemicellulose and sawdust of the white poplar (Populus alba L.). *The Journal of Supercritical Fluids*, *162*, p.104846.
- Monedero, E., Lapuerta, M., Pazo, A., Díaz-Robles, L.A., Pino-Cortés, E., Campos, V., Vallejo, F., Cubillos, F. and Gómez, J., 2019. Effect of hydrothermal carbonization on the properties, devolatilization, and combustion kinetics of Chilean biomass residues. *Biomass and Bioenergy*, *130*, p.105387.
- Bridgwater, A.V., 2003. Renewable fuels and chemicals by thermal processing of biomass. *Chemical engineering journal*, *91*(2-3), pp.87-102.
- Shafizadeh, F., 1981. Basic principles of direct combustion. In *Biomass conversion processes for energy and fuels* (pp. 103-124). Boston, MA: Springer US.
- Jenkins, B.M., 1989. Physical properties of biomass. *Biomass handbook*, pp.860-891.

- Biagini, E., Lippi, F., Petarca, L. and Tognotti, L., 2002. Devolatilization rate of biomasses and coal–biomass blends: an experimental investigation. *Fuel*, *81*(8), pp.1041-1050.
- Idris, S.S., Abd Rahman, N., Ismail, K., Alias, A.B., Abd Rashid, Z. and Aris, M.J., 2010. Investigation on thermochemical behaviour of low rank Malaysian coal, oil palm biomass and their blends during pyrolysis via thermogravimetric analysis (TGA). *Bioresource technology*, *101*(12), pp.4584-4592.
- Aboyade, A.O., Görgens, J.F., Carrier, M., Meyer, E.L. and Knoetze, J.H., 2013. Thermogravimetric study of the pyrolysis characteristics and kinetics of coal blends with corn and sugarcane residues. *Fuel Processing Technology*, *106*, pp.310-320.
- Wang, J., Yan, Q., Zhao, J., Wang, Z., Huang, J., Gao, S., Song, S. and Fang, Y., 2014. Fast co-pyrolysis of coal and biomass in a fluidized-bed reactor. *Journal of Thermal Analysis and Calorimetry*, *118*, pp.1663-1673.
- Wang, X., Xu, Z., Wei, B., Zhang, L., Tan, H., Yang, T., Mikulčić, H. and Duić, N., 2015. The ash deposition mechanism in boilers burning Zhundong coal with high contents of sodium and calcium: A study from ash evaporating to condensing. *Applied Thermal Engineering*, *80*, pp.150-159.
- Messina, L.G., Bonelli, P.R. and Cukierman, A.L., 2015. Copyrolysis of peanut shells and cassava starch mixtures: Effect of the components proportion. *Journal of analytical and applied pyrolysis*, *113*, pp.508-517.
- Yan, L.J., Bai, Y.H., Kong, X.J. and Li, F., 2016. Effects of alkali and alkaline earth metals on the formation of light aromatic hydrocarbons during coal pyrolysis. *Journal of Analytical and Applied Pyrolysis*, *122*, pp.169-174.
- Dalluge, D.L., Kim, K.H. and Brown, R.C., 2017. The influence of alkali and alkaline earth metals on char and volatile aromatics from fast pyrolysis of lignin. *Journal of Analytical and Applied Pyrolysis*, *127*, pp.385-393.
- Guo, F., Li, X., Wang, Y., Liu, Y., Li, T. and Guo, C., 2017. Characterization of Zhundong lignite and biomass co-pyrolysis in a thermogravimetric analyzer and a fixed bed reactor. *Energy*, *141*, pp.2154-2163.
- Li, H., Shi, S., Lin, B., Lu, J., Ye, Q., Lu, Y., Wang, Z., Hong, Y. and Zhu, X., 2019. Effects of microwave-assisted pyrolysis on the microstructure of bituminous coals. *Energy*, *187*, p.115986.

- Wu, Z., Ma, C., Jiang, Z. and Luo, Z., 2019. Structure evolution and gasification characteristic analysis on co-pyrolysis char from lignocellulosic biomass and two ranks of coal: Effect of wheat straw. *Fuel*, *239*, pp.180-190.
- Zhu, J., Jin, L., Luo, Y., Hu, H., Xiong, Y., Wei, B. and Wang, D., 2020. Fast co-pyrolysis of a massive Naomaohu coal and cedar mixture using rapid infrared heating. *Energy Conversion and Management*, *205*, p.112442.
- Zhang, P., Chen, Z., Zhang, Q., Zhang, S., Ning, X. and Zhou, J., 2022. Co-pyrolysis characteristics and kinetics of low metamorphic coal and pine sawdust. *RSC advances*, *12*(34), pp.21725-21735.
- Zhou, S., Tang, S., Li, G., Xin, S., Huang, F., Liu, X., Mi, T., Huang, K. and Zeng, L., 2023. Catalytic fast pyrolysis of herbal medicine wastes over zeolite catalyst for aromatic hydrocarbons production. *Fuel*, *333*, p.126311.
- Subagyono, R.D.J.N., Masdalifa, W., Aminah, S., Nugroho, R.A., Mollah, M., Londong Allo, V. and Gunawan, R., 2021. Kinetic Study of Copyrolysis of the Green Microalgae Botryococcus braunii and Victorian Brown Coal by Thermogravimetric Analysis. *ACS omega*, *6*(47), pp.32032-32042.
- Onay, Ö., Bayram, E. and Koçkar, Ö.M., 2007. Copyrolysis of seyitömer− lignite and safflower seed: influence of the blending ratio and pyrolysis temperature on product yields and oil characterization. *Energy & fuels*, *21*(5), pp.3049-3056.
- Chen, T., Zhang, K., Zheng, M., Yang, S., Yellezuome, D., Zhao, R., Liu, G. and Wu, J., 2021. Thermal properties and product distribution from pyrolysis at high heating rate of Naomaohu coal. *Fuel*, *292*, p.120238.
- Ismail, T.M., Banks, S.W., Yang, Y., Yang, H., Chen, Y., Bridgwater, A.V., Ramzy, K. and Abd El-Salam, M., 2020. Coal and biomass co-pyrolysis in a fluidized-bed reactor: Numerical assessment of fuel type and blending conditions. *Fuel*, *275*, p.118004.
- Zhao, Y., Cao, H., Yao, C., Li, R. and Wu, Y., 2020. Synergistic effects on cellulose and lignite co-pyrolysis and co-liquefaction. *Bioresource technology*, *299*, p.122627.
- Yang, F., Zhou, A., Zhao, W., Yang, Z. and Li, H., 2019. Thermochemical behaviors, kinetics and gas emission analyses during co-pyrolysis of walnut shell and coal. *Thermochimica Acta*, *673*, pp.26-33.

- Zhu, Y., Kwong, C.W., Van Eyk, P.J., de Nys, R., Wang, D. and Ashman, P.J., 2015. Pyrolysis characteristics and char reactivity of Oedogonium sp. and Loy Yang coal. *Energy & Fuels*, *29*(8), pp.5047-5055.
- Wang, J., Zhang, S.Y., Guo, X., Dong, A.X., Chen, C., Xiong, S.W., Fang, Y.T. and Yin, W.D., 2012. Thermal behaviors and kinetics of Pingshuo coal/biomass blends during copyrolysis and cocombustion. *Energy & fuels*, *26*(12), pp.7120-7126.
- Naik, D.V., Kumar, R., Tripathi, D., Singh, R. and Kanaujia, P.K., 2016. Co-pyrolysis of Jatropha curcas seed cake and bituminous coal: Product pattern analysis. *Journal of Analytical and Applied Pyrolysis*, *121*, pp.360-368.
- Wang, Z., Wan, K., Xia, J., He, Y., Liu, Y. and Liu, J., 2015. Pyrolysis characteristics of coal, biomass, and coal–biomass blends under high heating rate conditions: effects of particle diameter, fuel type, and mixing conditions. *Energy & Fuels*, *29*(8), pp.5036-5046.
- Zhao, Y., Chang, L., Huang, T., Yin, G., He, W., Zhang, L., Cui, M., Xu, S. and Liu, Z., 2022. Simultaneous Pyrolysis of Coal and Biomass in a Drop-Tube–Fixed-Bed Reactor. *ACS omega*, *7*(10), pp.8717-8723.
- Zhang, P., Chen, Z., Zhang, Q., Zhang, S., Ning, X. and Zhou, J., 2022. Co-pyrolysis characteristics and kinetics of low metamorphic coal and pine sawdust. *RSC advances*, *12*(34), pp.21725-21735.
- Wu, Z., Zhang, J., Fan, Y., Zhang, B., Guo, W., Zhang, R., Li, Y. and Yang, B., 2021. Synergistic effects from co-pyrolysis of lignocellulosic biomass with low-rank coal: A perspective based on the interaction of organic components. *Fuel*, *306*, p.121648.
- Li, Y., Huang, S., Wang, Q., Li, H., Zhang, Q., Wang, H., Wu, Y., Wu, S. and Gao, J., 2019. Hydrogen transfer route and interaction mechanism during co-pyrolysis of Xilinhot lignite and rice husk. *Fuel Processing Technology*, *192*, pp.13-20.
- Zhu, J., Zhao, S., Wei, B., Xu, J., Hu, H. and Jin, L., 2021. Enhanced co-pyrolysis synergies between cedar and Naomaohu coal volatiles for tar production. *Journal of Analytical and Applied Pyrolysis*, *160*, p.105355.
- Yan, J., Shi, K., Pang, C., Lester, E. and Wu, T., 2016. Influence of minerals on the thermal processing of bamboo with a suite of carbonaceous materials. *Fuel*, *180*, pp.256-262.

- Khawam, A. and Flanagan, D.R., 2006. Solid-state kinetic models: basics and mathematical fundamentals. *The journal of physical chemistry B*, *110*(35), pp.17315-17328.
- Yang, J., McCoy, B.J. and Madras, G., 2005. Kinetics of nonisothermal polymer crystallization. *The Journal of Physical Chemistry B*, *109*(39), pp.18550-18557.
- Burnham, A.K., Weese, R.K. and Weeks, B.L., 2004. A distributed activation energy model of thermodynamically inhibited nucleation and growth reactions and its application to the β− δ phase transition of HMX. *The Journal of Physical Chemistry B*, *108*(50), pp.19432-19441.
- Graetz, J. and Reilly, J.J., 2005. Decomposition kinetics of the AlH3 polymorphs. *The Journal of Physical Chemistry B*, *109*(47), pp.22181-22185.
- Wang, S., Gao, Q. and Wang, J., 2005. Thermodynamic analysis of decomposition of thiourea and thiourea oxides. *The Journal of Physical Chemistry B*, *109*(36), pp.17281-17289.
- Sbirrazzuoli, N., 2013. Determination of pre-exponential factors and of the mathematical functions f (α) or G (α) that describe the reaction mechanism in a model-free way. *Thermochimica Acta*, *564*, pp.59-69.
- Borchardt, H.J. and Daniels, F., 1957. The application of differential thermal analysis to the study of reaction kinetics1. *Journal of the American Chemical Society*, *79*(1), pp.41-46.
- Sharp, J.H., Brindley, G.W. and Achar, B.N., 1966. Numerical data for some commonly used solid state reaction equations. *Journal of the American Ceramic Society*, *49*(7), pp.379-382.
- Coats, A.W. and Redfern, J.P., 1964. Kinetic parameters from thermogravimetric data. *Nature*, *201*(4914), pp.68-69.
- Van Krevelen, D.W., Van Heerden, C. and Huntjens, F.J., 1951. Physicochemical aspects of the pyrolysis of coal and related organic compounds. *Fuel*, *30*(11), pp.253-259.
- Horowitz, H.H. and Metzger, G., 1963. A new analysis of thermogravimetric traces. *Analytical chemistry*, *35*(10), pp.1464-1468.
- Sharp, J.H. and Wentworth, S.A., 1969. Kinetic analysis of thermogravimetric data. *Analytical chemistry*, *41*(14), pp.2060-2062.

- Kennedy, J.A. and Clark, S.M., 1997. A new method for the analysis of non-isothermal DSC and diffraction data. *Thermochimica Acta*, *307*(1), pp.27-35.
- Kissinger, H.E., 1957. Reaction kinetics in differential thermal analysis. *Analytical chemistry*, *29*(11), pp.1702-1706.
- Freeman, E.S. and Carroll, B., 1958. The application of thermoanalytical techniques to reaction kinetics: the thermogravimetric evaluation of the kinetics of the decomposition of calcium oxalate monohydrate. *The Journal of Physical Chemistry*, *62*(4), pp.394-397.
- Friedman, H.L., 1964. Kinetics of thermal degradation of char-forming plastics from thermogravimetry. Application to a phenolic plastic. In *Journal of polymer science part C: polymer symposia* (Vol. 6, No. 1, pp. 183-195). New York: Wiley Subscription Services, Inc., A Wiley Company.
- Ozawa, T., 1965. A new method of analyzing thermogravimetric data. *Bulletin of the chemical society of Japan*, *38*(11), pp.1881-1886.
- Flynn, J.H. and Wall, L.A., 1966. General treatment of the thermogravimetry of polymers. *Journal of research of the National Bureau of Standards. Section A, Physics and chemistry*, *70*(6), p.487
- Ozawa, T., 1992. Estimation of activation energy by isoconversion methods. *Thermochimica acta*, *203*, pp.159-165.
- Tang, W., Liu, Y., Zhang, H. and Wang, C., 2003. New approximate formula for Arrhenius temperature integral. *Thermochimica Acta*, *408*(1-2), pp.39-43.
- Madhusudanan, P.M., Krishnan, K. and Ninan, K.N., 1986. New approximation for the p (α) function in the evaluation of non-isothermal kinetic data. *Thermochimica acta*, *97*, pp.189-201.
- Starink, M.J., 2003. The determination of activation energy from linear heating rate experiments: a comparison of the accuracy of isoconversion methods. *Thermochimica acta*, *404*(1-2), pp.163-176.
- Miura, K. and Maki, T., 1998. A simple method for estimating f (E) and k 0 (E) in the distributed activation energy model. *Energy & Fuels*, *12*(5), pp.864-869.
- Vyazovkin, S. and Wight, C.A., 1999. Model-free and model-fitting approaches to kinetic analysis of isothermal and nonisothermal data. *Thermochimica acta*, *340*, pp.53-68.

- Perejón, A., Sánchez-Jiménez, P.E., Criado, J.M. and Pérez-Maqueda, L.A., 2011. Kinetic analysis of complex solid-state reactions. A new deconvolution procedure. *The journal of physical chemistry B*, *115*(8), pp.1780-1791.
- Scott, S.A., Dennis, J.S., Davidson, J.F. and Hayhurst, A.N., 2006. An algorithm for determining the kinetics of devolatilisation of complex solid fuels from thermogravimetric experiments. *Chemical engineering science*, *61*(8), pp.2339-2348.
- Chen, Z., Hu, M., Zhu, X., Guo, D., Liu, S., Hu, Z., Xiao, B., Wang, J. and Laghari, M., 2015. Characteristics and kinetic study on pyrolysis of five lignocellulosic biomass via thermogravimetric analysis. *Bioresource technology*, *192*, pp.441-450.
- Naya, S., Cao, R., de Ullibarri, I.L., Artiaga, R., Barbadillo, F. and García, A., 2006. Logistic mixture model versus Arrhenius for kinetic study of material degradation by dynamic thermogravimetric analysis. *Journal of Chemometrics: A Journal of the Chemometrics Society*, *20(3-4)*, pp.158-163.
- Cai, J.M., Chen, S.Y. and Liu, R.H., 2009. Weibull mixture model for iso-conversional kinetic analysis of biomass oxidative pyrolysis. *Journal of the Energy Institute*, *82*(4), pp.238-241.
- Cheng, Z., Wu, W., Ji, P., Zhou, X., Liu, R. and Cai, J., 2015. Applicability of Fraser–Suzuki function in kinetic analysis of DAEM processes and lignocellulosic biomass pyrolysis processes. *Journal of Thermal Analysis and Calorimetry*, *119*(2), pp.1429-1438.
- Hu, M., Chen, Z., Wang, S., Guo, D., Ma, C., Zhou, Y., Chen, J., Laghari, M., Fazal, S., Xiao, B. and Zhang, B., 2016. Thermogravimetric kinetics of lignocellulosic biomass slow pyrolysis using distributed activation energy model, Fraser–Suzuki deconvolution, and iso-conversional method. *Energy Conversion and Management*, *118*, pp.1-11.
- De Caprariis, B., De Filippis, P., Herce, C. and Verdone, N., 2012. Double-Gaussian distributed activation energy model for coal devolatilization. *Energy & Fuels*, *26*(10), pp.6153-6159.
- Wang, J., Li, P., Liang, L., Yang, J., Hao, X., Guan, G. and Huang, W., 2016. Kinetics modeling of low-rank coal pyrolysis based on a three-Gaussian distributed activation energy model (DAEM) reaction model. *Energy & Fuels*, *30*(11), pp.9693-9702.

- Vand, V., 1943. A theory of the irreversible electrical resistance changes of metallic films evaporated in vacuum. *Proceedings of the Physical Society (1926-1948)*, *55*(3), p.222.
- Pitt, G.J., 1962. The kinetic of the evolution of volatile products from coal. *Fuel*, *41*, pp.267-274.
- Dhaundiyal, A. and Singh, S.B., 2016, March. Distributed activation energy modelling for pyrolysis of forest waste using Gaussian distribution. In *Proceedings of the Latvian Academy of Sciences* (Vol. 70, No. 2, p. 64). De Gruyter Poland.
- Soria-Verdugo, A., Goos, E., Arrieta-Sanagustín, J. and García-Hernando, N., 2016. Modeling of the pyrolysis of biomass under parabolic and exponential temperature increases using the Distributed Activation Energy Model. *Energy Conversion and Management*, *118*, pp.223-230.
- Dong, Z., Yang, Y., Cai, W., He, Y., Chai, M., Liu, B., Yu, X., Banks, S.W., Zhang, X., Bridgwater, A.V. and Cai, J., 2018. Theoretical analysis of double Logistic distributed activation energy model for thermal decomposition kinetics of solid fuels. *Industrial & Engineering Chemistry Research*, *57*(23), pp.7817-7825.
- Giuntoli, J., De Jong, W., Arvelakis, S., Spliethoff, H. and Verkooijen, A.H.M., 2009. Quantitative and kinetic TG-FTIR study of biomass residue pyrolysis: Dry distiller's grains with solubles (DDGS) and chicken manure. *Journal of analytical and applied pyrolysis*, *85*(1-2), pp.301-312.
- Bhatia, S.K. and Perlmutter, D. D., 1981. A random pore model for fluid-solid reactions: II. Diffusion and transport effects. AUChE Journal, 27(2), pp.247-254.
- He, C., Tang, C., Liu, W., Dai, L. and Qiu, R., 2020. Co-pyrolysis of sewage sludge and hydrochar with coals: Pyrolytic behaviors and kinetics analysis using TG-FTIR and a discrete distributed activation energy model. *Energy conversion and management*, *203*, p.112226.
- De Micco, G., Nasjleti, A. and Bohé, A.E., 2012. Kinetics of the gasification of a Rio Turbio coal under different pyrolysis temperatures. *Fuel*, *95*, pp.537-543.
- Rafsanjani, H.H. and Jamshidi, E., 2008. Kinetic study and mathematical modeling of coal char activation. *Chemical Engineering Journal*, *140*(1-3), pp.1-5.
- Bhatia, S.K. and Vartak, B.J., 1996. Reaction of microporous solids: The discrete random pore model. *Carbon*, *34*(11), pp.1383-1391.

- Seo, D.K., Lee, S.K., Kang, M.W., Hwang, J. and Yu, T.U., 2010. Gasification reactivity of biomass chars with CO_2. *Biomass and Bioenergy*, *34*(12), pp.1946-1953.
- Homma, S., Ogata, S., Koga, J. and Matsumoto, S., 2005. Gas–solid reaction model for a shrinking spherical particle with unreacted shrinking core. *Chemical Engineering Science*, *60*(18), pp.4971-4980.
- Vuthaluru, H.B., 2004. Thermal behaviour of coal/biomass blends during co-pyrolysis. *Fuel processing technology*, *85*(2-3), pp.141-155.
- Kumar, R. and Strezov, V., 2021. Thermochemical production of bio-oil: A review of downstream processing technologies for bio-oil upgrading, production of hydrogen and high value-added products. *Renewable and Sustainable Energy Reviews*, *135*, p.110152.
- Chai, M., Liu, R. and He, Y., 2020. Effects of SiO_2/Al_2O_3 ratio and Fe loading rate of Fe-modified ZSM-5 on selection of aromatics and kinetics of corn stalk catalytic pyrolysis. *Fuel processing technology*, *206*, p.106458.
- Zheng, Y., Wang, J., Wang, D. and Zheng, Z., 2022. Advanced catalytic upgrading of biomass pyrolysis vapor to bio-aromatics hydrocarbon: A review. *Applications in Energy and Combustion Science*, p.100061.
- Hernando, H., Hernández-Giménez, A.M., Ochoa-Hernández, C., Bruijnincx, P.C., Houben, K., Baldus, M., Pizarro, P., Coronado, J.M., Fermoso, J., Čejka, J. and Weckhuysen, B.M., 2018. Engineering the acidity and accessibility of the zeolite ZSM-5 for efficient bio-oil upgrading in catalytic pyrolysis of lignocellulose. *Green Chemistry*, *20*(15), pp.3499-3511.
- Furusawa, T., Saito, K., Kori, Y., Miura, Y., Sato, M. and Suzuki, N., 2013. Steam reforming of naphthalene/benzene with various types of Pt-and Ni-based catalysts for hydrogen production. *Fuel*, *103*, pp.111-121.
- Wang, S., Dai, G., Yang, H. and Luo, Z., 2017. Lignocellulosic biomass pyrolysis mechanism: a state-of-the-art review. *Progress in energy and combustion science*, *62*, pp.33-86.
- H.V.Ly, J.W.Park, S.S.Kim, H.T.Hwang, J.Kim, H.C.Woo, Catalytic pyrolysis of bamboo in a bubbling fluidized-bed reactor with two different catalysts: HZSM-5 and red mud for upgrading bio-oil. Renewable Energy, 149 (2020) 1434-1445.

- Ren, J., Cao, J.P. and Zhao, X.Y., 2021. Fabrication strategies of Ni-based catalysts in reforming of biomass tar/tar model compounds. *Applications in Energy and Combustion Science*, p.100053.
- Wang, S., Wang, K., Liu, Q., Gu, Y., Luo, Z., Cen, K. and Fransson, T., 2009. Comparison of the pyrolysis behavior of lignins from different tree species. *Biotechnology Advances*, *27*(5), pp.562-567.
- Xu, L., Wang, F., Chen, M., Yang, H., Nie, D., Qi, L. and Lian, X., 2017. Alkaline-promoted Ni based ordered mesoporous catalysts with enhanced low-temperature catalytic activity toward CO 2 methanation. *RSC advances*, *7*(30), pp.18199-18210.
- Lin, J., Ma, C., Luo, J., Kong, X., Xu, Y., Ma, G., Wang, J., Zhang, C., Li, Z. and Ding, M., 2019. Preparation of Ni based mesoporous Al_2O_3 catalyst with enhanced CO_2 methanation performance. *RSC advances*, *9*(15), pp.8684-8694.
- Li, J., Yan, R., Xiao, B., Liang, D.T. and Du, L., 2008. Development of nano-NiO/Al_2O_3 catalyst to be used for tar removal in biomass gasification. *Environmental science & technology*, *42*(16), pp.6224-6229.
- Li, J., Xiao, B., Yan, R. and Liu, J., 2009. Development of a nano-Ni-La-Fe/Al_2O_3 catalyst to be used for syn-gas production and tar removal after biomass gasification. *BioResources*, *4*(4), pp.1520-1535.
- Muley, P.D., Henkel, C., Abdollahi, K.K. and Boldor, D., 2015. Pyrolysis and catalytic upgrading of pinewood sawdust using an induction heating reactor. *Energy & Fuels*, *29*(11), pp.7375-7385.
- Nandini A., Pant K.K. and Dhingra S.C., 2005. K-, CeO_2-, and Mn-promoted Ni/Al_2O_3 catalysts for stable CO_2 reforming of methane. *Applied Catalysis A: General.* 290 (1-2), pp.166-174. https://doi.org/10.1016/j.apcata.2005.05.016.
- Yang, H., Ji, G., Clough, P.T., Xu, X. and Zhao, M., 2019. Kinetics of catalytic biomass pyrolysis using Ni-based functional materials. *Fuel Processing Technology*, *195*, p.106145.
- Ji, G., Xu, X., Yang, H., Zhao, X., He, X. and Zhao, M., 2017. Enhanced hydrogen production from sawdust decomposition using hybrid-functional Ni-CaO-Ca2SiO4 materials. *Environmental science & technology*, *51*(19), pp.11484-11492.
- Cruz-Hernández, A., Mendoza-Nieto, J.A. and Pfeiffer, H., 2017. NiO-CaO materials as promising catalysts for hydrogen production through carbon dioxide capture and subsequent dry methane reforming. *Journal of energy chemistry*, *26*(5), pp.942-947.

- Gupta, S. and Mondal, P., 2021. Catalytic pyrolysis of pine needles with nickel doped gamma-alumina: Reaction kinetics, mechanism, thermodynamics, and products analysis. *Journal of Cleaner Production*, *286*, p.124930.
- Yang, Y., Li, T., Jin, S., Lin, Y. and Yang, H., 2011. Catalytic pyrolysis of tobacco rob: Kinetic study and fuel gas produced. *Bioresource Technology*, *102*(23), pp.11027-11033.
- Williams, P.T. and Nugranad, N., 2000. Comparison of products from the pyrolysis and catalytic pyrolysis of rice husks. *Energy*, *25*(6), pp.493-513.
- Sun, M., Wang, Q., He, C., Gao, J., Wang, R., Zhang, Y., Xu, L., Yao, Q. and Ma, X., 2019. Pyrolysis characteristics of Shendong coal by CH_3OH-THF swelling coupled with in-situ loading of metal ions. *Fuel*, *253*, pp.409-419.
- Dorado, C., Mullen, C.A. and Boateng, A.A., 2014. H-ZSM5 catalyzed co-pyrolysis of biomass and plastics. *ACS Sustainable Chemistry & Engineering*, *2*(2), pp.301-311.
- Yao, W., Li, J., Feng, Y., Wang, W., Zhang, X., Chen, Q., Komarneni, S. and Wang, Y., 2015. Thermally stable phosphorus and nickel modified ZSM-5 zeolites for catalytic co-pyrolysis of biomass and plastics. *Rsc Advances*, *5*(39), pp.30485-30494.
- Yang, Q., Yao, Q., Ma, D., Liu, Y., He, L., Zhou, R., Sun, M. and Ma, X., 2022. Investigation of the (catalytic) co-pyrolysis of Shendong coal and coal tar based on rapid pyrolysis and ANN modelling. *Journal of Analytical and Applied Pyrolysis*, *163*, p.105486.
- Yan, L.J., Bai, Y.H., Kong, X.J. and Li, F., 2016. Effects of alkali and alkaline earth metals on the formation of light aromatic hydrocarbons during coal pyrolysis. *Journal of Analytical and Applied Pyrolysis*, *122*, pp.169-174.
- Quan, C. and Gao, N., 2016. Copyrolysis of biomass and coal: a review of effects of copyrolysis parameters, product properties, and synergistic mechanisms. *BioMed research international*, *2016*.
- Zhao, Y., Xing, C., Shao, C., Chen, G., Sun, S., Chen, G., Zhang, L., Pei, J., Qiu, P. and Guo, S., 2020. Impacts of intrinsic alkali and alkaline earth metals on chemical structure of low-rank coal char: Semi-quantitative results based on FT-IR structure parameters. *Fuel*, *278*, p.118229.
- Hong, W., Zhang, Y., Jiang, H., Li, S., Chen, J. and Zhang, L., 2022. Co-pyrolysis of corn stalk and coal fly ash: A case study on catalytic pyrolysis behavior, bio-oil yield and its characteristics. *Case Studies in Thermal Engineering*, *38*, p.102346.

- Bie, N., Wang, J., Lv, P., Zhang, Y., Bai, Y., Song, X., Su, W. and Yu, G., 2023. In-situ release characteristic of alkali metals during co-pyrolysis of coal and biomass in a visual fixed bed combined with laser-induced breakdown spectroscopy. *Fuel*, *331*, p.125868.
- Song, Y.C., Li, Q.T., Li, F.Z., Wang, L.S., Hu, C.C., Feng, J. and Li, W.Y., 2019. Pathway of biomass-potassium migration in co-gasification of coal and biomass. *Fuel*, *239*, pp.365-372.
- Tian, B., Zhao, W., Guo, Q. and Tian, Y., 2022. A comprehensive understanding of synergetic effect and volatile interaction mechanisms during co-pyrolysis of rice husk and different rank coals. *Energy*, p.124388.
- Chansa, O., Luo, Z., Eddings, E.G. and Yu, C., 2021. Determination of alkali release during oxyfuel co-combustion of biomass and coal using laser-induced breakdown spectroscopy. *Fuel*, *289*, p.119658.
- Dayton, D.C., Belle-Oudry, D. and Nordin, A., 1999. Effect of coal minerals on chlorine and alkali metals released during biomass/coal cofiring. *Energy & fuels*, *13*(6), pp.1203-1211.

CHAPTER III
MATERIALS AND METHODS

3.1 Introduction

This chapter describes the preparation and characterization techniques used for the characterization of the feedstocks, biomass and coal. A detailed assessment of thermal pyrolytic parameters such as devolatilization, reactivity, and pyrolysis index were carried out for raw and blended fuels. The catalysts, 10 % and 20 % NiO and Ni (II) aluminate nano-composite catalysts prepared were characterized. A thermo-gravimetric analyzer (TGA) was employed to discern the pyrolytic characteristics of the feed samples with and without the employment of catalysts, 10 % and 20 % NiO and Ni (II) aluminate nano-composite catalysts. Interpretation of kinetics and thermodynamics was evaluated by the model-free integral kinetic method, Kissinger-Akahira-Sunose (KAS method) which has its significance and accuracy in pyrolysis kinetics as previously established in literature as given in Chapter 2. The theoretical reaction mechanism was evaluated by Criado plot for both thermal and catalytic pyrolysis kinetics of biomass and co-pyrolysis of coal and biomass blends. The development of the fixed-bed reactor unit was further emphasized in this Chapter for thermal pyrolysis of coal and biomass along with the thermal co-pyrolysis of its blends. Implications of catalytic pyrolysis of biomass and catalytic co-pyrolysis of coal-biomass blends after detailed optimization strategy of (catalyst/biomass) ratio and (catalyst/blend) ratio on evaluation of product distribution profile was carried out.

3.2 Materials

3.2.1 Preparation of feedstock

The raw materials used in the work were North-Eastern coal retrieved from Meghalaya of sub-bituminous origin and lignocellulosic biomass of the agricultural waste and forestry residue which are profusely available in the North-Eastern region of the Indian subcontinent. The coal was ball and hammer-milled for its physical breakage to its smaller counterparts. Further, it was meshed to a particle size of 300 µm and further oven-dried overnight to remove the inherent moisture. Sawdust (teak wood) was collected from a local sawdust mill in Guwahati, Assam (latitude 26.14^{o} and longitude 91.73^{o}). Sawdust of such variety was considered as the candidate biomass feedstock for the work. It was initially washed with warm water 2-3 times and dried overnight above 373 K in a hot air oven. For the preparation and its further usage in thermal degradation and pyrolysis experiments, coal, and sawdust were initially sun-dried to remove the excess moisture, and ball and hammer-milled for its physical breakage to its smaller counterparts. Further, it was meshed to a particle size of 300 µm and further oven-dried overnight to remove the inherent moisture. A lesser particle size of 300 µm was incorporated to minimize the external heat and mass transfer effects during

thermogravimetric and pyrolysis experiments. All the pyrolysis experiments were performed by taking the sized sample to obtain more accurate outcomes *(Bhattacharyya et al., 2022).*

3.2.2 Preparation of co-pyrolysis samples

Sawdust at 10 %, 30 %, 50 %, 70 %, 90 %, 100 %, and 200 % of the coal samples was blended with coal on a weight basis and coded as 10 % blending, 30 % blending, 50 % blending, and so on. During co-pyrolysis, the weight of coal was constant which was 100 g. Different weight % of sawdust from 10-200 % was added with the coal. Accordingly, the total weight of the feed for co-pyrolysis varied. 10 % means the feed is a mixture of 100 g of coal and 10 g of sawdust. Correspondingly, 200 % blend indicates 200 g of sawdust added to 100 g of coal as it shows coal:sawdust ratio = 1:2. Appropriate mixing of coal and sawdust was achieved using a mixture grinder and reserved carefully for experimental purposes *(Bhattacharyya et al., 2022).*

3.2.3 Preparation of catalyst

Nickel nitrate hexahydrate [Ni $(NO_3)_2.6H_2O$] (CAS no. of nickel nitrate is 13478-00-7) and aluminum oxide (CAS no. for Al_2O_3 is 1344-28-1) were purchased from Thermo Fischer Scientific India Pvt. Ltd. The minimum assay for nickel nitrate is 98 %. The pH of the solution of 5% aq. solution (in carbon dioxide – free water) according to the National laboratory Test (NLT) was 3.5. The maximum limits of impurities were chloride 0.005 %, sulfate 0.05%, iron 0.02 %, and cobalt 0.1 %. The alumina-supported Ni nano-composite catalyst was prepared at 10 % and 20 % Ni loading by impregnating metallic precursor (Ni $(NO_3)_2.6H_2O$) onto the support material. The process is termed as wetness impregnation method.

To prepare 100 g of 10 % Ni/Al_2O_3 catalyst material, 29.089 g of Ni $(NO_3)_2.6H_2O$ was mixed with 500 mL of distilled H_2O to make (0.2 M) Ni $(NO_3)_2.6H_2O$ solution. However, to prepare 20 % Ni/Al_2O_3 catalyst material, 58.178 g of Ni $(NO_3)_2.6H_2O$ was mixed with 500 mL of distilled H_2O to make (0.2 M) Ni $(NO_3)_2.6H_2O$ solution. The Ni $(NO_3)_2.6H_2O$ solution was slowly impregnated onto Al_2O_3 support (70.911 g of support for 10 % Ni/Al_2O_3 catalyst) and (41.822 g of support for 20 % Ni/Al_2O_3 catalyst). This was for maintaining the proper heat and mass transfer limitations while stirring at 350-380 rpm in a round bottom flask at 423 K temperature. The metallic precursor was added drop wise to the support while the process continued till a slurry solution was formed. The solution was maintained in a hot-air oven at 393 K overnight. The sample was covered in a crucible and was calcined for 873 K for 4 h in a muffle furnace (air atmosphere). This changed Ni (II) nitrate/Al_2O_3 to become

$Ni(O)/Al_2O_3$. The process of calcination was repeated each time the sample was set to any characterization technique or pyrolysis experiments.

3.3 Experimental methods

3.3.1 Characterization of the feed samples

The characterization of the raw materials was carried out by proximate, ultimate analysis, heating value and mineral content analysis. The proximate compositions of the coal, biomass, and blend samples were determined using ASTM procedures: E871-82 (moisture), E872-82 (volatile) and D1102-84 (Ash) using the standard procedures as explained by Shadangi and Mohanty *(Shadangi and Mohanty, 2014)*. The ultimate analysis (carbon, hydrogen, sulfur, and nitrogen) was ascertained using CHNS Elemental Analyzer (Make: Eurovector, Model: Eurovector EA3000). However, the oxygen content was evaluated by difference on as received-basis (Eq. 3.1),

(%) O (as received-basis) = 100 – (%) C - (%) H - (%) N - (%) S (3.1)

The calorific value (MJ kg^{-1}) was determined by using an oxygen bomb calorimeter (Make: PARR, Model: 1341) by purging in pure oxygen.

A Zeiss Sigma 300 FESEM instrument (Make: Zeiss, Germany, Model: Sigma 300) equipped with the Thermo-energy dispersive X-ray spectrometer (EDS) was used to notice the presence of mineral contents in the sample.

Gemini Field Emission Scanning Electron Microscope instrument (Make: Zeiss, Model: Gemini) equipped with a Schottky type of field emitter and windowless EDS detector system is a high-performance instrument for achieving high-resolution images (0.8 nm at 15 kV and 1.4 nm at 1 kV) from low to high accelerating voltages (0.02-30 kV) up to a magnification from 500X-10.0KX. The sample was placed on a stub using double-sided carbon tape, double gold-coated, and inserted into the chamber which operated at 15 kV operating voltage. High-resolution images were taken in the range of 500X, 1.0KX, 5.0KX and 10.0KX for raw coal and sawdust samples.

X-ray Diffraction Spectrometry was used to measure the chemical composition, crystallinity, crystal size, and in-plane scattering of the coal and sawdust samples. An X-ray Diffraction Spectrometer (Make: SmartLab, Model: Rigaku Technologies, Japan) having a high-resolution diffractometer with a high-flux 9 kW rotating anode X-ray source, in-plane arm (5-axis goniometer), 3 kW sealed X-ray-tube and a D/teX Ultra 250 silicon strip detector was used and the XRD images of the coal and sawdust samples were measured at a diffraction angle from 10-90 ($2\Theta^{o}$) respectively. Cu-K Beta filter was used in the instrumentation.

The FTIR analysis of the feed samples was studied using an FTIR analyzer (Model: IRAffinity-1; Make M/s Shimadzu, Japan). The samples were prepared using KBr and measured within a 4000-450 cm^{-1} wavelength range.

The laser micro-Raman spectrometer system (Make: Horiba JobinYvon, Model: LabRam HR) is based on the inelastic scattering of monochromatic light, from the laser source of wavelength 633 nm for the measurement of Stokes and anti-Stokes lines of scattering of the coal and the biomass feedstocks.

The ESR analysis of the feed samples was studied using an ESR instrument (Make: Jeol, Model: JES FA200) which employed powdered feed samples into the sample holder.

3.3.2 Characterization of catalyst

X-ray Diffractometry was used to measure the chemical composition, crystallinity, crystal size, and in-plane scattering of the support and the catalyst samples. An X-ray Diffractometer (Make: Smart Lab, Model: Rigaku Technologies, Japan) has a high-resolution diffractometer with a high-flux 9 kW rotating anode X-ray source, in-plane arm (5-axis goniometer), 3 kW sealed X-ray tube, and a D/teX Ultra 250 silicon strip detector was used and the XRD diffractogram of the catalyst samples was measured at a diffraction angle from 10-90 ($2\Theta^{o}$) respectively. Cu-K Beta filter was used in the instrumentation. Debye Scherrer Equation gives the crystallite size (nm) of the sample which is given in Eq. (3.2),

$$\text{Crystallite size (D) (nm)} = = \frac{k\lambda}{\beta cos\theta} \quad (3.2)$$

where D is the crystallite size of the particle (nm), K is known as the Scherer's constant (k=0.94), λ is the X-ray wavelength (1.54060 Å), β is full width at half maximum (FWHM) of the diffraction peak in radian located at any 2θ in the pattern.

The Crystallinity (%) as given in Eq. (3.3) was calculated as,

$$\text{Crystallinity (\%)} = \frac{Area\ of\ crystalline\ peaks}{Total\ area\ of\ (crytsalline+amorphou\ )\ peaks} \times 100\% \quad (3.3)$$

The attendance of mineral contents in the catalyst samples was gauged by a Sigma 300 FESEM instrument (Make: Zeiss, Model: Sigma 300) armed with an Energy-dispersive X-ray spectrophotometer (EDS) machine.

Field Emission Scanning Electron Microscope instrument (Make: Zeiss, Model: Sigma 300) equipped with a Schottky type of field emitter and windowless EDS detector system is a high-performance instrument for achieving high-resolution images (1.2 nm at 15 kV and 2.2 nm at 1 kV) from low to high accelerating voltages (0.02-30 kV) up to a magnification from 5.0-150.0KX. The sample was placed on a stub using double-sided carbon tape, double gold-

coated, and inserted into the chamber. High-resolution images were taken in the range of 5.0 KX and 150.0 KX for the composite catalyst with an InLens SE detector.

Atomic Force Microscope (Make: Oxford Instruments, Model: Cypher S) was used for topographical imagery analysis of the nano-scaled samples in non-contact mode between the probe and the sample.

Field Emission Transmission Electron Microscope (Make: Jeol, Model: 2100F) equipped with a ZrO/W (100) Schottky type of field emitter which is essential for ultrahigh resolution in scanning transmission microscopy and analysis of a nano-scaled sample is used. The powdered samples were dispersed in an acetone solution and vigorously sonicated for 20 min in an ultra-sonicator. The dispersed solution of 10 uL (sample + ethanol) was mounted in a Cu grid which was placed in a clean Petri dish and dried overnight in a hot air oven at 378 K.

The surface area and pore size distribution of the support material and the catalyst samples were studied using a surface area analyzer (Make: Quantachrome, Model: Autosorb-IQ MP). The samples were degassed under nitrogen as a purge gas for 4 h at 393 K and adsorption/desorption isotherms were generated. Total pore volume and multi-point Brunnaeur-Emmett-Teller surface area were estimated. DFT pore volume and DFT surface area were also estimated. The pore size distribution curve according to BJH distribution was also correlated.

Fourier Transform Infrared Spectroscope (FTIR instrument) (Make: M/s Shimadzu, Japan, Model: IRAffinity-1) was used for the identification of functional groups in the catalyst samples.

X-ray photoelectron spectroscope (XPS instrument) (Make: M/s Physical electronics, USA, Model: Phi 5000 Versus Probe III) equipped with an X-ray source of monochromatic K-Alpha (1486.7 eV) and focus (<10–300 μm) was used for calculating the binding energies of the mineral oxides present in the sample.

To compute the thermal stability of the catalysts, a thermo-gravimetric analyzer (TGA) (Model: Perkin Elmer 4000) was appraised which operated at a temperature range of 303-1173 K in the presence of 99.99% pure N_2 gas flow at 20 mL min^{-1} at 1.9 bar gas pressure.

3.3.3 Thermal pyrolytic experiment

A Perkin-Elmer 4000, thermo-gravimetric analyzer (TGA) was employed to discern the pyrolytic characteristics of the feed samples. The TGA was performed in between 303-1173 K temperature ranges in the presence of 99.99% pure N_2 gas flow at 20 mL min^{-1} at 1.9 bar gas pressure. Upon culminating at 1173 K temperature, nitrogen gas was imported into the

furnace to scrap off the remaining volatile products. The analysis was executed by compelling approximately 6.500 mg of samples (-300 mesh size) in a ceramic crucible. The TGA analysis of coal, sawdust, and its blended samples was conducted at a single heating rate (20 K min^{-1}). At the single heating rate, the effect of sawdust blending with coal on the thermal stability and the rate of degradation was observed. The comparative degradation analysis between the feed samples settled the optimum blending condition where the rate of degradation was higher. At the optimum conditions, the influence of the heating rate was studied at 10, 20, 30 and 40 K min^{-1}. The degradation kinetic parameters were studied by using the iso-conversional method, the Kissinger-Akahira-Sunose (KAS) Method. Further, the calculated values were used for the determination of thermodynamic parameters. To get proper results each experiment was conducted three times and accurate results were used for further studies.

3.3.4 Performance metrics of pyrolysis

3.3.4.1 Determination of rate of decomposition (R_d)

On the grounds of evaluating the execution of releasing of volatile matter during thermal degradation, the maximum rate of decomposition (mg min^{-1}), initial devolatilization temperature (K), and the temperature at which maximum loss of mass takes place (peak temperature) are represented by R_{max}, T_{in}, T_{max} respectively.

R_d is the rate of decomposition and is determined by using (Eq. 3.4).

$$R_d = -dw_t/dt \tag{3.4}$$

where the mass loss rate of volatiles was considered as dw_t/dt.

3.3.4.2 Determination of comprehensive pyrolysis index (CPI)

The pyrolysis reactivity of the samples was calculated as CPI by using (Eq. 3.5) *(Li et al., 2018),*

$$\text{CPI} = \frac{Dmax}{Tmax(Tf - Ti)} \tag{3.5}$$

where D_{max} shows the highest peak value noticed from the DTG profile and T_{max} is the corresponding temperature. However, the initial pyrolysis temperature and the final pyrolysis temperature are denoted as T_i and T_f. respectively.

Equation 3.6 shows the way to calculate the final pyrolysis temperature.

$$T_f = 2T_{max} - T_i \tag{3.6}$$

3.3.4.3 Determination of instantaneous reactivity (R_i)

The instantaneous reactivity *(R_i)* for the weight loss of the sample (w_i) was studied by (Eq. 3.7) *(Kirtania and Bhattacharyya, 2013),*

$R_i = -1/w_i\ (dw/dt)_i$ (3.7)

3.3.4.4 Determination of intrinsic reaction rate (ρ)

The reactivity of the fuel or intrinsic reaction rate *(ρ)* was appraised using (Eq. 3.8) *(Zhu et al., 2008),*

$$Reactivity\ (R) = -\frac{1}{1-\alpha}\left(\frac{d\alpha}{dt}\right) \quad (3.8)$$

3.3.5 Determination of chemical synergistic interactions in the blends

The theoretical DTG curves of the blends were calculated as the sum of the weight loss rates of each component and compared with the experimental DTG curves to investigate whether synergistic interactions existed between the components of the blends *(Gil et al., 2010; Kastanaki et al., 2002).* So, the chemical synergistic interactions between the coal and biomass feeds during the co-pyrolysis can be modeled as given in (Eq. 3.9),

$$\frac{dw}{dt} = x_{coal}\frac{dw}{dt}_{coal} + x_{Biomass}\frac{dw}{dt}_{Biomass} \quad (3.9)$$

where $\frac{dw}{dt}_{coal}$, $\frac{dw}{dt}_{Biomass}$ are the normalized weight loss rates of the individual fuels and $x_{coal}, x_{Biomass}$ are the mass fractions of coal and biomass in the coal-sawdust blends respectively.

3.3.6 Theory of mathematical modelling

Theoretical and mathematical modeling gives a welter of information to recognize strategically the thermal characteristics of the feedstock. The reaction kinetics of the feedstock were studied by such mathematical techniques.

Solid-state decomposition follows the following stoichiometric equation (Eq. 3.10) *(Khawam and Flanagan, 2006),*

$A_{solid} \dashrightarrow B_{solid} + C_{gas}$ (3.10)

At the very outset, the fundamental rate equation can be recounted for describing the decomposition process. The rate of the equation (Eq. 3.11) can be appraised under three variable factors: temperature, *T*; pressure, *P* and the extent of conversion, *α (Vyazovkin et al., 2011),*

$$\frac{d\propto}{dt} = k(T)f(\propto)h(P) \quad (3.11)$$

The partial pressure of the gaseous reductant in a solid-gas phase reaction directly affects the kinetics of decomposition. The total pressure of the system collates to the local concentration of the reactive product which could be manifested in Power-law form (Eq. 3.12) *(Vyazovkin et al., 2011),*

$h(P) = P^n$ (3.12)

The deduction of the expression leads to *h(P)*=constant and hence can be neglected in the kinetic equation, denoting only two variables, *T* and *α (Vyazovkin et al., 2011).*

The conversion, *α*, depicts the loss of a mass fraction of the feedstock is defined as (Eq. 3.13) *(Khawam and Flanagan, 2006),*

$$\alpha = (m_0 - m_t) / (m_0 - m_f) \quad (3.13)$$

where, m_0 and m_f are appraised as the weight % of the reactant at the initialization of the reaction and the final residue % at the end of the reaction respectively, whereas m_t is the weight % at an instantaneous time *t*. Thus, conversion % is equilibrated in terms of actual weight % from thermal degradation data in this study.

The Arrhenius equation is encouraged to count the rate of mass decay with the rise in the temperature. The rate of the reaction can be parameterized by the temperature (*T)* and the extent of conversion (*α*) as shown in Eq. (3.14 & 3.15).

$$\frac{d\propto}{dt} = k(T)f(\propto) \quad (3.14)$$

$$\frac{d\propto}{dt} = A\exp\left(-\frac{E}{RT}\right)f(\propto) \quad (3.15)$$

when the temperature program is non-isothermal, *T= T(t),* time changes the heating rate linearly such that *β= dT/dt=* constant in (Eq. 3.16),

$$\beta\frac{d\propto}{dT} = A\exp\left(-\frac{E}{RT}\right)f(\propto) \quad (3.16)$$

where, the heating rate (K min^{-1}), pre-exponential factor (min^{-1}), activation energy at a particular conversion (kJ mol^{-1}), universal gas constant (8.314 $\times 10^{-3}$ kJ mol^{-1} K^{-1}), and absolute temperature are denoted by the terms *β, A*, *E, R,* and *T* respectively. The differential temperature integral which is solved by numerical method approximation as $f(\propto)$.

The inception and the occurrence of the precise value of the heating rate reduces the relevance of (Eq. 3.11) to the optimization of processes where the sample temperature is relative to the reference temperature. Integration of (Eq. 3.16) resulted in an outcome as (Eq. 3.17):

$$g(\alpha) = \int_0^{\propto} \frac{d(\propto)}{f(\propto)} = A \int \exp\left(-\frac{E}{RT}\right)dT \quad (3.17)$$

where *g(α)* is the integral form of the reaction model.

For a constant heating rate, the integral form concerning the temperature is manifested as a priority. The following expression, (Eq. 3.18) introduces the precise value of the heating rate as,

$$g(\alpha) = \int_0^{\propto} \frac{d(\propto)}{f(\propto)} = A/\beta \int \exp\left(-\frac{E}{RT}\right)dT \quad (3.18)$$

3.3.6.1 Kissinger-Akahira-Sunose method

Each constituent module in the Arrhenius equation is associated with a theoretical concept, *E* with the energy barrier, *A* with the number of collisions of the activated complex, and *f(α)* or *g(α)* with the reaction mechanism.

Integration of (Eq. 3.18) leads to (Eq. 3.19)

$$g(\alpha) = \int_0^{\propto} \frac{d(\propto)}{f(\propto)} = \frac{A}{\beta} \int \exp\left(-\frac{E}{RT}\right) dT = \frac{A}{\beta}\frac{E}{R}\ \mathrm{P(u)} \quad (3.19)$$

where *g(α)* denotes the reaction function representing the integral form, *P*(*u*) represents the integral temperature function, *u* is a variable which is defined as:

$$u = E/RT \quad (3.20)$$

Murray and White temperature integral approximation is indicated in (Eq. 3.21) *(Akahira and Sunose 1971, Kissinger 1957),*

$$\mathrm{P(u)} = \exp(-u)/u^2 \quad (3.21)$$

Combining Equations. (Eq. 3.18) and (Eq. 3.21) give (Eq. 3.22),

$$ln\frac{\beta}{T^2} = ln\frac{AR}{E\alpha\, g(\propto)} - \frac{E}{RT\alpha} \quad (3.22)$$

where the slope gives the activation energy by plotting *ln (β/T²)* vs. *1/T* and the intercept gives the pre-exponential factor. This is the Kissinger-Akahira-Sunose (KAS) equation.

3.3.6.2 Determination of the thermodynamic parameters

The thermodynamic parameters such as enthalpy *(ΔH,* kJ mol^{-1}*),* Gibbs free energy (*ΔG,* kJ mol^{-1}), and entropy of the system (*ΔS,* kJ mol^{-1} K^{-1}*)* were calculated based on the obtained values of activation energy (E_a, kJ mol^{-1}) and collision frequency (A, s^{-1}) by using the following (Eq. 3.23-3.25) *(Varma et al., 2020),*

$$\Delta H = \Delta E_a - RT_m \quad (3.23)$$

$$\Delta G = E_a + RT_m\, ln\,(k_B\, T_m/hA) \quad (3.24)$$

$$\Delta S = \frac{\Delta H - \Delta G}{T_m} \quad (3.25)$$

The peak temperature (K), the gas constant, 8.314 × 10^{-3} (kJ mol^{-1} K^{-1}), the Plank's constant, 6.626 × 10 $^{-34}$ J s^{-1}, the Boltzmann constant, 1.381 × 10^{-23} J K^{-1} are notified by the terms T_m, R, h and k_B respectively.

3.3.6.3 Determination of reaction mechanism

A solid-state reaction mechanism can be determined by the Criado method and is implemented by Doyle's approximation *p(α) (Gotor et al., 2000).* To propose the issue of the designated thermal process for ascertaining the reaction mechanism, the theoretical and experimental master plots are tallied to conversions for *f(α)* and *g(α)* values of solid-state reaction models.

$$g(\propto) = \int_0^{\propto} \frac{d(\propto)}{f(\propto)} = AE\ p(\alpha)/\beta R \quad (3.26)$$

where, p(α) is $\alpha = E/RT$ (3.27)

According to Doyle's approximation,

$$p(\alpha) = 0.00484\ e - 1.0516\alpha \quad (3.28)$$

At conversion reference point ($\alpha = 0.5$), where $\alpha_{0.5} = E/RT_{0.5}$ and $T_{0.5}$ is the temperature at $\alpha = 0.5$,

$$g(0.5) = A.E.p(\alpha_{0.5})/\beta.R \quad (3.29)$$

The integral master-plots by dividing Eq. (3.26) and Eq. (3.29) are thus deduced as,

$$\frac{g(\alpha)}{g(0.5)} = \frac{p(\alpha)}{p(\alpha 0.5)} \quad (3.30)$$

The Criado differential-integral method is implemented as given in (Eq. 3.31),

$$\frac{Z(\propto)}{Z(0.5)} = \frac{f(\propto)\times g(\propto)}{f(0.5)\times g(0.5)} \quad (3.31)$$

The reaction pathway based on solid-state kinetic models along with the kinetic and thermodynamic parameters is ascertained using the formulas given in Table 3.1.

Table 3.1 Estimation of kinetic, reaction mechanism, and thermodynamic parameters

Sl No.	Value (Unit)	Equation	Significance	Reference
1.	Activation energy *(E_a)* (kJ mol^{-1})	Kissinger-Akahira-Sunose equation (KAS) $ln\frac{\beta}{T^2} = ln\frac{AR}{E\alpha\, g(\propto)} - \frac{E}{RT\alpha}$	The slope gives the E_a when the graph is drawn between *ln* (β/T^2) vs. *1/RT*	*Akahira and Sunose 1971, Kissinger 1957*
2.	Pre-exponential factor *(A)* (s^{-1})	Kissinger-Akahira-Sunose equation (KAS) $ln\frac{\beta}{T^2} = ln\frac{AR}{E\alpha\, g(\propto)} - \frac{E}{RT\alpha}$	Intercept of $ln\frac{AR}{E\alpha\, g(\propto)}$ gives the pre-exponential factor	*Akahira and Sunose 1971, Kissinger 1957*
3.	Enthalpy *(ΔH)* (kJ mol^{-1})	$\Delta H = \Delta E_a - RT_m$ where T_m and R are the peak temperature (K) and the gas constant	This signifies the heat evolved or absorbed when a reaction takes place at a constant pressure.	*Varma et al., 2020*
4.	Gibbs free energy *(ΔG)* (kJ mol^{-1})	$\Delta G = E_a + RT_m\, ln\,(k_B\, T_m/hA)$ where T_m, R, h, and k_B is the peak temperature (K), the gas constant, 8.314 × 10^3 (kJ mol^{-1} K^{-1}), the Plank's constant, h, 6.626 × 10^{-34} J s^{-1} and the Boltzmann constant, k_B, 1.381 × 10^{-23} J K^{-1}	Signifies whether the reaction is exothermic or endothermic	*Varma et al., 2020*
5.	Entropy *(ΔS)* (kJ mol^{-1}min^{-1})	$\Delta S = \frac{\Delta H - \Delta G}{T_m}$	Signifies the randomness of a reaction	*Varma et al., 2020*
6.	Reaction Mechanism	$\frac{Z(\propto)}{Z(0.5)} = \frac{f(\propto) \times g(\propto)}{f(0.5) \times g(0.5)} = \left(\frac{T_\alpha^2}{T_{0.5}^2}\right) \cdot \left(\frac{\frac{\delta\alpha}{\delta t}\alpha}{\frac{\delta\alpha}{\delta t}0.5}\right)$	Signifies the theoretical and experimental Z master plots	*Gotor et al., 2000*

3.3.7 Thermo-catalytic degradation study of sawdust and blends

The thermal degradation of sawdust and 100 % and 200 % blends in the absence and presence of the catalyst was studied using the thermogravimetry analysis. The thermally stable catalyst (studied at the heating rate of 20 K min^{-1}) was used for the thermo-catalytic

degradation of sawdust and the blends were individually performed. The catalytic effect of 10 % and 20 % NiO and Ni (II) aluminate composite nano-catalysts on the degradation of sawdust was evaluated by varying the catalyst loading by 5 %, 10 %, 15 %, and 20 % in weight (%) in sawdust at a single heating rate of 20 K min^{-1} from 303-1173 K temperature. The optimum catalyst wt.% was selected based on the observed highest degradability of sawdust and the blends. Further, the effect of heating rate on the catalytic effect was perceived at four heating rates (10, 20, 30 and 40 K min^{-1}) from 303-1173 K temperature. The analysis was executed by compelling approximately 6.5 mg of sample in a ceramic crucible at the precedence of N_2 inert gas flow rate of 20 mL min^{-1}.

3.3.8 Studies on pyrolysis experiment for pyrolytic behavior of biomass and coal as feedstocks

Thermal pyrolysis of coal and sawdust and its co-pyrolysis experiments were carried out in a horizontal tubular pyrolyzer. The pyrolyzer was made of SS 316 and had a length of 600 mm and inner diameter of 76.5 mm, was powered by 2000 W electrical heating and had a central heating zone of 150 mm. The volume of the reactor was 2700 mL which was insulated from outside region. The experiments were carried out at reaction temperatures of 773 K, 823 K and 873 K. The furnace was controlled by a PID controller, which had temperature feedback from a K-type thermocouple placed in the reaction zone. The entire set-up was placed in dual clamp, insulated bricks which can sustain high-temperature reactions. Nitrogen of 99.9% purity was supplied by Assam Air Gas Company Private Limited. The reactor chamber was purged with nitrogen gas for 20 min before the pyrolysis experiments. The gas flow rate was maintained at 300 mL min^{-1} (18 L h^{-1}) and the heating rate was maintained at 30 K min^{-1}. The samples were kept in an alumina boat of 80 mL volume. The evolved gas was condensed in a glass condenser and the oil was collected in a separating funnel. The condenser water temperature was maintained at 280–283 K. The char residue was collected at the end of the experiment for further analysis.

Initially, three sets of experiments were designed and conducted consisting of thermal (non-catalytic) pyrolysis of coal and sawdust and co-pyrolysis of coal-sawdust blends by blending 100 % sawdust to coal. For the thermal experiments, three temperature ranges were considered for experimentation, 773 K, 823 K and 873 K with pressure 1 bar and a heating rate of 30 K min^{-1}. The reaction temperature of 773 K, 823 K and 873 K denoted the temperatures inside the reactor furnace. Initial inventory of coal was 50 g (approx.), sawdust was 10 g (approx.) and blended mixtures was 20 g (approx.) in the alumina tray crucible. The reaction time was evaluated as 0.75 h till the final evolution of volatile gas from the reactor

outlet and the residence time was 0.15 h as calculated for each feed component inside the reactor. Further co-pyrolysis of other coal-sawdust blend samples (50 % and 200 % sawdust addition to coal) were evaluated at 873 K reaction temperature.

Catalytic upgradation experiments on product oil, biochar residue and evolved pyrolytic gas were evaluated by integrating composite catalysts of NiO and Ni (II) aluminates with sawdust in the crucible. In this scenario, (the catalyst/sawdust) ratio plays a prime role in estimating the optimum catalyst % with the highest degradability in the thermogravimetric experiment. This ensures that (the catalyst/sawdust) ratio is the optimization criteria for the initial feedstock inventory integrated for the catalytic pyrolysis experiment. The bio-oil was collected in a separating funnel and the char residue was collected at the end of the experiment for further analysis and characterization. However, the recyclability of the catalysts was not performed in the present context as the focus lies in the further utilization of the char residue in experiments. Similar catalytic upgradation experiments on pyrolyzed products were done for 100 % and 200 % coal and sawdust blends by integrating composite catalysts of NiO and Ni (II) aluminates. A brief outlay of the tubular fixed-bed pyrolyzer unit is shown in Fig. 3.1.

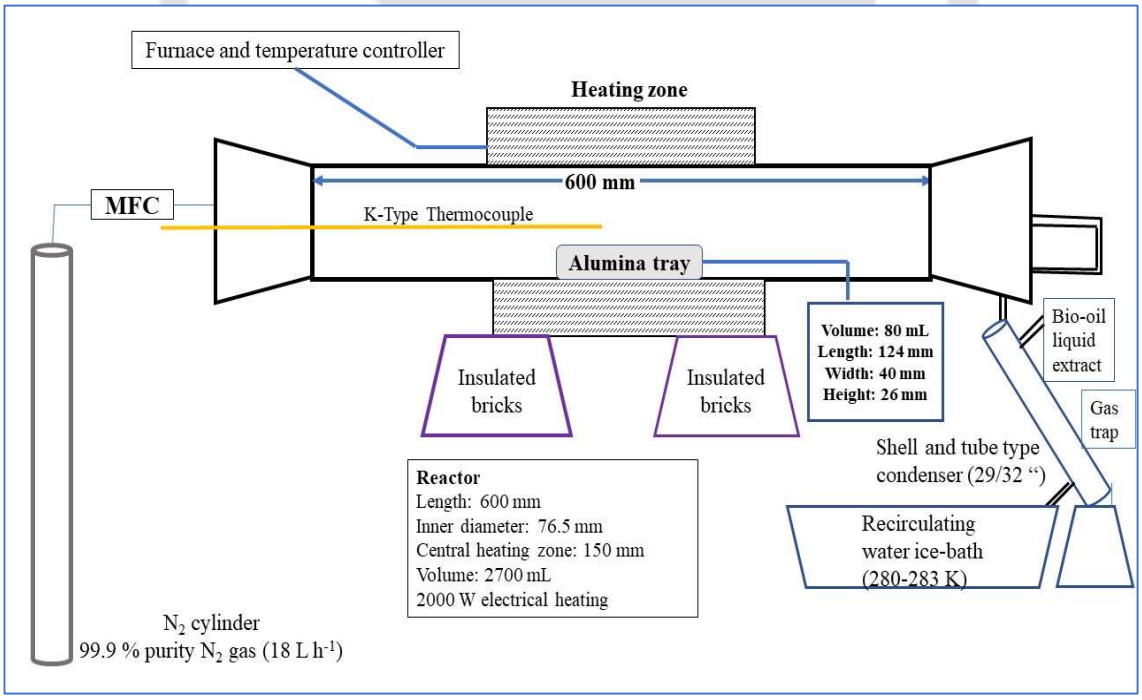

Fig. 3.1 Tubular fixed-bed pyrolyzer unit

3.3.8.1 Determination of the product yield

Product yield comprising of (liquid oil, char residue and evolved volatiles) are estimated based on weight %. Whereas the liquid oil yield is estimated based on the weight of the the

measuring flask before and after the completion of the reaction as reported by Cao et al. *(Cao et al., 2020),* char yield is estimated based on the amount of char residues after completion of the reaction as reported by Shen and Yoshikawa et al. *(Shen and Yoshikawa, 2014).*

For thermal pyrolysis of coal and sawdust, the yield of pyrolysis products and conversion was calculated as reported by Cao et al. and Shen and Yoshikawa et al. (*(Cao et al., 2020, Shen and Yoshikawa, 2014).*

$$\text{Liquid oil yield (wt. \%)} = ((X2 - X1)/Y2) * 100\ \% \quad (3.32)$$

$$\text{Char yield (wt. \%)} = \frac{Amount\ of\ solid\ residues\ (g)}{Total\ amount\ of\ feedstock} * 100\ \% \quad (3.33)$$

Yield of non-condensable gases = 100 – Liquid oil yield – Char yield (3.34)

Conversion = Yield of the liquid oil + Yield of non-condensable gases (3.35)

X1: Initial weight of the measuring flask, g

X2: Weight of measuring flask after completion of the reaction, g

Y2: Weight of feed, g

3.3.8.2 Characterization of the pyrolyzed product

3.3.8.2.1 Characterization of liquid oil product

FTIR analysis of the liquid oil extracts was carried out by an FTIR spectrometer (Model No.: Spectrum Two; Make: Perkin Elmer, Singapore) comprising of a liquid sampler. It carries the detection up to a depth of 30 cm at a temperature range of 278-293 K and operates at 4 scans per minute.

GC/MS analysis of the liquid oil samples was carried out with a Gas chromatography-mass spectrometer (Model No.: Clarus 680 GC; Make: Perkin Elmer, USA; amp.: Clarus 600C MS) comprising a liquid auto-sampler. The samples were first passed through a 0.25 µm mesh size nylon-membraned syringe filter and diluted in hexane with a dilution factor of 200 µL sample dissolved in 800 µL of solvent. The Software used in the system was TurboMass Ver. 5.4.2. The peaks were analyzed using data analysis software NIST-2014. The capillary column used was 'Elite-5MS' having dimensions- length-60 m, ID-0.25 mm, and film thickness of 0.25 µm and the stationary phase is 5 % diphenyl and 95 % dimethyl polysiloxane. Helium gas (99.99 %) was used as carrier gas (mobile phase) at a flow rate of 1 mL/min. An injection volume of 2 µL was employed in splitless mode. The injector temperature is 280°C and the ion-source temperature is 180°C. The oven temperature was programmed at 60°C (for 1 min), with an increase at the rate of 7°C/min to 200°C (hold for 3 min) then again increased at a rate of 10°C/min to 300°C (hold for 5 min). The total run time is ~39 min. Solvent delay was kept for 8 mins. MS Protocol Mass Spectra was taken in

Electron Impact positive (EI+) mode at 70 eV. A solvent delay of 8 min was there for the MS scan. Mass range, m/z range is 50-600 amu *(Swargiary and Daimari, 2021; Sarkar and Kalita, 2022).*

Differential Scanning Calorimeter (Model No.: DSC 1; Make: M/s Mettler Toledo, Switzerland) is used to measure the thermal properties (glass transition temperature, specific heat capacity (kJ kg^{-1} K^{-1}), heat flow (mW mg^{-1}), heat of fusion (J g^{-1}) and peak temperatures) of the liquid oil samples. The sample was placed in a covered alumina crucible and run under nitrogen purge gas (40 mL min^{-1}) and nitrogen as protective gas (60 mL min^{-1}) from 303-873 K at a constant heating rate of 20 K min^{-1} at 5.0 µV voltage.

For ^{1}H NMR spectroscopy analysis of bio-oil samples, the samples were diluted with DMSO (dimethyl sulfoxide) in the dilution factor of 10 µL of the sample with 100 µL of DMSO. The NMR spectroscope (Make: Bruker; Model: ASCEND 600) is used to measure the relative concentration of aliphatic and aromatic hydrocarbons in the bio-oil samples.

3.3.8.2.2 Characterization of thermal and catalytic char residue

The ultimate analysis (carbon, hydrogen, sulfur, and nitrogen) of the char residue samples was ascertained using CHNS Elemental Analyzer (Make: Eurovector, Model: Eurovector EA3000).

The proximate composition of the char residue samples was determined using ASTM procedures: E4442-20 (moisture), E872-82 (volatile) and E1755-01 (Ash) which were evaluated using the standard procedures.

X-ray Diffractometry was used to measure the chemical composition, crystallinity, crystal size, and in-plane scattering of the char samples. An X-ray Diffractometer (Make: SmartLab, Model: Rigaku Technologies, Japan) has a high-resolution diffractometer. Cu-K Beta filter was used in the instrumentation.

Gemini Field Emission Scanning Electron Microscope instrument (Make: Zeiss, Model: Gemini) equipped with Schottky type of field emitter and windowless EDS detector system is a high-performance instrument for achieving high-resolution images (0.8 nm at 15 kV and 1.4 nm at 1 kV) from low to high accelerating voltages (0.02-30 kV) up to a magnification from 1.0 KX. The sample was placed on a stub using double-sided carbon tape, double gold-coated and inserted into the chamber which operated at 15 kV operating voltage. High-resolution images were taken in the 1.0 KX, 5.0 KX and 10.0 KX magnification.

Field Emission Transmission Electron Microscope (Make: Jeol, Model: 2100F) equipped with a ZrO/W (100) Schottky type of field emitter is essential for ultrahigh resolution in scanning transmission microscopy and analysis of a nano-scaled sample. The

powder samples were dispersed in an isopropyl alcohol solution and vigorously sonicated for 20 mins in an ultra-sonicator. The dispersed solution of 5 µL (sample + isopropyl alcohol) was mounted in a (Cu) grid which was placed in a clean Petri dish and dried overnight in a hot air oven at 378 K.

FTIR analysis of the solid samples was carried out by an FTIR spectrometer (Model No.: Spectrum Two; Make: Perkin Elmer, Singapore) comprising a solid sampler. It carries the detection up to a depth of 30 cm and a temperature range of 278-293 K.

The ESR analysis of the feed samples was studied using an ESR instrument (Make: Jeol, Model: JES FA200) which employed powdered feed samples into the sample holder.

3.3.8.2.3 Characterization of fuel gas

Fuel gas was analyzed by a gas chromatography analyzer (Make: Nucon, Model: Series 5765) with both F.I.D. and T.C.D. detectors and a molecular sieve 5A column. The length of the column was 6 feet, the outer diameter was 1/8 mm, the inner diameter was 2 mm and the mesh size was 60–80. The purge gas used was nitrogen inert gas (flow rate: 30 mL min^{-1}) for the detection of hydrogen gas. The oven temperature was 70°C, the injector temperature was 180°C and the detector temperature was 200°C. Fuel gas was also analyzed by Testo 350 flue gas analyzer for the presence of gas components (CO, CO_2, O_2, NO_2, NO_x, SO_x, HC's). The gas flow rate at the outer surface of the analyzer probe was measured for each reaction run.

References

- Bhattacharyya, M., Shadangi, K.P., Mahanta, P. and Mohanty, K., 2022. Co-pyrolysis of coal-biomass: study on reaction kinetics and thermodynamics. *Biofuels, Bioproducts and Biorefining*, *16*(3), pp.725-742.
- Shadangi, K.P. and Mohanty, K., 2014. Kinetic study and thermal analysis of the pyrolysis of non-edible oilseed powders by thermogravimetric and differential scanning calorimetric analysis. *Renewable Energy*, *63*, pp.337-344.
- Li, L., Huang, Y., Zhang, D., Zheng, A., Zhao, Z., Xia, M. and Li, H., 2018. Uncovering structure–reactivity relationships in pyrolysis and gasification of biomass with varying severity of torrefaction. *ACS Sustainable Chemistry & Engineering*, *6*(5), pp.6008-6017.
- Kirtania, K. and Bhattacharya, S., 2013. Pyrolysis kinetics and reactivity of algae–coal blends. *Biomass and Bioenergy*, *55*, pp.291-298.
- Zhu, W., Song, W. and Lin, W., 2008. Catalytic gasification of char from co-pyrolysis of coal and biomass. *Fuel Processing Technology*, *89*(9), pp.890-896.
- Gil, M.V., Casal, D., Pevida, C., Pis, J.J. and Rubiera, F., 2010. Thermal behaviour and kinetics of coal/biomass blends during co-combustion. *Bioresource technology*, *101*(14), pp.5601-5608.
- Kastanaki, E., Vamvuka, D., Grammelis, P. and Kakaras, E., 2002. Thermogravimetric studies of the behavior of lignite–biomass blends during devolatilization. *Fuel processing technology*, *77*, pp.159-166.
- Khawam, A. and Flanagan, D.R., 2006. Solid-state kinetic models: basics and mathematical fundamentals. *The journal of physical chemistry B*, *110*(35), pp.17315-17328.
- Vyazovkin, S., Burnham, A.K., Criado, J.M., Pérez-Maqueda, L.A., Popescu, C. and Sbirrazzuoli, N., 2011. ICTAC Kinetics Committee recommendations for performing kinetic computations on thermal analysis data. *Thermochimica acta*, *520*(1-2), pp.1-19.
- Varma, A.K., Singh, S., Rathore, A.K., Thakur, L.S., Shankar, R. and Mondal, P., 2020. Investigation of kinetic and thermodynamic parameters for pyrolysis of peanut shell using thermogravimetric analysis. *Biomass Conversion and Biorefinery*, pp.1-12.

- Akahira, T.J.R.R.C.I.T. and Sunose, T., 1971. Method of determining activation deterioration constant of electrical insulating materials. *Res Rep Chiba Inst Technol (Sci Technol)*, *16*(1971), pp.22-31.
- Kissinger, H.E., 1957. Reaction kinetics in differential thermal analysis. *Analytical chemistry*, *29*(11), pp.1702-1706.
- Gotor, F.J., Criado, J.M., Malek, J. and Koga, N., 2000. Kinetic analysis of solid-state reactions: the universality of master plots for analyzing isothermal and nonisothermal experiments. *The journal of physical chemistry A*, *104*(46), pp.10777-10782. https://doi.org/10.1021/jp0022205.
- Shen, Y. and Yoshikawa, K., 2014. Tar conversion and vapor upgrading via in situ catalysis using silica-based nickel nanoparticles embedded in rice husk char for biomass pyrolysis/gasification. *Industrial & Engineering Chemistry Research*, *53*(27), pp.10929-10942.
- Cao, Z., Niu, J., Gu, Y., Zhang, R., Liu, Y. and Luo, L., 2020. Catalytic pyrolysis of rice straw: Screening of various metal salts, metal basic oxide, acidic metal oxide and zeolite catalyst on products yield and characterization. *Journal of Cleaner Production*, *269*, p.122079.
- Swargiary, A. and Daimari, M., 2021. GC–MS analysis of phytocompounds and antihyperglycemic property of Hydrocotyle sibthorpioides Lam. *SN Applied Sciences*, *3*(1), p.36.
- Sarkar, R.D. and Kalita, M.C., 2022. Green synthesized Se nanoparticle-mediated alleviation of salt stress in field mustard, TS-36 variety. *Journal of Biotechnology*, *359*, pp.95-107.

Chapter IV

Characterization of Feed and Catalyst

4.1 Introduction

This chapter describes the characterization of the feedstock materials and the prepared catalysts, 10 % and 20 % NiO and Ni (II) aluminate nano-composite catalysts for their applications in thermal and catalytic pyrolysis of biomass and co-pyrolysis reactions of coal and biomass blends. Detailed characterization and analysis of catalysts were done to delve into its design aspects which define the utilization efficiency of the catalyst by unifying the physico-chemical environment of its active sites. This substantially necessitates the profundity of its structure-activity-relationship implications through the precise engineering and design of its active site structure and functionalities.

4.2 Experimental validation

Feedstocks were characterized by surface morphological studies by FESEM analysis, the presence of functional groups by FTIR analysis, the presence of free radicals by ESR analysis and the presence of crystallinity by XRD analysis. Characterization of catalyst entails elemental characterization through EDX analysis, surface morphological characteristics such as microstructure and nanostructure morphology along with particle size distribution, surface height and roughness of the catalysts through FESEM, FETEM and AFM analysis, presence of crystallinity by XRD analysis, presence of functional groups by FTIR analysis, determination of pore surface area and pore size distribution analysis through BET-N_2 physisorption technique, effect of surface binding energies of the catalysts by XPS measurements and studies on its thermal stability by TG-DTG analysis.

4.3 Highlights of the chapter

- The physicochemical characterization of the feedstocks revealed that coal has higher ash content and lower volatile matter content than sawdust.
- Sawdust contains considerable volatile matter and lesser ash with higher quantities of alkali and alkaline earth metals (AAEM's) in the decreasing order of Al>Ca>Si>K>Mg>Fe>P.
- FESEM images showed a rough irregular polyhedral fractal surface of coal while sawdust revealed a flat and smooth surface with micropores. FTIR spectra showed the presence of various functional groups in coal and sawdust.
- The preparation method concocts a facile preparatory process of impregnation of the metal precursor into an acidic metal oxide (Al_2O_3) support and controlled morphology and particle sizes of the nanocomposite catalysts.

- XRD analysis portrayed the catalysts as nano-composite materials due to the presence of various phases such as nickel di-aluminate, nickel aluminum iron oxide, alumina, and nickel-oxide phases for both 10 % and 20 % nickel loaded catalysts. FETEM analysis visualized the occurrence of as nanoclusters with a particle size of 3.47 nm and 10.96 nm for 10 % and 20 % nickel loaded catalysts respectively.
- EDX analysis showed the nickel content prioritized in (weight %) as 8.6 % and 15.2 %, aluminum as 50.3 % and 36.9 % and oxygen content as 40.3 % and 47.4 %. This indicated the increase in oxygen content due to the presence of increased oxide phases with enhanced nickel and aluminum content in a 20 % nickel-loaded catalyst.
- FESEM images distinctly showed metal active nanoclusters onto the alumina support forming random nanocluster shapes which formed agglomerates with higher metal loading. Also, due to a higher number of active sites (high metal loading in 20 % Ni loaded catalyst) and increased support size, oxygen carrying capacity significantly increased with an increase in catalyst activity per surface area rendering it active in substrate reactivity.
- Multilayer adsorption was seen in 20 % Ni loaded due to the gradual curvature in pore filling during the adsorption process with an H3 hysteresis loop for 10 % and 20 % Ni loaded catalysts respectively from BET-N_2 isotherm.
- The catalysts were thermally stable up to a temperature of 1173 K.

4.4 Characterization of raw feeds

4.4.1 Physicochemical characterization

The proximate, ultimate and calorific value analysis are estimated for raw feeds, coal, and sawdust samples. Table 4.1 portrays the physico-chemical properties of the feed samples. It was observed that coal was low-rank since it has higher ash content and a lower calorific value index. Coal was less in moisture, volatile matter, and fixed carbon content compared to sawdust. However, the HHV of coal was significantly higher than that of sawdust Similar results are found in other literatures *(Vasilatos et. al., 2022)*. Since sawdust is softer than coal; the diffusion of moisture content during the sample preparation from the bulk to the surface is also possible.

Table 4.1 Physico-chemical properties of individual raw materials

Proximate analysis						
Feeds	**M, %**	**VM, %**	**A, %**	**FC, %**	**HHV, MJ kg^{-1}**	**HHV, MJ kg^{-1}** *****(Theoretical value)***
Coal	0.86	39.19	31.73	28.21	15.12	14.19
Sawdust	8.45	52.75	2.47	36.33	9.22	17.10

Ultimate analysis							
Feeds	**C, %**	**H, %**	**O, %**	**S, %**	**N, %**	**H/C**	**O/C**
Coal	35.80	3.89	27.23	1.425	31.64	1.302	0.573
Sawdust	47.14	5.15	36.15	0.2	11.34	1.309	0.578

**M: Moisture content, VM: Volatile Matter content, A: Ash content, FC: Fixed carbon content*

***Note: HHV (cal/g) as calculated by Dulong formula = 1/100[8080C +(34500 (H-N/8))) + (22400S)]*

The elemental composition of the raw materials by weight % (average values) is shown in Table 4.2. The analysis confirmed that the concentration of Si was higher in coal than the sawdust. Among the occurrence of alkaline earth metals and alkali metals, potassium and calcium showed higher weight percentages in sawdust at 3.68 % and 4.53 % than in coal which was 0.53 % and 0.70 % respectively. This visualized an intricate attribute of the catalytic property during pyrolysis reaction. Magnesium was found to be low (0.21 %) in coal compared to sawdust (2.48 %). Whereas sodium was more or less equal. Among the other minor elements, iron was found to be higher in coal (1.34 %) than sawdust (1.28 %). The presence of phosphorus was also higher in sawdust 0.45 % than in coal 0.13 %. The occurrence of manganese 0.18 % and titania 0.3 % in sawdust was minimal indicating the presence of mineral matter in sawdust. Copper content was higher in coal 0.11 % than in sawdust 0.03 %, whereas zinc was almost similar in the feeds (0.08 % in the coal and 0.10 % in the sawdust). Chlorine was negligible in coal at 0.03 % while the presence of chlorine in sawdust was 0.08 %. Other trace metals found in both coal and sawdust were ruthenium, rhodium, cobalt, silver, nickel, and zirconia with trace amounts of chromium in sawdust which is absent in coal.

The presence of abundant alkali and alkaline earth metals (AAEM) directly affected the chemical composition and product distribution of the pyrolysis end-products as reported by Liu et al. *(Liu et al., 2017).* Some trace elements such as iron content 1.28 %, phosphorus 0.45 % and manganese 0.18 % were also seen. Literature suggests poplar sawdust is rich in K and Ca with minor P content as reported by Wu et al. which is similar to the present study *(Wu et al., 2020)*. The presence of such minerals in sawdust behaves as catalysts to enhance

the rate of thermal degradation to generate pyrolytic vapors. As a result, secondary cracking reactions occurred in the reaction pathway upgrading the pyrolytic end-products. It is reported that Cu and Fe have a higher affinity towards K, thus inducing potassium chemical transformation pathways. Biochar cracking takes place inherently due to the secondary cracking of volatiles catalyzed by certain K-containing compounds generating higher amounts of evolved volatiles (e.g., CO, H_2, CH_4, C_2H_4, CO) *(Bridgewater, 2012).* The free ionic forms of AAEM's can be released to a larger extent than their hydro-oxide and carbonate species. Ca and Mg are more likely to be retained in the biochar phase than Na and K as reported by Liu et al. *(Liu et al., 2017).* The mass transfer of AAEM's from biochar to a vapor phase and then through condensation to bio-oil occurs via an interaction between organic volatiles and free radical forms of AAEM's *(Oudenhoven et al. 2015).* Heavy metals (Cu, As, Cd, Co, Zn, Fe, Ni, Pb, Ti, Ag, Cr, Zr) have a dual role in the transformation and distribution of residual biochar and bio-oil during biomass pyrolysis. The effect of low-temperature states that 723 K is the optimum temperature for the transformation of minimal amounts of Zn and Cd into bio-oil *(Stals et al., 2010)* and Pb as maximum in the biochar than bio-oil. Richardson et al. stated that despite nickel being in trace quantities, it has an affinity towards inducing catalytic reactions in the biomass pyrolysis reaction as they are embedded in the residual biochar in the form of biochar-supported metallic (Ni) nanoparticles. This is instigated due to the less temperature induced reduction (723 K) of an amorphous $Ni_xO_yH_z$ phase with carbon atoms to metallic (Ni) nanoparticles which is in a catalytically active phase for selective tar reduction and hydrogen production *(Richardson et al., 2010).* In addition to this, inorganic metal elements might also influence the acid-base ratios of ash elements when combustion and gasification systems were studied for their ash fusibility tests, a phenomenon atypical in slow-rate inducing pyrolysis reactions. However, during pyrolytic vapour combustion or reforming reactions, the presence of AAEM in the biomass resulted in the deposition of chlorinated species leading to higher corrosion in the walls of the reactor.

Table 4.2 EDX analysis of raw materials

Element	Coal	Standard deviation	Sawdust	Standard deviation
Si	6.51	2.03	4.05	3.47
P	0.13	0.08	0.45	0.12
K	0.53	0.18	3.68	1.0
Ca	0.7	0.25	4.53	1.1
Fe	1.34	0.47	1.28	0.70
Cl	0.03	0.01	0.08	0.02
Cu	0.11	0.10	0.03	0.02
Co	0.03	0.03	0.03	0.02
Mg	0.21	0.08	2.48	0.57
Mn	0.05	0.05	0.18	0.07
Ti	0.45	0.16	0.3	0.02
Ru	0.01	0.01	0.002	0.01
Rh	0.01	0.01	0.05	0.07
Zr	0.05	0.03	0.18	0.17
Na	0.09	0.06	0.1	0.07
Mo	0.09	0.09	0.08	0.12
Zn	0.08	0.05	0.1	0.01
Ag	0.01	0.02	0.05	0.1
Ni	0.03	0.012	0.05	0.05
Cr	-	-	0.03	0.02

** The values are expressed in wt.%.*

4.4.2 XRD analysis

PDF Card No.: 00-005-0625 Quality: O of coal reveals the chemical name, chemical formula, chemical composition, crystal system and atomic planes (in-plane scattering). The chemical name of coal is graphite (inorganic, mineral, alloy) and the chemical formulae is C. PDF Card No.: 00-057-0503 Quality: I of sawdust also revealed the chemical name, chemical formula, chemical composition, crystal system and atomic planes (in-plane scattering). The chemical name of sawdust was potassic-chloro-pargasite and the chemical formulae was [(K, Na) Ca_2 (Mg, Fe^{+2})$_4$ Al (Si_6 Al_2) O_{22} (Cl, $OH)_2$]. The chemical composition of the raw sample in weight % was Na_2O: 1.22 %, K_2O: 3.03 %, CaO: 11.41 %, MgO: 9.08 %, FeO: 16.63 %, Al_2O_3: 15.05 %, TiO_2: 0.26 %, SiO_2: 38.71%, Cl: 4.33 %, OCl_2: 0.98 %. The observed density was 3.29 g/cc while the calculated density was 2.33 g/cc.

The XRD analysis of the feed samples is shown in Fig. 4.1. It is noticed that coal shows a crystalline XRD diffractogram. The XRD diffractogram of coal is measured at a diffraction

angle of 26.59°-102.46° (2-Theta°) at a scan speed of 21.67°/min with a step width of 0.0300°. The peaks are obtained at 2-Theta° of 26.59°, 42.40° 44.37°, 50.64°, 54.76°, 59.98°, 77.55°, 83.75°, 87.20°, 98.87°, 102.03° and 102.46°, where the peak with the highest intensity was at 26.59°. The (h, k, l) parameters of coal at 2-Theta° of 26.59° is (0, 0, 2), 42.40° (1, 0, 0), 44.37° (1, 0, 1), 50.64° (1, 0, 2), 54.76° (0, 0, 4), 59.98° (1, 0, 3), 77.55° (1, 1, 0), 83.75° (1, 1, 2), 87.20° (0, 0, 6) 98.87°, 102.03° and 102.46° respectively. The lattice structure of coal is hexagonal structure and the lattice parameters are a=2.4620, b=2.4620, and c=6.7010. The space group of the lattice structure is 0. However, sawdust shows a polycrystalline XRD diffractogram. The XRD diffractogram of sawdust is measured at a diffraction angle of 10-90 (2-Theta°) at a scan speed of 21.67°/min with a step width of 0.0300°. It indicated various peaks with variable peak positions, peak intensity, and peak width at the consequent (2-Theta°) diffraction angle. The peaks are obtained at 2-Theta° of 14.90°, 18.39°, 22.43°, 29.94°, 32.14°, 33.96°, 37.25°, and 44.10° respectively. Peak intensity is observed to be the highest at 22.43° (2-Theta°) among all the other peaks. This is due to the superimposition effect of the constructive and destructive contribution of the atoms in the lattice structure. The crystallinity percent is 95.5 % and the crystallite size is 197.3 nm according to the Debbye Scherrer equations, Eq. (3.2) and Eq. (3.3). The d-planar spacing is seen to be the highest initially at 14.90° (2-Theta°) and with increasing (2-Theta°) diffraction angle, the d-spacing decreased. The peak width is also seen to be broader at 14.90° (2-Theta°) due to the non-uniform strain in the peak. The (h, k, l) parameters at 2-Theta° of 14.90° was (0, 2, 0), 18.39° (3, 1, 0), 22.43° (4, 0, 0), 29.94° (2, 0, 2), 32.14° (2, 4, 0), 33.96° (6, 0, 0), 37.25° (8, 2, 0) and 44.10° (-5, 3, 2) respectively. The lattice structure of sawdust is of the monoclinic structure (b) and the lattice parameters are a=1.59, b=1.18 and c=0.669. The space group of the lattice structure is 12: C 12/m1, unique b, cell-1 with a Z factor of 2 and Z' factor of 0.250.

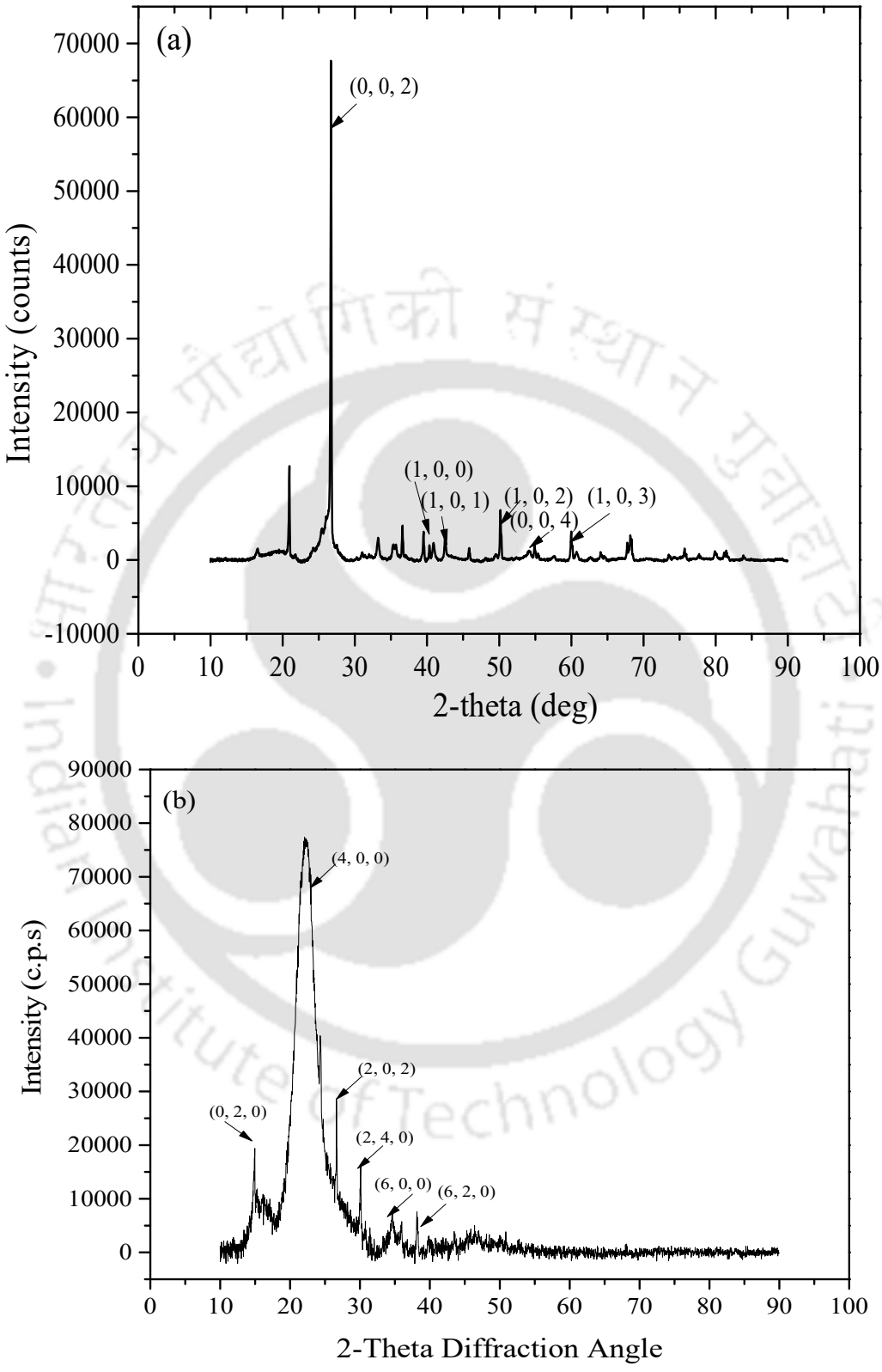

Fig. 4.1 X-ray Diffractogram of (a) Coal and (b) Sawdust

4.4.3 FESEM analysis

The FESEM analysis of the feed samples, coal and sawdust is shown in Fig 4.2. It is noticed that the surface morphological and topological study of the feed samples produced its microstructure images. Images were taken at the magnifications: 500X, 1.0KX, 5.0KX and 10.0KX. Fig. 4.2 (a-d) represents an irregular rough polyhedral fracture surface of the coal particles with a great number of staggered fractures with sharp edges seen at a particle size of 20 µm. It shows a very minimal number of pores with micropores densely distributed where structures are fractured. This is seen at higher magnifications of 5.0KX and 10.0KX of particle sizes of 5 µm and 3 µm respectively. Fig. 4.2 (e-h) represented a flat and smooth surface of the sawdust sample with micro-porous structures. Images are taken at the magnification 500X, 3.0KX, 5.0 KX and 10.0 KX with particle sizes of 30 µm, 20 µm and 2 µm respectively. It indicates a highly porous structure of the sawdust sample with pore diameters of 14.54 µm and 16.35 µm respectively. Pores are visualized such that they occur almost linearly placed in the raw sawdust particle.

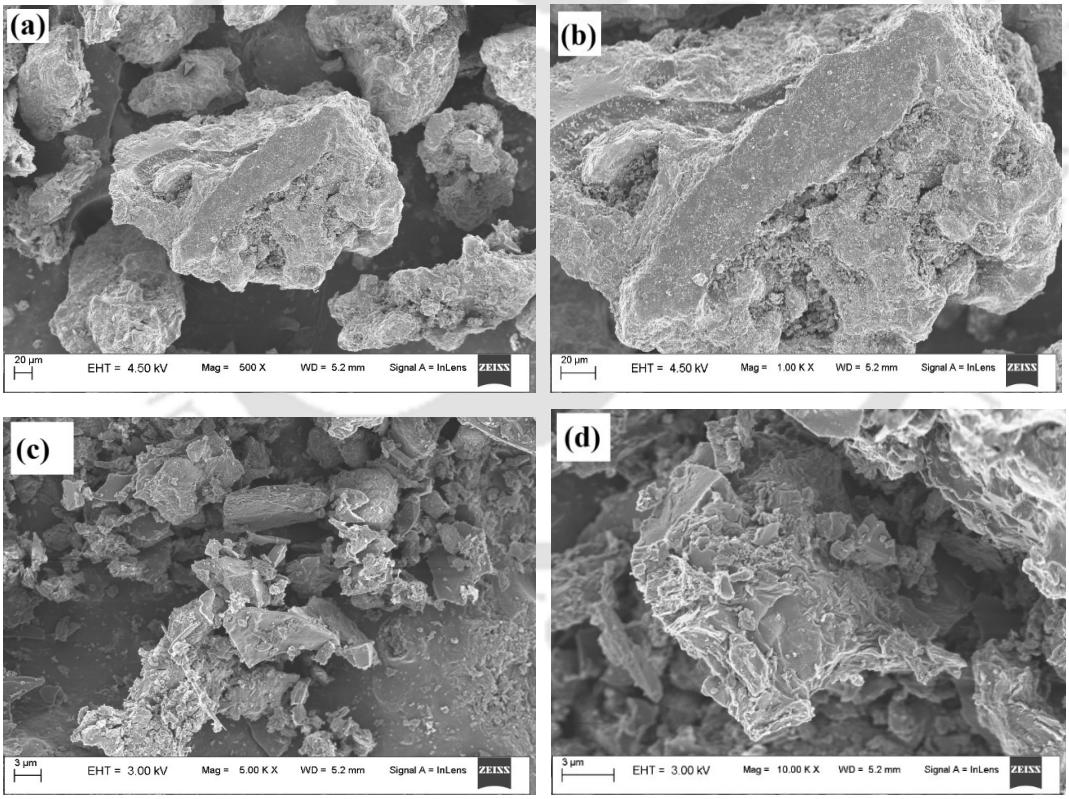

(Continued)

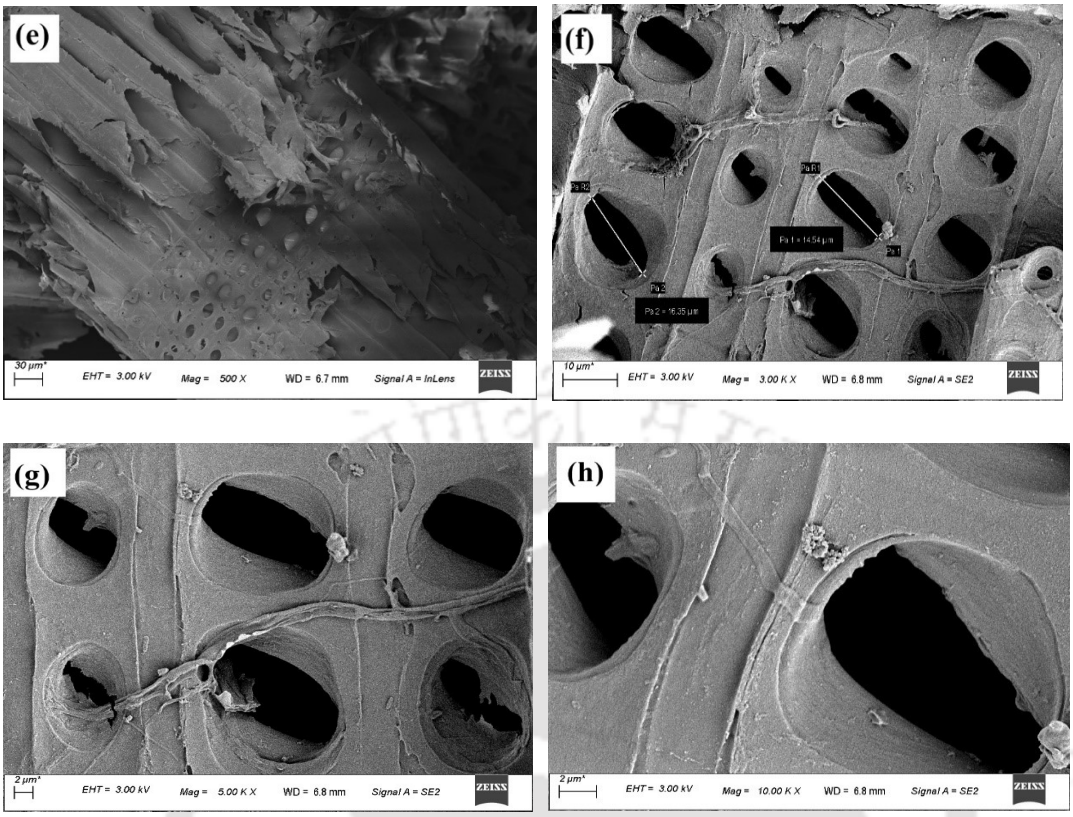

Fig 4.2 FESEM Images of (a-d) Meghalaya Coal and (e-h) Sawdust at magnifications 500.0 X, 1.0KX, 5.0KX and 10.0KX

4.4.4 FTIR analysis

The FTIR analysis of the feed samples is shown in Fig. 4.3. It was noticed that most of the peaks obtained in sawdust and coal had the same wavenumber with variations in absorbance. The intensity of the absorbance peak noticed at 3438 cm^{-1} was due to the presence of OH group (hydroxyl radical) may be related to the presence of moisture content. A small peak noticed at 2900 cm^{-1} shows the presence of cellulose. It is the occurrence of methylene group in the cellulose and allocated as C–H stretching vibration. The peak obtained at 1376 cm^{-1} visualized the incidence of C-H bond bending vibrations, denoted the appearance of molecules of cellulose and hemicelluloses. The presence of cellulose and hemicellulose was noticed at 1073 cm^{-1} shows the stretching vibration of C–O–C *(Zhang et al., 2019).* However, the existence of lignin was identified at 1627 cm^{-1}, accredited to the benzene ring in the molecules of lignin. It also says about the attendance of nitrogen in the ring. Hydroxyl groups including aliphatic, condensed phenolic, guaiacyl phenolic, p-hydroxyl phenyl and carboxylic hydroxyl groups are present in the biomass components. The occurrence of aromatic C-H vibrations observed at 2355 cm^{-1} was noticed at both the coal and

sawdust respectively. C-H bending vibrations of the alkane group was perceived at 1472 cm^{-1}. The hydroxyl group in coal is not only because of the presence of water. It also shows the indication of several chemical compounds such as pyridine and polycyclic aromatic compounds present in the coal *(Solomon and Carangelo, 1988; Li et al., 2017)*. The occurrence of such compounds are the cause of the higher thermal stability of coal over sawdust *(Li et al., 2017)*.

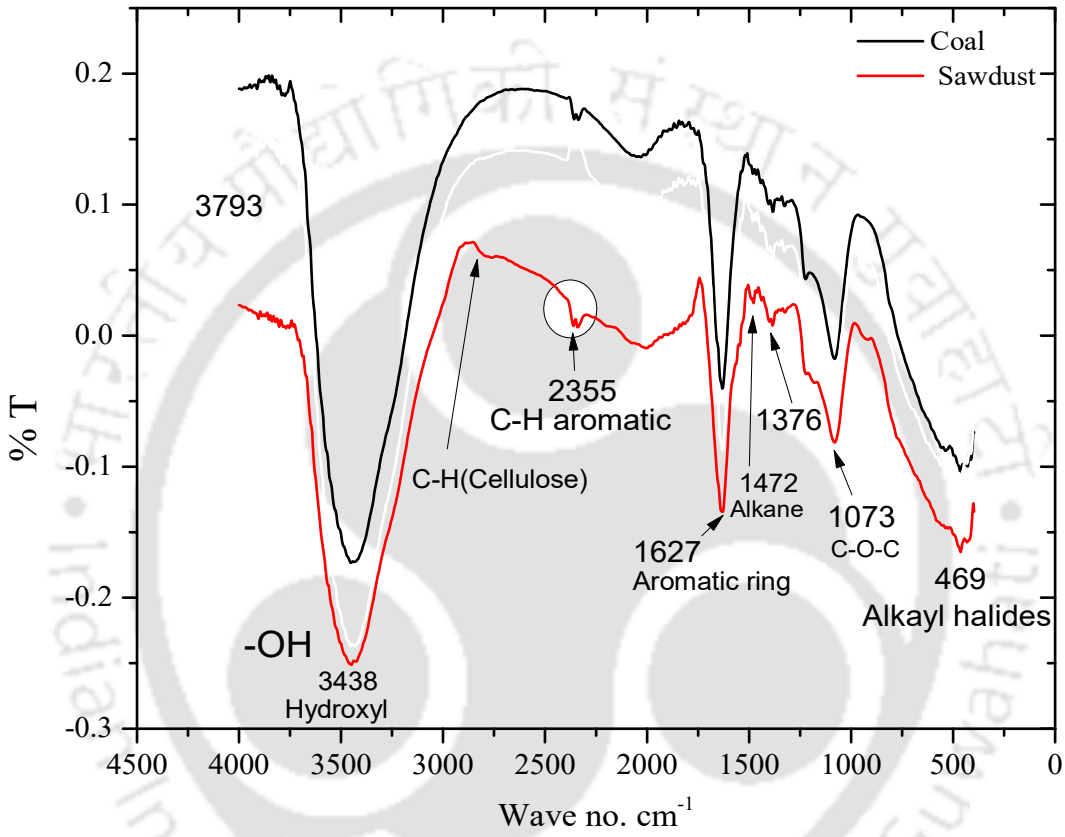

Fig 4.3 FTIR spectra of coal and sawdust

4.4.5 Raman analysis

Fig. 4.4 portrays the Raman spectra of coal and sawdust. Raman spectra of coal detected the presence of D band and G band at 1300 cm^{-1} and 1575 cm^{-1} Raman shift. Raman spectra of sawdust detects the presence of cellulose, hemicellulose, and lignin. For the presence of cellulose, intense peaks or bands are observed at 900-1200 cm^{-1}, 1200-1500 $cm^{-1,}$ and 2600-3000 cm^{-1} Raman shift, amongst which peaks at Raman shift 951 cm^{-1}, 1053 cm^{-1}, 1120 cm^{-1}, 1326 cm^{-1} and 1423 cm^{-1} are the sharpest. The intensive peak at 951 cm^{-1}, 1053 $cm^{-1,}$ and 1120 cm^{-1} was due to stretching vibrations of C-C and C-O bonds and C-C and C-O-C bonds of cellulose respectively *(Xu et al., 2020)*. Another peak was observed at 853 cm^{-1} due to the

C-C bond of cellulose. The sharp peaks at 1326 cm^{-1} and 1423 cm^{-1} were due to the aliphatic O-H bend and HCC, HCO, and HOC bending along with the presence of the CH_2 functional group of cellulose *(Xu et al., 2020)*. For the presence of lignin, intense peaks were observed at 1053 cm^{-1}, 1598 cm^{-1}, and 2812 cm^{-1} which denotes the presence of the C-O bond of aryl-H_3 group, aryl-OH group of lignin, C=C bond in the aromatic ring of lignin and C-H stretch of -OCH_3 group of lignin respectively *(Xu et al., 2020)*. I_L/I_C refers to the intensity ratio of the band for lignin at 1600 cm^{-1} to the band for holocellulose at 2812 cm^{-1}.

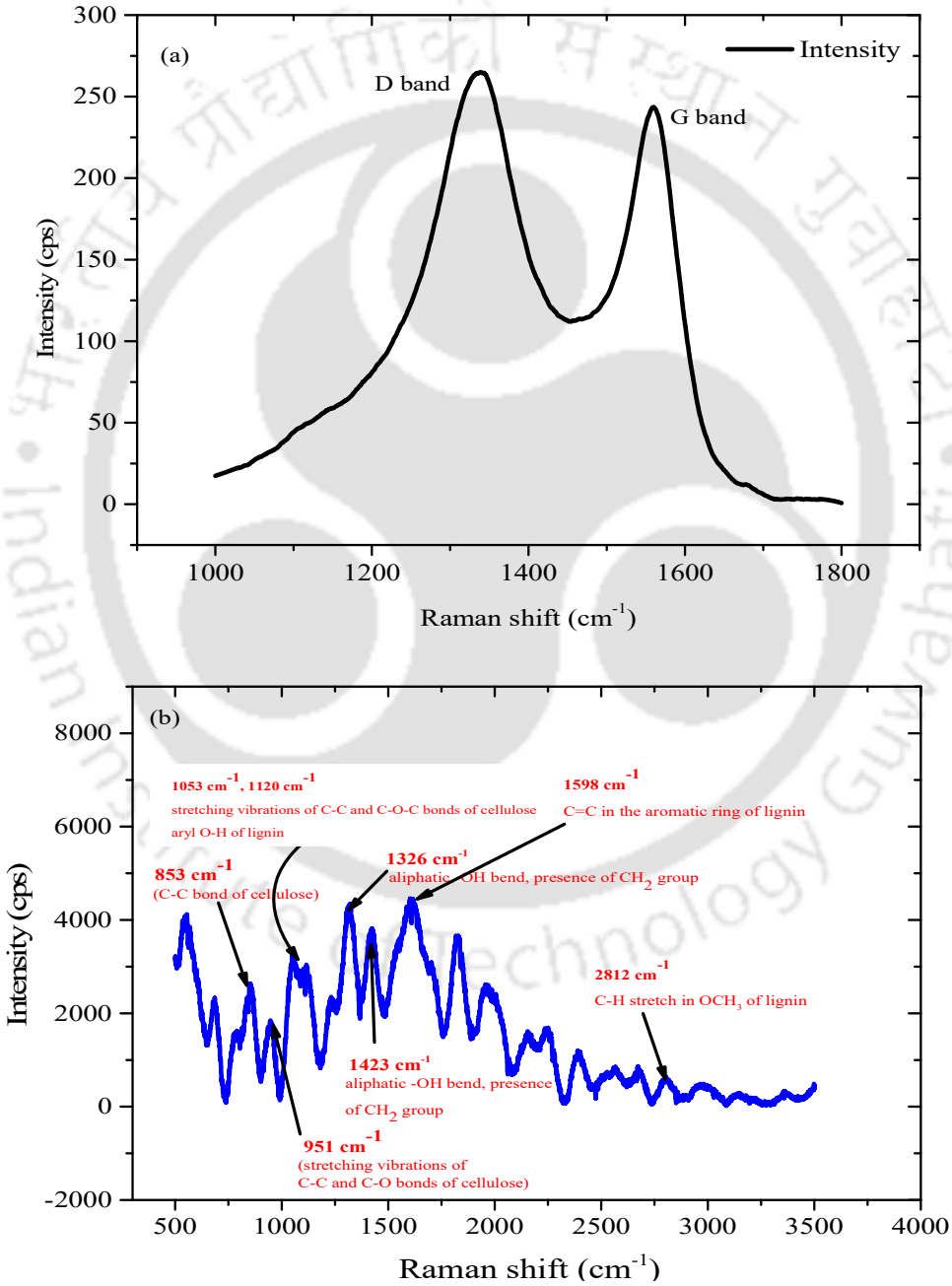

Fig. 4.4 Raman spectra of (a) Coal and (b) sawdust

4.4.6 ESR analysis

Fig. 4.5 depicts the ESR spectra of coal and sawdust with a variance in peak position, peak area, and peak profile according to Zeeman transitions of the unpaired electrons of paramagnetic species. The paramagnetic species might be chemically reactive organic free radicals or point defects in solids. Multiple paramagnetic species are seen in coal molecular structure. Hence the ESR spectra of coal is a smooth curve without the hyperfine spectral splitting structure. It was observed that the ESR spectral intensity of sawdust was lesser than coal because of the presence of oxygen-free radicals which interacted strongly with the carbon-centered radicals of sawdust. The g-factor indicates the higher heteroatom content of the feeds, which was 2.015 for coal and 2.00255 for sawdust. This indicated graphitic structure for coal and aliphatic π type radicals located on hydrocarbons for sawdust *(Trubetskaya et al., 2016, Petrakis and Grandy, 1978).* Morgan and Kandiyoti reviewed the pyrolysis of coal and biomass and analysis of their thermal breakdown *(Morgan and Kandiyoti, 2014).* Singer and co-workers stated that the ESR spectra of coal reflect stable free-radical populations embedded within coal matrices *(Singer and Lewis, 1982).*

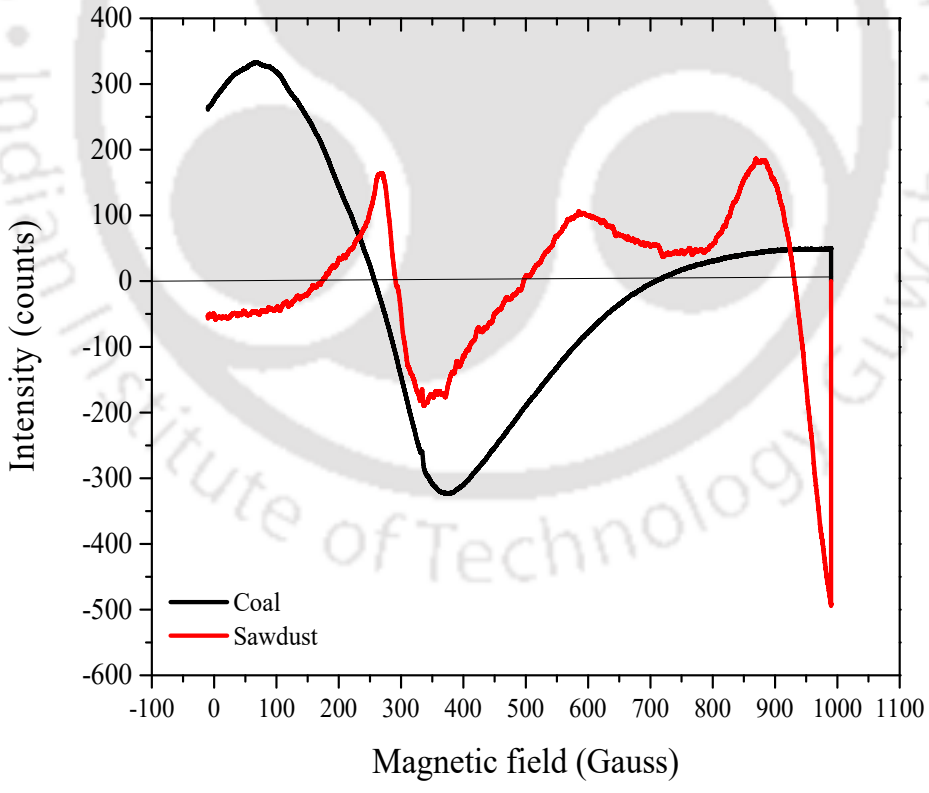

Fig. 4.5 ESR Spectra of coal and sawdust

4.5 Characterization of blended fuels

4.5.1 Physicochemical characterization

The effect of sawdust blending from 10% to 200% with coal resulted in increasing the moisture, volatile matter, and fixed carbon content of the blended sample. The values of such characteristic properties were less in the blended samples compared to the sawdust and higher compared to the coal. The value of ash content was found to decrease with the increase in the % of sawdust in the blended sample and comparison, with coal, it was less. However, no direct relation was noticed on the HHV as the % sawdust blending was raised. In comparison with the coal, the HHV of the 100% sawdust blended sample was higher. The result of less moisture content even in the 100% blended sample was lower than the sawdust. This could be due to the release of moisture during sample preparation. Since the sample was prepared by grinding, the generation of heat would be possible. The increase in the sample temperature would help in the release of some of the moisture present in the bulk of the sawdust during the sample preparation. The decrease in the amount of oxygen in the sample was also confirmed by the ultimate analysis. The presence of less oxygen and hydrogen in the 100% blends could be the cause of increasing the HHV. The oxygen content in the 100% blend was less compared to sawdust but higher than the coal. The impact of sample preparation was also noticed on the N_2 concentration in the blends. The N_2 content decreased in the blends compared to the coal. However, the sulfur concentration in the blends was close to the sum of the % present in the coal and sawdust. This confirmed that the preparation of samples also plays an important role in the composition of the blended samples. As the sawdust and coal blends yielded a little higher HHV compared to coal and sawdust, it can be predicted that the yield of pyrolytic vapor will be higher during pyrolysis. So, co-pyrolysis is a better option to produce a better quality of pyrolytic vapor.

Table 4.3 Physico-chemical properties of various blending conditions of coal and sawdust

Proximate analysis						
Feed	**M, %**	**VM, %**	**A, %**	**FC, %**	**HHV, MJ kg^{-1}**	**HHV, MJ kg^{-1}** ***(Theoretical value)*****
Sawdust	8.45	52.75	2.47	36.33	9.22	17.10
Coal	0.86	38.19	31.73	28.21	15.12	14.19
10% blend	1.55	40.42	29.07	28.96	12.56	14.37
30% blend	2.61	42.31	24.97	30.11	16.24	15.14
50% blend	3.42	43.71	21.97	30.90	11.07	15.59
70% blend	3.98	44.77	19.68	31.57	11.66	15.94
90% blend	4.00	45.61	17.87	32.52	12.29	16.34
100% blend	4.65	45.97	17.10	32.28	16.00	16.35
200% blend	5.92	48.23	12.22	33.63	-	16.07

Ultimate analysis							
	C, %	**H, %**	**O, %**	**S, %**	**N, %**	**H/C**	**O/C**
Sawdust	47.14	5.15	36.15	0.2	11.34	1.309	0.578
Coal	35.80	3.89	27.23	1.425	31.64	1.302	0.573
10% blend	36.83	4.01	28.04	1.445	29.66	1.303	0.573
30% blend	38.43	4.18	29.29	1.485	29.60	1.304	0.574
50% blend	39.57	4.31	30.19	1.525	24.38	1.305	0.575
70% blend	40.48	4.41	30.90	1.562	22.63	1.305	0.575
90% blend	41.46	4.51	31.59	1.605	20.81	1.303	0.574
100% blend	41.47	4.52	31.69	1.622	20.67	1.306	0.576
200% blend	43.36	4.73	33.19	0.608	18.10	1.309	0.574

**M: Moisture content, VM: Volatile Matter content, A: Ash content, FC: Fixed carbon content*

***Note: HHV (cal/g) as calculated by Dulong formula = 1/100[8080C +(34500 (H-N/8))) + (22400S)]*

4.5.2 EDX analysis

The impact of mixing on the mineral composition was also noticed perfectly. The increase in the sawdust % in the blends increased the occurrence of the mineral elements. This confirmed that during the sample preparation process, no degradation of mineral content in the sample occurred.

Table 4.4 EDX analysis of raw materials

Element	10 % Blend	30 % Blend	50 % Blend	70 % Blend	90 % Blend	100 % Blend	200 % Blend
Si	4.7	6.0	6.4	8.6	9.91	10.56	9.21
P	0.46	0.48	0.68	0.53	0.5	0.57	0.43
K	3.72	3.83	5.53	4.04	4.14	4.2	2.98
Ca	4.59	4.73	6.82	5.01	5.15	5.22	3.72
Fe	1.4	1.67	1.97	2.21	2.47	2.61	2.19
Cl	0.07	0.08	0.11	0.09	0.09	0.1	0.08
Cu	0.03	0.05	0.04	0.1	0.12	0.13	0.13
Co	0.02	0.03	0.03	0.04	0.04	0.05	0.05
Mg	2.49	2.53	3.72	2.62	2.66	2.68	1.86
Mn	0.18	0.19	0.26	0.21	0.22	0.22	0.17
Ti	0.345	0.43	0.47	0.61	0.7	0.75	0.65
Ru	0.001	0.003	0.0006	0.008	0.01	0.012	0.01
Rh	0.05	0.05	0.07	0.05	0.06	0.06	0.04
Zr	0.18	0.19	0.26	0.21	0.22	0.22	0.17
Na	0.1	0.12	0.15	0.16	0.17	0.18	0.16
Mo	0.08	0.1	0.11	0.13	0.15	0.16	0.14
Zn	0.1	0.12	0.15	0.15	0.16	0.17	0.15
Ag	0.05	0.05	0.07	0.05	0.06	0.06	0.04
Ni	0.05	0.05	0.07	0.06	0.07	0.07	0.06
Cr	0.02	0.02	0.03	0.02	0.025	0.02	0.02

** The values are expressed in average wt. %*

4.6 Characterization of catalyst

4.6.1 XRD Analysis

The XRD diffractogram of 10 %, 20 % Ni loaded catalyst and alumina support is shown in Fig. 4.6 and the crystal structure, crystallinity %, and crystallite size are depicted in Table S1, S2, and S3 in Annexure. The PDF Card No.: 00-008-0013, Quality: O was reported for activated alumina support. It is a synthetic form of alumina, produced at a lower temperature which is a mixture of new "kappa" and theta alumina. The XRD diffractograms of the alumina support are depicted in Fig. 4.6 (a). The elemental phase peaks were seen at various 2θ diffraction angles of 15.62°, 37.45°, 43.65°, 45.63° and 67°. The crystallite size of Al_2O_3 support with Al_2O_3 phase was 11.52 nm from the Debyye-Scherrer equation from (Eq. 3.2) and crystallinity % was seen as 93.66 % from (Eq. 3.3). Three main peaks of calcined

alumina support at 2-Theta diffraction angles of 37.69°, 45.23° and 66.63° respectively are considered for their calculations and as mentioned in Table S2 - S3.

For the 10 % NiO/Al_2O_3 composite catalyst, the PDF Card No.: 00-001-1303 Quality: B was reported for the alumina phase which is an inorganic, alloy metal, cement and hydration product. It has a cubic form of lattice structure and would transform into a hexagonal lattice under the effect of temperature from 1023.15 – 1273.15 K. The Al_2O_3 phase peaks were seen at 2θ° of 45.79° and 66.76° respectively. The PDF Card No.: 01-075-9711 Quality: B was reported for the nickel di-aluminate phase. The $NiAl_2O_4$ peaks were seen at 2θ° of 19.29°, 37.43°, 45.53°, and 66.36°. The PDF Card No.: 00-010-0339 Quality: S was reported for nickel aluminum oxide. The $NiAl_2O_4$ phase peaks with cubic crystal lattice structure were seen at 2θ° of 19.49°, 37.01°, 45.00°, 46.08° and 66.33° respectively. The PDF Card No.: 00-037-1292 Quality: I was reported for $NiAl_{10}O_{16}$ with monoclinic crystal lattice with phase peaks at 2θ° of 37.59°, 45.53°, 59.66° and 65.54° respectively. The PDF Card No.: 00-020-0777 Quality: I was reported for $NiAl_{32}O_{49}$ with monoclinic crystal lattice with phase peaks at 2θ° of 37.41°, 37.72°, 45.43° and 46.36° respectively. The PDF Card No.: 01-079-5342 Quality: I was reported for nickel aluminum iron oxide with formulae $(Fe_{0.35}Ni_{0.12}Al_{0.53})$ $(Ni_{0.88}Fe_{0.15}Al_{0.97})$ O_4 and a cubic crystal lattice system. Phase peaks of nickel aluminum iron oxide were seen at 2θ° of 36.70° and 64.95° respectively. The PDF Card No.: 01-081-8430 Quality: I was reported for $NiFe_{1.5}Al_{0.5}O_4$ whereas PDF Card No.: 01-081-8429 Quality: I was reported for $NiFe_{1.75}Al_{0.25}O_4$. Phase peaks of $NiFe_{1.5}Al_{0.5}O_4$ were seen at 2θ° of 35.83° and 63.29° and for $NiFe_{1.75}Al_{0.25}O_4$ were seen at 2θ° of 35.68° and 63.00° respectively. The PDF Card No.: 01-088-2326 Quality: B was reported for nickel, syn metal crystal with cubic lattice whereas PDF Card No.: 00-001-1239 Quality: B was reported for NiO (Bunsenite) with cubic lattice structure. Nickel, syn metal crystal peaks were seen at 2θ° of 45.50° and NiO phase peaks were seen at 2θ° of 37.44°, 43.47° and 63.20° respectively. The PDF Card No.: 00-014-0481 Quality: O was reported for Ni_2O_3, nickel oxide with hexagonal lattice and with phase peaks at 31.94°, 51.60°, and 56.78°. The crystallite size was 16.107 nm from the Debbye-Scherrer equation from (Eq. 3.2) and crystallinity % was 96.29 % from (Eq. 3.3) as mentioned in Table S2-S3. The three main phase peaks of 10 % Ni-loaded catalyst composite at a 2-Theta diffraction angle of 37.69°, 45.23° and 66.63° respectively are considered for their calculations.

For 20 % NiO/Al_2O_3 composite catalyst, PDF Card No.: 00-001-1303 Quality: B, reported for the alumina phase which is an inorganic, alloy metal, cement and hydration product. Alumina phase peaks were seen at 2θ° of 45.79° and 66.76°. The PDF Card No.: 01-

073-6579 Quality: I was reported for $Al_{2.66}O_4$ peaks which inherit cubic lattice with $Al_{2.66}O_4$ phase peaks at 2θ° of 37.71°, 45.88° and 66.89°. The PDF Card No.: 01-075-9711 Quality: B was reported for the nickel di-aluminate phase. The $NiAl_2O_4$ peaks were seen at 2θ° of 19.29°, 37.43°, 45.53° and 66.36°. The PDF Card No.: 01-079-5342 Quality: I was reported for nickel aluminum iron oxide with formulae $(Fe_{0.35}Ni_{0.12}Al_{0.53})$ $(Ni_{0.88}Fe_{0.15}Al_{0.97})$ O_4 and cubic crystal lattice system. The $(Fe_{0.35}Ni_{0.12}Al_{0.53})$ $(Ni_{0.88}Fe_{0.15}Al_{0.97})$ O_4 phase peaks were seen at 2θ° of 36.70° and 64.95° respectively. The PDF Card No.: 01-081-8430 Quality: I was reported for $NiFe_{1.5}Al_{0.5}O_4$ with a cubic lattice and phase peaks at 2θ° of 35.83°, 43.55°, 57.62° and 63.29° respectively. The PDF Card No.: 00-013-0458 Quality: I was reported for Fe_2O_3 (iron oxide) with a tetragonal lattice system, whereas PDF Card No.: 00-003-0862 Quality: O was reported for Fe_3O_4 (magnetite) with a cubic lattice system. The Fe_3O_4 phase peaks were seen at 2θ° of 30.17°, 35.45°, 37.28°, 43.25°, 53.55°, 57.56° and 62.26° respectively. The PDF Card No.: 01-077-3085 Quality: B was reported on nickel, syn phase with a cubic lattice, whereas PDF Card No.: 00-001-1239 Quality: B was reported on NiO (Bunsenite) phase with a cubic lattice structure. Nickel, syn phase peaks were seen at 43.94° and 51.19° and NiO phase peaks were seen at 37.44°, 43.47° and 63.20° respectively. However, PDF Card No.: 01-078-0553 Quality: I was reported for spinel (Cu, Ni) $(Cu_{0.25}Ni_{0.75}Al_2O_4)$ with a cubic lattice structure. Crystallite size was 16.10 nm from the Debbye-Scherrer equation from (Eq. 3.2) and crystallinity % was seen as 93.35 % from (Eq. 3.3) as mentioned in Table S2-S3. The three main phase peaks of 20 % Ni loaded catalyst at a 2-Theta diffraction angle of 37.69°, 45.23°, and 66.63° respectively are considered for its calculations.

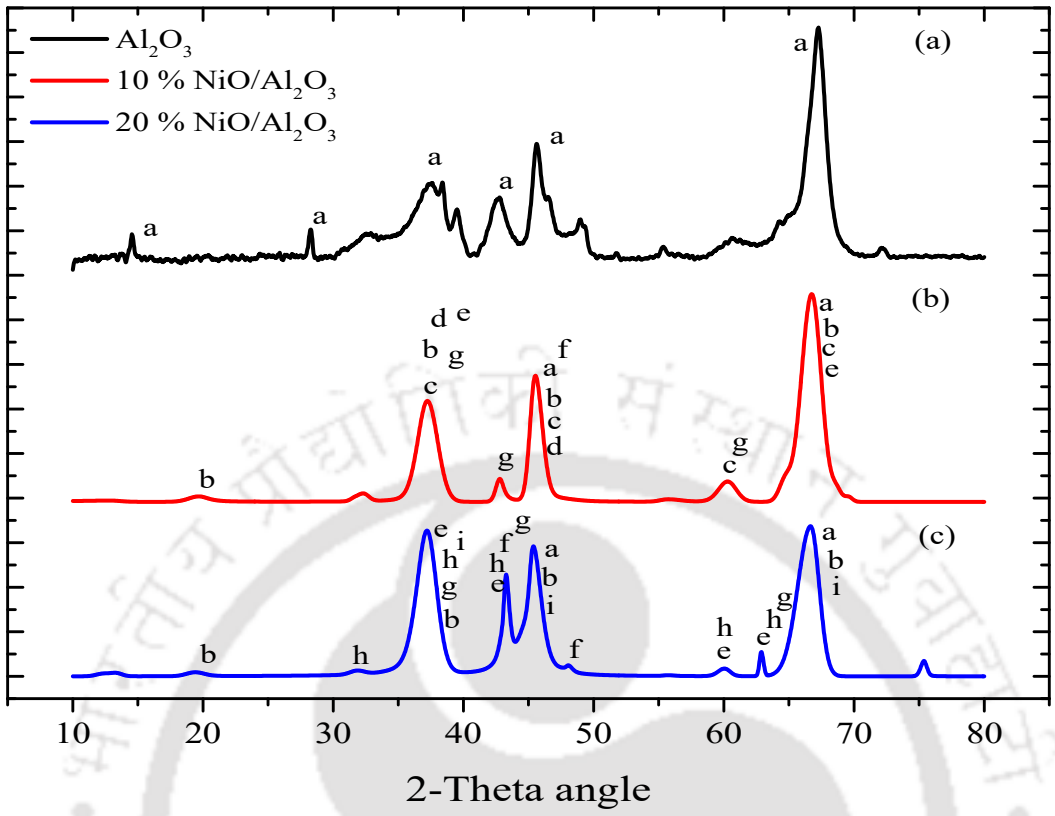

Al_2O_3 : a **$NiAl_2O_4$: b** **$NiAl_{10}O_{16}$: c**

$NiAl_{32}O_{49}$: d **Nickel-aluminium-iron oxide: e** **Ni, syn metal: f**

NiO: g **Fe_3O_4: h** **$Al_{2.66}O_4$: i**

Fig. 4.6 XRD Diffractogram of (a) alumina support and (b) 10 % and (c) 20 % NiO/Al_2O_3 composite catalyst

4.6.2 EDX Analysis

The EDX spectra of 10 % and 20 % Ni-loaded catalysts are shown in Fig. 4.7 (a, b). It indicated the purity of the samples. The actual weight % composition of the NiO/Al_2O_3 – 10% and 20% Ni loading was prioritized by nickel content of 8.6 % and 15.2 % respectively. However, at 10 % and 20 % Ni loading, the aluminum was 50.3 % and 36.9 % and had an oxygen content of 40.3 % and 47.4 % respectively. Other trace metals or impurities such as sulfur, iron, cobalt, and chlorine were also seen in the samples. The EDX mapping images of the composite catalysts are also shown in Fig. 4.6. In the mapping of the spectrum, different color indices were used to represent the elements whereas major elements such as aluminum, oxygen, and nickel showed a vivid color representation of the images. It was observed that the Al, O, and Ni are homogeneously dispersed on the surface of the catalyst. The Ni content in 20 % loading was more than 10 % as evident from the EDX mapping images. It confirmed that Ni and Al's oxides are homogeneously dispersed.

As evident from EDX analysis, the oxygen content in 20 % Ni-loaded catalyst increased due to the formation of oxide phases with enhanced nickel and aluminum content. This was observed from the XRD peaks (20 % loaded catalyst) with more intensity and phases as compared to 10 %, except for the peak noticed at 66.85° (2θ°) diffraction angle. This substantiates the fact that a 20 % NiO/Al_2O_3 catalyst has a greater number of active phases with higher surface area in the support which can increase its catalytic activity.

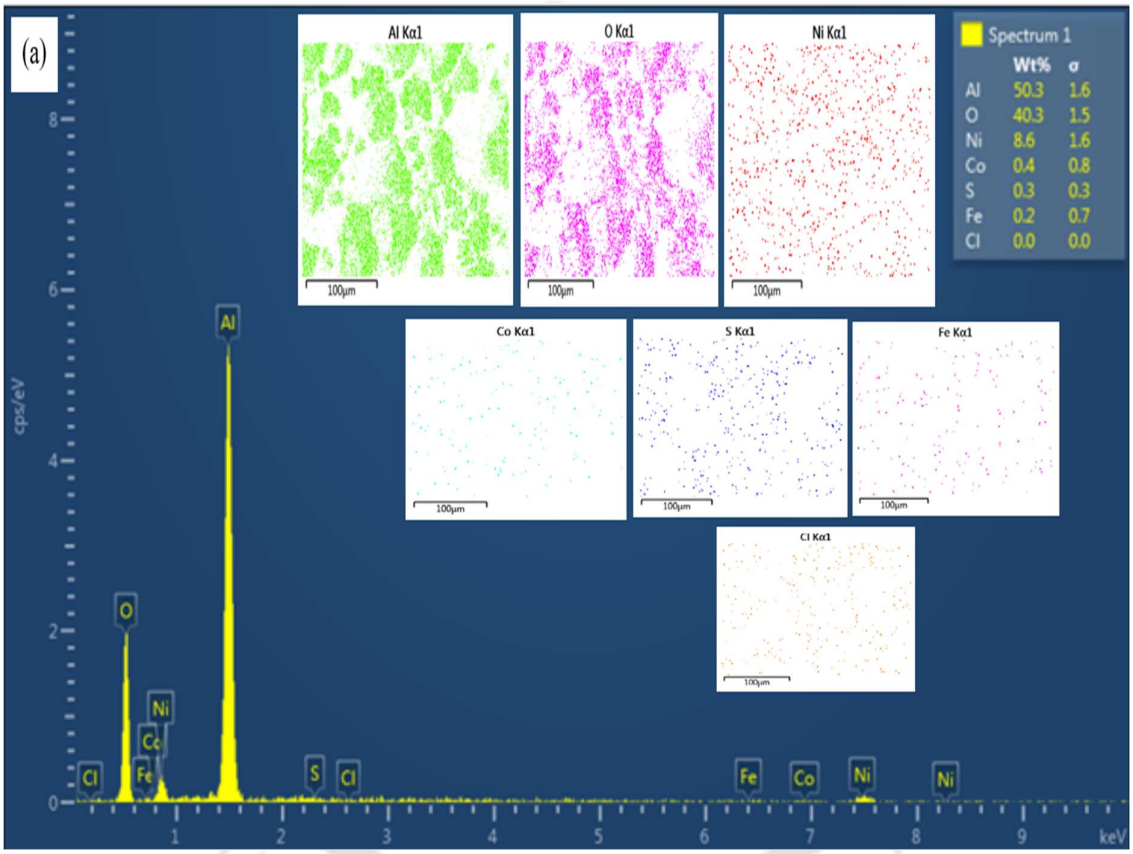

(Continued)

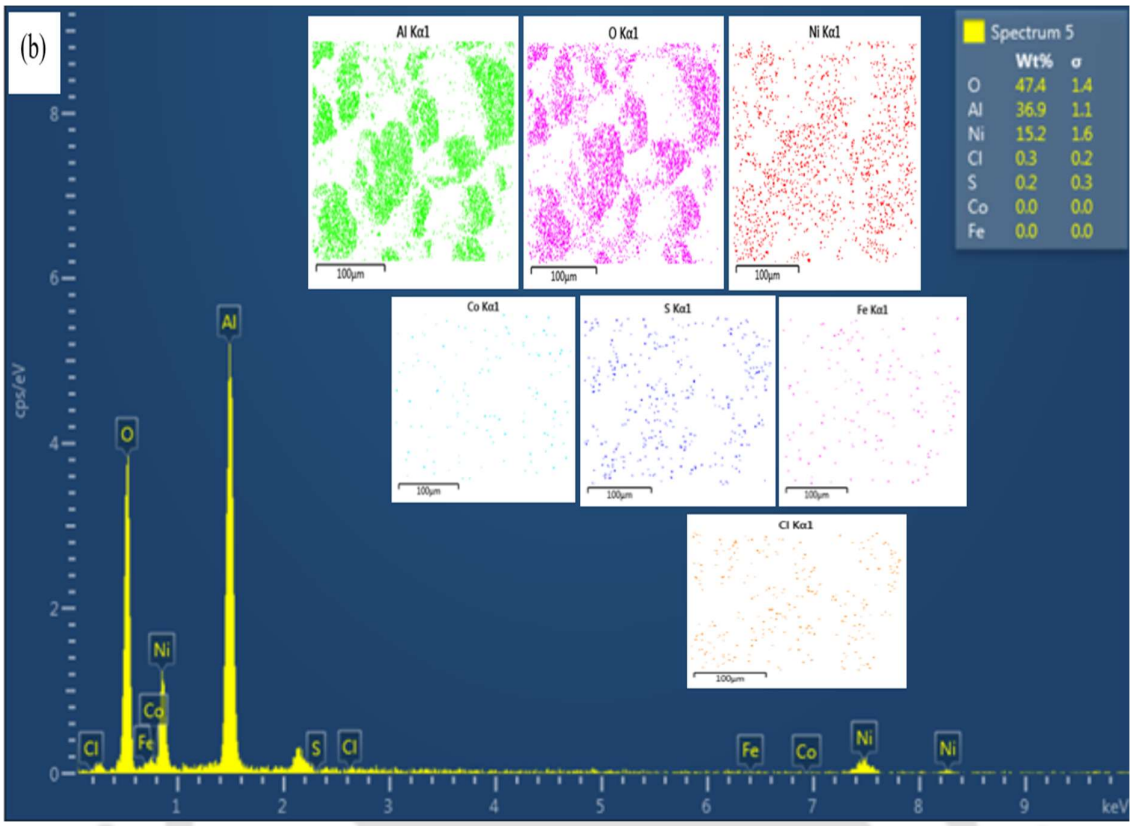

Fig. 4.7 EDX spectrum and EDX mapping images of (a) 10% and (b) 20% Ni loading in Ni(O)(II)/Al_2O_3 nano-composite catalyst

4.6.3 FESEM analysis

The FESEM microstructure images of the 10 % and 20 % NiO/Al_2O_3 composite catalyst samples were denoted in Fig. 4.8. These were at magnifications of 5.0 KX, 50.0 KX, 100.0 KX, and 150.0 KX respectively for better comparison between the SEM micrographs. The range of particle sizes at magnifications of 5.0 KX, 50.0 KX, 100.0 KX, and 150.0 KX was 5 µm, 500 nm, and 200 nm (for both 100.0 KX and 150.0 KX) respectively for both the catalysts. The shape, morphology and topography of the surface characteristics of the materials were indicated as spherical structures for the metal nanoparticles and hexagonal for the alumina support. The production of backscattered electrons differs based on the weight of the element. Heavier elements because of their bigger nuclei, can deflect incident electrons more strongly than lighter elements. The heavier elements such as Ni and Fe appear bright as compared to lighter elements such as O and Al which appear dark in the composite catalyst samples. When the FESEM images of the catalyst samples were magnified to 150.0 KX, it indicated the metal active nanoparticles embedded on the alumina support forming random nanocluster shapes. Increasing the Ni content, increased the agglomeration of the particles in

a 20 % NiO (II)/Al_2O_3 composite catalyst. Spaces among the solid particles are seen in FESEM images of Fig. 4.8 (g) and (h). The agglomeration of particles occurred in a 20 % loading catalyst. This was due to the increase in the nickel di-aluminate phases (as observed from the XRD diffractogram). This can also be substantiated by the explanation of atomic force microscopy results of the composite catalyst which is discussed in the next section. It was also noticed that the upper layer of the particles was bigger than the lower particles by 20% due to the agglomeration of the heavier elements. When the particle sizes were measured along with the particles diagonally for the individual catalyst samples, small (Ni) based metal particles were measured as 39.55 nm, 34.57 nm and 31.87 nm respectively which was calculated as 35.33 nm average particle size for Ni metal for 10 % Ni loaded catalyst, whereas 30.23 nm, 27.68 nm and 28.13 nm respectively which was calculated as 28.68 nm average particle size for Ni metal for 20 % Ni loaded catalyst respectively. However, the average particle size of the alumina support for 10 % and 20 % Ni loaded catalyst was 99.06 nm and 254.3 nm respectively. This proved the efficiency of the 20 % Ni loading for enhanced thermal degradation since the size of the active metal particles over the support and their probable distribution over the support are significant. Also, the surface-specific activity (turnover frequency), product selectivity and catalyst stability enhanced by local particle density are desirable factors for maximizing activity per unit volume of catalysts. Henceforth, as compared to 10 %, the 20 % Ni-loaded catalyst is preferred due to its high density of active sites (high metal loading). Due to the reduction in the size of metal nanoparticles in a 20 % Ni-loaded catalyst, the number of surface-active sites was enhanced and the oxygen-carrying capacity increased leading to a greater number of active phases in the support, thus increasing its support size. Due to the lesser surface area (fewer surface catalytic sites) of the smaller nanoparticles in a 20% Ni-loaded catalyst, the catalytic activity per surface area increased with decreasing size with an increase in substrate reactivity *(Mandic et al., 2017).* This was due to the interplay between weaker substrate binding to the catalytic site and substrate adsorption constant at each active site *(Mandic et al., 2017).*

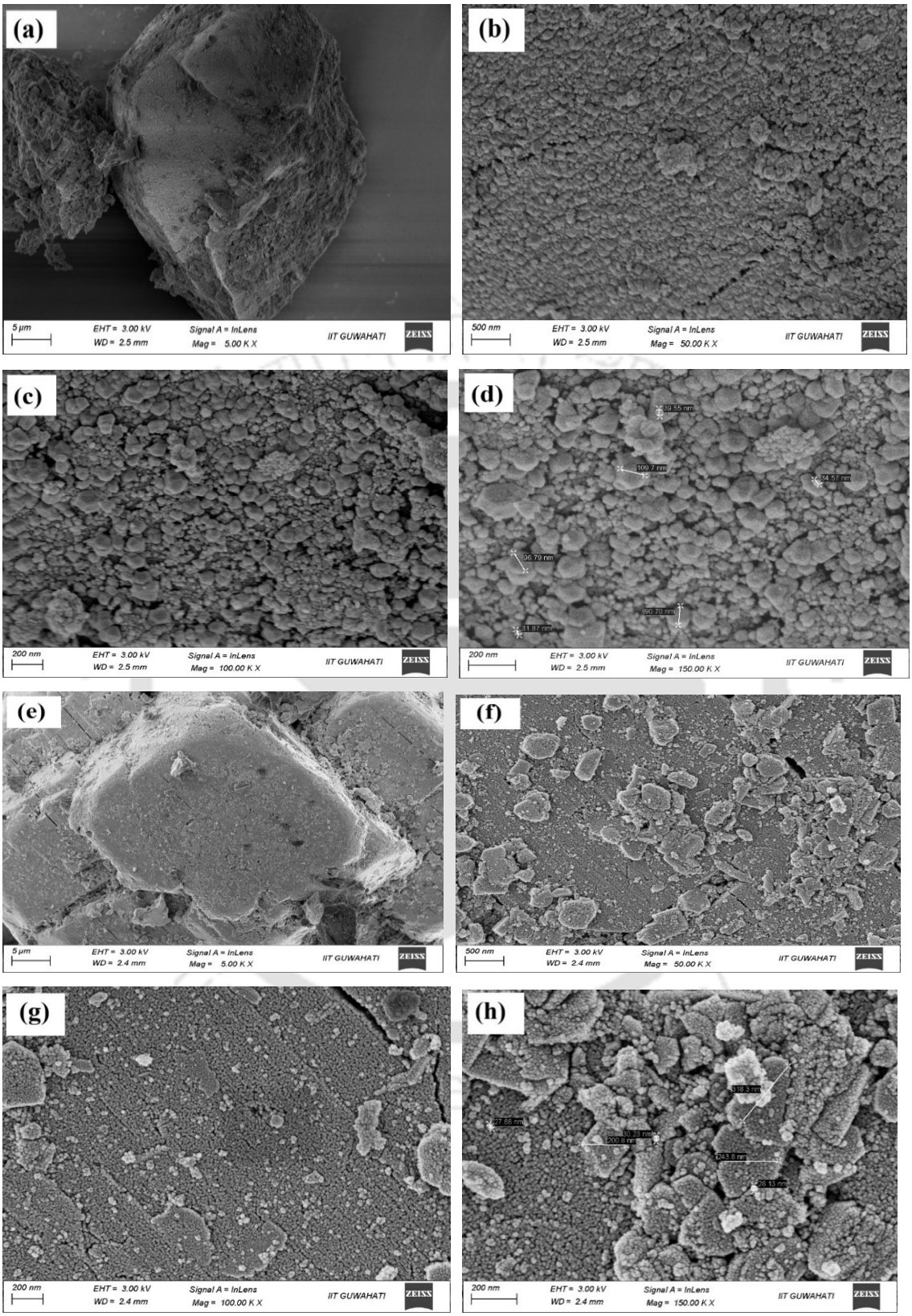

Fig. 4.8 FESEM images of (a-d) 10 % Ni loaded Ni(O)(II)/Al_2O_3 composite catalyst and (e-h) 20 % Ni loaded Ni(O)(II)/Al_2O_3 composite catalyst

4.6.4 AFM Analysis

The AFM analysis interprets the surface roughness and height profile of the composite catalyst. The height profile and 3-D view of the composite catalysts are shown in Fig. 4.9 (a, b) and Fig. 4.9 (c, d) respectively. The statistical parameters were deduced by Gwyddion software for both the composite catalyst and given in Table 4.5. The analysis visualized a higher value of all the statistical parameters for a 20 % Ni-loaded catalyst as compared to 10 %. The 3-D view indicated agglomeration of the particles in the 20 % Ni-loaded catalyst as compared to 10 %. The agglomeration of the particles was also substantiated by the FESEM analysis (Fig. 4.8).

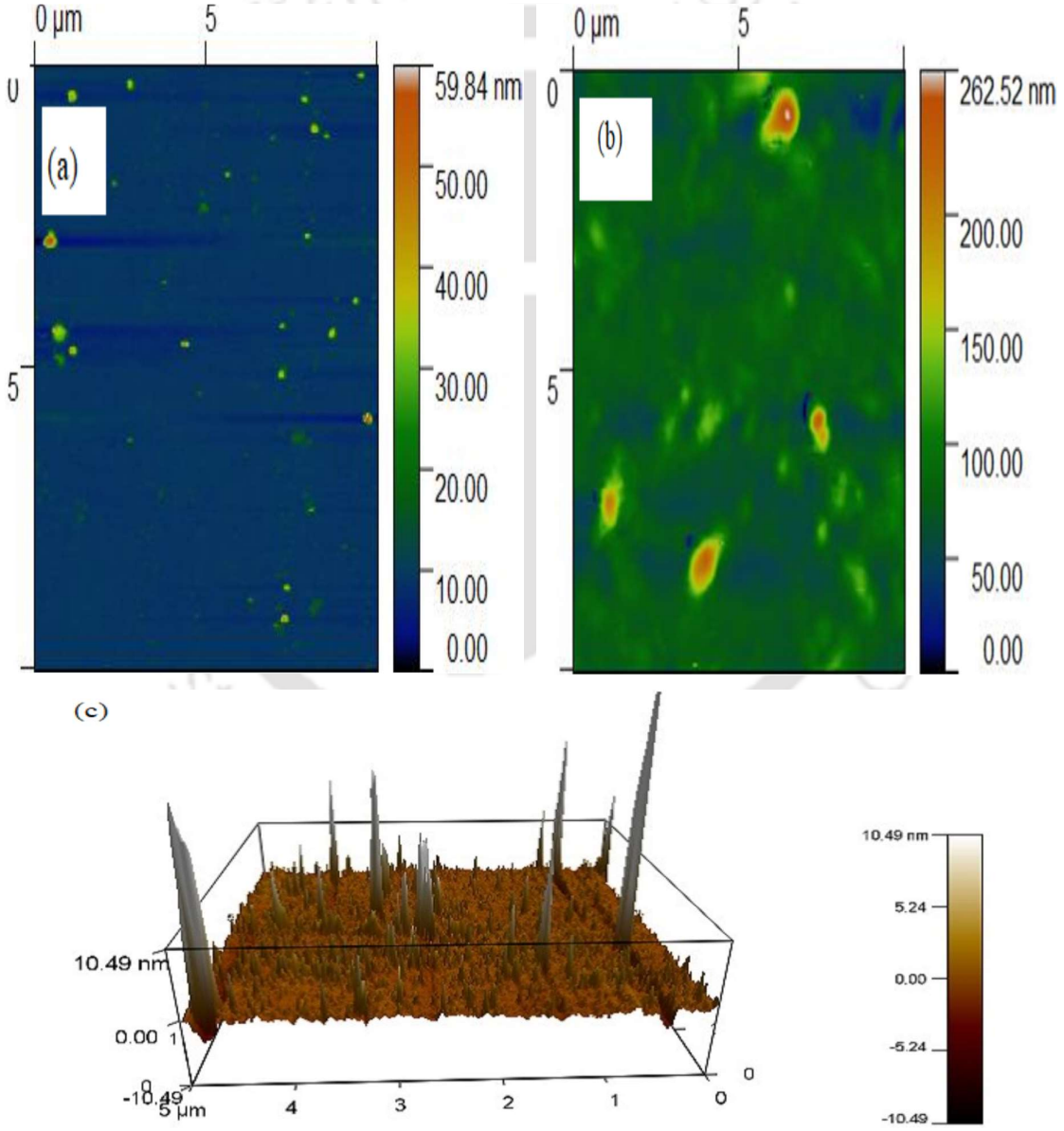

(Continued)

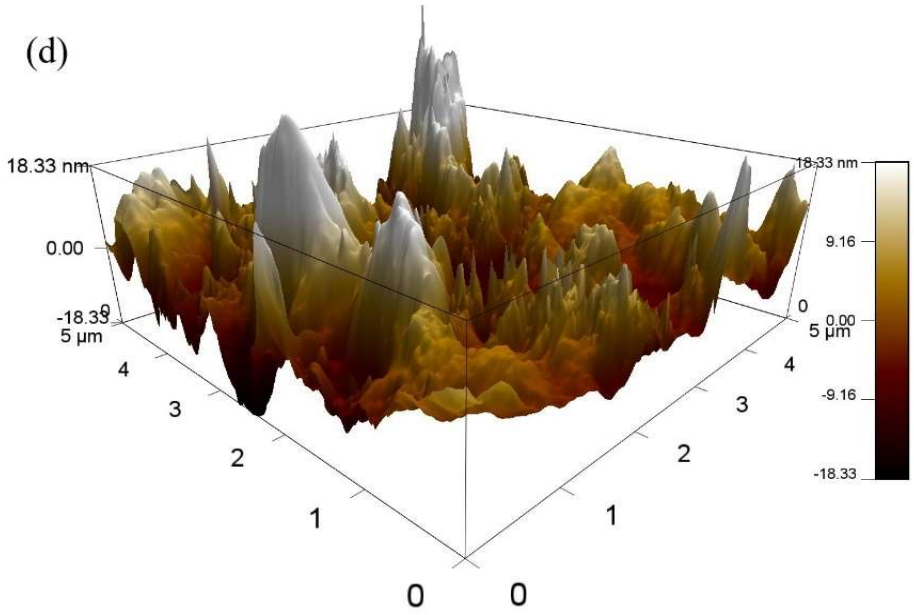

Fig. 4.9 AFM images indicating (a, b) height profile of 10 % Ni loaded Ni(O)(II)/Al_2O_3 nano-composite catalyst and 20 % Ni loaded Ni(O)(II)/Al_2O_3 nano-composite catalyst and (c, d) 3-D view of 10 % Ni loaded Ni(O)(II)/Al_2O_3 nano-composite catalyst and 20 % Ni loaded Ni(O)(II)/Al_2O_3 nano-composite catalyst

Table 4.5 Representation of statistical parameters of 10 % and 20 % NiO (II)/Al_2O_3 nano-composite catalyst by AFM analysis

Statistical parameter	**10 % NiO (II)/Al_2O_3 composite catalyst**	**20 % NiO (II)/Al_2O_3 composite catalyst**
Maximum height	59.84 nm	262.5 nm
Maximum peak height	50.74 nm	186.9 nm
Maximum pit depth	9.10 nm	75.6 nm
Mean roughness	0.670 nm	12.0 nm
Maximum height of roughness	5.099 nm	55.84 nm
Maximum peak to valley roughness	5.099 nm	55.84 nm
Maximum roughness valley depth	2.570 nm	19.80 nm
Grain-wise roughness	2.192 nm	20 nm
Average maximum height of the roughness	3.219 nm	25.31 nm

4.6.5 FETEM Analysis

The FETEM micrographs of the 10 % and 20 % NiO and Ni (II) aluminate composite catalysts are shown in Fig. 4.10. For better comparison, the TEM micrographs Fig. 4.10 (a, b) were obtained at a single magnification (50 nm) for both 10 % and 20 % loaded catalysts. The agglomeration/sintering of particles due to thermal effects could not be seen in these images of a 10 % loaded catalyst, whereas it was noticed in a 20 % loaded catalyst. The appearance of bigger particles might be due to the formation of nickel di-aluminate and $NiAl_{10}O_{16}$ as evident from the XRD diffractogram (Fig. 4.6). This might be explained by the Newton's concept of intermolecular force. The Netwon's concept of intermolecular forces depend upon electrostatic attraction or electronegativity which increases from left to right side and from bottom to top in the periodic table. As electronegativity decreases from O>Al>Ni in the periodic table, electron-donating capacity also increases. The Lewis dot structure of Al_2O_3 renders 6 valence electrons from oxygen to aluminum to make it a stable structure with a complete octet configuration. According to VSEPR theory, lone pair-lone pair have higher repulsion than lone pair-bond pair electrons present in the outer shell of the oxygen orbital. This forms a highly resonating stable structure of Al_2O_3. As evident from the XRD diffractogram, it was noticed that the catalyst also contains NiO (Bunsenite), and nickel aluminate iron oxide (EDX analysis also confirms). However, nickel due to its partially d-subshells with two valence electrons in the outermost orbital is electropositive with its electronic configuration as [Ar] $3d^8$, $4s^2$ (most stable), and [Ar] $3d^9$, $4s^1$. The electronegativity of an atom is a function of its atomic radii. Due to the increase in size of the atom from Ni<Al<O with the increase in electronegativity, the positively charged nucleus is shielded by more electrons. This attraction completes the octet, or s-p-d subshells with argon by electron donation from a nickel to neighboring aluminum and oxygen atoms and might form a co-ordination complex of $NiAl_2O_4$. Another reason might be the homonuclear bonding or covalent bonding amongst Ni-Ni metal interactions. This proves the increase in electron radii size in 20 % catalysts due to higher electronegativity and repulsive forces in their phases. Fig. 4.10 (c, d) showed the particle size distribution of both 10% and 20% catalyst which proved that the maximum frequency of particles appears in the particle diameter range of 4–6 nm. The frequency of particles decreases further with the increasing diameter of the particles. The average particle size was 3.47 nm for a 10 % Ni-loaded catalyst. Fig. 4.10 (d) showed the particle size distribution of a 20 % Ni-loaded catalyst. which proved that the maximum frequency of particles appears in the particle diameter range of 1–20 nm with an average particle size of 10.96 nm. The analysis confirmed that the average particle size of 20

% Ni loading was higher compared to 10 % Ni catalyst. The SAED patterns (selected area electron diffraction pattern) are shown in Fig. 4.10 (e, f) which shows the crystallographic structure of the material. It showed a single crystal structure enveloped with polycrystalline structure between the Ni metal and the matrix for 10 % catalyst however for 20 % catalyst. Enhancing the resolution to higher magnification (20 nm) notable agglomeration was seen in 20 % catalyst which was lacking in 10 % can be observed in Fig. 4.10 (g, h). The SAED pattern. Fig. 4.10 (i, j) showed a single crystal structure of both the materials at these locations with a cubic pattern crystallographic lattice structure. The inter-particle distance or d-spacing is one of the desirable factors for alleviating the activity per unit volume of the catalysts. Fig. 4.9 (k) depicted that the HRTEM image of the 10 % catalyst showed a d-spacing of 0.216 nm. This was calculated by First Fourier Transform (FFT) calculations in the HRTEM image as shown in Fig. 4.10 (l, m). The HRTEM image of the 20 % catalyst can be observed in Fig. 4.10 (n). It denoted a regular d-spacing of the crystal image, where 20 % Ni loading notified a d-spacing of 0.26 nm, 0.26 nm and 0.29 nm for three consecutive planes.

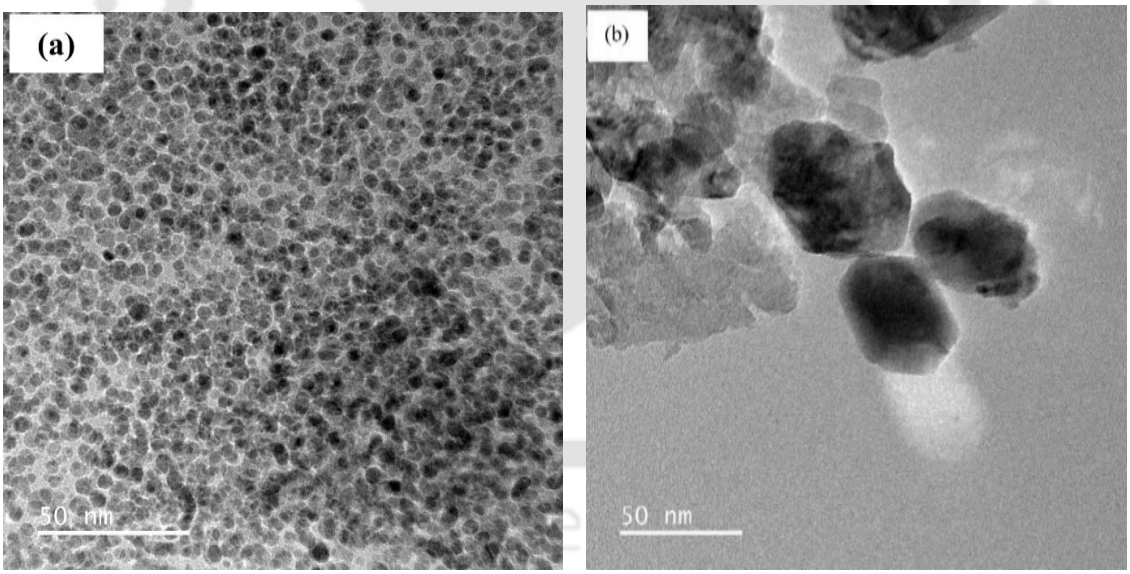

(Continued)

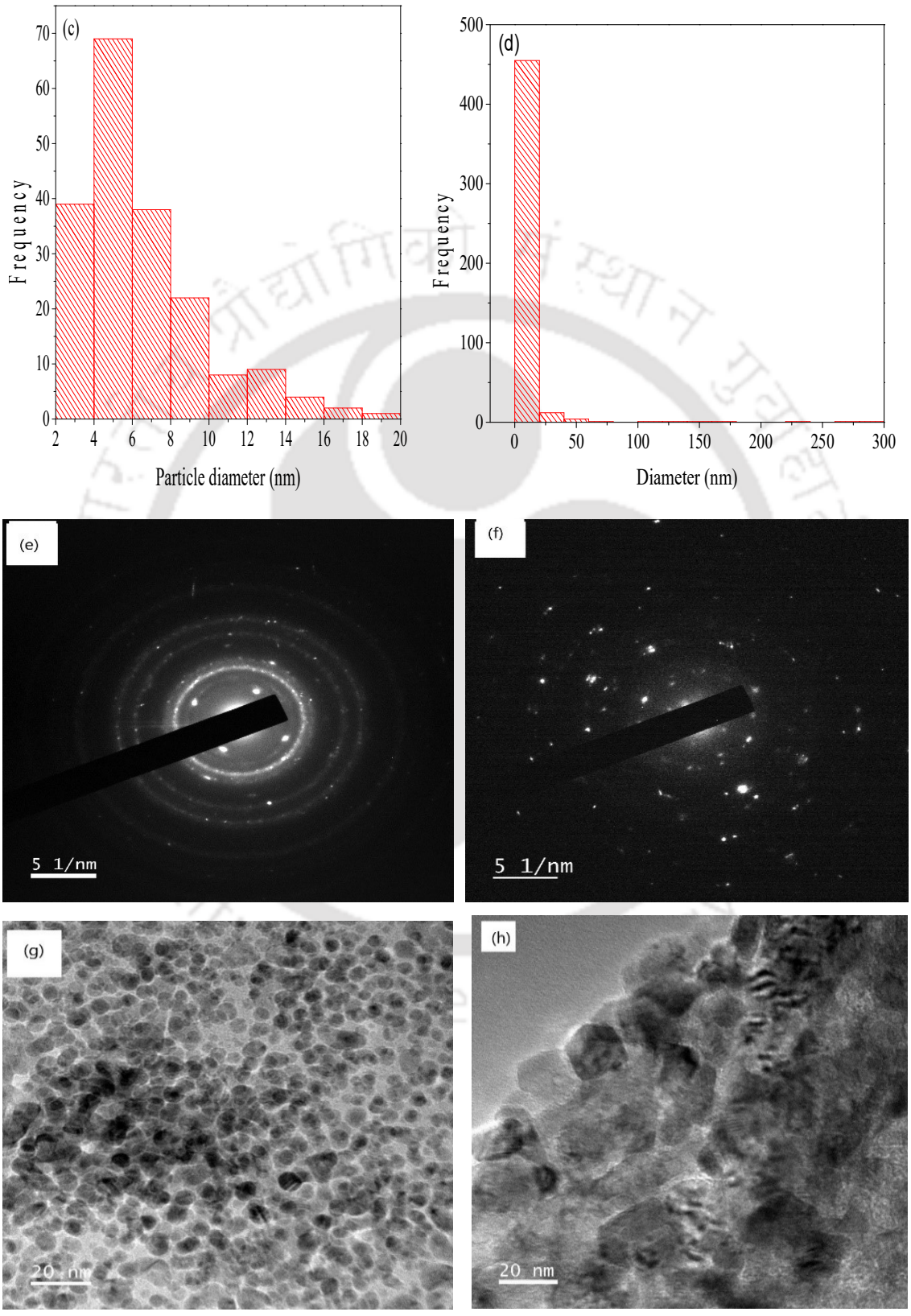

(Continued)

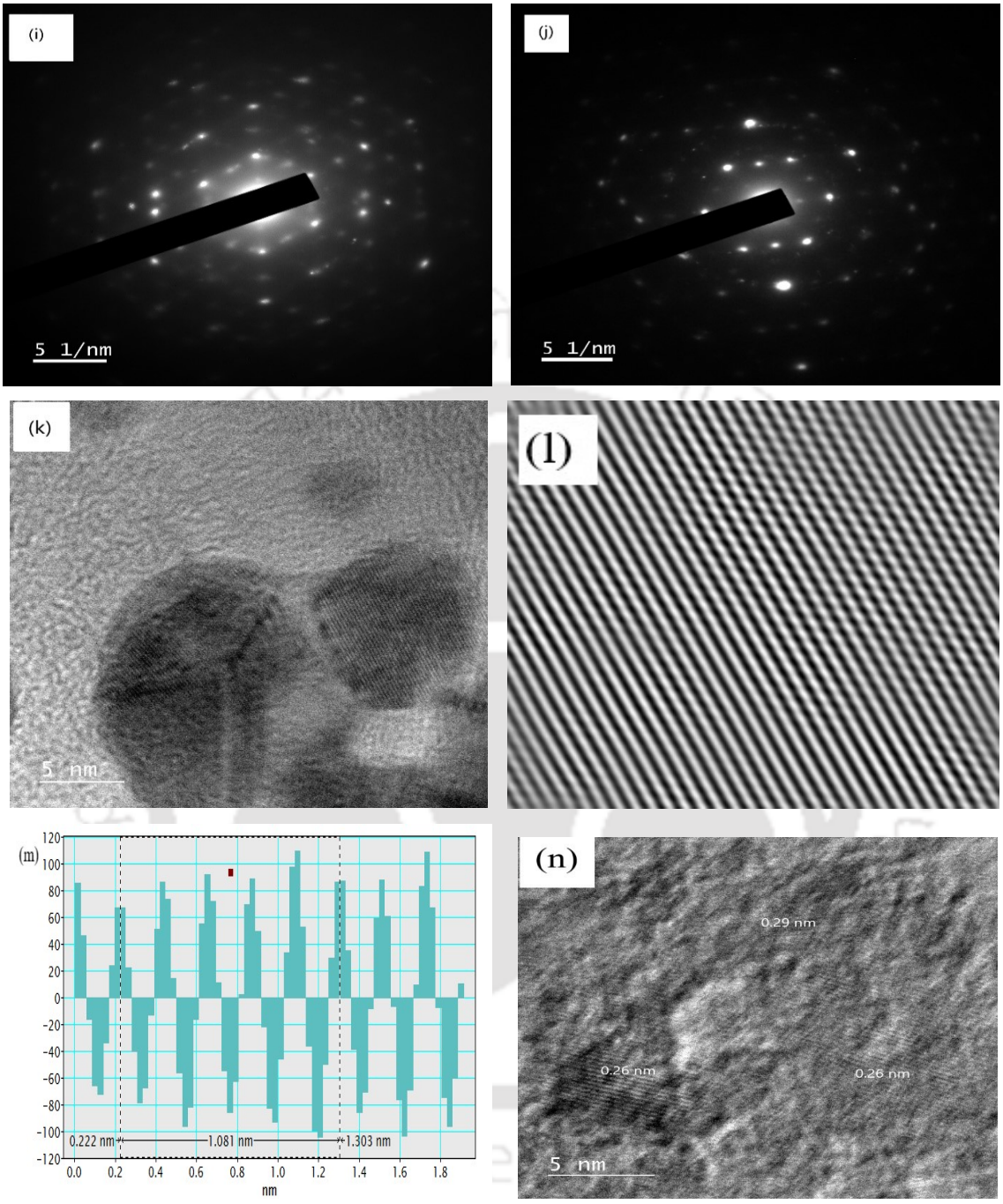

Fig. 4.10 FETEM micrograph images at 50 nm magnification, (a) 10 % NiO(II)/Al_2O_3 catalyst and (b) 20 % NiO(II)/Al_2O_3 catalyst, particle size distribution (c) 10 % NiO(II)/Al_2O_3 catalyst, and (d) 20 % NiO(II)/Al_2O_3 catalyst, SAED pattern at 50 nm magnification (e) 10 % NiO(II)/Al_2O_3 catalyst, and (f) 20 % NiO(II)/Al_2O_3 catalyst, FETEM micrograph images at 20 nm magnification (g) 10 % NiO(II)/Al_2O_3 catalyst, (h) 20 % NiO(II)/Al_2O_3 catalyst, SAED pattern at 20 nm magnification (i) 10 % NiO(II)/Al_2O_3 catalyst, (j) 20 % NiO(II)/Al_2O_3

catalyst, (k) HRTEM images at 5 nm magnification of 10 % NiO(II)/Al_2O_3, FFT calculations for d-spacing (l) 10 % NiO(II)/Al_2O_3 catalyst, and (m) 20 % NiO(II)/Al_2O_3 catalyst, (n) HRTEM images at 5 nm magnification of 20 % NiO(II)/Al_2O_3

4.6.6 FTIR analysis

The FTIR analysis of the prepared composite catalyst is shown in Fig. 4.11. The broad peak obtained at 3465 cm^{-1} corresponds to H bonded -OH stretching, which showed the presence of moisture and hydroxyl groups. A small peak noticed at 1375 cm^{-1} was related to -OH in-plane bend in 10 % Ni(O) (II)/Al_2O_3 composite catalyst, while sharp intense peaks at lower wavenumbers, 552 cm^{-1} and 774 cm^{-1} wavenumbers correspond to -OH out-of-plane bend in both the composite catalysts. The peaks noticed at the region of low frequency (1000 and 400 cm^{-1}), indicated the sorption peaks resemble the lattice vibration approaches of Al-O, Ni-O bonding. The bending vibrations of water δ (H_2O) were observed from the peaks obtained at 1645 cm^{-1}. The formation of aluminate can be observed from the peak obtained at 1022 and 1098 cm^{-1} *(Lebon et al., 2008)*.

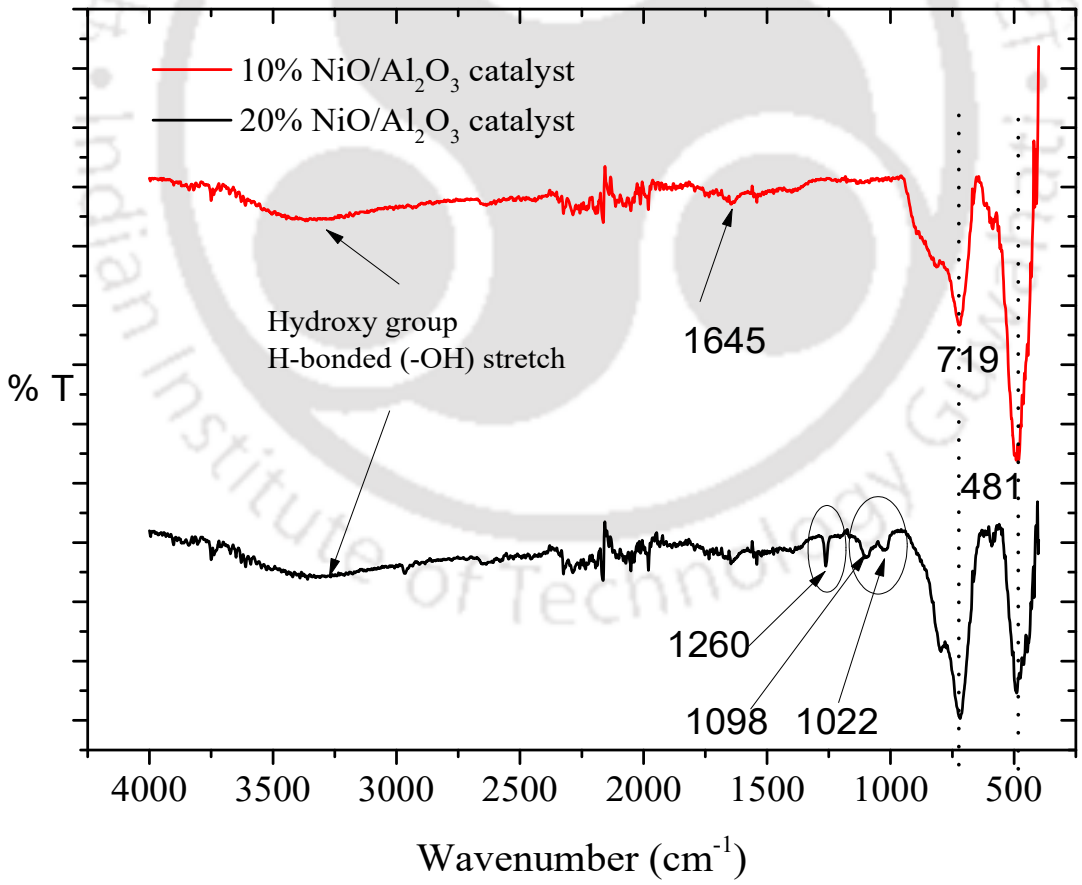

Fig. 4.11 FTIR spectra of the Ni(O) (II)/Al_2O_3 nano-composite catalyst

4.6.7 Surface area analysis

The multi-point BET surface area, total pore volume, average pore diameter, and its non-linear density functional theory values of the alumina support and the 10 % and 20 % Ni-loaded catalyst are mentioned along with the Isotherm type and hysteresis loop of the samples in Table 4.6. Both the prepared catalysts and the support show reversible Type IV isotherm for the physisorption of nitrogen gas with an H3 hysteresis loop as observed in Fig. 4.12 *(Thommes et al., 2015)*. The shape was the result of unrestricted monolayer-multilayer adsorption up to high p/p_0. The knee was sharper in alumina support, at the beginning of the middle linear section – corresponding to the completion of monolayer coverage. A more gradual curvature in a 20 % Ni-loaded catalyst indicated a significant amount of overlap of monolayer coverage and the onset of multilayer adsorption. The thickness of the adsorbed multilayer appeared to increase without limit when $p/p_0=1$. H3 hysteresis loops have characteristics of desorption shoulders and lower closure points rendering slit-type pores. This analysis confirmed a reduction in the BET surface area and DFT surface area in 10 % and 20 % Ni-loaded catalysts compared to the alumina support. However, the upsurge in the pore diameter was observed in a 10 % Ni-loaded catalyst compared to others. The pore volume in the catalysts was higher in both the prepared catalysts compared to the calcined alumina support. It was noticed that the pore-filling occurred between 5–15 nm pore diameter with a significant amount of pore filling in active alumina support. As the metal content increased in the Ni-based catalysts, pore filling decreased substantially due to the presence of various Ni (II) aluminates and NiO impregnated onto the support and blocking the active pores.

The ratio S_{BET}/S_{av} is a linear function of the average pore width and offers a quantitative explanation for the difference in surface areas from the BET-N_2 physisorption analysis and NLDFT model. Non-local DFT stands as a more versatile approach in calculating pore structure parameters in comparison to the conventional BET-N_2 physisorption approach. Lander's (2013) density functional theory (DFT) method is used for calculating the adsorption characterization of microporosity and meso-porosity in materials. With the predictions of the Dubinin – Radushkevich equation supported by Monte Carlo simulations, a reliable assessment of surface areas can be obtained rather than a single determination. In the Monte Carlo modeling of nitrogen adsorption, the total surface area exceeds the effective surface area due to the prominence of gas-solid characteristic energy in narrow pores (w <1.1 nm), which further decreases. DFT approach leads to an average surface area, S_{av} which probably corresponds to a good estimate of S_{total} for microporous materials. The BET area

diverges from it as expressed quantitatively and the two values are similar only for pore widths around 0.9 nm *(Landers, 2013)*.

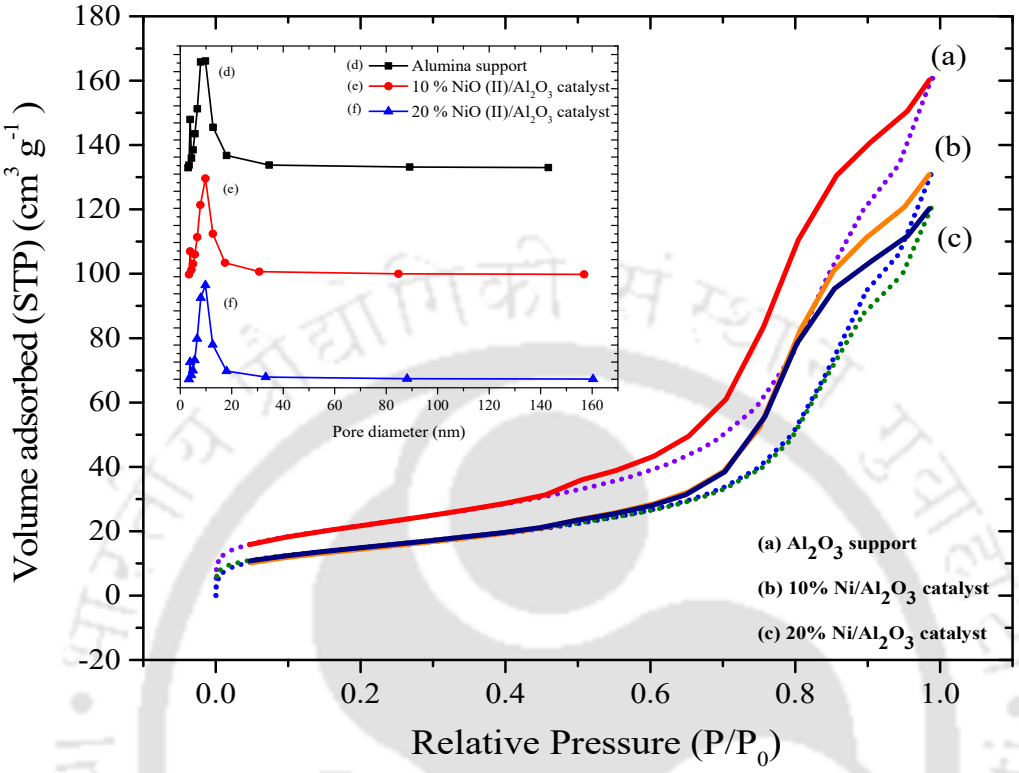

Fig. 4.12 BET-N_2 Isotherm of (a) Alumina support, (b) 10 % NiO/Al_2O_3 and (c) 20 % NiO/Al_2O_3 composite catalysts (Inset: BJH Pore size distribution curve of pore diameter (nm) versus dV(D) of (d) Alumina support, (e) 10 % NiO/Al_2O_3 and (f) 20% NiO/Al_2O_3))

Table 4.6 Characterization of support and catalyst using BET-N_2 physisorption analysis

Sl No.	**Material**	**Multi-point BET Surface Area (m^2 g^{-1})**	**Isotherm Type**	**Hysteresis Loop Type**	**Mean Pore diameter (nm)**	**Total Pore Volume (m^3 g^{-1})**	**DFT Pore Surface Area (m^2 g^{-1})**	**DFT Pore Surface Volume (m^3 g^{-1})**
1.	Al_2O_3 support	77.98	IV	H3	12.75	0.248	59.626	0.230
2.	10 % Ni in Ni(O)(II)/Al_2O_3 composite catalyst	52.64	IV	H3	15.51	0.204	43.542	0.186
3.	20 % Ni in Ni(O)(II)/Al_2O_3 composite catalyst	53.77	IV	H3	13.98	0.188	41.681	0.172

4.6.8 XPS analysis

Fig. 4.13 represents the XPS spectra specific to Ni and Al(2p) of the 10 % and 20 % composite catalysts with an indication of Co and Fe. Corresponding to the main peaks, two forms of Ni species were observed which were $Ni(OH)_2$ and NiO at binding energies of 533.31 eV and 854.5 eV respectively. From XRD data in Section 4.6.1, it can be inferred that there might be NiO and $NiAl_2O_4$ on the catalyst surface. Al (2p) hybridized orbital state is seen at a lower binding energy of 74.5 eV, while other forms of alumina which were Al_2O_3 and $Al(OH)_3$ were seen at a binding energy of 533.31 eV in their oxidized state. CoO was observed in its valence (II) state at the same binding energy of 533.31 eV for a 10 % Ni composite catalyst while Fe_2O_3 was found in the binding energy of 640.7 eV. As can be seen from the curves, the binding energy of the Al(2p) peak for NiO/Al_2O_3 is at 74 eV, which is typical of Al^{3+} in the spinel phase, but for NiO/Al_2O_3 the binding energy is lesser *(Ashok et al., 2008)*.

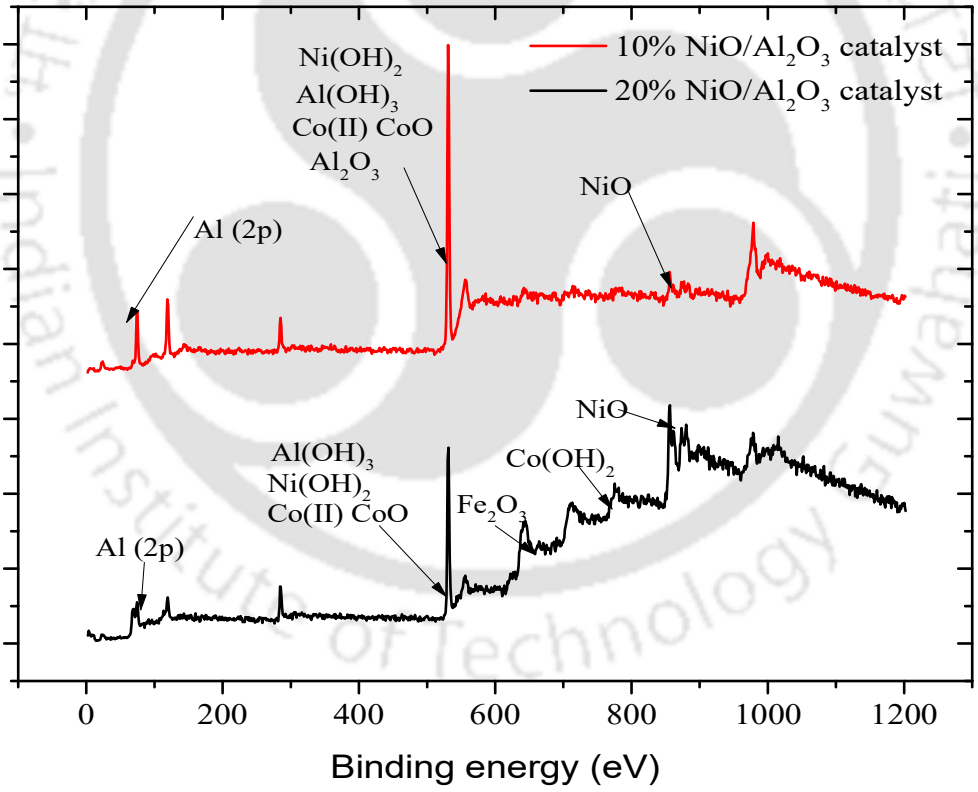

Fig. 4.13 XPS spectra of 10% and 20% NiO and Ni (II) aluminate composite catalysts

4.6.9 Thermal stability analysis

Fig. 4.14 denotes the TG-DTG analysis of the catalysts. The TG curve depicts the thermal degradation profile of the catalyst while the DTG curve denotes the rate of mass

degradation (% min^{-1}) of the catalyst samples. For the 10 % and 20 % Ni-loaded catalysts, the final residue % was 95.21 % and 94.50 % respectively as evaluated from the TG curve. The peak temperature was observed as 350 K where maximum degradation of the sample takes place. The thermal degradation profile of the catalysts proved that they are thermally stable to a temperature of 1173 K, which makes it feasible for the catalytic pyrolysis of sawdust and catalytic co-pyrolysis of blends.

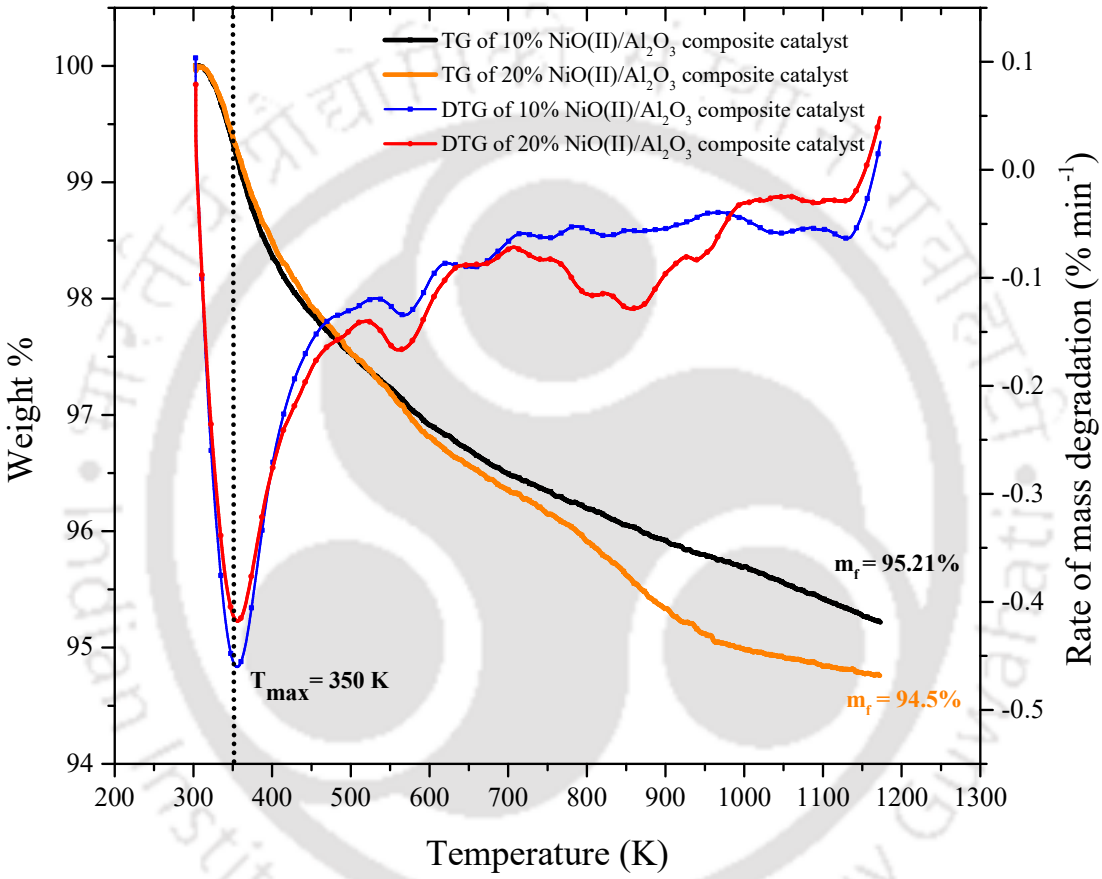

Fig. 4.14 TG-DTG analysis of 10 % and 20 % NiO and Ni (II) aluminate composite catalysts

4.7 Summary of the chapter

This chapter reports the characterization of two feedstocks, coal and sawdust, and their respective blends in specific proportions (10 %, 30 %, 50 %, 70 %, 90 %, 100 % and 200 % of biomass addition to coal). From this analysis, it has been observed that coal has higher ash and lower volatile matter content than sawdust with considerable calorific value. Sawdust has considerable volatile matter content and lesser ash content with higher quantities of alkali ana alkaline earth metals (AAEM) content in the decreasing order of Al>Ca>Si>K>Mg>Fe>P which makes it a potential source of pyrolysis reaction. Due hydroxyl group in coal, increases

the thermal stability of the irregular macromolecular polymeric aromatic structure while the presence of cellulose, hemicellulose, and lignin content increases the devolatilization and reactivity potential of sawdust. However, an increase in sawdust addition to coal increases its devolatilization attributes its volatile content in these blends is higher than coal-sawdust blends with higher coal proportion. This chapter also comprehensively elucidates the characterization of catalysts, 10% and 20% NiO and Ni (II) aluminate composite catalysts by various analytical techniques to comprehend its purity in elemental composition, microstructure, and nanostructure visualizations, purity in crystal phase structure, presence of functional groups, presence of surface binding energies, determination of surface area and pore size distribution and studies on its thermal stability.

References

- Vasilatos, C., Dimitris, C., Theodorou, T., Stouraiti, C., Andreadi, M. and Koukouzas, N., 2022. A Comparative Study of Selected Properties of Biomass and Coal Fuels from Greece. *materials proceedings*, *5*(1), p.108.
- Du, C., Liu, L. and Qiu, P., 2017. Importance of volatile AAEM species to char reactivity during volatile–char interactions. *RSC advances*, *7*(17), pp.10397-10406.
- Wu, L., Xue, X., Yu, H., Zhang, C., Wei, X., Liang, J. and Sun, Y., 2020. Catalytic pyrolysis of poplar sawdust: Excellent hydrocarbon selectivity and activity of hollow zeolites. *Bioresource Technology*, *317*, p.123954.
- Bridgwater, A.V., 2012. Review of fast pyrolysis of biomass and product upgrading. *Biomass and bioenergy*, *38*, pp.68-94.
- Oudenhoven, S.R.G., Westerhof, R.J.M. and Kersten, S.R., 2015. Fast pyrolysis of organic acid leached wood, straw, hay and bagasse: Improved oil and sugar yields. *Journal of analytical and applied pyrolysis*, *116*, pp.253-262.
- Stals, M., Thijssen, E., Vangronsveld, J., Carleer, R., Schreurs, S. and Yperman, J., 2010. Flash pyrolysis of heavy metal contaminated biomass from phytoremediation: influence of temperature, entrained flow and wood/leaves blended pyrolysis on the behaviour of heavy metals. *Journal of Analytical and Applied Pyrolysis*, *87*(1), pp.1-7.
- Richardson, Y., Blin, J., Volle, G., Motuzas, J. and Julbe, A., 2010. In situ generation of Ni metal nanoparticles as catalyst for H2-rich syngas production from biomass gasification. *Applied Catalysis A: General*, *382*(2), pp.220-230.
- Zhang, M., Zhang, S., Chen, Z., Wang, M., Cao, J. and Wang, R., 2019. Preparation and characterization of superabsorbent polymers based on sawdust. *Polymers*, *11*(11), p.1891.
- Solomon, P.R. and Carangelo, R.M., 1988. FT-ir analysis of coal: 2. Aliphatic and aromatic hydrogen concentration. *Fuel*, *67*(7), pp.949-959.
- Li, L., Fan, H. and Hu, H., 2017. Distribution of hydroxyl group in coal structure: A theoretical investigation. *Fuel*, *189*, pp.195-202.
- Xu, J., He, Q., Xiong, Z., Yu, Y., Zhang, S., Hu, X., Jiang, L., Su, S., Hu, S., Wang, Y. and Xiang, J., 2020. Raman spectroscopy as a versatile tool for investigating thermochemical processing of coal, biomass, and wastes: recent advances and future perspectives. *Energy & Fuels*, *35*(4), pp.2870-2913.

- Morgan, T.J. and Kandiyoti, R., 2014. Pyrolysis of coals and biomass: analysis of thermal breakdown and its products. *Chemical reviews*, *114*(3), pp.1547-1607.
- Singer, L.S. and Lewis, I.C., 1982. Applications of ESR to carbonaceous materials. *Applied Spectroscopy*, *36*(1), pp.52-57.
- Trubetskaya, A., Jensen, P.A., Jensen, A.D., Glarborg, P., Larsen, F.H. and Andersen, M.L., 2016. Characterization of free radicals by electron spin resonance spectroscopy in biochars from pyrolysis at high heating rates and at high temperatures. *Biomass and Bioenergy*, *94*, pp.117-129.
- Petrakis, L. and Grandy, D.W., 1978. Electron spin resonance spectrometric study of free 0.84radicals in coals. *Analytical Chemistry*, *50*(2), pp.303-308.
- Mandić, M., Todić, B., Živanić, L., Nikačević, N. and Bukur, D.B., 2017. Effects of catalyst activity, particle size and shape, and process conditions on catalyst effectiveness and methane selectivity for Fischer–Tropsch reaction: a modeling study. *Industrial & Engineering Chemistry Research*, *56*(10), pp.2733-2745.
- Lebon, M., Reiche, I., Fröhlich, F., Bahain, J.J. and Falguères, C., 2008. Characterization of archaeological burnt bones: contribution of a new analytical protocol based on derivative FTIR spectroscopy and curve fitting of the ν 1 ν 3 PO 4 domain. *Analytical and Bioanalytical Chemistry*, *392*, pp.1479-1488.
- Thommes, M., Kaneko, K., Neimark, A.V., Olivier, J.P., Rodriguez-Reinoso, F., Rouquerol, J. and Sing, K.S., 2015. Physisorption of gases, with special reference to the evaluation of surface area and pore size distribution (IUPAC Technical Report). *Pure and applied chemistry*, *87*(9-10), pp.1051-1069.
- Landers, J., Gor, G.Y. and Neimark, A.V., 2013. Density functional theory methods for characterization of porous materials. *Colloids and Surfaces A: Physicochemical and Engineering Aspects*, *437*, pp.3-32.
- Ashok, J., Raju, G., Reddy, P.S., Subrahmanyam, M. and Venugopal, A., 2008. Catalytic decomposition of CH4 over NiO–Al_2O_3–SiO_2 catalysts: influence of catalyst preparation conditions on the production of H_2. *International Journal of Hydrogen Energy*, *33*(18), pp.4809-4818.

CHAPTER V

Thermal Pyrolysis and Co-pyrolysis Kinetics of Coal-Biomass Blends

5.1 Introduction

This chapter describes the kinetic (using the KAS method) and thermodynamic study of coal-sawdust co-pyrolysis that are calculated away from the evaporation zone. The effects of heating rates on co-pyrolysis are compared to individual pyrolysis in subsection 5.4. This study clarifies the effect of biomass on the thermal stability of coal during co-pyrolysis. This is explicated by the conversion % in the three thermal zones of coal pyrolysis and the active pyrolytic zone of sawdust and coal/sawdust blend co-pyrolysis. Kinetic and thermodynamic study along with estimation of reaction mechanism on individual samples and coal/biomass blends is explained in subsection 5.5. Co-pyrolysis of sawdust with coal helps in increasing the rate of thermal degradation at low-temperature degradation zones by reducing the activation energy and Gibbs free energy. This process can be a better option to produce CO_2-neutral fuel since the presence of higher H-content in the biomass helps in the degradation of coal and increases the yield of liquid.

5.2 Experimental validation

In this Chapter, a detailed and comprehensive study on kinetics and thermodynamics was done on coal, sawdust, and coal-sawdust blends (100 % and 200 % sawdust addition to coal). A thermo-gravimetric analyzer (TGA) was employed to discern the pyrolytic characteristics of the feed samples. TGA was performed in between 303-1173 K temperature range in the presence of 99.99 % pure N_2 gas flow at 20 mL min^{-1} at 1.9 bar gas pressure. Upon culminating at 1173 K temperature, nitrogen gas was imported into the furnace to scrap off the remaining volatile products. The TGA analysis of coal, sawdust, and its blended samples was conducted at a single heating rate (20 K min^{-1}). At the single heating rate, the effect of sawdust blending with coal on the thermal stability and the rate of degradation was observed. The comparative degradation analysis between the individual and blended samples settled the optimum blending conditions where the rate of degradation was higher. At the optimum conditions, the influence of the heating rate was studied at 10, 20, 30 and 40 K min^{-1}. The degradation kinetic parameters were studied by using the KAS Method.

5.3 Highlights of the chapter

- The present investigation visualizes the positive and negative upshots of the blending of sawdust on the thermal stability of coal during the co-pyrolysis process.
- Coal degraded less than sawdust due to its presence of more ash content and lesser volatile matter content.

- Sawdust degradation visualized a three-stage degradation profile while four-stage profiles were perceived from the coal degradation with very less mass loss.
- This study clarifies the effect of biomass on the thermal stability of coal during co-pyrolysis, where with the increase in sawdust blending on coal, the rate of thermal degradation increased. This is evident from conversion % in the active pyrolytic zone and also from values of instantaneous rate, intrinsic reaction rate, and comprehensive pyrolysis index at a single heating rate, 20 K min^{-1}.
- Synergistic interactions were observed for 10 %, 70 %, 90 %, 100 % and 200 % blends.
- The co-pyrolysis kinetics and thermodynamics of coal and sawdust are studied at 100 % and 200 % blending of sawdust. The effect of heating rate on the coal pyrolysis and co-pyrolysis was also elaborated along with their effects on kinetics and thermodynamics by using the Kissinger-Akahira-Sunose (KAS) method.
- The alternation in the value of activation energy from positive to negative occurs beyond the active pyrolytic zone. The overall E_a of coal pyrolysis (196 kJ mol^{-1}) shows a value higher than the co-pyrolysis of coal and 100 % sawdust blend (100.63 kJ mol^{-1}) and co-pyrolysis of coal and 200 % sawdust blend (122.408 kJ mol^{-1}).

5.4 Thermogravimetric analysis (TGA)

5.4.1 TG analysis of coal and sawdust

The thermal degradation profile of coal and sawdust at 20 K min^{-1} heating rate is shown in Fig. 5.1. The TGA/DTG analysis showed that coal degraded less than the sawdust as shown in Table 5.1, due to the presence of more ash, lesser volatile matter and higher density. Sawdust degradation visualized a three-stage degradation profile while four-stage profiles were perceived from the coal degradation. The moisture evaporation zone was observed at 506 K for both samples. Less moisture (0.63 %) was released from coal compared to sawdust (6.08 %). Further, a sharp decrease in mass loss (63.18 %) was noticed during sawdust degradation and notified as an active pyrolytic zone (506-717 K). During coal pyrolysis, beyond the drying zone, the rate of mass loss was very slow and continued up to the end temperature (1173 K). For coal, the mass loss in the 3rd and 4th stages was very low. However, the loss of mass in coal within 506-717 K (2nd) was only 1.14 %. During the 3rd and 4th stages of degradation within 717-1173, K was 3.18 %. In the 3rd stage of sawdust degradation, about 16.94 % mass loss was perceived from sawdust. The amount of char formed by the pyrolysis of coal and sawdust was 95.05 % and 13.80 % respectively. This

study showed that the overall degradation of sawdust and coal within the entire temperature range was about 86.2 % and 4.92 % respectively except for the moisture content. The active pyrolytic zone says that the de-volatilization of hemicellulose and cellulose present in the sawdust while the 3rd stage shows the degradation of lignin. However, the more volatile components exit in the coal released during the pyrolysis of coal. Moreover, it can be said that the rate of mass loss depends on the composition of the samples. Hence, this statement can be established that coal is more thermally stable than sawdust and the active pyrolytic zone lied between 506-1173 K. In comparison to available literature for coal pyrolysis, Idris et al. reported on the thermal decomposition of Mukaah Balingian coal which results in one major DTG peak in the higher temperature range of 380-580°C at a pyrolysis thermal temperature of 900°C with a final char residue of 60 %. The DTG peak corresponds to the carbon-containing volatile matter *(Idris et al., 2010).* However, Shi et al. worked on the pyrolysis of 34 different varieties of Chinese coals and showed that with the decrease in carbon content in the coal samples, lower-grade coal ensues higher weight loss at lower temperatures. However, large DTG peaks were also seen for certain coal varieties at higher temperatures of 700°C which indicated the decomposition of carbonates in coals because it is entitled to CO_2 release *(Shi et al., 2013).* In another study, Wang et al. reported on the thermal pyrolysis of four selected low-rank coals from China which decomposed within the temperature range of 110-900°C. The respective peak temperatures of the coal samples were 407.20°C, 411.0°C, 415°C and 435.70°C with a maximum mass loss at the main degradation stage as 37.34 %, 40.25 %, 31 % and 23.90 % respectively. The emphasis was on a three-stage pyrolysis process for coal pyrolysis with different kinetics behaviors and kinetic distribution *(Wang et al., 2016).* However, in another interesting study, Pitt et al. assumed that coal pyrolysis should include a large number of irreversible, independent, and parallel first-order reactions with different activation energies which can be predominantly represented by a distribution of activation energy function, f €. *(Pitt, 1962).* The C=C bond available in the coal is stronger than the R-O-R bond of biomass which breaks faster and the transfer of OH radicals and H helps in the breaking of aromatic associations of coal during co-pyrolysis. This can be stated by the fact that the structure of coal comprises crosslinked aromatics bonded by C=C with a bond dissociation energy of 1000 kJ mol^{-1} *(Aboyade et al., 2013)* whereas biomass consists of weak ether bonds R-O-R with a bond dissociation energy of 380-420 kJ mol^{-1} *(Vuthaluru, 2004).* Higher thermal reactivity and volatile matter content facilitate a synergistic interaction during the co-pyrolysis process which occurs due to hydrogen availability of C-H bond dissociation to coal and coal pyrolysis intermediates *(Park*

et al., 2010). This also develops a higher yield of liquid and gaseous products and reduces the char yield.

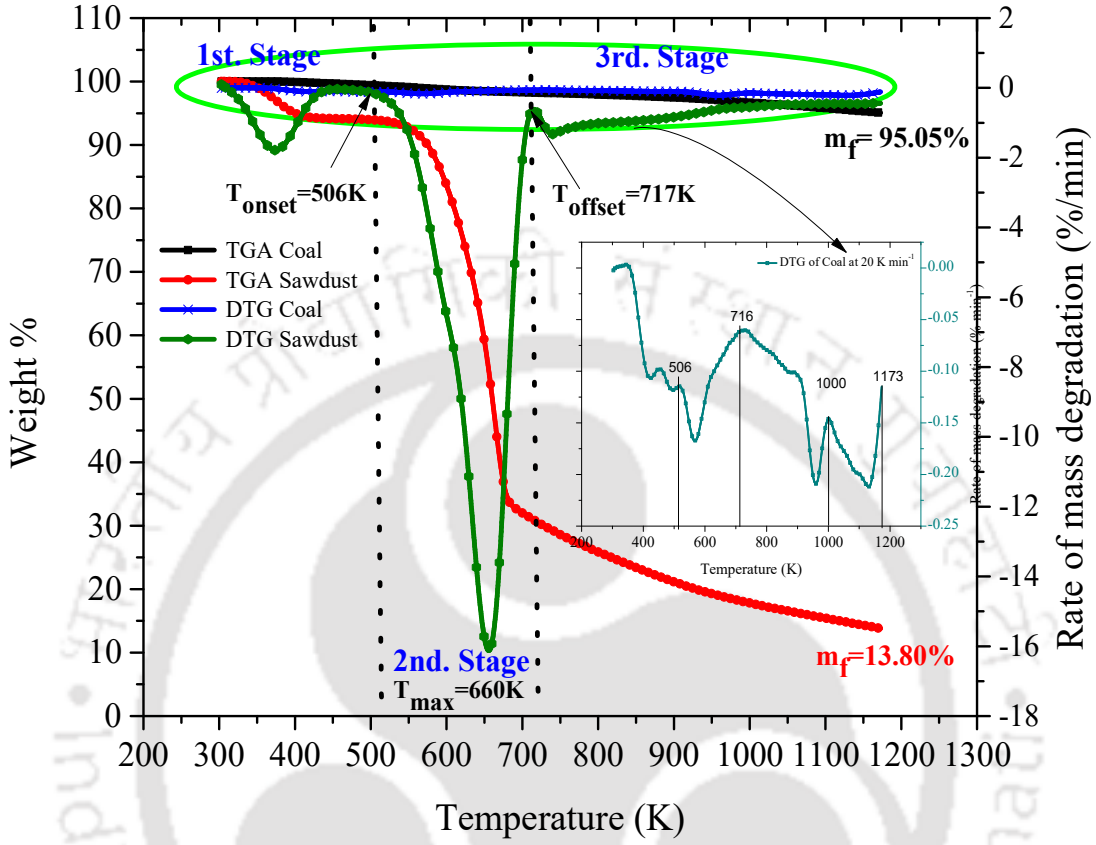

Fig. 5.1 TGA/DTG profile of coal and biomass at 20 K/min heating rate.

Table 5.1 Stages of thermal degradation of coal and sawdust

Sample	Drying zone (1st. stage)		Active pyrolytic zone (2nd. stage)		Carbonization zone (3rd. stage)		% char remaining
	Temp. K	% evaporation	Temp. K	Weight %	Temp. K	Weight %	
Sawdust	Up to 506	6.08	506-717	63.18	1173	16.94	13.80
	Drying zone (1st. stage)		**Active pyrolytic zone (3 stages)**				
			506-1173 K				
	Up to 506 K		**506-717**	**717-1000**	**1000-1173**		
Coal	0.63		1.14	1.24	1.94		95.05

5.4.2 TG analysis of coal and sawdust blends (Co-pyrolysis)

The thermal degradation profile of the co-pyrolysis samples is shown in Fig. 5.2 (a, b). It also displays the pyrolysis of coal and sawdust. The comparison of the thermal degradation profile is well understood between the co-pyrolysis samples and the individuals. The TG

profile of coal did not visualize any clear active pyrolytic zone whereas this zone was noticed as the sawdust blended. The increase in the mass loss in Fig 5.2 (a) was observed with the rise in the % sawdust in the co-pyrolysis sample. As a result, the char residue was reduced. The final char residue decreased from 84.05-20.87 % as blending of sawdust increased in coal at the end pyrolysis temperature. If the mass loss is considered in the active pyrolytic zone, then it can be stated that during the co-pyrolysis process, the mass of the sample degraded in the active pyrolytic zone was also increased linearly with the rise in the sawdust blending. The active pyrolytic zone for the sawdust and coal blend (100 %) was analogous with sawdust with a maximum degradation temperature of about 660 K. This can be observed from the TG/DTG curve. The active pyrolytic zone for the blended mixtures was analogous to each other and lied within 506-712 K (having a peak temperature at 660 K). In this zone, the % conversion of devolatilization increased from 60.67-73.37 % as blending of sawdust to coal increased respectively. This confirmed that the blending of biomass with coal helped in decreasing the thermal stability of coal. This also indicated the best utilization of low-grade coal and waste biomass to produce alternative fuels. A higher content of volatiles in the sawdust increases the thermochemical reactivity and acts as H_2-donors during the co-pyrolysis of biomass and coal and produces more volatile products. Literature reported that biomass pyrolytic oil has several disadvantages and needs proper upgrading techniques *(Park et al., 2010)*. Co-pyrolysis with coal will generate a better quality of pyrolytic oil to use as fuel since the hydrocarbon present in the coal helps in the formation of a better-quality pyrolytic oil. Also, it will reduce the cost of upgrading. The co-pyrolysis of coal and biomass will help in the transformation of N_2 into char rather than emitting more as pyrolytic vapor. The transformation of N_2 will enhance the fertility of char *(Tian et al., 2007)*. Since most of the low-temperature volatiles are released as pyrolytic vapors, the pyrolytic char contains very little volatile matter content and a higher C/H ratio and also the calorific value of the char increases. The high carbon and minimum volatile content char can be a good feed for gasification purposes to produce gaseous fuel *(Lu et al., 2013)*. Hence, it can be used as solid fuel also *(Benedetti et al., 2017)*. It is also reported that as biomass proportion increased in coal-biomass blended mixtures, there was an increase in the maximum devolatilization rate of the peaks representing coal while reducing the maximum devolatilization rates of peaks corresponding to biomass. To add on, the biomass-coal mix ratio is also a function of the volatiles yield *(Aboyade et al., 2013)*.

The cause for the decrease in the stability of coal with the addition of sawdust during thermal degradation can be proved if the degradation kinetics are studied. Without knowing

the detailed composition and reaction mechanism it is quite difficult to provide any statement regarding the cause. Hence, the kinetics study is performed further with the hope of explaining the reason for the decrease in stability based on the activation energy.

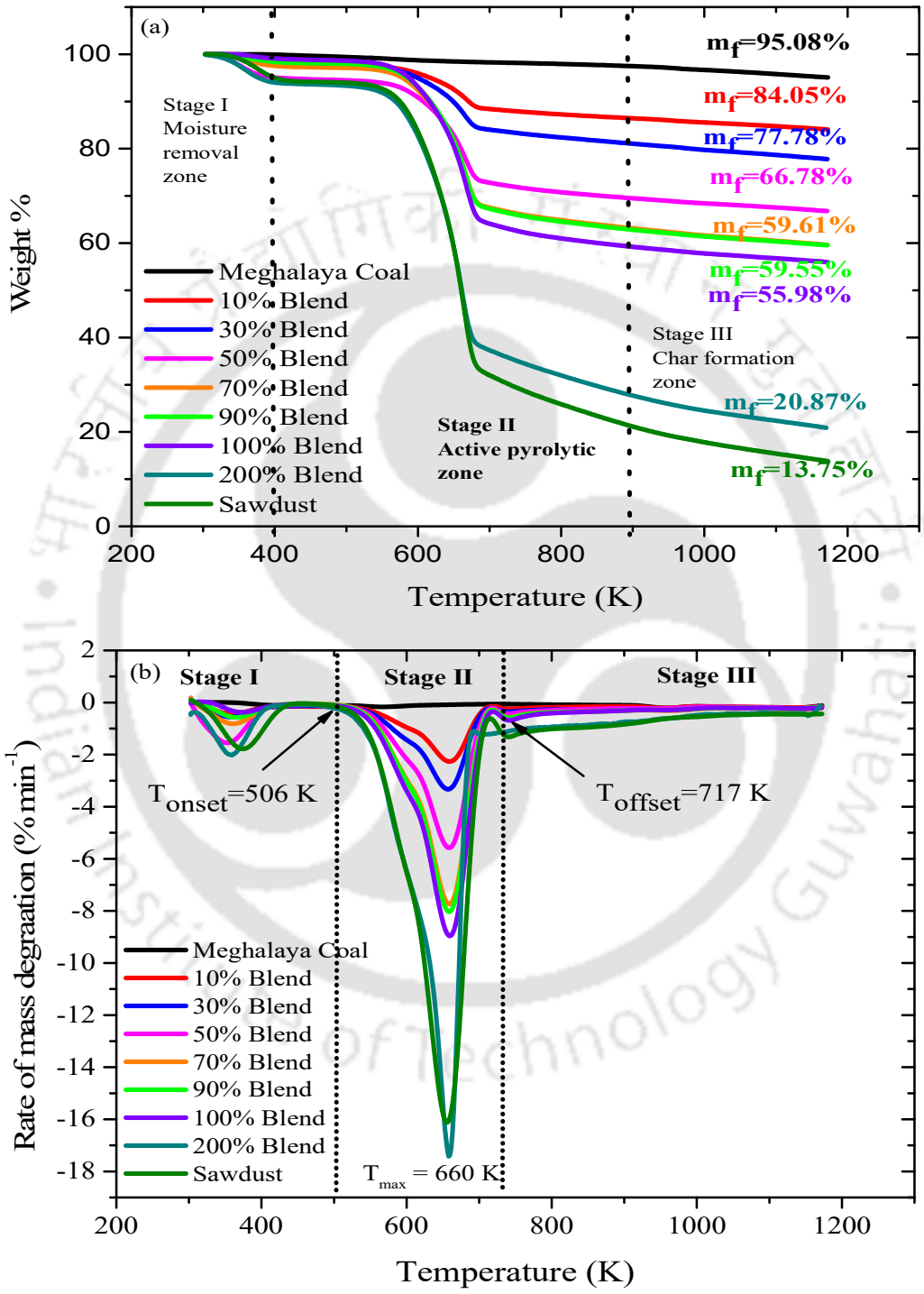

Fig. 5.2 Thermal degradation profile (a) TG, (b) DTG of coal, sawdust, and its blends at a single heating rate, 20 K min^{-1}

5.4.3 Assessment of performance metrics on thermal degradation

In Table 5.2, various parameters such as R_d, *CPI*, R_i, and ρ are indicated which affect the thermal degradation profile of the raw feed samples observed at a single heating rate, 20 K min^{-1} according to Eq. (3.4–3.8) mentioned in Chapter 3. R_i and intrinsic reaction rate, ρ of the biomass feedstock is seen as apposite to coal. The R_i of sawdust was 0.045 mg min^{-1}, whereas the intrinsic reaction rate was -0.228 min^{-1}. The R_i of coal was 0.0004 mg min^{-1}, whereas the intrinsic reaction rate was -0.180 min^{-1}. Comprehensive pyrolysis index *(CPI),* which was used to indicate the pyrolysis reactivity in the biomass sample was 27.77 × 10^{-6} % min^{-1} K^{-2}, whereas for coal it was much lesser 0.2032 × 10^{-6} % min^{-1} K^{-2}. The reactivity, R_i, and the intrinsic reaction rate, ρ increased with the increase in sawdust addition to coal. Comprehensive pyrolysis index (CPI) also increased with an increase in biomass addition to coal from 3.97 × 10^{-6} - 27.84 × 10^{-6} % min^{-1} K^{-2}.

Table 5.2 Reactivity (R_i), Intrinsic reaction rate (ρ), and Comprehensive pyrolysis index (CPI) for coal, sawdust, and its mixtures at a single heating rate, 20 K min^{-1} pyrolyzed under nitrogen atmosphere

Feed	**T_{onset} (K)**	**T_{offset} (K)**	**T_{in} (K)**	**T_{max} (K)**	***W_{mean}* (mg min^{-1})**	***R_{max}* (mg min^{-1})**	***R_d* (mg min^{-1})**	***R_i* (mg min^{-1})**	***ρ* (min^{-1})**	***CPI* (10^{-6} % min^{-1} K^{-2})**
Coal	423	1150	423	950	0.007	0.026	0.013	0.0004	-0.180	0.2032
Sawdust	506	712	505	660	0.135	1.44	0.72	0.045	-0.228	27.77
10 % Blend	506	717	506	660	0.020	0.195	0.097	0.003	-0.203	3.97
30 % Blend	506	717	506	660	0.030	0.169	0.084	0.005	-0.208	5.66
50 % Blend	506	717	506	660	0.038	0.076	0.456	0.228	-0.218	9.60
70 % Blend	506	717	506	660	0.067	0.756	0.378	0.011	-0.224	13.10
90 % Blend	506	717	506	660	0.073	0.860	0.430	0.011	-0.233	13.93
100 % Blend	514	720	514	720	0.074	0.172	0.086	0.013	-0.233	14.19
200 % Blend	514	714	514	663	0.145	1.43	0.715	0.0357	-0.0083	27.84

**T_1= Temperature at which devolatilization starts (K or onset temperature (K)), T_2= Temperature at which active pyrolytic zone ends (K) or offset temperature (K), T_{in}= Initial devolatilization temperature (K), T_{max}= peak temperature (K), W_{mean}= average mass degradation rate (mg min^{-1}), R_{max}= Maximum rate of mass degradation (mg min^{-1}), R_d= Rate at which maximum rate of degradation halves (mg min^{-1})*

5.4.4 Effect of chemical synergistic interactions in blends

For the determination of synergism in the blends, the deviation between the experimental and calculated values of mass loss and mass loss rate were calculated *(Tauseef et al., 2022, Merdun and Laouge, 2021).* The synergistic effect in the coal-sawdust blends during pyrolysis is reflected by any positive deviation in calculated and experimental values

obtained from the TGA of individual fuels. Positive chemical synergistic effects were seen in the blends (10 %, 70 %, 100 % and 200 %) when calculated from (Eq. 3.9) as mentioned in Chapter 3. The degree of synergy in blends is an intrinsic factor during co-pyrolysis. This is predominantly seen when biomass proportion is enhanced in coal-biomass blends. Synergistic interaction during the co-pyrolysis process occurs due to hydrogen availability of C-H bond dissociation to coal and coal pyrolysis intermediates *(Park et al., 2010).* Despite this fact, synergy may not be linearly dependent on the amount of biomass in the blended mixture due to lower thermal conductivity and packing density of biomass than coal particles. The effect of an increase in biomass proportion in the mixture decreases the heating rate capacity of the blends which results in higher residence time of volatiles such as OH and H radicals. These radicals in return, catalyses the coal tar formed during the process increasing the liquid yield and also the gas yield, thus increasing the conversion *(Park et al., 2010 and Sonobe et al., 2008).* Synergistic interactions might be also due to the presence of alkali and alkaline earth metals in sawdust which interacts with the polyaromatic hydrocarbons of coal and also during the volatile-char interface interactions during the reaction. As an addendum, the porous macrostructure of char formed after devolatilization in co-pyrolysis may also lead to a synergistic effect by increasing the volatile emissions and consequently increasing the weight loss. However, negative synergism was seen in the 30 % and 50 % blends, with the highest synergistic interaction in the 200 % blend. Volatile-volatile interactions and volatile-char interaction might be the added factor in positive chemical synergistic effects in 10 %, 70 %, 100 % and 200 % blends. This might be explained by the increased stable radicals as detected by the ESR signal for coal and sawdust in Fig. 4.5 in Chapter 4. Coal and sawdust thermal covalent bond breakage individually results in the generation of volatile free radicals and stable radicals, where due to the poor mobility of stable radicals, they recombine with each other easily *(He et al., 2021).* A series of crosslinking reactions and random fission reactions occur due to the simultaneous breakage of covalent bonds in the blends at higher temperatures, resulting in more volatile free radicals, effectuating the volatile-volatile and volatile-char interactions. Negative synergism might be due to the formation of biochar solid phases which might block the pores of the coal molecule as volatiles are driven out *(Chen et al., 2012).*

5.4.5 Effect of heating rate on coal degradation

The degradation of coal concerning the heating rate is shown in Fig. 5.3. It was observed that the rate of weight loss increased with the rise in the heating rate. The releasing of instantaneous thermal energy to the reaction system resulted in a higher rate of

devolatilization and hence the increase in the height of the DTG peak was perceived. However, the heating rate did not show any positive effect on the mass loss. The char yield increased with increasing the heating rate from 10-40 K min^{-1}. The yield of char increased from 94.48–95.81 % from 10–40 K min^{-1} respectively. According to the different temperature ranges, the active pyrolytic zone is segregated into different thermal degradation stages based on degradation pattern and maximum peak temperature. In coal pyrolysis, three stages of thermal degradation were duly observed in the active pyrolytic zone along with the moisture removal zone from 303-506 K which is considered as the first zone of degradation. With an increase in heating rates from 10–40 K min^{-1}, the temperature zone of thermal degradation increased due to the increased heat transfer effect as given in Table 5.3. For Stage I of thermal degradation, the temperature range was from 500-710.3 K at 10 K min^{-1} heating rate, 506-717 K at 20 K min^{-1} heating rate, 500-749.87 K at 30 K min^{-1} heating rate and 505-806.06 K at 40 K min^{-1} heating rate. For Stage II of thermal degradation, the temperature range was from 710.3-988.29 K at 10 K min^{-1} heating rate, 717-1000.5 K at 20 K min^{-1} heating rate, 749.87-1036.9 K at 30 K min^{-1} heating rate and 806.06 - 1052.2 K at 40 K min^{-1} heating rate. For Stage III of thermal degradation, the temperature range was from 988.29-1173 K at 10 K min^{-1} heating rate, 1000.5-1173 K at 20 K min^{-1} heating rate, 1036.91173 K at 30 K min^{-1} heating rate and 1052.2-1173 K at 40 K min^{-1} heating rate.

At the lower heating rates, the effect of heating on coal particles occurs more gradually to the inner core. This instills the cracking process to be more efficient in the form of weight loss of volatiles *(Moghtaderi et al., 2004).* Weight loss increased as the temperature range of the active pyrolytic zone increased. However, with an increase in the heating rates from 10-40 K min^{-1}, peak temperature shifts towards the right side (higher temperature zone). From this study, it could be observed that due to the higher thermal stability of coal, it needs more time inside the reactor to degrade. Hence at the low heating rate, the degradation was greater.

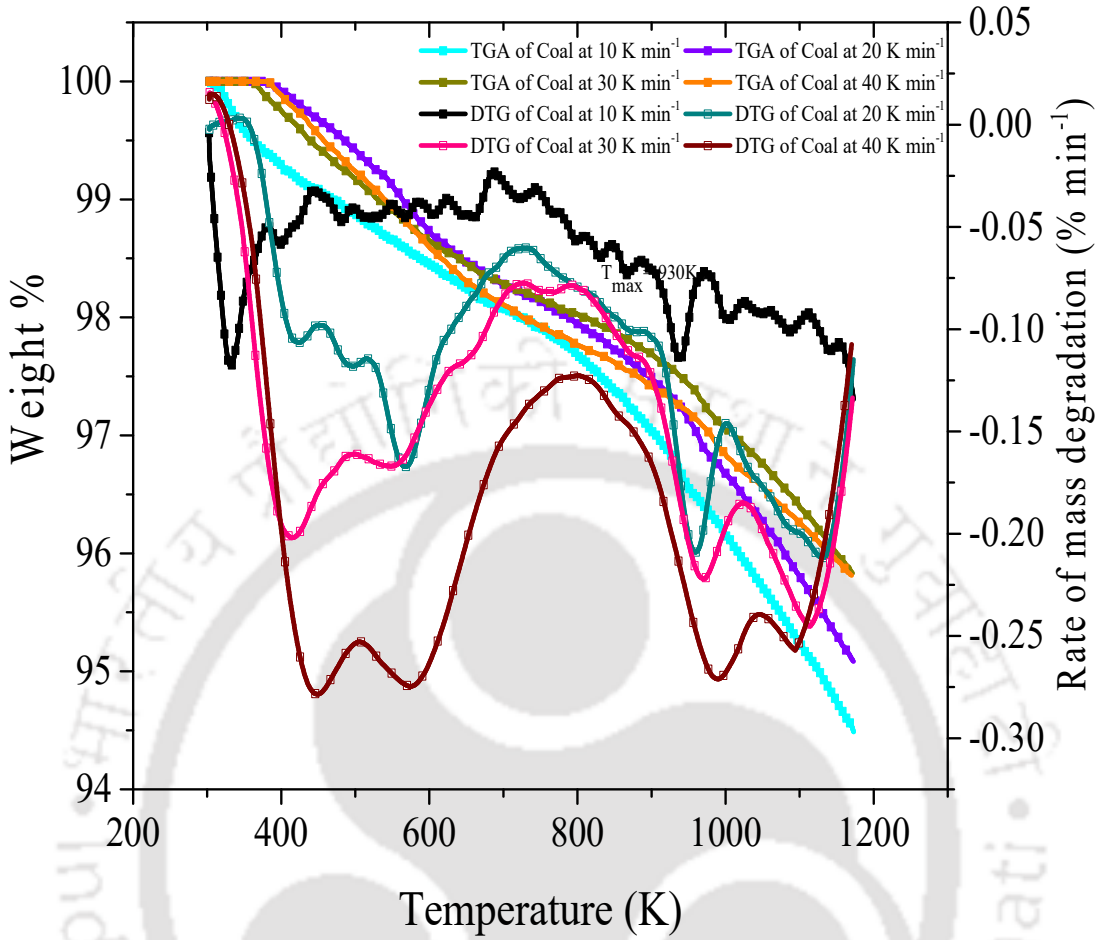

Fig. 5.3 Effect of heating rate on coal degradation (TGA/DTG)

Table 5.3 Stages of thermal degradation of coal as per heating rate

Coal	Drying zone (1st stage)		Active pyrolytic zone (3 Stages)									% Char residue
			Stage I			Stage II			Stage III			
β (K min^{-1})	Temp. K	Wt. loss %	Temp. K	Wt. loss %	T_{max} (K)	Temp. K	Wt. loss %	T_{max} (K)	Temp. K	Wt. loss %	T_{max} (K)	
10	303-500	1.16	500-710.3	0.82	-	710.3-988.29	1.77	930	988.29-1173	1.79	-	94.48
20	303-506	0.63	506-717	1.14	580	717-1000.5	1.24	950	1000.5-1173	1.94	1140	95.05
30	303-500	0.82	500-749.87	1.01	570	749.8-1036.9	1.31	970	1036.9-1173	1.007	1120	95.83
40	303-505	0.79	505-806.06	1.45	580	806.06 - 1052.2	1.19	990	1052.2-1173	0.727	1100	95.81

5.4.6 Effect of heating rate on sawdust degradation

The (TG/DTG) curve of sawdust is explicated in Fig. 5.4 which represents its thermal degradation pattern, weight (%) and rate of mass degradation (% min^{-1}) from 303-1173 K temperature at four heating rates 10, 20, 30 and 40 K min^{-1} respectively. The thermal stability and degradation profile of the lignocellulosic biomass components: cellulose, hemicellulose and lignin significantly differ according to the chemical structure and variations in the elemental composition of the feedstock. A single (TG/DTG) curve at 20 K min^{-1} can be considered for accurate estimation of the effect of temperature on the thermal degradation of the pseudo lignocellulosic components of sawdust. Before pseudo-component decomposition, the moisture removal zone (dehydration) (Stage I) was prevalent from 303-504 K releasing H_2O molecules from both extrinsic and intrinsic hydrated biomolecular regions of sawdust. The subsequent region (Stage II) was the zone of active pyrolysis from 505-712 K with a significant peak temperature at 660 K along with a higher rate of degradation as compared to other biomass feedstocks as evident from the literature. Initially, hemicellulose degradation happens and it demonstrates two peaks, one a shoulder peak from 505-550 K and another a sharp peak from 550-575 K, both encasing a two-stage pyrolysis profile. Hemicellulose (polyose) (mainly xylan, glucuronoxylan, arabinoxylan, glucomannan, and xyloglucan) is a matrix-embedded heteropolysaccharide comprising of a diverse range of sugars (prominently D-pentose sugars), five-carbon sugars- xylose and arabinose, six-carbon sugars- glucose, mannose and galactose and the six-carbon deoxy sugar rhamnose having several backbone linkages and branched side-groups. Most of the hemicelluloses, cellulose, and extractives get decomposed within the active pyrolytic zone. Typically, cellulose degradation occurs followed by hemicelluloses. In contrast to hemicellulose, cellulose decomposition encompasses a significant sharp peak at 660 K due to its rapid thermal cracking reaction occurring within a narrow temperature range of 550-712 K. Due to an incessant unbranched straight-chain polymeric structure alongside D-glucose units with β (1, 4–glycosidic linkages) and multiple hydroxyl groups linked to both intramolecular and intermolecular oxygen atoms through hydrogen bonds, it proves to be more resilient to thermal cracking within a narrow temperature gap as compared to hemicellulose. Thus, it has higher thermal stability than hemicellulose because of its higher tensile strength and strong microfibril structure. However, % conversion of 73.37 % sawdust degradation occurred by producing a final char residue of 13.75 % within the active pyrolytic zone. The % conversion to the pyrolytic vapor phase was higher at this stage. However, lignin degradation transpired at higher temperatures (713-1173 K) resulting in char residue at the end of the process. Lignin is a complex organic polymer

made up of phenylpropane precursor units. The cross-linked lignols are comprised of coniferyl alcohol, sinapyl alcohol, and para-coumaryl alcohol. The hydrophobic nature of the biomass was due to the higher aromaticity of lignin which makes it highly thermally stable. However, lignin degradation transpired at higher temperatures resulting in char at the end of the process. The higher the lignin content in the biomass, the higher the char residue at the end of thermal degradation. The decreasing trend of final char residue % is in the order, of lignin > hemicellulose > cellulose. The bio-extractives degrade slowly and occur within the degradation temperature of cellulose.

Figure 5.4 also demonstrates the effect of increasing heating rate on sawdust pyrolysis through (TG/DTG) curves. The pseudo-components of lignocellulosic biomass have a temperature gradient due to varying chemical structure and degree of polymerization factor engulfing various bond breakage and random scission during the pyrolytic process. Increasing the heating rate (10-40 K min^{-1}) pacifies the formation of a heat sink and intensifies the temperature gradient, providing an addendum to a thermal hysteresis phenomenon during the pyrolytic degradation of sawdust. It is seen that the % residue formation increased with an increase in heating rates, 10, 20, 30 and 40 K min^{-1} from 11.89 – 17.64 % and the % conversion within the active pyrolytic zone was enhanced and from 69.69–85.79 % at the four heating rates respectively as shown in Table 5.4. This confirmed that though a higher heating rate enhances de-volatilization in the active pyrolytic zone and better evaporation of moisture, due to the fast release of the pyrolytic vapors the biomass gets squeezed at a higher rate and the resultant is a higher char yield.

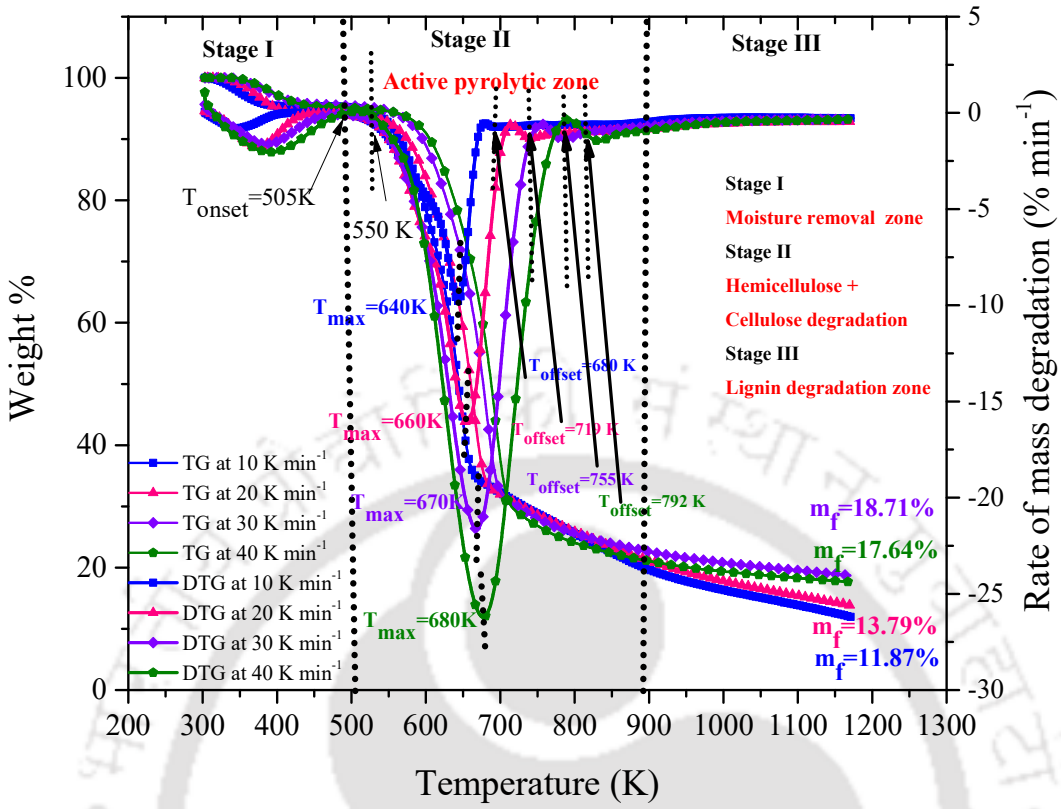

Fig. 5.4 Thermal degradation pattern of sawdust

Table 5.4 Final residue %, offset temperature (K), peak temperature (K), and conversion % at active pyrolytic zone in sawdust pyrolysis as per heating rate

Heating rate, K min^{-1}	T_{offset}	% α	T_{max}	Final residue, %
10	680 K	69.69 %	640 K	11.87 %
20	719 K	73.37 %	660 K	13.79 %
30	755 K	83.29 %	670 K	18.71 %
40	792 K	85.79 %	680 K	17.64 %

5.4.7 Effect of heating rate on co-pyrolysis (coal and 100% sawdust)

The effect of heating rate on the degradation profile (TG/DTG profile) of coal and 100 % sawdust blends at 10, 20, 30 and 40 K min^{-1} heating rates is depicted in Fig. 5.5. It was observed that co-pyrolysis at higher heating rate enhanced the conversion by yielding less amount of char. At 10 K min^{-1}, the mean conversion was 27.54 % and increased to 32.43 % at 20 K min^{-1}. Further increasing the heating rate to 30 K min^{-1} and 40 K min^{-1}, the conversion was accelerated to 31.05 % and 39.19 % respectively. As the conversion proceeded faster at a higher heating rate, the yield of char was also reduced. The final char residue was 58.14 %,

55.98 %, 53.30 %, and 49.42 % at 10, 20, 30 and 40 K min^{-1} respectively. The effect of the heating rate on the weight loss profile also visualized a shift in the curve (active pyrolytic zone) towards a higher temperature zone. It was confirmed that the degradation started at a particular temperature for all the heating rates and terminated at dissimilar temperatures.

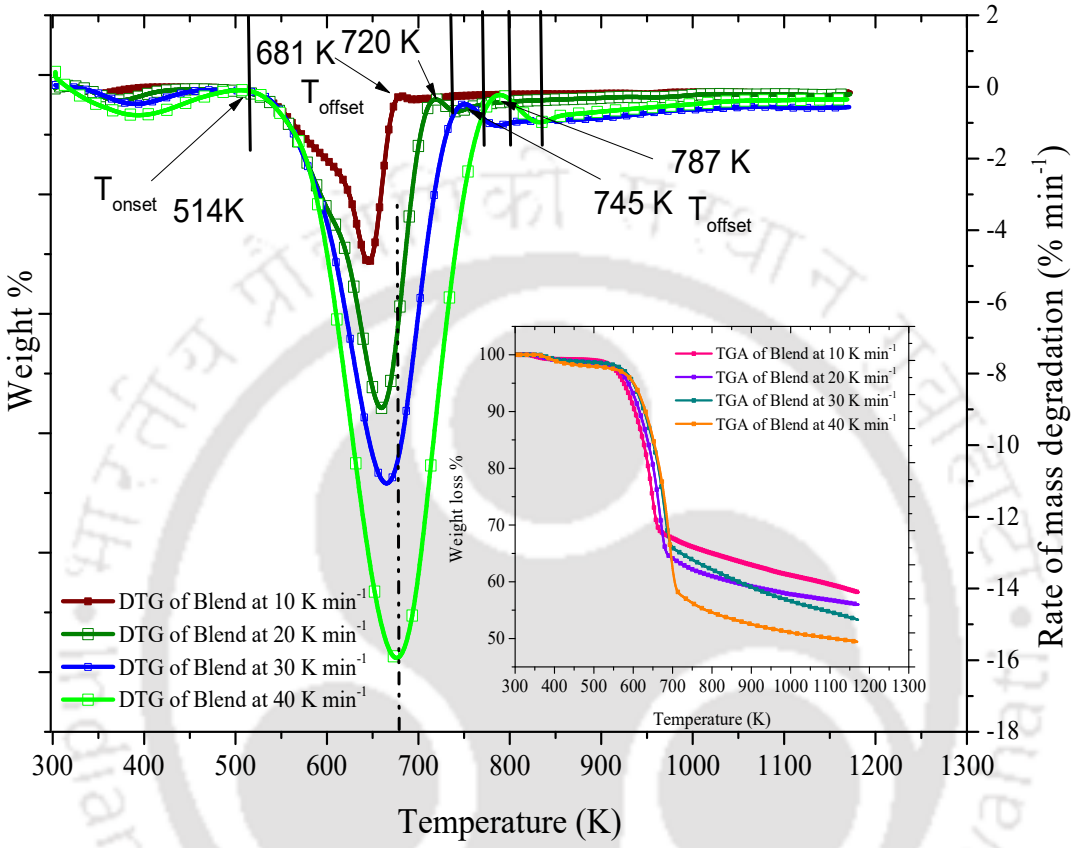

Fig 5.5 Effect of heating rate on thermal degradation of coal and 100 % sawdust blend

Table 5.5 Final residue %, offset temperature (K), peak temperature (K), and mean conversion % at active pyrolytic zone in coal and 100 % sawdust blend co-pyrolysis as per heating rate

Heating rate, K min^{-1}	**T_{offset}**	**% α**	**T_{max}**	**Final residue, %**
10	681 K	27.54 %	638 K	58.14 %
20	720 K	32.43 %	654 K	55.98 %
30	745 K	31.05 %	668 K	53.30 %
40	787 K	39.19 %	679 K	49.42 %

The onset pyrolytic temperature for the entire heating rate was 514 K. However, the offset temperature was 618 K for 10 K min^{-1}, 720 K for 20 K min^{-1}, 745 K for 30 K min^{-1} and

787 K for 40 K min^{-1}. Since the active pyrolytic zone continued for a longer temperature range, the conversion increased and yielded less char at the end of the pyrolysis. Correspondingly, pyrolysis at a higher heating rate reduced the time of pyrolysis by providing fewer yields of char. The slow pyrolysis required more time to heat the sample and to reach the pyrolysis temperature *(Arni, 2018).* The vapor residence time (VPR) is much longer at a slow heating rate than the higher heating rate that helps in the formation of char at low temperatures. The formation of char at a low temperature reduces thermal degradation. Especially, a lower heating rate is adopted to produce char from biomass which is known as carbonization *(Ronsee et al., 2015).* So as per the requirement of the yield, the rate of heating may be accepted. If the aim is to produce char as a solid fuel, then a lower heating rate and for liquid or gaseous fuel higher heating rate will be selected. However, optimization of the process parameters is important to produce the highest yield of pyrolytic oil of good quality. The releasing of pyrolytic volatiles from biomass and coal overlapped *(Ganeshan et al., 2018)* due to the volatile-volatile interaction and volatile-char interactions. It was observed that the composition plays an important role in the degradation. Since coal and sawdust are different in composition the effect of heating rate was found to be opposite.

5.4.8 Effect of heating rate on co-pyrolysis (coal and 200% sawdust)

The effect of heating rate on the degradation profile (TG/DTG profile) of coal and 200 % sawdust blends at 10, 20, 30 and 40 K min^{-1} heating rate is depicted in Fig. 5.6, which represents its thermal degradation pattern, weight (%) and rate of mass degradation (% min^{-1}) from 303-1173 K temperature. Moisture removal zone (dehydration) (Stage I) was prevalent from 303-514 K releasing H_2O molecules, subsequent region (Stage II) was the zone of active pyrolysis from 515-714 K with a significant peak temperature at 663 K and carbonization zone transpired at higher temperatures (715-1173 K) by resulting in char residue at the end of the process. As shown in Table 5.6, at 10 K min^{-1}, the conversion was 52.87 % and increased to 73.37 % at 20 K min^{-1}. Further increasing the heating rate to 30 K min^{-1} and 40 K min^{-1}, the conversion was accelerated to 79.03 % and 85.60 % respectively. As the conversion proceeded faster at a higher heating rate, the yield of char was also reduced. The final char residue was 23.91 %, 20.87 %, 46.54 % and 42.93 % at 10, 20, 30 and 40 K min^{-1} respectively. Due to effective heat and mass transfer rate conditions, peak temperatures shifted towards the right from 10–40 K min^{-1} heating rate as 633 K, 663 K, 677 K and 685 K respectively.

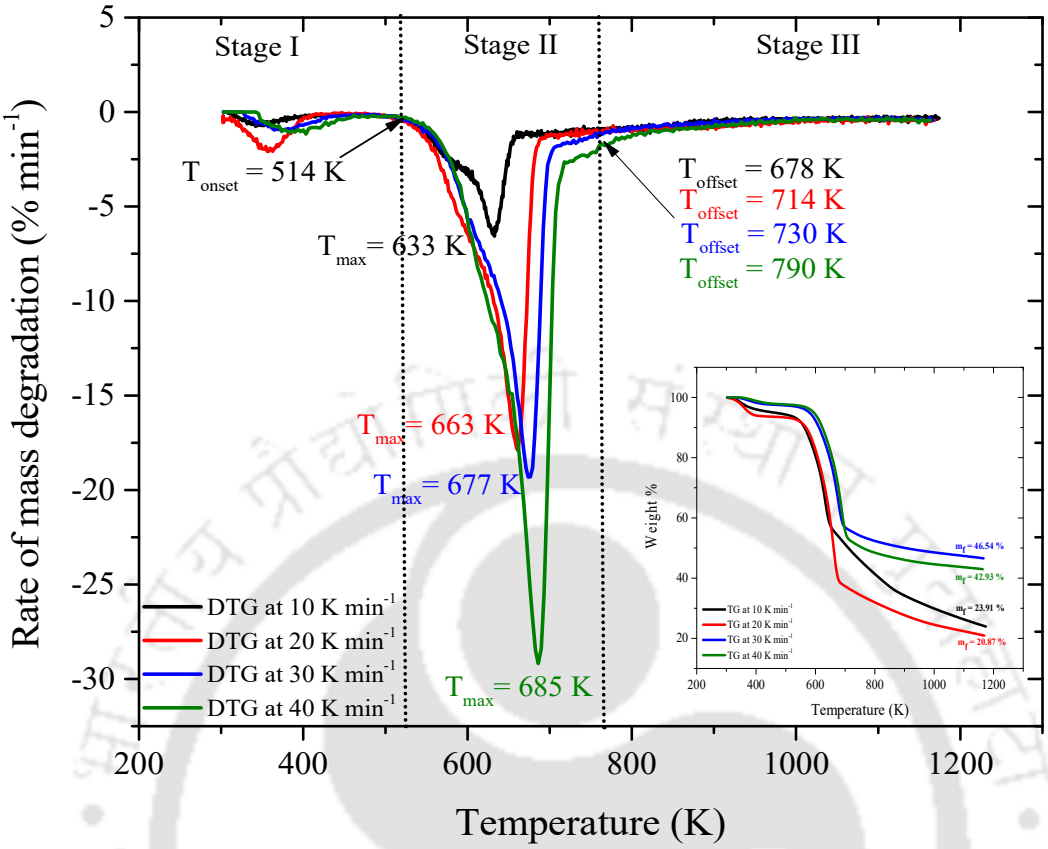

Fig 5.6 Effect of heating rate on thermal degradation of coal and 200% sawdust blend

Table 5.6 Final residue %, offset temperature (K), peak temperature (K), and conversion % at active pyrolytic zone in coal and 200 % sawdust blend co-pyrolysis as per heating rate

Heating rate, K min^{-1}	**T_{offset}**	**% α**	**T_{max}**	**Final residue, %**
10	678 K	52.87 %	633 K	23.91 %
20	714 K	73.37 %	663 K	20.87 %
30	730 K	79.03 %	677 K	46.54 %
40	790 K	85.60 %	685 K	42.93 %

5.5 Kinetics and thermodynamics study

The pyrolysis and co-pyrolysis kinetics and thermodynamics were studied except for the moisture removal zone since the moisture removal zone is not under the pyrolysis zone.

5.5.1 Degradation kinetics of coal pyrolysis

The active pyrolytic zone of coal is segregated into three stages depending on the temperature range. For each stage, a degradation peak (T_{max}) and rate of degradation are

observed. Non-isothermal iso-conventional model-free integral kinetics (KAS method) is used in this study. The iso-conventional calculation is estimated for each degradation stage from a conversion range of 5%<α<95%. The *p(x)* iso-conventional term as approximated by Murray and White approximation is used for the KAS method *(Akahira and Sunose, 1971).*

The plots generated by plotting ln (β/T^2) vs. 1/T in the conversion range of 5%< α<95% were used to determine the activation energy which is shown in Fig. S1 (a-b). It was observed that the linear plots were mostly straight lines and demonstrated parallel behaviors between the conversions. The kinetic parameters evaluated from the slope of the plots are exemplified in Table 5.7-5.8. Stage I of active pyrolysis rendered very less regression coefficient values and hence the model is not linearly fitted for this pyrolysis zone. For Stage II, the linear regression lines were wider between 10–50 % conversion indicating the fact that activation energy would be wider in range. However, the conversion (α) range between 50-95 % which indicated that the required activation energy would be closer. The result obtained visualized the increase in the activation energy achieved as the conversion (α) was intensified from 10-95 %. A significant increase in the E_α value from 5–95 % was perceived eventually. This is because at Stage II of thermal degradation, the rate of degradation is higher accounting for the increase in E_α value. The main reason encompassing this fact is that many dissociation reactions take place at this juncture due to the endothermicity of the reaction. Due to increased crosslinking and free-radical stabilization reactions, the resulting phenomenon occurs accounting for a higher E_α value. Consequently, a lesser E_a value is accountable for a lesser rate of degradation. The average value of E_α within 10%<α<95% for Stage II of thermal degradation of coal was 99.47 kJ mol^{-1}. The value of the pre-exponential factor (A, s^{-1}) also followed a different trend as the activation energy. The pre-exponential factor (A, s^{-1}) decreased from 5-95% due to fewer collisions in the reaction mixture. Regression coefficients are however higher as obtained by linear fitting regression analysis.

For Stage III of thermal degradation, the parallel lines were closer in the conversion *(α)* range between 5–70 % indicating that the required activation energy would be closer. The result obtained visualized the increase in the activation energy achieved as the conversion *(α)* was intensified from 5–85 % with a further decrease from 85–95 %. This is because, at Stage III of thermal degradation, the rate of degradation is higher accounting for the increase in E_α value as compared to the prior two stages of thermal degradation. However, the decrease in E_α value might be because char has already formed at this conversion stage and no further reaction is being carried out. The main reason encompassing this fact is that many dissociation reactions take place at this juncture due to the endothermicity of the reaction

encompassing its higher E_a value. The negative activation energy is due to the slow rate of degradation; hence the activation energy gets reduced to a lower value. Due to very less regression coefficients, these values are correspondingly not depicted in Table 5.8. Pyrolysis is an endothermic process that is associated with many dissociation reactions in the polymer chain. However, the addition reaction shows negative activation energy. This confirmed that the pyrolysis reaction stopped once the negative activation energy was observed *(Velden et al., 2010, Arseneau, 1971, Mettler et al., 2012).* The average value of E_α within 5%<α<70% for Stage III of thermal degradation of coal was 402.04 kJ mol^{-1}. The value of the pre-exponential factor (A, s^{-1}) also followed the same trend as the activation energy. Regression coefficients are however higher as obtained by linear fitting regression analysis. It was observed in Table 5.7 and 5.8 that R^2 values were significant for Stage II and Stage III of coal pyrolysis indicating that coal pyrolysis was favorable at higher temperature stages of 717-1000 K and 1000-1173 K respectively.

Table 5.7 Kinetic Parameters of Coal Pyrolysis for Stage II of Active Pyrolytic Zone

α, %	Model equation	R^2	E, (kJ mol-1)	A, (s-1)
10	Y= -6808.81X-1.73	0.811	56.60	1.10×10^2
15	Y= -7578.46X-1.05	0.852	63.00	3.52×10^2
20	Y= -7683.72X-1.19	0.863	63.88	4.06×10^2
25	Y= -7774.79X-1.31	0.862	64.63	4.50×10^2
30	Y= -9280.27X+0.24	0.931	77.15	3.06×10^3
35	Y= -9539.41X+0.31	0.944	79.31	3.90×10^3
40	Y= -10068.15X+0.70	0.942	83.70	6.94×10^3
45	Y= -10719.95X+1.21	0.982	89.12	1.38×10^4
50	Y= -11422.41X+1.79	0.998	94.96	2.91×10^4
55	Y= -12245.41X+2.51	0.99	101.80	7.04×10^4
60	Y= -15072.98X+5.30	0.978	125.31	1.54×10^6
65	Y= -15042.34X+5.13	0.991	125.06	1.41×10^6
70	Y= -16013.53X+5.99	0.989	133.13	3.79×10^6
75	Y= -16023.08X+5.83	0.982	133.21	3.48×10^6
80	Y= -15322.54X+4.96	0.962	127.39	1.49×10^6
85	Y= -14662.41X+4.12	0.939	121.90	6.51×10^5
90	Y= -14695.60X+3.97	0.943	122.17	5.95×10^5
95	Y= -15419.90X+4.50	0.93	128.20	1.12×10^6

Table 5.8 Kinetic Parameters of Coal Pyrolysis for Stage III of Active Pyrolytic Zone

α, %	**Model equation**	R^2	E, kJ mol^{-1}	A, s^{-1}
5	Y= -20216.98X+8.80	0.88	168.08	6.77×10^{6}
10	Y= -21804.25X+10.15	0.881	181.28	5.12×10^{7}
15	Y= -24139.27X+12.20	0.889	200.69	6.45×10^{8}
20	Y= -26743.98X+14.48	0.897	222.34	9.10×10^{9}
25	Y= -29187.67X+16.56	0.891	242.66	9.84×10^{10}
30	Y= -32485.94X+19.39	0.894	270.08	2.23×10^{12}
35	Y= -36222.09X+22.59	0.907	301.15	7.08×10^{13}
40	Y= -41616.43X+27.33	0.91	345.99	1.06×10^{16}
45	Y= -45705.41X+30.77	0.885	379.99	4.07×10^{17}
50	Y= -52291.97X+36.43	0.87	434.75	1.48×10^{20}
55	Y= -60739.43X+43.70	0.851	504.98	2.70×10^{23}
60	Y= -72303.53X+53.65	0.834	601.13	7.39×10^{27}
65	Y= -90516.83X+69.34	0.849	752.55	6.54×10^{34}
70	Y= -123046.10X+97.55	0.755	1023.0	1.70×10^{47}

5.5.2 Degradation kinetics of sawdust pyrolysis

Fig. S2 represents the relation between $\ln(\beta/T^2)$ vs. 1/T for KAS in the conversion range of 5%<α<75% at distinct heating rates and the evaluated kinetic parameters are given in Table 5.9. It could be noticed in Fig. S2 that the linear regression graph comprised of straight parallel lines which were close by in the conversion (α) range between 10–75 %. This indicated that the required activation energy would be closer to that range. A greater gap was observed between the curves obtained for α = 5 %, α = 10 % and α > 75 %. The result visualized that the reduction in the activation energy was achieved as the conversion (α) was intensified from 5–10 %. A sudden increase in the activation energy was perceived again as α increased to 75 %. Further, negative activation energy appeared at 75%>α<95%. A distinct decline in the E_α value from 175.83–91.46 kJ mol^{-1} was observed when the conversion was increased from 5–10 %. The increase in the conversion from 10–70 % resulted in the alleviation in the activation energy from 91.46–123.21 kJ mol^{-1}. The activation energy was 123.21 kJ mol^{-1} at α = 70% which was higher than the activation energy obtained between 10%>α<75% and lower as compared to 5 %. At α = 80 % and 95 %, the negative values of activation energy were perceived. The activation energies at these particular conversions were not considered. Hence, it could be confirmed that higher heat energy is required to start

the thermal degradation or to release the initial lower-temperature volatile contents from the sawdust. Since thermal degradation is an endothermic process; it requires more energy to initiate the reaction.

The pre-exponential factor *(A)* illustrates the density of collisions between reactant molecules. However, according to the Arrhenius equation, the rate equation and the value of the frequency factor do not affect the temperature sensitivity of the reaction. For thermal pyrolysis of sawdust, higher values of A at low conversions ($\alpha<10$ %) and high conversions ($\alpha > 65$ %) as 2.73×10^{6} (s^{-1}) and 1.50×10^{-1} (s^{-1}) were seen respectively, owing to the solid-phase surface reaction and greater collisions occurring at higher conversions. The zone of active pyrolysis manifested frequency values ranging from $6.81\times10^{-3} – 1.50\times10^{-1}$ (s^{-1}) for the KAS method at conversions ($10\%>\alpha>70\%$) respectively. These values indicate reaction chemistry which is quite simple concerning the peak conversion temperature integral.

For bimolecular reactions, degrees of freedom are lost as reactants proceed along the potential energy surface. If the transition state is loose, these will be replaced by internal rotations with similar contributions to the average kinetic energy. Also, the potential energies will be essentially unchanged in forming the transition state. If the reaction proceeds via a tight transition state, classical degrees of freedom will be replaced with vibrational modes. These, if stiff, will contribute very little to the average internal energy; as a result, the average kinetic energy will decrease. However, such a transition state generally requires the breaking and forming of bonds with a substantial increase in potential energy. This will generally be much larger than the decrease in kinetic energy. For a tight transition state with a very low potential energy, E_a proceeds via a stable intermediate. If the second transition state (TS2) is tight and the first (TS1) is loose, the equilibrium constant will be much less and the decomposition of stable intermediate to products would be rate determining. The tight transition state would have a significant threshold energy relative to the intermediate but may have a small, or even negative, potential energy relative to the reactants. If the energy to reach the transition state is sufficiently negative, then the second step will be faster than the first despite TS2 being tighter. The reduction in the number of classical degrees of freedom can then produce a negative activation energy for the overall process. As activation energies are negative, reactants with lower energy react faster than higher energy, which directly affects the pre-exponential factor values as there are no molecular collisions due to the short-life span of the intermediates. However, for higher negative values of activation energies, the rate of the reaction would be directly dependent as a product of equilibrium constant and rate constant, defined by the potential energy of the transition state relative to the reactants, and

thus higher negative values of pre-exponential factor is seen *(Mozurkewich and Benson, 1984).* Also, at distinct higher conversion values of subsequent bimolecular reactions of biomass pyrolysis, char evolution, and decomposition act as blockage of volatiles released from peculiar nucleation sites. This might manifest a rate-determining step with a negative potential energy transition state for the stable intermediates to products step, resulting in negative values of activation energies and pre-exponential factors.

Table 5.9 Estimation of thermal pyrolysis kinetics for sawdust

α, %	**Model Equation**	R^2	*E, (kJ mol^{-1})*	*A, (s^{-1})*
5	Y= -21148.74X+29.51	0.976	175.83	2.73E+06
10	Y= -11000.75X+9.00	0.974	91.46	6.81E-03
15	Y= -11326.35X+9.03	0.976	94.167	7.10E-03
20	Y= -11859.1X+9.51	0.971	98.597	1.14E-02
25	Y= -12409.35X+10.06	0.973	103.17	1.97E-02
30	Y= -12781.7X+10.35	0.976	106.27	2.67E-02
35	Y= -12959.48X+10.36	0.976	107.75	2.74E-02
40	Y= -13315.67X+10.67	0.974	110.71	3.80E-02
45	Y= -13315.82X+10.47	0.974	110.71	3.21E-02
50	Y= -13316.51X+10.29	0.974	110.71	2.79E-02
55	Y= -13577.60X+10.54	0.975	112.88	3.61E-02
60	Y= -14389.92X+11.59	0.961	119.64	1.01E-01
65	Y= -14061.23X+10.98	0.975	116.91	5.79E-02
70	Y= -14819.48X+11.96	0.971	123.21	1.50E-01

5.5.3 Co-pyrolysis kinetics of coal and 100 % sawdust blend

The linear plot between ln (β/T^2) vs. 1/T in the conversion range of 5%<α<70% is shown in Fig. S3 and the determined kinetic parameters are reported in Table 5.10. The regression lines were parallel and very close to each other between 5-65 % conversion. A greater gap was observed between the curves α > 65 % which were not parallel. The value of E_α was increased from 94.67–117.02 kJ mol^{-1} as the conversion enhanced from 5-65 % and further decreased till the end of the process. However, negative values of activation energies were perceived between 75-95 % conversion. Beyond α =75%, the rate of degradation was very slow and char formation occurred due to this negative activation energy. Henceforth, the activation energy values are not considered in this particular conversion. The value of pre-exponential factor *'A'* was also increased from α =5-65 %. The average activation energy obtained from the co-pyrolysis of coal and 100 % sawdust was 108.84 kJ mol^{-1} between α = 5-65 %. As compared to the coal pyrolysis the activation energy was less, this confirmed that

co-pyrolysis of coal with sawdust decreases the activation energy and as a result, the rate of degradation increased along with the mass loss. The negative activation energy was not because of the spontaneous reactions which occurred during the pyrolysis process. Hence, these steps are not an endothermic process. The negative activation energy appeared once the depolymerization of cellulose and hemicellulose was completed and the char was formed *(Velden et al., 2010, Arseneau, 1971, Mettler et al., 2012).*

For thermal pyrolysis of coal and 100% sawdust blend, higher values of *A* at low conversions (α < 10 %) and high conversions (α = 65 %) as 8.96×10^{6} (s^{-1}) and 3.84×10^{-8} (s^{-1}) were seen respectively, owing to the solid-phase surface reaction and greater collisions occurring at higher conversions *(Chong et al., 2019).* The zone of active pyrolysis manifested frequency values ranging from 1.70×10^{7} – 3.84×10^{8} (s^{-1}) for the KAS method at conversions (10%>α>70%) respectively. These values indicate reaction chemistry which is quite simple concerning the peak conversion temperature integral.

Table 5.10 Kinetic parameters of coal and 100% sawdust blend

α, %	**Model equation**	R^2	*E, (kJ mol^{-1})*	*A, (s^{-1})*
5	Y= -11387.5X+9.66	0.98	94.67	8.96×10^{6}
10	Y= -11715.1X+9.67	0.981	97.39	1.70×10^{7}
15	Y= -12236.5X+10.11	0.984	101.73	4.03×10^{7}
20	Y= -12643.6X+10.41	0.981	105.11	7.38×10^{7}
25	Y= -12969.6X+10.61	0.981	107.82	1.14×10^{8}
30	Y= -13277.6X+10.81	0.983	110.39	1.71×10^{8}
35	Y= -13327.2X+10.64	0.977	110.80	1.68×10^{8}
40	Y= -13506.1X+10.71	0.979	112.29	2.09×10^{8}
45	Y= -13456.8X+10.46	0.978	111.88	1.81×10^{8}
50	Y= -13698.1X+10.68	0.982	113.88	2.55×10^{8}
55	Y= -13908.5X+10.85	0.982	115.63	3.38×10^{8}
60	Y= -13997.4X+10.84	0.977	116.37	3.66×10^{8}
65	Y = -14075X+10.81	0.956	117.02	3.84×10^{8}

5.5.4 Co-pyrolysis kinetics of coal and 200 % sawdust blend

The linear plot between ln (β/T^2) vs. 1/T in the conversion range of 5%<α<50% is shown in Fig. S4 and the determined kinetic parameters are signified in Table 5.11. The regression lines were parallel and very close to each other between 10-50 % conversion. The value of E_α was increased from 191.03–128.24 kJ mol^{-1} as the conversion enhanced from 5-50 % and further decreased till the end of the process. However, negative values of activation

energies were perceived between 70-95 % conversion. The value of pre-exponential factor *'A'* was also increased from α = 5-60 % and decreased beyond. The average activation energy obtained from the co-pyrolysis of coal and 200 % sawdust was 122.40 kJ mol^{-1} between α = 5-65 %. As compared to the coal pyrolysis the activation energy was less, this confirmed that co-pyrolysis of coal with sawdust decreases the activation energy and as a result, the rate of degradation increased along with the mass loss. However, as compared to coal with a 100 % sawdust blend, the activation energy of coal and 200 % sawdust was higher since the char formation zone which rendered negative activation energy values occurred at a lesser conversion α > 65% and also at a lesser temperature zone.

For thermal pyrolysis of coal and 200 % sawdust blend, higher values of A at low conversions (α < 10%) and high conversions (α > 45%) as 1.06×10^{12} (s^{-1}) and 7.36×10^{5} (s^{-1}) were seen respectively, owing to the solid-phase surface reaction and greater collisions occurring at higher conversions. The zone of active pyrolysis manifested frequency values ranging from 7.82×10^{2} – 7.36×10^{5} (s^{-1}) for the KAS method at conversions (10%>α>45%) respectively. For bimolecular reactions of coal-biomass co-pyrolysis, char evolution and decomposition act as blockage of volatiles released from peculiar nucleation sites *(Vyas et al., 2017).* This would manifest a rate-determining step with a negative potential energy transition state for the stable intermediates to products step, resulting in negative values of activation energies and pre-exponential factors *(Mozurkewich and Benson, 1984).* Here, Table 5.11 specifies the co-pyrolysis kinetics of coal and 200 % sawdust blend.

Table 5.11 Kinetic parameters of coal and 200 % sawdust blend

α, %	**Model equation**	R^2	*E, (kJ mol^{-1})*	*A, (s^{-1})*
5	Y= -21774.3X+30.36	0.918	191.03	1.06E+12
10	Y= -10856.8X+8.78	0.91	181.03	7.82E+02
15	Y= -11684.09X+9.66	0.92	90.263	1.36E+03
20	Y= -12892.74X+11.23	0.904	97.141	9.33E+03
25	Y= -14068.60X+12.75	0.904	107.19	5.78E+04
30	Y= -14349.45X+12.84	0.904	116.96	8.27E+04
35	Y= -14385.25X+12.60	0.899	119.30	7.70E+04
40	Y= -14987.15X+13.30	0.933	119.59	1.76E+05
45	Y= -15425.14X+13.76	0.913	124.60	3.27E+05
50	Y= -16012.68X+14.44	0.889	128.24	7.36E+05

5.5.5 Interpretation of kinetic analysis

The kinetics of coal, sawdust, and their blends are comprehensively interpreted and compared with prior works. Higher values of regression coefficients stated that coal pyrolysis was favorable at higher temperature stages of 717-1000 K and 1000-1173 K. Sawdust pyrolysis resulted in the decline in the E_α value from 175.83–91.46 kJ mol^{-1} as observed when the conversion was increased from 5-10 % and increased linearly from 91.46–123.21 kJ mol^{-1} as conversion increased from 10–70 % as evaluated by KAS method. Biagini et al. worked on three biomass fuels, rice husks, olive cake (exhausted), and cacao shells (particle size of 90-125 μm) at a constant heating rate programmed to 1220 K with 5, 10, 15, 20, 40, 60 and 100 K/min heating rates in a TG analyzer. Three methods (Friedman, Flynn Wall, and Kissinger) are selected for evaluating the kinetic parameters of biomass fuels. For both Friedmann and OFW methods, E_a varies strongly with the extent of conversion, 135.5 kJ mol^{-1} and 128.1 kJ mol^{-1} for rice husks, 119.1 kJ mol^{-1} and 117.8 kJ mol^{-1} for olive cake and 127.7 kJ mol^{-1} and 129.6 kJ mol^{-1} for cacao shells respectively. However, the Kissinger method shows lower activation energy values than those from the other methods, 112.5 kJ mol^{-1}, 103.2 kJ mol^{-1} and 65.3 kJ mol^{-1} for rice husks, olive cake and cacao shells respectively as it focuses on the peak temperature weight loss % as a single reaction step *(Biagini et al., 2008).* In the similarly reported literature, a VEB (Variable activation Energy model for Biomass devolatilization) model is developed where the average values of the activation energy obtained by using the three methods are input in a first-order reaction model and pre-exponential factor is calculated from the best-fit with the experimental results of all set of runs (5–100 K/min). The model is optimized by considering the widest interval ($\alpha1$, $\alpha2$) for each biomass sample and varying E_{on} and E_{off} to the characteristic temperatures (T_{onset} and T_{offset}, respectively). The optimal interval ($\alpha1$, $\alpha2$) is (0.2,0.55) for rice husks, (0.2,0.45) for olive cake, (0.25,0.5) for cacao shells, respectively of pre-exponential factor values *(Biagini et al., 2008).*

In the co-pyrolysis kinetics of Meghalaya coal and sawdust of the present work, activation energies increased from 94.67–117.02 kJ mol^{-1} as conversion increased from 10-65 %. Increasing the sawdust proportion in the blend, led to activation energies from 191.03–107.19 KJ mol^{-1} as conversion increased from 5–20 % and increased from 107.17–161.25 kJ mol^{-1} as conversion increased from 20–60 %. In a study reported by Lu et al., anthracite coal from Australia and C. japonica biomass from Taiwan were meshed in a 100-200 μm particle size and blended in the biomass blending percentages of 100, 75, 50, 25 and 0 wt.%,

subjected to TG analyzer at 1073 K temperature under nitrogen atmosphere. When the Coats-Redfern method was employed, the activation energies of W_{Raw}, TW_{250} and TW_{300} in the second stage were compared with each other, TW_{250} at a given BBR generally has the highest value in that relatively more cellulose is contained in the sample. In the third stage, lignin plays an important role in determining the activation energy and the relative amount of lignin in TW_{300} is the highest. As a consequence, the activation energy is characterized by $TW_{300}>TW_{250}>W_{Raw}$ *(Lu et al., 2013)*. In another study for pyrolysis of banana agro-waste residues, the activation energy increased from 0.1-0.7 fractional conversion and then decreased due to insufficient amounts of cellulose and hemicellulose *(Singh et al., 2022)*. Aboyade et al. worked on non-isothermal thermo-kinetics of the co-pyrolysis of sugarcane bagasse and corn residue blended with coal at mix ratios (by mass): 90:10, 80:20, 70:30, 60:40 and 50:50. In the 0.1-0.8 conversion range, where the correlation coefficient was high (>0.95), the apparent activation energy *E* for the biomass fuels increased with apparent *E* for coal as more or less constant. The average apparent E_a values for coal–BG blends were 240, 183, and 173 kJ mol^{-1} while for coal–CC blends they were 220, 243 and 195 kJ mol^{-1} for concentrations of 10 wt. %, 20, wt. % and 40 wt. % respectively. Initial devolatilization in the blends is attributed to the biomass fraction, while at higher conversion, it was mainly due to coal devolatilization. The conversion values indicated the mass contribution that biomass made to the total volatile yield, 34%, 50% and 70% conversion at 10 wt. %, 20, wt. % and 40 wt. % respectively of biomass concentration *(Aboyade et al., 2013)*. Idris et al. reported on the thermal decomposition of Mukaah Balingian coal and oil palm biomass blends at 20 %, 40 %, 50 %, 60 % and 80 % biomass blending percentage to coal with a particle size of < 212 μm. Encompassing a differential kinetic method, activation energies, and pre-exponential factors were determined *(Bamford and Tipper, 1980)*. Similar trends of activation energies were observed in the second thermal evolution profile for coal and palm mesocarp fibre blends and coal and palm kernel shell blends which increased with an increase in conversion and an exception for coal and empty fruit brunch blended mixtures which decreased with an increase in conversion. This is due to the mean reactivity in the order of empty fruit brunch> palm kernel shell> palm mesocarp fiber>coal. The activation energies due to the decomposition of cellulose (thermal evolution profile 2) present in biomass showed the highest value (174–227 kJ mol^{-1}), then that due to the decomposition of hemicellulose (thermal evolution profile 1) (140–166 kJ mol^{-1}). It was also noticed that the higher the values of average activation energies, the higher the mean pre-exponential factor values for each blended mixture *(Idris et al., 2010)*. Singh et al. worked on co-pyrolysis of pet-coke from a

delayed coker unit of an Indian petrochemical origin and banana agro-waste and according to the model-free kinetic methods, KAS, OFW, Starink, Kissinger, Friedman, Vyazovkin and Vyazovkin AIC explored their kinetics parameters. The average value of activation energy estimated from KAS, FWO, Starink, Vyazovkin's method, Vyazovkin's AIC and Friedman method for pet coke pyrolysis, banana waste pyrolysis and their co-pyrolysis was 258.05 kJ mol^{-1}, 257.14 kJ mol^{-1}, 256.51 kJ mol^{-1}, 256.12 kJ mol^{-1}, 260.83 kJ mol^{-1} and 251.685 kJ mol^{-1} respectively, 222.32 kJ mol^{-1}, 220.75 kJ mol^{-1}, 222.54 kJ mol^{-1}, 226.89 kJ mol^{-1}, 226.43 kJ mol^{-1} and 237.98 kJ mol^{-1} respectively, and 165.77 kJ mol^{-1}, 166.12 kJ mol^{-1}, 164.52 kJ mol^{-1}, 164.28 kJ mol^{-1}, 169.23 kJ mol^{-1} and 170.94 kJ mol^{-1} respectively *(Singh et al., 2022).* At lower E_a, the value of A is low, and vice versa *(Singh et al., 2021).* The reactivity of biomass is more than that of coal as the pre-exponential factor rises when the biomass blending ratio increases. The pre-exponential factor is raised to compensate for the significant reduction in chemical kinetics due to the growth of the exponential term *(Lu et al., 2013).* In a study reported by Guo et al., Zhundong lignite and pine sawdust (particle size: 150–250 μm) were considered for blending at biomass mass ratios of 100, 75, 50, 25 and 0 % (weight %, dry basis), activation energies were estimated by distributed activation energy model from 84.7-346.9 kJ mol^{-1}, 87.9-326.4 kJ mol^{-1}, 87.4-280.2 kJ mol^{-1}, 85.5-284.9 kJ mol^{-1} and 73.4-245.1 kJ mol^{-1} for coal, ZD: PS= 3:1, ZD: PS=1:1, ZD: PS=1:3 and pine sawdust *(Guo et al., 2017).* The values of activation energies increase gradually with the increasing conversion (*a*). The DAEM was applied by Goldfarb et al. to analyse the pyrolysis kinetics of Pennsylvania coal and three different biomass samples, yielding activation energies ranging from 304-522 kJ mol^{-1} for coal, 164–304 kJ mol^{-1} for the biomasses and 218–530 kJ mol^{-1} for the coal–biomass blends *(Goldfarb et al., 2015).*

5.5.6 Reaction mechanism

Theoretical Z plots and experimental Z plots for different solid-state kinetic mechanisms of thermal pyrolysis kinetics of coal, sawdust, and coal-sawdust blends are observed in Fig. S5. The kinetics of these solid-state reactions have been elucidated by various nucleation models *(Khawam, 2006).* However, the shape of the curve is indicative of the dedicated mechanism and the solid-state kinetic model of the process but is independent of the heating rate of the reaction.

5.5.6.1 Prediction of the reaction mechanism of coal pyrolysis kinetics

As shown in Fig. S5 (a), in a coal pyrolysis reaction, decomposition occurs through the first-order rate kinetics method. Based on the Criado equation given in Section 3.3.6.3 and

Table 3.1 in Chapter 3, coal pyrolysis kinetics incorporates several consequent reaction models till a particular conversion.

5.5.6.2 Prediction of the reaction mechanism of sawdust pyrolysis kinetics

As shown in Fig. S5 (b), in sawdust pyrolysis reaction, decomposition occurs through a sequence of parallel and series reactions converging into a complex multistep reaction. The developing char crystal during the reaction has fluctuating local energies from imperfections due to cracks, impurities, dislocations, surface edges, and point defects. Such imperfections are considered reaction nucleation sites since reaction activation is minimized at these points. Random nucleation points or cleavage sites in the crystal act as specific sites for further growth of the nucleus. It is observed that at a conversion of 10 %, the curve is closer to the A4 reaction mechanism which is the Avrami-Erofeev nucleation model according to solid-state kinetic model theory, which occurs due to ingestion or coalescence of the growing nucleation sites *(Khawam 2006).* At a conversion of 20 %, the curve is closer to the R3 reaction mechanism which is a geometrical contracting sphere/cubical shape. Due to rapid nucleation happening on the surface of the crystal, it incorporated an R2 reaction mechanism which is a geometrical contracting cylinder reaction model from conversion 20-70 %. The rate of sawdust degradation happens with the reaction interface progressing towards the core of the crystal very speedily. This is also true for the R3 reaction mechanism. Beyond 70 % conversion, the curve deviates from the R2 reaction model pattern to engulf other reaction models in its vicinity. Further, the reaction mechanism ascertains a first-order kinetics pattern beyond 70 % conversion as indicative of the Criado method. However, order-based models are similar to homogeneous kinetics where the order of the reaction is proportional to the concentration of the reactant, that is the reactant conversion.

5.5.6.3 Prediction of the reaction mechanism of 100 % and 200 % coal-sawdust blend co-pyrolysis kinetics

As shown in Fig. S5 (c-d), in the coal-sawdust blend co-pyrolysis reaction, decomposition occurs through a sequence of parallel and series reactions converging into a complex multistep reaction. Based on the Criado equation given in Section 3.3.6.3 and Table 3.1 in Chapter 3, coal-sawdust blend co-pyrolysis kinetics incorporates a similar R2 reaction mechanism towards 80 % conversion and later converges to first–order reaction mechanism. However, as evident from literature at higher conversions (α>70 %) of pyrolysis and co-pyrolysis reactions, carbonization and polycondensation reactions of the macromolecules take place where the disordered carbon become more orderly and lose their active reaction sites.

Henceforth, there is no proper agreement with R^2 at this juncture *(Goldfarb and Ceylan, 2015, Cai et al., 2013).*

5.5.7 Thermodynamics of pyrolysis and co-pyrolysis of blends

5.5.7.1 Change in enthalpy (ΔH, kJ mol^{-1})

The change in the enthalpy during coal and sawdust pyrolysis and co-pyrolysis is given in Table 5.12-5.15. It was observed that the higher the value of activation energy, the higher the enthalpy value since they are linearly proportional. A seen in Table 5.12, for Stage II of coal pyrolysis, the *ΔH* value was 44.3 kJ mol^{-1} at α=5 % after which it further increased till α = 15% as 54.94 kJ mol^{-1}. It increased till α=75 % after which it linearly decreased with an increase in conversion. Stage II of thermal degradation of coal thus gave an outcome of an increase in enthalpy with an increase in conversion. However, Stage III of coal pyrolysis gave an outcome of an increase in enthalpy with an increase in conversion, but with a higher value. The change in the enthalpy during thermal pyrolysis of sawdust is shown in Table 5.13. It was observed that the lofty values of enthalpy accounted for the higher values of activation energy since they are linearly proportional. For sawdust pyrolysis, the change in enthalpy was found within the range between 85.97-170.3 kJ mol^{-1}. However as seen in Table 5.14, the change in enthalpy for the co-pyrolysis for 100% blend was started from 89.18 kJ mol^{-1} and increased continuously to 111.53 kJ mol^{-1} when 5%<α<70% and decreased further and resulted in negative enthalpy. As seen in Table 5.15, the change in enthalpy for the co-pyrolysis for 200% blend was started from 185.51 kJ mol^{-1} and decreased continuously to 91.62 kJ mol^{-1} when 5%<α<20% and increased significantly to 155.73 kJ mol^{-1} when 25%<α<65% and decreased further. The average enthalpy was 242.087 kJ mol^{-1} for coal pyrolysis, 103.35 kJ mol^{-1} for 100 % blend co-pyrolysis and 122.019 kJ mol^{-1} for 200 % blend co-pyrolysis. The occurrence of a potential energy barrier between the activated complex and the product was appraised as a difference of 3-5 kJ mol^{-1} approximately between the activation energy and the enthalpy.

5.5.7.2 Change in entropy (ΔS, kJ mol^{-1}K^{-1})

The random disorder in a reaction is defined by the entropy of the system. In the case of biomass pyrolysis, it might account for the number of carbon layers that emerged during the thermal degradation process, and in the case of coal-biomass co-pyrolysis, it might be due to the same interpretation of the char formed during the process. The change in entropy of a system is a positive or a negative value, where the positive value indicates that thermal equilibrium is not achieved during the process while the negative value apposite the contrast of it and that a thermal product is formed during the process. The change in the entropy

during pyrolysis of coal and sawdust and its co-pyrolysis of blends is shown in Table 5.12 – 5.15. As shown in Table 5.9, the entropy value obtained ranged between -1.21 to -1.12 kJ mol^{-1} K^{-1} and -0.09 to -1.13 kJ mol^{-1} K^{-1} for coal pyrolysis at Stage II and Stage III of the thermal degradation stages respectively. In Table 5.13, the values were estimated at each conversion factor measuring very few entropy values for sawdust pyrolysis. The average entropy value for sawdust pyrolysis ranged between –0.301 to - 0.137 kJ mol^{-1} K^{-1}. This indicated the highly unstable nature of the sample during the initial stages of thermal degradation at α=5%, whereas till 75% conversion it almost reached its thermal equilibrium. This indicated a higher degree of randomness at higher conversions (α>75%), whereas almost a thermal equilibrium point was attained at α=75%. This manifested that a stable product was produced at α=75% after the attainment of the thermal equilibrium, while a higher degree of randomness at higher conversions (α>75%) was perceived for sawdust pyrolysis. However as seen in Table 5.14, the entropy value was from 0.09 to 0.28 kJ mol^{-1} K^{-1} for coal and 100% sawdust blend co-pyrolysis with a decrease in entropy values from 5-65 %. As seen in Table 5.15, the entropy value was from 0.148 to 0.467 kJ mol^{-1} K^{-1} for 200 % sawdust blend co-pyrolysis with a decrease in entropy values from 5–65 %. This confirmed that the entropy value was positive for co-pyrolysis and negative for coal pyrolysis. Hence, it can be said that co-pyrolysis thermal equilibrium is not achieved during the process. The average value of entropy was -0.905 kJ mol^{-1} K^{-1} for coal, 0.101 kJ mol^{-1} K^{-1} for coal and 100 % sawdust blend co-pyrolysis and 0.158 kJ mol^{-1} K^{-1} for coal and 200 % sawdust blend co-pyrolysis. This manifested that a stable product was produced at α = 80 % for coal for Stage III of thermal degradation and α = 65 % for the coal co-pyrolysis process after the attainment of the thermal equilibrium. Since the thermal equilibrium attends at higher conversion for co-pyrolysis the conversion was higher.

5.5.7.3 Change in Gibbs free energies (ΔG, kJ mol^{-1})

The change in Gibbs free energy, ΔG is the sum of the enthalpy and product of the temperature and the entropy of the system. Higher Gibbs free energy indicates that more amount of energy was taken up by the system for thermal degradation which is irreversible and non-spontaneous. The change in the Gibbs free energy during pyrolysis of coal and sawdust and its co-pyrolysis is shown in Table 5.12-5.15. It was noticed that with an increase in the conversion the value of Gibbs free energy increased for both coal pyrolysis and co-pyrolysis. However, the value was much higher for coal pyrolysis compared to co-pyrolysis. The average value of Gibbs free energy for coal was 1207.48 kJ mol^{-1} and 1409.02 kJ mol^{-1} for coal co-pyrolysis at the two thermal degradation stages respectively. The overall average

value of Gibbs free energy for coal was 1308.25 kJ mol^{-1} for the three stages of thermal degradation. With an increase in conversion from 5-70%, there was a linear increase in Gibbs free energy values from 260.5–299.6 kJ mol^{-1} for sawdust pyrolysis. However, average Gibb's free energy value was 173.35 kJ mol^{-1} for coal and 100 % sawdust blend co-pyrolysis. In Table 5.15, average Gibbs free energy value was 226.772 kJ mol^{-1} for coal and 200 % sawdust blend co-pyrolysis. Lower value of Gibbs free energy indicated that the product formation was favorable at a lower energy supply. Hence, it can be said that coal and sawdust require less energy for conversion than coal pyrolysis alone for the production of pyrolytic volatiles.

Table 5.12 Thermodynamic parameters obtained from pyrolysis of coal

	Coal (2nd Stage)			**Coal (3rd Stage)**		
α, %	***Δ H* (kJ mol^{-1})**	***Δ G* (kJ mol^{-1})**	***Δ s* (kJ $mol^{-1}K^{-1}$)**	***Δ H* (kJ mol^{-1})**	***Δ G* (kJ mol^{-1})**	***Δ s* (kJ $mol^{-1}K^{-1}$)**
5	-	-	-	158.8	1423.2	-1.13
10	48.54	1212.8	-1.2	172	1417.5	-1.11
15	54.94	1209.8	-1.19	191.4	1413.4	-1.09
20	55.82	1209.6	-1.19	213	1410.4	-1.07
25	56.58	1209.5	-1.19	233.4	1408.5	-1.05
30	69.09	1206.6	-1.17	260.8	1406.9	-1.02
35	71.25	1206.7	-1.17	291.8	1405.7	-0.99
40	75.64	1206.5	-1.17	336.7	1404.0	-0.95
45	81.06	1206.4	-1.16	370.7	1404.0	-0.92
50	86.9	1206.2	-1.15	425.4	1403.8	-0.87
55	93.74	1205.9	-1.15	495.7	1404.2	-0.81
60	117.3	1204.6	-1.12	591.8	1405.2	-0.73
65	117	1205.0	-1.12	743.2	1407.6	-0.59
70	125.1	1205.1	-1.11	1014	1411.9	-0.36
75	125.2	1205.9	-1.11	-	-	-
80	119.3	1206.9	-1.12	-	-	-
85	113.8	1208.1	-1.13	-	-	-
90	114.1	1209.1	-1.13	-	-	-
95	120.1	1210.0	-1.12	-	-	-

Table 5.13 Thermodynamic parameters obtained from pyrolysis of sawdust

α, %	ΔH (kJ mol^{-1})	ΔG (kJ mol^{-1})	Δs (kJ mol^{-1}K^{-1})
5	170.3	260.5	-0.137
10	85.97	284.8	-0.301
15	88.68	287.3	-0.301
20	93.11	289.2	-0.297
25	97.68	290.7	-0.292
30	100.8	292.2	-0.29
35	102.3	293.5	-0.29
40	105.2	294.7	-0.287
45	105.2	295.6	-0.288
50	105.2	296.4	-0.29
55	107.4	297.1	-0.287
60	114.2	298.2	-0.279
65	111.4	298.5	-0.284
70	117.7	299.6	-0.276

Table 5.14 Thermodynamic parameters obtained from co-pyrolysis of coal and 100 % sawdust blend

α, %	Coal and 100 % sawdust blend		
	ΔH (kJ mol^{-1})	ΔG (kJ mol^{-1})	Δs (kJ mol^{-1}K^{-1})
5	89.18	173.22	0.12
10	91.91	172.42	0.12
15	96.24	172.03	0.11
20	99.63	172.1	0.11
25	102.34	172.42	0.10
30	104.90	172.76	0.10
35	105.31	173.27	0.10
40	106.80	173.56	0.10
45	106.39	173.93	0.10
50	108.39	174.07	0.09
55	110.14	174.27	0.09
60	110.88	174.57	0.09
65	111.53	174.95	0.09

Table 5.15 Thermodynamic parameters obtained from co-pyrolysis of 200 % blend

α, %	Coal and 200 % sawdust blend		
	Δ H **(kJ mol^{-1})**	***Δ G*** **(kJ mol^{-1})**	***Δ s*** **(kJ mol^{-1}K^{-1})**
5	185.51	205.20	0.03
10	175.51	311.09	0.204
15	84.75	217.25	0.2
20	91.62	213.53	0.184
25	101.67	213.53	0.169
30	111.45	221.33	0.166
35	113.78	224.06	0.166
40	114.08	219.79	0.159
45	119.09	221.38	0.154
50	122.73	220.56	0.148

5.6 Summary of the chapter

Co-pyrolysis of sawdust with coal is a viable option to use low-grade Indian coal for the production of pyrolytic oil. Co-pyrolysis of sawdust with coal helps in increasing the rate of thermal degradation in low-temperature regions by reducing the activation energy and Gibbs free energy. Since low-rank coal has a low calorific value and is more thermally stable, co-pyrolyzing with the use of waste biomass is a suitable technique to produce solid, liquid, and gaseous products. As most of the volatiles get removed from the feed the activation energy changed from a positive value to a negative value. The negative activation energy was obtained during the char formation. The co-pyrolysis of coal-sawdust resulted in higher conversion as a result the negative activation energy was obtained at a higher conversion compared to the coal pyrolysis alone. For bimolecular reactions of coal-biomass co-pyrolysis, char evolution, and decomposition act as a blockage for volatiles release. This would manifest a rate-determining step with a negative potential energy transition state for the stable intermediates to products step, resulting in the negative values of activation energies and pre-exponential factor values. For sawdust pyrolysis, the R2 reaction mechanism which is a geometrical contracting cylinder reaction model from conversion 20-70 % is observed beyond which first-order reaction order is incorporated in contrast to first-order reaction kinetics for coal pyrolysis. Coal-sawdust blend co-pyrolysis kinetics incorporates a similar R2 reaction mechanism till 70% and 80% conversion and later converges to first – order reaction mechanism.

References

- Idris, S.S., Abd Rahman, N., Ismail, K., Alias, A.B., Abd Rashid, Z. and Aris, M.J., 2010. Investigation on thermochemical behaviour of low rank Malaysian coal, oil palm biomass and their blends during pyrolysis via thermogravimetric analysis (TGA). *Bioresource technology*, *101*(12), pp.4584-4592.
- Shi, L., Liu, Q., Guo, X., Wu, W. and Liu, Z., 2013. Pyrolysis behavior and bonding information of coal—A TGA study. *Fuel Processing Technology*, *108*, pp.125-132.
- Wang, J., Li, P., Liang, L., Yang, J., Hao, X., Guan, G. and Huang, W., 2016. Kinetics modeling of low-rank coal pyrolysis based on a three-Gaussian distributed activation energy model (DAEM) reaction model. *Energy & Fuels*, *30*(11), pp.9693-9702.
- Pitt, G.J., 1962. The kinetic of the evolution of volatile products from coal. *Fuel*, *41*, pp.267-274.
- Aboyade, A.O., Carrier, M., Meyer, E.L., Knoetze, H. and Görgens, J.F., 2013. Slow and pressurized co-pyrolysis of coal and agricultural residues. *Energy Conversion and Management*, *65*, pp.198-207.
- Bamford, C.H., Tipper, C.F.H. (Eds.), 1980. Decomposition reactions of solids. In: Green, N. (Ed.), Comprehensive Chemical Kinetics, vol. 22. Elsevier, New York, pp. 115–246.
- Vuthaluru, H.B., 2004. Thermal behaviour of coal/biomass blends during co-pyrolysis. *Fuel processing technology*, *85*(2-3), pp.141-155.
- Park, D.K., Kim, S.D., Lee, S.H. and Lee, J.G., 2010. Co-pyrolysis characteristics of sawdust and coal blend in TGA and a fixed bed reactor. *Bioresource technology*, *101*(15), pp.6151-6156.
- Kim, S.D., Lee, S.H. and Lee, J.G., 2010. Co-pyrolysis characteristics of sawdust and coal blend in TGA and a fixed bed reactor. *Bioresource technology*, *101*(15), pp.6151-6156.
- Tian, F.J., Yu, J., McKenzie, L.J., Hayashi, J.I. and Li, C.Z., 2007. Conversion of fuel-N into HCN and NH_3 during the pyrolysis and gasification in steam: a comparative study of coal and biomass. *Energy & fuels*, *21*(2), pp.517-521.
- Lu, L., Devasahayam, S. and Sahajwalla, V., 2013. Evaluation of coal for metallurgical applications. *The coal handbook: towards cleaner production*, pp.352-386.

- Benedetti, V., Patuzzi, F. and Baratieri, M., 2017. Gasification char as a potential substitute of activated carbon in adsorption applications. *Energy Procedia*, *105*, pp.712-717.
- Merdun, H. and Laougé, Z.B., 2021. Kinetic and thermodynamic analyses during co-pyrolysis of greenhouse wastes and coal by TGA. *Renewable Energy*, *163*, pp.453-464.
- Tauseef, M., Ansari, A.A., Khoja, A.H., Naqvi, S.R., Liaquat, R., Nimmo, W. and Daood, S.S., 2022. Thermokinetics synergistic effects on co-pyrolysis of coal and rice husk blends for bioenergy production. *Fuel*, *318*, p.123685.
- Sonobe, T., Worasuwannarak, N. and Pipatmanomai, S., 2008. Synergies in co-pyrolysis of Thai lignite and corncob. *Fuel processing technology*, *89*(12), pp.1371-1378.
- He, W., Yin, G., Zhao, Y., Zhang, L., Xu, S., Huang, T., Chang, L. and Lu, H., 2021. Interactions between free radicals during co-pyrolysis of lignite and biomass. *Fuel*, *302*, p.121098.
- Chen, C., Ma, X. and He, Y., 2012. Co-pyrolysis characteristics of microalgae Chlorella vulgaris and coal through TGA. *Bioresource technology*, *117*, pp.264-273.
- Moghtaderi, B., Meesri, C. and Wall, T.F., 2004. Pyrolytic characteristics of blended coal and woody biomass. *Fuel*, *83*(6), pp.745-750.
- Wu, Z., Wang, S., Zhao, J., Chen, L. and Meng, H., 2014. Thermal behavior and char structure evolution of bituminous coal blends with edible fungi residue during co-pyrolysis. *Energy & fuels*, *28*(3), pp.1792-1801.
- Arni, S., 2018. Comparison of slow and fast pyrolysis for converting biomass into fuel. *Renewable Energy*, *124*, pp.197-201.
- Ronsse, F., Nachenius, R.W. and Prins, W., 2015. Carbonization of biomass. In *Recent advances in thermo-chemical conversion of biomass* (pp. 293-324). Elsevier.
- Ganeshan, G., Shadangi, K.P. and Mohanty, K., 2018. Degradation kinetic study of pyrolysis and co-pyrolysis of biomass with polyethylene terephthalate (PET) using Coats–Redfern method. *Journal of Thermal Analysis and Calorimetry*, *131*, pp.1803-1816.
- Akahira T, Sunose T (1971) Method of determining activation deterioration constant of electrical insulating materials. Report of Research Institute. Chiba Institute of Technology (Science Technology) 16:22–31.

- Van de Velden, M., Baeyens, J., Brems, A., Janssens, B. and Dewil, R., 2010. Fundamentals, kinetics and endothermicity of the biomass pyrolysis reaction. *Renewable energy*, *35*(1), pp.232-242.
- Arseneau, D.F., 1971. Competitive reactions in the thermal decomposition of cellulose. *Canadian Journal of Chemistry*, *49*(4), pp.632-638.
- Mettler, M.S., Paulsen, A.D., Vlachos, D.G. and Dauenhauer, P.J., 2012. Pyrolytic conversion of cellulose to fuels: levoglucosan deoxygenation via elimination and cyclization within molten biomass. *Energy & Environmental Science*, *5*(7), pp.7864-7868.
- Biagini, E., Fantei, A. and Tognotti, L., 2008. Effect of the heating rate on the devolatilization of biomass residues. *Thermochimica Acta*, *472*(1-2), pp.55-63.
- Mozurkewich, M. and Benson, S.W., 1984. Negative activation energies and curved Arrhenius plots. 1. Theory of reactions over potential wells. *The Journal of Physical Chemistry*, *88*(25), pp.6429-6435.
- Lu, K.M., Lee, W.J., Chen, W.H. and Lin, T.C., 2013. Thermogravimetric analysis and kinetics of co-pyrolysis of raw/torrefied wood and coal blends. *Applied energy*, *105*, pp.57-65.
- Singh, R.K., Patil, T., Pandey, D., Tekade, S.P. and Sawarkar, A.N., 2022. Co-pyrolysis of petroleum coke and banana leaves biomass: Kinetics, reaction mechanism, and thermodynamic analysis. *Journal of Environmental Management*, *301*, p.113854.
- Chong, C.T., Mong, G.R., Ng, J.H., Chong, W.W.F., Ani, F.N., Lam, S.S. and Ong, H.C., 2019. Pyrolysis characteristics and kinetic studies of horse manure using thermogravimetric analysis. *Energy Conversion and Management*, *180*, pp.1260-1267.
- Singh, B., Singh, S. and Kumar, P., 2021. In-depth analyses of kinetics, thermodynamics and solid reaction mechanism for pyrolysis of hazardous petroleum sludge based on isoconversional models for its energy potential. *Process Safety and Environmental Protection*, *146*, pp.85-94.
- Vyas, A., Chellappa, T. and Goldfarb, J.L., 2017. Porosity development and reactivity changes of coal–biomass blends during co-pyrolysis at various temperatures. *Journal of analytical and applied pyrolysis*, *124*, pp.79-88.

- Guo, F., Li, X., Wang, Y., Liu, Y., Li, T. and Guo, C., 2017. Characterization of Zhundong lignite and biomass co-pyrolysis in a thermogravimetric analyzer and a fixed bed reactor. *Energy*, *141*, pp.2154-2163.
- Goldfarb, J.L. and Ceylan, S., 2015. Second-generation sustainability: application of the distributed activation energy model to the pyrolysis of locally sourced biomass–coal blends for use in co-firing scenarios. *Fuel*, *160*, pp.297-308.
- Khawam, A. and Flanagan, D.R., 2006. Solid-state kinetic models: basics and mathematical fundamentals. *The journal of physical chemistry B*, *110*(35), pp.17315-17328.
- Cai, J., Wu, W., Liu, R. and Huber, G.W., 2013. A distributed activation energy model for the pyrolysis of lignocellulosic biomass. *Green Chemistry*, *15*(5), pp.1331-1340.

Chapter VI

Thermo-catalytic Pyrolysis Kinetics of Biomass and Thermo-catalytic Co-pyrolysis Kinetics of Coal-Biomass Blends

6.1 Introduction

This chapter describes the kinetic and thermodynamic study (using the KAS method) of sawdust catalytic pyrolysis and coal-sawdust blends catalytic co-pyrolysis that are calculated away from the evaporation zone using 10 % and 20 % NiO and Ni (II) aluminate composite catalysts. The effects of catalytic pyrolysis on sawdust on activation energy (E_a) and thermodynamic parameters are given in subsection 6.4 and catalytic co-pyrolysis of 100 % and 200 % blends in subsections 6.5 and 6.6 respectively. This study clarifies the effect of (catalyst/sawdust) ratio and (catalyst/blend) ratio on the conversion % in the active pyrolytic zone. The effect of heating rate was studied for the (catalyst/sawdust) ratio and (catalyst/blend) ratio with the highest degradability and conversion % in the active pyrolytic zone of the respective feedstocks.

6.2 Experimental validation

In this Chapter, a detailed and comprehensive study on kinetics and thermodynamics was done on catalytic pyrolysis of sawdust and catalytic co-pyrolysis of coal-sawdust blends (100 % and 200 % sawdust addition to coal) using 10 % and 20 % NiO and Ni (II) aluminate composite catalysts. A thermo-gravimetric analyzer (TGA) was employed to discern the pyrolytic characteristics of the feed samples. TGA was performed in between 303-1173 K temperature range in the presence of 99.99 % pure N_2 gas flow at 20 mL min^{-1} at 1.9 bar gas pressure. Upon culminating at 1173 K temperature, nitrogen gas was imported into the furnace to scrap off the remaining volatile products. TGA analysis of catalyst/sawdust and catalyst/blend samples was conducted at a single heating rate (20 K min^{-1}) using four concentrations of catalyst, 5 %, 10 %, 15 % and 20 %. At the single heating rate (20 K min^{-1}), the effect of catalyst/sawdust ratio and catalyst/blend ratio on the conversion % in the active pyrolytic zone and the rate of degradation (DTG peak with the highest degradability) was observed. The comparative degradation analysis between the individual and feed loaded with catalyst samples settled the optimum blending conditions where the rate of degradation was higher. At the optimum conditions, the influence of the heating rate was studied at 10, 20, 30 and 40 K min^{-1}. The degradation kinetic parameters were studied by using the KAS Method.

6.3 Highlights of the chapter

- This study reports the effect of catalyst/sawdust ratio and catalyst/blend ratio on the conversion % in the active pyrolytic zone. The effect of heating rate was studied for the catalyst/sawdust ratio and catalyst/blend ratio with the highest degradability and conversion % in the active pyrolytic zone of the respective feedstocks.

- For sawdust catalytic pyrolysis, the % conversion in the active pyrolytic zone was highest for catalyst/sawdust ratio = 0.15 and 0.10 for 10 % and 20 % NiO and Ni (II) aluminate composite catalysts respectively.
- The % final char residues decreased with the increase in heating rate from 10–40 K min^{-1} for sawdust catalyzed by 10 % and 20 % NiO and Ni (II) aluminate composite catalysts.
- For 100 % blend catalytic co-pyrolysis, the % conversion in the active pyrolytic zone was highest for catalyst/sawdust ratio = 0.20 and 0.05 for 10 % and 20 % NiO and Ni (II) aluminate composite catalysts respectively.
- For catalytic co-pyrolysis of 100 % blend with 10 % NiO/Al_2O_3 catalyst, E_α was decreased from 157.78–84.334 kJ mol^{-1} as the conversion enhanced from 5–10 %. A significant increase in the E_α value from 84.334–139.28 kJ mol^{-1} by the KAS method was observed when the conversion was increased from 10% to 65%. Similarly, for 20% catalyst, E_α was decreased from 175.83–91.082 kJ mol^{-1} as the conversion enhanced from 5-10 %. A significant increase in the E_α value from 91.082–234.3 kJ mol^{-1} was observed when the conversion was increased from 10-80 %.
- For 200 % blend catalytic co-pyrolysis, the % conversion in the active pyrolytic zone was highest for catalyst/blend ratio = 0.10 for both 10 % and 20 % NiO and Ni (II) aluminate composite catalysts respectively.
- For the 200 % blend, a significant increase in the E_α value from 76.6–103 kJ mol^{-1} was observed when the conversion was increased from 10–65 % with 10 % NiO/Al_2O_3 catalyst, an E_α value of 99.06 – 145.9 kJ mol^{-1} was observed when the conversion was increased from 10– 65% with 20 % NiO/Al_2O_3 catalyst.

6.4 Catalytic pyrolysis of sawdust

6.4.1 Effect of (catalyst/biomass) ratio on the degradation

Fig. 6.1 (a, b) depicts the catalytic degradation pattern of sawdust with NiO and Ni (II) aluminate composite catalysts at (a) 10 % and (b) 20 % Ni loading from 303-1173 K temperature at the heating rate of 20 K min^{-1} at four concentrations of catalyst, 5 %, 10 %, 15 % and 20 % which is at a (catalyst/sawdust) ratio of 0.05, 0.10, 0.15 and 0.20 respectively. There were three zones relevant from Fig. 6.1 (a, b): moisture removal zone, active pyrolytic zone, and char formation zone *(Ganeshan et al., 2018).* The moisture removal zone was prevalent in between 303-500 K for these cases. The moisture removal zone varied with the rise in the catalyst concentration on biomass. It was observed that the release of moisture

increased from 4.97-5.06 % at 10 % Ni-loaded catalyst and decreased from 8.33-7.05 % at 20% Ni-loaded catalyst where the catalyst/sawdust ratio was maintained at 0.05, 0.10, 0.15 and 0.20 respectively. The active pyrolytic zone was prevalent between 500 - 730 K and 550-738 K in presence of 10 % and 20 % Ni-loaded catalysts respectively. This was the region where maximum degradation occurred. The T_{onset} rendered the value 500 K, while T_{offset} rendered the values 730 K and 738 K for both 10 % and 20 % Ni-loaded catalysts respectively. Lowering the onset temperatures for catalyzed reactions suffices the energy required in the process, which lessens the activation energy required for the reaction to take place. The peak temperature was 664 K for 10 % Ni loading and 663.15 K for 20 % Ni loading which was almost similar. The peak temperatures were similar in each case since it was for the same feedstock with a different metal-loaded catalyst. This confirmed that peak temperature did not vary with the Ni loading. However, the % of conversion within the active pyrolytic zone varied with catalyst concentration at different Ni loading. The 20 % Ni-loaded catalyst is better in activity than the 10 % loaded since it has a higher conversion % at all the catalyst/sawdust ratios. Beyond 750 K temperature, the char formation occurred. The rising in the % final residue was noticed as the concentration of the catalyst accelerated.

Gupta and Mondal worked on the effect of catalysts on the degradation pattern of biomass, pine needle biomass with gamma-Al_2O_3 (AO) and Ni/gamma-Al_2O_3 (NAO) catalysts (biomass to catalyst ratio 1:1). On the addition of catalysts, DTG peak height increases indicating the improvement of reaction rate on addition of catalyst, where mass loss rate has been increased from 17.26 (mass %)/min for PN pyrolysis to 18.94 (mass %)/min and 21.18 (mass %)/min for PN-AO and PN-NAO *(Gupta and Mondal, 2021).* Yang et al. worked on the catalytic pyrolysis of three biomasses (cellulose, sawdust and straw) in the presence of catalyst, Ni-CaO-Ca_2SiO_4 and Ni-Ca_2SiO_4 as functional materials using four iso-conversional kinetic methods, OFW, KAS, Starink and DAEM. The residual mass fraction of cellulose, sawdust and straw pyrolysis was 4.9 %, 16.3 %, and 30.8 % respectively, whereas CaO addition to the biomass led to a lower residual mass at the end of the pyrolysis. The addition of catalyst (in weight %) was not included in final char residue % in the TG-DTG degradation pattern *(Yang et al., 2019).* Subramanian and Ragula in an interesting paper worked on the thermal and catalytic pyrolysis of Nerium oleander, which is a non-edible plant to both humans and cattle and grown in arid and semi-arid regions throughout the year. It is stated that from the leaves of *Nerium Oleander*, the mass % remaining under catalytic pyrolysis by zeolite 5A catalyst is higher than the non-catalytic pyrolysis. This is due to the amount of catalyst (approximately 1 mg) that remains at the end of the experiment. From

DTG graphs, it is seen that the derivative mass is lower for catalytic degradation of the leaves of Nerium oleander by zeolite 5A catalyst when compared to its non-catalytic degradation *(Subramanian and Ragula, 2020)*. Ratnasari et al. worked on non-catalytic and catalytic pyrolysis of beech wood with H-ZSM-5 and MCM-41 catalysts *(Ratnasari et al., 2019)*.

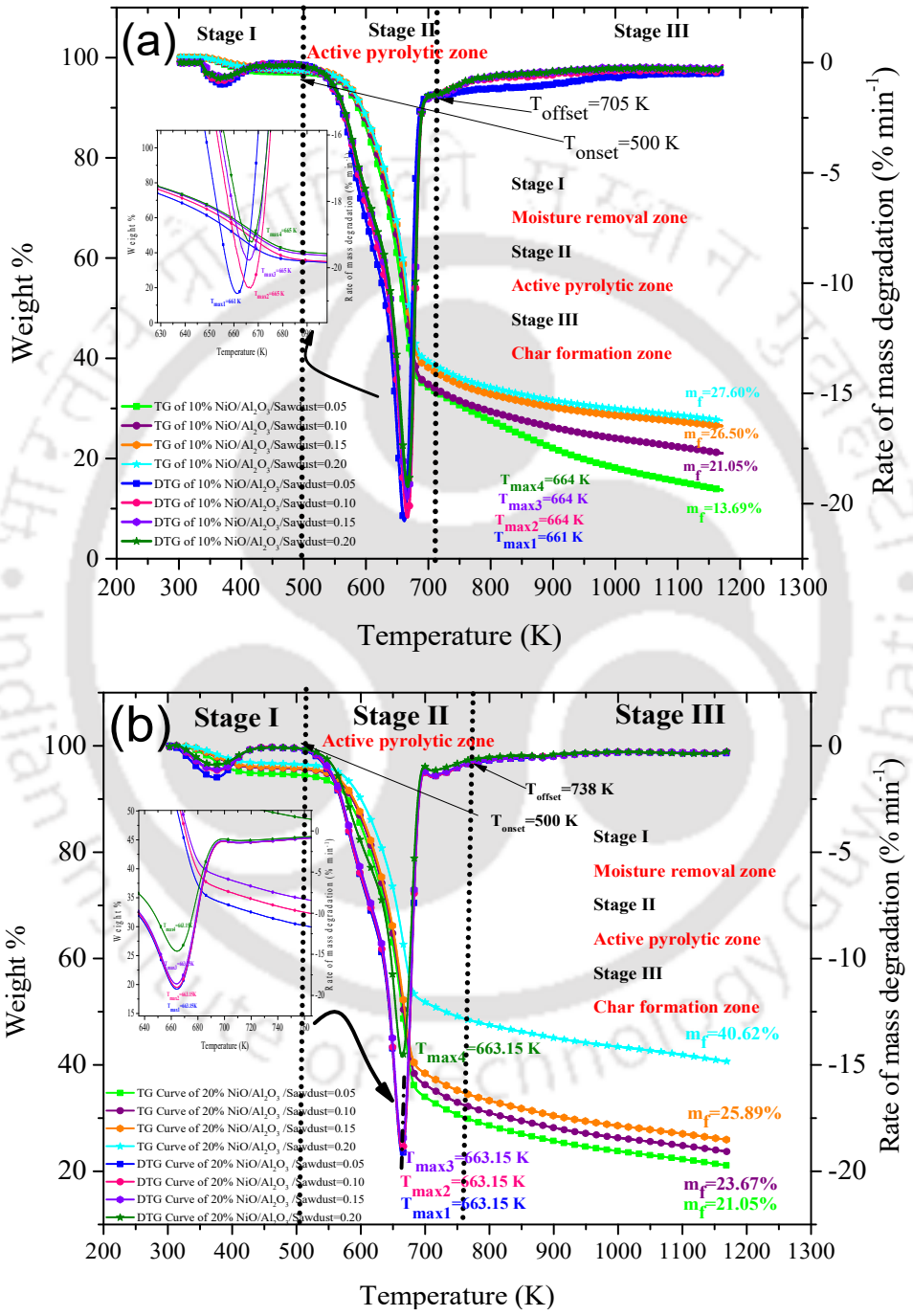

Fig. 6.1 Thermal degradation pattern of sawdust with (a) 10 % NiO/Al_2O_3 catalyst, (b) 20 % NiO/Al_2O_3 catalyst at a catalyst/biomass ratio (0.05, 0.10, 0.15 and 0.20) and at a single heating rate, 20 K min^{-1}

Table 6.1 Effect of (Catalyst/Sawdust) ratio on the % conversion and peak characteristics for catalytic pyrolysis of sawdust with 10 % and 20 % NiO/Al_2O_3 catalyst at 20 K min^{-1} heating rate and a (catalyst/sawdust) ratio (0.05, 0.10, 0.15 and 0.20)

(Catalyst /Sawdust)ratio	10 % NiO/Al_2O_3 catalyst					20 % NiO/Al_2O_3 catalyst				
	T_{offset}	% α	T_{max}	Final residue % with catalyst	Final residue % without catalyst	T_{offset}	% α	T_{max}	Final residue % with catalyst	Final residue % without catalyst
0.05	705 K	73.17	661 K	13.69	8.69	738 K	80.07	663.15 K	21.05	16.05
0.10	705 K	79.17	664 K	21.05	11.05	738 K	81.31	663.15 K	23.67	13.67
0.15	705 K	81.48	664 K	26.50	11.50	738 K	80.91	663.15 K	25.89	10.89
0.20	705 K	80.81	664 K	27.60	7.60	738 K	78.91	663.15 K	40.62	20.62

6.4.2 Effect of the heating rate at lower (catalyst/biomass) ratio

Fig. 6.2 depicts the effect of heating rate (10, 20, 30 and 40 K min^{-1}) at catalyst/sawdust ratios of 0.05 and 0.10 for both the 10 % and 20 % Ni loaded catalysts in the temperature range of 303-1173 K. The three-stage weight loss curves are the moisture removal zone, active pyrolytic zone, and char formation zone *(Bhattacharyya et al., 2022).* The moisture removal zone was within 303-500 K. The active pyrolytic zone was prevalent from 500 K (T_{onset}) for every heating rate for both catalysts. However, T_{offset} (temperature where the active pyrolytic zone ends) increased as the heating rate amplified from 10-40 K min^{-1} (Table 6.2). Similarly, the peak temperature (T_{max}) also increased as the heating rate augmented due to the uneven distribution of heat transfer on the fluid particle.

The moisture removal zone was observed between 303-500 K for every heating rate. It was noticed that the dehydration process takes place in this zone. The active pyrolytic zone was prevalent from beyond 500 K (T_{onset}) for both the catalytic run and this was the region where maximum degradation occurred. The final stage is the char formation stage where lignin is mainly degraded to produce complex carbon structures.

With the increased heating rate from 10-40 K min^{-1}, the T_{offset} (temperature where active pyrolytic zone ends) increased. T_{offset} rendered the values at four heating rates 10, 20, 30, and 40 K min^{-1} as 690 K, 705 K, 724 K and 800 K for sawdust with 10% NiO/Al_2O_3 catalyst whereas T_{offset} at the heating rate of 10, 20, 30 and 40 K min^{-1} emerged as 675 K, 698 K, 715.67 K and 781.3 K for sawdust catalytic pyrolysis with 20% NiO/Al_2O_3 catalyst. The conversion % increased with the increase in the heating rate for both the catalytic pyrolysis

processes. This was due to an increase in the activity of the catalyst loaded with 20% Ni due to an increase in metal active sites. The maximum degradation temperature, peak temperature (T_{max}) and conversion % also increased with an increase in the heating rate from 10–40 K min^{-1}. However, the % char residue decreased linearly with an increase in heating rate. The effect of the heating rate at a a lower (catalyst/sawdust) ratio on conversion % and final char residue % is based on Table 6.2.

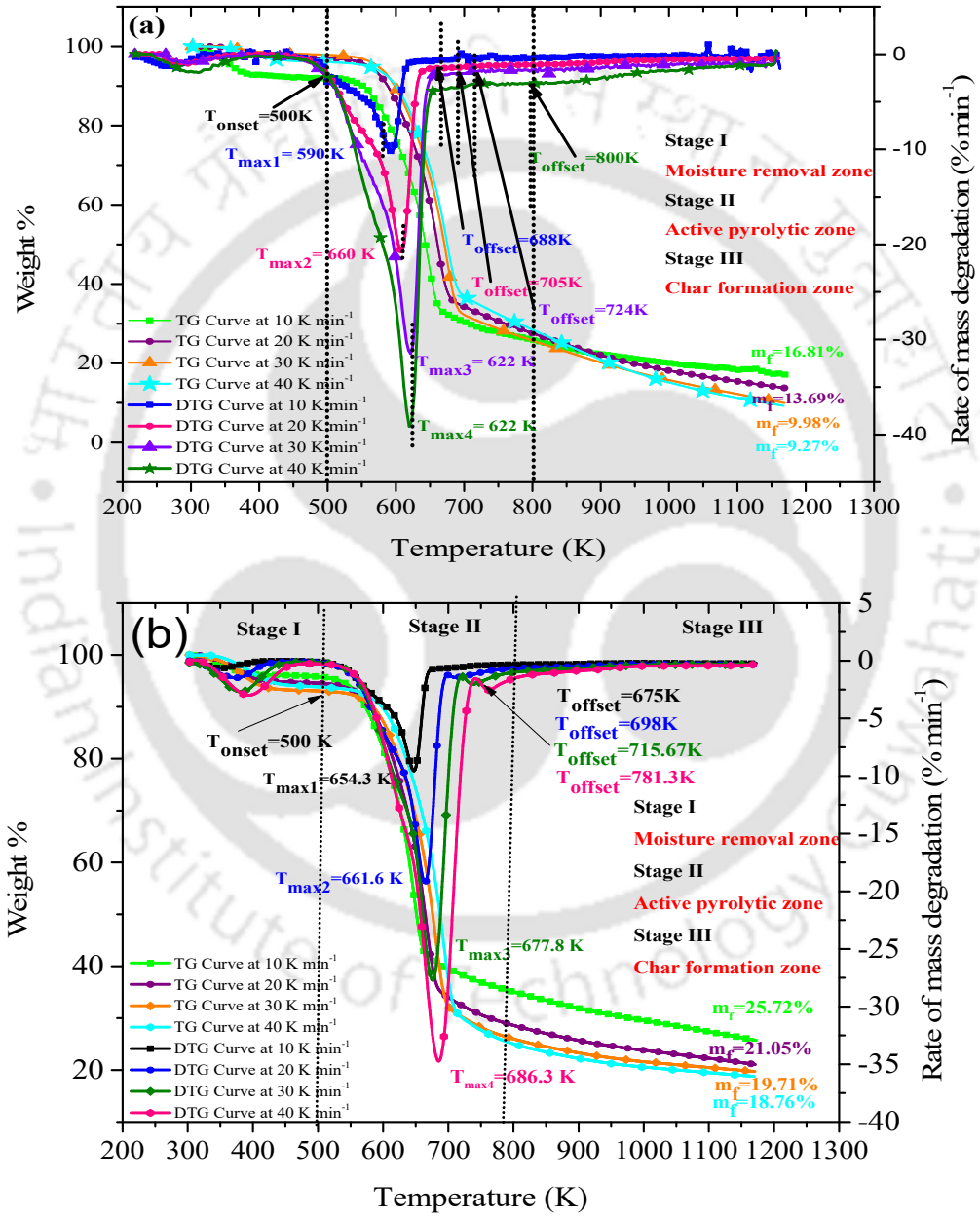

Fig. 6.2 Catalytic degradation pattern of sawdust with (a) 10 % NiO/Al_2O_3 composite catalyst, (b) 20 % NiO/Al_2O_3 composite catalyst at heating rates 10, 20, 30 and 40 K min^{-1} at (catalyst/sawdust) ratio of 0.05 and 0.10 respectively

Table 6.2 Effect of heating rate on the conversion in the active pyrolytic zone at 0.05 and 0.10 (catalyst/sawdust) ratio for 10 % and 20 % NiO/Al_2O_3 catalyst

Heating rate, K min^{-1}	10 % NiO/Al_2O_3 catalyst					20 % NiO/Al_2O_3 catalyst				
	T_{offset}	% α	T_{max}	Final residue % with catalyst	Final residue % without catalyst	T_{offset}	% α	T_{max}	Final residue % With catalyst	Final residue % without catalyst
10	690 K	72.80 %	590 K	16.81 %	11.8 %	675 K	70.76 %	654.3 K	25.72 %	15.72 %
20	705 K	73.17 %	661 K	13.69 %	8.69 %	698 K	75.10 %	661.6 K	21.05 %	11.05 %
30	724 K	74.52 %	676 K	9.98 %	4.98 %	715 K	76.98 %	677.8 K	19.71 %	9.71 %
40	800 K	74.86 %	673 K	9.27 %	4.27 %	781 K	83.02 %	686.3 K	18.76 %	8.76 %

6.4.3 Prediction of the reaction mechanism of sawdust catalytic pyrolysis kinetics

Theoretical Z plots and experimental Z plots for different solid-state kinetic mechanisms of catalytic pyrolysis kinetics of sawdust with 10 % and 20 % Ni-loaded catalysts are observed in (Fig. S6 (a, b)). The kinetics of these solid-state reactions have been elucidated by various nucleation models *(Khawam and Flanagan, 2006)*. However, the shape of the curve is indicative of the dedicated mechanism and the solid-state kinetic model of the process but is independent of the heating rate of the reaction. In a sawdust pyrolysis reaction, decomposition occurs through a sequence of parallel and series reactions converging into a complex multistep reaction. Based on the Criado equation given in Table 3.1 in Chapter 3, catalytic pyrolysis kinetics of sawdust with 10 % and 20 % Ni loading composite catalysts incorporate several consequent reaction models till a particular conversion. The developing char crystal during the reaction has fluctuating local energies from imperfections due to cracks, impurities, dislocations, surface edges and point defects. Such imperfections are considered reaction nucleation sites since reaction activation is minimized at these points. Random nucleation points or cleavage sites in the crystal act as specific sites for further growth of the nucleus. In the case of catalytic pyrolysis kinetics of sawdust with 10 % and 20 % NiO/Al_2O_3 composite catalysts, the mechanism was almost similar to its thermal pyrolysis. At a conversion of 10 %, the curve is similar to the A4 reaction mechanism which is an Avrami-Erofeev pattern, and at a conversion of 20%, the curve is similar to the F1 reaction mechanism which is a first-order reaction. From conversion 20-80 %, the experimental curve takes the shape of an R2 reaction mechanism which is a geometrical contracting cylinder similar to the experimental curve of sawdust. The effect of catalysts can be used in the

increased rate of volatile gaseous emissions due to secondary pyrolysis at lower temperatures. Catalytic tar cracking takes place when sawdust is pyrolyzed in the presence of a NiO/Al_2O_3 composite catalyst which dissociates C-C and C-O bonds and increases the yield of light gases. Catalytic reforming reactions also take place during this catalytic process which cleaves the C-H bonds forming lighter hydrocarbons, thus enhancing the gas yield. The evolution of these volatile emissions and lighter hydrocarbons occurs through the medium of the Avrami-Erofeev nucleation and growth model, which occurs due to the ingestion or coalescence of the growing nucleation sites *(Khawam and Flanagan, 2006).* This specifies nucleation growth (where n=2) as an exponential law. Another model which explicates the growth kinetics is the geometrical contracting cylinder reaction model where the rate of the reaction progresses towards the center of the crystal very fast. This reaction pattern is not seen beyond 80 % conversion. This corresponds to the fact that coke deposition has taken place in the NiO/Al_2O_3 composite catalyst, further deactivating and decreasing its activity. First-order reaction rate kinetics is seen beyond 80 % for both cases (a) and (b). The reaction mechanism beyond 80 % is the rate-determining step since the reactant becomes the limiting reagent for the pyrolysis reaction.

6.4.4 Catalytic pyrolysis kinetics of sawdust

6.4.4.1 Activation energy (E, kJ mol^{-1})

The evaluated kinetic parameters for the catalytic pyrolysis kinetics of sawdust are given in (Table 6.3, 6.4). It could be noticed in (Fig. S7a) that the linear regression representations were mostly un-deviated lines and portrayed parallel characteristics between the conversions. A greater break was noted between the curves obtained for α = 5 % and α = 10 % and α > 50%. The gap between the parallel lines was more significant at α>75% depicting the alteration in the activation energy required during the thermal degradation process. The measured kinetic parameters are given in (Table 6.3). E_α was decreased from 182.22–95.13 kJ mol^{-1} as the conversion enhanced from 5-10 % for pyrolysis of sawdust with 10% NiO/Al_2O_3 catalyst. A significant increase in the E_α value from 95.13–159.68 kJ mol^{-1} was observed when the conversion was increased from 10–65%.

Fig. S7b represents the relation between ln (β/T^2) vs. 1/T in the conversion range of 5% < α < 75% for pyrolysis of sawdust with 20 % NiO/Al_2O_3 catalyst. The measured kinetic parameters are given in (Table 6.4). It could be noticed (Fig. S7b) that the linear plots depicted a similar pattern of regression plot as Fig. S7a. A similar gap was ascertained between the curves obtained for α = 5 %, α = 10 % and α > 50 %. E_α was decreased from 189.6–96 kJ mol^{-1} as the conversion enhanced from 5-10 %. The increase in E_α continued till

75 % conversion from 10 % conversion. A significant decrease in the E_α value from 96.0–121.7 kJ mol^{-1} was observed when the conversion was increased from 10 – 75%. The activation energy was 121.7 kJ mol^{-1} by the KAS method at α=75% which was higher than the activation energy obtained between 10%>α<75% and lower as compared to 5 %. The E_α value increased further from 80-95% conversion giving negative values of activation energies since char has already been formed and there is less chance for the reaction to take place. At higher conversions, the activation energies values are therefore not depicted here. Similar results were perceived from both methods.

6.4.4.2 Pre-exponential factor (s^{-1})

For catalytic pyrolysis kinetics of sawdust with 10 % NiO/Al_2O_3 catalyst, higher values of A at low conversions (α < 5%) as 1.19×10^{9} (s^{-1}) were seen, whereas 4.28×10^{7} (s^{-1}) were perceived for its pyrolysis with 20 % Ni/Al_2O_3 catalyst. The zone of active pyrolysis manifested frequency values ranging from 9.21×10^{5}–1.06×10^{-1} (s^{-1}) which decreased with an increase in conversion % at conversions (5>α>70%) for catalytic pyrolysis of sawdust with 10 % NiO/Al_2O_3 catalyst. The zone of active pyrolysis manifested frequency values ranging from 4.28×10^{7}–9.47×10^{-4} (s^{-1}) which decreased with an increase in conversion % at conversions (5 >α >70%) for catalytic pyrolysis of sawdust with 20 % NiO/Al_2O_3 catalyst.

In chemical kinetics, the rate constant ascertains the rate and direction of a chemical reaction. It could be confirmed that the rate constant for thermal and catalytic pyrolysis of sawdust with 10 % and 20 % NiO/Al_2O_3 catalysts, decreased linearly with the increase in the conversion. This indicated that the rate of the reaction was higher in the case of catalytic pyrolysis with 10 % and 20 % NiO/Al_2O_3 than in thermal pyrolysis itself. This might be due to active metal (Ni) content which catalyzes the reaction and its interaction with the alkali and alkaline earth metals (AAEM) in the biomass.

Table 6.3 Estimation of catalytic pyrolysis kinetics of sawdust with 10 % NiO/Al_2O_3 composite catalyst

α, %	**Model Equation**	R^2	**Activation energy, kJ mol^{-1}**	**Pre-exponential factor, s^{-1}**
5	Y= -21917.87X+31.18	0.996	182.22	1.94E+10
10	Y= -11442.58X+9.79	0.995	95.13	1.06E+01
15	Y= -12105.14X+10.38	0.998	100.64	3.07E+01
20	Y= -12844.35X+11.18	0.998	106.78	9.78E+01
25	Y= -13517.77X+11.90	0.997	112.38	2.69E+02
30	Y= -14031.12X+12.40	0.999	116.65	5.59E+02
35	Y= -13527.46X+11.30	0.994	112.46	2.13E+02
40	Y= -12980.68X+10.19	0.990	107.92	7.83E+01
45	Y= -13143.58X+10.25	0.992	109.27	9.63E+01
50	Y= -13592.38X+10.77	0.995	113.007	1.91E+02
55	Y= -15158.77X+13.03	0.983	126.03	2.28E+03
60	Y= -15820.92X+13.84	0.994	131.53	5.99E+03
65	Y= -19206.39X+18.58	0.899	159.68	9.21E+05

Table 6.4 Estimation of catalytic pyrolysis kinetics of sawdust with 20 % NiO/Al_2O_3 composite catalyst

α, %	**Model Equation**	R^2	**Activation energy, kJ mol^{-1}**	**Pre-exponential factor, s^{-1}**
5	Y= -22807.6X+32.34	0.966	189.6	4.28E+07
10	Y= -11546.9X+9.91	0.973	96.00	1.61E-02
15	Y= -10646.4X+7.86	0.943	88.51	2.33E-03
20	Y= -9859.75X+6.19	0.908	81.97	4.99E-04
25	Y= -10439.7X+6.85	0.915	86.79	9.47E-04
30	Y= -10824.7X+7.2	0.918	89.9	1.36E-03
35	Y= -11255X+7.66	0.929	93.5	2.13E-03
40	Y= -11711.20X+8.16	0.94	97.3	3.52E-03
45	Y= -13283.7X+10.44	0.981	110.4	3.12E-02
50	Y= -13243.6X+10.20	0.982	110.1	2.56E-02
55	Y= -13499.1X+10.44	0.985	112.2	3.30E-02
60	Y= -13630.6X+10.50	0.983	113.3	3.58E-02
65	Y= -13627.3X+10.36	0.983	113.2	3.22E-02
70	Y= -14045.4X+10.86	0.987	116.7	5.28E-02
75	Y= -14644.2X+11.61	0.974	121.7	1.74E-01

6.4.5 Thermodynamics study of thermal and catalytic pyrolysis kinetics of sawdust

6.4.5.1 Change in enthalpy (ΔH, kJ mol^{-1})

The change in the enthalpy during both thermal and catalytic pyrolysis of sawdust is shown in Table 6.5. It was observed that the lofty values of enthalpy accounted for the higher values of activation energy since they are linearly proportional. For sawdust pyrolysis, the change in enthalpy was found within the range between -179.0 to +193.9 kJ mol^{-1}. The presence of a potential energy barrier between the activated complex and the product was appraised as a difference of 3-5 kJ mol^{-1} approximately. A similar difference for catalytic pyrolysis of sawdust with 10 % and 20 % NiO/Al_2O_3 catalyst was noticed in Table 6.5 where the change in enthalpy ranged between 31.77 to +176.72 kJ mol^{-1} and -160.3 to +183.8 kJ mol^{-1} respectively. The wide difference in enthalpy was recounted to the difference in activation energies in thermal and catalytic pyrolyzed samples of sawdust where sawdust had a higher enthalpy change than either of the catalyzed samples. There was an abrupt decrease in enthalpy change from 5-10 % conversion after which it increased simultaneously to 75 % conversion. This was in correspondence to the activation energy change at each conversion % for sawdust, where enthalpy change was directly proportional. However, for sawdust-catalyzed samples, there was an abrupt decrease in enthalpy change from 5-10 % conversion after which it increased simultaneously to 65 % conversion. It decreased further to 75 % conversion after which there was a slight increase in enthalpy change.

6.4.5.2 Change in Entropy (ΔS, kJ $mol^{-1}K^{-1}$)

The change in entropy of a system is indicative of its thermal equilibrium. In Table 6.5, the values were estimated at each conversion factor measuring very few entropy values. The average entropy value for sawdust pyrolysis ranged between –0.301 to - 0.137 kJ mol^{-1} K^{-1}. This indicated the highly unstable nature of the sample during the initial stages of thermal degradation at α=5%, whereas till 75 % conversion it almost reached its thermal equilibrium. This indicated a higher degree of randomness at higher conversions (α>75%), whereas almost a thermal equilibrium point was attained at α=75%. This manifested that a stable product was produced at α=75% after the attainment of the thermal equilibrium, while a higher degree of randomness at higher conversions (α>75%) was perceived for sawdust pyrolysis. However, catalytic pyrolysis of sawdust with 10 % NiO/Al_2O_3 catalyst and 20 % NiO/Al_2O_3 catalyst evinced the average entropy values ranging between -0.34 to -0.15 kJ mol^{-1} K^{-1} and -0.028 to – 0.009 kJ mol^{-1} K^{-1} respectively. A higher degree of randomness was exhibited in the initial stages of its catalytic pyrolysis reaction with 10 % NiO/Al_2O_3 catalyst at α = 5 %, after which it decreased significantly till α = 65 %. A m uch higher entropy value was achieved at α = 5 % for catalytic pyrolysis of sawdust with 20 % NiO/Al_2O_3 catalyst, after which it decreased further till α = 80 %.

6.4.5.3 Change in Gibbs free energies (ΔG, kJ mol^{-1})

Higher Gibbs free energy indicates that more amount of energy was taken up by the system for thermal degradation and that the process was irreversible and non-spontaneous. As shown in Table 6.5, with an increase in conversion from 5–75 %, there was a linear increase in Gibbs free energy values from 260.5 – 304.2 kJ mol^{-1} for sawdust pyrolysis, 218.37–250.64 kJ mol^{-1} for catalytic pyrolysis of sawdust with 10 % NiO/Al_2O_3 catalyst and 259.5–297.6 kJ mol^{-1} for catalytic pyrolysis of sawdust with 20 % NiO/Al_2O_3 catalyst. Some reactions are suppressed over catalytic pyrolysis which occurs very slowly. The variations observed in the ΔG correspond to the modifications in the sawdust degradation path in the presence of a catalyst. A positive ΔG and a large free energy value (kJ mol^{-1}) confirmed that the process reactants were favored at equilibrium conditions and very few products were available at equilibrium. A negative Gibbs free energy indicated that the product formation was more prevalent at a lower energy supply, which was not seen in this case.

Table 6.5 Thermodynamic estimation of catalytic pyrolysis kinetics of sawdust using 10 % and 20 % NiO/Al_2O_3 composite catalysts

α, %	**Enthalpy, kJ mol^{-1}**	**Gibbs free energy, kJ mol^{-1}**	**Entropy, kJ mol^{-1} K^{-1}**	**Enthalpy, kJ mol^{-1}**	**Gibbs free energy, kJ mol^{-1}**	**Entropy, kJ mol^{-1} K^{-1}**
	Catalytic pyrolysis of sawdust with 10 % NiO/Al_2O_3 composite catalyst			**Catalytic pyrolysis of sawdust with 20 % NiO/Al_2O_3 composite catalyst**		
5	176.72	218.37	-0.06	183.8	259.5	-0.01
10	89.625	248.69	-0.24	90.2	285	-0.025
15	95.135	248.35	-0.23	82.71	288.1	-0.027
20	101.28	248.11	-0.22	76.17	290	-0.028
25	106.88	248.14	-0.21	80.99	291.3	-0.027
30	111.15	248.38	-0.21	84.1	292.4	-0.027
35	106.96	249.5	-0.22	87.7	293.6	-0.027
40	102.42	250.47	-0.22	91.5	294.6	-0.026
45	103.77	250.68	-0.22	104.6	295.7	-0.025
50	107.5	250.65	-0.22	104.3	296.5	-0.025
55	120.53	250.02	-0.2	106.4	297.2	-0.025
60	126.03	250.2	-0.19	107.5	297.9	-0.025
65	154.18	250.64	-0.15	107.4	298.4	-0.025
70	-	-	-	110.9	299.1	-0.024
75	-	-	-	115.9	297.6	-0.024

6.4.6 Interpretation of kinetic analysis

Fig. 6.3 depicts the plot of conversion versus activation energy for both thermal and catalytic pyrolysis kinetics of sawdust. A significant increase in the E_α value from 95.13–159.68 kJ mol^{-1} was observed when the conversion was increased from 10–65 % for catalytic pyrolysis of sawdust with 10 % NiO/Al_2O_3 catalyst, an E_α value of 96–175.4 kJ mol^{-1} was observed when the conversion was increased from 10–75 % for catalytic pyrolysis of sawdust with 20 % NiO/Al_2O_3 catalyst and an E_α value of 91.46-199.35 kJ mol^{-1} was manifested only for sawdust. There was a slight alteration in the reduction of activation energies observed for the 20% NiO/Al_2O_3 catalyzed sawdust sample which was 96 – 175.4 kJ mol^{-1}. This correlates to the fact that due to higher nickel loading in the 20 % NiO/Al_2O_3 catalyzed sawdust sample than in the 10 % NiO/Al_2O_3 catalyzed sawdust sample, it might lead to CO_2 methanation reaction, reforming the evolved volatiles from catalytic pyrolysis of sawdust *(Xu, et al., 2017).* It might also result in synthesis gas upgrading via a water-gas shift reaction for enhanced hydrogen production. This was due to the higher metal surface area of the 20 % NiO/Al_2O_3 catalyst which led to higher activity and reforming of more hydrocarbons. Also, the enhanced activity was an impact of metal nanoparticle particle size of 20 % NiO/Al_2O_3 catalyst which increased the number of active sites per gram of catalyst. This was specifically observed in the active pyrolytic zone where maximum degradation takes place from α=20-45%. For manifesting higher productivity in a given reactor volume, intraparticle diffusional limitations are to be avoided by incorporating smaller catalyst particles (<100 μm) *(Mandic et al., 2017).* This was seen in the case of the 20 % NiO/Al_2O_3 catalyst as evident from characterization results. However, the catalyst undergoes thermal sintering due to the existence of hot spots in the catalyst bed *(Xu et al., 2017).* Prior literature on Ni-CaO-Ca_2SiO_4 catalytic materials specified an optimal Ni loading of 20 wt.% for maximizing hydrogen production *(Yang et al., 2011).* Activation energies of catalyzed samples were seen to be more or less similar to sawdust kinetics except for 10 % NiO/Al_2O_3 catalyzed sawdust. The char formation region started at a conversion of α = 75 % for sawdust, while for the catalytically pyrolyzed samples was observed at α = 65 % and α = 80 %. In this region, negative values of activation energies were seen because high energy was required for the degradation of the samples. Coke was already formed in the catalysts, thus deactivating the catalyst and ensuring that more energy was required for the breakdown of the C-C bonds. The entire process of thermal pyrolysis and catalytic pyrolysis of sawdust are explained below comprehensively.

Depolymerization of cellulose, hemicellulose, and lignin present in sawdust is explained in the presence of NiO/Al_2O_3 catalyst. The support Al_2O_3 with higher Lewis acidic sites renders suitable performance towards catalytic cracking of sawdust and shows higher selectivity towards hydrocarbons. Alumina when impregnated with nickel-based transition metal salt precursor (with a stable oxidation state and valence d-electrons) accentuates the selectivity towards catalytic cracking of hydrocarbons due to the creation of de-novo Lewis acidic sites *(Zheng et al., 2022).* Cellulose consists of a variety of bonds such as H-O, H-H, and C-O bonds whose bond dissociation energies are in the order of 460 kJ mol^{-1}>436 kJ mol^{-1}>350 kJ mol^{-1}. Due to the lower bond dissociation energy and smaller bond order (which gives higher stability to the bond), the C-O linkage breaks between the consequent cellulose molecules which were linked together by the catalyst complex (Ni-O-Al). This might generate a bulky lone pair carbon-free radical which acts as a strong nucleophile in attacking the meta-hydroxyl group of the cellulose molecule. This might lead to β-elimination of the β-hydrogen atom from the OH bond-forming a glycosidic ring oxygen bridge in the cellulose complex. The hydrogen atom now might act as an electrophile to bind with the lone pair of electrons on the oxygen atom of the cellulosic complex to form a hydroxyl group. However, it is important to state that the proposed reaction mechanism is under study for thermal and catalytic pyrolysis of sawdust using NiO/Al_2O_3 catalyst through the characterization of various pyrolytic end compounds. Cellulose-derived model compounds are prone to higher reactivity and increased activity and hemicellulose-derived model compounds have higher activity but more dismal coke formation. However, lignin-derived model compounds have low aromatic yield due to their high stability of the polyaromatic ring structure *(Zheng et al., 2022).* This phenomenon might be substantiated and resonated with the estimation of yields of pyrolytic end-products and their functionalities.

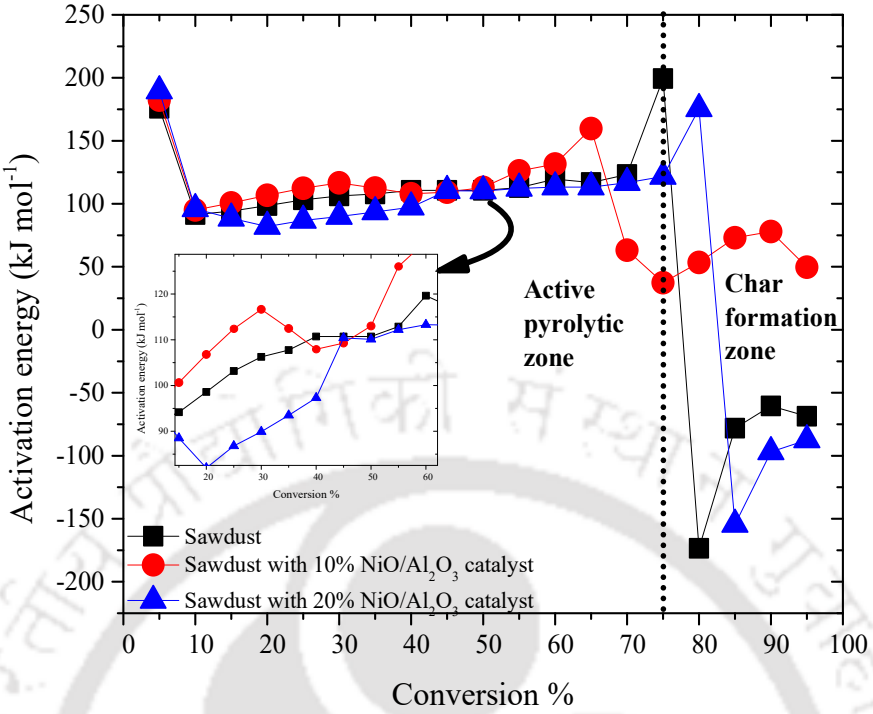

Fig. 6.3 Comparison between the activation energies obtained from thermal and catalytic pyrolysis kinetics reaction of sawdust

6.5 Catalytic co-pyrolysis of coal and 100 % sawdust blend

6.5.1 Effect of (catalyst/blend) ratio on blend degradation

Fig. 6.4 (a, b) depicts the catalytic degradation pattern of coal and 100 % sawdust blend with NiO/Al_2O_3 catalyst at (a) 10 % and (b) 20 % Ni loading from 303-1173 K temperature at the heating rate of 20 K min^{-1} for four concentrations of catalyst, 5 %, 10 %, 15 % and 20 % which is at a (catalyst/blend) ratio of 0.05, 0.10, 0.15 and 0.20 respectively. The moisture removal zone was prevalent between 303-514 K for these cases. The moisture removal zone varied with the rise in the catalyst concentration on the blend. The active pyrolytic zone was prevalent between 514 - 717 K and 540-720 K in the presence of 10 % and 20 % NiO/Al_2O_3 catalyst respectively. This was the region where maximum degradation occurred. The T_{onset} rendered the value 514 K, while T_{offset} rendered the values 717 K and 720 K for both 10 % and 20 % Ni-loaded NiO/Al_2O_3 catalysts respectively. Lowering the onset temperatures for catalyzed reactions suffices the energy required in the process, which lessens the activation energy required for the reaction to take place. The peak temperature was 665 K for 10 % Ni loading and 660 K for 20 % Ni loading NiO/Al_2O_3 catalyst which was almost similar. The peak temperatures were similar in each case since it was for the same feedstock with a different metal-loaded catalyst. This confirmed that peak temperature did not vary with the Ni

loading. However, the % of conversion within the active pyrolytic zone varied with catalyst concentration at different Ni loading. The % conversion increased eventually for 10 % loaded NiO/Al_2O_3 catalyst and decreased for 10 % loaded NiO/Al_2O_3 catalyst from 81.21-82.35% and 76.70 - 74.11 % respectively at (catalyst/blend) ratio of 0.05, 0.10, 0.15 and 0.20. This showed that 10 % loaded NiO/Al_2O_3 is better in activity than 20 % loaded NiO/Al_2O_3 catalyst since it has a higher conversion % at all the catalyst/blend ratio. Beyond 717 K temperature, the char formation occurred. If the catalyst weight is deducted from the % char residue since it is the unreacted component, the final residue % decreases with an increase in the (catalyst/blend) ratio for both 10 % and 20 % NiO/Al_2O_3 composite catalysts as shown in Table 6.6.

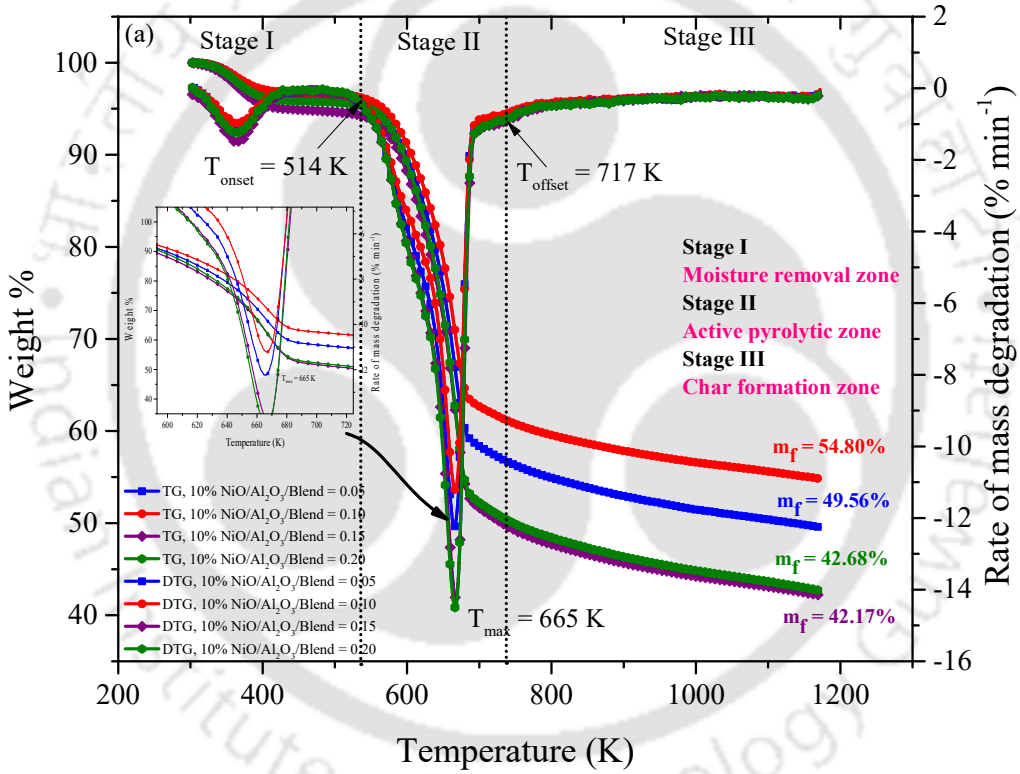

(Continued)

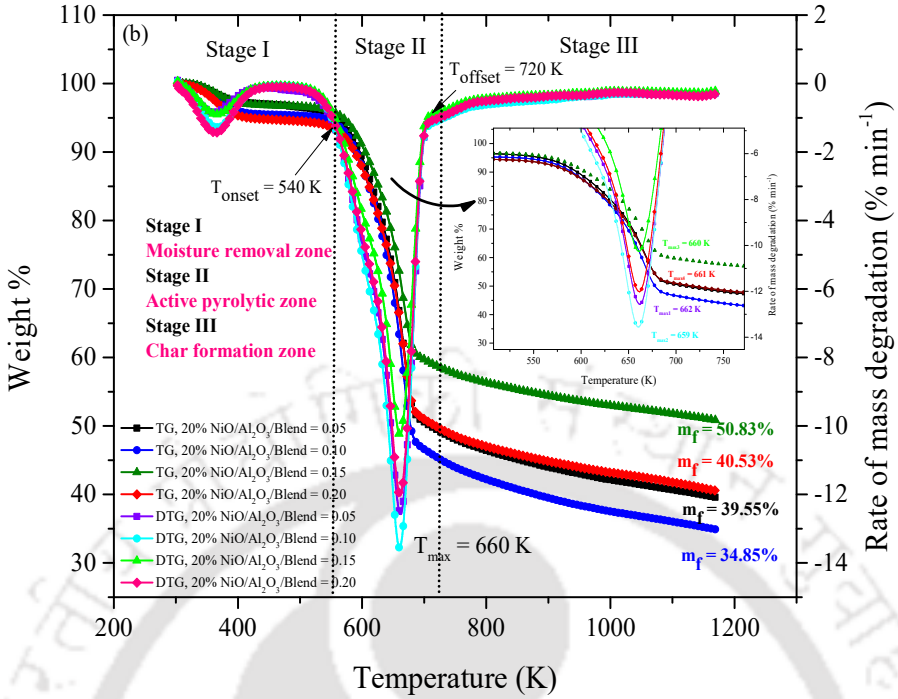

Fig. 6.4 Thermal degradation pattern of 100 % blend with (a) 10 % NiO/Al_2O_3 nano-catalyst (b) 20 % NiO/Al_2O_3 nano-catalyst at a (catalyst/blend) ratio (0.05, 0.10, 0.15 and 0.20)

Table 6.6 Effect of (Catalyst/Blend) ratio on the % conversion and peak characteristics for catalytic pyrolysis of blend with 10 % and 20 % NiO/Al_2O_3 composite catalysts

(Catalyst /Blend) ratio	10 % NiO/Al_2O_3 composite catalyst					20 % NiO/Al_2O_3 composite catalyst				
	T_{offset}	% α	T_{max}	Final residue % without catalyst	Final residue % with catalyst	T_{offset}	% α	T_{max}	Final residue % without catalyst	Final residue % with catalyst
0.05	717 K	81.21 %	665 K	44.56 %	49.56 %	720 K	76.70 %	662 K	34.55 %	39.55 %
0.10	717 K	81.76 %	665 K	44.80 %	54.80 %	720 K	75.88 %	659 K	24.85 %	34.85 %
0.15	717 K	81.05 %	665 K	27.17 %	42.17 %	720 K	76.22 %	660 K	35.83 %	50.83 %
0.20	717 K	82.35 %	665 K	22.68 %	42.68 %	720 K	74.11 %	661 K	20.53 %	40.53 %

6.5.2 Effect of the heating rate at higher (catalyst/blend) ratio

Fig. 6.5 depicts the effect of heating rate (10, 20, 30 and 40 K min^{-1}) at (catalyst/blend) ratios of 0.20 and 0.05 for both the 10 % and 20 % NiO/Al_2O_3 catalyst in the temperature range of 303-1173 K. The three-stage weight loss curve was also noticed in each case. The moisture removal zone was within 303-514 K. It was noticed that the dehydration process takes place in this zone. The active pyrolytic zone was prevalent from 514 K (T_{onset}) for every

heating rate for 100 % blend for both the 10 % and 20 % NiO/Al_2O_3 catalyst respectively. However, T_{offset} (temperature where the active pyrolytic zone ends) increased as the heating rate amplified from 10-40 K min^{-1} as shown in Table 6.7. Similarly, the peak temperature (T_{max}) was also increased as the heating rate augmented due to the uneven distribution of heat transfer on the fluid particle. The final stage is the char formation stage where lignin is mainly degraded to produce complex carbon structures. 100 % coal-sawdust blend with 10 % NiO/Al_2O_3 catalyst at heating rates 10, 20, 30 and 40 K min^{-1}. % char residue increased with an increase in heating rate from 10-40 K min^{-1} for 10 % Ni loaded catalyst with 100 % blend with a slight decrease at 20 K min^{-1} heating rate as 22.68 %. Similarly for catalyst with 100 % blend at 20 % Ni loaded catalyst, % final char residue increased with an increase in heating rate from 10-40 K min^{-1} with a slight decrease at 20 K min^{-1} heating rate.

With the increased heating rate from 10-40 K min^{-1}, the T_{offset} (temperature where active pyrolytic zone ends) increased. T_{offset} increased at four heating rates 10, 20, 30 and 40 K min^{-1} as 640-694 K and from 640-690 K for 100 % blend with 10 % NiO/Al_2O_3 catalyst and for 100 % blend catalytic co-pyrolysis with 20 % NiO/Al_2O_3 catalyst. However, the % conversion within the active pyrolytic zone was 68.71-83.05 % for 100 % blend catalytic co-pyrolysis with 10 % NiO/Al_2O_3 catalyst whereas the % of conversion within the active pyrolytic zone was enhanced by 73.63-80.02 % for 100 % blend catalytic co-pyrolysis with 20 % NiO/Al_2O_3 catalyst as the heating rate increased from 10 - 40 K min^{-1} respectively. This was due to an increase in activity of the catalyst loaded with 20 % nickel due to an increase in metal nanoparticles active sites. The maximum degradation temperature of sawdust catalytic pyrolysis with NiO/Al_2O_3 catalyst increased with an increase in heating rate from 10– 40 K min^{-1}. Peak temperatures at the four heating rates 10, 20, 30, and 40 K min^{-1} increased as 640 K, 667 K, 680 K and 694 K for 100 % blend catalytic co-pyrolysis with 10 % NiO/Al_2O_3 catalyst, and also 640 K, 657.5 K, 678 K and 690 K for 100 % blend catalytic co-pyrolysis with 20 % NiO/Al_2O_3 catalyst. The peak temperatures augmented towards the right with the increase in heating rates due to the uneven distribution of heat transfer on the fluid particle. Similarly, the peak temperature (T_{max}) was also increased as the heating rate was alleviated due to the uneven distribution of heat transfer on the fluid particle.

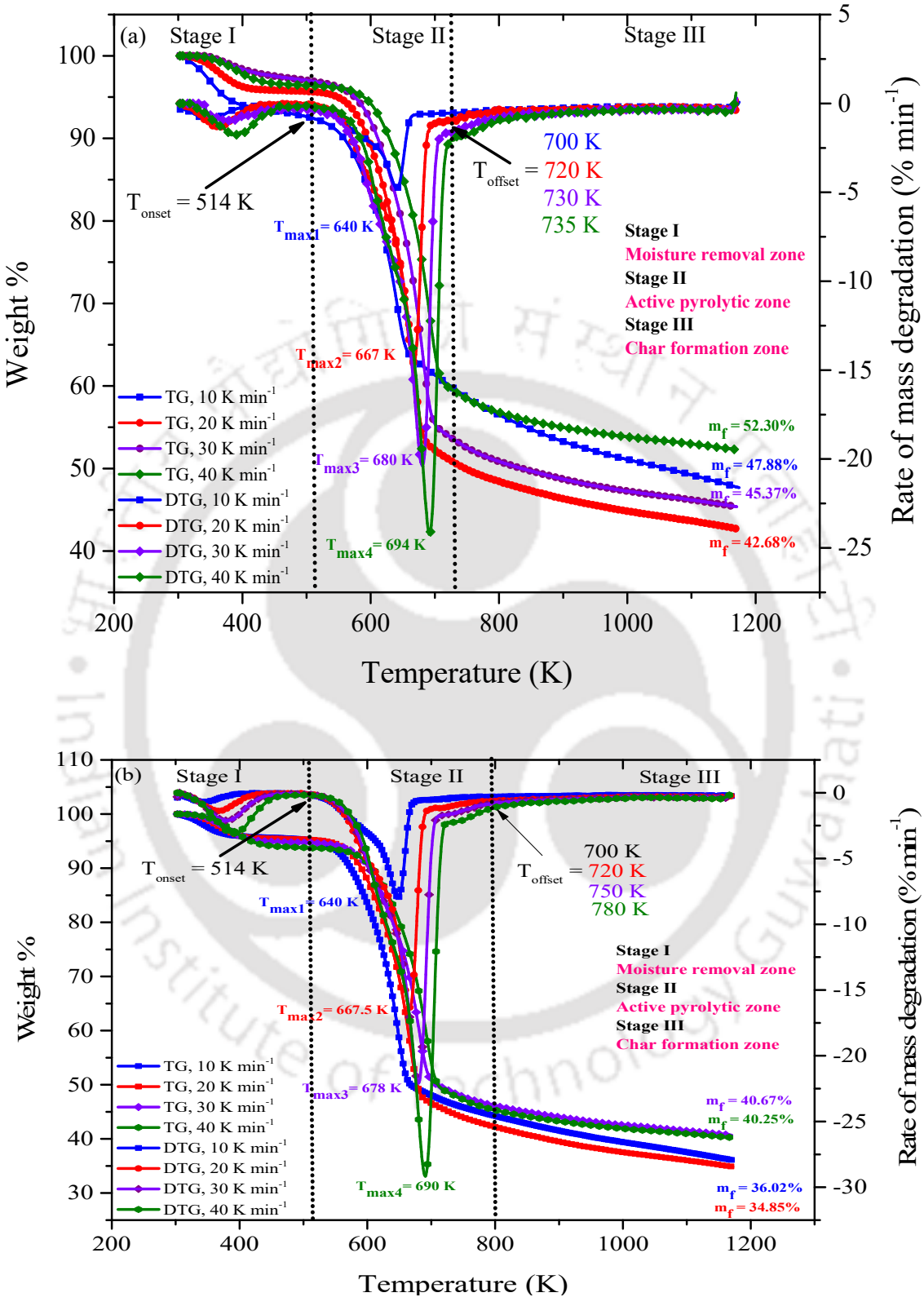

Fig. 6.5 Catalytic degradation pattern of blend with (a) 10 % NiO/Al_2O_3 composite catalyst and (b) 20 % NiO/Al_2O_3 composite catalyst at heating rates 10, 20, 30 and 40 K min^{-1}

Table 6.7 Effect of heating rate on the conversion in the active pyrolytic zone for lower (catalyst/blend) ratio at 10 % and 20 % NiO/Al_2O_3 nano-composite catalysts

Heating rate, K min^{-1}	10 % NiO/Al_2O_3 composite catalyst					20 % NiO/Al_2O_3 composite catalyst				
	T_{offset}	% α	T_{max}	Final residue % without catalyst	Final residue % with catalyst	T_{offset}	% α	T_{max}	Final residue % without catalyst	Final residue % with catalyst
10	700 K	68.7 %	640 K	27.88 %	47.88 %	700 K	73.63 %	640 K	31.02 %	36.02 %
20	720 K	82.3 %	667 K	22.68 %	42.68 %	720 K	76.42 %	657.5 K	29.85 %	34.85 %
30	730 K	84.3 %	680 K	25.37 %	45.37 %	750 K	82.66 %	678 K	35.67 %	40.67 %
40	735 K	83.0 %	694 K	32.30 %	52.30 %	780 K	80.02 %	690 K	35.25 %	40.25 %

6.5.3 Prediction of Reaction Mechanism of 100 % Blend Catalytic Co-pyrolysis Kinetics

Theoretical Z plots and experimental Z plots for different solid-state kinetic mechanisms of catalytic co-pyrolysis kinetics of 100 % blend with 10 % and 20 % Ni-loaded catalysts are shown in Fig. S8 (a, b). The mechanism of catalytic co-pyrolysis of 100 % blend was almost similar to its thermal co-pyrolysis. At a conversion of 10 %, the curve is similar to the A4 reaction mechanism which is an Avrami-Erofeev pattern, and at a conversion of 20 %, the curve is similar to the F1 reaction mechanism which is a first-order reaction. From conversion 20-80%, the experimental curve takes the shape of an R2 reaction mechanism which is a geometrical contracting cylinder similar to the experimental curve of sawdust. Another model which explicates the growth kinetics is the geometrical contracting cylinder reaction model where the rate of the reaction progresses towards the center of the crystal very fast. This reaction pattern is not seen beyond 80% conversion. This corresponds to the fact that coke deposition has taken place in the NiO/Al_2O_3 composite catalyst, further deactivating and decreasing its activity. First-order reaction rate kinetics is seen beyond 80 % for both cases (a) and (b). The reaction mechanism beyond 80 % is the rate-determining step since the reactant becomes the limiting reagent for the pyrolysis reaction.

6.5.4 Catalytic co-pyrolysis kinetics of 100 % coal-sawdust blend

6.5.4.1 Activation energy, E (kJ mol^{-1})

The evaluated kinetic parameters for the catalytic co-pyrolysis kinetics of 100 % blend are given in (Table 6.8, 6.9). It could be noticed in (Fig. S9a) that the linear regression representations were mostly un-deviated lines and portrayed parallel characteristics between

the conversions. A greater break was noted between the curves obtained for α = 5% and α = 10% and α>80%. The gap between the parallel lines was more significant at α>80 % depicting the alteration in the activation energy required during the thermal degradation process. The measured kinetic parameters are given in (Table 6.8). E_α was decreased from 157.78–84.33 kJ mol^{-1} as the conversion enhanced from 5-10 % for pyrolysis of 100 % blend with 10 % NiO/Al_2O_3 catalyst. A significant increase in the E_α value from 84.33–139.28 kJ mol^{-1} was observed when the conversion was increased from 10–65 %. The activation energy was 139.28 kJ mol^{-1} at α = 65 % which was lower as compared to 5 %.

Fig. S9b represents the relation between ln (β/T^2) vs. 1/T in the conversion range of 5% < α < 95% for pyrolysis of 100 % blend with 20 % NiO/Al_2O_3 catalyst. The measured kinetic parameters are given in (Table 6.9). It could be noticed (Fig. S9b) that the linear plots depicted a similar pattern of regression plot as Fig. S9a. A similar gap was ascertained between the curves obtained for α = 5 %, α = 10 % and α>80%. E_α was decreased from 175.83–91.08 kJ mol^{-1} as the conversion enhanced from 5-10%. The increase in E_α continued till 80% conversion from 10 % conversion with an abrupt decrease at 85 % conversion. A significant increase in the E_α value from 91.08–234.3 kJ mol^{-1} by the KAS method was observed when the conversion was increased from 10 - 80%. The activation energy was 125.13 kJ mol^{-1} by the KAS method at α = 75 % which was higher than the activation energy obtained between 10%>α<75% and lower as compared to 5 %. The E_α value decreased further from 85-95 % conversion giving negative values of activation energies since char has already been formed and there is less chance for the reaction to take place. Similar results were perceived from both methods.

6.4.4.2 Pre-exponential factor (s^{-1})

For catalytic co-pyrolysis kinetics of 100 % blend with 10 % NiO/Al_2O_3 catalyst, higher values of A at low conversions (α < 5%) as 8.50×10^{13} (s^{-1}) were seen, whereas 4.63×10^{15} (s^{-1}) were perceived for its pyrolysis with 20 % NiO/Al_2O_3 catalyst. The zone of active pyrolysis manifested frequency values ranging from 1.80×10^{6}–7.66×10^{8} (s^{-1}) which decreased with an increase in conversion % at conversions (5>α>60%) for catalytic co-pyrolysis of 100 % blend with 10 % NiO/Al_2O_3 catalyst. The zone of active pyrolysis manifested frequency values ranging from 7.22×10^{6}–4.20×10^{17} (s^{-1}) which increased with an increase in conversion % at conversions (5>α>80%) for catalytic co-pyrolysis of 100 % blend with 20 % NiO/Al_2O_3 catalyst.

Table 6.8 Estimation of catalytic co-pyrolysis kinetics of 100 % Blend with 10 % NiO/Al_2O_3

α, %	**Model Equation**	R^2	**Activation energy, kJ mol^{-1}**	**Pre-exponential factor, s^{-1}**
5	Y= -18977.9X+25.21	0.94	157.78	8.50E+13
10	Y= -10143.6X+7.56	0.94	84.334	1.80E+06
15	Y= -11037.7X+8.56	0.95	91.768	7.70E+06
20	Y= -11782.5X+9.38	0.96	97.959	2.47E+07
25	Y= -12346.8X+9.95	0.96	102.65	5.66E+07
30	Y= -12711X+10.22	0.96	105.68	9.08E+07
35	Y= -13114.2X+10.58	0.96	109.03	1.56E+08
40	Y= -13315.3X+10.65	0.96	110.7	1.93E+08
45	Y= -13404.6X+10.59	0.96	111.45	2.05E+08
50	Y= -13634.6X+10.75	0.97	113.36	2.73E+08
55	Y= -13777.03X+10.81	0.97	114.54	3.20E+08
60	Y= -14372.16X+11.56	0.96	119.49	7.66E+08
65	Y= -16752.05X+14.89	0.85	139.28	2.72E+10

Table 6.9 Estimation of catalytic co-pyrolysis kinetics of 100 % Blend with 20 % NiO/Al_2O_3

α, %	**Model Equation**	R^2	**Activation energy, kJ mol^{-1}**	**Pre-exponential factor, s^{-1}**
5	Y= -21148.3X+29.10	0.98	175.83	4.63E+15
10	Y= -10955.3X+8.88	0.99	91.082	7.22E+06
15	Y= -11435.6X+9.18	0.99	95.075	1.48E+07
20	Y= -11920.7X+9.58	0.98	99.108	3.03E+07
25	Y= -12313.2X+9.87	0.98	102.37	5.19E+07
30	Y= -12625X+10.07	0.98	104.96	7.75E+07
35	Y= -12979.1X+10.36	0.99	107.91	1.23E+08
40	Y= -13444.1X+10.85	0.98	111.77	2.37E+08
45	Y= -13468.3X+10.68	0.99	111.98	2.27E+08
50	Y= -13488.3X+10.54	0.99	112.14	2.19E+08
55	Y= -13491.6X+10.41	0.97	112.17	2.10E+08
60	Y= -13773.1X+10.69	0.99	114.51	3.09E+08
65	Y= -13773.1X+10.55	0.99	114.51	2.92E+08
70	Y= -13952.6X+10.70	0.98	116	3.68E+08
75	Y= -15050.2X+12.16	0.98	125.13	1.83E+09
80	Y= -28181.9X+30.72	0.73	234.3	4.20E+17
85	Y= 26328.74X-46.41	0.77	-218.9	-1.31E-16
90	Y= 13259.29X-27.06	0.97	-110.2	-1.77E-08
95	Y= 12917X-24.91	0.98	-107.4	-1.56E-07

6.5.5 Thermodynamics study of catalytic co-pyrolysis kinetics of 100 % Blend

6.5.5.1 Change in enthalpy (ΔH, kJ mol^{-1})

The change in the enthalpy during catalytic co-pyrolysis of 100 % coal-sawdust blend is shown in Table 6.10. It was observed that the lofty values of enthalpy accounted for the higher values of activation energy since they are linearly proportional. As mentioned in Chapter 5 for 100 % blend co-pyrolysis, the change in enthalpy was found within the range between -179.0 to +193.9 kJ mol^{-1}. The presence of a potential energy barrier between the activated complex and the product was appraised as a difference of 3-5 kJ mol^{-1} approximately between the activation energy and the enthalpy. A similar difference for catalytic co-pyrolysis of 100 % coal-sawdust blend with 10% and 20% NiO/Al_2O_3 catalyst was noticed in Table 6.10 where the change in enthalpy ranged between 86.22 to +152.2 kJ mol^{-1} and -224.4 to +228.8 kJ mol^{-1} respectively. The wide difference in enthalpy was recounted to the difference in activation energies in both thermal and catalytic co-pyrolyzed samples of the 100 % blend where the 100 % blend had a higher enthalpy change than either of the catalyzed samples as mentioned in Chapter 5. There was an abrupt decrease in enthalpy change from 5-10 % conversion after which it increased simultaneously to 65 % conversion and 80 % conversion for 10 % and 20 % Ni loaded catalyst samples respectively. This was in correspondence to the activation energy change at each conversion % for the blend-catalyzed samples, where enthalpy change was directly proportional.

6.5.5.2 Change in Entropy (ΔS, kJ mol^{-1}K^{-1})

The change in entropy of a system is indicative of its thermal equilibrium. In Table 6.10, the values were estimated at each conversion factor measuring very few entropy values. As mentioned in Chapter 5, the average entropy value for 100% blend co-pyrolysis ranged between 0.09-0.28 kJ mol^{-1} K^{-1}, where initially it was lesser. This indicated the highly unstable nature of the sample during the initial stages of thermal degradation at α=5%, whereas till 75 % conversion it almost reached its thermal equilibrium. However, catalytic co-pyrolysis of 100 % blend with 10 % NiO/Al_2O_3 catalyst and 20 % NiO/Al_2O_3 catalyst evinced the average entropy values ranging between -0.06 to 0.007 kJ mol^{-1} K^{-1} and -0.08 to + 0.079 kJ mol^{-1} K^{-1} respectively. A higher degree of randomness was exhibited in the initial stages of its catalytic co-pyrolysis reaction with 10 % NiO/Al_2O_3 catalyst at α = 5 %, after which it decreased significantly till α=65%. A much higher entropy value was achieved at α = 5% for catalytic co-pyrolysis of 100 % blend with 20 % NiO/Al_2O_3 catalyst, after which it decreased further till α=75%. This indicated a higher degree of randomness at lower conversions (α<5%), whereas almost a thermal equilibrium point was attained at α = 65% and

α = 80 % for 10 % and 20 % Ni loading catalysts. This manifested that a stable product was produced at α=70% and α=80% after the attainment of the thermal equilibrium, while a higher degree of randomness at lower conversions (α<5%) was perceived for 100 % blend catalytic co-pyrolysis.

6.5.5.3 Change in Gibbs free energies (ΔG, kJ mol^{-1})

Higher Gibbs free energy indicates that more amount of energy was taken up by the system for thermal degradation and that the process was irreversible and non-spontaneous. As shown in Table 6.10, with an increase in conversion from 5 - 75%, there was a linear increase in Gibbs free energy values from 147.74–173.85 kJ mol^{-1} for catalytic co-pyrolysis of 100 % blend with 10 % NiO/Al_2O_3 catalyst and 143.54–177.02 kJ mol^{-1} for catalytic co-pyrolysis of 100 % blend with 20 % NiO/Al_2O_3 catalyst. Further positive ΔG values were manifested for catalytic co-pyrolysis of 100 % blend with both 10 % NiO/Al_2O_3 and 20 % NiO/Al_2O_3 catalyst. A positive ΔG and a large free energy value (kJ mol^{-1}) confirmed that the process reactants were favored at equilibrium conditions and very few products were available at equilibrium. A negative Gibbs free energy indicated that the product formation was more prevalent at a lower energy supply, which was not seen in this case.

Table 6.10 Thermodynamic estimation of catalytic co-pyrolysis kinetics of 100 % blend at 10 % and 20 % NiO/Al_2O_3 composite catalyst

α, %	**Enthalpy, kJ mol^{-1}**	**Gibbs free energy, kJ mol^{-1}**	**Entropy, kJ mol^{-1} K^{-1}**	**Enthalpy, kJ mol^{-1}**	**Gibbs free energy, kJ mol^{-1}**	**Entropy, kJ mol^{-1} K^{-1}**
	Catalytic co-pyrolysis of 100 % blend with 10 % NiO/Al_2O_3 composite catalyst			**Catalytic co-pyrolysis of 100 % blend with 20 % NiO/Al_2O_3 composite catalyst**		
5	152.2	147.74	0.007	170.4	143.54	0.041
10	78.79	172.29	-0.14	85.62	171.25	-0.13
15	86.22	171.65	-0.13	89.61	171.26	-0.12
20	92.41	171.39	-0.12	93.64	171.33	-0.12
25	97.11	171.48	-0.11	96.91	171.6	-0.11
30	100.1	171.89	-0.11	99.5	171.97	-0.11
35	103.5	172.25	-0.1	102.4	172.35	-0.11
40	105.2	172.72	-0.1	106.3	172.59	-0.1
45	105.9	173.15	-0.1	106.5	173.03	-0.1
50	107.8	173.46	-0.1	106.7	173.39	-0.1
55	109	173.76	-0.1	106.7	173.65	-0.1
60	113.9	173.87	-0.09	109	173.84	-0.1
65	133.7	173.85	-0.06	109	174.16	-0.1
70	-	-	-	110.5	174.37	-0.1
75	-	-	-	119.7	174.61	-0.08
80	-	-	-	228.8	177.02	0.079
85	-	-	-	-224.4	-	-
90	-	-	-	-115.7	-	-
95	-	-	-	-112.9	-	-

6.5.6 Interpretation of kinetic analysis

Fig. 6.6 depicts the plot of conversion versus activation energy for both thermal and catalytic co-pyrolysis kinetics of 100 % blend. A significant increase in the E_α value from 84.33–139.28 kJ mol^{-1} was observed when the conversion was increased from 10–65% for catalytic co-pyrolysis of blend with 10 % NiO/Al_2O_3 catalyst, an E_α value of 91.08–234.3 kJ mol^{-1} was observed when the conversion was increased from 10–80 % for catalytic co-pyrolysis of blend with 20 % NiO/Al_2O_3 catalyst. There was a slight alteration in the reduction of activation energies observed for the 20 % NiO/Al_2O_3 catalyzed blend sample which was 91.082–114.51 kJ mol^{-1}. This correlates to the fact that due to higher nickel loading in the 20 % NiO/Al_2O_3 catalyzed sawdust sample than in the 10 % NiO/Al_2O_3

catalyzed sawdust sample. As reported by Aho et al. (2010), catalytic deoxygenation of cellulose pyrolytic vapors using zeolites using MCM-41 mesoporous materials is studied for catalytic upgradation experiments of pyrolytic vapors *(Aho et al., 2010)*. The influence of catalysts such as ZSM-5, Pd/C, and MCM-41 on thermo-catalytic degradation of wheat bran instilled an increase of solid char residue and a decrease of volatile matter content due to the deactivation of the catalysts *(Lazdovica et al., 2016)*. This might hold for catalytic co-pyrolysis reactions since coal is another major ingredient taking part in the reaction.

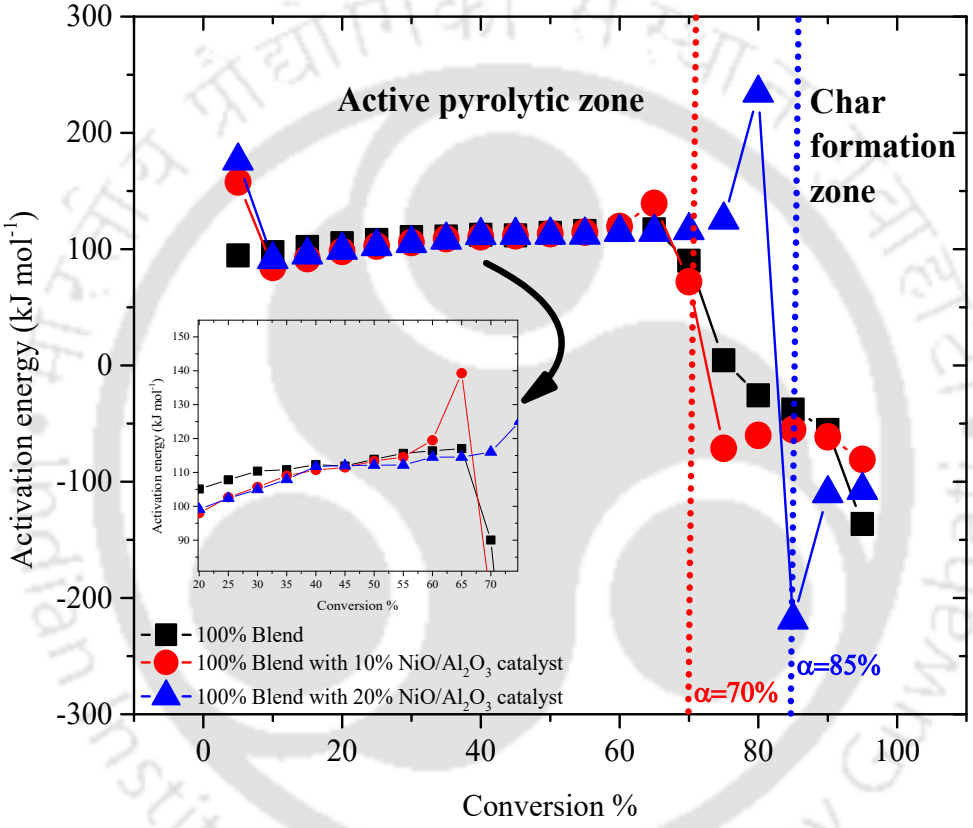

Fig. 6.6 Comparison between the activation energies obtained from thermal and catalytic co-pyrolysis kinetics reaction of 100 % blend

6.6 Catalytic co-pyrolysis of coal and 200 % sawdust blend

6.6.1 Effect of (catalyst/blend) ratio on blend degradation

Fig. 6.7 (a, b) depicts the catalytic degradation pattern of coal and 200 % sawdust blend with NiO/Al_2O_3 catalyst at (a) 10 % and (b) 20 % Ni loading from 303 -1173 K temperature at the heating rate of 20 K min^{-1} for four concentrations of catalyst, 5 %, 10 %, 15 % and 20 % which is at a (catalyst/blend) ratio of 0.05, 0.10, 0.15 and 0.20 respectively. The moisture removal zone was prevalent in between 303-500 K for these cases. The moisture removal

zone varied with the rise in the catalyst concentration on the blend. The active pyrolytic zone was prevalent between 500-800 K and 500-730 K in the presence of 10 % and 20 % NiO/Al_2O_3 catalyst respectively. This was the region where maximum degradation occurred. The T_{onset} rendered the value 500 K, while T_{offset} rendered the values 800 K and 730 K for both 10 % and 20 % Ni-loaded NiO/Al_2O_3 catalysts respectively. Lowering the onset temperatures for catalyzed reactions suffices the energy required in the process, which lessens the activation energy required for the reaction to take place. The peak temperature was 664.3 K for 10 % Ni loading and 665 K for 20 % Ni loading NiO/Al_2O_3 catalyst which was almost similar. The peak temperatures were similar in each case since it was for the same feedstock with a different metal-loaded catalyst. This confirmed that peak temperature did not vary with the Ni loading. However, the % conversion within the active pyrolytic zone varied with catalyst concentration at different Ni loading. The % conversion decreased from 65.72-52.97 % with a slight increase at the (catalyst/blend) ratio of 0.10 as 73.20 % for 10 % loaded NiO/Al_2O_3 catalyst and increased from 61.06-64 % at the (catalyst/blend) ratio of 0.05, 0.10, 0.15 and 0.20 for 20 % loaded NiO/Al_2O_3 catalyst respectively. This showed that 20 % loaded NiO/Al_2O_3 is better in activity than 10 % loaded NiO/Al_2O_3 catalyst since it has a higher conversion % at all the (catalyst/blend) ratios. Beyond 730 K temperature, the char formation occurred. In the presence of 0.05, 0.10, 0.15 and 0.20 (catalyst/blend) ratios, the % final residue increased from 40.13-57.37 % with a slight decrease at 0.20 (catalyst/blend) ratio as 48.25 % for 10 % Ni loading catalyst as shown in Table 6.11. However, for 20 % Ni loading, the % final residue increased from 24.66-32.81 % as (catalyst/blend) ratio increased from 0.05-0.10 and further decreased from 32.81-19.78 % as (catalyst/blend) ratio increased from 0.10-0.15 as shown in Table 6.11.

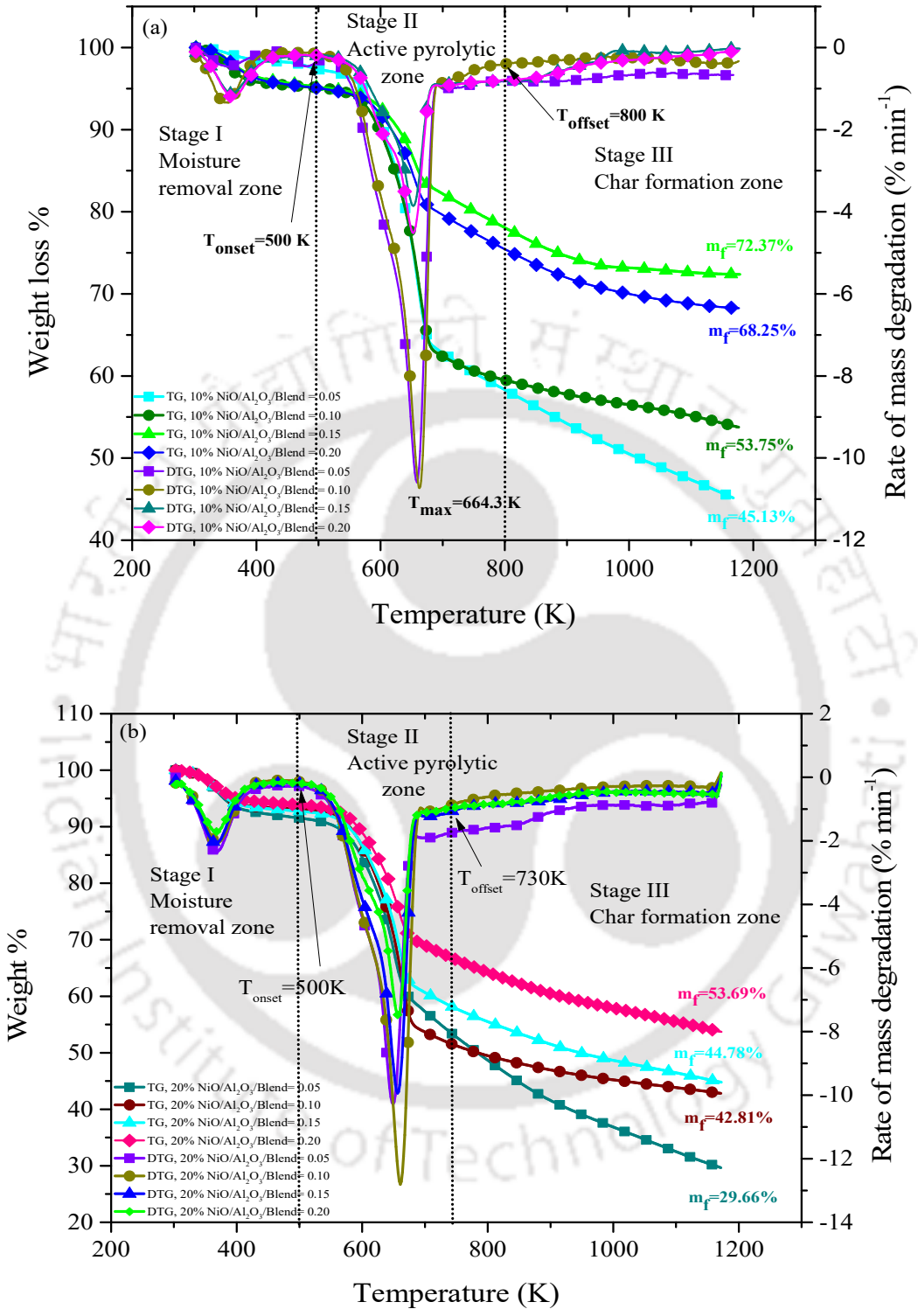

Fig. 6.7 Thermal degradation pattern of 200 % blend with (a) 10 % NiO/Al_2O_3 nanocomposite catalyst (b) 20 % NiO/Al_2O_3 composite catalyst at a (catalyst/blend) ratio (0.05, 0.10, 0.15 and 0.20)

Table 6.11 Effect of (Catalyst/Blend) ratio on the % conversion and peak characteristics for catalytic pyrolysis of blend with 10 % and 20 % NiO/Al_2O_3 composite catalysts

Catalyst/ Blend ratio	10 % NiO/Al_2O_3 composite catalyst					20 % NiO/Al_2O_3 composite catalyst				
	T_{offset}	% α	T_{max}	Final residue % without catalyst	Final residue % with catalyst	T_{offset}	% α	T_{max}	Final residue % without catalyst	Final residue % with catalyst
0.05	800 K	65.72 %	664 K	40.13 %	45.13 %	730 K	61.0 %	665 K	24.66 %	29.66 %
0.10	800 K	73.20 %	664 K	43.75 %	53.75 %	730 K	76.3 %	665 K	32.81 %	42.81 %
0.15	800 K	51.74 %	664 K	57.37 %	72.37 %	730 K	67.4 %	665 K	19.78 %	44.78 %
0.20	800 K	52.97 %	664 K	48.25 %	68.25 %	730K	64.0 %	665 K	33.69 %	53.69 %

6.6.2 Effect of the heating rate at a lower (catalyst/blend) ratio

Fig. 6.8 depicts the effect of heating rate (10, 20, 30 and 40 K min^{-1}) at (catalyst/blend) ratios of 0.10 for both the 10 % and 20 % NiO/Al_2O_3 catalyst in the temperature range of 303-1173 K. The three-stage weight loss curve was also noticed in each case. The moisture removal zone was within 303-490 K. It was noticed that the dehydration process takes place in this zone. The active pyrolytic zone was prevalent from 490 K (T_{onset}) for every heating rate for 200 % blend for both the 10 % and 20 % NiO/Al_2O_3 catalyst respectively. However, T_{offset} (temperature where the active pyrolytic zone ends) increased as the heating rate amplified from 10-40 K min^{-1} as shown in Table 6.12.

Similarly, the peak temperature (T_{max}) was also increased as the heating rate augmented due to the uneven distribution of heat transfer on the fluid particle. This increased from 650-700 K at (catalyst/blend) ratios of 0.10 for 10 % NiO/Al_2O_3 catalyst as the heating rate increased from 10–40 K min^{-1}. However, for 20 % NiO/Al_2O_3 catalyst, the peak temperatures increased from 645-685 K as the heating rate increased from 10–40 K min^{-1}. The final stage is the char formation stage where lignin is mainly degraded to produce complex carbon structures. Coal-sawdust blend with 10 % NiO/Al_2O_3 catalyst at heating rates 10, 20, 30 and 40 K min^{-1} resulted in an increase in char residue % from 20.53-55.37 % residues whereas with 20% NiO/Al_2O_3 catalyst resulted in a decrease in % char residue from 34.05-22.83 % with a sudden increase at 40 K min^{-1} as 44.94 % final residues.

With the increased heating rate from 10-40 K min^{-1}, the T_{offset} (temperature where active pyrolytic zone ends) increased. T_{offset} rendered the values at four heating rates 10, 20, 30 and

40 K min^{-1} as 690 K, 700 K, 730 K and 750 K for sawdust with 10 % NiO/Al_2O_3 catalyst whereas T_{offset} at the heating rate of 10, 20, 30 and 40 K min^{-1} emerged as 700 K, 730 K, 750 K and 780 K for 200 % blend catalytic co-pyrolysis with 20 % NiO/Al_2O_3 catalyst. However, the % conversion within the active pyrolytic zone increased from 62.20-74.40 % with a sudden decrease to 67.98 % for blend catalytic co-pyrolysis with 10 % NiO/Al_2O_3 catalyst whereas the % of conversion within the active pyrolytic zone was enhanced by 67.01-75.17 % with a slight decrease till 73.24 % with 20 % NiO/Al_2O_3 catalyst as the heating rate increased from 10- 40 K min^{-1} respectively as shown in Table 6.12.

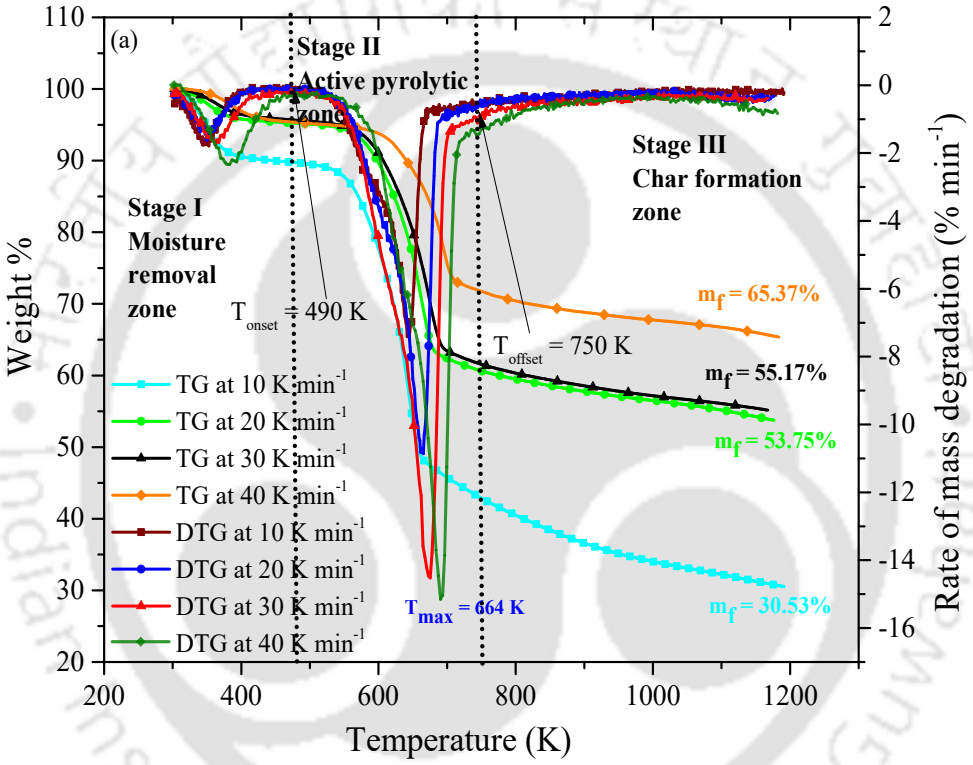

(Continued)

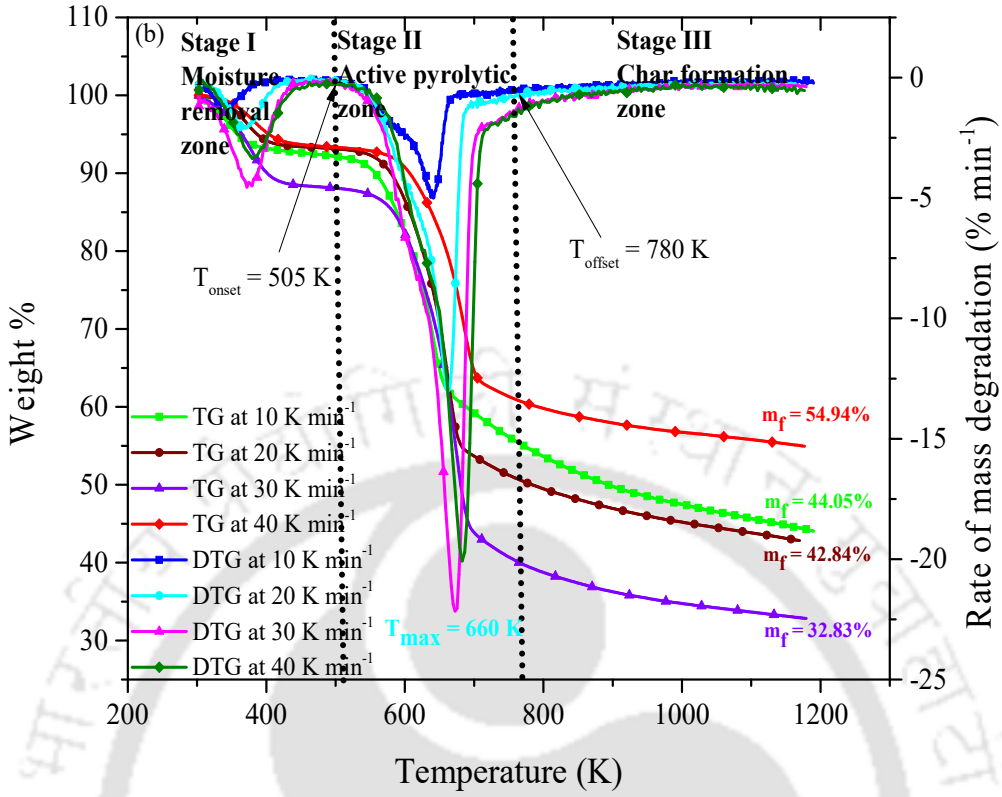

Fig. 6.8 Catalytic degradation pattern of 200 % blend with (a) 10% NiO/Al_2O_3 composite catalyst and (b) 20 % NiO/Al_2O_3 composite catalyst at heating rate 10, 20, 30 and 40 K min^{-1}

Table 6.12 Effect of heating rate on the % conversion and peak characteristics for catalytic pyrolysis of 200 % blend with 10 % and 20 % NiO/Al_2O_3 composite catalyst

Heating rate (K min^{-1})	10% NiO/Al_2O_3 nanocomposite catalyst					20% NiO/Al_2O_3 nanocomposite catalyst				
	T_{offset}	% α	T_{max}	Final residue % without catalyst	Final residue % with catalyst	T_{offset}	% α	T_{max}	Final residue % without catalyst	Final residue % with catalyst
10	690 K	62.20 %	650 K	20.53 %	30.53 %	645 K	67.0 %	700 K	34.05 %	44.05 %
20	700 K	73.20 %	664 K	43.75 %	53.75 %	660 K	75.1 %	730 K	32.84 %	42.84 %
30	730 K	74.40 %	680 K	45.17 %	55.17 %	675 K	72.3 %	750 K	22.83 %	32.83 %
40	750 K	67.98 %	700 K	55.37 %	65.37 %	685 K	73.2 %	780 K	44.94 %	54.94 %

6.6.3 Prediction of reaction mechanism of 200 % blend catalytic co-pyrolysis kinetics

Theoretical Z plots and experimental Z plots for different solid-state kinetic mechanisms of catalytic co-pyrolysis kinetics of 200 % blend with 10 % and 20 % Ni-loaded catalysts are

shown in Fig. S10 (a, b). The mechanism of catalytic co-pyrolysis of 200 % blend was almost similar to its thermal co-pyrolysis. From conversion 20-80 %, the experimental curve takes the shape of an R2 reaction mechanism which is a geometrical contracting cylinder similar to the experimental curve of sawdust. Another model which explicates the growth kinetics is the geometrical contracting cylinder reaction model where the rate of the reaction progresses towards the center of the crystal very fast. This reaction pattern is not seen beyond 80 % conversion. This corresponds to the fact that coke deposition has taken place in the NiO/Al_2O_3 composite catalyst, further deactivating and decreasing its activity. First-order reaction rate kinetics is seen beyond 80 % for both cases (a) and (b). The reaction mechanism beyond 80% is the rate-determining step since the reactant becomes the limiting reagent for the pyrolysis reaction.

6.6.4 Catalytic co-pyrolysis kinetics of 200 % coal-sawdust blend

6.6.4.1 Activation energy, E (kJ mol^{-1})

The evaluated kinetic parameters for the catalytic co-pyrolysis kinetics of 200 % Blend are given in (Table 6.13, 6.14). It could be noticed in (Fig. S11a) that the linear regression representations were mostly un-deviated lines and portrayed parallel characteristics between the conversions. A greater break was noted between the curves obtained for α=5% and α=10% and α>60%. The measured kinetic parameters are given in (Table 6.13). E_α was decreased from 140.9–76.6 kJ mol^{-1} as the conversion enhanced from 5–10 % for pyrolysis of 200 % blend with 10 % NiO/Al_2O_3 catalyst. The increase in E_α continued till 65 % conversion from 10 % conversion. A significant decrease in the E_α value from 76.5–103 kJ mol^{-1} was observed when the conversion was increased from 10–65 %. The activation energy was 103 kJ mol^{-1} at α = 65 % which was higher as compared to 5 %.

Fig. S11b represents the relation between $\ln(\beta/T^2)$ vs. 1/T in the conversion range of 5%<α<65% for pyrolysis of 200 % blend with 20 % NiO/Al_2O_3 catalyst. The measured kinetic parameters are given in (Table 6.14). It could be noticed (Fig. S11b) that the linear plots depicted a similar pattern of regression plot as Fig. S11a. A similar gap was ascertained between the curves obtained for α=5% α =10% and α>80%. E_α was decreased from 203.4–99.06 kJ mol^{-1} as the conversion enhanced from 5-10 %. The increase in E_α continued till 60 % conversion from 10 % conversion. A significant increase in the E_α value from 99.06–145.9 kJ mol^{-1} by the KAS method was observed when the conversion was increased from 10-65 %. The activation energy was 163.1 kJ mol^{-1} by the KAS method at α = 65 % which was higher than the activation energy obtained between 10%>α<65% and lower as compared to 5 %.

6.4.4.2 Pre-exponential factor (s^{-1})

For catalytic co-pyrolysis kinetics of 200 % blend with 10 % NiO/Al_2O_3 catalyst, higher values of A at low conversions (α<5%) as 7.09×10^{11} (s^{-1}) were seen, whereas 7.06×10^{17} (s^{-1}) were perceived for its pyrolysis with 20 % NiO/Al_2O_3 catalyst The zone of active pyrolysis manifested frequency values ranging from 3.33×10^{4}–8.27×10^{5} (s^{-1}) which increased with increase in conversion % at conversions (5>α>60%) for catalytic co-pyrolysis of 200 % blend with 10 % NiO/Al_2O_3 catalyst. The zone of active pyrolysis manifested frequency values ranging from 4.38×10^{6}–3.03×10^{9} (s^{-1}) which increased with an increase in conversion % at conversions (5>α>55%) for catalytic co-pyrolysis of 200 % blend with 20 % NiO/Al_2O_3 catalyst.

Table 6.13 Estimation of catalytic co-pyrolysis kinetics of 200 % Blend with 10 % NiO/Al_2O_3 composite catalyst

α, %	**Model Equation**	R^2	**Activation energy, kJ mol^{-1}**	**Pre-exponential factor (s^{-1})**
5	Y= -16941.9X+22.28	0.736	140.9	7.09E+11
10	Y= -9213.02X+5.97	0.769	76.6	3.33E+04
15	Y= -9626.94X+6.21	0.796	80.04	4.60E+04
20	Y= -9645.51X+5.90	0.754	80.19	3.54E+04
25	Y= -10041.94X+6.25	0.774	83.49	5.47E+04
30	Y= -10021.10X+5.96	0.761	83.31	4.25E+04
35	Y= -9901.78X+5.55	0.744	82.32	2.88E+04
40	Y= -10410.2X+6.17	0.751	86.55	5.81E+04
45	Y= -10576.2X+6.26	0.769	87.93	6.69E+04
50	Y= -10798.6X+6.44	0.812	89.78	8.50E+04
55	Y= -11209.5X+6.95	0.811	93.2	1.52E+05
60	Y= -11684.1X+7.55	0.823	97.14	2.99E+05
65	Y= -12393.9X+8.48	0.864	103	8.27E+05

Table 6.14 Estimation of catalytic co-pyrolysis kinetics of 200 % Blend with 20 % NiO/Al_2O_3 composite catalyst

α, %	**Model Equation**	R^2	**Activation energy, kJ mol^{-1}**	**Pre-exponential factor (s^{-1})**
5	Y= -24470X+35.73	0.943	203.4	7.06E+17
10	Y= -11914.3X+10.59	0.955	99.06	4.38E+06
15	Y= -12625.1X+11.22	0.962	105	9.11E+06
20	Y= -13620.9X+12.42	0.956	113.2	3.39E+07
25	Y= -13757.3X+12.24	0.961	114.4	2.99E+07
30	Y= -14198.6X+12.59	0.962	118	4.56E+07
35	Y= -14633.6X+12.99	0.961	121.7	7.24E+07
40	Y= -14655.7X+12.77	0.954	121.8	6.03E+07
45	Y= -14977X+13.04	0.944	124.5	8.40E+07
50	Y= -15964.5X+14.37	0.945	132.7	3.49E+08
55	Y= -16790.5X+15.34	0.955	139.6	1.09E+09
60	Y= -17552.3X+16.37	0.92	145.9	3.03E+09

6.6.5 Thermodynamics studies of catalytic co-pyrolysis kinetics of 200 % Blend

6.6.5.1 Change in enthalpy (ΔH, kJ mol^{-1})

The change in the enthalpy during catalytic co-pyrolysis of 200 % coal-sawdust blend is shown in Table 6.15. A difference for catalytic co-pyrolysis of 200 % coal-sawdust blend with 10 % and 20 % NiO/Al_2O_3 catalyst was noticed in Table 6.15 where the change in enthalpy ranged between +135.4 to +74.52 kJ mol^{-1} and +197.9 to +93.57 kJ mol^{-1} respectively. The wide difference in enthalpy was recounted to the difference in activation energies in both thermal and catalytic co-pyrolyzed samples of the 200 % blend where it had a higher enthalpy change than either of the catalyzed samples as mentioned in Chapter 5. There was an abrupt decrease in enthalpy change from 5-10 % conversion after which it increased simultaneously to 65 % conversion and 60 % conversion for 10 % and 20 % Ni loaded catalyst samples respectively. This was in correspondence to the activation energy change at each conversion % for the blend-catalyzed samples, where enthalpy change was directly proportional.

6.6.5.2 Change in Entropy (ΔS, kJ mol^{-1}K^{-1})

Catalytic co-pyrolysis of 200 % blend with 10 % NiO/Al_2O_3 catalyst and 20 % NiO/Al_2O_3 catalyst evinced the average entropy values ranging between +0.18 to -0.06 kJ mol^{-1} K^{-1} and -0.02 to + 0.39 kJ mol^{-1} K^{-1} respectively. A higher degree of randomness was exhibited in the initial stages of its catalytic co-pyrolysis reaction with 10 % NiO/Al_2O_3 catalyst at α=5%,

after which it decreased significantly till α=65%. A much higher entropy value was achieved at α=5% for catalytic co-pyrolysis of 200 % blend with 20 % NiO/Al_2O_3 catalyst, after which it decreased further till α = 65 %. This indicated a higher degree of randomness at lower conversions (α<5%), whereas almost a thermal equilibrium point was attained at α=65% and α=60 % for 10 % and 20 % Ni loading catalysts respectively.

6.6.5.3 Change in Gibbs free energies (ΔG, kJ mol^{-1})

Higher Gibbs free energy indicates that more amount of energy was taken up by the system for thermal degradation and that the process was irreversible and non-spontaneous. As shown in Table 6.15, with an increase in conversion from 10-70 %, there was a linear decrease in Gibbs free energy values from 109–91.3 kJ mol^{-1} for catalytic co-pyrolysis of 200 % blend with 10 % NiO/Al_2O_3 catalyst and 82.1–46.2 kJ mol^{-1} for catalytic co-pyrolysis of 200 % blend with 20 % NiO/Al_2O_3 catalyst. Further positive ΔG values were manifested for catalytic co-pyrolysis of 200 % blend with both 10 % NiO/Al_2O_3 and 20 % NiO/Al_2O_3 catalyst.

Table 6.15 Thermodynamic estimation of catalytic co-pyrolysis kinetics of 200 % blend at 10 % and 20 % NiO/Al_2O_3 composite catalyst

α, %	**Enthalpy, kJ mol^{-1}**	**Gibbs free energy, kJ mol^{-1}**	**Entropy, kJ mol^{-1} K^{-1}**	**Enthalpy, kJ mol^{-1}**	**Gibbs free energy, kJ mol^{-1}**	**Entropy, kJ mol^{-1} K^{-1}**
	Catalytic co-pyrolysis of 200 % blend with 10 % NiO/Al_2O_3 composite catalyst			**Catalytic co-pyrolysis of 200 % blend with 20 % NiO/Al_2O_3 composite catalyst**		
5	135.4	16.3	0.18	197.9	-59.5	0.39
10	71.08	109	-0.06	93.57	82.1	0.02
15	74.52	107	-0.05	99.51	78.1	0.03
20	74.67	109	-0.05	107.7	70.9	0.06
25	77.97	106	-0.04	108.9	71.5	0.06
30	77.79	108	-0.05	112.5	69.2	0.07
35	76.8	110	-0.05	116.2	66.7	0.08
40	81.03	106	-0.04	116.3	67.7	0.07
45	82.41	105	-0.03	119.0	65.9	0.08
50	84.26	104	-0.03	127.2	58.1	0.10
55	87.68	101	-0.02	134.1	51.8	0.12
60	91.62	96.9	-0.01	140.4	46.2	0.14
65	97.48	91.3	0.01	-	-	-

6.6.6 Interpretation of kinetic analysis

Fig. 6.9 depicts the plot of conversion versus activation energy for both thermal and catalytic co-pyrolysis kinetics of 200 % blend. A significant increase in the E_α value from 76.6–103.0 kJ mol^{-1} was observed when the conversion was increased from 10–65% for catalytic co-pyrolysis of blend with 10 % NiO/Al_2O_3 catalyst, an E_α value of 99.06–145.9 kJ mol^{-1} was observed when the conversion was increased from 10–60 % for catalytic co-pyrolysis of blend with 20 % NiO/Al_2O_3 catalyst. A significant decrease in activation energies is seen for 200 % blend with 10 % Ni loaded catalyst due to added autocatalytic effect of AAEM's with the catalyst. The higher metal loading in 20 % Ni loaded catalyst might resulted in the weight of the catalyst thus decreasing its reaction rate efficiency. In a study by Hong et al. on industrial solid waste coal fly ash and agricultural solid waste corn stalk studied on its catalytic co-pyrolysis aspects, bio-oil yield was improved as the content of oxy-compounds decreased from 43.32-32.44 % upon integration of coal fly ash to corn stalk due to ketonization taking place. The selectivity of aliphatic hydrocarbons was also increased by 7.89 % due to coal fly ash acting as a catalyst. industrial solid waste coal fly ash and agricultural solid waste corn stalk is studied on its catalytic co-pyrolysis aspects *(Hong et al., 2022)*.

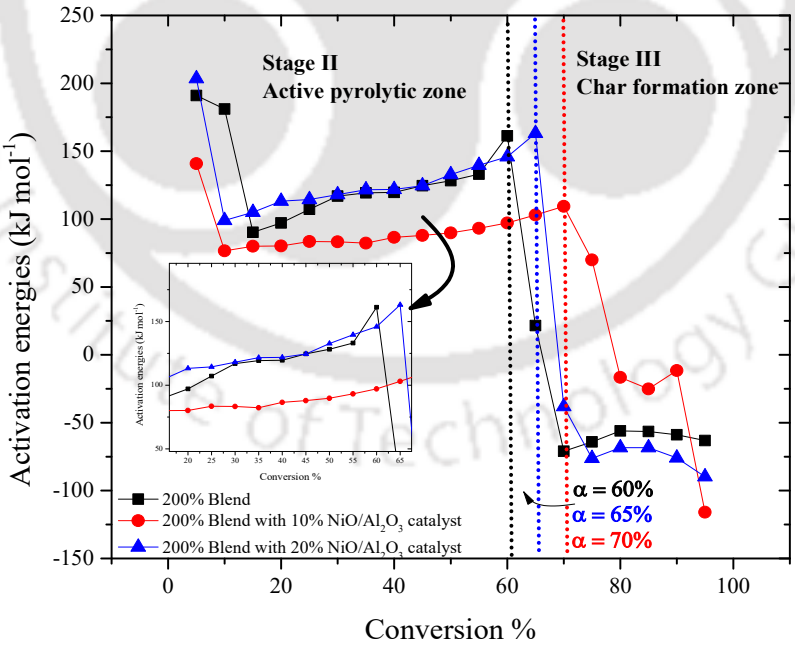

Fig. 6.9 Comparison between the activation energies obtained from thermal and catalytic co-pyrolysis kinetics reaction of 200 % blend with 10 % and 20 % NiO/Al_2O_3 nanocomposite catalyst

6.7 Summary of the Chapter

This chapter describes the kinetic and thermodynamic study (using the KAS method) of sawdust catalytic pyrolysis and coal-sawdust blends catalytic co-pyrolysis that are calculated away from the evaporation zone using 10 % and 20 % NiO and Ni (II) aluminate composite catalysts. This study clarifies the effect of catalyst/sawdust ratio and catalyst/blend ratio on the conversion % in the active pyrolytic zone. The effect of heating rate was studied for the catalyst/sawdust ratio and catalyst/blend ratio with the highest degradability and conversion % in the active pyrolytic zone of the respective feedstocks. For sawdust catalytic pyrolysis, the % conversion in the active pyrolytic zone was highest for (catalyst/sawdust) ratio = 0.05 and 0.10 for 10 % and 20 % NiO and Ni (II) aluminate composite catalysts respectively, whereas for 100 % blend catalytic co-pyrolysis, the % conversion in the active pyrolytic zone was highest for (catalyst/blend) ratio = 0.20 and 0.05 for 10% and 20% NiO and Ni (II) aluminate composite catalysts respectively. However, for 200 % blend catalytic co-pyrolysis, the % conversion in the active pyrolytic zone was highest for (catalyst/blend) ratio = 0.10 for both 10 % and 20 % NiO and Ni (II) aluminate composite catalysts respectively. Upon estimation of activation energies for sawdust catalytic pyrolysis, E_α was decreased from 182.22–95.13 kJ mol^{-1} as the conversion enhanced from 5-10 % for pyrolysis of sawdust with 10 % NiO/Al_2O_3 catalyst. The increase in E_α continued till 65 % conversion from 10 % conversion. The activation energy was 159.68 kJ mol^{-1} at α=65% which was lower as compared to 5 %. Sawdust catalyzed with 20 % Ni loading resulted in E_α from 189.6-96 kJ mol^{-1} as the conversion enhanced from 5–10 % and a significant increase in the E_α value from 96–121.7 kJ mol^{-1} by the KAS method was observed when the conversion was increased from 10-75 %. The activation energy was 121.7 kJ mol^{-1} by the KAS method at α = 75% which was higher than the activation energy obtained between 10%> α <75% and lower as compared to 5 %. E_α was decreased from 157.78 – 84.33 kJ mol^{-1} as the conversion enhanced from 5-10% for catalytic co-pyrolysis of 100 % blend with 10 % NiO/Al_2O_3 catalyst and a significant decrease in the E_α value from 84.33–139.28 kJ mol^{-1} was observed when the conversion was increased from 10–65 %. The activation energy was 139.28 kJ mol^{-1} at α=65 % which was lower as compared to 5 %. For catalytic co-pyrolysis of 100 % blend with 20 % NiO/Al_2O_3 catalyst, E_α was decreased from 175.83 – 91.08 kJ mol^{-1} as the conversion enhanced from 5-10 %. A significant increase in the E_α value from 91.08 – 234.3 kJ mol^{-1} by the KAS method was observed when the conversion was increased from 10-80 %. The activation energy was 125.13 kJ mol^{-1} by the KAS method at α=75% which was higher than the activation energy obtained between 10%>α<75% and lower as compared to 5 %.

However, for 200% blend, a significant increase in the E_α value from 76.6–103 kJ mol^{-1} was observed when the conversion was increased from 10–65 % with 10% NiO/Al_2O_3 catalyst, an E_α value of 99.06–145.9 kJ mol^{-1} was observed when the conversion was increased from 10–60 % with 20 % NiO/Al_2O_3 catalyst.

References

- Ganeshan, G., Shadangi, K.P. and Mohanty, K., 2018. Degradation kinetic study of pyrolysis and co-pyrolysis of biomass with polyethylene terephthalate (PET) using Coats–Redfern method. *Journal of Thermal Analysis and Calorimetry*, *131*, pp.1803-1816.
- Gupta, S. and Mondal, P., 2021. Catalytic pyrolysis of pine needles with nickel doped gamma-alumina: reaction kinetics, mechanism, thermodynamics and products analysis. Journal of Cleaner Production, 286, p.124930.
- Yang, H., Ji, G., Clough, P.T., Xu, X. and Zhao, M., 2019. Kinetics of catalytic biomass pyrolysis using Ni-based functional materials. Fuel Processing Technology, 195, p.106145.
- Subramanian, S. and Ragula, U.B.R., 2020. Kinetics of catalytic and non-catalytic pyrolysis of Nerium Oleander. Fuel, 280, p.118591.
- Ratnasari, D.K., Yang, W. and Jönsson, P.G., 2019. Kinetic study of an H-ZSM-5/Al–MCM-41 catalyst mixture and its application in lignocellulose biomass pyrolysis. Energy & Fuels, 33(6), pp.5360-5367.
- Bhattacharyya, M., Shadangi, K.P., Mahanta, P. and Mohanty, K., 2022. Co-pyrolysis of coal-biomass: study on reaction kinetics and thermodynamics. *Biofuels, Bioproducts and Biorefining*, *16*(3), pp.725-742.
- Mandić, M., Todić, B., Živanić, L., Nikačević, N. and Bukur, D.B., 2017. Effects of catalyst activity, particle size and shape, and process conditions on catalyst effectiveness and methane selectivity for Fischer–Tropsch reaction: a modeling study. *Industrial & Engineering Chemistry Research*, *56*(10), pp.2733-2745.
- Xu, L., Wang, F., Chen, M., Yang, H., Nie, D., Qi, L. and Lian, X., 2017. Alkaline-promoted Ni based ordered mesoporous catalysts with enhanced low-temperature catalytic activity toward CO 2 methanation. *RSC advances*, *7*(30), pp.18199-18210.
- Yang, Y., Li, T., Jin, S., Lin, Y. and Yang, H., 2011. Catalytic pyrolysis of tobacco rob: Kinetic study and fuel gas produced. *Bioresource Technology*, *102*(23), pp.11027-11033.
- Zheng, Y., Wang, J., Wang, D. and Zheng, Z., 2022. Advanced catalytic upgrading of biomass pyrolysis vapor to bio-aromatics hydrocarbon: A review. *Applications in Energy and Combustion Science*, p.100061.

- Aho, A., Käldström, M., Fardim, P., Kumar, N., Eränen, K., Salmi, T., Holmbon, B., Hupa, M. and Murzin, D.Y., 2010. Catalytic deoxygenation of cellulose pyrolysis vapours over mesoporous materials. *Cellul. Chem. Technol*, *44*, pp.89-96.
- Lazdovica, K., Liepina, L. and Kampars, V., 2016. Catalytic pyrolysis of wheat bran for hydrocarbons production in the presence of zeolites and noble-metals by using TGA-FTIR method. *Bioresource technology*, *207*, pp.126-133.
- Hong, W., Zhang, Y., Jiang, H., Li, S., Chen, J. and Zhang, L., 2022. Co-pyrolysis of corn stalk and coal fly ash: A case study on catalytic pyrolysis behavior, bio-oil yield and its characteristics. *Case Studies in Thermal Engineering*, *38*, p.102346.

Chapter VII
Studies on Thermal and Catalytic Pyrolysis of Biomass

7.1 Introduction

Based on the formulations described in chapters 5 and 6, the results in the experimental validation of thermal (non-catalytic) and catalytic pyrolysis of sawdust are explained. Catalytic pyrolysis of sawdust in the presence of synthesized NiO and Ni (II) aluminate composite catalysts is elucidated in this chapter, further substantiated with detailed product analysis and characterization.

7.2 Experimental validation

Sawdust was integrated into a fixed-bed reactor and assessed for product profile distribution from a temperature range of 773 K, 823 K and 873 K at 30 K min^{-1} heating rate under nitrogen purge gas (300 mL min^{-1}). The evolved gas was condensed in a glass condenser and the bio-oil was collected in a separating funnel. The condenser water temperature was maintained at 280–283 K. The bio-char residue was collected at the end of the experiment for further analysis and characterization. Catalytic upgradation experiments on product bio-oil, thermal and catalytic char residue, and evolved gas was evaluated by integrating in-situ 10% and 20% synthesized NiO and Ni (II) aluminate composite catalysts with sawdust in the alumina crucible.

7.3 Highlights of the chapter

- A significant comparative study was done on thermal and catalytic pyrolysis of sawdust via 10 % and 20 % NiO/Al_2O_3 nano-composite catalyst.
- In thermal pyrolysis of sawdust, with an increase in temperature from 773–873 K, bio-oil yield increased while biochar yield decreased significantly.
- In catalytic pyrolysis of sawdust, with the effect of 10 % and 20 % NiO/Al_2O_3 nano-catalyst, bio-oil yield decreased whereas gas yield increased for 10 % NiO/Al_2O_3 nano-catalyst.
- From thermal bio-oil characterization, it was observed that D-Allose is the prominent compound present along with Beta-D-Glucopyranose-1,6-Anhydro with a remarkable C_p value of 2.00 kJ kg^{-1} K^{-1} and an ignition temperature of 397.95 K.
- Catalytic upgradation of bio-oil using 10 % and 20 % NiO/Al_2O_3 nano-catalyst resulted in phosphonic acid, (p-hydroxyphenyl)- and 6-Hepten-3-one, 5-Hydroxy-4-Methyl- as the candidate compounds with slightly decreased C_p values of 0.095 kJ kg^{-1} K^{-1} and 0.826 kJ kg^{-1} K^{-1} respectively due to catalytic tar cracking of polyaromatic hydrocarbons present in the bio-oil.

- With the increase in temperature, aromatic content decreased as aromatic rings break into short oligomer aliphatic chains. Aromatics content increased for bio-oil with 10% Ni loading catalyst and aldehyde content decreased while alcohol content increased with decrease in furan content. Aromatics content increased significantly for bio-oil with 20% Ni loading catalyst and aldehyde content decreased, alcohol content increased with decrease in furan content. This proves the fact that due to catalytic cracking at higher temperatures, furans, and aromatic rings break into short oligomer aliphatic chains.
- Characterization of the biochar revealed amorphous graphitic multilayer sheets with polycrystalline and hexagonal crystal lattice structure. Carbon content as evaluated from EDS-FETEM analysis was 91.78 % in this sample with the presence of aromatic ring structures and -CN stretching as evident from FTIR analysis.
- The highest yield % of hydrogen in fuel gas was observed to be maximum for pyrolysis of sawdust at 873 K, which indicated that with the increase in temperature, the hydrogen yield % increased.

7.4 Thermal and catalytic pyrolysis of biomass

The study imbibes on the thermal pyrolysis of sawdust in a fixed-bed reactor unit at temperatures, 773 K, 823 K and 873 K at 30 K min^{-1} heating rate under nitrogen purge gas (flow rate: 18 L h^{-1}). Priorly, when thermal degradation analysis of sawdust was done in a TG-DTG analyzer under nitrogen purge gas (20 mL min^{-1}) from 303-1173 K temperature at 10, 20, 30 and 40 K min^{-1} heating rates, it indicated significant mass loss at active pyrolytic zone due to its high volatile matter content as mentioned in Chapter 5. This was due to the reason of the thermal breakdown of the ligno-cellulosic biomass structure consisting of cellulose, hemicellulose, and lignin at higher temperatures where thermal stability of the pseudo components was given priority. In this chapter, to study the pyrolytic behaviour of sawdust experimentally, a fixed-bed reactor unit was implemented with 2700 mL volume capacity. Catalytic pyrolysis of sawdust was performed experimentally in presence of 10 % and 20 % synthesized NiO and Ni (II) aluminate composite catalysts at optimized (catalyst/biomass) ratio which showed highest degradability in the active pyrolytic zone in thermogravimetric analysis as mentioned in Chapter 6. The product distribution profile at the mentioned temperatures, 773 K, 823 K and 873 K was evaluated extensively for bio-oil, evolved non-condensable gas, and biochar. Detailed product characterization was further carried out.

7.4.1 Effect of pyrolysis temperature and catalyst on the product distribution profile

The variance of temperature was a candidate factor in the design of thermal experiments for sawdust pyrolysis. The distribution of pyrolysis products (evolved non-condensable gas, bio-oil (water and condensable organics), and biochar) by thermal and catalytic pyrolysis of sawdust is shown in Table 7.1. The increase in yield % (17.34–20.51 %) of bio-oil, and a decrease in yield % (58.66–56.33 %) of evolved gas, decreasing the yield % (24.00-23.15 %) of biochar and a rise in conversion (%) was significantly seen with an increase in temperature from 773–873 K. Therefore, based on maximum bio-oil yield and conversion, wt. %, 873 K was chosen as the optimum temperature for further investigation on catalytic pyrolysis of sawdust. Higher pyrolysis temperature instigated the rapid thermal cracking of the lignocellulosic biomass linkages, leading to faster bond breakage and random scission reactions further lowering the char residue. Researchers reported on the decrease in the production of char residue from 45–33.5% with an increase in temperature from 673–973 K *(Chandra and Bhattacharyya, 2019)*. Cao et al reported on the decrease in char residue from 48.6–35.2 %, increase in bio-oil yield from 26.7–32.5 % and increase in gas yield from 24.7–32.3% from 623–773 K temperature *(Cao et al., 2019)*.

The effect of metal loading % on the activated support of the catalyst and the (catalyst/biomass) ratio are two primal features on the product distribution profile of the catalytic pyrolysis of sawdust as shown in Table 7.1. For a (catalyst/biomass) ratio of 0.05 and 0.10 for 10 % and 20 % Ni loading composite catalysts, bio-oil, and bio-char were accessed at the optimized pyrolytic temperature of 873 K. It was observed that for a 10% composite catalyst, the yield % of evolved volatiles enhanced from 56.34-67.7 %, yield % of biochar, and yield % of bio-oil decreased from 23.15-23.03 % and 20.51-9.27 % at (catalyst/sawdust) ratio of 0.05 respectively. From Table 7.1, it was observed that for 20 % composite catalyst, the yield % of evolved volatiles increased substantially, the yield % of biochar decreased and the yield % of bio-oil decreased at (catalyst/sawdust) ratio of 0.10. The % conversion was 76.97 % for sawdust over 10 % catalyst and 90.19 % for sawdust over 20 % catalyst. Similar trends in product distribution were observed in pine wood and cellulose pyrolysis over HZSM-5/Al_2O_3 catalyst *(Murillo et al., 2021)*. The product profile distribution for non-catalytic pyrolysis of pine wood showed 15 % water yield, 46 % organics yield, 16 % evolved gas yield and 18% char yield, whereas 22 % water yield, 28 % organics yield, 22 % gas yield, 18% char yield % and 2% coke yield was seen for catalytic pyrolysis of pine wood over HZSM-5/Al_2O_3 catalyst for 3 h TOS (time on stream). The product profile distribution for non-catalytic pyrolysis of cellulose showed 24 % water yield, 43 % organics yield, 9 %

gas yield and 13 % char yield, whereas 24 % for water yield, 36 % organics yield, 19 % gas yield and 13 % char yield % and 1 % coke yield for catalytic pyrolysis of cellulose over HZSM-5/Al_2O_3 catalyst for 3 h TOS (time on stream). In another study on the catalytic pyrolysis of poplar wood with ZSM-5 and hollow HZSM-5 catalysts in a fixed-bed reactor, product profile distribution and composition of bio-oil was vividly studied. It was observed that at the expense of solid yield, liquid oil yield decreased due to coke deposition and deactivation of the catalyst ZSM-5. However, in comparison to ZSM-5 catalyst, hollow HS-ZSM-5(α) decreased the solid yield by 9.7 wt. %, while increasing the yield of liquid and gas by 4.8 and 4.9 wt. %, respectively *(Wu et al., 2020)*. The activity of the catalyst thus plays an important role in upgrading product fractions by enhancing both primary and secondary reaction pathways during catalytic pyrolysis of biomass which would be explained further. Transition metal salt precursors are partially covalent in nature and in this scenario fine tuning of the catalyst structure plays an emissive role in modifying the structure-activity relationship of the catalyst. However, in the present case, the catalytic char samples were not recycled to estimate the stability of the catalysts in similar pyrolytic experiments of sawdust.

Table 7.1 Effect of pyrolytic reaction temperature and 10 % and 20 % NiO and Ni (II) aluminate composite catalyst on thermal and catalytic pyrolysis of sawdust

Temperature (K)	Bio-oil, wt.%	Char residue, wt.%	Gas, wt.%	Conversion, wt.%
773	17.34±1.86	24±1.25	58.66	76±1.25
823	18.4±1.57	23.92±1.64	57.68	76.08±1.64
873	20.51±1.94	23.15±1.83	56.34	76.85±1.83
		Catalyst		
10 % Ni loading	9.27±1.27	23.03±1.54	67.7	76.97±1.54
20 % Ni loading	8.818±1.32	9.81±1.44	81.372	90.19±1.44

**Note: Gas wt. % = {(Wt. of feed - (Wt. of bio-oil + Wt. char))/Wt. of feed} × 100*

7.4.2 Product characterization

7.4.2.1 Characterization of bio-oil compounds

7.4.2.1.1 FTIR analysis of bio-oil

The FTIR analysis of the bio-oil samples produced at different temperatures, 773 K, 823 K, and 873 K from thermal and catalytic pyrolysis of sawdust is denoted in Fig. 7.1 (a, b). As shown in Fig. 7.1 (a), the intensity of a sharp broad peak for transmittance % was perceived at 3475 cm^{-1} which was due to O-H stretching (hydroxyl radical) inherent in the H_2O molecules of the bio-oil product. A sharp intense peak was observed at 1725 cm^{-1} due to C=O stretching, whereas small moderate peaks indicating C-O stretching were seen at

wavenumber 1000 cm^{-1} and 1250 cm^{-1} respectively due to both carbonyl and carboxyl functional groups. The peak at 1000 cm^{-1} wavenumber also indicated S-O stretching due to the presence of thiol groups (sulfonated compounds) in the bio-oil samples. A sharp peak with significant intensity was observed in a lower range wavenumber of 585 cm^{-1} indicating C-Cl stretching due to the presence of chlorinated compounds in the bio-oil samples. However a significant observation was with an increase in reaction temperature, the peak intensity increased in the bio-oil samples with the maximum intensity as shown in spectra of bio-oil produced at a temperature of 873 K. The FTIR analysis of the bio-oil samples with catalysts is given similarly in Fig. 7.1 (b) for FTIR spectra of transmittance % at X-axis with respect to wavenumber (cm^{-1}) at Y-axis. A strong broad peak was denoted at wavenumber 3425 cm^{-1} due to O-H stretching (hydroxyl radical) inherent in the H_2O molecules of the bio-oil product, a strong peak at 1642 cm^{-1} due to C=O stretching small sharp peak at 1300 cm^{-1} due to C-N stretching another small sharp peak at 1073 cm^{-1} due to C-O stretching and another small peak at 610 cm^{-1} was due to C-Cl stretching.

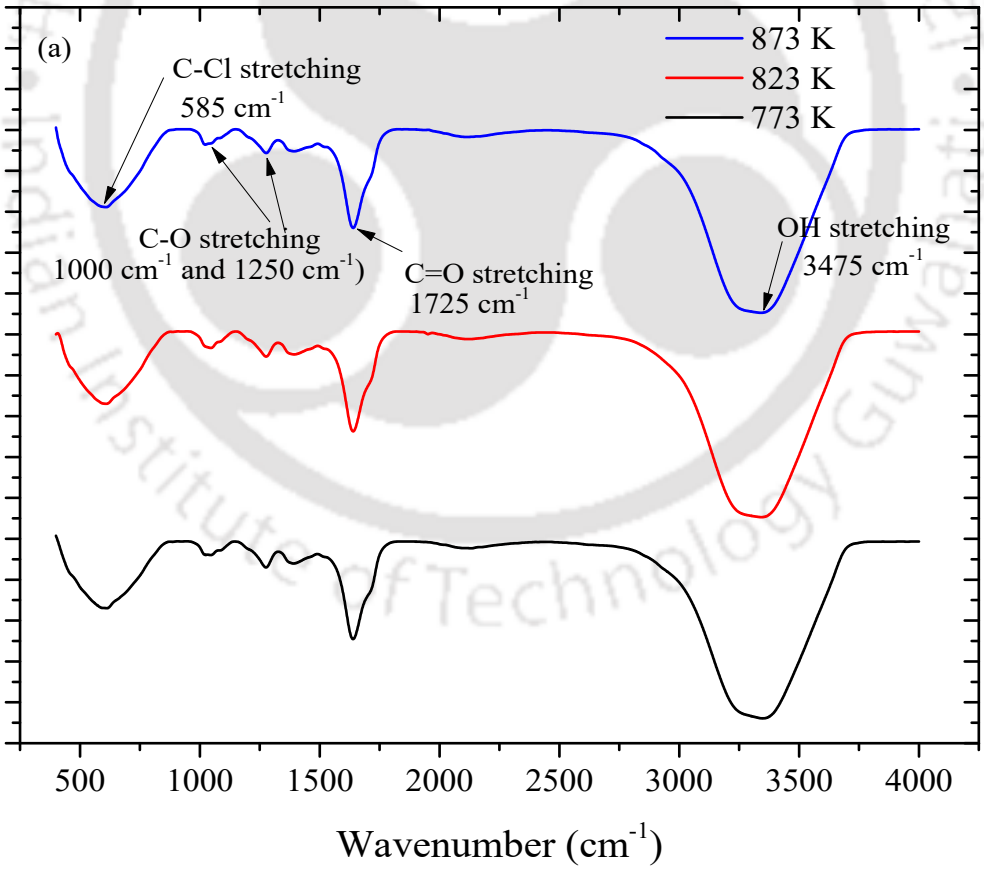

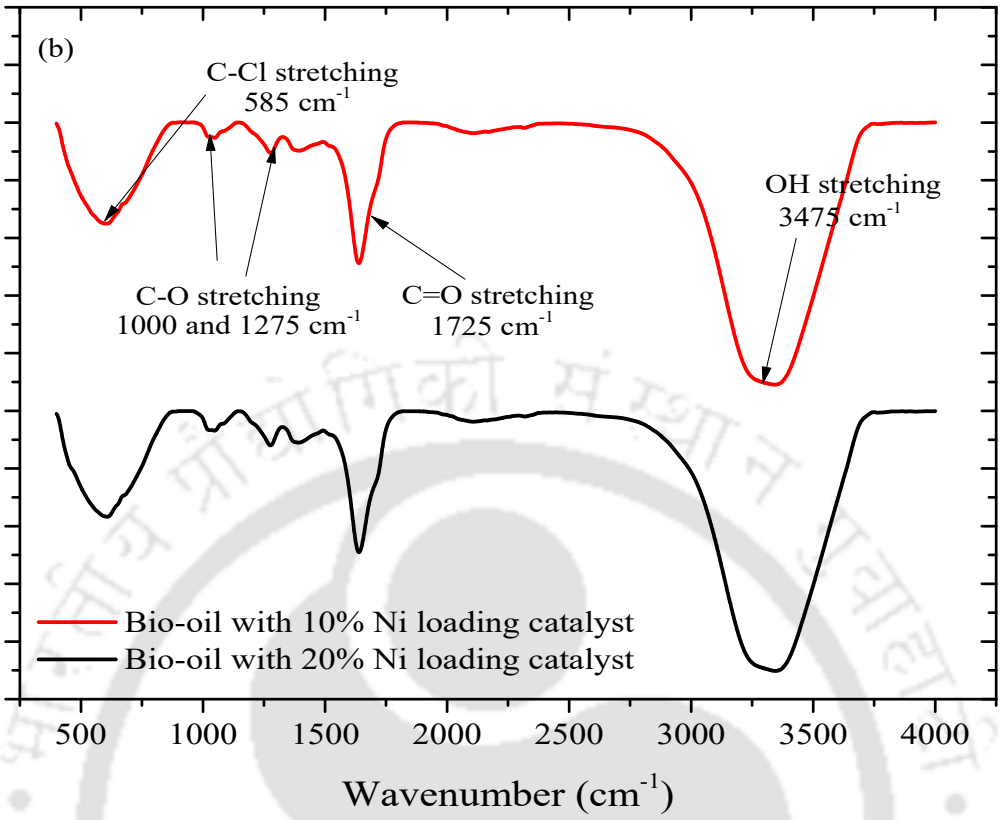

Fig. 7.1 FTIR Spectra of bio-oil produced during (a) thermal pyrolysis of sawdust and (b) catalytic pyrolysis of sawdust at 873 K using 10 % and 20 % NiO and Ni (II) aluminate composite catalyst

7.4.2.1.2 DSC analysis of bio-oil

Bio-oil from thermal and catalytic pyrolysis of sawdust was subjected to differential scanning calorimetry (DSC) analysis as shown in Fig. 7.2 (a, b) which indicated the exothermic of heat flowing out of the bio-oil samples. The various features such as glass transition temperature - melting temperature (peak temperature), specific heat capacity *(C_p),* heat flow characteristics, the heat of fusion, very fast purity determination, and heat released *(Q)* can be determined at constant heating rates for DSC analysis as mentioned in Table 7.2.

Table 7.2 Thermal characteristics of thermal and catalytic bio-oil

Temperature (K)	Glass transition temperature					Specific heat (*Cp*) (J/g. K)	Heat of fusion (J/g)	Specific heat flow (mW/mg)
	Onset temp. (K)	Mid temp. (K)	Inflection temp. (K)	End temp. (K)	Peak temp. (K)			
773	308.55	330.87	387.95	408.85	401.75	1.131	-1979	-28.95
823	301.05	342.65	400.95	408.95	402.85	0.862	-2180	-30.75
873	305.2	331.65	400.25	607.75	397.95	2.000	-1924	-32
Composite catalyst								
10 % Ni loading	304.45	341.05	402.65	611.45	400.15	0.095	-2192	-30.11
20 % Ni loading	387.15	440.85	394.05	464.45	390.55	0.826	-1249	-19.02

The result confirmed that the heat flow characteristics of thermal pyrolysis oil increased for the oil obtained at higher temperature. However, the heat flow was less in catalytic pyrolytic oil compared to thermal. This might be due to the catalytic cracking of the process which manifests a distillation temperature gradient in the samples causing the materials to hinder the proper flow of heat. Phase transition exhibited in the bio-oil samples with the increase in rising temperature and various first-order derivative transitions occur (melting, evaporation, sublimation, crystal-to-crystal transition) causing a difference in its glass transition temperatures (*Ehrenfest, 1933).* A directional heat pathway may cause such transitions in an exponential rise of heat flow until a steady-state condition is achieved which was T_s = 435 K in these samples. Peak temperatures decreased for bio-oil at 873 K which was 397.95 K rather than bio-oil at 773 K and 823 K since a lesser temperature was required for its ignition.

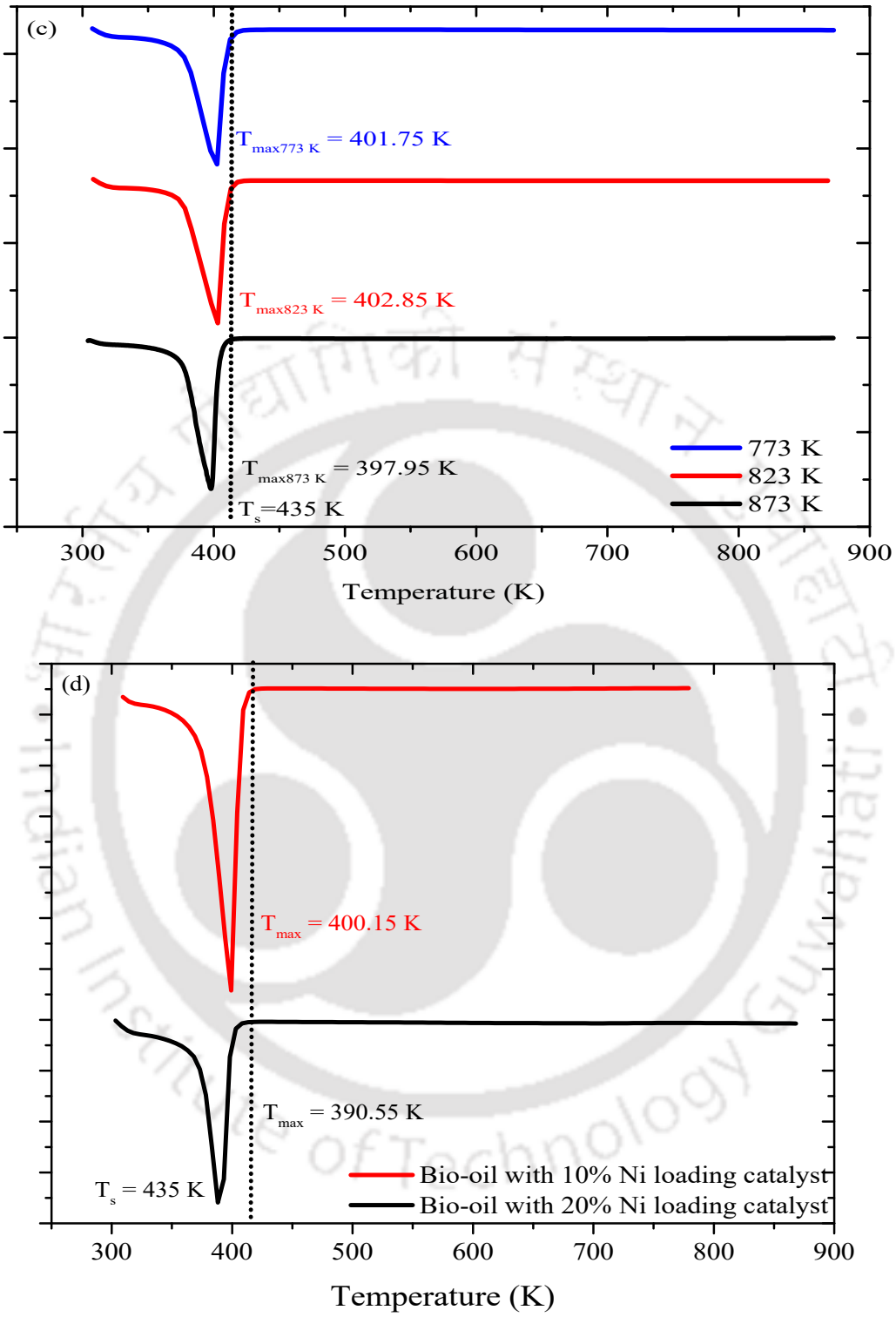

Fig. 7.2 DSC of bio-oil produced during (a) thermal pyrolysis of sawdust and (b) catalytic pyrolysis of sawdust at 873 K using 10 % and 20 % NiO and Ni (II) aluminate composite catalyst

7.4.2.1.3 GC/MS analysis of bio-oil compounds

Bio-oil produced from sawdust pyrolysis can be classified into ketones, alcohols, acids, esters, aldehydes, furans, alkanes, alkenes, and phenols. The peak area % of bio-oil component groups was used to characterize the formation characteristics of the bio-oil samples. An in-depth GC/MS analysis of each bio-oil component identification observed concerning retention time is listed in Table S4 and shown in Fig. S12 in Annexure. At the retention time of 22.55 min, bio-oil samples produced at temperatures 823 K and 873 K showed the peak area of the component D-Allose, while bio-oil samples at temperatures 773 K showed a peak area of 13.981%. However, D-Allose was seen to be prominent in bio-oil samples produced from 773 K at the retention time of 22.83 min, bio-oil samples produced at 823 K, and 873 K at a retention time of 22.55 min resulted in a peak area of 5.005% and 5.461 % respectively. D-Allose is a rare aldohexose with a carbonyl group at the end-most carbon atom of the carbon backbone chain and a hydroxyl group bonded to the other carbon atoms. It is a sugar found in less abundance in nature, is largely regioselective in protective reactions and glycosidation reactions, and has stupendous pharmacological and alimentary biological properties as reported by Vigo et al. *(Vigo et al., 2022).* It can be widely used as an antioxidant (phytochemicals) and an anti-tumor agent as reported by Zhang et al *(Zhang et al., 2020).* Other compounds found in bio-oil produced at reaction temperature 723 K in abundant quantities were 3-methyl-2-(2-oxopropyl) furan (7.166 %), phosphonic acid, (p-hydroxyphenyl)- (5.080 %), 2-ethyl-5-propylcyclopentanone, cyclopentanone and 2-(1-methylpropyl)- (4.529 %), phenol-2-Methyl (2.836 %), phenol-2,6 dimethoxy- (2.220 %), catechol and resorcinol (1.923 %), 3-(4,8,12)-trimethyl tridecyl (Furan) and bicyclo (5, 3, 0) decane (Cis) (1.642 %) and carbamic acid, hydroxy-ethyl ester (1.745 %) as compared to bio-oil produced at temperatures 823 K and 873 K. The compound 3-methyl-2-(2-oxopropyl) furan has bioactive potential as compared to its natural product form in plant species, *Euphorbia hirta* while phosphonic acid, (p-hydroxyphenyl)- shows antioxidant potential. 6-Hepten-3-one-5-Hydroxy-4-Methyl- was found in abundant quantities in the liquid oil produced at temperatures 823 K and 873 K where peak area was 2.482 % and 3.538 % respectively. Carbamic acid, hydroxy-ethyl ester was also found in fantastic amounts in the liquid oil produced at temperatures 823 K and 873 K where peak area was 4.175 % and 4.018 % respectively. Carbamic acid, hydroxy-ethyl ester contains many such therapeutic properties. Other compounds found in bio-oil produced at reaction temperature 823 K were 3-(4,8,12)-trimethyl tridecyl (Furan) and bicyclo (5, 3, 0) decane (Cis) (4.017 %), phosphonic acid, (p-hydroxyphenyl)- (2.935 %), 2-Ethyl-5-Propylcyclopentanone (3.358 %), phenol-2-

methyl (2.256 %) and creosol (1.726 %). Similar compounds were found in bio-oil produced at reaction temperature 873 K along with pyridine with a peak area of 3.355 % which has medicinal properties. The GC/MS analysis of the bio-oil samples from catalytic pyrolysis of sawdust at 873 K pyrolysis temperature using 10 % and 20 % NiO and Ni (II) aluminate composite catalysts is given in Table S5 and compared to thermal bio-oil produced at 873 K pyrolysis temperature. At the retention time of 22.554 min, bio-oil samples produced at temperatures 823 K and 873 K showed a peak area of 13.981 % of the component D-Allose, while the bio-oil with 10 % and 20 % Ni loaded catalysts showed peak area % of 5.005 % and 5.461 % respectively. Pyridine was also found in abundant quantities with a peak area of 3.304 % and 6.165 % for bio-oil with 10 % and 20 % catalysts respectively. 6-Hepten-3-one, 5-Hydroxy-4-Methyl- and 3-(4,8,12)-Trimethyl Tridecyl (Furan) present in thermal bio-oil was catalytically cracked in bio-oil with 10 % and 20 % catalysts as it showed negligible peak area. Compounds such as 1-phenyl-5-methylheptane, silacyclopentane, 1-methyl cyclopropane methanol, 2 (5H)-furanone and trifluoromethyl t-butyl disulphide were seen in bio-oil with 10 % composite catalyst with peak area of 1.754 %, 2.222 %, 0.802 %, 1.845 % and 3.719 % respectively. Other compounds such as 1-pentene-3-ol, 4-methyl, carbamic acid-hydroxy-ethyl ester, 3-trans-(1,1-di-methyl-ethyl)-4, cis-methoxycyclohexan-1-ol, 1-silacyclo hexa-2,5-diene, phenol-2-methyl, catechol and resorcinol, phosphonic acid, phenol-2, 6-dimethoxy and 2 (5H)-furanone were seen in bio-oil with 20 % composite catalyst with peak area of 3.885 %, 2.477 %, 1.191 %, 1.265 %, 2.353 %, 1.487 %, 3.298 %, 1.301 % and 2.031 % respectively.

As observed in Fig. 7.3 (a, b), the total peak area % of compounds from GC/MS of bio-oil produced from thermal pyrolysis of sawdust at temperatures 773 K, 823 K and 873 K and catalytic pyrolysis of sawdust using 10 % and 20 % NiO and Ni (II) aluminate composite catalyst is observed. As given in Fig. 7.2 (a), aromatics content and furan content decreased with increase in temperature from 773-873 K, whereas ester content and tertiary amine content increased with increase in temperature from 773-873 K. However, bio-oil produced at 823 K was seen to be lesser for aldehyde content and higher for ketone, carboxylic acid content and alcohol content. This proves the fact that with increase in temperature, aromatic content decreased as aromatic rings break into short oligomer aliphatic chains. Cellulose upon its degradation forms levoglucosan, hydroxyl-acetone, furans and glycolaldehyde, whereas hemicellulose degrades into water, hydroxyl-1-butanone, hydroxyl-1-propanone, 2-methylfuran, formic acid, acetic acid, etc by a free radical mechanism. Xylose reacts with H^+ and OH^- ions of D-Allose in its vicinity forming xylosyl cation and undergoing subsequent

glycosidic bond cleavage. D-Allose is the main component released from cellulose degradation where it is an epimer at C3 position of glucose units *(Vigo et al., 2022).* In another study, non-catalytic pyrolysis of poplar sawdust yielded phenol, methyl phenol and alkoxy phenol. Incorporating ZSM-5 into the catalytic pyrolysis of poplar sawdust yielded increased selectivity towards alkoxy phenols while decreased selectivity for methyl phenols. However, with the inclusion of HZSM-5 into the mixture, selectivity towards alkoxy phenols increased substantially due to the enhanced adsorption of active intermediates into the biomass vapor *(Wu et al., 2020)*. Alkoxy phenol, on the other hand, could be converted to methyl phenol and phenol through alkylation and de-methoxylation reactions *(Fan et al., 2018).* Phenol products such as phenol-2-methyl, phenol-2, 6- dimethoxy are mainly products of lignin pyrolysis. Hence in a summary of GC/MS analysis, the total aromatics are the combined BTX (benzene, toluene and xylene) and substituted polycyclic aromatic hydrocarbons and oxygenates are the non-catalytic products of biomass pyrolysis.

Catalytic pyrolysis of sawdust significantly reduces the content of oxygenated compounds such as ketones, furans, acids, sugars, etc. as well as nitrogen-containing compounds with increment in the hydrocarbon and phenolic content of the bio-oil through deoxygenation (decarboxylation, decarbonylation, and dehydration), cracking and reforming pathways. As mentioned in Fig. 7.3 (b), aromatics content increased for bio-oil with 10 % Ni loading catalyst and aldehyde content decreased, alcohol content increased with decrease in furan content. Aromatics content increased significantly for bio-oil with 20 % Ni loading catalyst and aldehyde content decreased, alcohol content increased with decrease in furan content. This proves the fact that due to catalytic cracking at high temperatures, furans, and aromatic rings break into short oligomer aliphatic chains. This also proves the deoxygenation and cracking capability of the catalysts enhancing breakage of C-O and C-C bonds. Due to increase in phenolic content in catalysed bio-oil samples, it can be stated from previous literatures that Ni/Al_2O_3 catalysts decreases the oxygen and nitrogen content due to presence of metal active sites in addition to Lewis acidic sites. Reduction in the oxygen content after catalytic cracking of bio-oil increases the fuel quality of bio-oil. Reduction of carboxylic acids from 0.775-0.689 % and 0.44 % with 10 % and 20 % Ni loading reduces the corrosivity of the bio-oil, thus increasing its stability. However, there was an increase in nitro-geneous compounds such as cyannamide in the catalytic samples, resulting in NOx emissions. Henceforth, addition of catalysts sustains significant improvement in the quality of bio-oil as compared to non-catalytic bio-oil. Further, incorporation of nano-catalysts into biomass

pyrolysis enhances aromatic hydrocarbon production as compared to conventional catalysts as stated by Yi et al. Jatropha seeds de-oil cake (called JS cake), peanut shell, corncob and bagasse were chosen as the biomass samples and catalytic pyrolysis of biowastes was conducted in a dual-catalyst fixed-bed reactor system with a lab-scale continuous feeder. Two types of CaO catalysts were used in the upgrading of bio-oil experiments, the conventional CaO was prepared from calcium hydroxide (called for CH-CaO) and CaO derived from calcium D-gluconate monohydrate and two ZSM-5 catalysts were chosen which were nanosized ZSM-5 (NZSM-5) and the micro-sized ZSM-5 (MZSM-5). Here the proportion of aromatic hydrocarbons in bio-oil obtained from pyrolysis of JS cake with Org-CaO/NZSM-5 is up to 93 % which is much more than that with CH-CaO/MZSM-5 which was 26 % due to the formation of naphthalenes mainly as naphthalene and methylnaphthalene. The increase of NZSM-5 promoted more formation of BTX and naphthalenes *(Yi et al., 2019).*

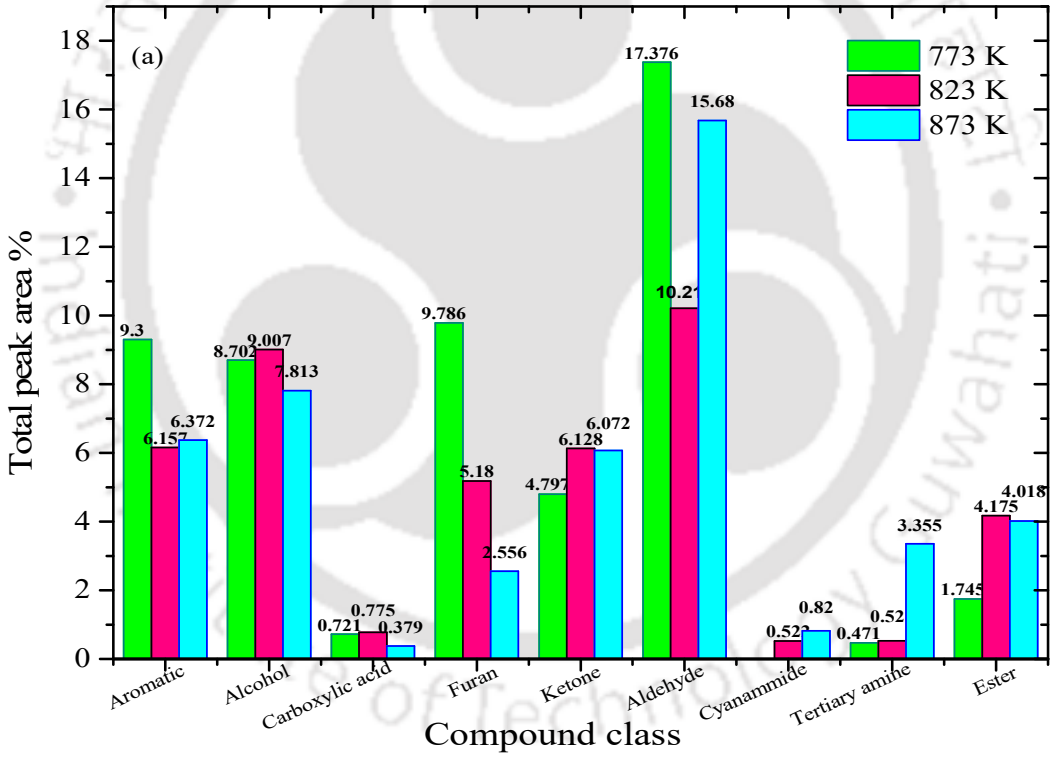

(Continued)

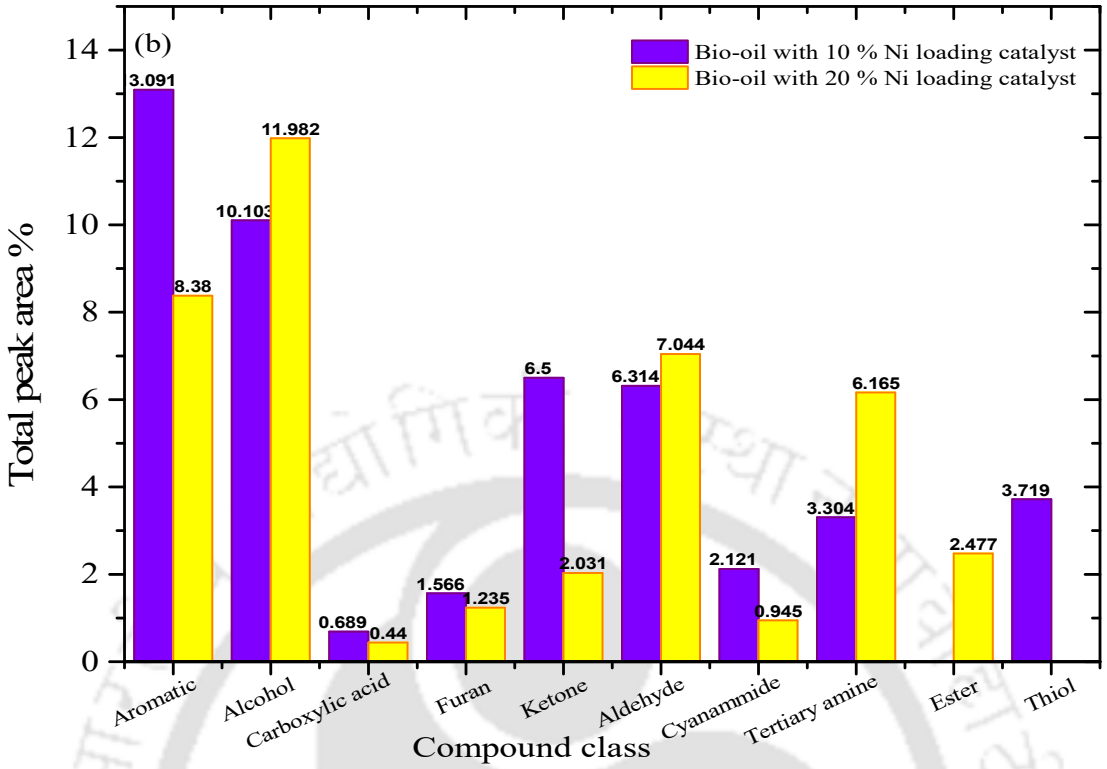

Fig. 7.3 Total peak area % of compounds from GC/MS of bio-oil produced from a) thermal and b) catalytic pyrolysis oil

7.4.2.1.4 NMR spectroscopy analysis of bio-oil compounds

The NMR spectra of thermal and catalytic bio-oil samples are shown in Fig. 7.4 (a-e) where a small peak was found in the chemical shift region (^{1}H ppm) of 1.4-1.9 ppm which accounts to CH_2, CH_β to Ar and a larger peak at 3.4-4.5 ppm which accounts to CH_2, CH_α to two Ar. The spectra is divided into methyl (CH_3), methylene (CH_2) and methine (CH) groups, combined with the distance of the alkyl group from the aromatic nucleus: α, β and γ (aliphatic region: 0.5-4.5 ppm, inter-unit aliphatic region/oxygenated aliphatic region: 2.8-5.7 ppm and an aromatic region: 4.0-9.2 ppm) *(Mattson et al., 2016).* Most of the cross-peaks in the bio-oil fractions were found to be connected in the α-position to an aromatic ring, which indicates a shortening of the aliphatic chains in the bio-oil.

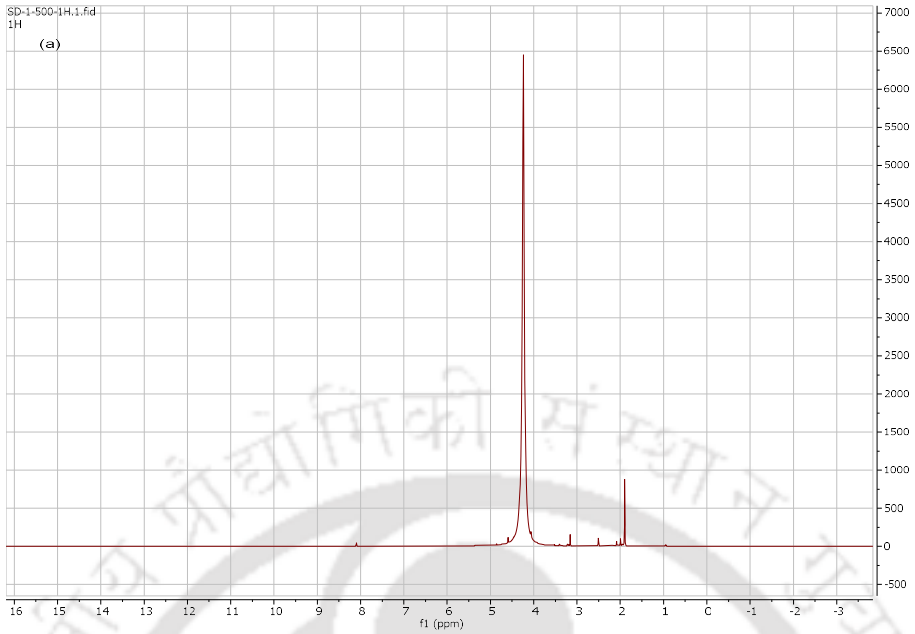

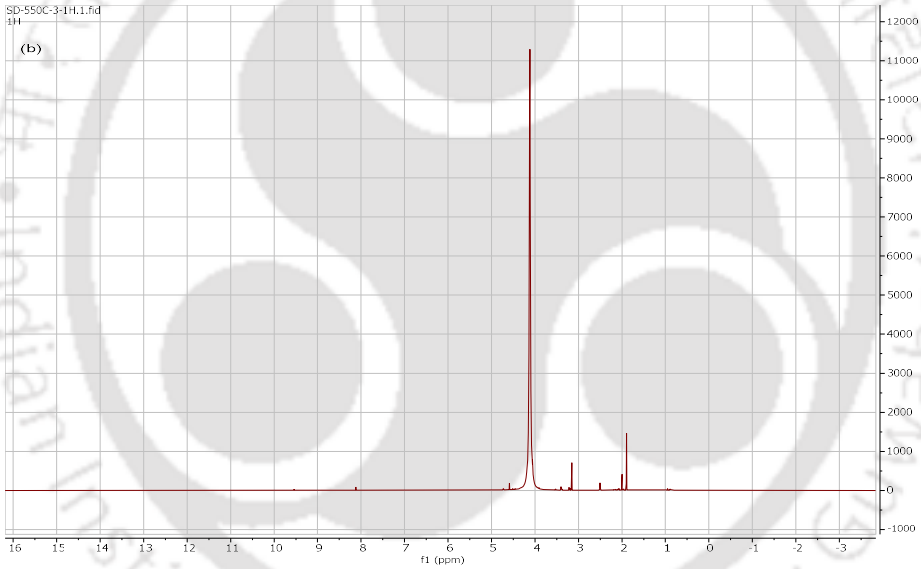

(Continued)

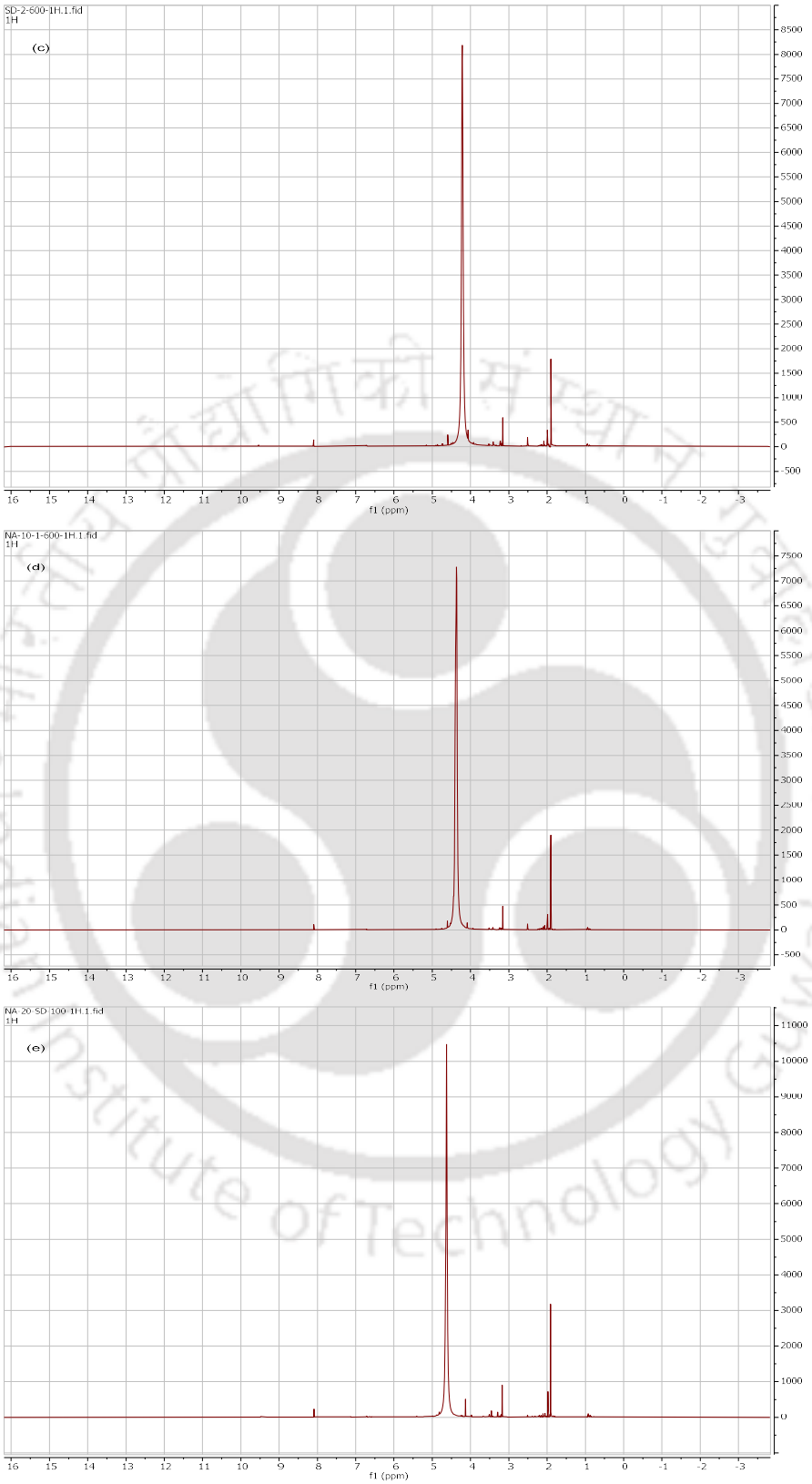

Fig. 7.4 NMR spectra of bio-oil produced from (a-c) thermal and (d, e) catalytic pyrolysis of sawdust

7.4.2.2 Characterization of thermal and catalytic biochar residue

7.4.2.2.1 Composition of biochar

As given in Table 7.3, proximate analysis and ultimate analysis of biochar from thermal and catalytic pyrolysis of sawdust are explained. In the thermal pyrolysis of sawdust, the effect of temperature plays a dual role in physico-chemical properties of char. The decrease in the moisture content, rise in volatile matter content from 52.81-60.34 %, increase in ash content from 15.65-16.43 %, and decrease in fixed carbon content is seen in biochar as the pyrolysis temperature rises from 773-873 K. In comparison of biochar at the temperature of 873 K, catalytic char taken at 873 K pyrolysis temperature resulted in increase in moisture content and a significant decrease in volatile matter content with increase in nickel loading from 10-20%. Ash content increased significantly with increase in nickel metal content along with the decrease in fixed carbon as compared to biochar evaluated at 873 K pyrolysis temperature. The ultimate analysis determined the carbon content, hydrogen content, sulfur content, nitrogen content, and oxygen content (by difference). Carbon content increased with an increase in pyrolysis temperature from 773-873 K, an increase in hydrogen content and a decrease in the oxygen content with negligible sulfur content was visualized respectively. In comparison to biochar taken at 873 K pyrolysis temperature, catalytic char decreased in carbon content, increase in hydrogen content, decrease in nitrogen content with significant increase in oxygen content with the increase in nickel metal content from 10-20 %. With the increase in temperature, yield of biochar residue decreases with the increase in fixed carbon content, because the volatile matter (e.g., H_2O, CO_2, CO, NH_3, HCN, and $C_xH_yO_z$) is released randomly. With a further increase in temperature, the release of carbon-rich compounds, such as $C_xH_yO_z$, from the biochar significantly decreases, while other compounds with less carbon (e.g., CO, CO_2, and NO_x) content are continuously released. This results in an increase in fixed carbon content of the remained biochar *(Liu et al., 2015)*.

The atomic H/C ratio and atomic O/C ratio stand as indicators of the degree of carbonization, demethanation, dehydration, decarboxylation, and oxidation reactions. The atomic H/C ratio and atomic O/C ratio for biochar are plotted and compared with sawdust in Fig. 7.5, which serve as coordinates in X-axes and Y-axes. The atomic H/C ratio of biochar increases with an increase in pyrolysis temperature from 773-873 K, while the atomic O/C ratio subsequently decreases with an increase in pyrolysis temperature. This shows that biochar produced at 873 K was led by higher carbonization, demethanation, and decarboxylation reactions. However, the biochar produced at 773 K and 823 K showed lesser

carbonization and comparable demethanation, and decarboxylation reactivity as compared to biochar at 873 K. Catalytic char with 10 % and 20 % catalyst instilled higher atomic H/C ratio of 0.6069 and 0.8096 and higher atomic O/C ratio of 0.250 and 0.452 respectively, as compared to biochar produced at 873 K. This shows higher demethanation reaction, lesser decarbonization, and higher oxidation occurring with an increase in nickel loading in the char s. In this scenario, oxygen existing in the biochar product might be included in hydroxyl groups, ether groups, and heterocyclic oxygen compounds. Hence, the H/C ratio culminates in the hydrocarbon carbon skeletal structure in biochar.

Table 7.3 Proximate and ultimate analysis of biochar pyrolytic product residue from thermal and catalytic pyrolysis of sawdust

Temperature (K)	**Proximate Analysis**						
	M, %	**VM, %**	**A, %**	**FC, %**	**(FC/VM) × 100 %**		
773	0.420	52.81	15.65	31.12	58.92		
823	0.106	55.20	15.94	28.75	52.09		
873	0.0167	60.34	16.43	23.21	38.64		
	Catalytic biochar residue						
10 % Ni/Al_2O_3	0.229	49.711	22.07	27.99	56.30		
20 % Ni/Al_2O_3	0.204	46.426	43.87	9.50	20.46		
Temperature (K)	**Ultimate Analysis**						
	C, %	**H, %**	**S, %**	**N, %**	**O, %**	**H/C**	**O/C**
773	71.28	0.83	-	0.631	27.259	0.1397	0.286
823	76.62	1.85	-	0.882	20.648	0.2897	0.202
873	80.71	2.18	-	0.616	16.494	0.3241	0.153
	Catalytic biochar residue						
10 % NiO/Al_2O_3	72.169	3.650	-	0.112	24.069	0.6069	0.250
20 % NiO/Al_2O_3	59.800	4.032	-	0.078	36.09	0.8096	0.452

(M: Moisture Content, VM: Volatile matter content, A: Ash content, FC: Fixed carbon content, C %: Carbon content, H %: Hydrogen content, S %: Sulphur content, N %: Nitrogen content, O %: Oxygen content)

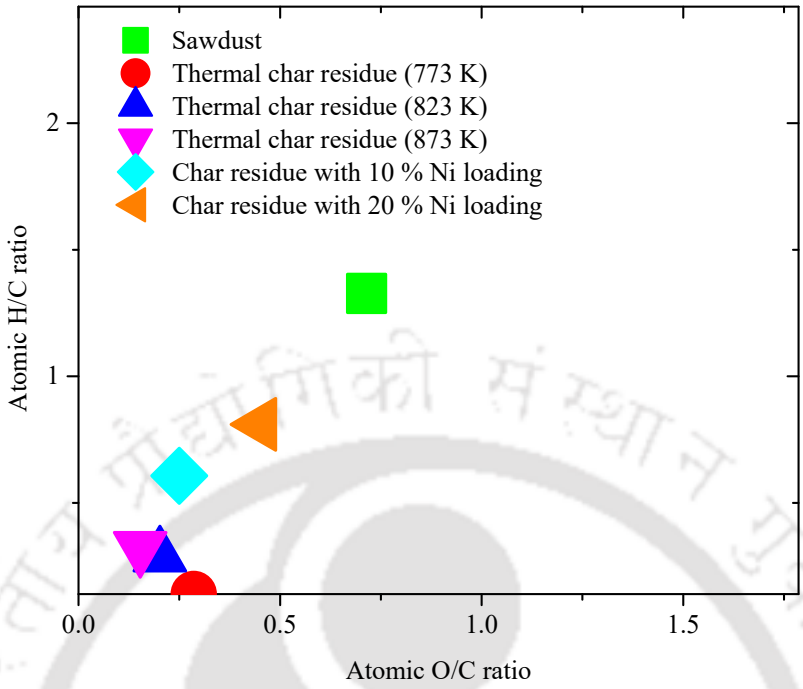

Fig. 7.5 Van Krevelen diagram of atomic O/C ratio with atomic H/C ratio for thermal and catalytic biochar residue

7.4.2.2.2 FESEM analysis of the biochar

FESEM analysis of the biochar produced at 873 K reaction temperature and the catalytic char residue with 10 % and 20 % NiO and Ni (II) aluminates is depicted in Fig. 7.6 (a-c) respectively. This showed its morphological and topological microstructure of each thermal and catalytic char residue at a magnification of 1.0 KX. Distinct macro-pores were seen evenly on the surface of the biochar produced and their morphology tend to became smoother with the appearance of some micropore structures. This might have the possibility of providing sites for nutrient adsorption and soil microbe colonization. However, catalytic char residue with 10 % and 20 % Ni loading render spherical structures on the topological surface blocking the pores of the biochar material. Likewise, due to increased nitrogen content in the catalytic chars, they might be subsequently used for bioaccumulation in soil for nutrient adsorption. It might also be rendered as energy storage material due to its high hydrogen storing capacity as seen from CHNS analysis. Liu et al. also stated on porous biochar materials for energy storage and bioremediation potential *(Liu et al., 2017).*

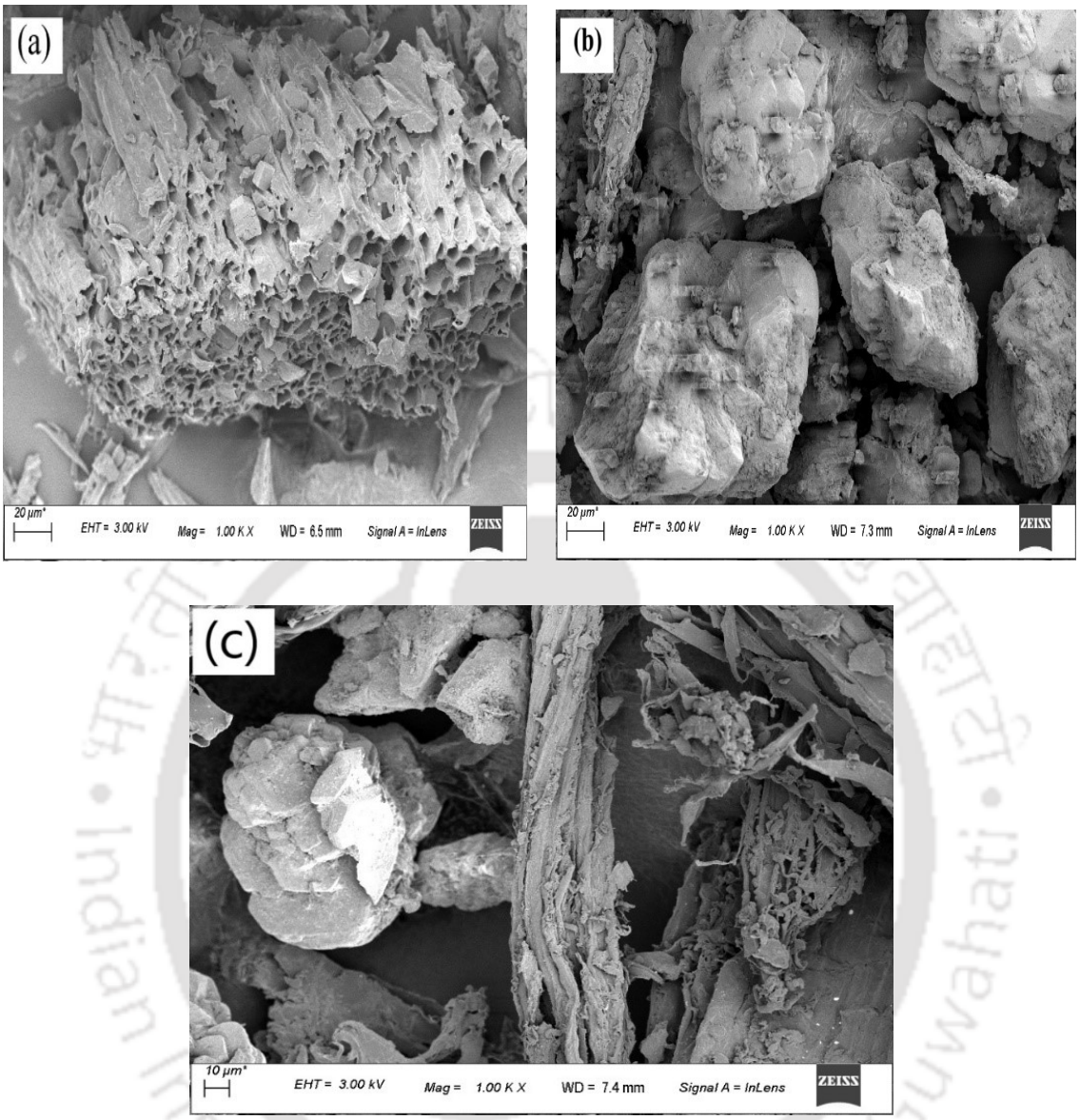

Fig. 7.6 FESEM analysis of (a) Biochar from thermal pyrolysis of sawdust, (b, c) Catalytic biochar residue with 10 % and 20 % Ni loading

7.4.2.2.3 FETEM analysis of the biochar

FETEM analysis of the pyrolyzed biochar at 873 K reaction temperature and the biochar residue with 10 % NiO and Ni (II) aluminates is depicted in Fig. 7.7 (a-i), which showed its morphological and topological microstructure FETEM images, selected area electron diffraction pattern (SAED pattern) at selected locations of FETEM image and the high-resolution transmission electron microscopy (HRTEM) images. FETEM images for biochar were seen in Fig. 7.7 (a, b) at magnification 200 nm and 100 nm which showed multilayer hexagonal nano-sheets stacked on one top of another respectively. The SAED pattern in Fig.

7.7 (c) was single crystalline as notified from the distinct atomic planes and was hexagonal in crystal shape. Fig. 7.7 (d) notified the FETEM image at magnification of 50 nm which showed distinct porous structures of biochar. The SAED pattern was notified in Fig. 7.7 (e) with single crystalline and hexagonal structure. However, Fig. 7.7 (f) and (g) showed the FETEM image and the SAED pattern of the catalytic biochar residue with 10 % Ni loading. It showed spherical agglomerated structures and a single crystalline pattern of SAED. Fig. 7.7 (h) and (i) depicted the FETEM microstructure images and SAED pattern of the catalytic biochar residue with 20 % Ni loading. FETEM images showed the larger agglomerated structures of the catalytic biochar residue at 100 nm magnification. At this location, SAED pattern was denoted which notified the amorphous nature of the catalytic char residue with three ringed atomic planes visible. The EDS measurements for elemental weight % and atomic % as given in Table 7.4, showed carbon content of 91.78 %, an oxygen content of 3.89 %, the aluminum content of 1.35 %, silica content of 1.09 %, the iron content of 0.65 %, the potassium content of 0.58 %, the calcium content of 0.34 %, the magnesium content of 0.18 %, sulfur content of 0.06 %, titanium content of 0.03 %, phosphorus content of 0.03 % and chlorine content of 0.02 % for biochar. Similarly, catalytic biochar residue with 10 % Ni loading showed a carbon content of 38.80 %, iron content of 26.22 %, cobalt content of 17.46 %, the oxygen content of 11.06 %, the aluminum content of 2.78 %, silica content of 1.09 %, the nitrogen content of 1.85 %, the chlorine content of 0.99 %, sulfur content of 0.84 % and with negligible magnesium, potassium, calcium, nickel, phosphorus, and titanium content. Catalytic biochar residue with 20 % Ni loading showed carbon content of 47.63 %, iron content of 0.37 %, chromium content of 1.19 %, oxygen content of 12.85 %, aluminium content of 0.10 %, silica content of 1.16%, nitrogen content of 6.02 %, chlorine content of 7.03 %, sulphur content of 14.89 %, magnesium content of 1.66 %, potassium content of 1.04 %, calcium content of 4.27 % and negligible phosphorus, zirconia, bromine and nickel contents.

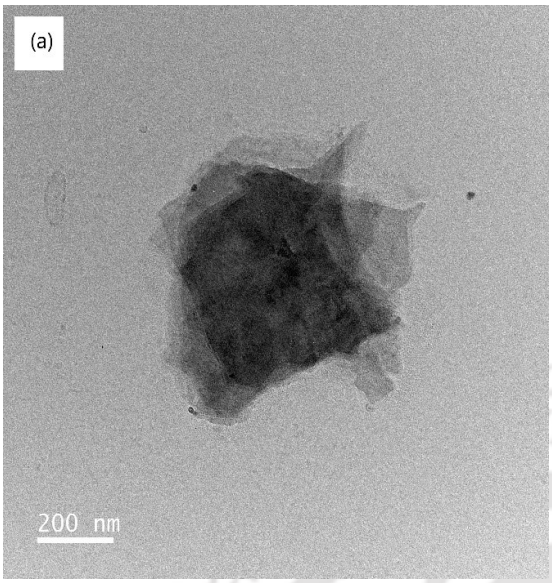

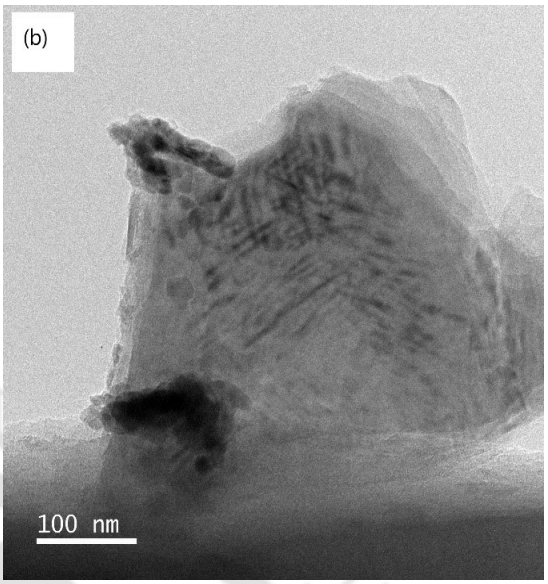

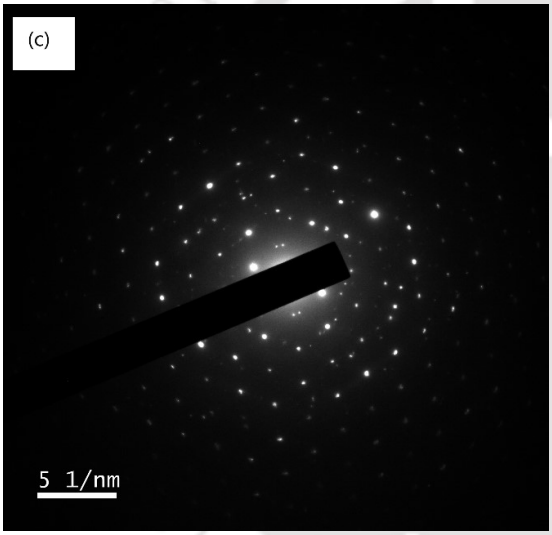

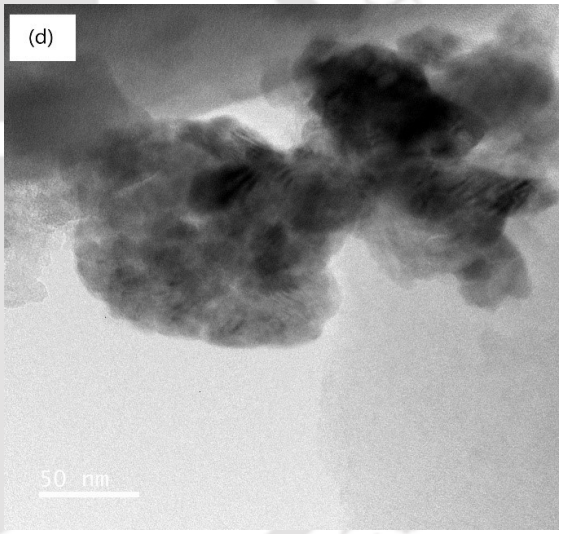

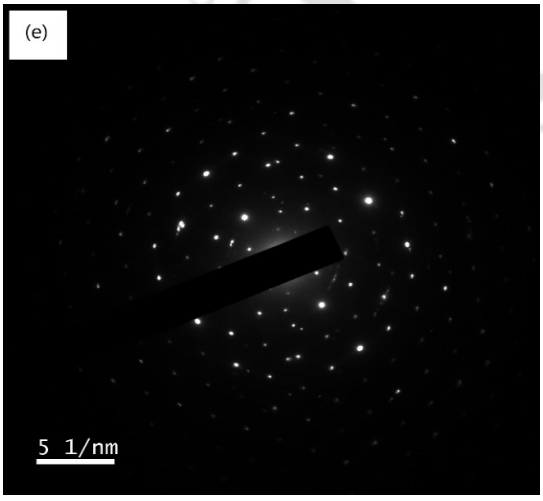

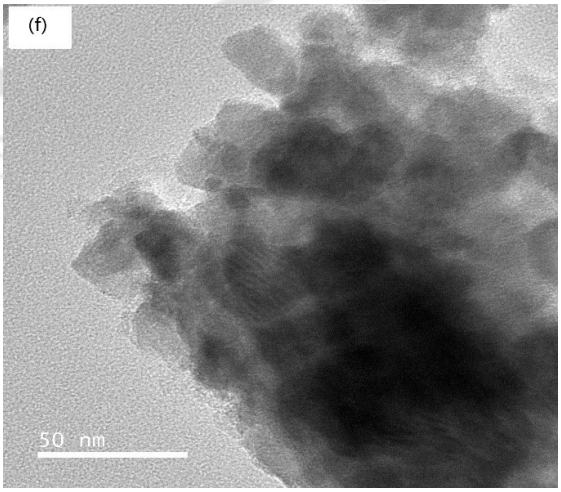

(Continued)

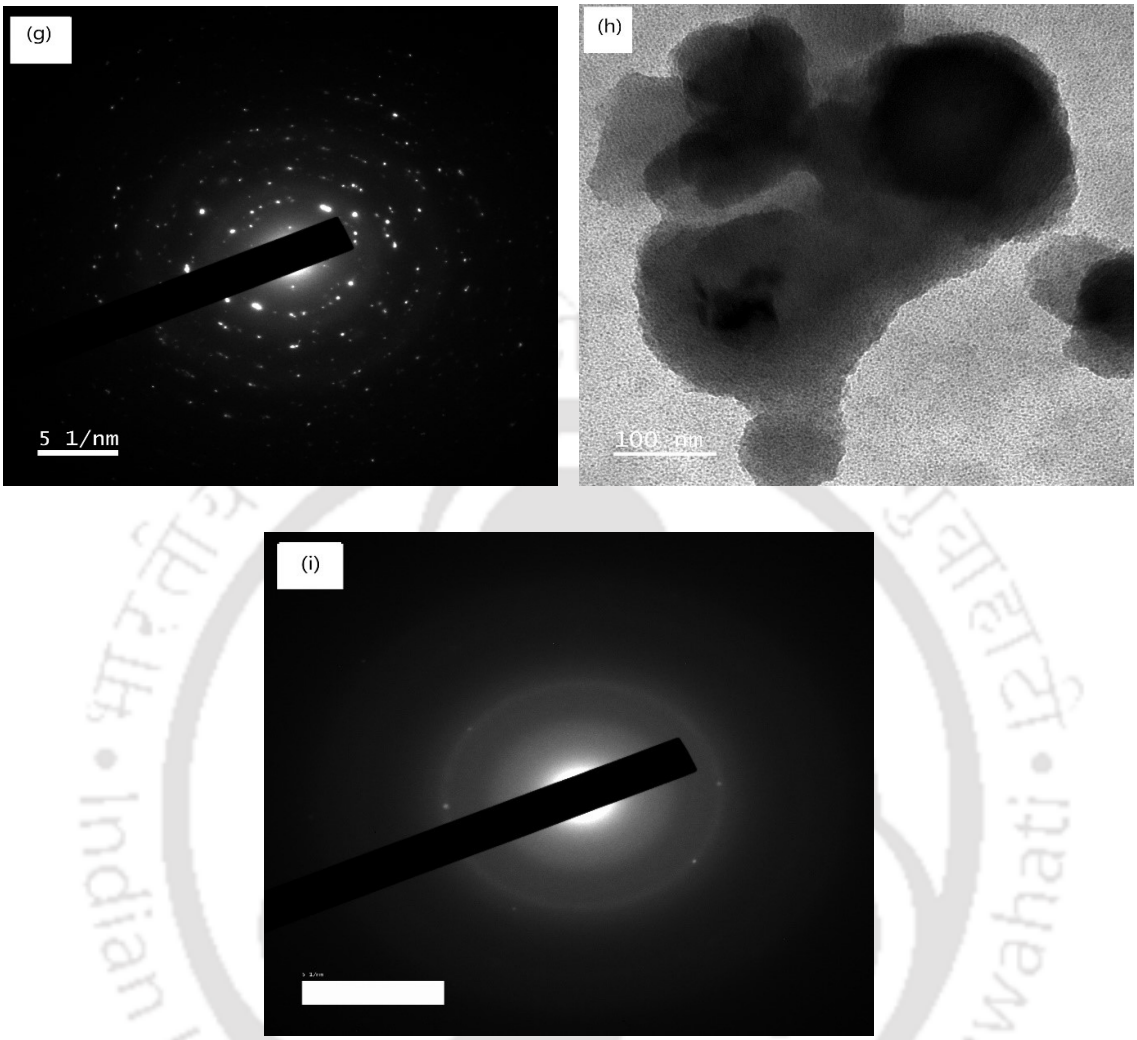

Fig. 7.7 FETEM analysis of (a-e) Biochar residue from thermal pyrolysis of sawdust, (f, g) Catalytic biochar residue with 10 % Ni loading catalyst, (h, i) Catalytic biochar residue with 20 % Ni loading catalyst

Table 7.4 Elemental weight (%) and atomic (%) of pyrolyzed thermal and catalytic biochar residue with 10 % and 20 % Ni loading catalyst by EDS FETEM analysis

Element	Biochar residue		Catalytic biochar residue with 10 % Ni loading catalyst		Catalytic biochar residue with 20 % Ni loading catalyst	
	Elemental weight (%)	Atomic (%)	Elemental weight (%)	Atomic (%)	Elemental weight (%)	Atomic (%)
Carbon	91.78	95.28	38.80	64.91	47.63	64.41
Oxygen	3.89	3.03	11.06	13.89	12.85	13.04
Magnesium	0.18	0.09	-	-	1.66	1.11
Aluminium	1.35	0.62	2.78	2.07	0.10	0.06
Silica	1.09	0.49	1.09	0.49	1.16	0.67
Phosphorus	0.03	0.01	-	-	-	-
Sulfur	0.06	0.02	0.84	0.53	14.89	7.55
Chlorine	0.02	0.02	0.99	0.56	7.03	3.22
Potassium	0.58	0.18	-	-	1.04	0.43
Calcium	0.34	0.11	-	-	4.27	1.73
Titanium	0.03	0.01	-	-	-	-
Iron	0.65	0.15	26.22	9.43	0.37	0.11
Nitrogen	-	-	1.85	2.65	6.02	6.99
Cobalt	-	-	17.46	5.95	-	-
Zirconia	-	-	-	-	1.82	0.32
Bromine	-	-	-	-	-	-
Nickel	-	-	-	-	-	-
Chromium	-	-	-	-	1.19	0.03

7.4.2.2.4 XRD analysis of the biochar

The XRD analysis of pyrolyzed thermal and catalytic biochar residues is shown in Fig. 7.8 (a, b). It indicated various peaks with variable peak positions, peak intensity, and peak width at the consequent (2-Theta^o) diffraction angle. The peaks as shown in Fig. 7.8 (a) were obtained at 2-Theta^o of 22.43^o and a small peak at 40.02^o. Peak intensity was observed to be the highest at 22.43^o (2-Theta^o). This was due to the superimposition effect of the constructive and destructive contribution of the atoms in the lattice structure. The peak width was also seen to be broader at 22.43^o (2-Theta^o) due to the non-uniform strain in the peak. PDF Card No.: 01-089-7213 Quality: S revealed the graphitic composition of the peaks. The lattice structure of thermal biochar was of the hexagonal structure and the lattice parameters were a= 2.4640, b= 2.4640, and c=6.7110. However, Fig. 7.8 (b) shows the peaks at 20.64^o

and 23.33° (2-Theta°) PDF Card No.: 00-001-0378 Quality: I, PDF Card No.: 00-011-0817 Quality: O and PDF Card No.: 01-072-1682 Quality: I revealed the tridymite (SiO_2) composition of peaks at 20.64° and 23.33° (2-Theta°), iron oxalate (FeC_2O_4) at 17.04°, 22.49°, 24.10° and 37.44° (2-Theta°) and tetra-aluminium tetra-oxide carbide (Al_4O_4C) at 20.98°, 22.99° and 28.62° (2-Theta°) respectively.

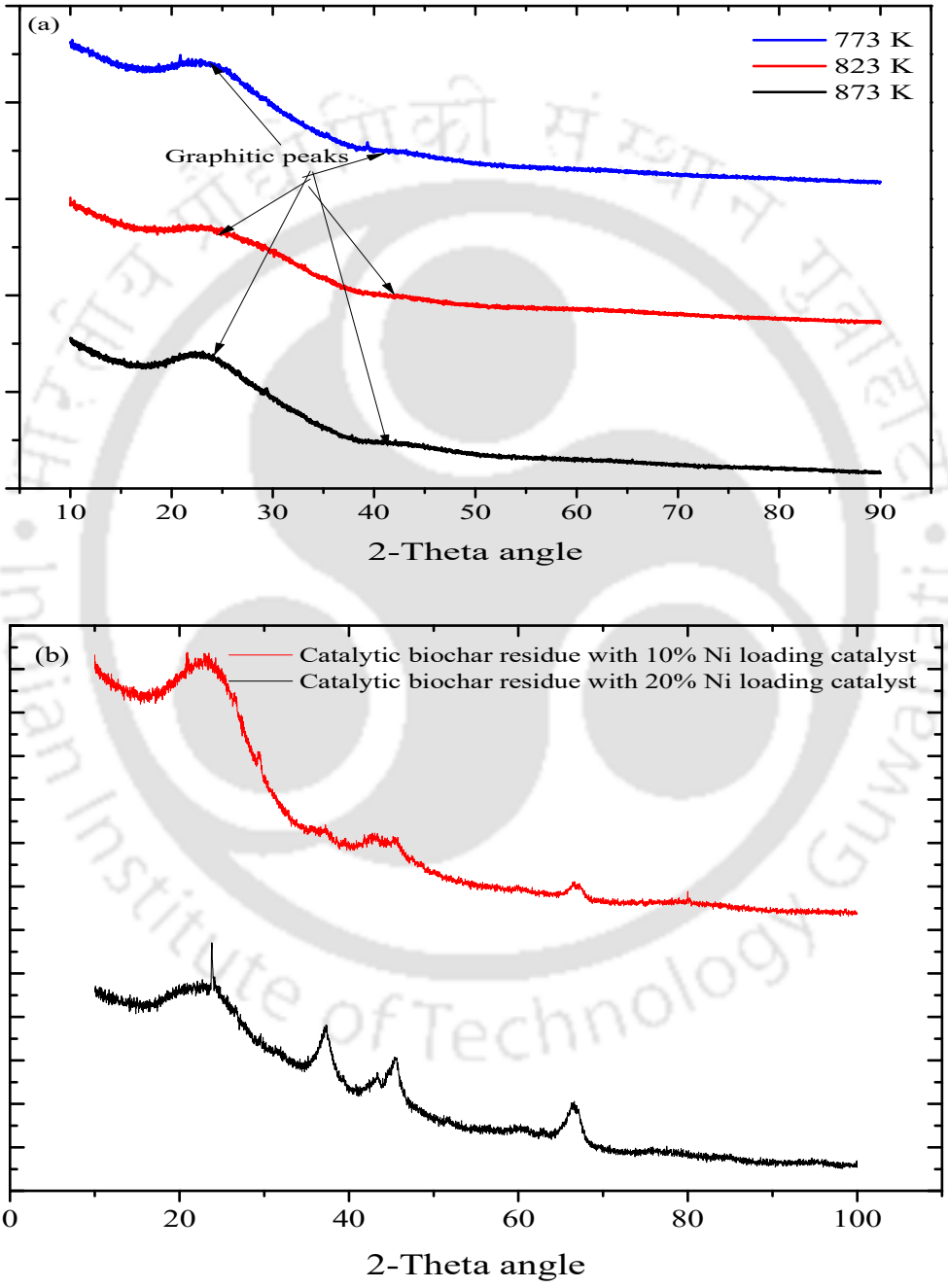

Fig. 7.8 XRD diffractogram of biochar produced during (a) thermal pyrolysis of sawdust and (b) catalytic pyrolysis of sawdust at 873 K

7.4.2.2.5 FTIR analysis of the biochar

FTIR analysis of the pyrolyzed thermal and catalytic biochar residues at 773 K, 823 K and 873 K is given in Fig. 7.9 (a, b). As shown in Fig. 7.9 (a), a small sharp peak at 1627 cm^{-1} wavenumber represents an aromatic ring in the pyrolyzed thermal biochar residue produced at 773 K and 823 K, while there was no representation of peaks for biochar produced at 873 K reaction temperature. The small broad peak at 1300 cm^{-1} wavenumber represents C-N stretching, while several small peaks at 800 cm^{-1} wavenumbers manifest a polycyclic aromatic skeleton. The absence of O-H groups indicates that there were no hydroxyl groups in the samples. Even the biochar residue samples were devoid of C=O stretching, C-O stretching and S-O stretching due to the high-temperature effect. However, aromaticity increased with an increase in pyrolysis temperature. Due to the rate of loss of long-chain aliphatic groups due to homolytic dissociation, thermal breaking of C-C and C-H bonds, and formation of more stable hydrocarbons as seen from FTIR spectra, carbon content increased in the biochar residue samples. Fig. 7.9 (b) represents the FTIR spectra of catalytic biochar residues with 10 % and 20 % Ni loading catalysts. At wavenumber 757 cm^{-1}, cis CH out-of-plane bend was observed for both the catalytic char residues with 10 % and 20 % Ni loading, and at 1175 cm^{-1} wavenumber, aromatic CH in-plane bend was formed. However, C=C-C aromatic ring stretch and cis/trans CH stretch was found at wavenumber 1783 cm^{-1} and 3024 cm^{-1} respectively for biochar residue with 20 % Ni loading catalyst.

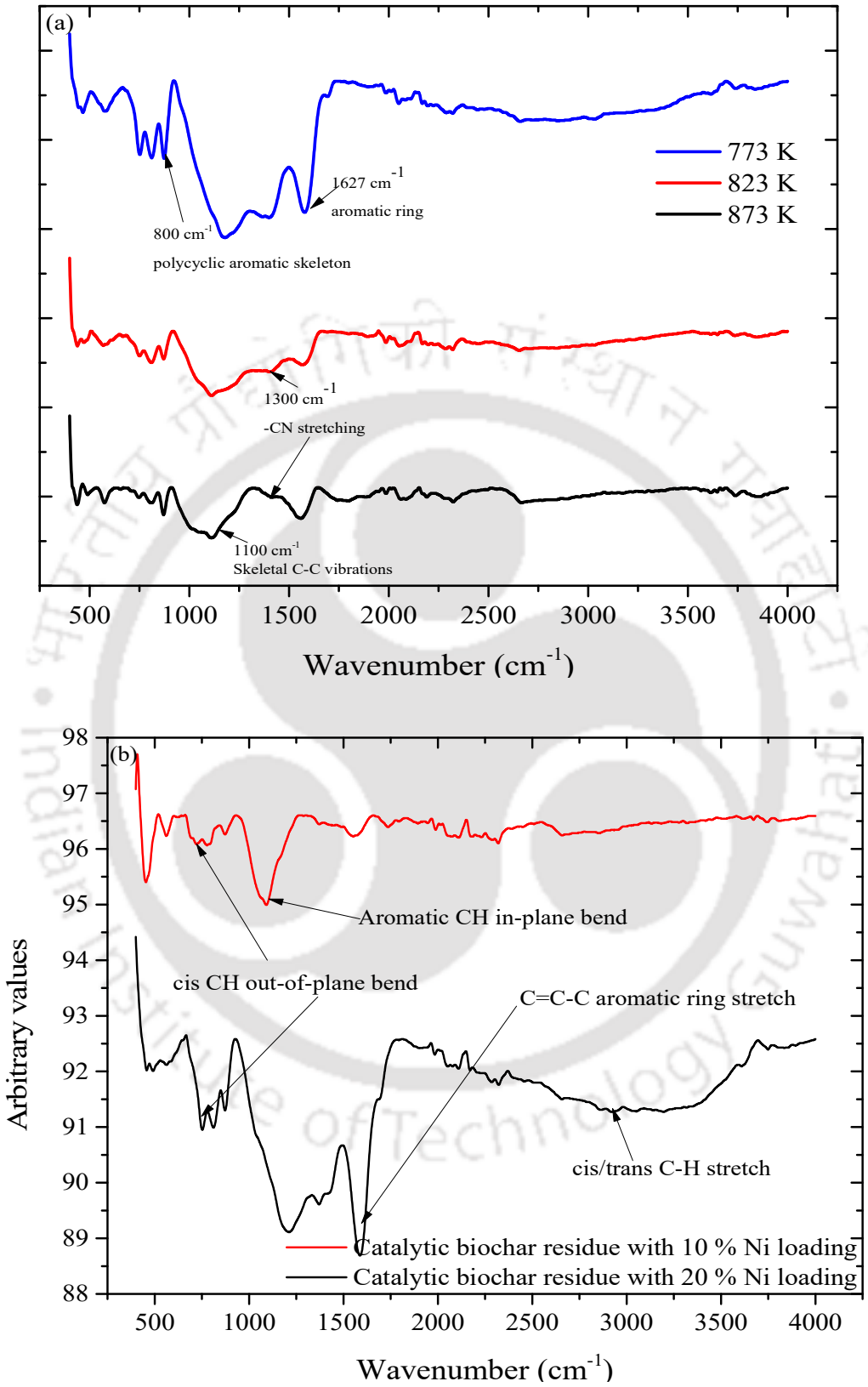

Fig. 7.9 FTIR spectra of biochar produced during (a) thermal pyrolysis of sawdust and (b) catalytic pyrolysis of sawdust at 873 K

7.4.2.2.6 ESR analysis of the biochar

ESR analysis of the thermal and catalytic chars at 773 K, 823 K, and 873 K is given in Fig. 7.10 (a, b). It was observed that the ESR spectra (first derivative of the absorbed microwave signal) are highly intense in the case of thermal biochar residue because of the presence of oxygen free radicals which interacted strongly with the carbon-centered radicals of biochar. A similar case was seen with catalytic biochar residues where the ESR signal was higher in catalytic residues with 10 % Ni loading.

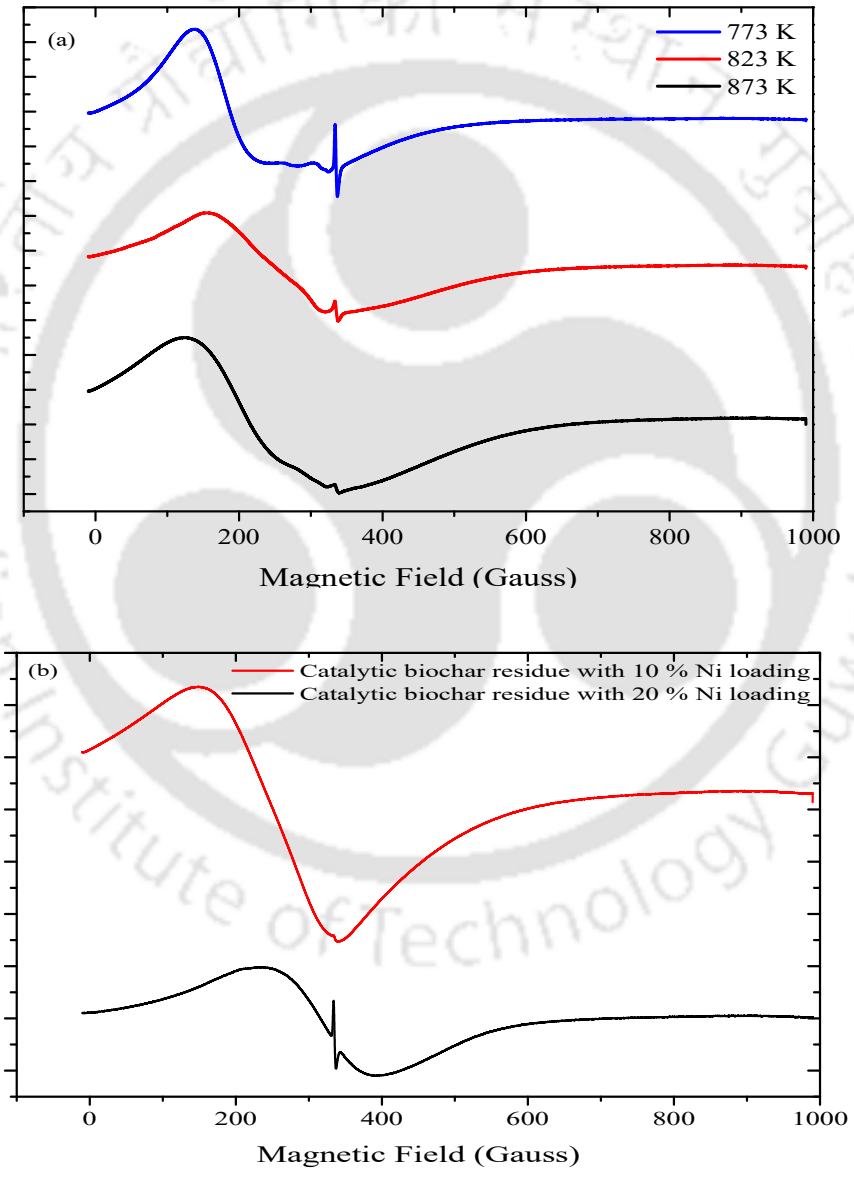

Fig. 7.10 ESR spectra of biochar produced during (a) thermal pyrolysis of sawdust and (b) catalytic pyrolysis of sawdust at 873 K

7.4.2.3 Fuel gas analysis

Pyrolysis gases consist of a mixture of CO, CO_2, CH_4, and H_2. In thermal pyrolysis, CO_2 and CO are the major components of a gaseous mixture with the presence of H_2 and CH_4 in comparatively lesser proportion. The decomposition of carbonyl and carboxylic group compounds releases CO and CO_2 whereas, the cracking of methoxy and aromatic groups at higher temperatures results in the generation of H_2 and CH_4 gases *(Gupta and Mondal, 2021).* Further, the inclusion of catalysts in biomass pyrolytic systems at higher temperatures decreases the CO_2 content in the pyrolytic gas and increases the H_2 and CH_4 content due to reverse water-gas shift reactions and methane disproportionation (Sabatier reaction). Bio-oil deoxygenation contributes to the formation of CO and CO_2. This is accountable due to the metal active sites in the catalyst along with its Lewis acidic sites which have a higher oxygen removal potential by generating more hydrocarbons in bio-oil along with the evolution of a substantial amount of H_2 gas. As observed in Fig. 7.11 (a), hydrogen content in the pyrolytic gas increased from 2.719-14.3 % from 773-873 K temperature. However, with the catalytic reforming of pyrolytic fuel gas with NiO on aluminate composite catalysts, hydrogen evolution was 6.208–5.612 % at 10 % and 20 % Ni-loaded catalysts at reaction temperature 873 K as observed in Fig. 7.11 (b). In comparison to the present study, tar conversion and vapor gas upgrading via in situ catalysis using silica-based nickel nanoparticles embedded in rice husk char for biomass pyrolysis were studied by Shen et al. *(Shen and Yoshikawa, 2014).* In another study, Yue et al. worked on catalytic pyrolysis of corn cob by using a Ni/Ca bifunctional catalyst. Ni/Ca bifunctional catalysts were synthesized using citric acid as a complexing agent in combination with the sol-gel method and by changing the calcination temperatures to 650ºC, 750ºC, 850ºC and 950ºC, the obtained catalysts were denoted as Ni_1Ca_7-650, Ni_1Ca_7-850, and Ni_1Ca_7-950, respectively. The Ni_1Ca_7-750 exhibited the best catalytic performance. The total gas volume was increased from 257.47 mL g^{-1} biomass for pure pyrolysis to 661.63 mL g^{-1} biomass for the Ni_1Ca_7-750 catalyst, which increased the total gas volume by 156.97 % due to synergistic interactions between the catalyst and the biomass. It was observed that the H_2 concentration in the pyrolysis gas increased from 11.82 vol. % to 68.62 vol. % with Ni_1Ca_7-750 catalyst. The syngas ratio of Ni_1Ca_7-750 catalyst reached 85.81 vol. % and the large particles of $CaCO_3$ decomposed and the catalyst activity increased for the NiO active phase *(Yue et al., 2023).*

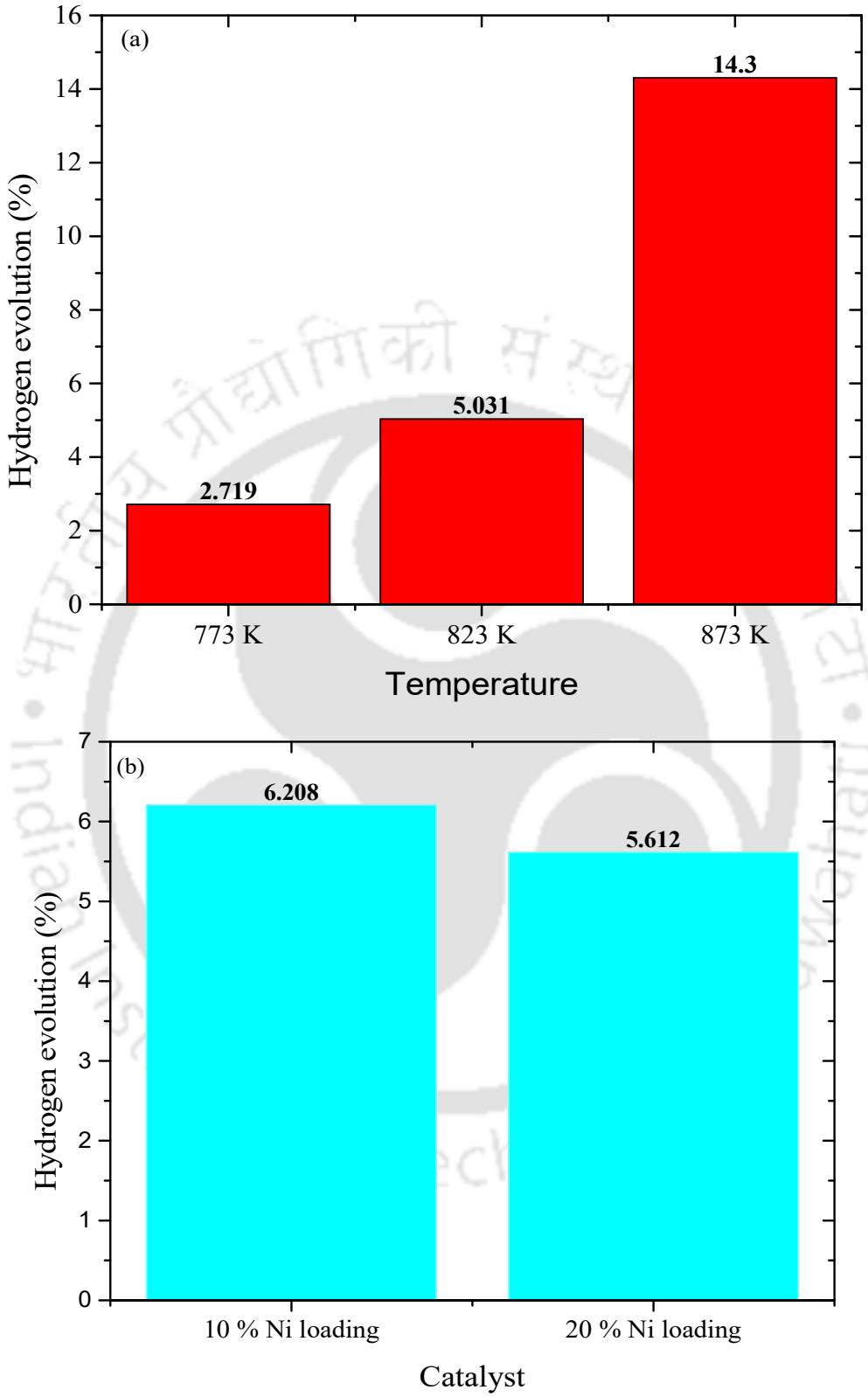

Fig. 7.11 Fuel gas evaluation (a) Effect of temperature and (b) Effect of catalyst on hydrogen gas yield %

7.5 Summary of the chapter

It is concluded that thermal pyrolysis of sawdust leads to a product profile distribution of bio-oil, biochar, and evolved volatile gas as production of a higher yield of bio-oil, less tar yield in the bio-oil content through thermal cracking, production of more evolved volatiles from non-condensable gases and a highly stable porous biochar. With an increase in temperature, bio-oil yield increases while biochar yield decreases. Characterization of liquid pyrolytic products concluded that compounds (C_3–C_{20}) were mainly present in bio-oil with D-Allose, Beta-D-Glucopyranose-1,6-Anhydro, Phosphonic acid, (p-hydroxyphenyl)-, 2-Ethyl-5-Propylcyclopentanone, Phenol, 3-Methyl, Phenol, 2-Methyl and 3-(4,8,12-Trimethyl Tridecyl (Furan) as the prominent compounds and a higher C_p value of 2.000 kJ kg^{-1} K^{-1}. Nickel-based nano-catalysts were designed for the catalytic pyrolysis of sawdust by the wetness impregnation method. This resulted in a higher concentration of 6-Hepten-3-one, 5-Hydroxy-4-Methyl-, phosphonic acid, (p-hydroxyphenyl)- organic compounds in catalytically active bio-oil with slightly decreased C_p values for both 10 % and 20 % NiO/Al_2O_3 catalysts respectively. Biochar revealed amorphous graphitic multilayer nanosheets with polycrystalline and hexagonal crystal system with a porous carbon structure. Carbon content as evaluated from EDS FETEM analysis was 91.78 % in the biochar residue with presence of aromatic ring structures and C-N stretching as evident from FTIR analysis. Biochar produced at higher temperatures was led by higher carbonization, demethanation, and decarboxylation reactions, whereas with an increase in nickel loading in the catalytic char residue, higher demethanation reaction, lesser decarbonization and higher oxidation occurred. The highest yield % of hydrogen in fuel gas was observed to be maximum for pyrolysis of sawdust at 873 K, which indicated that with the increase in temperature, the hydrogen yield % increased.

References

- Chandra, S. and Bhattacharya, J., 2019. Influence of temperature and duration of pyrolysis on the property heterogeneity of rice straw biochar and optimization of pyrolysis conditions for its application in soils. *Journal of Cleaner Production*, *215*, pp.1123-1139.
- Cao, Z., Niu, J., Gu, Y., Zhang, R., Liu, Y. and Luo, L., 2020. Catalytic pyrolysis of rice straw: Screening of various metal salts, metal basic oxide, acidic metal oxide and zeolite catalyst on products yield and characterization. *Journal of Cleaner Production*, *269*, p.122079.
- Murillo, H.A., Díaz-Robles, L.A., Santander, R.E. and Cubillos, F.A., 2021. Conversion of residual biomass into valuable biofuels by co-hydrothermal carbonization for utilization in household pellet stoves. *Biomass and Bioenergy*, *151*, p.106153.
- Wu, L., Xue, X., Yu, H., Zhang, C., Wei, X., Liang, J. and Sun, Y., 2020. Catalytic pyrolysis of poplar sawdust: Excellent hydrocarbon selectivity and activity of hollow zeolites. *Bioresource Technology*, *317*, p.123954.
- Ehrenfest, P., 1933. Phase changes in the ordinary and extended sense classified according to the corresponding singularities of the thermodynamic potential. In *Proc Acad Sci Amsterdam* (Vol. 36, pp. 153-157).
- Del Vigo, E.A., Stortz, C.A. and Marino, C., 2022. D-Allose, a rare sugar. Synthesis of D-allopyranosyl acceptors from glucose, and their regioselectivity in glycosidation reactions. *Organic & Biomolecular Chemistry*, *20*(22), pp.4589-4598.
- Zhang, H., Jiang, M. and Song, F., 2020. D-allose is a critical regulator of inducible plant immunity in tomato. *Physiological and Molecular Plant Pathology*, *111*, p.101507.
- Fan, L., Chen, P., Zhou, N., Liu, S., Zhang, Y., Liu, Y., Wang, Y., Omar, M.M., Peng, P., Addy, M. and Cheng, Y., 2018. In-situ and ex-situ catalytic upgrading of vapors from microwave-assisted pyrolysis of lignin. *Bioresource technology*, *247*, pp.851-858.
- Yi, L., Liu, H., Li, S., Li, M., Wang, G., Man, G. and Yao, H., 2019. Catalytic pyrolysis of biomass wastes over Org-CaO/Nano-ZSM-5 to produce aromatics: Influence of catalyst properties. *Bioresource technology*, *294*, p.122186.

- Mattsson, C., Andersson, S.I., Belkheiri, T., Åmand, L.E., Olausson, L., Vamling, L. and Theliander, H., 2016. Using 2D NMR to characterize the structure of the low and high molecular weight fractions of bio-oil obtained from LignoBoost™ kraft lignin depolymerized in subcritical water. *Biomass and bioenergy*, *95*, pp.364-377.
- Liu, W.J., Jiang, H. and Yu, H.Q., 2015. Development of biochar-based functional materials: toward a sustainable platform carbon material. Chemical reviews, 115(22), pp.12251-12285.
- Gupta, S. and Mondal, P., 2021. Catalytic pyrolysis of pine needles with nickel doped gamma-alumina: reaction kinetics, mechanism, thermodynamics and products analysis. *Journal of Cleaner Production*, *286*, p.124930.
- Shen, Y. and Yoshikawa, K., 2014. Tar conversion and vapor upgrading via in situ catalysis using silica-based nickel nanoparticles embedded in rice husk char for biomass pyrolysis/gasification. *Industrial & Engineering Chemistry Research*, *53*(27), pp.10929-10942.
- Yue, W., Ma, X., Yu, Z., Liu, H., Li, M. and Lu, X., 2023. Ni-CaO bifunctional catalyst for biomass catalytic pyrolysis to produce hydrogen-rich gas. *Journal of Analytical and Applied Pyrolysis*, *169*, p.105872.

Chapter VIII

Studies on Thermal and Catalytic Co-pyrolysis of Coal/Biomass Blends

8.1 Introduction

Based on the formulation described in chapters 5 and 6, the results in the experimental validation of thermal (non-catalytic) pyrolysis of coal and co-pyrolysis of coal-sawdust blends are explained. Catalytic co-pyrolysis of blends in the presence of 10 % and 20 % NiO and Ni (II) aluminates nano-composite catalyst is elucidated in this chapter, further substantiated with detailed product analysis and characterization.

8.2 Experimental validation

Coal and coal-sawdust blends were integrated into a fixed-bed reactor and assessed for product profile distribution and analysis from a temperature range of 773 K, 823 K and 873 K at 30 K min^{-1} heating rate under nitrogen purge gas (300 mL min^{-1}). The evolved gas was condensed in a glass condenser and the liquid oil with tar was collected in a separating funnel. The condenser water temperature was maintained at 280 – 283 K. The char residue was collected at the end of the experiment for further analysis and characterization. The optimized condition evaluated for thermal co-pyrolysis was similarly performed for 50 % and 200 % blend co-pyrolysis and the products were characterized. Catalytic upgradation experiments on product liquid oil, thermal and catalytic char residue, and evolved gas were evaluated by integrating in-situ 10 % and 20 % NiO and Ni (II) aluminates nanocomposite catalyst with coal-sawdust blends in an alumina crucible.

8.3 Highlights of the chapter

- Coal pyrolysis revealed negligible liquid oil generation with maximum coal char generation and very little evolved volatiles gas product. Char residue revealed that graphitic multilayer sheets were formed with 70.28 % carbon with hexagonal single-crystal lattice structures.
- In thermal co-pyrolysis of coal and 100 % sawdust blend, with an increase in temperature from 773–873 K, liquid oil yield increased while biochar yield decreased significantly.
- At a coal-sawdust blending ratio of 50 %, 100 % and 200 %, the conversion, wt. % increased from 27.97 % and 37.35 % to a significant rise of 92.8 % respectively.
- From liquid oil produced from co-pyrolysis of blends, it was observed that D-Allose is the prominent compound present along with Beta-D-Glucopyranose-1,6-Anhydro with a remarkable C_p value of 5.300 kJ kg^{-1} K^{-1} pyrolyzed at 823 K reaction temperature.

- Char residue from thermal co-pyrolysis of coal-sawdust blends revealed multilayer graphitic layers sheet-like structures and nano-rod-like structures with distinct single crystalline SAED patterns.
- A significant comparative study was done on thermal and catalytic co-pyrolysis of coal-sawdust blend via metal-induced active site bonded 10 % and 20 % NiO/Al_2O_3 nano-catalyst.
- In catalytic co-pyrolysis of blends, with the effect of 10 % and 20 % NiO/Al_2O_3 nano-catalyst, oil yield decreased whereas gas yield increased for 10% NiO/Al_2O_3 nano-catalyst.
- Catalytic upgradation of liquid oil from catalytic co-pyrolysis of 100 % and 200 % blends using 10 % and 20 % NiO/Al_2O_3 nano-catalyst resulted in phosphonic acid, (p-hydroxyphenyl)- and 6-Hepten-3-one, 5-Hydroxy-4-Methyl- as the candidate compounds with slightly decreased C_p values of 0.150 kJ kg^{-1} K^{-1} and 0.345 kJ kg^{-1} K^{-1} respectively due to catalytic tar cracking of polyaromatic hydrocarbons present in the 100 % blend-oil. C_p values of 0.573 kJ kg^{-1} K^{-1} and 0.602 kJ kg^{-1} K^{-1} respectively due to catalytic tar cracking of polyaromatic hydrocarbons present in the 200 % blend-oil with 10 % and 20 % NiO/Al_2O_3 nano-catalyst.

8.4 Thermal pyrolysis of coal

This study imbibes the pyrolysis of low-grade coal in a fixed-bed reactor unit at temperatures, 773 K, 823 K and 873 K at 30 K min^{-1} heating rate under nitrogen as purge gas (flow rate: 18 L h^{-1}). Priorly, when thermal degradation analysis of coal was done, it indicated very little mass loss due to its high ash and less volatile matter. This was the reason for the higher thermal stability of the coal which required higher temperatures for its thermal breakdown. To study the pyrolytic behavior of coal experimentally, a fixed-bed reactor unit was implemented in the study with a 2700 mL volume capacity. The product distribution profile at temperatures, 773 K, 823 K and 873 K was evaluated intensively with its detailed product characterization and analysis in Sections 8.4.1 and 8.4.2.

8.4.1 Effect of pyrolysis temperature on the product distribution profile

The variance of temperature was a candidate factor in the design of thermal experiments for coal pyrolysis. The distribution of pyrolysis products (evolved non-condensable gas and coal char as co-product) from thermal pyrolysis of coal is shown in Table 8.1. The effect of temperature (773 K, 823 K and 873 K) on the pyrolytic product distribution profile heavily relies on the degree of its optimization. As seen in Table 8.1 with an increase in temperature

from 773 – 873 K, coal char yield decreased, while gas yield increased slightly. The gas yield % was much lesser in comparison to char yield %. There was no observation of liquid oil production in coal pyrolysis. Henceforth, the estimation of conversion in terms of liquid oil product and evolved gas was negligible.

Table 8.1 Product profile distribution of coal pyrolysis based on temperature variance from 773-873 K

Temperature (K)	Char, wt. (yield %)	Volatile gas, wt. (yield %)
773	97.8	2.2
823	98.68	1.32
873	97.67	2.33

8.4.2 Product characterization

The physicochemical characteristics of the derived coal char structure as a co-product were vividly studied. Surface morphological structure, presence of functional groups, and determination of free radicals were some such attributes. Further, the concentration of the individual gas components in the fuel gas was comprehensively studied with prominence in hydrogen evaluation.

8.4.2.1 Characterization of coal char

8.4.2.1.1 Composition of coal char

As given in Table 8.2, the ultimate analysis of coal char from thermal pyrolysis of coal is explained. The ultimate analysis determined the carbon content, hydrogen content, sulfur content, nitrogen content, and oxygen content (by difference). The carbon content of char increased with an increase in pyrolysis temperature from 773-873 K, decreasing the oxygen content with negligible hydrogen content. This was due to more release of hydrocarbons, CO_2, and CO greenhouse gases at higher temperatures. Due to the acute severage of C-C linkages, rather than the C-H linkages in the intricate aromatic structure of coal (Haber's rule) and consequent oxidation reactions, this was accountable. There was negligible sulfur content for coal char produced at 773 K. However, the atomic O/C ratio decreases with an increase in temperature.

Table 8.2 Ultimate analysis of coal char residue from thermal pyrolysis of coal

Temperature (K)	C (%)	H (%)	S (%)	N (%)	O (%)	H/C	O/C
773	58.143	-	-	0.689	41.168	-	0.531
823	59.027	-	0.924	0.741	39.308	-	0.499
873	60.397	-	0.873	0.663	38.067	-	0.472

(C %: Carbon content, H %: Hydrogen content, S %: Sulphur content, N %: Nitrogen content, O %: Oxygen content)

8.4.2.1.2 XRD analysis of coal char

XRD diffractogram of pyrolytic coal char produced at temperatures, 773 K, 823 K and 873 K is shown in Fig. 8.1. It showed a sharp peak at 26.54° of 2-theta diffraction angle and several small peaks at 21.23°, 42.36° and 50.70° of 2-theta diffraction angle at the three reaction temperatures, 773 K, 823 K and 873 K. PDF Card No.: 00-056-0159 Quality: S was reported for coal char indicating graphitic peak with a hexagonal crystal structure with a space group of P63/MMC (194). The values of cell parameters which are a, b and c equals 2.4617, 2.4617 and 6.7106 and α, β and γ are 90, 90 and 120 respectively. The volume is 35.218 cm^3 g^{-1} and Z parameter is 4. The (h, k, l) parameters are (0, 0, 2) at 26.54° of 2- theta diffraction angle, (1, 0, 0) at 42.36° of 2- theta diffraction angle and (1, 0, 2) at 50.70° of 2-theta diffraction angle.

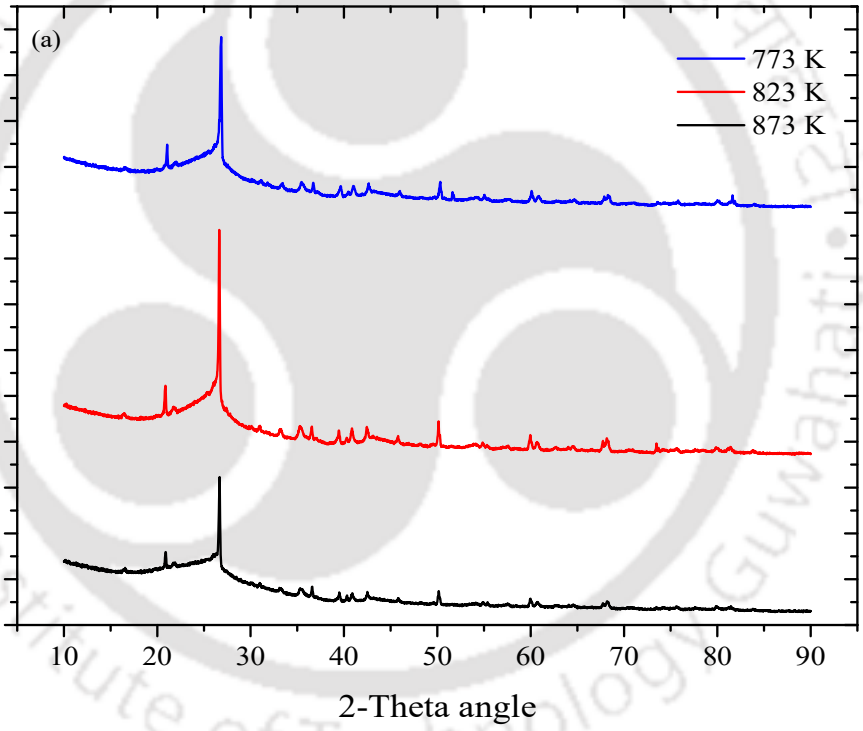

Fig. 8.1 XRD diffractogram of coal char residue

8.4.2.1.3 FESEM analysis of coal char

FESEM analysis of coal char residue produced at 873 K reaction temperature is depicted in Fig. 8.2. It shows its morphological and topological microstructure image at a magnification of 1.0 KX, 5.0 KX and 10.0 KX. Fractal apertures in the char particle increased as compared to raw coal particle as shown in Fig. 4.2 in Chapter 4. Cell pores encased within

such fractures get enlarged and the thickness of the cell walls become thinner. Few smaller porous structures were seen indicating simultaneous evolution of volatiles gases (CO_2, CO, CH_4, C_2H_6) with pore diameters of 0.93 µm and 0.86 µm. This reflects that the pore structure of coal char particles is directly linked to porosity and mean pore diameter *(Li et al., 2022)*. Prior works by Wedlar et al. revealed that with the increase in pyrolysis temperature, mesopores dominate the micropores in the evolution of char particles *(Wedlar et al., 2020)*. Odeh reported that diffusion of oxygen within coal char particles affects the rate of char burning and hence change in char morphology (Odeh, 2015). Solum et al. revealed that the eventual removal of oxygen functional groups in coal leads to the structural modification of aromatic clusters to a densely packed structure further decreasing its pore surface area *(Solum, Pugmire, Jagtoyen, & Derbyshire, 1995)*.

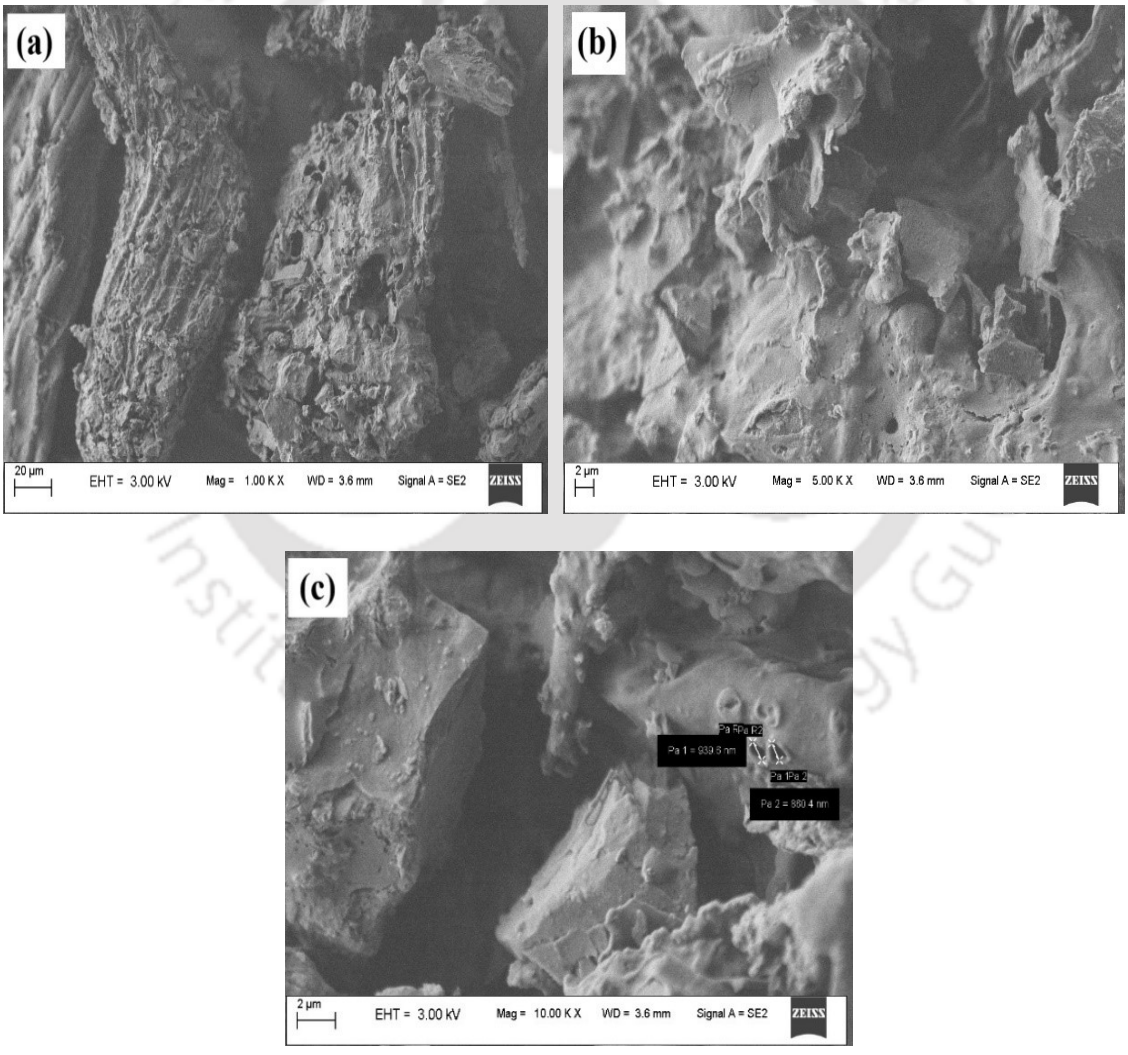

Fig. 8.2 FESEM images of coal char at magnification (a) 1.0 KX, (b) 5.0 KX, (c) 10.0 KX

8.4.2.1.4 FETEM analysis of coal char

FETEM analysis of coal char is shown in Fig. 8.3 where FETEM microstructure images are shown in Fig. 8.3 (a) and (c) and their respective SAED (selected area electron diffraction pattern) in Fig. 8.3 (b) and (d). Fig. 8.2 (a) denotes graphitic multilayer arrays of the coal char sample at a magnification of 200 nm. Fig. 8.3 (b) shows it as a single crystal with a hexagonal lattice crystal system. Fig. 8.3 (c) denotes the hexagonal ring structure of the char sample at 100 nm magnification with a SAED pattern constituting an intercalation of a single crystal embedded in the polycrystalline matrix.

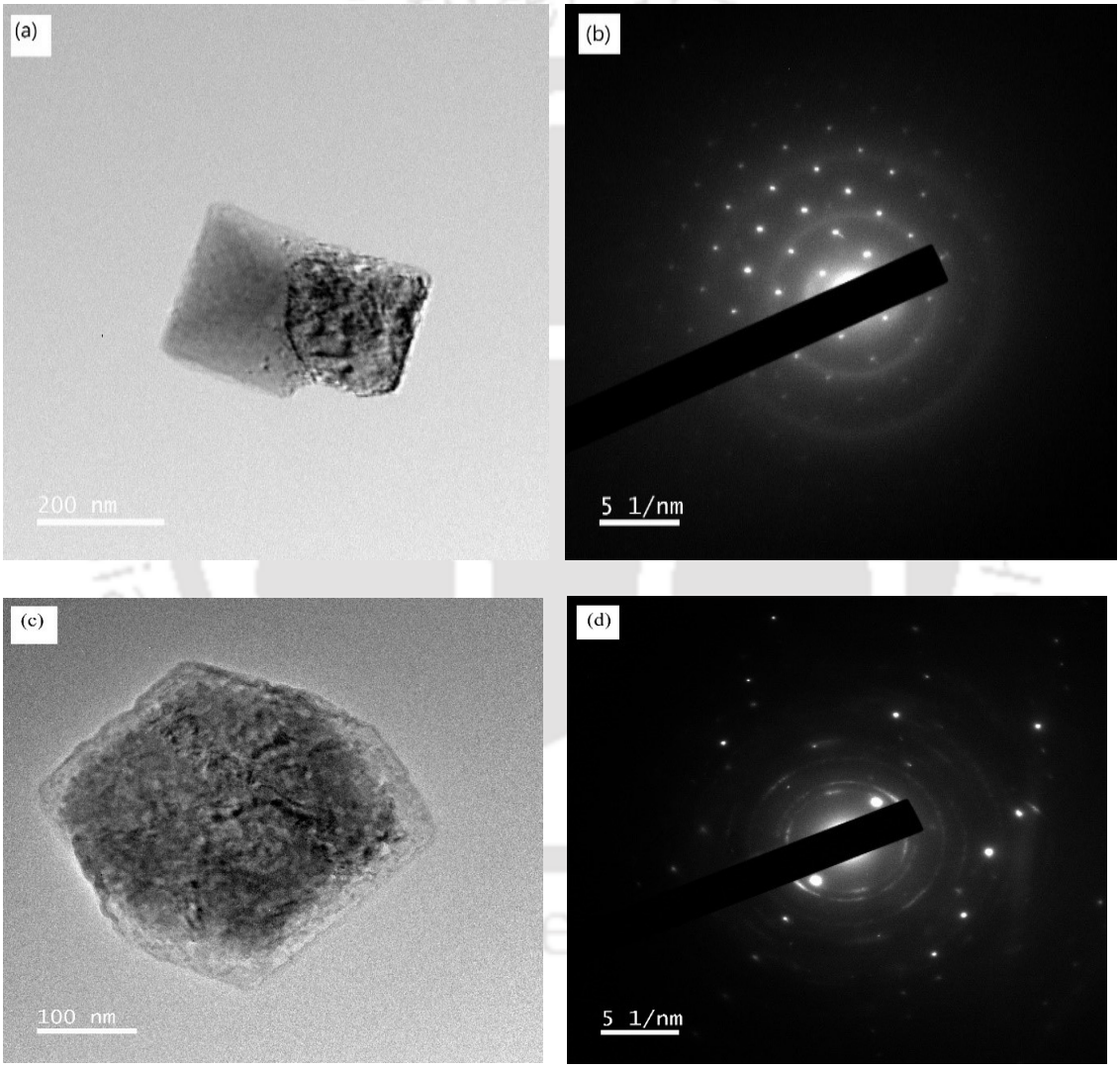

Fig. 8.3 FETEM images of coal char at magnification (a) 200 nm and (b) SAED Pattern (c) 100 nm and (d) SAED pattern

EDS FETEM analysis of coal char residue produced at 873 K reaction temperature is given in Table 8.3 with elemental weight (%) and atomic (%) as the measured values. Carbon

content was highest in coal char with 70.11 %, iron content was 10.82 %, the oxygen content was 9.65 %, silica content was 2.94 %, magnesium content was 2.72 %, aluminum was 1.33 %, potassium content was 0.80 %, sulfur content was 0.49 %, bromine content was 0.33 %, calcium content was 0.29 %, manganese content was 0.17 %, phosphorus content was 0.13 %, chromium content was 0.10, titanium content was 0.07 % and chlorine content was 0.0%.

Table 8.3 Elemental weight (%) and atomic (%) of coal char by EDS FETEM analysis

Element	**C, %**	**Fe, %**	**O, %**	**Si, %**	**Mg, %**	**Al, %**	**K, %**	**S, %**	**Br, %**	**Ca, %**	**Mn, %**	**P, %**	**Cr, %**	**Ti, %**	**Cl, %**
Elemental weight (%)	70.11	10.8	9.65	2.94	2.72	1.33	0.80	0.49	0.33	0.29	0.17	0.13	0.10	0.07	0.05
Atomic (%)	83.88	2.78	8.66	1.50	1.61	0.71	0.29	0.22	0.06	0.11	0.05	0.06	0.03	0.02	0.02

8.4.2.1.5 FTIR analysis of coal char

FTIR analysis of pyrolyzed coal char produced at three different temperatures, 773 K, 823 K and 873 K is explained in Fig. 8.4. FTIR spectra of coal char samples are plotted for determination of functional groups at wavenumber (cm^{-1}) with its transmittance % in intensity (a.u). It is seen that with an increase in pyrolysis temperature (773–873 K), the intensities of the respective peaks of the coal char samples increase. Two small peaks were perceived at 2918 cm^{-1} and 2575 cm^{-1} indicating aliphatic C-H and asymmetric Ar-CH_3 stretching and S-H stretching. However, a small sharp peak was indicated at 1720 cm^{-1} imbuing carbonyl group (C=O group) cleavage. Another small peak with less intensity was observed at 1300 cm^{-1} wavenumber indicating C-N stretching. This indicates the presence of heterocyclic CN char form. However, a strong and intense broad peak was observed at 1073 cm^{-1} wavenumber indicating C-O-C bonded groups. However, with the absence of the -OH group, it showed negligible hydrogen content in the coal such that a dehydration reaction took place during pyrolysis.

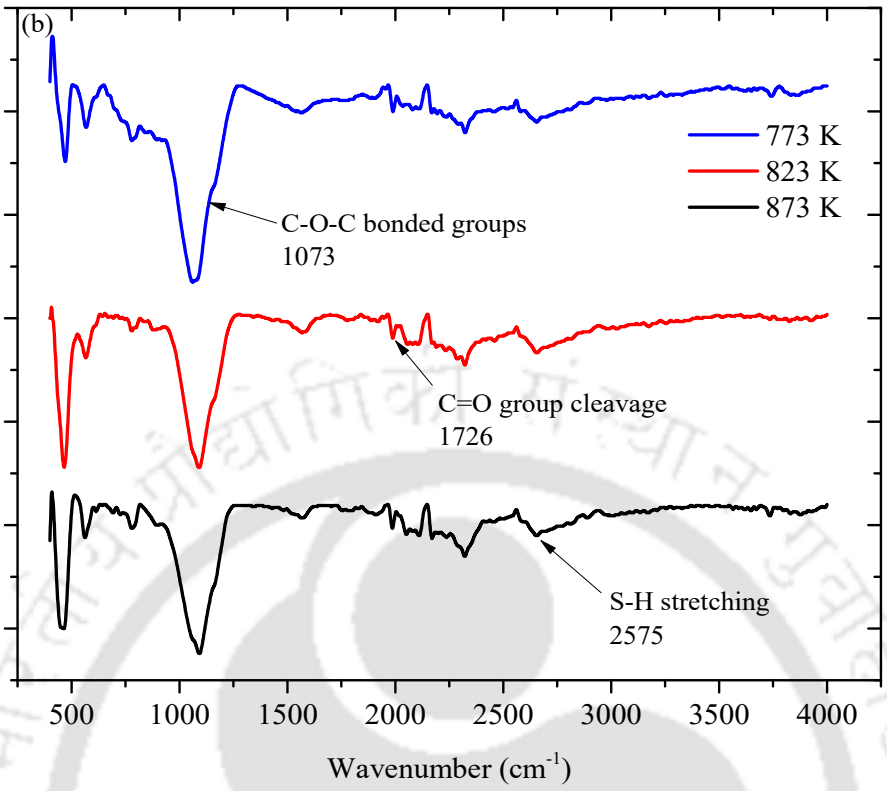

Fig. 8.4 FTIR spectra of coal char

8.4.2.2 Fuel gas analysis

Fuel gas analysis from coal pyrolysis revealed the release of carbon mono-oxide (CO), NO_x, SO_x, NO, hydrocarbons in ppm levels whereas carbon dioxide (CO_2), hydrogen (H_2), and oxygen (O_2) in percentage (%) concentration. For an increasing trend in pyrolysis temperature: 773 K, 823 K and 873 K, it revealed significant outcomes for each volatile gas component at subsequent residence time. It was observed in Table 8.4 that with the increase in pyrolysis temperature, H_2 yield and CO_2 levels increased significantly whereas O_2 levels decreased at subsequent residence time. However it was observed that concentration of CO increased with the increase in pyrolysis temperature from 773-873 K at each final residence time. A remarkable observation was the higher concentration of hydrocarbons (CH_4, C_2H_6) in the fuel gas exceeding >1500 ppm level. The concentration of hydrocarbons increased linearly with increase in temperature (773-873 K). The concentration of SO_x decreased at subsequent residence times at 773 K pyrolysis temperature, whereas higher temperatures showed negligible SO_x levels. Similarly, NO_x and NO levels were negligible at the given temperature conditions.

Table 8.4 Concentration of gas components in (%) and ppm levels in the fuel gas from coal pyrolysis under N_2 inert gas at residence time of 300, 900 and 1800 s

Gas component	773 K			823 K			873 K		
	300 s	900 s	1800 s	300 s	900 s	1800 s	300 s	900 s	1800 s
H_2 (%)	0.169	0.015	0.005	0.189	0.107	0.270	0.421	0.288	0.041
CO_2 (%)	1.16	1.1	1.09	1.48	1.45	1.16	2.84	1.76	1.54
O_2 (%)	19.32	19.01	19.62	18.33	18.48	19.41	13.75	14	14.21
CO (ppm)	67	36	24	115	49	27	674	902	800
NO (ppm)	-	-	-	-	-	-	1	-	-
NO_x (ppm)	-	-	-	-	-	-	1	-	-
SO_x (ppm)	23	5	4	-	-	-	40	-	-
HC (ppm)	41	122	201	155	173	200	1314	1066	1662

8.5 Thermal co-pyrolysis of coal/sawdust blends

This study incorporates coal and sawdust as potential feed sources for thermal co-pyrolysis process. The effect of pyrolysis temperature (773–873 K) on product distribution profile was studied in a fixed-bed reactor unit for 100 % blend at 30 K min^{-1} heating rate under nitrogen (18 L h^{-1}) as purge gas as given in Section 8.5.1. The derived liquid oil product, char residue and evolved volatile gas were evaluated for detailed product characterization as given in Section 8.5.2. Further the studies on the effect of feedstock composition (50 % and 200 % biomass blending) on the product distribution profile was studied at the optimized temperature condition was analysed in Section 8.5.3. Subsequent product characterizations were done as given in Section 8.5.4.

8.5.1 Effect of pyrolysis temperature on the product distribution profile

Table 8.5 shows the product distribution profile of co-pyrolysis of coal-sawdust blend (100% sawdust blending with coal) at 773–873 K temperature. With a rise in temperature of 773 K, 823 K and 873 K, it yielded an increase in (oil + tar) yield, decrease in char yield and gas yield respectively. Oil yield was maximum at 873 K temperature along with conversion %. Previous literatures suggest on the effect of pyrolysis temperature on the product distribution profile of co-pyrolysis of blends. Wu et al. worked on cellulose, hemicellulose, lignin, wheat straw and lignite coal in a drop-tube furnace from 600-1000ºC *(Wu et al., 2019).* They suggested that positive synergistic effect on the component of H_2 was seen from 873-1073 K for all the feeds and negative synergistic effects were observed at even higher temperatures. For the component of CO, positive synergy was seen at 600ºC and 700ºC,

whereas at higher temperatures negative synergy was seen. One significant finding was that of HHV value, 17.74 MJN m^{-3} was highest at 626ºC as compared to HHV values at higher temperatures. Nyoni et al. worked on low-grade bituminous coal and algal biomass and reported on kiln temperature on the yield of resultant oils at a final temperature of 800ºC at heating rates of 50, 100 and 200ºC min^{-1} in a rotary kiln unit *(Nyoni et al., 2023).* For coal pyrolysis, resultant oils containing long chain paraffins (52.6 %) ranging from dodecane to heneicosane and presence of polyaromatic hydrocarbons (31.7 %) was effectuated at 550ºC. However, yield of oil from this process was quite low 6.9 %. Therefore, with the pyrolysis of algae and co-pyrolysis of coal-algae blends, resulted in higher yields of oil, which increased with the increase in pyrolysis temperature till 550ºC. These studies thus substantiate the fact that a temperature range between 823-873 K is most effective for higher yields of oils and conversion, wt.% with higher gas yields.

Table 8.5 Effect of reaction temperature on the product distribution profile of thermal co-pyrolysis of coal and 100 % sawdust blend

Temperature (K)	Oil, wt. %	Char residue, wt. %	Gas, wt. %	Conversion, wt. %
773	16.45	63.75	19.79	36.24
823	17.11	63.62	19.27	36.38
873	19.19	62.65	18.16	37.35

8.5.2 Product characterization

8.5.2.1 Characterization of liquid oil product

8.5.2.1.1 FTIR analysis of liquid oil

The FTIR analysis of the liquid oil product samples produced at different temperatures, 773K, 823 K and 873 K from co-pyrolysis of coal and 100% sawdust blend is denoted in Fig. 8.5. The FTIR spectra of transmittance % with wavenumber (cm^{-1}) was plotted on X-axes and Y axes respectively. As shown in Fig. 8.5, the intensity of a sharp broad peak in transmittance % was perceived at 3348 cm^{-1} which was due to O-H stretching (hydroxyl radical) inherent in the H_2O molecules of the oil product. A broad less intense peak is seen at 2110 cm^{-1} wavenumber due to C=C stretching. A sharp intense peak was observed in 1652 cm^{-1} due to C=O stretching, whereas small moderate peaks indicating C-O stretching was seen at 1290 cm^{-1} and 1052 cm^{-1} wavenumbers respectively due to both carbonyl and carboxyl functional groups. A small peak indicating O-H bending is seen at 1402 cm^{-1} wavenumber whereas a small peak is seen at 1290 cm^{-1} wavenumber indicating C-O

stretching. The peak at 1000 cm^{-1} wavenumber also indicated S-O stretching due to the presence of thiol groups (sulfonated compounds) in the liquid oil samples. A sharp peak with significant intensity was observed in a lower range wavenumber of 610 cm^{-1} indicating C-Cl stretching due to the presence of chlorinated compounds in the oil samples.

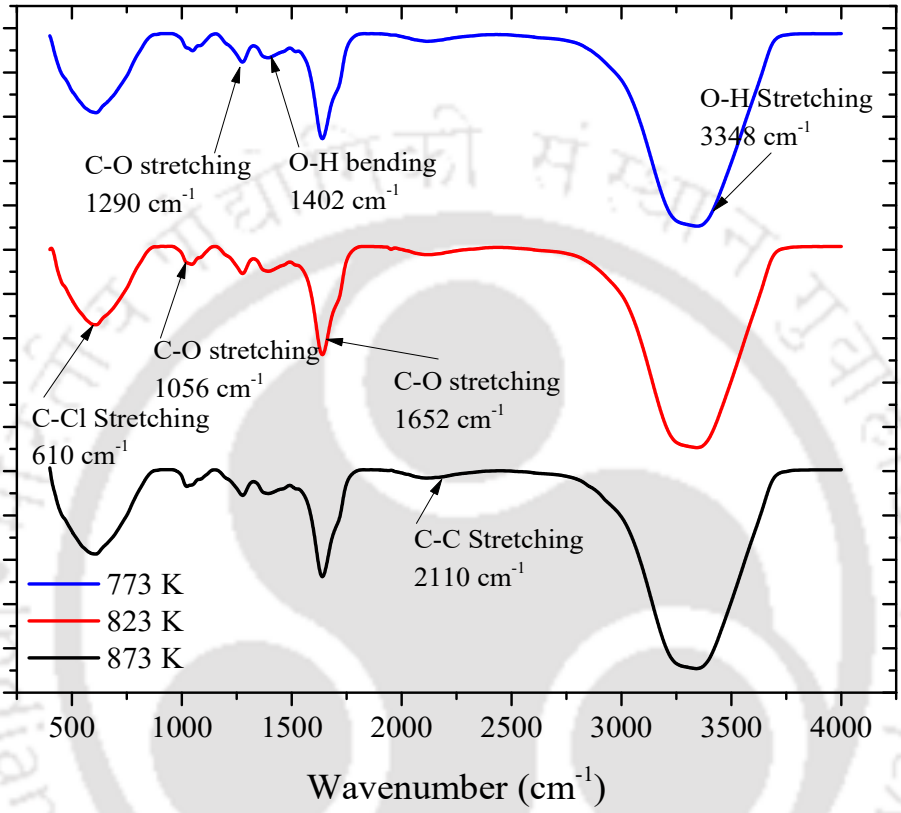

Fig. 8.5 FTIR spectra of liquid oil from co-pyrolysis of coal and 100 % sawdust blend

8.5.2.1.2 DSC analysis of liquid oil

The liquid oil samples from thermal co-pyrolysis of coal and 100 % sawdust blend at reaction temperatures, 773 K, 823 K and 873 K was subjected to differential scanning calorimetry (DSC) analysis as mentioned in Fig. 8.6. The various features of liquid oil such as glass transition temperature - melting temperature (peak temperature), specific heat capacity *(C_p),* heat flow characteristics, heat of fusion, fast purity determination can be determined at constant heating rates for a DSC analysis as mentioned in Table 8.6. Kinetic evaluation of the co-pyrolysis of coal and 100 % sawdust blend reaction such as cure, thermal and oxidative thermo-degradation is feasible which can be assessed for further investigation. Fig. 8.6 indicates an exotherm of heat flowing out of the liquid samples. With the increase in temperature for thermal co-pyrolysis of coal and 100 % sawdust blend from 773-873 K, heat

flow characteristics increased from -21.72 to -29.33 mW mg^{-1}, indicating higher heat flow out for oil sample at 873 K reaction temperature. With the increase in rise in temperature, phase transition exhibited in the oil samples along with various first-order derivative transitions (melting, evaporation, sublimation, crystal-to-crystal transition) causing a difference in glass transition temperature. A directional heat pathway may cause such transitions in an exponential rise of heat flow until a steady-state condition is achieved which was T_s=411.55 K. The specific heat capacity of the liquid oil samples increased till 1.094 J g^{-1} K^{-1} at 823 K with further decrease to 0.019 J g^{-1} K^{-1} at 873 K. Peak glass transition temperatures indicated that the liquid oil sample pyrolyzed at 773 K temperature ignited faster.

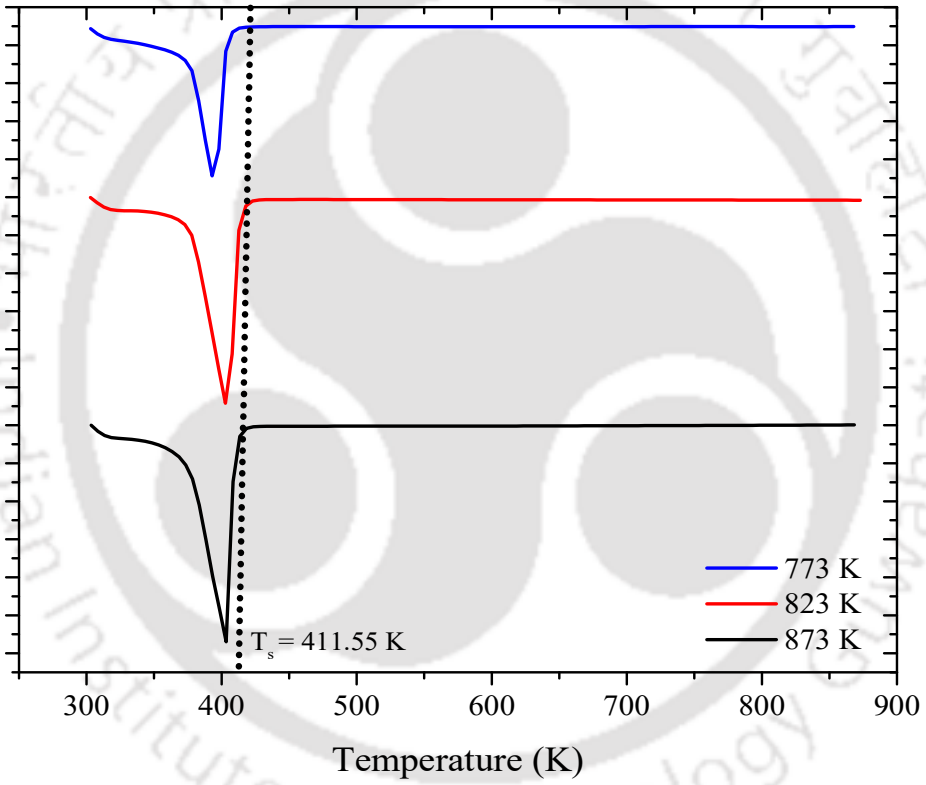

Fig. 8.6 DSC thermogram of liquid oil from co-pyrolysis of coal and 100 % sawdust blend

Table 8.6 Thermal characteristics of liquid oil from co-pyrolysis of 100 % blend

Temperature (K) at which liquid oil was obtained	Glass transition temperature					Γ Cp (J/g. K)	Heat of fusion (J/g)	Specific heat flow (mW/mg)
	Onset temp. (K)	Mid temp. (K)	Inflection temp. (K)	End temp. (K)	Peak temp. (K)			
773	374.05	-	393.45	401.95	395.35	0.827	-1512	-21.72
823	374.15	-	402.45	411.55	405.15	1.094	-2148	-27.8
873	395.15	-	399.55	408.95	402.75	0.019	-2201	-29.33

8.5.2.1.3 GC/MS analysis of liquid oil

Liquid oil product obtained from co-pyrolysis of coal and 100 % sawdust blend at three different reaction temperatures, 773 K, 823 K and 873 K revealed a multifarious range of compounds which is classified according to its chemical formulae, molecular weight, and carbon number *(C_n)* at specific retention times. The peak area % of liquid oil component groups were used to characterize its formation characteristics. An in-depth GC/MS chromatogram analysis of each liquid oil product component identification observed in relation to retention time is listed in Table S6. At the retention time of 22.58 min, it showed the peak area of 7.049 % and 13.644 % of the component D-Allose at temperatures 823 K and 873 K whereas at temperature 773 K, it showed a higher peak area of 30.21 %. As mentioned in Subsection 7.4.2.1.3, D-Allose has wide number of applications. Other compounds found in liquid oil produced at reaction temperature 773 K in abundant quantities were phosphonic acid, (p-hydroxyphenyl)-, 2-ethyl-5-propylcyclopentanone, cyclopentanone, 2-(1-Methylpropyl)-, 1,4:3,6-Dianhydro-Alpha-D-Glucopyranose, 3, 3'- Thiodipropanol, phenol-2-Methyl, phenol-2,6 dimethoxy-, catechol and resorcinol, furan, tetrahydro-2, 5-dimethoxy-, phenol, 2 – methoxy-, carbamic acid, hydroxy-ethyl ester, Hexacosyl acetate, 1,2-Benzenediol, 4-Methyl- and creosol. The compound phosphonic acid, (p-hydroxyphenyl)- shows an antioxidant potential, while 2-ethyl-5-propylcyclopentanone, cyclopentanone, 2-(1-Methylpropyl)- is a cyclic ketone compound. At reaction temperature 823 K, compounds in abundant quantities were Phosphonic acid (p-hydroxyphenyl), 2-Ethyl-5-Propylcyclopentanone, Phenol-2-Methyl, 6-Hepten-3-one, 5-Hydroxy-4-Methyl-, 3 3, 3'-Thiodipropanol, Catechol, Carbamic acid, Hydroxy-ethyl ester, Silacyclopentane (2.582 %), 2 (5H) – Furanone (2.217 %), Phenol, 2 – methoxy- (2.070 %), 1,2-Benzenediol, 4-Methyl- (1.99 %), 6-Hepten-3-one, 5-Hydroxy-4-Methyl- (1.514 %) Octadecane, 2,2,4,15,17,17-Hexamethyl-7, 12- Bis (3, 5,5 -Trimethylhexyl)- (1.244 %), 1,4:3,6-Dianhydro-Alpha-D-

Glucopyranose (1.099 %) and 1- Silacyclo-hexa-2,5 diene (1.083 %). Carbamic acid, hydroxy-ethyl ester contains many such therapeutic properties while the compound catechol is an ortho isomer of the three isomeric benzenediols. Compounds found in liquid oil produced at reaction temperature 873 K were Silacyclopentane (5.519 %), Phosphonic acid (p-hydroxyphenyl) (4.805 %), 6-Hepten-3-one, 5-Hydroxy-4-Methyl- (4.083 %), 2-Ethyl-5-Propylcyclopentanone (3.544 %), 3- (4, 8, 12 – Trimethyltridecyl) Furan (3.120%), Phenol-2-Methyl (2.824 %), Phosphonic acid (p-hydroxyphenyl) (2.686 %), Octadecane, 2,2,4,15,17,17-Hexamethyl-7, 12- Bis (3, 5,5 -Trimethylhexyl)- (2.132 %), 2 (5H) – Furanone (1.674 %), Phenol, 2–methoxy-(1.391 %), 1,4:3,6-Dianhydro-Alpha-D-Glucopyranose (1.391 %), Creosol (1.359 %), Phenol-2,6 Dimethoxy- (1.326%) and 3-Trans-(1,1-Dimethylethyl)-4, Cis, Methoxycyclohexane-1-ol (1.075%), Hexacosyl acetate (0.744 %) and 3,3'-Thiodipropanol (0.383 %). A significant observation in the GC/MS analysis is the detection of new compounds such as 1-Methyl cyclopropane methanol, 3, 3'-Thiodipropanol, 3- Trans-(1,1-Dimethylethyl)-4, Cis, Methoxycyclohexane-1-ol, 1, 1 -Dimethyl-1-Sinacyclobutane, Octadecane, 2,2,4,15,17,17-Hexamethyl-7, 12-Bis (3, 5,5-Trimethylhexyl), Creosol, 1,4:3,6-Dianhydro-Alpha-D-Glucopyranose, Hexacosyl acetate and 1,2-Benzenediol, 4-Methyl- in the liquid oil from co-pyrolyzed samples as comparted to bio-oil samples.

Fig. 8.7 denotes total peak area % of liquid oil product from thermal co-pyrolysis of coal and 100 % sawdust blend. This could be classified into ketones, alcohols, acids, esters, aldehydes, furans, alkanes, alkenes, aromatics, and phenols. With increase in temperature from 773–873 K, total peak area % of alkanes increased and aldehydes decreased.

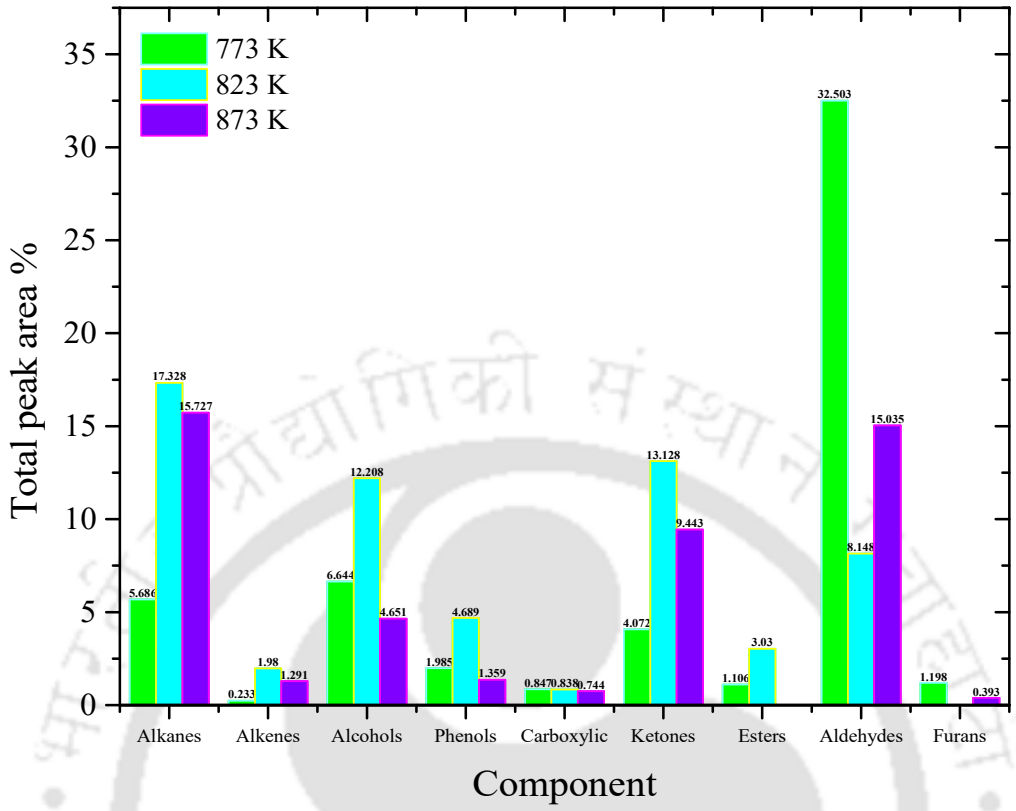

Fig. 8.7 Total peak area % of oil compounds from GC/MS analysis of thermal pyrolysis oil

8.5.2.2 Characterization of char residue

8.5.2.2.1 Composition of char residue

As given in Table 8.7, ultimate analysis of char residue from thermal co-pyrolysis of coal and 100 % sawdust blend obtained at reaction temperatures, 773 K, 823 K and 873 K is explained. The ultimate analysis determined the carbon content, hydrogen content, sulphur content, nitrogen content and oxygen content (by difference). With increase in pyrolysis temperature from 773 K, 823 K and 873 K, carbon and hydrogen content increased whereas oxygen content decreased respectively. Nitrogen content was 0.338 % for char residue at 773 K, 0.636 % for char residue at 823 K and 0.593 % at 873 K with negligible sulphur content.

The atomic H/C ratio and atomic O/C ratio stand as indicators of degree of carbonization, demethanation, dehydration, decarboxylation, and oxidation reactions. The atomic H/C ratio and atomic O/C ratio for char residues is plotted in Fig. 8.8, which serve as co-ordinates in Y-axes and X-axes. Atomic H/C ratio of char residues increases with increase in pyrolysis temperature 773 K, 823 K and 873 K, while atomic O/C ratio subsequently decreases. This shows that char residue produced at 873 K was led by higher carbonization, demethanation, and decarboxylation reactions. However, the char residue produced at 773 K

and 823 K showed lesser carbonization and comparable demethanation, and decarboxylation reactivity as compared to char residue at 873 K.

Table 8.7 Ultimate analysis of char residue from co-pyrolysis of coal and 100 % sawdust blend

Temperature (K)	Ultimate Analysis						
	C, %	H, %	S, %	N, %	O, %	H/C	O/C
773	61.829	0.373	-	0.593	37.205	0.072	0.451
823	73.582	1.110	-	0.636	24.672	0.181	0.251
873	82.099	1.506	-	0.338	16.057	0.22	0.146

(C %: Carbon content, H %: Hydrogen content, S %: Sulphur content, N %: Nitrogen content, O %: Oxygen content)

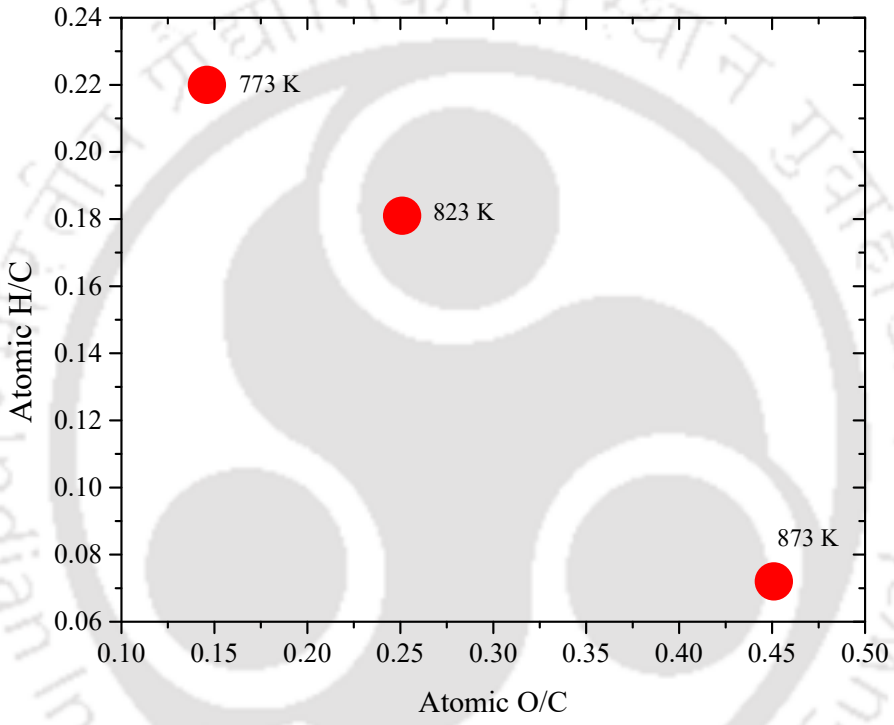

Fig. 8.8 Van Krevelen diagram of atomic O/C ratio with atomic H/C ratio for char residue

8.5.2.2.2 XRD analysis of char residue

XRD diffractogram of char residues produced at temperatures, 773 K, 823 K and 873 K is shown in Fig. 8.9. It showed a sharp peak at 27.54° (2-theta diffraction angle) and a small peak at 21.23° (2-theta diffraction angle) at the three reaction temperatures, 773-873 K.

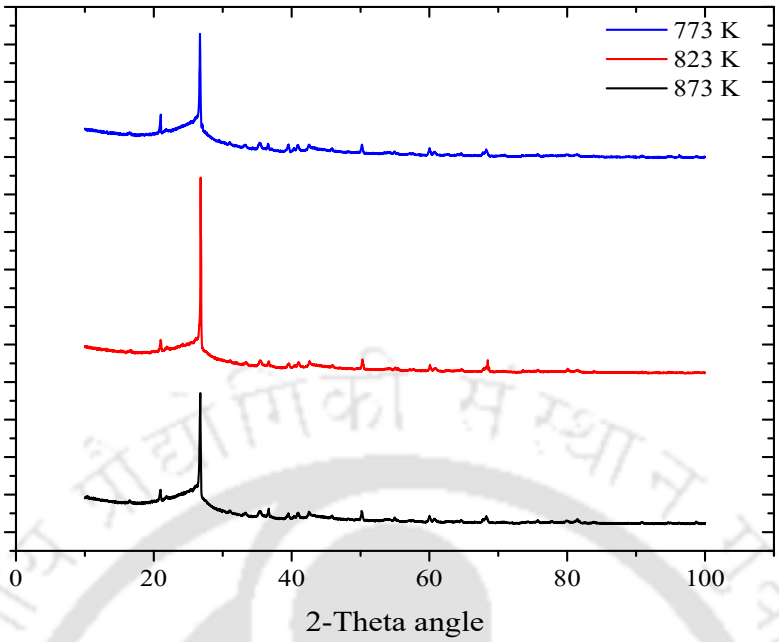

Fig. 8.9 XRD diffractogram of char residue from co-pyrolysis of 100 % blend

8.5.2.2.3 FESEM analysis of char residue

FESEM analysis of coal and 100 % sawdust char residue produced at 873 K reaction temperature is depicted in Fig. 8.10 (a, b). It shows its morphological and topological microstructure at a magnification of 1.0 KX and 5.0 KX respectively. Smaller porous structures were seen in the micro-structured images of the char residue indicating simultaneous evolution of volatiles gases (CO_2, CO, CH_4, C_2H_6) with pore diameter of 10.56 µm.

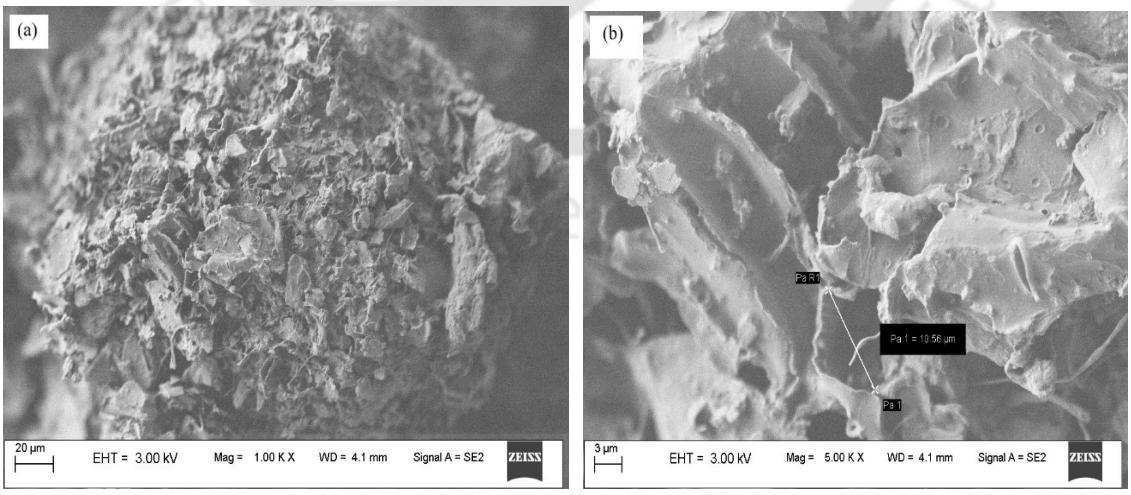

Fig. 8.10 FESEM analysis of char residue at magnification of (a) 1.0 KX and (b) 5.0 KX

8.5.2.2.4 FETEM analysis of char residue

FETEM analysis in Fig. 8.11 (a, b) showed an FETEM image and the SAED pattern of the char residue. Distinct nano-rod like microstructures at a magnification of 100 nm and a SAED pattern showed an amorphous ring like pattern of the char residue.

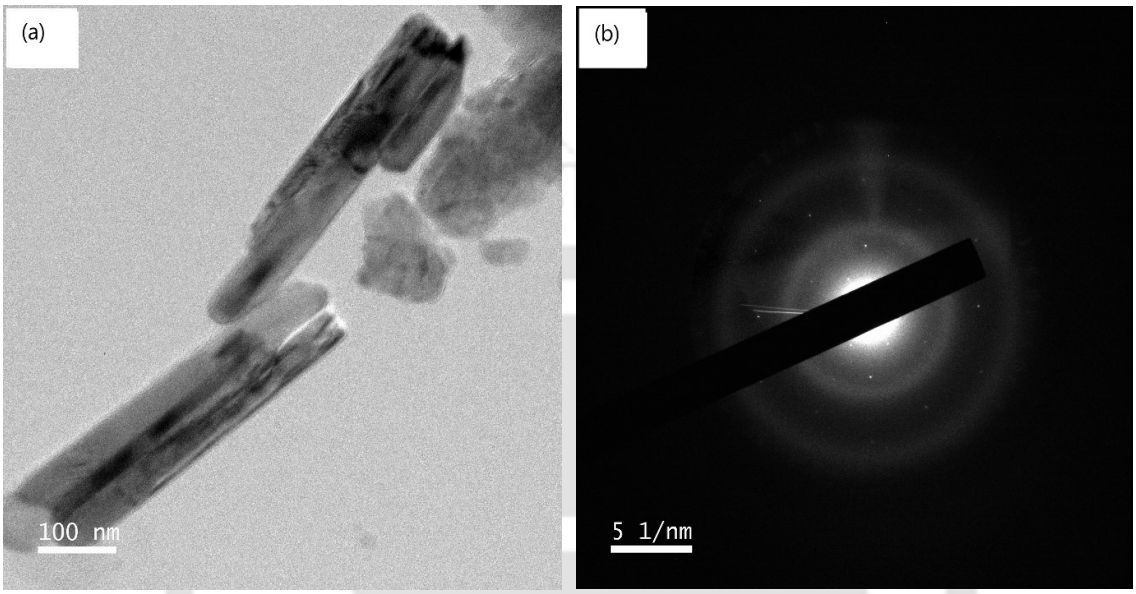

Fig 8.11 FETEM analysis of char residue at (a) magnification of 100 nm and (b) SAED pattern

8.5.2.2.5 FTIR analysis of char residue

FTIR analysis of char residue from thermal co-pyrolysis of coal and 100 % sawdust produced at three different temperatures, 773 K, 823 K and 873 K is explained in Fig. 8.12 which showed the similar functional groups as coal char residue. FTIR spectra of char residues are plotted for functional group determination at wavenumber (cm^{-1}) with its transmittance % shown in intensity (a.u). It is seen that with increase in pyrolysis temperature (773–873 K), the intensities of the respective peaks of the char residues increase. Two small peaks were perceived at 2918 cm^{-1} and 2575 cm^{-1} indicating aliphatic C-H and asymmetric Ar-CH_3 stretching and S-H stretching in the three respective coal char residue samples, whereas a small sharp peak was indicated at 1720 cm^{-1} imbuing carbonyl group (C=O group) cleavage. Another small peak with less intensity was observed at 1300 cm^{-1} wavenumber indicating C-N stretching. This indicates the presence of heterocyclic CN char form, however, a strong and intense broad peak was observed at 1073 cm^{-1} wavenumber indicated C-O-C bonded groups.

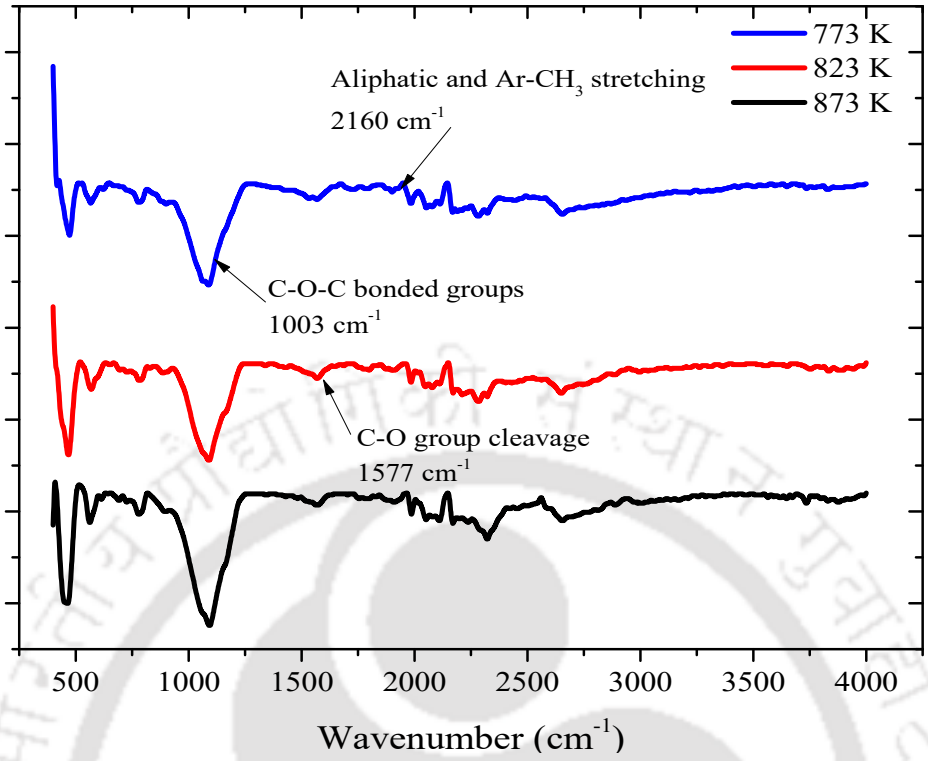

Fig. 8.12 FTIR spectra of char residue from co-pyrolysis of 100% blend

8.5.2.2.6 ESR analysis of char residue

ESR spectra of char residue from thermal co-pyrolysis of coal and 100 % sawdust at reaction temperatures, 773 K, 823 K and 873 K in Fig. 8.13. The graph shows first derivative of the ESR absorption signal of the electromagnetic radiation with the change or increase in electromagnetic field due to impact of microwave frequency on the sample. The point where there is an abrupt signal corresponds to maximum absorption peak of the radiation.

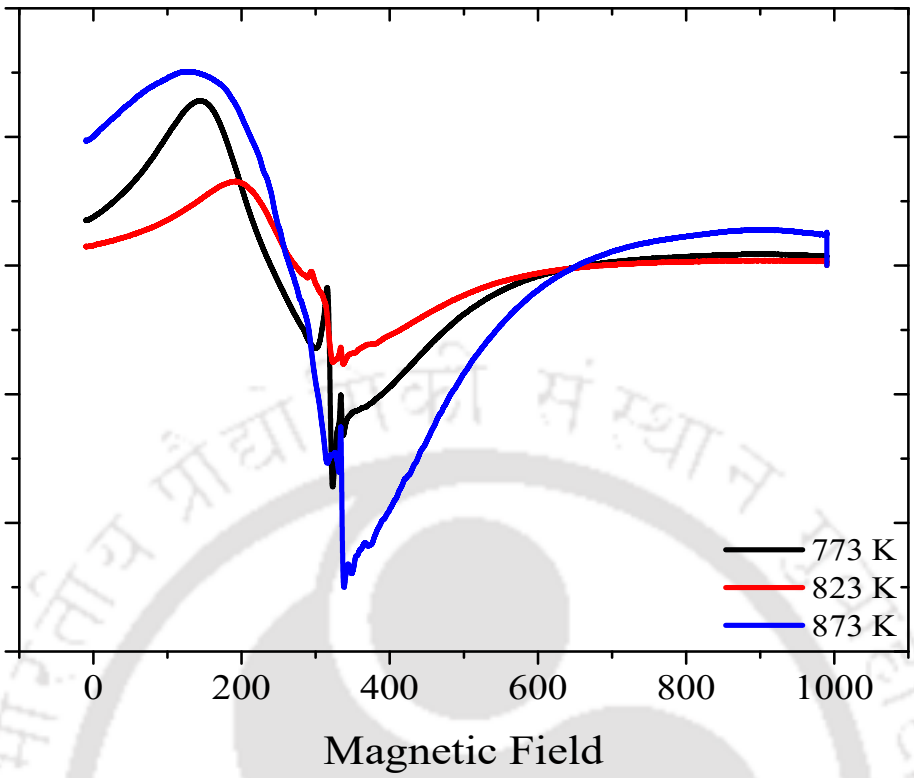

Fig. 8.13 ESR spectra of char residue from co-pyrolysis of 100 % blend

8.5.2.3 Fuel gas analysis

Fuel gas analysis from thermal co-pyrolysis of coal and 100 % sawdust blend revealed release of carbon mono-oxide (CO), NO_x, SO_x, NO, hydrocarbons in ppm levels whereas hydrogen (H_2), carbon dioxide (CO_2) and oxygen (O_2) in percentage (%) concentration. For an increasing trend in pyrolysis temperature conditions, 773 K, 823 K and 873 K, it revealed significant outcomes for each volatile gas component at subsequent residence time. It was observed in Table 8.8 that with the increase in pyrolysis temperature, hydrogen yield increased at 873 K with a slighter lesser hydrogen yield at 823 K as compared to 773 K. CO_2 levels decreased significantly at each residence time of 300 s, 900 s and 1800 s, whereas O_2 levels increased significantly. It was also observed that concentration of CO increased with the increase in pyrolysis temperature from 773 -873 K at subsequent residence time. A remarkable observation was the negligible concentration of hydrocarbons (CH_4, C_2H_6) in the fuel gas as compared to coal pyrolysis in Table 8.4. The concentration of SO_x released in the fuel gas increased at the residence of 300 s for the three consecutive temperatures at 773 K, 823 K and 873 K pyrolysis temperature. Similarly, NO levels increased with increase in

temperature from 773–873 K. However, NO_x levels decreased with the rise in temperature from 773–873 K at the three consecutive residence times.

Table 8.8 Concentration of gas components in (%) and ppm levels in fuel gas from thermal co-pyrolysis of coal and 100% sawdust blend

Gas component	773 K			823 K			873 K		
	300 s	900 s	1800 s	300 s	900 s	1800 s	300 s	900 s	1800 s
H_2 (%)	7.38	2.55	1.82	4.79	1.86	1.33	8.05	6.41	1.33
CO_2 (%)	13.24	9.58	9.12	10.19	-	14.38	9.31	2.04	2.02
O_2 (%)	9.64	9.84	9.92	10.19	-	14.38	11.92	13.67	13.95
CO (ppm)	2098	1634	1208	2283	1856	1406	4978	3967	3003
NO_x (ppm)	16	35	-	15	30	1	14	26	5
NO (ppm)	5	8	-	11	19	1	13	25	5
SO_x (ppm)	945	215	6	1054	386	8	1330	742	200
HC (ppm)	-	-	-	-	-	-	-	-	-

8.5.3 Effect of biomass blending on the product distribution profile

The product distribution profile of 100 % coal/sawdust blend co-pyrolysis made a significant observation of higher oil yields of 19.19 % at 873 K temperature as observed in Table 8.5. This substantiates the possibility of higher oil yields, wt. % for both 50 % and 200 % coal/sawdust blend co-pyrolysis at the optimized pyrolysis temperature 873 K respectively. Table 8.9 shows that increasing the biomass blending ratio in coal increases the oil content in product yield. At a biomass blending to coal of 50 %, 100 % and 200 %, the conversion wt. % increased to a significant rise of 92.8 % respectively. This was due to the high hydrogen in sawdust which catalyses the polyaromatic hydrocarbons in coal. The physical and chemical characteristics of coal and sawdust as feedstocks leads to different reactivities and thermal behaviour during co-processing as observed in Section 5.4.3 in Chapter 5. This elucidates the effect of chemical synergy or the sum of the fractional properties on of the individual fuels over the entire thermal process. Synergistic interactions of the alkali and alkaline earth metals (AAEM) in ligno-cellulosic sawdust which render an auto-catalytic effect in catalysing the polyaromatic hydrocarbon group chains of coal is the main crux of this effect. Chemical synergistic effect occurred maximum in 200 % blend as mentioned in Section 5.4.4 of Chapter 5, which proves its abundant rise in conversion, wt. %. This can be substantiated with the fact that peak height (DTG curve) as shown in Fig. 5.2 in Section 5.4.2 of Chapter 5 was maximum in 200 % blend surpassing even sawdust degradation due to its unique

elemental composition. Also, higher the H/C and O/C ratio in biomass helps to donate the H and the oxygen increases the reactivity during co-pyrolysis and simplify the degradation of coal. However, liquid yields diminishes with increasing temperatures for biomass pyrolysis while maximum liquid yield for coal pyrolysis occurs at 873 K *(Ismail et al., 2020).* Evidences of synergistic effects was seen in 773 K and 873 K rather than 973 K in this literature. At a higher blending of biomass to coal of 74 wt. % at higher temperatures of 873 K, reduces char yield by 14 % and increases liquid yields by 10 %.

Table 8.9 Effect of feedstock composition on the thermal co-pyrolysis of blend 50 %, 100 % and 200 % at 873 K reaction temperature

Biomass blending ratio	Oil, wt.%	Char residue, wt.%	Gas, wt.%	Conversion, wt.%
50 %	8.13	71.87	19.84	27.97
100 %	19.19	62.65	18.16	37.35
200 %	31.22	57.2	61.58	92.8

8.5.4 Product characterization

8.5.4.1 Characterization of liquid oil product

8.5.4.1.1 FTIR analysis of liquid oil

The FTIR analysis of the liquid oil product produced at temperature 873 K from co-pyrolysis of coal-sawdust blend (50 % and 200 %) is denoted in Fig. 8.14. The FTIR spectra of transmittance % with wavenumber (cm^{-1}) was plotted on X-axes and Y axes respectively. As shown in Fig. 8.14, the intensity of a sharp broad peak in transmittance % was perceived at 3348 cm^{-1} which was due to O-H stretching (hydroxyl radical) inherent in the H_2O molecules of the oil product. A broad less intense peak is seen at 2110 cm^{-1} wavenumber due to C=C stretching. A sharp intense peak was observed in 1652 cm^{-1} due to C=O stretching, whereas small moderate peaks indicating C-O stretching was seen at 1290 cm^{-1} and 1052 cm^{-1} wavenumbers respectively due to both carbonyl and carboxyl functional groups. A small peak indicating O-H bending is seen at 1402 cm^{-1} wavenumber whereas a small peak is seen at 1290 cm^{-1} wavenumber indicating C-O stretching. The peak at 1000 cm^{-1} wavenumber also indicated S-O stretching due to the presence of thiol groups (sulfonated compounds) in the oil samples. A sharp peak with significant intensity was observed in a lower range wavenumber of 610 cm^{-1} indicating C-Cl stretching due to the presence of chlorinated compounds in the oil samples.

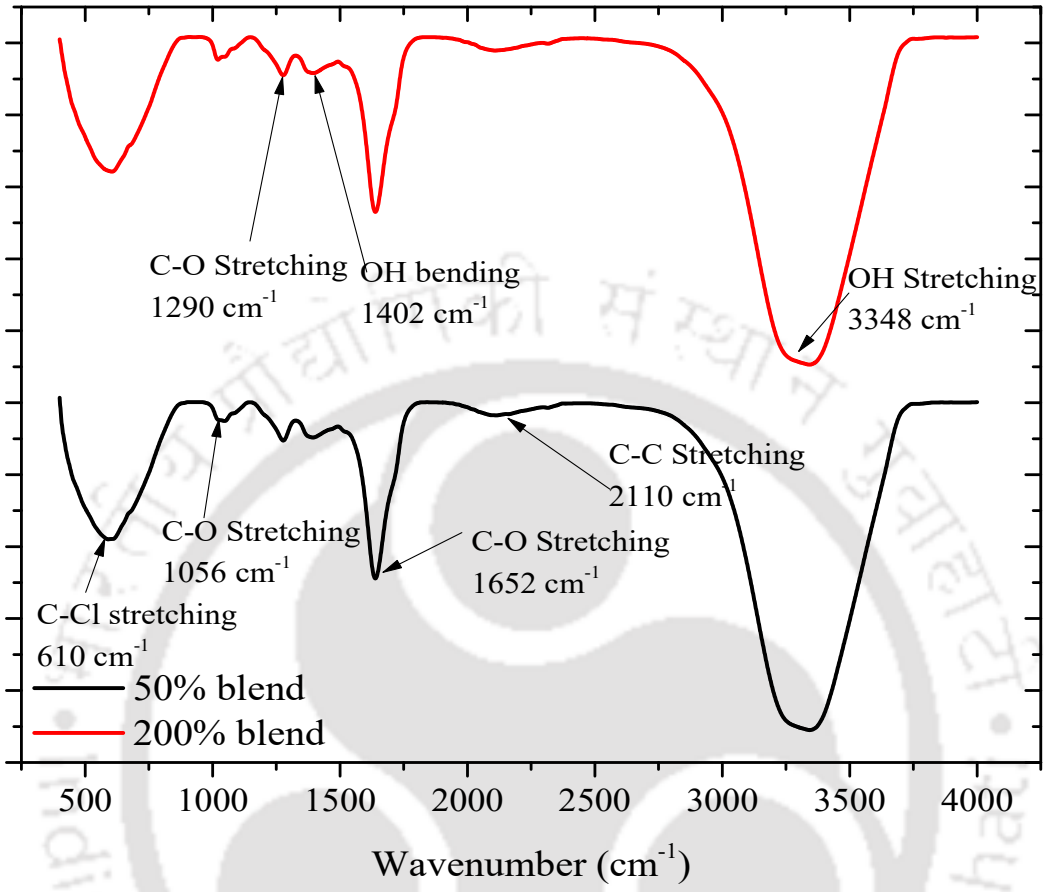

Fig. 8.14 FTIR spectra of liquid oil from co-pyrolysis of blends

8.5.4.1.2 DSC analysis of liquid oil

The liquid oil product from thermal co-pyrolysis of coal and 50 % sawdust blend and coal and 200 % sawdust blend was subjected to differential scanning calorimetry (DSC) analysis as observed in Fig. 8.15 respectively. The various features of liquid oil such as glass transition temperature - melting temperature (peak temperature), specific heat capacity *(C_p),* heat flow characteristics, heat of fusion, fast purity determination can be determined at constant heating rates for a DSC analysis as mentioned in Table 8.10.

Table 8.10 Thermal characteristics of liquid oil produced from thermal co-pyrolysis of coal and 50 % sawdust blend and coal and 200 % sawdust blend at temperature 873 K

Temperature (K) at which liquid was obtained	Glass transition temperature					Γ Cp (J/g. K)	Heat of fusion (J/g)	Specific heat flow (mW/mg)
	Onset temp. (K)	Mid temp. (K)	Inflection temp. (K)	End temp. (K)	Peak temp. (K)			
50 %	389.98	-	-	-	403.15	0.628	-1987	-32.25
200 %	397.25	-	404.55	414.25	408.3	0.271	-2240	-28.36

Fig. 8.15 indicates an exotherm of heat flowing out of the liquid samples. With the increase in temperature for thermal co-pyrolysis of coal and 50 % sawdust blend and 200 % blend at 873 K, heat flow characteristics increased, indicating higher heat flow out for oil sample produced at 873 K reaction temperature.

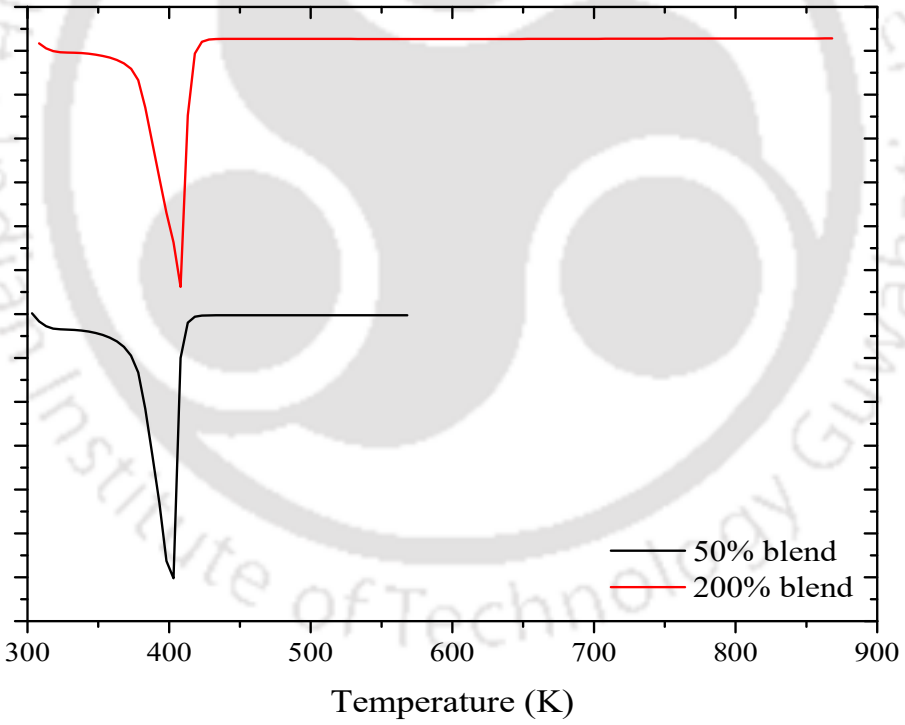

Fig. 8.15 DSC thermogram of liquid oil from co-pyrolysis of blends

8.5.4.1.3 GC/MS analysis of liquid oil compounds

Table S7 depicts the relative content of liquid oil samples from thermal co-pyrolysis of coal-sawdust blend. While the peak area % of coal and 100 % sawdust oil sample at 873 K

reaction temperature is explained comprehensively priorly in Subsection 8.5.2.1.3, the following discussion portends to GC/MS analysis of liquid oil from coal-sawdust blends (50 % and 200 %) respectively. In the liquid oil product from co-pyrolysis of coal and 50% sawdust blend, the main compounds were D-Allose, Phosphonic acid (p-hydroxyphenyl), Silacyclopentane, 1-Phenyl-5-Methylheptane, 2-Ethyl-5-Propylcyclopentanone, 3- (4, 8, 12 – Trimethyltridecyl) Furan, Phenol-2-Methyl, Propanoic acid, 1- Methylpropyl ester, Phosphonic acid (p-hydroxyphenyl), Octadecane, 2,2,4,15,17,17-Hexamethyl-7, 12- Bis (3, 5,5 -Trimethylhexyl)-, Creosol, Phenol-2,6 Dimethoxy-, Phenol, 2 – methoxy-, 6-Hepten-3-one, 5-Hydroxy-4-Methyl-, 3- Trans-(1,1-Dimethylethyl)-4, Cis, Methoxycyclohexane-1-ol, -Methyl-2-(2-Oxopropyl) furan, Tetrahydro-2, 5-dimethoxy-, Hexacosyl acetate and 1-Silacyclohexa-2, 5- diene arranged in their decreasing order in the concentration and peak area %. Whereas in the liquid oil product from co-pyrolysis of coal-sawdust blend (200 %), prominent compounds were D-Allose, Phosphonic acid (p-hydroxyphenyl), 2-Ethyl-5-Propylcyclopentanone, 6-Hepten-3-one, 5-Hydroxy-4-Methyl-, 3- (4, 8, 12 – Trimethyltridecyl) Furan, Phenol-2-Methyl, Propanoic acid, 1- Methylpropyl ester, Silacyclopentane, Phosphonic acid (p-hydroxyphenyl), Octadecane, 2,2,4,15,17,17-Hexamethyl-7, 12- Bis (3, 5,5 -Trimethylhexyl)-, 2 (5H) – Furanone, 1-Methyl cyclopropane methanol, Phenol-2,6 Dimethoxy-, Phenol, 2 – methoxy-, Creosol, 1-Silacyclohexa-2, 5-diene and 3- Trans-(1,1-Dimethylethyl)-4, Cis, Methoxycyclohexane-1-ol arranged in the decreasing order of their peak area %.

Fig. 8.16 denotes total peak area % of liquid product from co-pyrolysis of coal and sawdust blends. This could be classified into ketones, alcohols, acids, esters, aldehydes, furans, alkanes, alkenes and phenols. Total peak area % of alkanes was 13.204 % and 15.119 %, alkenes was 0.995 % and 1.889 %, alcohol was 3.978 % and 6.485 %, phenols was 2.557% and 2.952 %, carboxylic acids was 0.664 % and 0.475 %, ketones was 4.563 % and 2.878 %, esters was 17.81% and 5.996 % and aldehydes was 4.155 % and 4.488 % for 50 % and 200 % blends respectively.

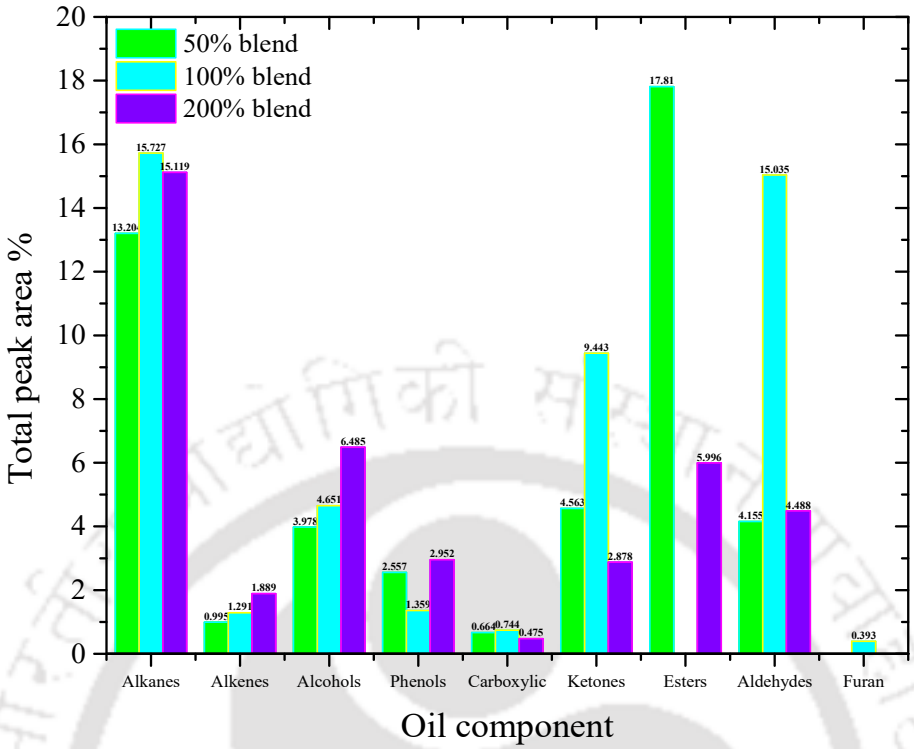

Fig. 8.16 Total peak area % of oil compounds from GC/MS analysis of thermal pyrolysis oil

8.5.4.2 Characterization of char residue

8.5.4.2.1 Composition of char residue

As given in Table 8.11, ultimate analysis of char residue from thermal co-pyrolysis of coal and 50% sawdust blend and coal and 200 % sawdust blend obtained at reaction temperature, 873 K is explained. The ultimate analysis determined the carbon content, hydrogen content, sulphur content, nitrogen content and oxygen content (by difference). Carbon content was 76.182 %, hydrogen content was 1.192 %, nitrogen content was 0.608 % and oxygen content was 21.818 % for coal and 50 % sawdust blend, whereas coal and 200 % sawdust blend revealed carbon content of 64.022 %, hydrogen content of 0.350 %, nitrogen content of 0.581% and oxygen content of 35.047 %, both with negligible sulphur content.

Table 8.11 Ultimate analysis of char residue from thermal co-pyrolysis of blends

Temperature (K)	**Ultimate Analysis**						
	C, %	**H, %**	**S, %**	**N, %**	**O, %**	**H/C**	**O/C**
50 %	76.182	1.392	-	0.608	21.818	0.219	0.214
200 %	64.022	0.350	-	0.581	35.047	0.656	0.410

(C %: Carbon content, H %: Hydrogen content, S %: Sulphur content, N %: Nitrogen content, O %: Oxygen content)

8.5.4.2.2 XRD analysis of char residue

As shown in Fig. 8.17, XRD diffractogram revealed a sharp peak at 26.54° (2-Theta angle).

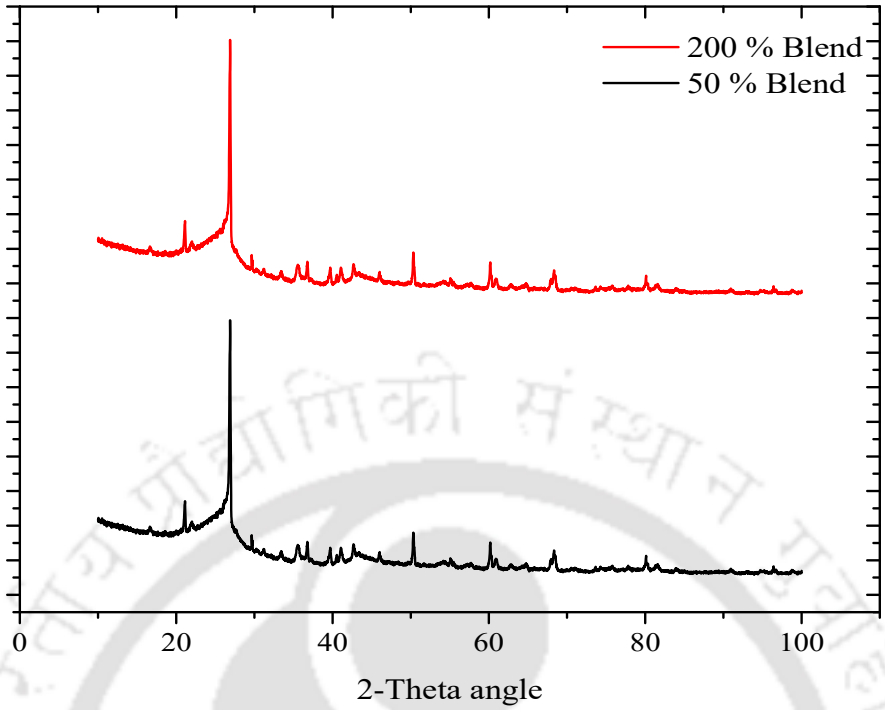

Fig. 8.17 XRD diffractogram of char residue from thermal co-pyrolysis of blends

8.5.4.2.3 FESEM analysis of char residue

FESEM analysis in Fig. 8.18 revealed the microstructure image at magnification 1.0 KX of char residue from thermal co-pyrolysis of 50 % and 200 % blends. It revealed a non-porous microstructure bulbous structure of a porous char residue from the blends due to higher biomass blending.

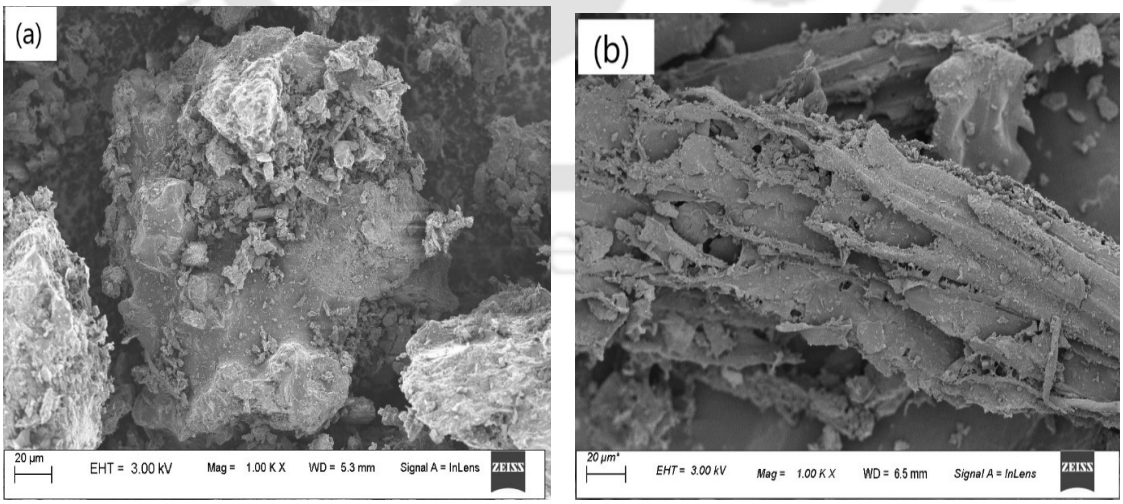

Fig. 8.18 FESEM analysis at magnification 1.0 KX of char residue from thermal co-pyrolysis of (a) 50 % blend and (b) 200 % blend

8.5.4.2.4 FETEM analysis of char residue

FETEM analysis was observed for char residue in Fig. 8.19 which showed multilayer sheets or plates of graphitic layers for char residue from 50 % blend while nano-rod like structures for char residue from 200 % blend. Distinct SAED pattern was seen for char residue from 50 % blend and 200 % blend with single crystalline lattice structure. EDS-FETEM analysis is shown in Table 8.12 which revealed a carbon content of 18.92 % and 48.60 % for 50 % and 200 % blends respectively along with the presence of other elements such as oxygen, magnesium, aluminium, silica, chromium, phosphorus, potassium, sulphur, titanium, and chlorine.

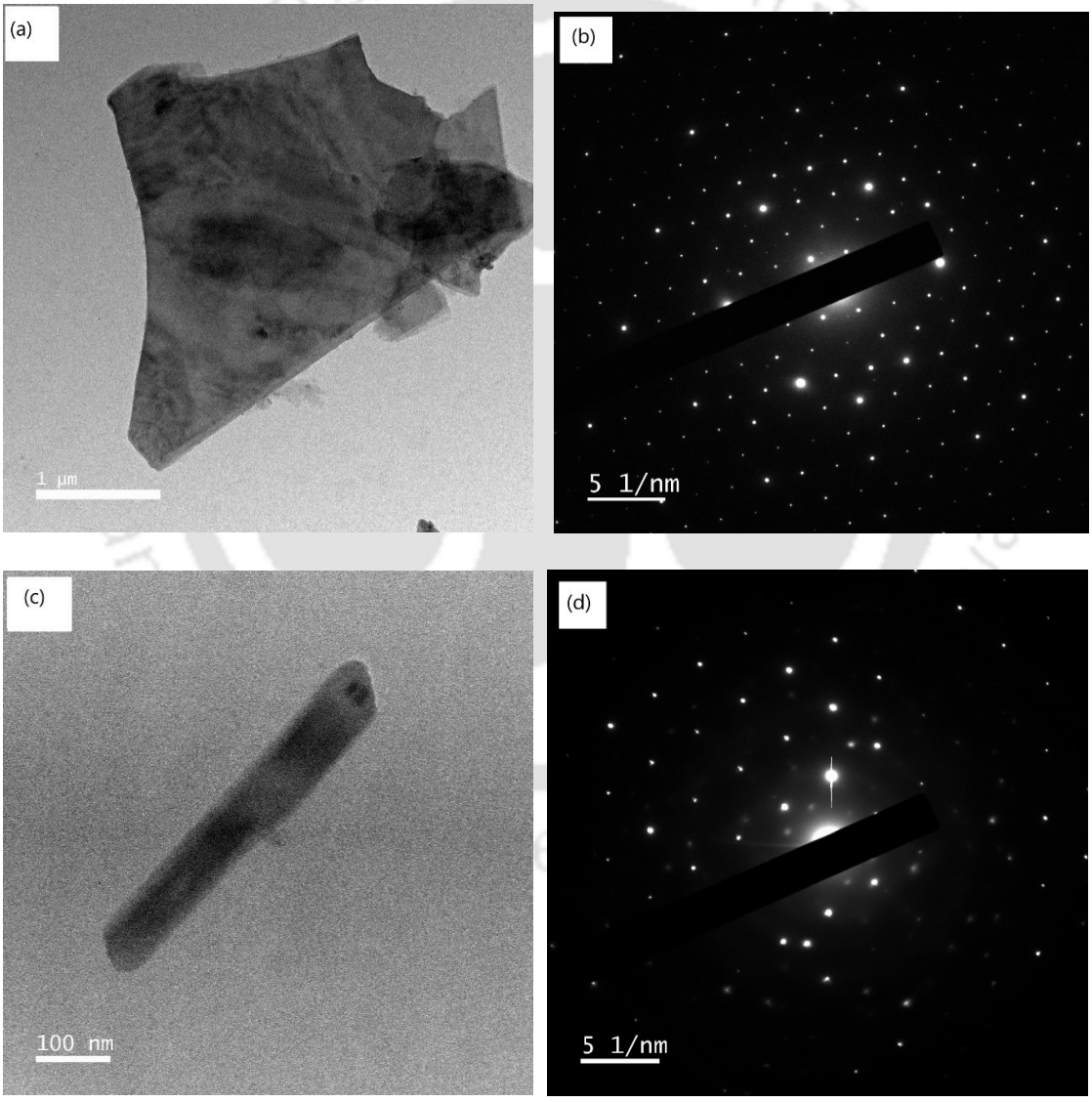

Fig. 8.19 FETEM analysis of char residue from thermal co-pyrolysis of blends (a, b) 50 % blend and (c, d) 200 % blend

Table 8.12 Elemental weight (%) and atomic (%) of char residue from thermal co-pyrolysis of blends by EDS FETEM analysis

Feed	Element	C, %	Fe, %	O, %	Si, %	Mg, %	Al, %	K, %	S, %	Co, %	Ca, %	Mn, %	P, %	Cr, %	Ti, %	Cl, %
50 % Blend	Elemental weight (%)	18.92	0.38	39.73	24.91	16.37	0.18	0.22	-	-	0.23	-	-	1.06	-	-
	Atomic (%)	25.63	0.12	45.17	16.13	12.25	0.12	0.10	-	-	0.11	-	-	0.37	-	-
200 % Blend	Elemental weight (%)	48.6	6.80	-	1.48	-	0.84	0.94	0.12	5.08	0.32	1.54	0.16	35.73	1.29	1.42
	Atomic (%)	82.7	2.49	-	1.08	-	0.64	0.49	0.08	1.76	0.16	0.57	0.11	14.05	0.55	0.82

8.5.4.2.5 FTIR analysis of char residue

FTIR analysis was observed in Fig. 8.20 which revealed C-O-C bonded groups at 1003 cm^{-1} wavenumber and C-O group bond cleavage at 1577 cm^{-1} wave number for both the blends respectively. There was no presence of hydroxyl -OH groups in the thermal char residue.

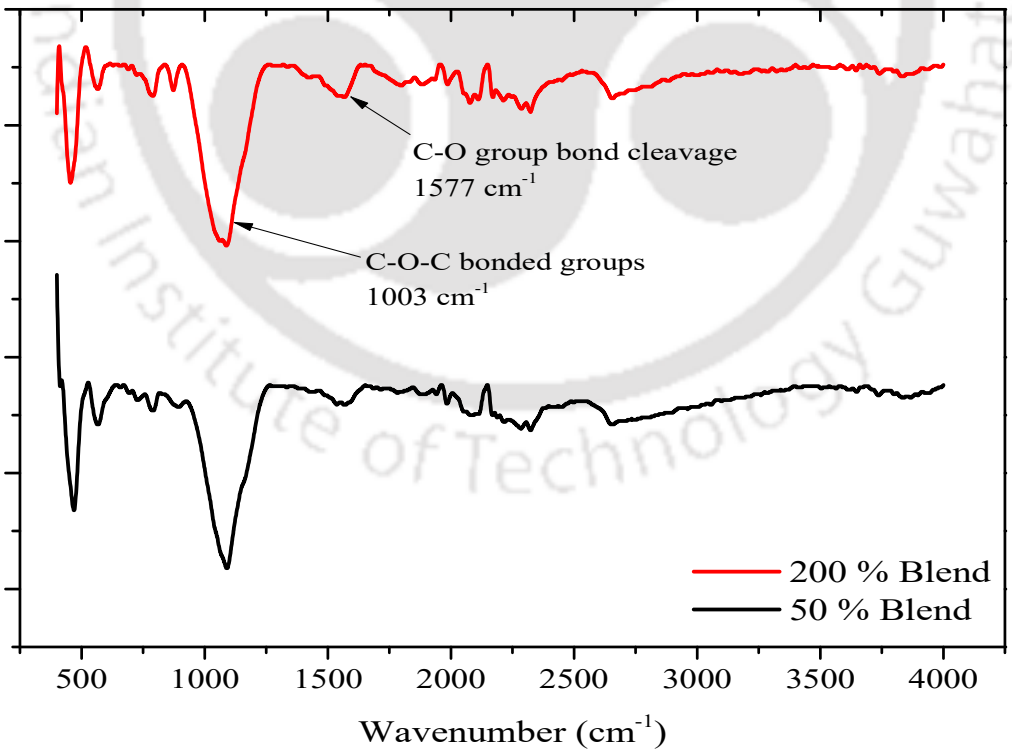

Fig. 8.20 FTIR spectra of char residue from thermal co-pyrolysis of blends

8.5.4.3 Fuel gas analysis

Fuel gas analysis from thermal co-pyrolysis of coal and 50 % sawdust blend and 200 % blend revealed the release of carbon mono-oxide (CO), NO_x, SO_x, NO, and hydrocarbons in ppm levels whereas hydrogen (H_2), carbon dioxide (CO_2), and oxygen (O_2) in percentage (%) concentration. An increasing trend in biomass blending to coal, revealed significant outcomes for each volatile gas component at subsequent residence time. It was observed in Table 8.13 that with the increase in biomass blending to coal, hydrogen yield increased for 200 % blend with a slightly lesser values for 100 % and 50 % blend for each residence time. This was due to presence of more hydrogen content in 200 % blend, and also releasing more volatile gas due to presence of higher volatile matter and degradation potentiality.

Table 8.13 Concentration of gas components in (%) and ppm levels in fuel gas from thermal co-pyrolysis of coal and 50 % sawdust blend and 200 % blend and compared to 100 % blend at a residence time of 300s, 900s and 1800s

Gas component	50% blend			100% blend			200% blend		
	300 s	900 s	1800 s	300 s	900 s	1800 s	300 s	900 s	1800 s
H_2 (%)	1.21	8.85	-	8.05	6.41	1.33	7.40	8.43	4.15

8.6 Catalytic co-pyrolysis of coal-sawdust blends

The study incorporates coal and sawdust as potential sources for thermal co-pyrolysis process and the effect of NiO and Ni (II) aluminate composite catalysts on its catalytic co-pyrolysis. The effect of feedstock composition at 100 % and 200 % coal-sawdust blend at reaction temperature 873 K on product distribution profile was studied in a fixed-bed reactor unit at 30 K min^{-1} heating rate under nitrogen (18 L h^{-1}) as purge gas as previously given in Section 8.5.1 and 8.5.3. Further the studies on effect of 10 % and 20 % NiO/Al_2O_3 composite catalysts on 100 % and 200 % blend feedstock on the product distribution profile was studied at the optimized reaction temperature condition as given in Section 8.6.1. The derived liquid oil product, catalytic char residue and evolved volatile gas were evaluated for detailed product characterization and analysis as given in Section 8.6.2.

8.6.1 Effect of catalyst (metal loading %) on the product distribution profile

Catalytic co-pyrolysis of 100 % and 200 % coal-sawdust blended mixtures was studied in presence of 10 % and 20 % NiO/Al_2O_3 composite catalyst at optimized (catalyst/blend) ratio which showed highest degradability and conversion % in the active pyrolytic zone of thermogravimetric degradation zones as elucidated in Chapter 6. The effect of metal loading

% on the activated support of the catalyst and the (catalyst/blend) ratio are two primal features on the product distribution profile of the catalytic co-pyrolysis of coal-sawdust blends (100 % and 200 %) as shown in Table 8.14. For coal and 100 % sawdust blend at a (catalyst/blend) ratio of 0.20 and 0.05 for 10 % and 20 % NiO/Al_2O_3 composite catalysts, a wide range of products of liquid oil, char and gas was accessed when the pyrolysis experiments were conducted at the temperature of 873 K. As shown in Table 8.14, it was observed that for a 10 % NiO/Al_2O_3 composite catalyst, yield % of liquid oil enhanced from 19.19–31.07 %, yield % of char decreased from 62.65–45.3 % and yield % of evolved volatiles increased from 18.16–23.63 % at (catalyst/blend) ratio 0.20. However, it was observed that for 20 % NiO/Al_2O_3 composite catalyst, yield % of evolved volatiles increased substantially from 18.16–31.57%, yield % of char decreased from 62.65–55.5 % and yield % of liquid oil decreased from 19.19–12.93% at (catalyst/blend) ratio of 0.05. The % conversion was 54.1 % for coal and 100 % sawdust blend with 10 % NiO/Al_2O_3 composite catalyst and 44.5 % for coal and 100 % sawdust blend with 20 % NiO/Al_2O_3 composite catalyst. However, for a coal and 200 % sawdust blend at a (catalyst/blend) ratio of 0.10 using 10 % and 20 % NiO/Al_2O_3 composite catalysts, liquid oil, char and gas was accessed when the pyrolysis experiments were conducted at the temperature of 873 K. As shown in Table 8.14, it was observed that for a 10 % NiO/Al_2O_3 composite catalyst, yield % of oil decreased from 31.22–27 %, yield % of char decreased from 57.2–41 % and yield % of evolved volatiles decreased substantially from 61.58–32 % at (catalyst/blend) ratio of 0.10. It was observed that for 20 % NiO/Al_2O_3 composite catalyst, yield % of evolved volatiles decreased from 61.58–65.4 %, yield % of char decreased from 57.2–21.53 % and yield % of bio-oil decreased from 31.22–13.67 % at (catalyst/blend) ratio of 0.10. The % conversion was 59 % for coal and 200 % sawdust blend with 10 % NiO/Al_2O_3 composite catalyst and 79.07 % for coal and 200 % sawdust blend with 20 % NiO/Al_2O_3 composite catalyst.

Table 8.14 Effect of catalyst (metal loading %) 10% and 20 % NiO/Al_2O_3 composite catalysts on catalytic co-pyrolysis of coal-sawdust blends (100 % and 200 %) at the pyrolysis temperature, 873 K

Feedstock	Oil, wt.%	Char residue, wt.%	Gas, wt.%	Conversion, wt.%
100 % blend with 10 % NiO/Al_2O_3	31.07	45.3	23.63	54.1
100 % blend with 20 % NiO/Al_2O_3	12.93	55.5	31.57	44.5
200 % blend with 10 % NiO/Al_2O_3	27.0	41.0	32.0	59.0
200 % blend with 20 % NiO/Al_2O_3	13.67	21.53	65.4	79.07

8.6.2 Product characterization

8.6.2.1 Characterization of liquid oil product

8.6.2.1.1 FTIR analysis of liquid oil

The FTIR analysis of the liquid oil produced at the temperature, 873 K from catalytic co-pyrolysis of coal and 100 % sawdust blend and coal and 200 % sawdust blend thermal co-pyrolysis and the effect of 10 % and 20 % NiO/Al_2O_3 catalyst on pyrolytic liquid oil is denoted in Fig. 8.21. FTIR spectra of liquid oil from blends with 10 % and 20 % NiO/Al_2O_3 catalyst showed similar functional groups as that of previously characterized oil samples.

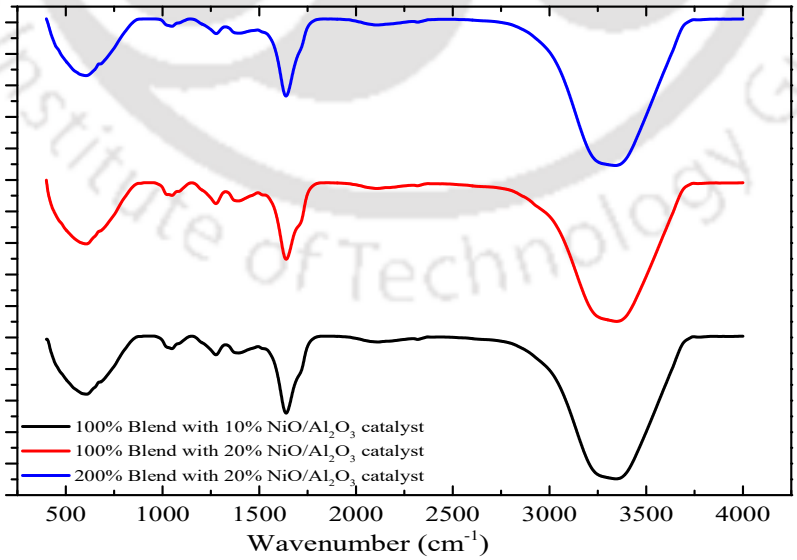

Fig. 8.21 FTIR spectra of liquid oil from catalytic co-pyrolysis of blends using 10 % and 20 % NiO/Al_2O_3 catalyst

8.6.2.1.2 DSC analysis of liquid oil

Fig. 8.22 indicates an exotherm of heat flowing out of the liquid oil samples from catalytic co-pyrolysis of blends using 10 % and 20 % NiO/Al_2O_3 catalyst. Specific heat flow decreased from -29.33 mW mg^{-1} to -29.24 mW mg^{-1} with the increase in metal loading % in the catalyst as given in Table 8.15. A directional heat pathway may cause such transitions in an exponential rise of heat flow until a steady-state condition is achieved which was T_s=435 K in these samples. Peak temperatures decreased for liquid oil which was 402.75 K since a lesser temperature was required for its ignition, indicating lesser release of heat. Specific heat capacity, C_p value was maximum for pyrolytic oil from catalytic co-pyrolysis of blends with 20 % NiO/Al_2O_3 which was 0.345 kJ kg^{-1} K^{-1}. The heat of fusion was -2000 J g^{-1} for pyrolytic oil from catalytic co-pyrolysis of coal and 100 % sawdust blend with 10 % NiO/Al_2O_3 catalyst and -2005 J g^{-1} for pyrolytic oil from catalytic co-pyrolysis of coal and 100 % sawdust blend with 20 % NiO/Al_2O_3 catalyst. The glass transition peak temperature of liquid oil from co-pyrolysis of coal and 200 % sawdust with 10 % NiO/Al_2O_3 catalyst and with 20 % NiO/Al_2O_3 catalyst as 400.25 K and 401.15 K rather than liquid oil from coal and 200 % sawdust blend catalytic co-pyrolysis sample which was 414.25 K indicating faster degradation in coal and 200 % sawdust with 10 % NiO/Al_2O_3 catalyst.

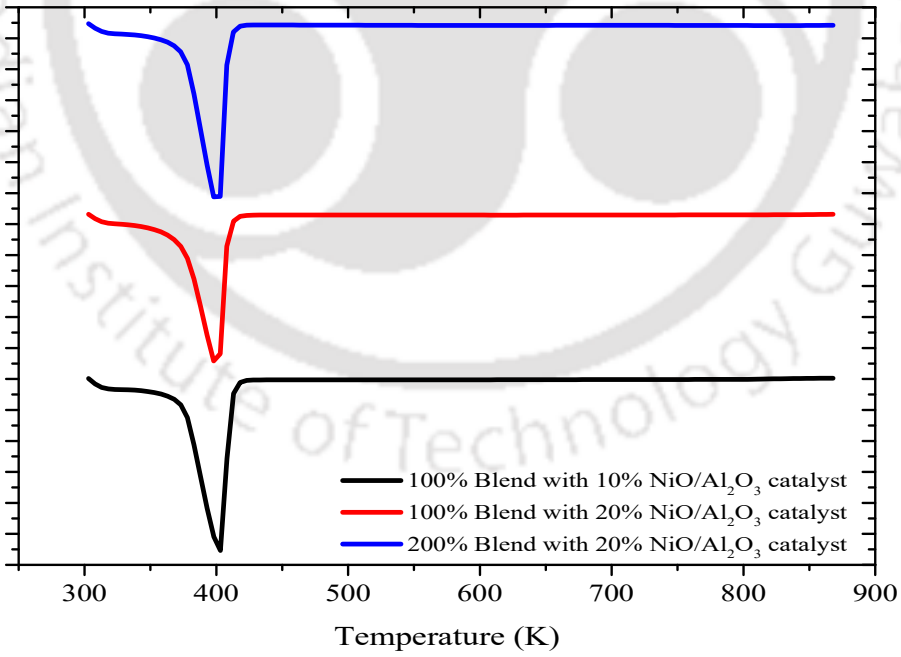

Fig. 8.22 DSC thermogram of liquid oil from catalytic co-pyrolysis of blends using 10 % and 20 % NiO/Al_2O_3 catalyst

Table 8.15 Thermal characteristics of liquid oil produced from catalytic co-pyrolysis of blends

Feedstock composition from which liquid oil was obtained	Glass transition temperature					Γ Cp (J/g. K)	Heat of fusion (J/g)	Specific heat flow (mW/mg)
	Onset temp. (K)	Mid temp. (K)	Inflection temp. (K)	End temp. (K)	Peak temp. (K)			
Coal and 100 % sawdust blend with 10 % NiO/Al_2O_3 catalyst	-	-	-	-	401.65	0.150	-2000	-25.23
Coal and 100 % sawdust blend with 20 % NiO/Al_2O_3 catalyst	402.65	412.85	404.65	402.35	404.95	0.345	-2005	-29.24
Coal and 200 % sawdust blend with 10 % NiO/Al_2O_3 catalyst	391.85	424.25	398.25	406.65	400.25	0.573	-2226	-28.55
Coal and 200 % sawdust blend with 20 % NiO/Al_2O_3 catalyst	419.05	421.95	404.55	424.85	401.15	0.602	-1794	-29.56

8.6.2.1.3 GC/MS analysis of liquid oil compounds

As shown in Table S8 and S9, catalytic upgradation of liquid oil from catalytic co-pyrolyzed samples using 10 % and 20 % NiO/Al_2O_3 composite catalyst resulted in phosphonic acid, (p-hydroxyphenyl)- and 6-Hepten-3-one, 5-Hydroxy-4-Methyl- as the candidate compounds with slightly decreased C_p values of 0.150 kJ kg^{-1} K^{-1} and 0.345 kJ kg^{-1} K^{-1} respectively due to catalytic tar cracking of polyaromatic hydrocarbons present in the 100 % co-pyrolyzed oil sample. C_p values of 0.573 kJ kg^{-1} K^{-1} and 0.602 kJ kg^{-1} K^{-1} respectively due to catalytic tar cracking of polyaromatic hydrocarbons present in the liquid oil from catalytic co-pyrolyzed samples with 10 % and 20 % NiO/Al_2O_3 composite catalyst. Table 8.16 denotes the total peak area % of the compounds present in liquid oil from catalytic co-pyrolysis of blends from the GC/MS analysis. It shows that alkanes were 12.23 % and 2.195 %, alkenes were 1.227 % and 1.017 %, alcohols were 6.024 % and 3.505 %, phenols were 4.457 %, carboxylic acid was 0.91 %, ketones were 5.005 % and 2.454 % and aldehydes were 9.803 % and 0.609 % in liquid oil from catalytic co-pyrolysis of coal and 100 % sawdust blend using 10 % and 20 % NiO/Al_2O_3 catalyst obtained at pyrolytic reaction temperature, 873 K. However, liquid oil from catalytic co-pyrolysis of 200 % blend using 20 % NiO/Al_2O_3

catalyst revealed alkane content of 9.194 %, alkene content of 0.795 %, alcohol content of 2.693 %, phenolic content of 2.627 %, carboxylic acid content of 3.971 %, ketone content of 10.457 %, aldehydes of 0.203 % and aromatic content of 8.122 %.

Table 8.16 Total peak area % of component groups in liquid oil product from catalytic co-pyrolysis of coal-sawdust blend (100 % and 200 %) in presence of 10 % and 20 % NiO/Al_2O_3 catalyst

Compound class	**Total peak area %**		
	100 % Blend with 10 % NiO/Al_2O_3 catalyst	**100 % Blend with 20 % NiO/Al_2O_3 catalyst**	**200 % Blend with 20 % NiO/Al_2O_3 catalyst**
Alkanes	12.23	2.195	9.194
Alkenes	1.227	1.017	0.795
Alcohols	6.024	3.505	2.693
Phenols	4.457	4.457	2.627
Carboxylic acids	0.91	-	3.971
Ketones	5.005	2.454	10.457
Aldehydes	9.803	0.669	0.203
Aromatic	-	-	8.122

8.6.2.2 Fuel gas analysis

Fuel gas analysis from catalytic co-pyrolysis of 50 % and 200 % blends at 873 K pyrolysis temperature revealed release of carbon mono-oxide (CO), NO_x, SO_x, NO, hydrocarbons in ppm levels whereas hydrogen (H_2), carbon dioxide (CO_2) and oxygen (O_2) in percentage (%) concentration. For an increasing trend in biomass blending in coal with the integration of catalysts, it revealed significant outcomes for each volatile gas component at subsequent residence time. It was observed in Table 8.17, that with the increase in biomass blending, hydrogen yield increased for 200 % blend with a slightly lesser values for 100 % blend for each residence time with the implementation of catalysts. The blends with NiO/Al_2O_3 nano-composite catalysts undergo reverse water-gas shift reaction and produce more of hydrogen gas. This holds true for higher metal loading % in the catalysts which generate more hydrogen gas evolution, which was significant with 16.0 % H_2 yield in pyrolytic syngas.

Table 8.17 Concentration of gas components in (%) and ppm levels in fuel gas from catalytic co-pyrolysis of coal and 100 % sawdust blend and 200 % blend with 10 % and 20 % Ni loaded catalyst at residence time of 300s, 900s and 1800s

Gas component	100 % Blend with 10 % NiO/Al_2O_3 catalyst			100 % Blend with 20 % NiO/Al_2O_3 catalyst		
	300 s	**900 s**	**1800 s**	**300 s**	**900 s**	**1800 s**
H_2 (%)	0.154	6.00	0.68	10.11	6.95	1.75

	200 % Blend with 10 % NiO/Al_2O_3 catalyst			200 % Blend with 20 % NiO/Al_2O_3 catalyst		
	300 s	**900 s**	**1800 s**	**300 s**	**900 s**	**1800 s**
H_2 (%)	-	-	-	7.11	16.00	6.94

8.7 Summary of the Chapter

It is concluded that thermal co-pyrolysis of coal-sawdust blends leads to a product profile distribution of oil, char and evolved volatile gas as production of a higher yield of liquid oil, less tar yield in the liquid oil through thermal cracking, production of more evolved volatiles from non-condensable gases and a highly stable porous char. However, coal pyrolysis revealed negligible liquid oil generation with maximum coal char generation and very less evolved volatiles gas product. The coal char characterized revealed that graphitic multilayer sheets were formed with 70.28 % carbon and hexagonal single crystal lattice structures. With an increase in temperature, liquid oil yield increases while char yield decreases. Characterization of liquid oil D-Allose is the prominent compound present along with Beta-D-Glucopyranose-1,6-Anhydro with a remarkable C_p value of 5.300 kJ kg^{-1} K^{-1} pyrolyzed ta 823 K reaction temperature. At a coal-sawdust blending ratio of 50 %, 100 % and 200 %, the conversion, wt% increased from 27.97 %, 37.35 % to a significant rise of 92.8 % respectively. This might be due to the synergistic interactions of the alkali and alkaline earth metals (AAEM) which render an auto-catalytic effect in catalysing the polyaromatic hydrocarbon group chains of coal linked with sawdust lignin and holocellulose components. In catalytic co-pyrolysis of blends, with the effect of 10 % and 20 % NiO/Al_2O_3 nano-catalyst, liquid oil yield decreased whereas gas yield increased for 10 % NiO/Al_2O_3 nano-catalyst. From GC/MS characterization liquid oil from thermal co-pyrolysis of blends, it was observed that alkanes is the main component along with esters and aldehydes with a remarkable C_p value of 5.300 kJ kg^{-1} K^{-1} pyrolyzed at 823 K reaction temperature. Catalytic upgradation of liquid oil using 10 % and 20 % NiO/Al_2O_3 composite catalysts resulted in ketones as the main compound present along with aromatics from GC/MS characterization

and fantastic C_p values of 0.573 kJ kg^{-1} K^{-1} and 0.602 kJ kg^{-1} K^{-1} respectively due to catalytic tar cracking of polyaromatic hydrocarbons present in the 200 % blend-oil with 10 % and 20 % NiO/Al_2O_3 composite catalyst. Also, higher metal loading % in the catalysts with a higher blending ratio of 200 % blend generates more hydrogen gas evolution, which was significant with 16.0 % H_2 yield in pyrolytic syngas.

References

- Li, X., Tian, J., Ju, Y. and Chen, Y., 2022. Permeability variations of lignite and bituminous coals under elevated pyrolysis temperatures (35–600° C): An experimental study. *Energy*, *254*, p.124187.
- Wedler, C., Span, R. and Richter, M., 2020. Comparison of micro-and macropore evolution of coal char during pyrolysis. *Fuel*, *275*, p.117845.
- Odeh, A.O., 2015. Oualitative and quantitative ATR-FTIR analysis and its application to coal char of different ranks. *Journal of Fuel Chemistry and Technology*, *43*(2), pp.129-137.
- Solum, M.S., Pugmire, R.J., Jagtoyen, M. and Derbyshire, F., 1995. Evolution of carbon structure in chemically activated wood. *Carbon*, *33*(9), pp.1247-1254.
- Wu, Z., Li, Y., Xu, D. and Meng, H., 2019. Co-pyrolysis of lignocellulosic biomass with low-quality coal: optimal design and synergistic effect from gaseous products distribution. *Fuel*, *236*, pp.43-54.
- Nyoni, B. and Hlangothi, S.P., 2023. Co-pyrolysis of low-grade bituminous coal and algal biomass in a rotary kiln: Effect of coal/algae ratio and kiln temperature on the yield and composition of the resultant oils. *Journal of Analytical and Applied Pyrolysis*, *171*, p.105950.
- Ismail, T.M., Banks, S.W., Yang, Y., Yang, H., Chen, Y., Bridgwater, A.V., Ramzy, K. and Abd El-Salam, M., 2020. Coal and biomass co-pyrolysis in a fluidized-bed reactor: Numerical assessment of fuel type and blending conditions. *Fuel*, *275*, p.118004.

Chapter IX

Conclusions and Scope for Future Work

9.1 Conclusions

In the present investigation, an attempt has been made to perform thermal pyrolysis of coal, sawdust, and its blends in a horizontal fixed bed reactor prior to its investigation on degradation kinetics in a thermogravimetric analyzer via Kissinger - Akahira – Sunose method. Further, catalytic pyrolysis of sawdust and co-pyrolysis of blends is conducted using two synthesized 10% and 20% NiO and Ni (II) aluminate nanocomposite catalysts in a horizontal fixed bed reactor prior to its kinetics estimation. Chapter-wise conclusions are presented in the following sub-sections.

9.1.1 Physico-chemical characterization of feeds and synthesized composite nano-catalyst

Characterization of feedstocks and synthesized catalysts were evaluated for its physicochemical characteristics by various analytical techniques such as proximate, ultimate analysis, FESEM, EDX, XRD, FETEM, AFM, XPS, FTIR, BET-N_2 and TGA. The key outcomes are presented below:

- Proximate analysis entails that coal has higher ash content and lower volatile matter content than sawdust with lower calorific value content. Sawdust has higher volatile matter content and lesser ash content with higher quantities of alkali and alkaline earth metals (AAEM) content in the decreasing order of Al>Ca>Si>K>Mg>Fe>P which makes it as a potential source of pyrolysis reaction.
- FTIR spectra showed the presence of functional groups in coal and sawdust with hydroxyl groups as the cause of the stability of coal.
- Characterization of synthesized catalysts, 10% and 20% NiO and Ni (II) aluminate composite catalysts by incipient wetness impregnation method showed a significant observation in its higher thermal stability, presence of functional groups (moisture and hydroxyl groups, OH in-plane bend and OH-out-of-plane bending) and surface binding energies ($Ni(OH)_2$ and NiO at binding energies of 533.31 eV and 854.5 eV, Al (2p) hybridized orbital state at 74.5 eV, Al_2O_3 and Al $(OH)_3$ at binding energy of 533.31 eV in its oxidized state, CoO (II) at 533.31 eV for 10% Ni composite catalyst while Fe_2O_3 at a binding energy of 640.7 eV) from TGA, FTIR and XPS results respectively.
- From XRD diffractogram, synthetic form of alumina, produced at a lower temperature which is a mixture of new “kappa” and theta alumina was observed for the calcined support. The crystallite size of Al_2O_3 support with Al_2O_3 phase was 11.52 nm from the Debyye-Scherrer equation and crystallinity % was seen as 93.66%. For the 10%

NiO/Al_2O_3 composite nano-catalyst, phases present were Al_2O_3, $NiAl_2O_4$, $NiAl_{10}O_{16}$ and $NiAl_{32}O_{49}$ with monoclinic crystal lattice, nickel aluminium iron oxide ($Fe_{0.35}Ni_{0.12}Al_{0.53}$) ($Ni_{0.88}Fe_{0.15}Al_{0.97}$) O_4 with a cubic crystal lattice system along with Ni $Fe_{1.5}Al_{0.5}O_4$, $NiFe_{1.75}Al_{0.25}O_4$, NiO (cubic), nickel, syn metal and Ni_2O_3, nickel oxide with hexagonal lattice. Whereas for 20% NiO/Al_2O_3 composite nano-catalyst, phases present were Al_2O_3 phase, $Al_{2.66}O_4$, $NiAl_2O_4$ (cubic), nickel aluminium iron oxide ($Fe_{0.35}Ni_{0.12}Al_{0.53}$) ($Ni_{0.88}Fe_{0.15}Al_{0.97}$) O_4 with a cubic crystal lattice system, $NiFe_{1.5}Al_{0.5}O_4$ (cubic), Fe_2O_3 (iron oxide) with tetragonal lattice, Fe_3O_4 (magnetite) with cubic lattice system, nickel, syn phase and NiO (Bunsenite) both with cubic lattice system. The crystallite size was 16.107 nm and crystallinity % was 96.29 % for 10 % Ni loaded catalyst and 16.10 nm and 93.35 % for 20 % Ni loaded catalyst from Debye-Scherrer equation.

- From FETEM results, average particle size was 3.47 nm for a 10 % Ni-loaded catalyst and 10.96 nm for 20 % Ni-loaded catalyst. The agglomeration/ sintering of particles due to thermal effects could not be seen in 10 % loaded catalyst, whereas it was noticed in a 20 % loaded catalyst. The appearance of bigger particles might be due to the formation of nickel di-aluminate and $NiAl_{10}O_{16}$ as also evident from XRD diffraction and AFM imaging.
- Selected area diffraction pattern (SAED pattern) showed a single crystal structure enveloped with polycrystalline structure between the Ni metal and the matrix for both 10 % catalyst and 20 % catalyst respectively.
- The inter-particle distance or d-spacing is one of the desirable factors for alleviating the activity per unit volume of the catalysts. HRTEM images of the 10 % catalyst showed a d-spacing of 0.216 nm whereas for 20 % catalyst, it denoted a d-spacing of 0.26 nm, 0.26 nm, and 0.29 nm for three consecutive planes.
- Physiosorption analysis revealed a multi-point BET surface area of 77.98 $m^2\ g^{-1}$, 52.64 $m^2\ g^{-1}$, and 53.77 $m^2\ g^{-1}$ along with mean pore diameter of 12.75 nm, 15.51 nm, and 13.98 nm for Al_2O_3 support, 10 % and 20 % Ni loaded catalysts respectively. It showed reversible Type IV isotherm for the physisorption of nitrogen gas with a H3 hysteresis loop. The shape was the result of unrestricted monolayer-multilayer adsorption up to high (p/p_0). However, the pore volume in the catalysts was higher in both the synthesized catalysts compared to the calcined alumina support. As the metal content increased in the Ni-based catalysts, pore filling decreased substantially due to

the presence of various Ni (II) aluminates and NiO impregnated onto the support, thereby blocking the active pores.

From this study, it is concluded that coal has higher ash content and lower volatile matter content than sawdust with considerable calorific value content. Sawdust has considerable volatile matter content and lesser ash content with higher quantities of alkali ana alkaline earth metals (AAEM) content. The purity in elemental composition, microstructure and nanostructure visualizations, purity in crystal phase structure, presence of functional groups, presence of surface binding energies, determination of surface area and pore size distribution of the 10 % and 20 % NiO and Ni (II) aluminate nano-composite catalysts is comprehended. The thermal degradation profile of the catalysts proved that they are thermally stable to a temperature of 1173 K, which makes it feasible for the catalytic pyrolysis of sawdust and catalytic co-pyrolysis of coal and sawdust blends.

9.1.2 Thermal pyrolysis and co-pyrolysis kinetics of coal and biomass blends

For discernment of pyrolysis studies, low-grade coal and sawdust were the candidate feedstock materials. A detailed and comprehensive study on pyrolysis kinetics and thermodynamics was done on coal, sawdust, and coal-sawdust blends (100 % and 200 % sawdust addition to coal) when evaluated in a thermogravimetric analyzer between 303-1173 K temperature range in presence of 99.99 % pure N_2 gas flow at 20 mL min^{-1} at 1.9 bar gas pressure from heating rates 10–40 K min^{-1}. The outcomes from the detailed study is presented below.

- Coal degraded least than sawdust due to its presence of more ash content and lesser volatile matter content with a four-stage degradation profile for coal and a three-stage degradation profile for sawdust. Higher the H/C and O/C ratio in biomass, higher the H donating capacity and increased oxygen reactivity during co-pyrolysis. The C=C bond in the coal is stronger than the R-O-R bond of biomass which breaks faster and the transfer of OH radicals and H helps in the breaking of aromatic associations of coal during co-pyrolysis. This also develops a higher yield of liquid and gaseous products and reduces the char yield.
- The study clarifies the effect of biomass on the thermal stability of coal during co-pyrolysis, where with increase in sawdust blending on coal, the rate of thermal degradation increased. This is evident from conversion % in the active pyrolytic zone and also from values of instantaneous rate, intrinsic reaction rate, and comprehensive pyrolysis index at a single heating rate, 20 K min^{-1}.

- Synergistic interactions were observed for 10 %, 70 %, 90 %, 100 % and 200 % blends due to the positive upshots of biomass blending on coal due to the presence of alkali and alkaline earth metals and negative synergistic effects were seen for 30% and 50% blends.
- Due to the higher thermal stability of coal, it needs more time inside the reactor to degrade. However, for sawdust pyrolysis, a higher heating rate enhances de-volatilization in the active pyrolytic zone and better evaporation of moisture. Due to the fast release of the pyrolytic vapours the biomass gets squeezed at a higher rate and the resultant is a higher char yield. % conversion of 73.37 % sawdust degradation occurred by producing a final char residue of 13.75 % within the active pyrolytic zone., while for coal degradation char residue was 95.05 % at 20 K min^{-1} heating rate. However, for the 100 % blend, % average conversion was 32.43 % and final char residue % was 55.98 % and for 200 % blend, % conversion was 73.37 % and final char residue was 20.87 %.
- A model free integral method (Kissinger-Akahira-Sunose method) was used for the estimation of degradation kinetics of coal, sawdust and the 100 % and 200 % coal-sawdust blends. The average value of E_α within 10%<α<95% for Stage II of thermal degradation of coal was 99.47 kJ mol^{-1} while for Stage III of coal pyrolysis was 402.04 kJ mol^{-1}. The activation energy was 123.21 kJ mol^{-1} at α=70% which was higher than the activation energy obtained between 10%>α<75% and lower as compared to 5 %. The average activation energy obtained from the co-pyrolysis of coal and 100 % sawdust was 108.84 kJ mol^{-1} between α = 5-65 % while for 200 % blend, it was 122.40 kJ mol^{-1} between α = 5-65%.
- The reaction mechanism for sawdust pyrolysis incorporated R2 (geometrical contracting cylinder) mechanism from 5–70 % conversion and beyond 70 % conversion, it ascertains a first-order reaction model and for coal, pyrolysis was first-order reaction model as estimated by the Criado method. However, coal-sawdust blend co-pyrolysis kinetics incorporates similar R2 reaction mechanism till 80% conversion and later converges to first – order reaction mechanism.
- For Stage II of coal pyrolysis, the ΔH value was 44.3 kJ mol^{-1} at α=5% after which it further increased till α = 15% as 54.94 kJ mol^{-1}. However, for Stage III of coal pyrolysis, the ΔH value was 158.8–1014 kJ mol-1. The average enthalpy was 242.087 kJ mol^{-1} for coal pyrolysis, 103.35 kJ mol^{-1} for 100 % blend co-pyrolysis and 122.019

kJ mol^{-1} for 200 % blend co-pyrolysis. With an increase in the conversion the value of Gibbs free energy increased for coal pyrolysis and co-pyrolysis as well. However, the value was much higher for coal pyrolysis as compared to co-pyrolysis of blends.

From this study, it is concluded that co-pyrolysis of sawdust with coal is a viable option to use low-grade coal for the production of pyrolytic oil. This confirmed that the blending of biomass with coal helped in decreasing the thermal stability of coal. This also indicated the best utilization of low-grade coal and waste biomass to produce alternative fuels.

9.1.3 Thermo-catalytic pyrolysis kinetics of biomass and catalytic co-pyrolysis kinetics of blends

The study describes the kinetic and thermodynamic study (using the KAS method) of sawdust catalytic pyrolysis and coal-sawdust blends catalytic co-pyrolysis that are calculated away from the evaporation zone using 10 % and 20 % NiO and Ni (II) aluminate composite catalysts when evaluated in a thermogravimetric analyzer between 303-1173 K temperature range in presence of 99.99 % pure N_2 gas flow at 20 mL min^{-1} at 1.9 bar gas pressure from heating rates 10–40 K min^{-1}. The outcomes from the detailed study is presented below.

- This study clarifies the effect of catalyst/sawdust ratio and catalyst/blend ratio on the conversion % in the active pyrolytic zone. The effect of heating rate was studied for the catalyst/sawdust ratio and catalyst/blend ratio with the highest degradability and conversion % in the active pyrolytic zone of the respective feedstocks.
- For sawdust catalytic pyrolysis, the % conversion in the active pyrolytic zone was highest for catalyst/sawdust ratio = 0.05 and 0.10 for 10 % and 20 % NiO and Ni (II) aluminate composite catalysts respectively.
- The KAS method was implemented for the catalytic pyrolysis of sawdust study. A significant increase in the E_α value from 95.13–159.68 kJ mol^{-1} was observed when the conversion was increased from 10–65 % for catalytic pyrolysis of sawdust with 10 % NiO/Al_2O_3 catalyst, an E_α value of 96–121.7 kJ mol^{-1} was observed when the conversion was increased from 10–75 % for catalytic pyrolysis of sawdust with 20 % NiO/Al_2O_3 catalyst.
- From conversion 20–80 %, the experimental curve takes the shape of an R2 reaction mechanism which is a geometrical contracting cylinder similar to the experimental curve of sawdust and beyond 80 % conversion, it was first order reaction model.
- For 100 % blend catalytic co-pyrolysis, the % conversion in the active pyrolytic zone was highest for (catalyst/blend) ratio = 0.20 and 0.05 for 10 % and 20 % NiO and Ni

(II) aluminate composite catalysts respectively. However, for 200 % blend catalytic co-pyrolysis, the % conversion in the active pyrolytic zone was highest for (catalyst/blend) ratio=0.10 for both 10 % and 20 % NiO and Ni (II) aluminate composite catalysts respectively

From this study, it can be concluded that using the KAS method, kinetics and thermodynamics can be calculated for sawdust catalytic pyrolysis and coal-sawdust blends catalytic co-pyrolysis away from the evaporation zone using 10 % and 20 % NiO and Ni (II) aluminate composite catalysts.

9.1.4 Thermal and catalytic pyrolysis of sawdust using NiO/Al_2O_3 composite catalyst

Thermal (non-catalytic) and catalytic pyrolysis of sawdust are explained. Catalytic pyrolysis of sawdust in the presence of synthesized NiO and Ni (II) aluminate composite catalysts is elucidated. The study is clarified by integrating sawdust into a fixed-bed reactor and assessment for its product profile distribution from a temperature range of 773 K, 823 K and 873 K at 30 K min^{-1} heating rate under nitrogen purge gas (300 mL min^{-1}). The key outcomes of the study include:

- In thermal pyrolysis of sawdust, with an increase in temperature from 773–873 K, bio-oil yield increased while biochar yield decreased significantly.
- In catalytic pyrolysis of sawdust, with the effect of 10 % and 20 % NiO/Al_2O_3 nano-catalyst, bio-oil yield decreased whereas gas yield increased for 10 % NiO/Al_2O_3 nano-catalyst.
- With the increase in pyrolysis temperature from 773–873 K, aromatic content decreased as aromatic rings break into short oligomer aliphatic chains. Aromatics content increased for bio-oil with 10 % Ni loading catalyst and aldehyde content decreased while alcohol content increased with a decrease in furan content. Aromatics content increased significantly for bio-oil with a 20 % Ni loading catalyst and aldehyde content decreased, alcohol content increased with a decrease in furan content.
- Characterization of the biochar revealed amorphous graphitic multilayer sheets with polycrystalline and hexagonal crystal lattice structures.
- The highest yield % of hydrogen in fuel gas was observed to be maximum for pyrolysis of sawdust at 873 K, which indicated that with the increase in temperature, the hydrogen yield % increased.

From this study, it is concluded that thermal pyrolysis with and without catalyst is a feasible technique for estimating the product profile distribution (liquid oil, fuel gas, and biochar residues) with (C_3–C_{20}) compounds present in bio-oil and a higher C_p value of 2.0 kJ kg^{-1} K^{-1}. Heat of fusion of bio-oil was -2192 J g^{-1} for sawdust pyrolyzed with 10% Ni loaded catalyst and maximum heat released was 4.35 kJ kg^{-1} for bio-oil at 873 K temperature. Due to the catalytic cracking at higher temperatures, furans, and aromatic rings break into short oligomer aliphatic chains. A highly stable porous biochar was observed with amorphous graphitic multilayer nanosheets with polycrystalline and hexagonal crystal system. With the increase in nickel loading in the catalytic char residue, higher demethanation reaction, lesser decarbonization and higher oxidation occurred. The highest yield % of hydrogen in fuel gas was observed at 873 K, which indicated that with the increase in temperature, the hydrogen yield % increased.

9.1.5 Thermal and catalytic co-pyrolysis of coal-sawdust blends with NiO/Al_2O_3 composite catalyst

Thermal (non-catalytic) pyrolysis of coal and co-pyrolysis of coal-sawdust blends are explained. Catalytic co-pyrolysis of blends in the presence of 10 % and 20 % NiO/Al_2O_3 catalysts is also elucidated by integrating the feedstocks into a fixed-bed reactor and assessment for its product profile distribution from a temperature range of 773 K, 823 K and 873 K at 30 K min^{-1} heating rate under nitrogen purge gas (300 mL min^{-1}). The key outcomes of the study include:

- For coal thermal pyrolysis, coal char yield % decreased from 97.8–97.67 % with an increase in temperature from 773–873 K due to carbonization, while gas yield % increased slightly from 2.2–2.33 % with no liquid oil as product.
- Coal-sawdust blend (100 % sawdust blending with coal) co-pyrolysis yielded an increase in oil yield % and a decrease in gas and char yield % with a rise in temperature from 773-873 K respectively.
- At a biomass blending ratio of coal of 50 %, 100 % and 200 %, the conversion wt. % increased from 27.97 %, 37.35 % to a significant rise of 92.8 % respectively.
- For a 10 % NiO/Al_2O_3 composite catalyst, yield % of liquid oil and char residue enhanced and yield % of evolved volatiles decreased at (catalyst/blend) ratio of 0.20 for the 100 % blend. Whereas for 200 % blend with the catalysts, the yield % of oil and char residue decreased and the yield % of evolved volatiles decreased substantially for 10 % Ni loaded catalyst, whereas for 20 % NiO/Al_2O_3 composite

catalyst, the yield % of evolved volatiles and char residue decreased and yield % of bio-oil decreased.

- Coal char characterized revealed that graphitic multilayer sheets were formed with 70.28 % carbon and hexagonal single crystal lattice structures.
- D-Allose is the prominent compound present in the liquid oil from thermal co-pyrolysis of blends with a remarkable C_p value of 5.300 kJ kg^{-1} K^{-1}. Heat of fusion of liquid oil increased with increased in temperature as seen from DSC thermogram results and maximum for 873 K as 2201 J g^{-1}.
- Catalytic upgradation of liquid oil using 10% and 20% NiO/Al_2O_3 composite catalyst resulted in ketones as the main compound present along with aromatics from GC/MS characterization and fantastic C_p values.

From this study, it is concluded that thermal pyrolysis of coal revealed good quality char with graphitic multilayer sheets and with negligible liquid oil generation. co-pyrolysis yielded an increase in oil yield % and a decrease in gas and char yield % with a rise in temperature. For catalytic co-pyrolysis of blends with 10% and 20% Ni-loaded catalysts, 20% Ni - loaded catalysts showed the highest conversion of 39.5% and 68.47% for 100% and 200% coal-sawdust blends respectively.

9.2 Application potential

The application potential of pyrolysis of sawdust and co-pyrolysis of blends with and without catalysts is tremendous from the point of view of its pyrolytic products. Liquid oil from sawdust pyrolysis imbibes functional groups, has high specific heat capacity value of 2.00 J g^{-1} K^{-1} as comparable to gasoline and diesel can be used as fuel for transport. D-Allose which was the predominant compound in bio-oil is largely regioselective in protective reactions and glycosidation reactions and has stupendous pharmacological and alimentary biological properties. It can be widely used as an antioxidant (phytochemicals) and an anti-tumor agent. The compound 3-methyl-2-(2-oxopropyl) furan has bioactive potential while phosphonic acid, (p-hydroxyphenyl)- shows antioxidant potential. Pyridine has medicinal properties whereas Carbamic acid, hydroxy-ethyl ester contains many such therapeutic properties. Another co-product of biomass pyrolysis along with evolved volatiles and liquid oil is biochar which can be used as a bio-fertilizer, catalyst carrier, precursor of activated carbon and carbon nanotubes (SWCNT and MWCNT), and a thermochemical energy storage material. Biochar usually has abundant surface functional groups (C−O, C=O, COOH and OH, etc.), which being highly modifiable act as a platform for the synthesis of various

functionalized carbon materials. Whereas coal char from thermal pyrolysis of coal revealed graphitic multilayer sheets formed with 70.28 % carbon and hexagonal single crystal lattice structures. Some rare compounds were found in liquid oil from thermal co-pyrolysis of blends such as Octadecane, 2,2,4,15,17,17-Hexamethyl-7, 12- Bis (3, 5,5 -Trimethylhexyl)- with maximum peak area for D – Allose. Distinct SAED pattern was seen for char residue from blend co-pyrolysis with single crystalline cubic lattice structure with graphitic multilayer sheets. Fuel gas generated consisting of pyrolytic syngas can be used for fine chemical synthesis using various catalytic bed materials in reactors, mainly CO_2 methanation reactions, water gas shift reactions, reforming reactions, and methanol generation. Hydrogen can be used as source of fuel for power generation and transport purposes.

9.3 Scope for future work

Advanced kinetic modelling techniques such as gaussian and logistic DAEM explaining the stepwise reaction mechanisms can be incorporated during kinetic studies for elucidating thermal degradative process. Catalysts with bimetallic active sites or promoted with metals (Ce, K, Mg, Na) can be fabricated for higher activity and selectivity towards selected products during the catalytic pyrolysis and co-pyrolysis process. Catalysts can be regenerated after post-treatment in such processes to effectuate their recyclability. Another milestone which could be achieved as future work potential would be the generation of single-walled and multi-walled carbon nanotubes from pyrolysis process. This would be the char residue which would have tremendous amount of potential as catalysts material, adsorbents and energy storage purposes. Char residue would also have tremendous potential if multilayer graphitic nanosheets are formed during pyrolysis process. This might create a breakthrough in carbon technology where it would serve as electrodes, super-capacitors, and adsorbents in soil remediation. Product liquid oil can be further studied for its usage in I.C. engine purposes and as fuel for transport.

Annexure

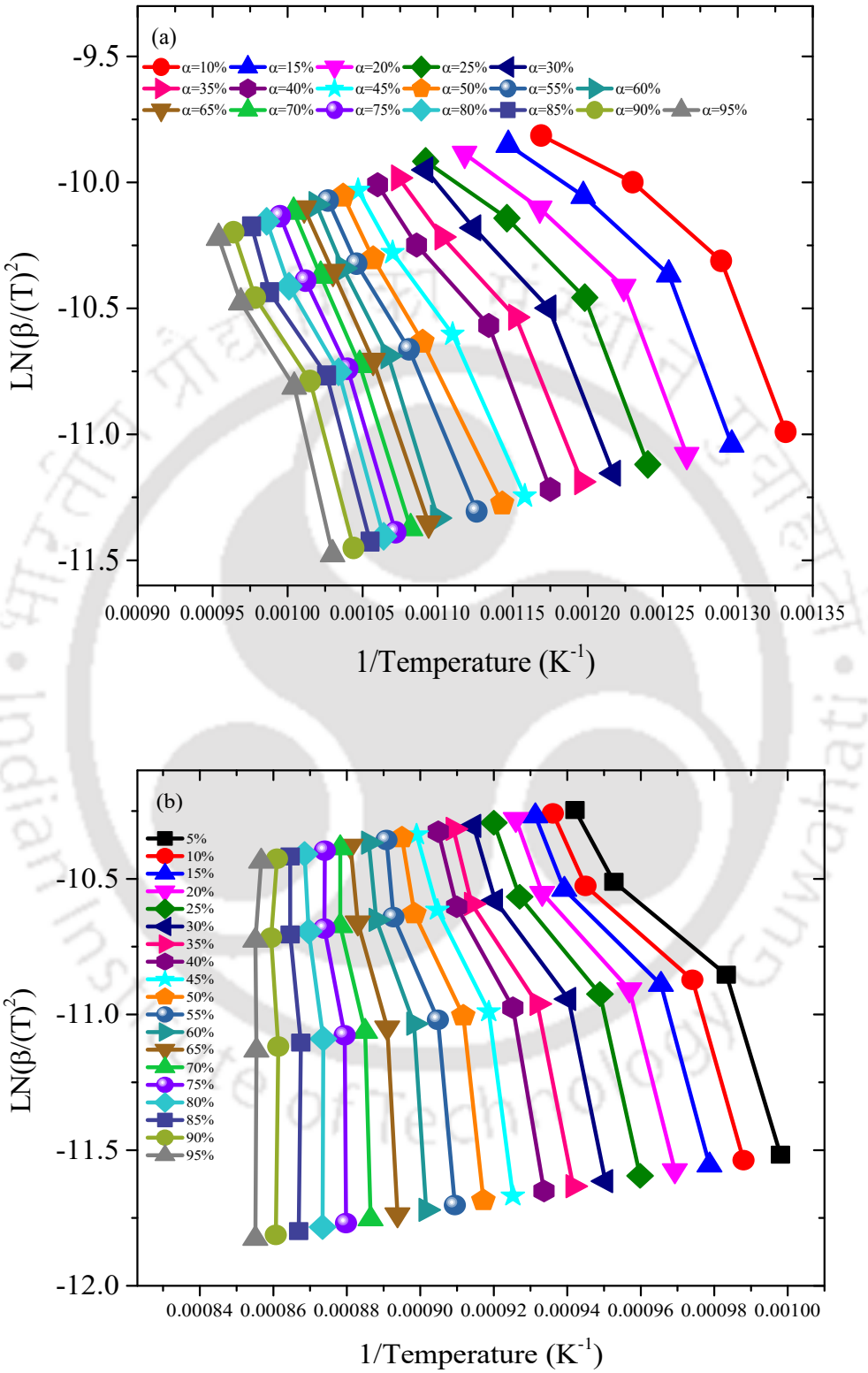

Fig. S1 Linear Regression plot of coal pyrolysis, $\ln(\beta/T^2)$ vs. 1/T in the conversion range of $5\% < \alpha < 95\%$ for a) Stage II and b) Stage III of Active Pyrolytic Zone

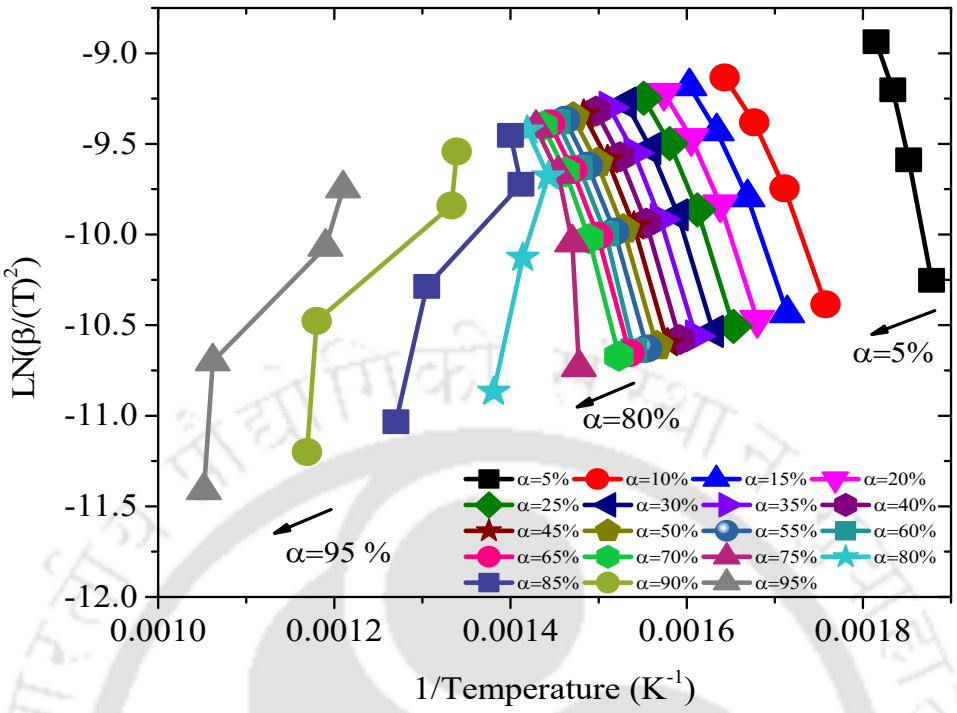

Fig. S2 Linear Regression Plots of thermal pyrolysis of sawdust, ln (β/T^2) vs. 1/T in the conversion range of 5% < α < 95%

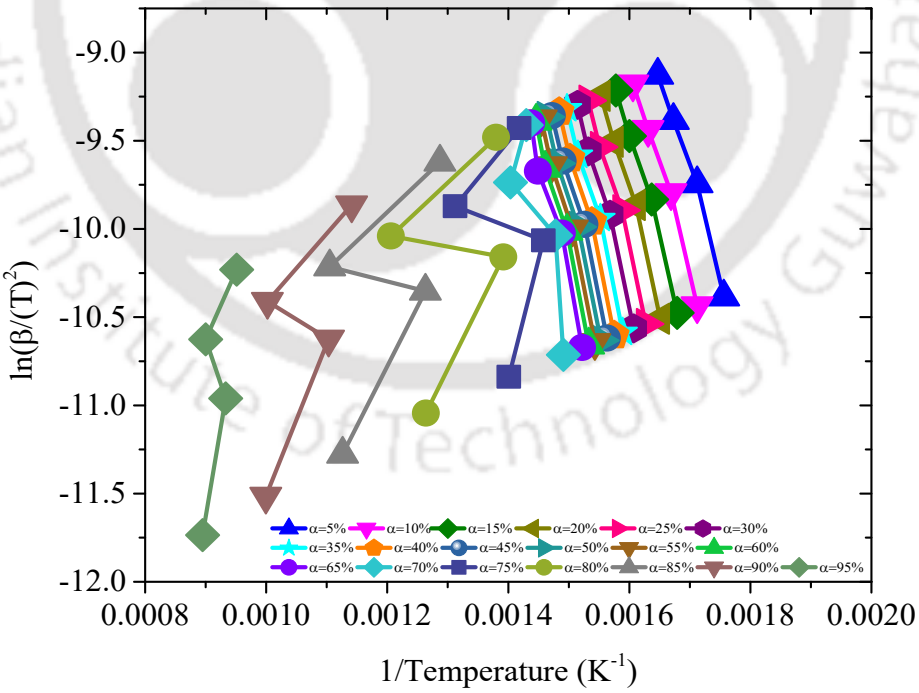

Fig. S3 Linear Regression plot of coal and 100% sawdust blend, ln(β/T^2) vs. 1/T in the conversion range of 5% < α < 95%

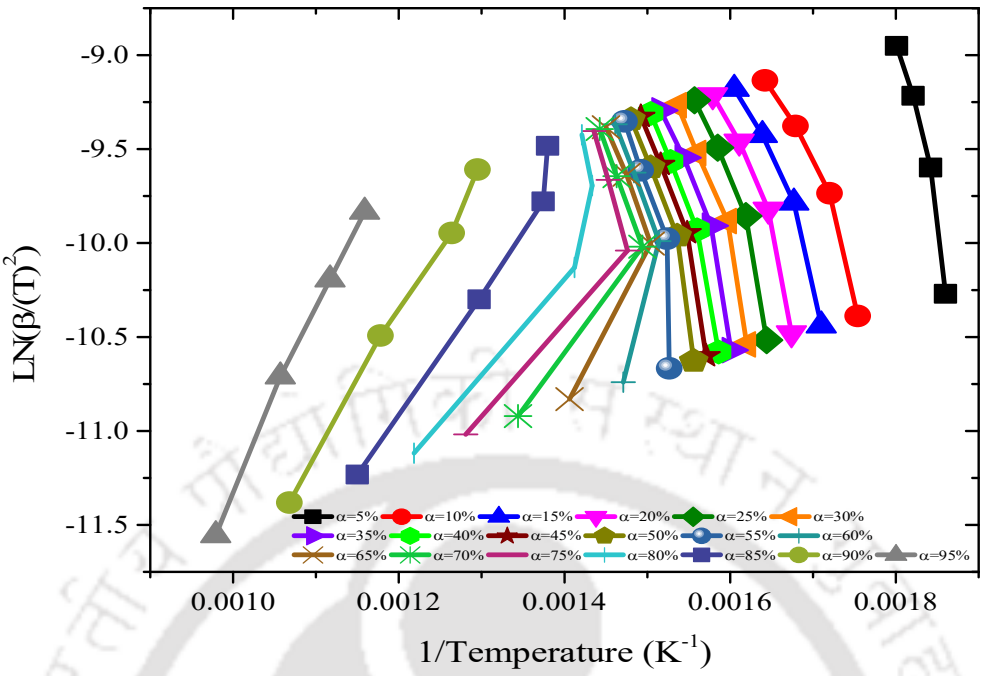

Fig. S4 Linear Regression plot of coal and 200% sawdust blend, $\ln(\beta/T^2)$ vs. 1/T in the conversion range of 5% < α < 95%

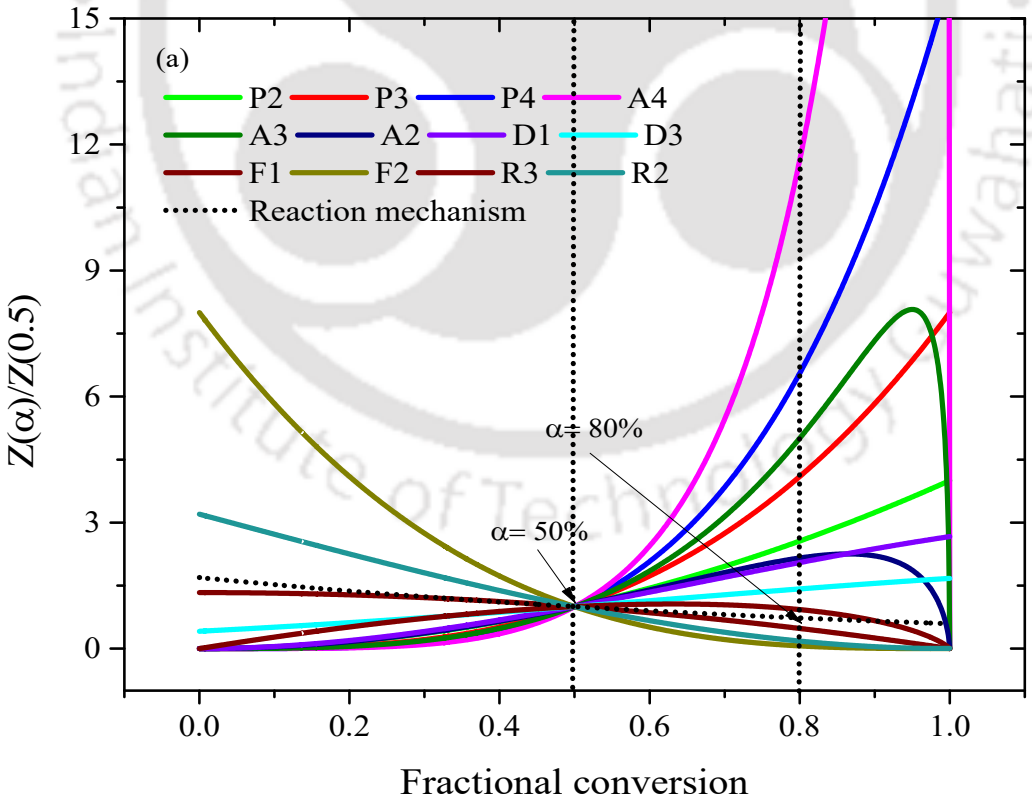

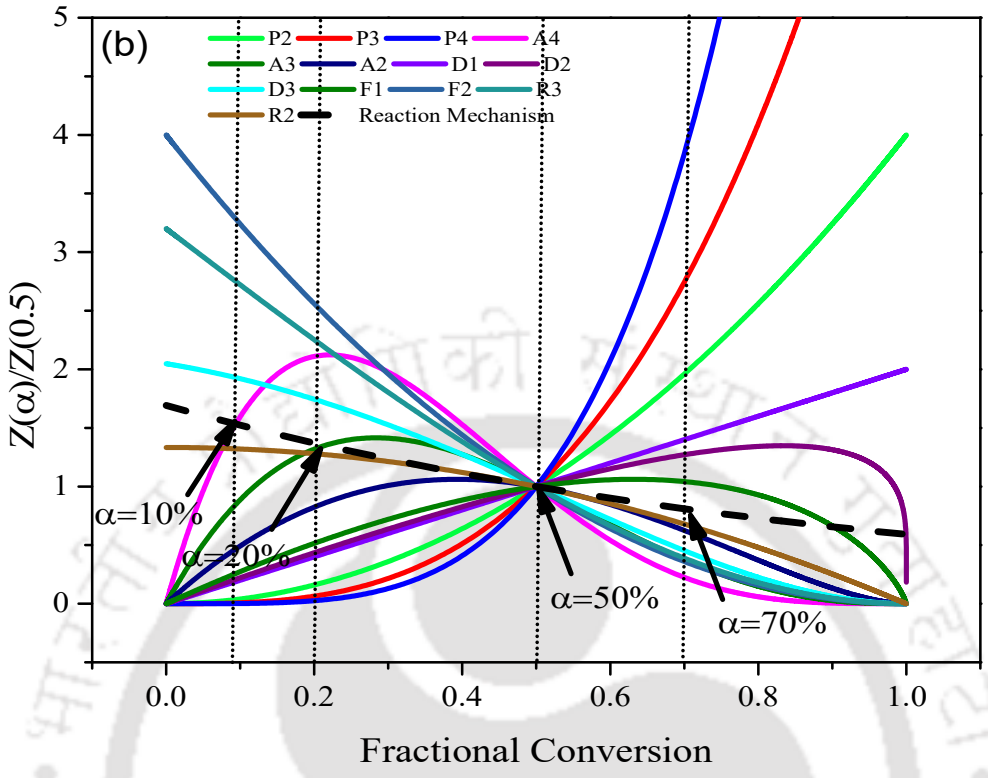

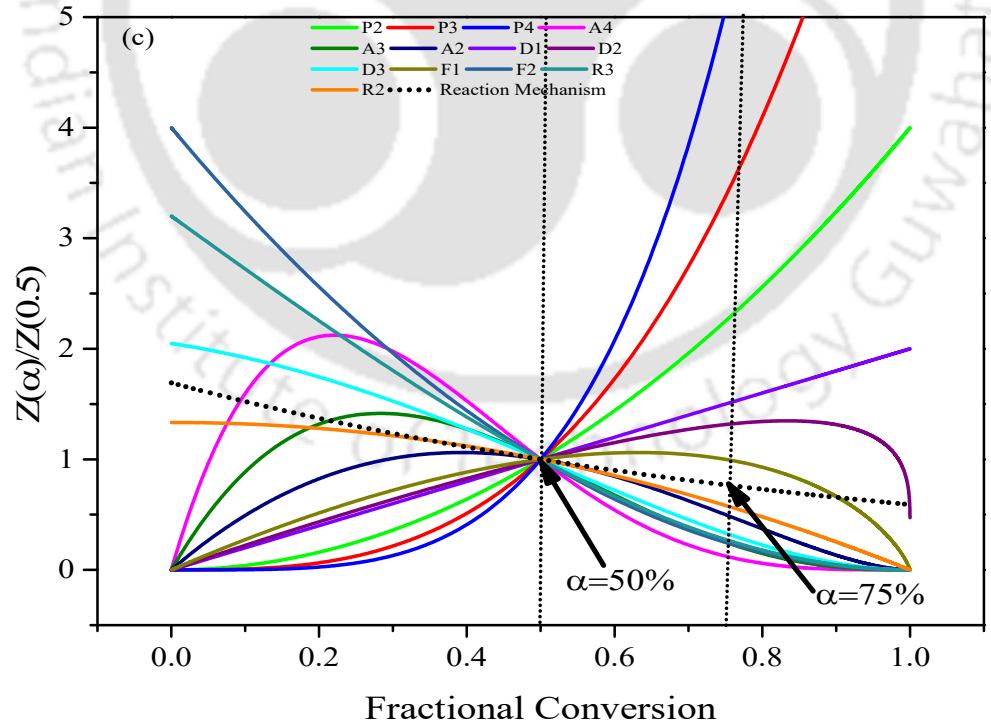

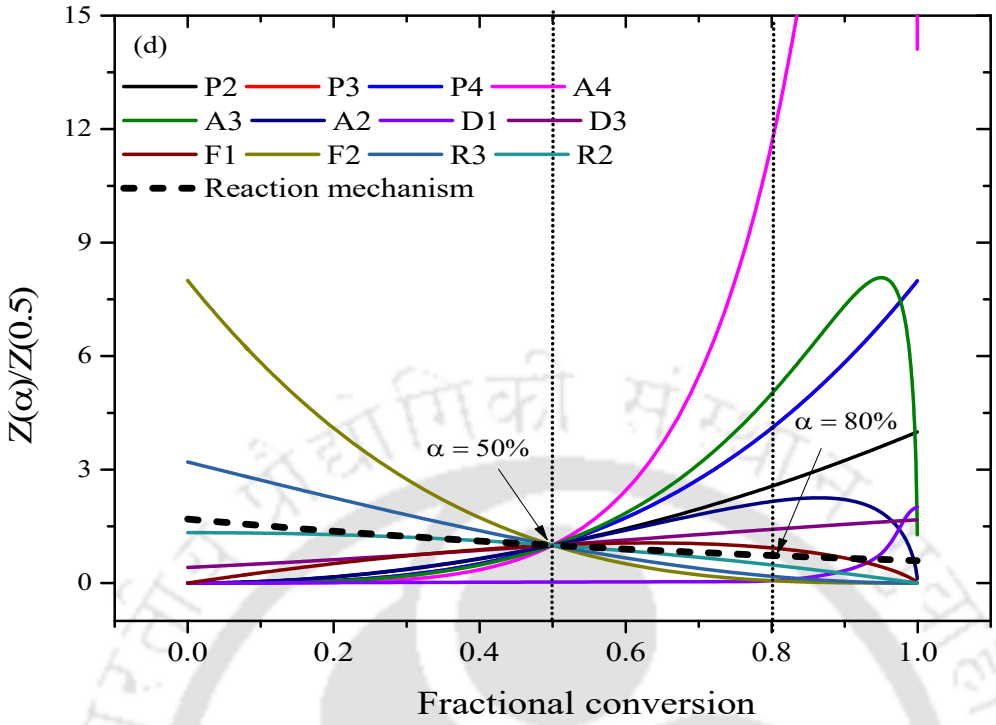

Fig. S5 Theoretical and experimental master curves in a differential−integral form representing f(α)/g(α) as a function of α for the different kinetic models describing solid-state reactions of a) Coal pyrolysis kinetics, b) Sawdust pyrolysis kinetics, c) 100% Coal-sawdust blend co-pyrolysis kinetics and d) 200% Coal-sawdust blend co-pyrolysis kinetics

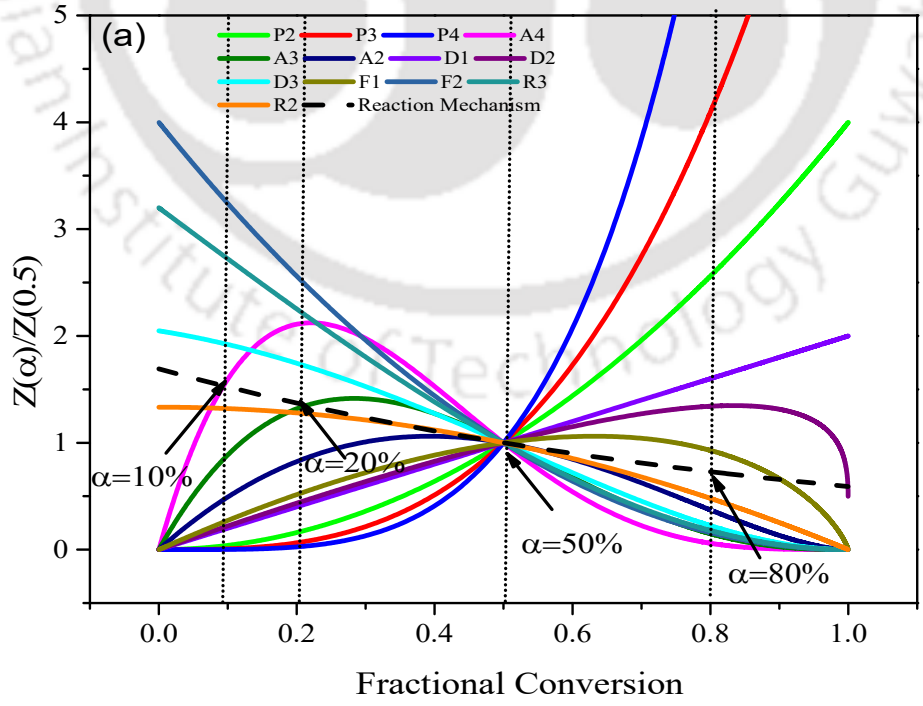

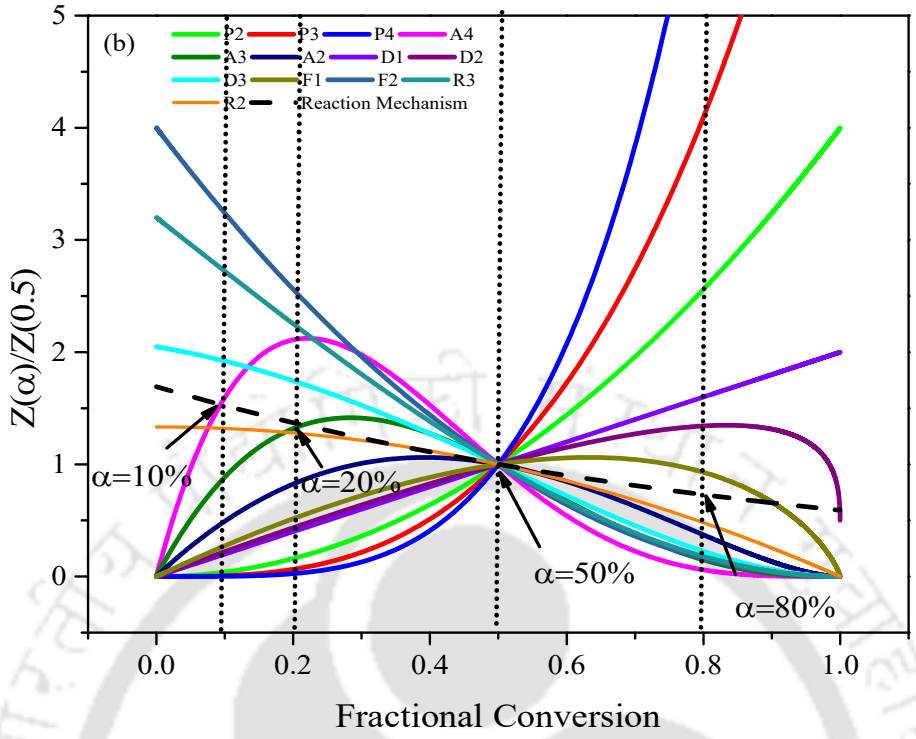

Fig. S6 Theoretical and experimental master curves in a differential−integral form representing f(α) g(α) as a function of α for the different kinetic models describing solid-state reactions of sawdust catalytic pyrolysis kinetics with a) 10% NiO/Al_2O_3 composite catalyst and b) 20% NiO/Al_2O_3 composite catalyst

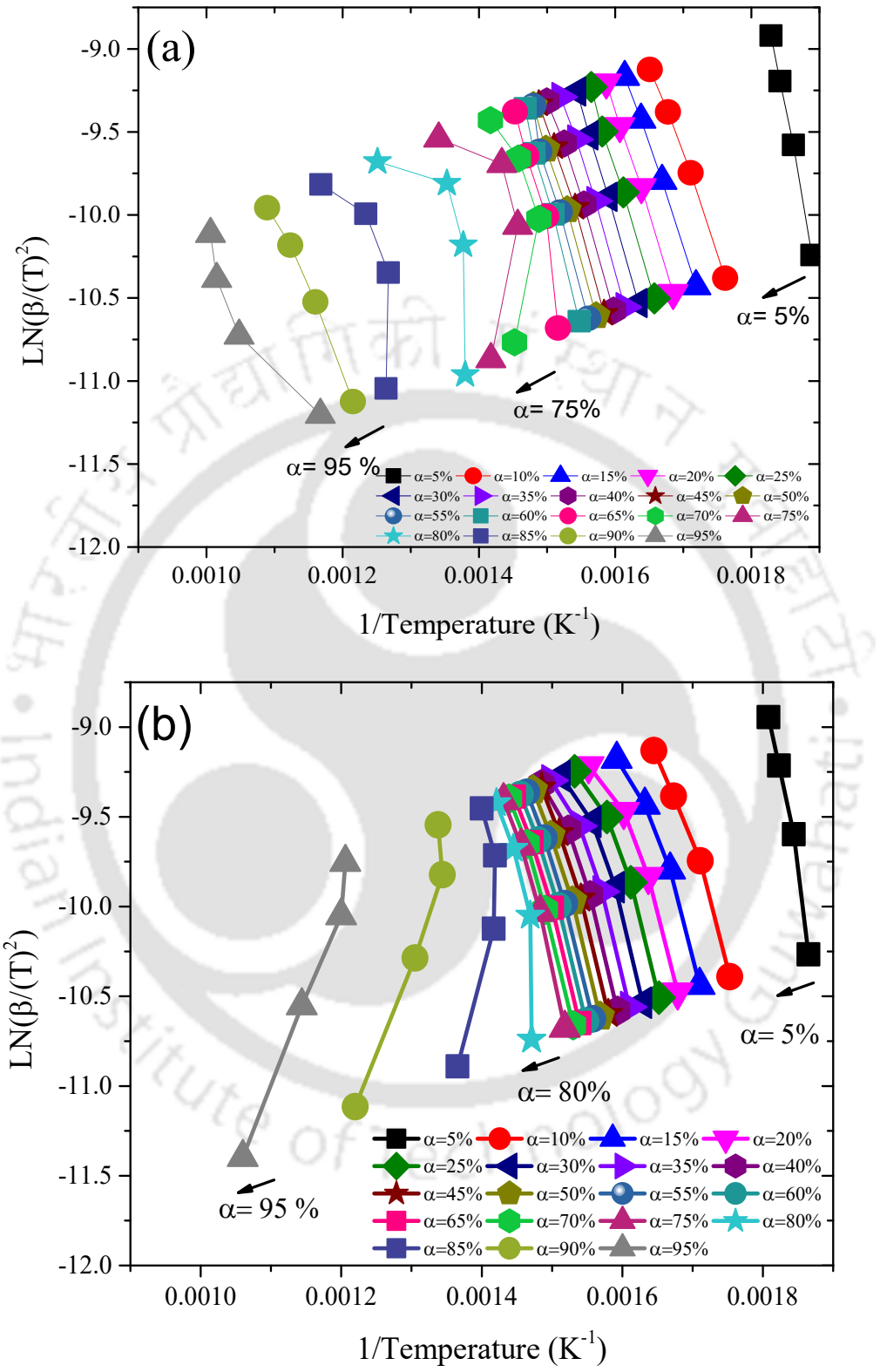

Fig. S7 Linear regression plots of catalytic pyrolysis kinetics of sawdust with (a) 10% NiO/Al_2O_3 composite catalyst, and (b) 20% NiO/Al_2O_3 composite catalyst

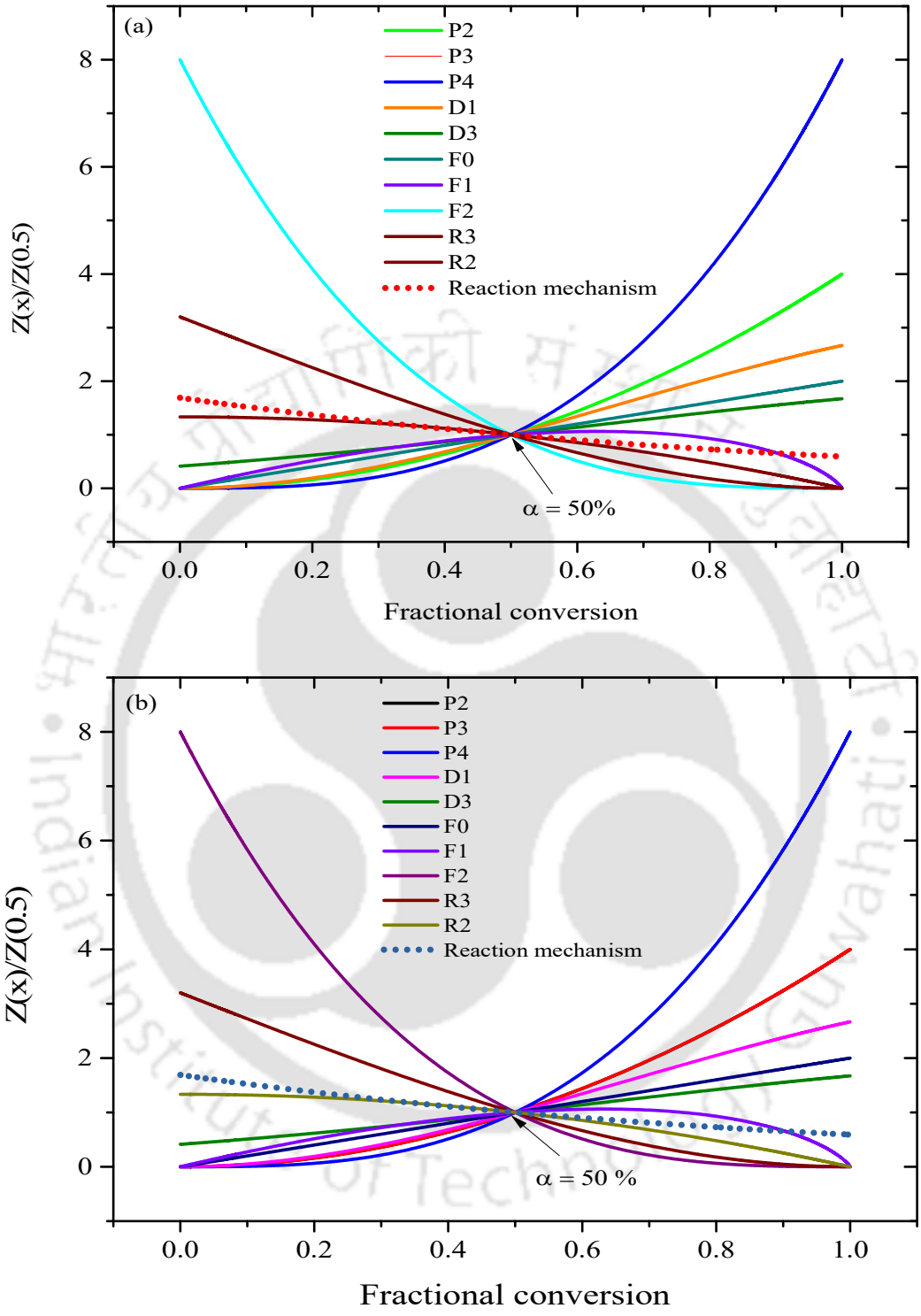

Fig. S8 Theoretical and experimental master curves in a differential−integral form representing f(α) g(α) as a function of α for the different kinetic models describing solid-state reactions of 100% blend catalytic co-pyrolysis kinetics with a) 10% NiO/Al_2O_3 composite catalyst and b) 20% NiO/Al_2O_3 composite catalyst

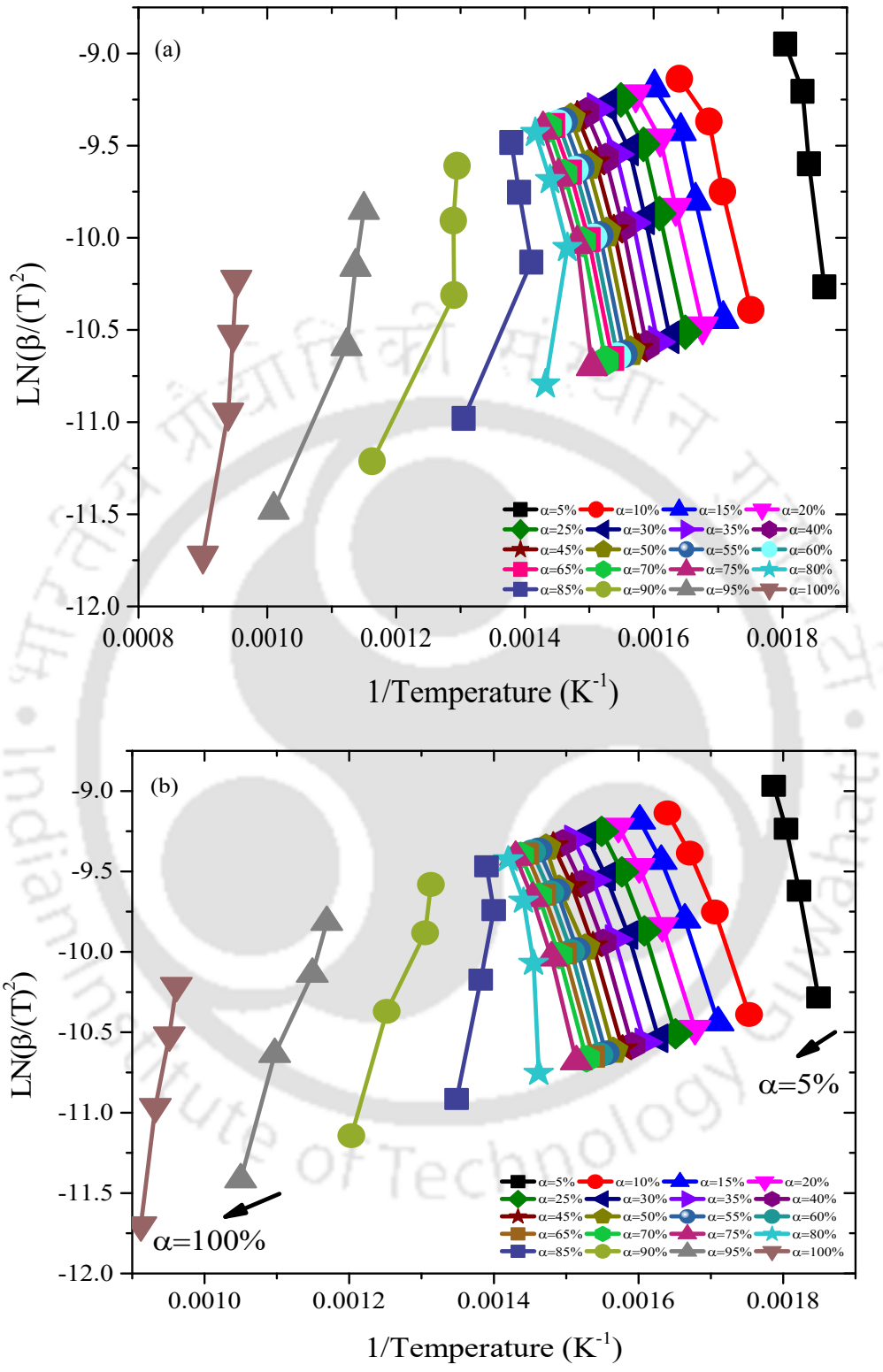

Fig. S9 Linear regression plots of catalytic co-pyrolysis kinetics of coal and 100% sawdust blend with (a) 10% NiO/Al_2O_3 composite catalyst, and (b) 20% NiO/Al_2O_3 composite catalyst

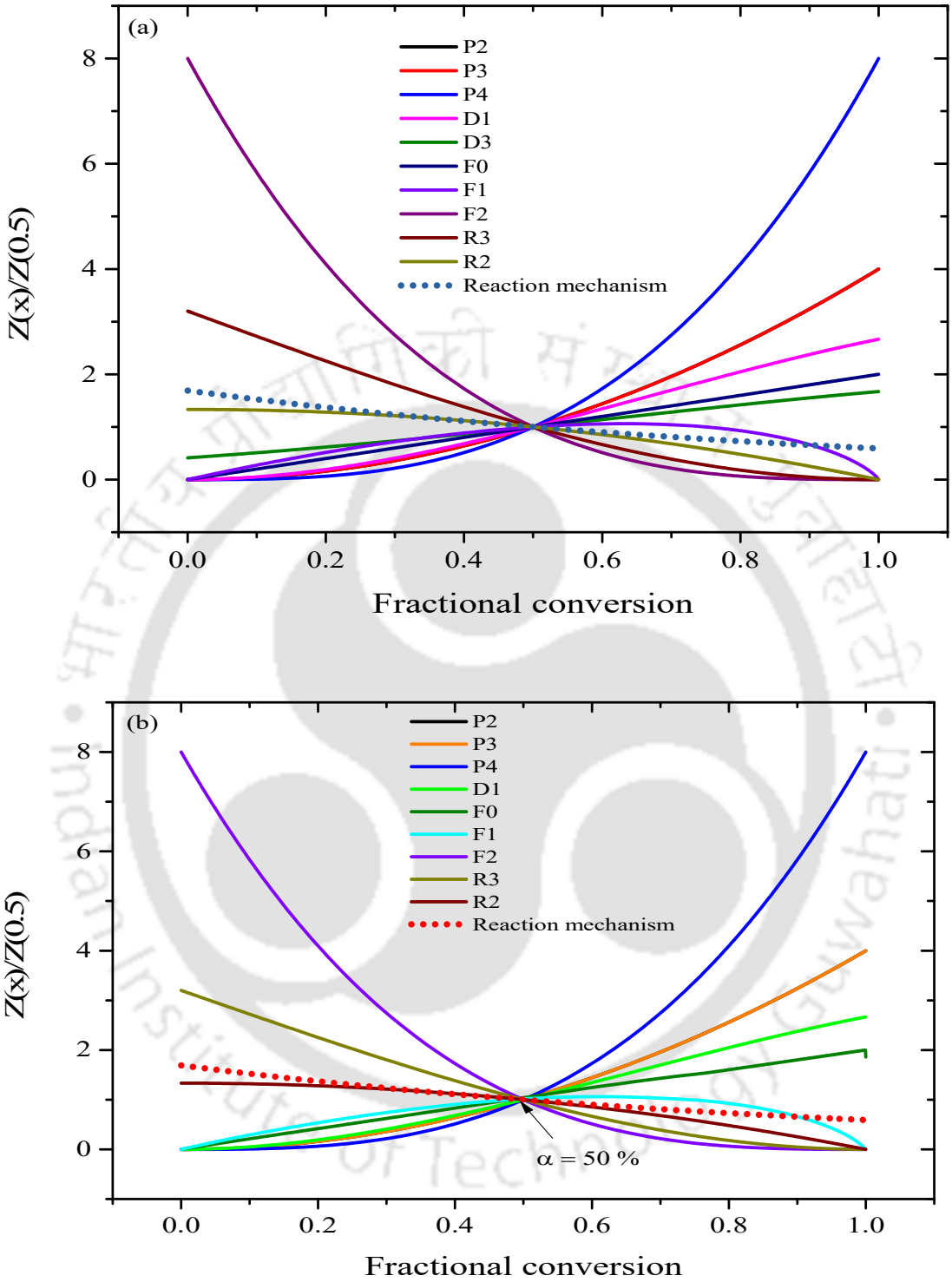

Fig. S10 Theoretical and experimental master curves in a differential−integral form representing f(α) g(α) as a function of α for the different kinetic models describing solid-state reactions of 200% blend catalytic co-pyrolysis kinetics with a) 10% NiO/Al_2O_3 composite catalyst and b) 20% NiO/Al_2O_3 composite catalyst

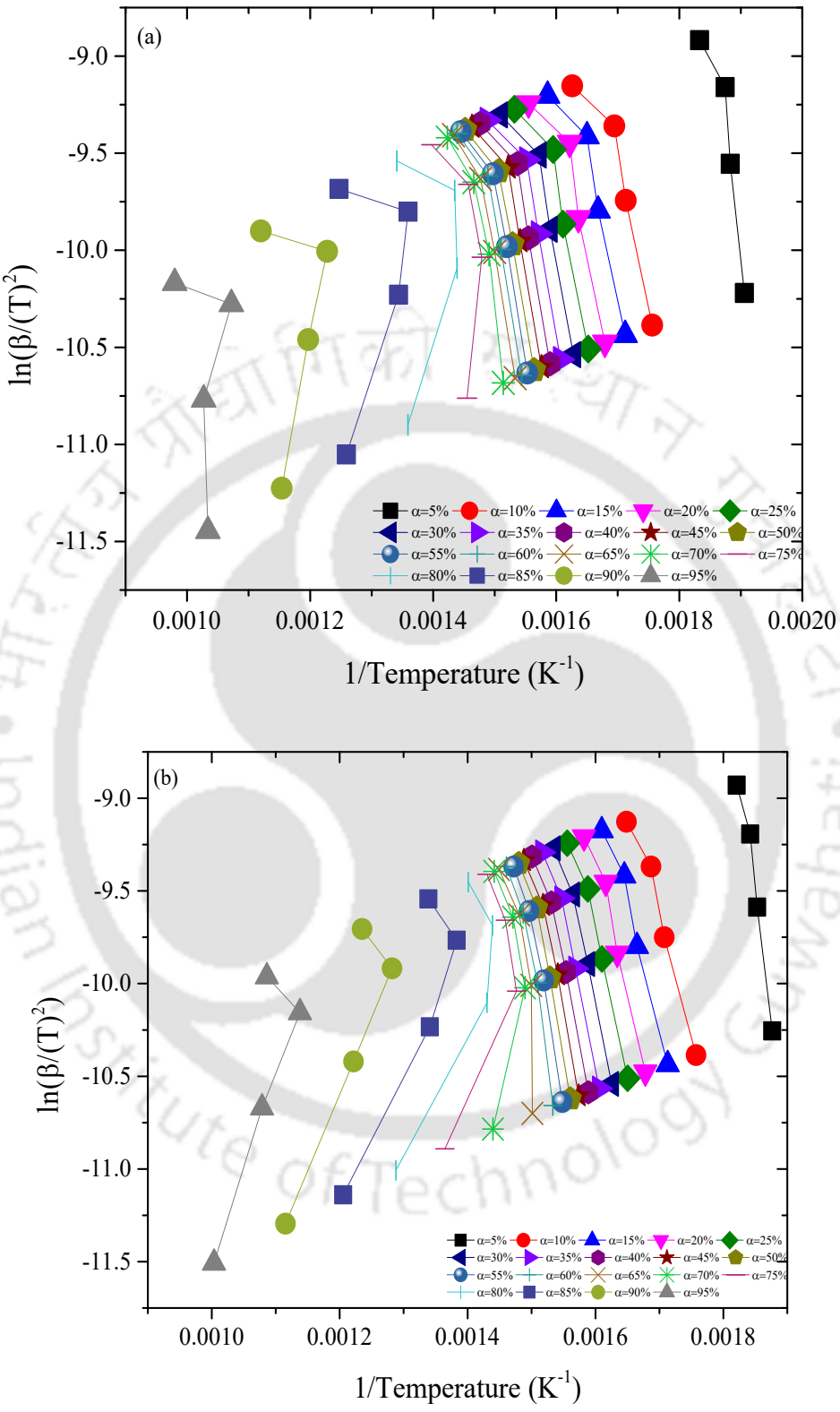

Fig. S11 Linear regression plots of catalytic co-pyrolysis kinetics of coal and 200% sawdust blend with (a) 10% NiO/Al_2O_3 nano-catalyst, and (b) 20% NiO/Al_2O_3 nano-catalyst

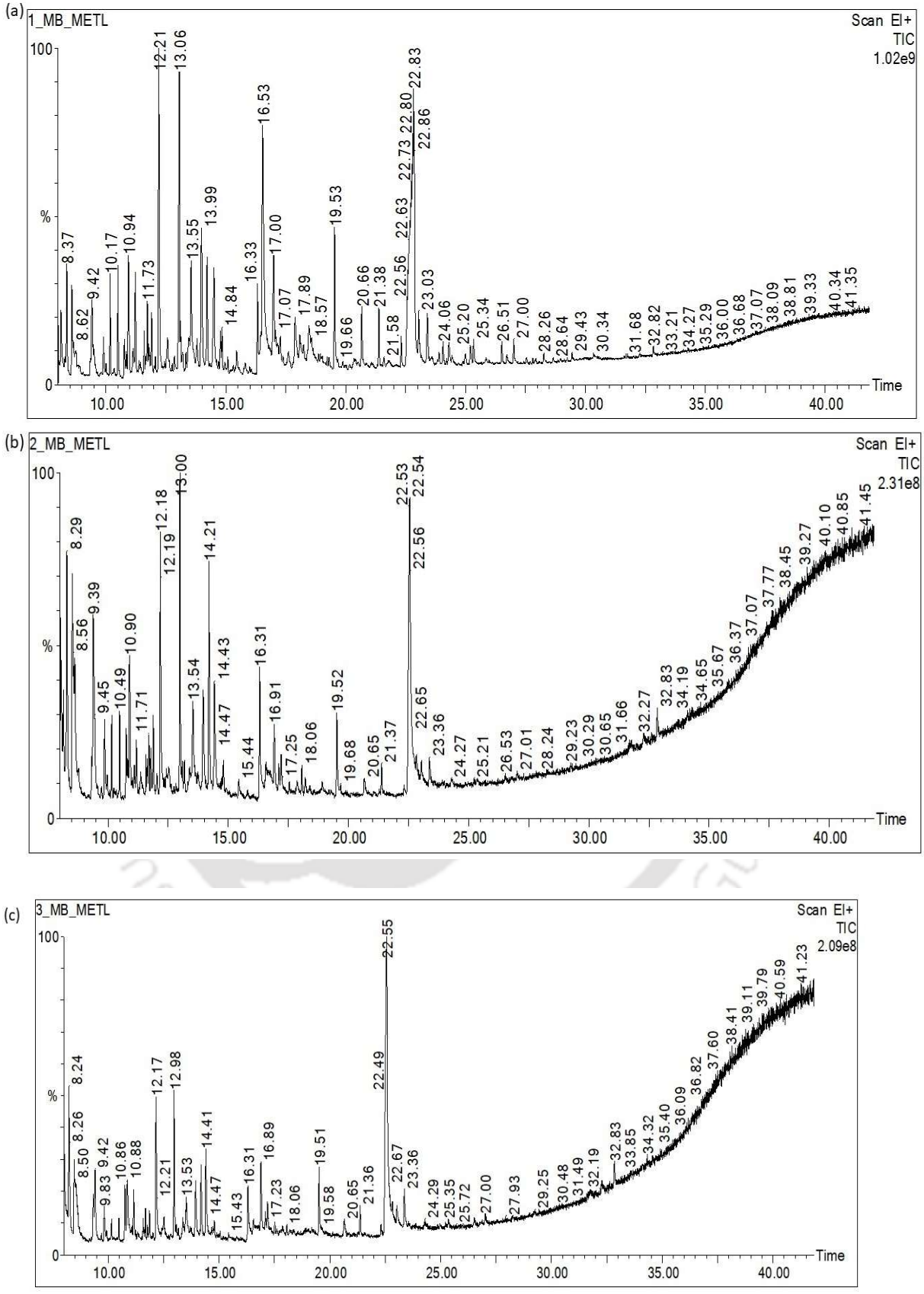

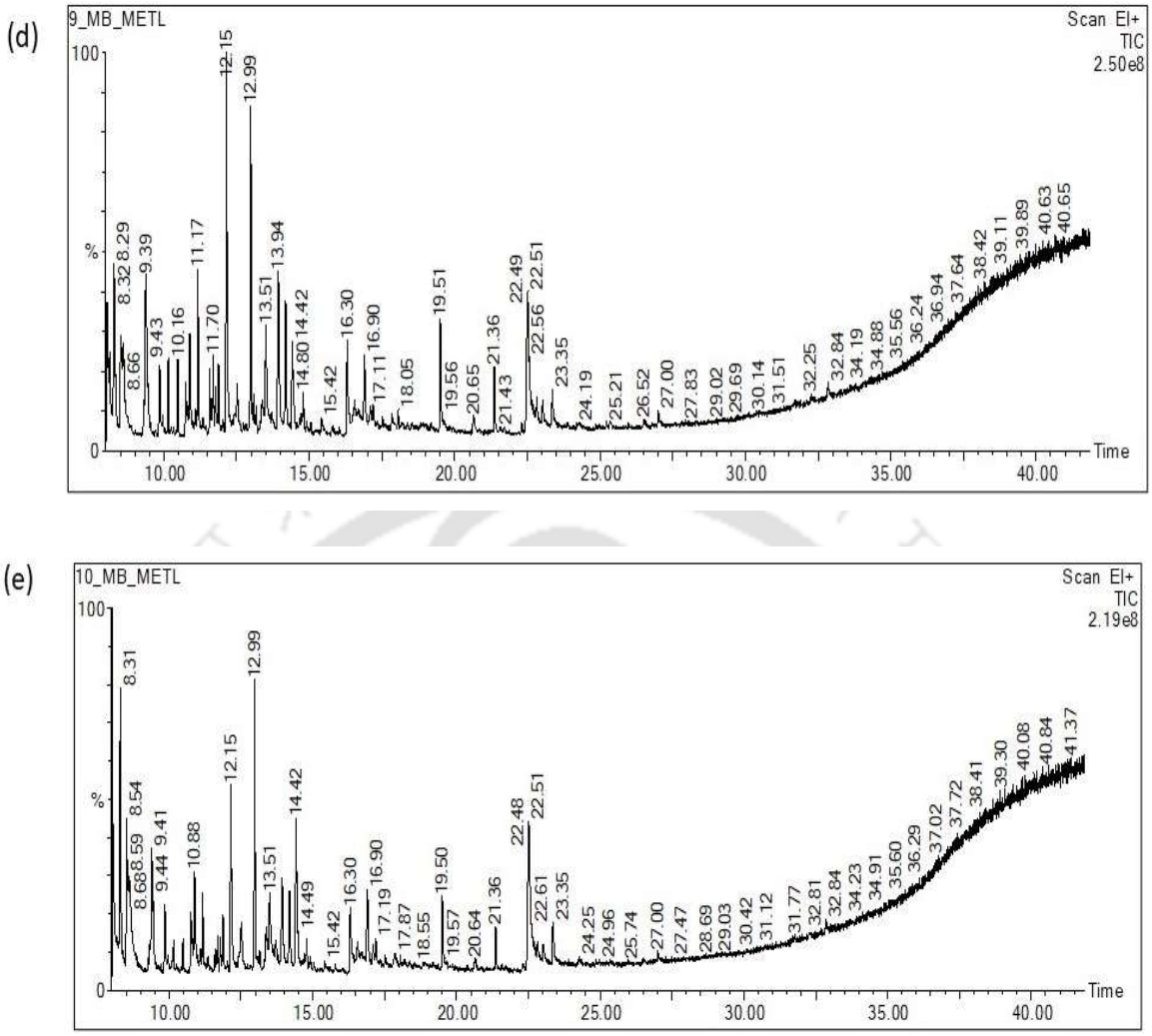

Fig. S12 GC/MS chromatogram of bio-oil from (a-c) thermal pyrolysis and (d, e) catalytic pyrolysis of sawdust using 10% and 20% NiO/Al_2O_3 nanocomposite catalyst

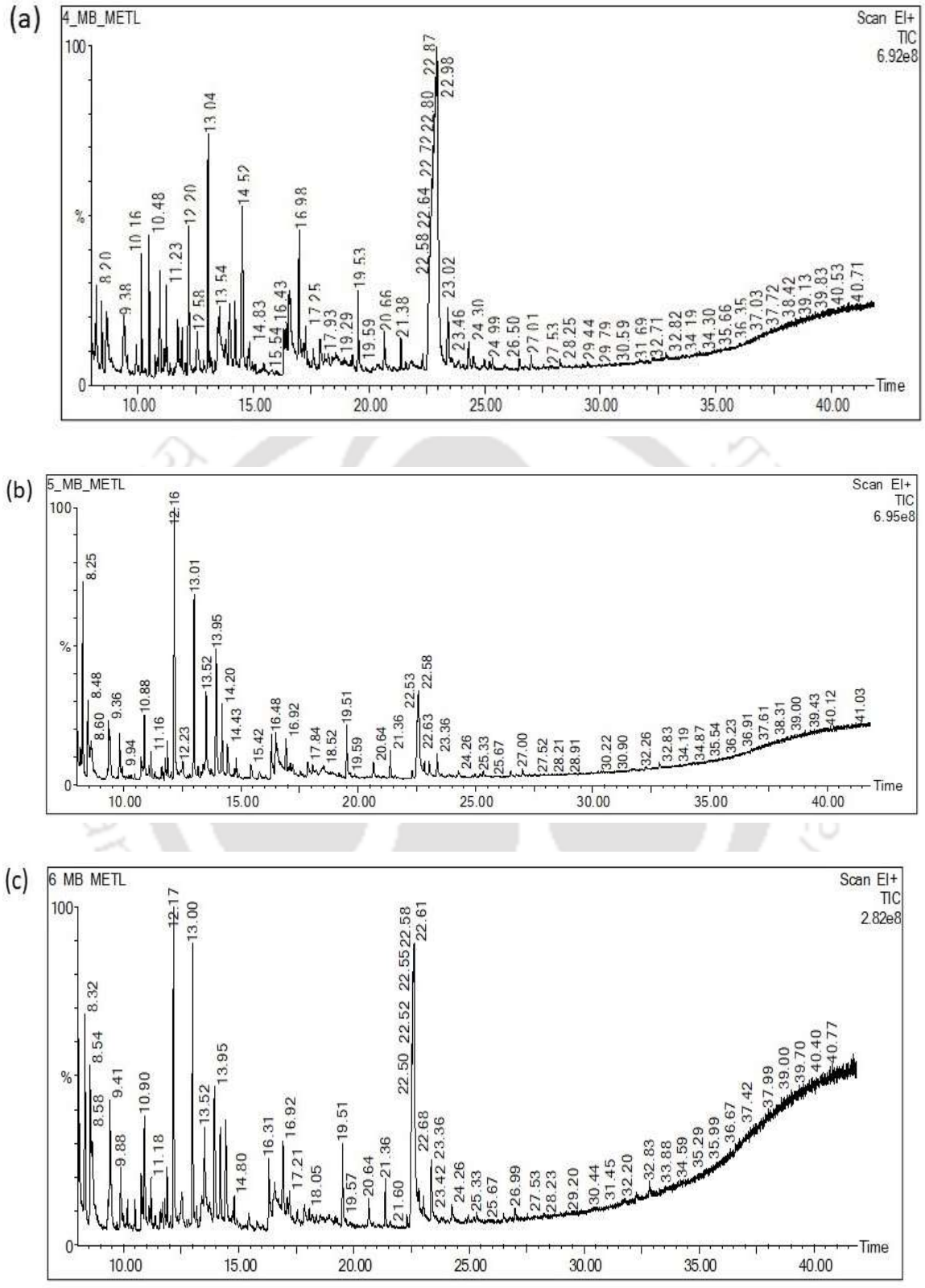

Fig. S13 GC/MS chromatogram of liquid oil product from (a-c) thermal co-pyrolysis of 100% blend at temperatures, 773 K, 823 K and 873 K

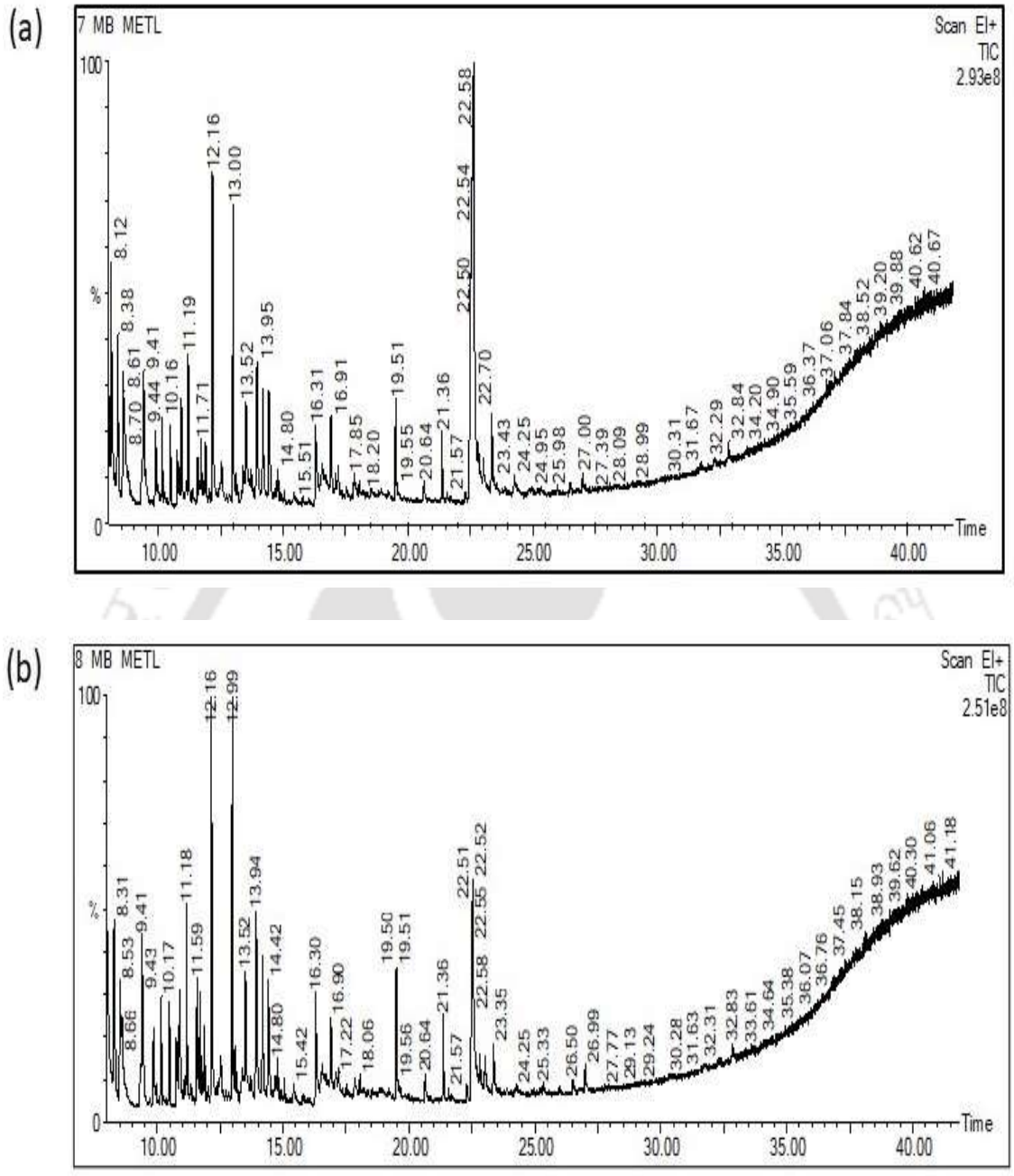

Fig. S14 GC/MS chromatogram of liquid oil from (a, b) thermal co-pyrolysis of 50% blend and 200% blend at temperature 873 K

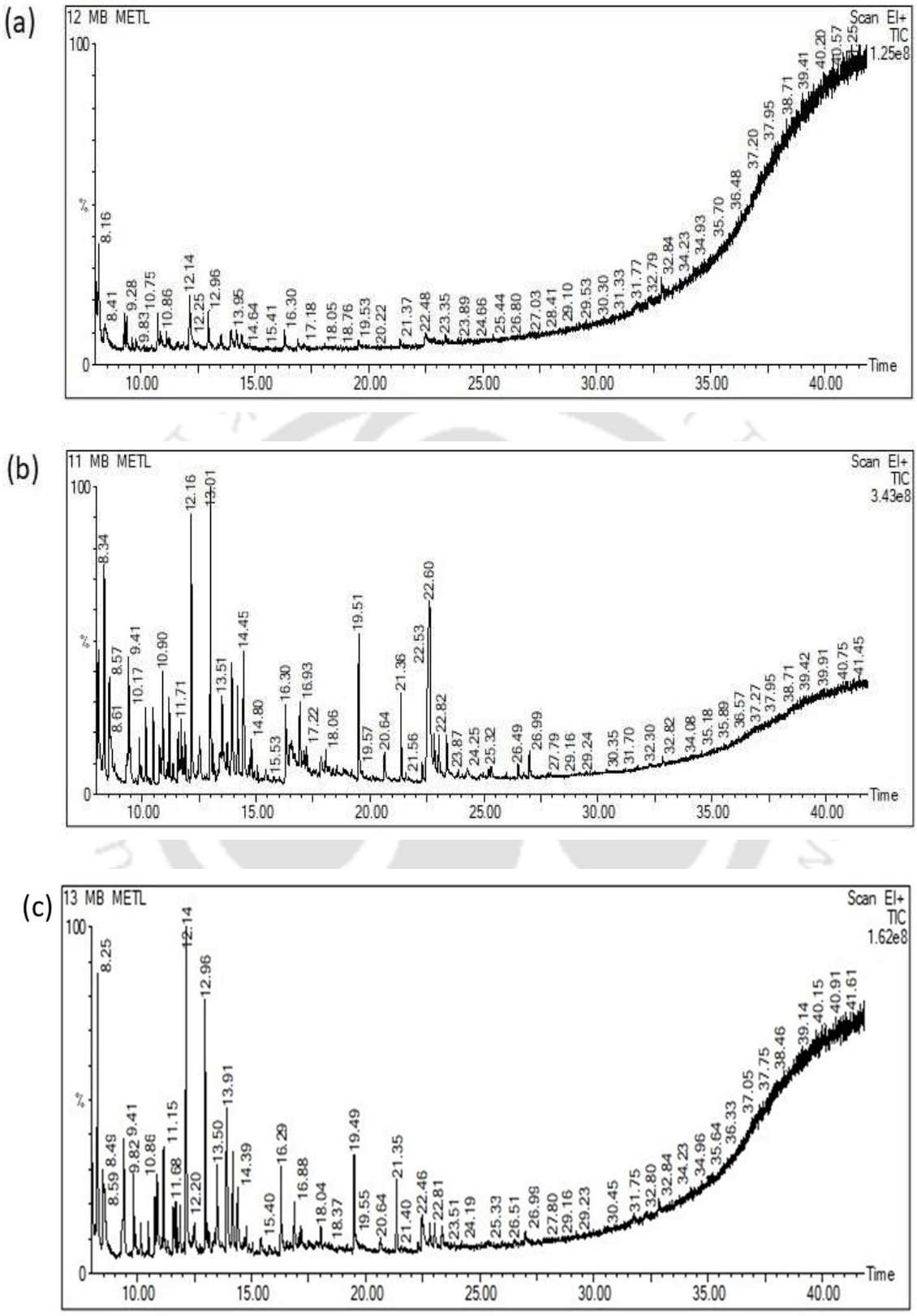

Fig. S15 GC/MS chromatogram of liquid oil from catalytic co-pyrolysis of (a, b) 50% and © 200% blends using 10% and 20% NiO/Al_2O_3 nanocomposite catalyst

Table S1. Determination of crystal structure from 2-theta angle, (h,k,l) parameters and d-spacing of each phase detected during XRD analysis for alumina support, 10% and 20% NiO/Al_2O_3 nano-composite catalyst

Crystal structure								
Alumina support			**10% NiO/Al_2O_3 composite catalyst**			**20% NiO/Al_2O_3 composite catalyst**		
Phase name	Chemical formulae	Crystal system and space group	Phase name	Chemical formulae	Crystal system and space group	Phase name	Chemical formulae	Crystal system and space group
Aluminum oxide	Al_2O_3	Cubic, Fd-3m (227)	Aluminum oxide	Al_2O_3	Cubic, Fd-3m (227)	Aluminum oxide	Al_2O_3	Cubic, Fd-3m (227)
							$Al_{2.66}O_4$	Cubic, Fd-3m (227)
			Nickel Aluminum Oxide	Al_2NiO_4	Cubic, Fd-3m (227)	Nickel Aluminum Oxide	Al_2NiO_4	Cubic, Fd-3m (227)
				$NiAl_{10}O_{16}$	Monoclinic, P21/b (14)			
				$NiAl_{32}O_{49}$	Monoclinic, 0			
			Nickel dialuminate	Ni (Al_2O_4)	Cubic, Fd-3m (227)	Nickel dialuminate	Ni (Al_2O_4)	Cubic, Fd-3m (227)
			Nickel Aluminum Iron Oxide	($Fe_{0.35}$ $Ni_{0.12}$ $Al_{0.53}$) ($Ni_{0.88}$ $Fe_{0.15}$ $Al_{0.97}$) O_4	Cubic, Fd-3m (227)	Nickel Aluminum Iron Oxide	($Fe_{0.35}$ $Ni_{0.12}$ $Al_{0.53}$) ($Ni_{0.88}$ $Fe_{0.15}$ $Al_{0.97}$) O_4	Cubic, Fd-3m (227)
				Ni $Fe_{1.5}$ $Al_{0.5}$ O_4			Ni $Fe_{1.5}Al_{0.5}$ O_4	
				Ni $Fe_{1.75}$ $Al_{0.25}$ O_4				
			Maghemite-Q, syn	Not present	-	Maghemite-Q, syn	Fe_2O_3	Tetragonal, P (0)
			Magnetite	Not present	-	Magnetite	Fe_3O_4	Cubic, Fd-3m (227)
			Nickel, syn	Ni	Cubic,	Nickel, syn	Ni	Cubic, Fm-3m

			Fm-3m (225)				(225)	
			Nickel		Cubic, Im-3m (229)	Nickel		Cubic, Im-3m (229)
			Bunsenite	NiO	Cubic, Fm-3m (225)	Bunsenite	NiO	Trigonal, R-3m (166)
								Cubic, Fm-3m (225)
			Nickel oxide	Ni_2O_3	Hexagonal, P (0)	Nickel oxide	Not present	-
			Spinel (Cu, Ni)	Not present	-	Spinel (Cu, Ni)	$Cu_{0.25}Ni_{0.75}Al_2O_4$	Cubic, Fd-3m (227)

Alumina support			**10% NiO/Al_2O_3 composite catalyst**			**20% NiO/Al_2O_3 composite catalyst**		
2-Theta angle	(h,k,l) parameters	d-value	2-Theta angle	(h,k,l) parameters	d-value	2-Theta angle	(h,k,l) parameters	d-value
	Al_2O_3			Al_2O_3			Al_2O_3	
29.26	-	3.050	19.45	(1,1,1)	4.560	19.45	(1,1,1)	4.560
31.36	-	2.850	31.94	(2,2,0)	2.800	31.94	(2,2,0)	2.800
31.94	-	2.800	37.60	(3,1,1)	2.390	37.60	(3,1,1)	2.390
32.90	-	2.720	45.86	(4,0,0)	1.977	45.86	(4,0,0)	1.977
34.88	-	2.580	60.90	(5,1,1)	1.520	60.90	(5,1,1)	1.520
36.65	-	2.450	67.03	(4,4,0)	1.395	67.03	(4,4,0)	1.395
38.96	-	2.310	-	-	-	-	-	-
42.61	-	2.120	-	-	-	-	-	-
42.83	-	2.020	-	-	-	-	-	-
48.62	-	1.871	-	-	-	-	-	-
60.03	-	1.540	-	-	-	-	-	-
67.64	-	1.384	-	-	-	-	-	-
	-			-			$Al_{2.66}O_4$	
						19.43	(1,1,1)	4.565
						31.99	(2,2,0)	2.795
						37.71	(3,1,1)	2.384
						45.88	(4,0,0)	1.977
						66.89	(4,4,0)	1.398
				Al_2NiO_4			Al_2NiO_4	
			19.29	(1,1,1)	4.597	19.29	(1,1,1)	4.597
			31.76	(2,2,0)	2.815	31.76	(2,2,0)	2.815

	37.43	(3,1,1)	2.401	37.43	(3,1,1)	2.401
	45.53	(4,0,0)	1.991	45.53	(4,0,0)	1.991
	60.35	(5,1,1)	1.532	60.35	(5,1,1)	1.532
	66.36	(4,4,0)	1.408	66.36	(4,4,0)	1.408
		$NiAl_{10}O_{16}$				
	19.49	(1,2,1)	4.551			
	32.26	(-2,1,2)	2.773			
	37.59	(-1,6,1)	2.391			
	45.53	(4,0,0)	1.990			
	60.52	(5,2,1)	1.529			
	66.33	(4,0,4)	1.408			
		$NiAl_{32}O_{49}$			-	
	37.41	(1,2,2)	2.402			
	37.72	(0,0,5)	2.383			
	45.43	(3,2,1)	1.995			
	46.36	(-2,0,6)	1.957			
	$(Fe_{0.35}\ Ni_{0.12}\ Al_{0.53})\ (Ni_{0.88}\ Fe_{0.15}\ Al_{0.97})\ O_4$			$(Fe_{0.35}\ Ni_{0.12}\ Al_{0.53})\ (Ni_{0.88}\ Fe_{0.15}\ Al_{0.97})\ O_4$		
	18.92	(1,1,1)	4.686	18.92	(1,1,1)	4.686
	36.70	(3,1,1)	2.447	36.70	(3,1,1)	2.447
	64.95	(4,4,0)	1.435	64.95	(4,4,0)	1.435
		$Ni\ Fe_{1.5}Al_{0.5}\ O_4$			$Ni\ Fe_{1.5}Al_{0.5}\ O_4$	
	18.49	(1,1,1)	4.795	18.49	(1,1,1)	4.795
	35.83	(3,1,1)	2.504	35.83	(3,1,1)	2.504
	63.29	(4,4,0)	1.468	63.29	(4,4,0)	1.468
		$Ni\ Fe_{1.75}\ Al_{0.25}\ O_4$			-	
	35.68	(3,1,1)	2.514			
	63.00	(4,4,0)	1.474			
		-			Fe_2O_3	
				30.34	(2,0,6)	2.944
				35.74	(1,1,9)	2.510
				43.43	(0,0,12)	2.082
				50.14	(2,1,12)	1.818
		-			Fe_3O_4	
				18.87	-	4.700
				30.17	(2,2,0)	2.960
				35.45	(3,1,1)	2.530
				43.25	(4,0,0)	2.090
				62.26	-	1.490
		Ni (syn)			Ni (syn)	

	43.94	(1,1,1)	2.059	43.94	(1,1,1)	2.059
	51.19	(2,0,0)	1.783	51.19	(2,0,0)	1.783
		Ni			-	
	45.62	(1,1,0)	1.987			
		NiO			NiO	
	37.44	(1,1,1)	2.400	37.44	(1,1,1)	2.400
	43.47	(2,0,0)	2.080	43.47	(2,0,0)	2.080
	63.20	(2,2,0)	1.470	63.20	(2,2,0)	1.470
		Ni_2O_3			-	
	31.94	(0,0,2)	2.800			
	39.13	(1,0,2)	2.300			
	44.83	-	2.020			
	51.60	(1,1,1)	1.770			
	57.68	(2,0,2)	1.620			
		-			$Cu_{0.25}\ Ni_{0.75}\ Al_2\ O_4$	
				36.99	(3,1,1)	2.428
				65.52	(4,4,0)	1.424

Table S2. Determination of crystallinity % from the peak area of amorphous and crystalline phases with area %, FWHM, and height of the peaks at 2- Theta diffraction angle for alumina support, 10% and 20% NiO/Al_2O_3 composite catalyst

Material	2-Theta angle	Area	Area %	FWHM	Height	Crystallinity %
Alumina support		1696.251	0.65009	0.55626	3232.829	
	28	3492.425	1.33847	0.54905	3896.434	
	37	42479.67	16.28031	1.65194	15139.41	
	38.9	5658.164	2.16849	0.38	15008.79	
	39	11183.22	4.28596	0.83847	14170.14	
	41	5339.041	2.04618	0.66	9182.863	
	41.7	6850.194	2.62533	41.84468	10695.47	93.66%
	43	15098.09	5.78634	1.12791	12065.42	
	43.6	12446.12	4.76997	45.17485	22096.17	
	45	22243.71	8.52489	0.99349	22096.17	
	47	11170.87	4.28123	1.80175	7383.173	
	65	77778.79	29.80868	1.02628	45666.51	
	70	35736.4	13.69596	0.57102	44346.34	
10% NiO/Al_2O_3 composite catalyst	15.11	140.815	1.42026	1.81821	61.61084	
	19.7	148.4866	1.49764	1.32759	95.53524	
	27.8	1189.414	11.99643	0.92214	1133.081	
	32.3	1043.934	10.52912	0.86284	1129.385	
	33.72	224.6533	2.26585	0.73516	258.448	96.29%
	37.24	1046.01	10.55006	0.68865	1415.807	
	42.93	772.5946	7.79239	0.45347	1282.308	
	45.54	61.74615	0.62277	1.92354	29.32412	
	55.76	397.1725	4.00588	1.60352	228.9822	
	60.32	2339.354	23.59473	65.81091	2312.841	
	66.76	2498.987	25.20479	0.95132	2331.436	
20% NiO/Al_2O_3 composite catalyst	12.9	80.15306	0.71462	1.97455	40.43815	
	19.5	92.63348	0.82589	1.67665	46.30418	
	31.9	182.2489	1.62487	1.96025	65.3659	
	37.2	1678.606	14.96593	36.24697	1618.96	
	43.39	1771.328	15.79261	0.98655	1635.699	93.35%
	45.38	675.799	6.02521	0.30836	1141.8	
	48.1	348.5614	3.10767	0.31074	1028.603	
	60.14	1082.568	9.65184	0.54618	1458.818	
	62.78	1215.211	10.83444	0.70186	1458.122	

66.66	1859.384	16.57769	65.50525	1668.368
75.48	1607.927	14.33578	0.90567	1685.857

Table S3. Determination of crystallite size (nm) from FWHM, width, distance (angstrom) and height of the peaks (counts) at 2- Theta diffraction angle for alumina support, 10% and 20% NiO/Al_2O_3 composite catalyst

Material	2-theta (deg)	d (ang.)	Height (counts)	FWHM (deg)	Int. W (deg)	Size (ang.)	Average crystallite size (nm)
Alumina support	28.2746	3.15377	4107.32	0.2815	0.3318	303.93	11.52
	32.6314	2.74196	2865.1	3.6897	4.2925	23.43	
	37.9091	2.37147	9935.98	2.7772	3.2203	31.59	
	39.4536	2.28212	4756.48	0.6103	0.6497	144.44	
	42.7083	2.11543	7147.07	1.5251	1.636	58.42	
	45.5831	1.98848	8837.3	0.6054	0.6494	148.66	
	46.1788	1.96421	7094.72	1.9858	2.1302	45.42	
	48.8527	1.86276	4030.1	1.2875	1.3811	70.78	
	60.9707	1.51837	2479.55	3.1661	5.4993	30.41	
	64.7165	1.43924	3704.67	2.8432	3.7768	34.55	
	67.2402	1.39122	29397.82	1.4983	1.9591	66.5	
10 % NiO/Al_2O_3 composite material	12.9428	6.83451	9.12	4.6025	5.0184	18.14	16.107
	19.6862	4.50596	40.76	1.8018	2.2766	46.74	
	31.5266	2.83548	11.19	0.5906	0.6301	145.99	
	32.2729	2.77159	58.8	1.0795	1.1516	80.02	
	37.2025	2.41487	758.11	1.7989	2.0094	48.67	
	42.7757	2.11226	174.47	0.7157	0.9267	124.5	
	45.4825	1.99265	948.22	1.0972	1.2357	82	
	47.2664	1.92151	14.39	2.632	2.9644	34.41	
	55.6673	1.64979	18.13	1.7741	1.8932	52.89	
	60.2428	1.53496	153.55	1.5892	1.7475	60.36	
	64.6439	1.44068	147.09	1.0137	1.0792	96.86	
	66.7025	1.40112	1567.46	1.7778	1.8927	55.87	
	68.6114	1.36672	86.96	0.8412	0.8956	119.41	
	69.5292	1.35091	39.3	0.6568	0.6993	153.78	
20 % NiO/Al_2O_3 composite material	12.2724	7.20626	18.22	1.1186	1.1936	74.6	16.10
	13.3094	6.64706	24.72	1.0917	1.1649	76.52	
	19.3943	4.57311	29.68	1.622	1.796	51.9	
	31.5981	2.82922	17.94	1.0617	1.1316	81.22	
	32.1509	2.78183	15.43	1.062	1.1319	81.31	
	37.1746	2.41662	1087.08	1.8174	2.1845	48.17	
	43.2164	2.09173	699.56	0.5294	0.8282	168.58	

	45.3132	1.99969	973.68	1.2305	1.9251	73.07
	48.0195	1.89312	49.89	0.5851	0.9154	155.24
	55.6352	1.65067	5.8	0.9567	1.0209	98.06
	60.0109	1.54034	57.5	1.068	1.1397	89.71
	62.8499	1.47741	218.19	0.2944	0.3138	330.26
	66.6287	1.4025	1130.96	1.9207	2.0468	51.69
	75.3498	1.26034	127.42	0.4965	0.5609	211.14

Table S4. Peak area % of the main compounds in bio-oil from thermal pyrolysis of sawdust

Retention time (min)	Component	Chemical formulae	Carbon number (C_n)	Mol. Weight (M.W.)	Peak area%		
					773 K	823 K	873 K
8.028	Pyridine	C_5H_5N	C_5	79	0.471	0.528	3.355
	Pyridine carboxylic acid	$C_5H_4N(CO_2H)$	C_5	123			
8.058	6-Hepten-3-one, 5-Hydroxy-4-Methyl-	$C_8H_{14}O_2$	C_8	142	0.268	2.482	3.538
	Carbamic acid, Hydroxy-ethyl ester	$C_3H_7NO_3$	C_3	105			
8.584	Carbamic acid, Hydroxy-ethyl ester	$C_3H_7NO_3$	C_3	105	1.745	4.175	4.018
9.42	3-(4,8,12)-Trimethyl Tridecyl (Furan)	$C_{20}H_{36}O$	C_{20}	292	1.642	4.017	1.921
	Bicyclo (5, 3, 0) Decane (Cis)	$C_{10}H_{18}$	C_{10}	138			
9.864	3-Trans-(1, 1- Di-Methyl-Ethyl)-4, Cis-Methoxycyclohexan-1-ol	$C_{13}H_{26}O_2$	C_{13}	186	0.548	0.988	0.229
10.17	Furan, Tetrahydro-2, 5-dimethoxy-	$C_6H_{12}O_3$	C_6	132	0.978	0.710	0.316
	1, 1 -Dimethyl-1-Sinacyclobutane	$C_6H_{10}N_2O_4Pt$	C_6	100			
11.175	2-MethylThiolane, S, S-Dioxide	$C_5H_{10}O_2S$	C_5	134	-	0.522	0.820
	Diethyl-cyanamide	$C_5H_{10}N_2$	C_5	98			
11.700	Norvaline-3-Hydroxy	$C_5H_{11}NO_3$	C_5	133	0.721	0.775	0.379
11.885	1-Silacyclo-hexa-2, 5-diene	$C_8H_8O_3$	C_8	96	0.728	0.770	0.389
	Cyclopentanone, 2-(1-MethylPropyl)-	$C_9H_{16}O$	C_9	140			
12.21	Phosphonic acid, (p-hydroxyphenyl)-	$C_6H_7O_4P$	C_6	174	5.080	2.935	3.075
	Phenol	C_6H_5OH	C_6	94			
12.530	1- Methyl Cyclopropane methanol	$C_5H_{10}O$	C_5	86	0.817	0.522	-
12.99	2-Ethyl-5-Propylcyclopentanone	$C_{10}H_{18}O$	C_{10}	154	-	3.358	2.249

	2-EthylThiolane, S, S-Dioxide	$C_6H_{12}O_2S$	C_6	148			
13.06	2-Ethyl-5-Propylcyclopentanone	$C_{10}H_{18}O$	C_{10}	154	4.529	0.288	0.285
	Cyclopentanone, 2-(1-Methylpropyl)-	$C_9H_{16}O$	C_9	140			
13.511	Phenol-2-Methyl	C_7H_8O	C_7	108	2.051	2.256	1.432
13.94	Phenol-2-Methyl	C_7H_8O	C_7	108	2.836	1.803	1.439
14.506	Phenol-2-Methyl	C_7H_8O	C_7	108	0.120	1.994	2.062
16.312	Creosol	$C_8H_{10}O_2$	C_8	138	0.927	1.776	1.287
16.53	3-Methyl-2-(2-Oxopropyl) furan	$C_8H_{10}O_2$	C_8	138	7.166	0.453	0.319
16.902	Catechol	$C_6H_6O_2$	C_6	110	1.923	0.990	1.490
	Resorcinol	$C_6H_6O_2$	C_6	110			
19.53	Phenol-2,6 Dimethoxy-	$C_8H_{10}O_3$	C_8	154	2.220	0.190	1.364
21.364	3, 5- Dimethoxy-4-Hydroxytoluene	$C_9H_{12}O_3$	C_9	168	0.752	0.418	0.598
22.55	D-Allose	$C_6H_{12}O_6$	C_6	180	0.403	9.547	13.981
	Beta-D-Glucopyranose-1,6-Anhydro	$C_6H_{10}O_5$	C_6	162			
22.83	D-Allose	$C_6H_{12}O_6$	C_6	180	15.999	0.667	0.768
	Beta-D-Glucopyranose-1,6-Anhydro	$C_6H_{10}O_5$	C_6	162			
23.355	Sedoheptulosan	$C_7H_{14}O_7$	C_7	192	0.974	-	0.931

Table S5. Peak area % of the main compounds in bio-oil from catalytic pyrolysis of sawdust with 10% and 20% NiO and Ni (II) aluminate catalyst at 873 K temperature

Retention time (min)	Component	Mol. Weight (M.W.)	Chemical formulae	Carbon number (C_n)	Peak area %	
					Bio-oil with 10% NiO and Ni (II) aluminate composite catalyst	Bio-oil with 20% NiO and Ni (II) aluminate composite catalyst
8.028	Pyridine	79	C_5H_5N	C_5	3.304	6.165
	Pyridine carboxylic acid	123	$C_5H_4N(CO_2H)$	C_5		
8.143	1- Phenyl-5-Methylheptane	190	$C_{14}H_{22}$	C_{14}	1.754	-
8.24	6-Hepten-3-one, 5-Hydroxy-4-Methyl-	142	$C_8H_{14}O_2$	C_8	-	-
	Carbamic acid, Hydroxy-ethyl ester	105	$C_3H_7NO_3$	C_3		
8.294	Trifluoromethyl T-Butyl Disulphide	190	$C_5H_9F_3S$	C_5	3.719	-
8.539	Silacyclopentane	86	$CH_{10}Si_5$	-	2.222	-
8.539	1-Pentene-3-ol, 4-Methyl	100	$C_6H_{12}O$	C_6	-	3.885
8.584	Carbamic acid, Hydroxy-ethyl ester	105	$C_3H_7NO_3$	C_3	-	2.477
9.42	3-(4,8,12)-Trimethyl Tridecyl (Furan)	292	$C_{20}H_{36}O$	C_{20}	-	-
	Bicyclo (5, 3, 0) Decane (Cis)	138	$C_{10}H_{18}$	C_{10}		
9.864	3-Trans-(1, 1- Di-Methyl-Ethyl)-4, Cis-Methoxycyclohexan-1-ol	186	$C_{13}H_{26}O_2$	C_{13}	1.239	1.191
10.17	Furan, Tetrahydro-2, 5-dimethoxy-	132	$C_6H_{12}O_3$	C_6	0.744	0.445
	1, 1 -Dimethyl-1-Silacyclobutane	100	$C_6H_{10}N_2O_4Pt$	C_6		
10.484	Furan, Tetrahydro-2,5-dimethoxy	132	$C_6H_{12}O_3$	C_6	0.822	0.391
10.765	1-Silacyclo hexa-2, 5-	96	$C_8H_8O_3$	C_8	0.667	1.265

	diene					
10.885	2 (5H)-Furanone	84	$C_4H_4O_2$	C_4	0.436	2.031
10.94	2 (5H)-Furanone	84	$C_4H_4O_2$	C_4	1.845	-
	Cyclopentanone, 2-(1-MethylPropyl)-	140	$C_9H_{16}O$	C_9		
11.175	2-MethylThiolane, S, S-Dioxide	134	$C_5H_{10}O_2S$	C_5	2.121	0.945
	Diethyl-cyanamide	98	$C_5H_{10}N_2$	C_5		
11.700	Norvaline-3-Hydroxy	133	$C_5H_{11}NO_3$	C_5	0.689	0.440
11.885	1-Silacyclo-hexa-2, 5-diene	96	$C_8H_8O_3$	C_8	0.725	0.720
12.15	Phosphonic acid, (p-hydroxyphenyl)-	174	$C_6H_7O_4P$	C_6	4.894	3.298
12.530	1- Methyl Cyclopropane methanol	86	$C_5H_{10}O$	C_5	0.802	-
12.99	2-Ethyl-5-Propylcyclopentanone	154	$C_{10}H_{18}O$	C_{10}	3.948	3.716
	2-EthylThiolane, S, S-Dioxide	148	$C_6H_{12}O_2S$	C_6		
13.06	2-Ethyl-5-Propylcyclopentanone	154	$C_{10}H_{18}O$	C_{10}	0.270	0.139
	Cyclohexanone-4-Methyl-	112	$C_9H_{16}O$	C_9		
13.511	Phenol-2-Methyl	108	C_7H_8O	C_7	2.603	2.353
13.94	Phenol-2-Methyl	108	C_7H_8O	C_7	3.087	1.917
16.312	Creosol	138	$C_8H_{10}O_2$	C_8	1.421	1.335
16.53	3- Methyl-2-(2-Oxopropyl) Furan	138	$C_8H_{10}O_2$	C_8	-	0.399
16.902	Catechol	110	$C_6H_6O_2$	C_6	1.173	1.487
	Resorcinol	110	$C_6H_6O_2$	C_6		
19.53	Phenol-2,6 Dimethoxy-	154	$C_8H_{10}O_3$	C_8	1.753	1.301
21.364	3, 5- Dimethoxy-4-Hydroxytoluene	168	$C_9H_{12}O_3$	C_9	0.955	0.665
22.554	D-Allose	180	$C_6H_{12}O_6$	C_6	5.005	5.461
	Beta-D-Glucopyranose-1,6-Anhydro	162	$C_6H_{10}O_5$	C_6		

22.83	D-Allose	180	$C_6H_{12}O_6$	C_6	0.591	0.623
	Beta-D-Glucopyranose-1,6-Anhydro	162	$C_6H_{10}O_5$	C_6		
23.355	Sedoheptulosan	192	$C_7H_{14}O_7$	C_7	0.718	0.960

Table S6. Peak area % of the main compounds in liquid oil product from thermal co-pyrolysis of coal and 100% sawdust blend

Retention time (min)	Component	Chemical formulae	Carbon number (C_n)	Mol. Weight (M.W.)	Peak area%		
					773 K	823 K	873 K
8.05	6-Hepten-3-one, 5-Hydroxy-4-Methyl-	$C_8H_{14}O_2$	C_8	142	0.818	1.514	4.083
8.25	6-Hepten-3-one, 5-Hydroxy-4-Methyl-	$C_8H_{14}O_2$	C_8	142	-	4.023	-
8.47	Carbamic acid, Hydroxy-ethyl ester	$C_3H_7NO_3$	C_3	105	1.106	3.030	-
8.59	Sila cyclopentane	$Cl_{10}Si_5$	-	86	-	2.582	5.519
8.62	1-Methyl cyclopropane methanol	$C_5H_{10}O$	C_5	86	2.131	-	-
9.33	3, 3'- Thiodipropanol	$C_6H_{14}O_2S$	C_6	150	1.819	3.731	0.383
9.40	3- (4, 8, 12 – Trimethyltridecyl) Furan	$C_3H_7NO_3$	C_3	292	-	-	3.120
9.82	3- Trans-(1,1-Dimethylethyl)-4, Cis, Methoxycyclohexane-1-ol	$C_{13}H_{26}O_2$	C_{13}	186	0.443	1.544	1.075
10.15	Furan, Tetrahydro-2, 5-dimethoxy-	$C_6H_{12}O_3$	C_6	132	1.198	-	0.393
	1, 1 -Dimethyl-1-Sinacyclobutane	$C_6H_{10}N_2O_4Pt$	C_6	100			
10.74	1-Silacyclohexa-2, 5- diene	$C_8H_8O_3$	C_8	96	0.233	1.083	0.553
10.88	2 (5H) - Furanone	$C_4H_4O_2$	C_4	84	0.207	2.217	1.674
11.86	1-Silacyclohexa-2, 5- diene	$C_8H_8O_3$	C_8	96	-	0.897	0.738
12.15	Phosphonic acid (p-hydroxyphenyl)	$C_6H_7O_4P$	C_6	174	2.284	8.023	4.805
12.99	2-Ethyl-5-Propylcyclopentanone	$C_{10}H_{18}O$	C_{10}	154	-	-	3.544
13.01	2-Ethyl-5-Propylcyclopentanone	$C_{10}H_{18}O$	C_{10}	154	3.047	5.374	0.142
	Cyclopentanone, 2-(1-Methylpropyl)-	$C_9H_{16}O$	C_9	140			
13.51	Phosphonic acid (p-hydroxyphenyl)	$C_6H_7O_4P$	C_6	174	2.209	3.721	2.686

13.94	Phenol-2-Methyl	C_7H_8O	C_7	108	1.508	4.936	2.824
14.19	Phenol, 2 – methoxy-	$C_7H_8O_2$	C_7	124	1.091	2.070	1.391
14.42	Octadecane, 2,2,4,15,17,17-Hexamethyl-7, 12- Bis (3, 5,5 -Trimethylhexyl)-			590	-	1.244	2.132
16.30	Creosol	$C_8H_{10}O_2$	C_8	138	0.723	1.437	1.359
16.47	Catechol	$C_6H_6O_2$	C_6	110	1.262	3.252	-
16.92	1,4:3,6-Dianhydro-Alpha-D-Glucopyranose	$C_6H_8O_4$	C_6	144	2.293	1.099	1.391
17.84	Hexacosyl acetate			424	0.847	0.838	0.744
18.45	1,2-Benzenediol, 4-Methyl-	$C_{11}H_{12}O_4$	C_{11}	124	0.280	0.887	-
18.53	1,2-Benzenediol, 4-Methyl-	$C_{11}H_{12}O_4$	C_{11}	124	0.463	1.110	0.369
19.50	Phenol-2,6 Dimethoxy-	$C_8H_{10}O_3$	C_8	154	1.193	1.758	1.326
22.58	D-Allose	$C_6H_{12}O_6$	C_6	180	30.21	7.049	13.644

Table S7. Total peak area % of the main compounds in pyrolytic liquid oil product from thermal co-pyrolysis of coal-sawdust blends each pyrolyzed at 873 K reaction temperature

Retention time (min)	Component	Chemical formulae	Carbon number (C_n)	Mol. Weight (M.W.)	Peak area%	
					50%	200%
8.05	6-Hepten-3-one, 5-Hydroxy-4-Methyl-	$C_8H_{14}O_2$	C_8	142	1.081	4.071
8.12	1-Phenyl-5-Methylheptane	$C_{14}H_{22}$	C_{14}	190	3.345	-
	(3-Bromo-1-Methylpropoxymethyl) Benzene	$C_{11}H_{15}BrO$	C_{11}	242		
8.31	Propanoic acid, 1-Methylpropyl ester	$C_7H_{14}O_2$	C_7	130	1.986	2.878
8.59	Silacyclopentane	$Cl_{10}Si_5$	-	86	3.542	2.428
8.62	1-Methyl cyclopropane methanol	$C_5H_{10}O$	C_5	86	-	1.919
9.33	3, 3'- Thiodipropanol	$C_6H_{14}O_2S$	C_6	150	0.476	0.652
9.40	3- (4, 8, 12 – Trimethyltridecyl) Furan	$C_3H_7NO_3$	C_3	292	2.724	3.594
9.82	3- Trans-(1,1-Dimethylethyl)-4, Cis, Methoxycyclohexane-1-ol	$C_{13}H_{26}O_2$	C_{13}	186	1.013	1.194
10.15	Furan, Tetrahydro-2, 5-dimethoxy-	$C_6H_{12}O_3$	C_6	132	0.713	0.999
	1, 1 -Dimethyl-1-Sinacyclobutane	$C_6H_{10}N_2O_4Pt$	C_6	100		
10.74	1-Silacyclohexa-2, 5- diene	$C_8H_8O_3$	C_8	96	0.418	1.206
10.88	2 (5H) - Furanone	$C_4H_4O_2$	C_4	84	0.235	1.921
11.86	1-Silacyclohexa-2, 5- diene	$C_8H_8O_3$	C_8	96	0.577	0.683
12.15	Phosphonic acid (p-hydroxyphenyl)	$C_6H_7O_4P$	C_6	174	4.297	4.973
12.99	2-Ethyl-5-Propylcyclopentanone	$C_{10}H_{18}O$	C_{10}	154	2.873	4.076
13.01	2-Ethyl-5-Propylcyclopentanone	$C_{10}H_{18}O$	C_{10}	154	0.374	0.417
	Cyclopentanone, 2-(1-Methylpropyl)-	$C_9H_{16}O$	C_9	140		
13.51	Phosphonic acid (p-	$C_6H_7O_4P$	C_6	174	1.806	1.999

	hydroxyphenyl)					
13.94	Phenol-2-Methyl	C_7H_8O	C_7	108	2.279	3.187
14.19	Phenol, 2 – methoxy-	$C_7H_8O_2$	C_7	124	1.390	1.841
14.42	Octadecane, 2,2,4,15,17,17-Hexamethyl-7, 12- Bis (3, 5,5 -Trimethylhexyl)-	-	-	590	1.781	1.962
16.30	Creosol	$C_8H_{10}O_2$	C_8	138	1.413	1.659
16.47	Catechol	$C_6H_6O_2$	C_6	110	-	0.120
	Resorcinol	$C_6H_6O_2$	C_6	110		
16.53	3-Methyl-2-(2-Oxopropyl) furan	$C_8H_{10}O_2$	C_8	138	0.718	0.656
16.92	Catechol	$C_6H_6O_2$	C_6	110	1.144	1.173
	Resorcinol	$C_6H_6O_2$	C_6	110		
17.84	Hexacosyl acetate	$C_{28}H_{56}O_2$	C_{28}	424	0.664	0.475
18.53	1,2-Benzenediol, 4-Methyl-	$C_{11}H_{12}O_4$	C_{11}	124	0.218	0.185
19.50	Phenol-2,6 Dimethoxy-	$C_8H_{10}O_3$	C_8	154	1.340	1.916
22.58	D-Allose	$C_6H_{12}O_6$	C_6	180	17.81	5.996

Table S8. Peak area % of the main compounds in pyrolytic liquid oil product from catalytic co-pyrolysis of coal and 100% sawdust blend in presence of 10% and 20% NiO/Al_2O_3 catalyst

Retention time (min)	Component	Chemical formulae	Carbon number (C_n)	Mol. Weight (M.W.)	Liquid oil from catalytic co-pyrolysis of 100% blend with 10 % NiO/Al_2O_3 catalyst	Liquid oil from catalytic co-pyrolysis of 100% blend with 20 % NiO/Al_2O_3 catalyst
8.05	6-Hepten-3-one, 5-Hydroxy-4-Methyl-	$C_8H_{14}O_2$	C_8	142	3.038	2.454
8.59	Sila cyclopentane	$Cl_{10}Si_5$	-	86	3.503	0.713
9.33	3, 3'-Thiodipropanol	$C_6H_{14}O_2S$	C_6	150	0.468	0.956
9.40	3- (4, 8, 12 – Trimethyltridecyl) Furan	$C_3H_7NO_3$	C_3	292	3.686	-
9.82	3- Trans-(1,1-Dimethylethyl)-4, Cis, Methoxycyclohexane-1-ol	$C_{13}H_{26}O_2$	C_{13}	186	0.900	-
10.15	Furan, Tetrahydro-2, 5-dimethoxy-	$C_6H_{12}O_3$	C_6	132	0.974	-
	1, 1 -Dimethyl-1-Sinacyclobutane	$C_6H_{10}N_2O_4Pt$	C_6	100		
10.74	1-Silacyclohexa-2, 5- diene	$C_8H_8O_3$	C_8	96	0.622	0.734
10.88	2 (5H) - Furanone	$C_4H_4O_2$	C_4	84	1.967	0.531
11.86	1-Silacyclohexa-2, 5- diene	$C_8H_8O_3$	C_8	96	0.605	0.283
12.15	Phosphonic acid (p-hydroxyphenyl)	$C_6H_7O_4P$	C_6	174	4.292	2.549
13.01	2-Ethyl-5-Propylcyclopentanone	$C_{10}H_{18}O$	C_{10}	154	4.510	-
	Cyclopentanone, 2-	$C_9H_{16}O$	C_9	140		-

	(1-Methylpropyl)-					
13.51	Phosphonic acid (p-hydroxyphenyl)	$C_6H_7O_4P$	C_6	174	2.050	0.679
13.94	Phenol-2-Methyl	C_7H_8O	C_7	108	2.710	0.916
14.19	Phenol, 2 – methoxy-	$C_7H_8O_2$	C_7	124	1.747	0.700
14.42	Octadecane, 2,2,4,15,17,17-Hexamethyl-7, 12-Bis (3, 5,5 - Trimethylhexyl)-	-	-	590	3.109	0.358
16.30	Creosol	$C_8H_{10}O_2$	C_8	138	1.701	0.838
16.47	Catechol	$C_6H_6O_2$	C_6	110	0.612	-
16.92	1,4:3,6-Dianhydro-Alpha-D-Glucopyranose	$C_6H_8O_4$	C_6	144	0.428	0.423
17.84	Hexacosyl acetate	-	-	424	0.910	-
18.53	1,2-Benzenediol, 4-Methyl-	$C_{11}H_{12}O_4$	C_{11}	124	0.364	-
19.50	Phenol-2,6 Dimethoxy-	$C_8H_{10}O_3$	C_8	154	2.594	0.445
22.58	D-Allose	$C_6H_{12}O_6$	C_6	180	9.375	0.246

Table S9. Peak area % of the main compounds in pyrolytic liquid oil product from catalytic co-pyrolysis of coal and 200% sawdust blend in the presence of 20% NiO/Al_2O_3 catalyst

Retention time (min)	Component	Chemical formulae	Carbon number (C_n)	Mol. Weight (M.W.)	Peak area %
					Liquid oil from catalytic co-pyrolysis of 200% blend with 20% NiO/Al_2O_3 catalyst
8.05	6-Hepten-3-one, 5-Hydroxy-4-Methyl-	$C_8H_{14}O_2$	C_8	142	2.170
8.12	1-Phenyl-5-Methylheptane	$C_{14}H_{22}$	C_{14}	190	0.692
	(3-Bromo-1-Methylpropoxymethyl) Benzene	$C_{11}H_{15}BrO$	C_{11}	242	
8.25	6-Hepten-3-one, 5-Hydroxy-4-Methyl-	$C_8H_{14}O_2$	C_8	142	4.809
8.47	Carbamic acid, Hydroxy-ethyl ester	$C_3H_7NO_3$	C_3	105	3.740
8.62	1-Methyl cyclopropane methanol	$C_5H_{10}O$	C_5	86	0.263
9.33	3, 3'- Thiodipropanol	$C_6H_{14}O_2S$	C_6	150	0.709
9.40	3- (4, 8, 12 – Trimethyltridecyl) Furan	$C_3H_7NO_3$	C_3	292	2.757
9.82	3- Trans-(1,1-Dimethylethyl)-4, Cis, Methoxycyclohexane-1-ol	$C_{13}H_{26}O_2$	C_{13}	186	1.529
10.15	Furan, Tetrahydro-2, 5-dimethoxy-	$C_6H_{12}O_3$	C_6	132	0.410
	1, 1 -Dimethyl-1-Sinacyclobutane	$C_6H_{10}N_2O_4Pt$	C_6	100	
10.74	1-Silacyclohexa-2, 5- diene	$C_8H_8O_3$	C_8	96	0.795
10.88	2 (5H) - Furanone	$C_4H_4O_2$	C_4	84	1.490
11.86	1-Silacyclohexa-2, 5- diene	$C_8H_8O_3$	C_8	96	0.592
12.15	Phosphonic acid (p-	$C_6H_7O_4P$	C_6	174	5.759

	hydroxyphenyl)				
12.99	2-Ethyl-5-Propylcyclopentanone	$C_{10}H_{18}O$	C_{10}	154	3.246
13.01	2-Ethyl-5-Propylcyclopentanone	$C_{10}H_{18}O$	C_{10}	154	0.232
	Cyclopentanone, 2-(1-Methylpropyl)-	$C_9H_{16}O$	C_9	140	
13.51	Phosphonic acid (p-hydroxyphenyl)	$C_6H_7O_4P$	C_6	174	1.990
13.94	Phenol-2-Methyl	C_7H_8O	C_7	108	3.546
14.19	Phenol, 2 – methoxy-	$C_7H_8O_2$	C_7	124	1.846
14.42	Octadecane, 2,2,4,15,17,17-Hexamethyl-7, 12- Bis (3, 5,5 -Trimethylhexyl)-	-	-	590	1.444
16.30	Creosol	$C_8H_{10}O_2$	C_8	138	1.674
16.53	3-Methyl-2-(2-Oxopropyl) furan	$C_8H_{10}O_2$	C_8	138	0.160
16.92	Catechol	$C_6H_6O_2$	C_6	110	0.953
	Resorcinol	$C_6H_6O_2$	C_6	110	
17.84	Hexacosyl acetate	$C_{28}H_{56}O_2$	C_{28}	424	0.231
18.53	1,2-Benzenediol, 4-Methyl-	$C_{11}H_{12}O_4$	C_{11}	124	0.192
19.50	Phenol-2,6 Dimethoxy-	$C_8H_{10}O_3$	C_8	154	2.038
22.58	D-Allose	$C_6H_{12}O_6$	C_6	180	0.203

Research Output

A) Manuscripts published in peer-reviewed journals

- Bhattacharyya, M., Shadangi, K.P., Purkayastha, R., Mahanta, P. and Mohanty, K., 2024. Catalytic upgradation of pyrolytic products by catalytic pyrolysis of sawdust using a synthesized composite catalyst of NiO and Ni (II) aluminates. *Renewable Energy*, *221*, p.119658. https://doi.org/10.1016/j.renene.2023.119658**.**
- Bhattacharyya, M., Shadangi, K.P., Mahanta, P. and Mohanty, K., 2023. Thermo-catalytic pyrolysis of sawdust by a synthesized NiO/Al2O3 composite catalyst: investigation on its reaction mechanism, kinetics, and thermodynamics. *Chemical Papers*, *77,* pp.4877-4903. https://doi.org/10.1007/s11696-023-02826-z.
- Bhattacharyya, M., Shadangi, K.P., Mahanta, P. and Mohanty, K., 2022. Co-pyrolysis of coal-biomass: study on reaction kinetics and thermodynamics. *Biofuels, Bioproducts and Biorefining*, *16*(3), pp.725-742. https://doi.org/10.1002/bbb.2333.

B) Book Chapter published (Original article)

Bhattacharyya, M., Mahanta, P. and Mohanty, K., 2022. Effect of Biomass Blending Ratio and Catalysts in the Kinetic Modelling of Coal and Duckweed Co-Pyrolysis. In *Advances in Thermofluids and Renewable Energy* (pp. 261-275). Springer, Singapore. https://doi.org/10.1007/978-981-16-3497-0_20.

C) Manuscripts to be communicated to peer-reviewed journals

- Bhattacharyya, M., Shadangi, K.P., Mahanta, P., Mohanty, K. Impact of Pyrolysis Reaction Temperature and Intrinsic Heating Effects on Co-pyrolysis of Coal and Sawdust Blend **(Under review)**
- Bhattacharyya, M., Shadangi, K.P., Mahanta, P., Mohanty, K. A Study on Chemical Synergy Effects on Enhanced pyrolytic syngas and liquid oil yield from co-pyrolysis of coal and biomass blends
- Bhattacharyya, M., Shadangi, K.P., Mahanta, P., Mohanty, K. A Review on Co-pyrolysis of Coal and Biomass: A Comprehensive Approach on Thermal and Catalytic Upgradation of Pyrolysis Products towards Platform Chemicals
- Bhattacharyya, M., Shadangi, K.P., Mahanta, P., Mohanty, K. Engineering the design aspects of a nano-catalyst NiO/MgO for studies in catalytic pyrolysis of sawdust and its comparative studies with industrial catalysts, Dolomite and Y-Zeolite

D) Conferences/ Symposiums

- **Impact of Pyrolysis Reaction Temperature and Intrinsic Heating Effects on Co-pyrolysis of Coal and Sawdust Blend**, International Conference on Petroleum, Hydrogen and Decarbonization (ICPHD 2023) organised by Department of Chemical Engineering, Indian Institute of Technology Guwahati from 3rd – 5th Nov 2023.
- **A comparative study on coal characteristics and its degradation kinetics for thermal pyrolysis processes,** 1st National Conference on Chemical and Bio-science (NCCBS 2023) (Hybrid mode), VSSUT, Burla from 25th – 26th March 2023.
- **Microwave pre-processing for Co-pyrolysis Kinetics of Coal-Sawdust Blends: Studies on its Kinetics, Reaction mechanism and Thermodynamics,** International Conference on Biotechnology, Sustainable Bioresources and Bioeconomy, IIT Guwahati, India from December 7 – 11, 2022.
- **Effect of Biomass Blending Ratio and Catalyst in the Kinetic Modelling of Co-pyrolysis of Coal and Duckweed Blends**, Proceedings of the International Conference on Recent Trends in Developments of Thermo-fluids and Renewable Energy, NIT Arunachal Pradesh, Yupia, India from November 26 – 28, 2020.
- **Kinetic Modelling of Raw and Torrefied Coal and Duckweed Blended Feedstocks for Co-pyrolysis by Briodo Method,** 2nd International Symposium on Analytical and Applied Pyrolysis (PYROASIA 2020) from 11th-13th Dec 2020.
- **The influence of pyrolysis temperature and heating rate on the co-pyrolysis of coal-sawdust blends: A kinetic study,** 1st International Symposium on Analytical and Applied Pyrolysis (PYROASIA 2019), IIT Madras from Dec 12-13th 2019.
- **Devolatilization and Reactivity Aspects of Coal-Duckweed Blends for Efficient Syngas Production in Co-pyrolysis process**, TEQIP 1st Online National Conference on Recent Trends in Thermal Sciences and Alternate Energy Resources, PG Thermal Engineering, Department of Mechanical Engineering, Government College of Technology Coimbatore and Department of Mechanical Engineering, National Institute of Technology, Arunachal Pradesh on July 01, 2020.
- **Thermogravimetric Analysis of Coal and Sawdust Blends for Efficient Syngas Production,** 2nd International Conference on Innovative Applied Energy (IAPE'2019) organized by St. Cross College, Oxford University, United Kingdom from 14-15th March 2019.

- **Compositional Analysis of Coal-Sawdust Blends for Co-gasification**, Indo Japan Bilateral Symposium (Future Perspectives on Bioresource Utilization in "North-East India") (IJBS 2018) jointly organized by Indian Institute of Technology Guwahati and Gifu University Japan, February 1-4, 2018.